

Doctoral thesis

Doctoral theses at NTNU, 2021:93

Andrea Broggi

Condensation of SiO and CO in silicon and ferrosilicon production

NTNU
Norwegian University of Science and Technology
Thesis for the Degree of
Philosophiae Doctor
Faculty of Natural Sciences
Department of Materials Science and Engineering



Norwegian University of
Science and Technology

Andrea Broggi

Condensation of SiO and CO in silicon and ferrosilicon production

Thesis for the Degree of Philosophiae Doctor

Trondheim, March 2021

Norwegian University of Science and Technology
Faculty of Natural Sciences
Department of Materials Science and Engineering



Norwegian University of
Science and Technology

NTNU

Norwegian University of Science and Technology

Thesis for the Degree of Philosophiae Doctor

Faculty of Natural Sciences

Department of Materials Science and Engineering

© Andrea Broggi

ISBN 978-82-326-6352-1 (printed ver.)

ISBN 978-82-326-5929-6 (electronic ver.)

ISSN 1503-8181 (printed ver.)

ISSN 2703-8084 (online ver.)

Doctoral theses at NTNU, 2021:93

Printed by NTNU Grafisk senter

«Finalmente la smetti di buttare via i soldi in aerei»

A mio nonno

Preface

The presented work is a monograph connecting articles published during my Doctoral work. All the experimental work was performed at NTNU in the period from July 2017 to January 2021.

The present study has been a part of the project 269431 – SiNoCO₂, financed by the Norwegian Research Council. The project is a cooperation between Elkem ASA NTNU, SINTEF and Norce. The project aim is to create an alternative technology for silicon production process, which can reduce costs, CO₂ emissions and energy consumption. The strategies through which this could be done are the creation of a closed process and a 100% yield furnace operation. The topic covered in this work - condensation of SiO(g) and CO(g) - is a common issue in both strategies.

Acknowledgment

I would like to express my gratitude to my supervisor Professor Merete Tangstad, Department of Material Science and Technology, NTNU, for the useful comments, remarks and engagement through the learning process of this thesis. I appreciated how she taught me to be effective and clear in every detail yet managing to explain things to the point. Her supervision was comprehensive, yet strict when needed, as it always should be to the fulfilment of the doctoral degree.

I would also like to thank my co-supervisor, Dr. Ing. Eli Ringdalen, SINTEF. Her multidisciplinary approach was of fundamental importance in the knowledge acquisition process. Her kindness, inputs and ideas have been a constant in the fulfilment of this doctoral degree, which constantly stimulated me to new challenges.

And, my supervisor from Elkem ASA Aasgeir Valderhaug. His contribution was mainly to imprint my work with an "industrial touch". Which means, first, having concrete and valuable results, ready to be discussed with people from different backgrounds. And second, to link my results to the industrial world. I am grateful for having learnt this approach. I am sure that it will turn out to be more useful also later in my life.

I would like to thank the participants in my survey, who have willingly shared their precious time with me during the process of researching. Special thanks go to Sethulakshmy Jayakumari, with whom I exchanged brilliant ideas and enlightening discussions for both our works. Our mutual help lead to amazing results, strong respect and gratitude to each other. Karin Jusnes and Marit Folstad, the best office companions, always up for a talk when I rarely stopped working. The people from Elkem ASA who have been interested in my work, especially Anne-Gry Messenlien, Odd-Arne Bariås, Edin Myrhaug and Halvard Tveit. Jan Kristen Lutro and the Elkem Bjølvfossen staff, for their kindness and availability during my visit to the plant. The collaboration with Manuel Sparta and Ulrik Thisted from Norce, for their input for useful data in my calculations. Brady Metherall and our long talks on the condensation model. Jonas Einan Gjøvik, Ivar André Ødegaard, Diego Ramos, Bartłomiej Gawel, Yingda Yi and Dmitry Slizovskiy for training me to use the laboratory equipment. Morten Peder Raanes for the EPMA and Ingeborg-Helen Svenum (SINTEF) for the XPS analysis. Ragnhild Sæterli and Per Erik Vullum for TEM and FIB.

I would like to thank my loved ones, who have kept me in harmony anytime I asked for help. The support of my grandfather Giuseppe and his attitude to work as hard as possible were fundamental. Moreover, my friend Jakob and bass player Jakob Kjerpeseth, brought away from cancer at the age of 21, fearless and rational until the end. And my friend Raafat Borhan Haska, a soul rich of feelings and beautiful thoughts, who disappeared too early from this world. I strongly believe this thesis proves what I have learnt from their stories. It has been a journey filled with Giuseppe's hard work, Jakob's rationality and Raafat's emotivity. May their souls rest in peace.

I would like to thank my parents and my brother Alberto, which encouraged me with their best wishes, as they did in those incredible years I have lived in Norway. The wonderful people I have met in both Norway and Italy, as well as the old friends from my two homelands. A special thought goes to Matteo Carlessi, Silvia Bianchi, Claudia Martinelli, Fabio Fortini, Silvia Stombelli, Nora Gigli, Henri Giudici, Davide Proserpio and Mauro Cerci. Finally, thanks to Ilaria, who gave the most real and tender support. Despite not being always physically with me, we could feed our connection through hard work and faith in each other and complete the hardest mission ever.

Thank you all for your patience and support. Now, it is time to go home.

Pensaci.
Quando a un bambino regalo una penna
E un foglio di carta
Non sai quale meraviglioso e terribile sortilegio
Hai evocato
Non sai che hai messo in moto
Una nuova misura del tempo.
Un orologio piccolo come un graffio di alfabeto
E grande come la biblioteca di tutti i sogni
(S. Benni)

*Think about it.
When you give a pen to a kid
And a piece of paper
You do not know what a marvelous and terrible sorcery
You have summoned.
You do not know you have established
A new time system.
A clock as small as a tear in the alphabet
And as large as the library of all dreams
(S. Benni)*

List of articles

The following list contains the citations of the articles assembled to compose this monograph. The articles are listed in chronological order, from the first published until the most recent.

A. Broggi and M. Tangstad, "Condensation of SiO and CO in silicon production - a literature review," presented at the Peter Hayes Symposium on Pyrometallurgical processing, Ottawa, Canada, 2018.

A. Broggi, M. Tangstad, E. Ringdalen, "Small scale experiments simulating condensation of SiO and CO in silicon production," presented at the Silicon for the Chemical and Solar Industry XIV, Svolve, Norway, 2018.

A. Broggi, M. Tangstad, E. Ringdalen, Characterization of Si-SiO₂ mixture generated from SiO and CO, Metallurgical and Materials Transactions B. 50 (2019) 2667–2680.

A. Broggi, E. Ringdalen, M. Tangstad, "Crystal defects and contact angle in SiC-SiO_x core-shell nanowires," poster presentation at the International Conference of Silicon Carbide and Related Materials, Kyoto, Japan, 2019.

A. Broggi, E. Ringdalen, M. Tangstad, "Empirical analysis of clogging of SiC charges: effect of condensation of SiO and CO", presented at the Silicon for the Chemical and Solar Industry XV, Trondheim, Norway, 2020.

A. Broggi, E. Ringdalen, M. Tangstad, Evolution of SiO_x Shell Layers on SiC-SiO_x Core-Shell Nanowires, Materials Science Forum. 1004 (2020) 479–489.

A. Broggi, M. Tangstad, E. Ringdalen, Characterization, Thermodynamics and Mechanism of Formation of SiC-SiO_x Core-shell Nanowires, Metallurgical and Materials Transactions B. 52 (2019) 339–350.

Table of contents

Preface	1
Acknowledgment	2
List of articles	4
Table of contents	5
List of figures	11
List of tables	22
List of reactions	24
Abstract	25
Sammendrag	27
Introduction	29
General background	29
Si production process	29
FeSi production process	30
Condensation in industrial furnaces.....	31
Objective for the thesis	33
Thesis outline.....	34
1. Theoretical background	35
A. Thermodynamics and kinetics	35
Si-C system	35
Phase diagram 35	
SiC polytypes 36	
The Si-O system.....	38
Thermodynamics stability of silicon monoxide	41
The scientific debate on the stability of solid SiO	41
Atomistic modelling of SiO and the concept of suboxide	43
SiO _x clustering in the gas phase.....	46
Si-C-O system	47
B. Industrial and pilot scale condensates.....	49
Stoking crust.....	50
Si-SiO ₂ mixtures 51	
SiO ₂ -SiC mixtures 53	
Crater crust.....	58
Side crust.....	60

Formation of the cavity	62
Condensates position in industrial excavations	66
Condensates in pilot-scale excavations.....	68
C. Laboratory-scale condensates	71
Si-SiO ₂ condensates.....	71
Brown condensate	71
Brown powder	74
SiC-SiO _x condensates.....	75
Blue condensate	75
White condensate	76
Other condensates.....	79
Summary	80
D. The oxide assisted growth of nanowires	82
Introduction	82
Mechanism.....	82
Final configurations.....	83
Melting point depression theory.....	84
2. Experimental method	87
A. Experimental method overview	87
B. Pellets characterization.....	89
SiO ₂ -SiC pellets	89
Si-SiO ₂ pellets	91
C. Characterization of substrates.....	92
SiC	93
Quartz A	94
Graphite tube.....	95
D. Experimental setups	96
Closed graphite tube (smaller scale)	96
Description	96
Procedure	97
Temperature gradients in condensation chamber.....	98
List of experiments.....	98
Open induction furnace (larger scale).....	100
Setup description	100
Procedure	101
List of experiments.....	102
E. Industrial samples	104
REC Solar	104
Salten	106
Wacker 1	106
Wacker 4	107
F. SEM (Scanning-Electron Microscopy) and EPMA (Electron Probe Micro-Analysis)	108
Sample preparation.....	108

	SEM and EPMA tools	108
G.	Transmission Electron Microscopy (TEM) and Focused-Ion Beam (FIB) preparation	109
	Thin layers analysis.....	109
	FIB preparation for thick condensate layers	109
H.	XPS analysis	110
	Technique description.....	110
	Procedure.....	110
I.	X-Ray Diffraction (XRD)	111
J.	ImageJ®	112
	Software description	112
	Procedure for particle size analysis on brown condensate.....	112
3.	Results	114
A.	SiC-SiO _x mixtures characterization.....	114
	Nanowire condensates.....	114
	Visual inspection and SEM analysis.....	114
	EPMA 117	
	TEM characterization	118
	XPS 122	
	XRD polytypes analysis.....	126
	Grey condensate	127
B.	Si-SiO ₂ condensate characterization.....	128
	Visual inspection and SEM analysis.....	128
	EPMA 129	
	TEM characterization	130
	XPS 133	
	XRD polytypes analysis.....	135
	Silicon spheres size distribution	136
C.	Industrial samples	141
	Summary	141
	Samples containing SiC-SiO _x condensates.....	142
	Samples containing Si-SiO ₂ condensates (and porous silica)	146
	Samples containing porous silica	147
	Samples containing grey condensate.....	148
D.	Temperature of formation.....	150
	Effect of experimental parameters	150
	Comparison between small and large-scale setup.....	150
	SiC and quartz substrates	151
	Effect of holding time (small-scale).....	152
	Effect of holding time (large-scale)	153
	Effect of partial pressure in small-scale setup (gas flow)	155
	Effect of partial pressure in large-scale setup (pellets composition)	156
	Effect of substrate particle size (large-scale).....	158
	Effect of substrate particle size (small-scale)	161
	Effect of target temperature and thermal history	163

Summary	164
Effect of parameters	164
Condensation on SiC (small-scale setup).....	165
Condensation on SiC (large-scale setup)	166
Condensation on quartz (small-scale)	166
E. Clogging.....	167
Overview of results	167
Clogging in small-scale experiments	167
Clogging in large-scale experiments.....	169
Comparison between large and small-scale setup	171
Effect of experimental parameters	171
Effect of target temperature (small-scale)	171
Effect of holding time (small-scale).....	172
Effect of holding time (large-scale)	173
Effect of substrate particle size (small-scale)	174
Effect of substrate particle size (large-scale).....	176
Effect of partial pressure in small-scale setup (gas flow)	177
Effect of partial pressure in large-scale setup (pellets composition)	178
Effect of substrate particle type (SiC vs Quartz).....	179
Summary	180
F. Mass balance.....	182
Condensate mass balance	182
Small-scale setup	182
Large-scale setup	183
Partially reacted pellets.....	185
Summary of mass balance.....	187
Distribution of SiC-SiO _x condensate in large-scale setup	189
4. Modeling	191
A. <i>p</i> _{SiO} -T calculation	191
Aim of the calculation	191
Procedure.....	191
Results	193
B. Kinetic modelling for SiO ₂ -SiC condensates (Reaction 1)	196
Aim of the model.....	196
Procedure.....	196
Reaction rate.....	198
Reaction time	198
Calculation and analysis of reaction rate for SiC-SiO ₂ condensation.....	199
Kinetic constants	202
5. Discussion	204
A. Formation and transformation of SiC-SiO _x nanowires (Reaction 1)	205
Generation and evolution of nodules	211
Back reaction to SiO(g) and CO(g)	214
B. Formation and transformation of Si-SiO ₂ condensate (Reaction 2)	215
Formation of SiC.....	221

C.	Mass balance, thermodynamics and kinetics	223
	p_{SiO} -T curves and equilibrium conditions	223
	Activation energy and statistical significance	227
	The driving force for condensation of SiC-SiO _x condensates	229
	Condensation yield, mass distribution and clogging	230
	Industrial interpretation of the results	236
	Considerations on condensation substrates	239
	SiO consumption by other reactions and SiO losses	239
D.	Production of SiO and CO	241
6.	Conclusions.....	243
	SiC-SiO _x condensate.....	243
	Si-SiO ₂ condensate	243
	Temperature of formation and clogging.....	244
	Mass balance, thermodynamics and industrial interpretation.....	245
	Reaction rate and kinetic model for SiC-SiO _x formation.....	246
7.	Further challenges	247
8.	References	248
9.	Appendix	253
A.	Condensates, SiC and Si formation on graphite	253
	SiC and Si formation in small scale setup	253
	SiC and Si formation in large-scale setup	255
	SiC whiskers in laboratory-scale experiments.....	256
	SiC whiskers in industrial samples.....	259
	Condensates formation on graphite	261
	Visual inspection: Large-scale setup	261
	Visual inspection: Small scale setup	262
	Microstructure, composition and temperature of formation	263
B.	FIB preparation	267
C.	Computation of temperature gradients	269
	Small scale	269
	Large-scale.....	271
	Vertical gradient	271
	Horizontal gradient	274
D.	Modeling calculation.....	276
	p_{SiO} -T model.....	276
	Kinetic model for Reaction 1.....	279
	Considerations on model 3b	284
E.	Reaction thermodynamics at 1.5 atm	287
F.	ImageJ® analysis on brown condensate particles.....	288
G.	Gauss propagation error law	292

Experimental errors.....	292
Error computation.....	292
Error on $k(T)$, E_a and k_0	292
Error on reaction rate <i>mcondtr</i>	294
Error on available surface for condensation (<i>A</i>).....	294
Error on partial pressure of SiO(g) (p_{SiO}).....	294
H. Spectra	295
XPS spectra.....	295
XRD spectra	295
I. Estimation of SiC in Figure 209	298
J. Condensation profiles.....	299
Small scale setup	299
Large-scale setup.....	302

List of figures

Figure 1: Overview of reactions involving SiO(g) and CO(g) in a silicon furnace. Revised after Ringdalen [13].	30
Figure 2: Stoking procedure in silicon furnaces [17].	33
Figure 3: Si-C phase diagram at atmospheric pressure. α and β stand for solid solutions [18].	35
Figure 4: Si-C phase diagram at atmospheric pressure [19].	36
Figure 5: Simple tetrahedral coordination of Si and C atoms: (a) Si ₄ C tetrahedron, C atom located at the tetrahedrons centroid and Si atoms at its vertices and (b) C ₄ Si tetrahedron, Si atom located at the tetrahedrons centroid and C atoms at its vertices. [21].	37
Figure 6: Left: Stacking sequences of tetrahedron layers of four most commonly occurring SiC polytypes at atmospheric pressure: (a) 3C-SiC; (b) 4H-SiC; (c) 6H-SiC; (d) 15R-SiC [21]. Right: unit cell of four SiC polytypes: (a) 3C, (b) 4H, (c) 6H and (d) 15R. Si atoms = red, C atoms = black [21].	38
Figure 7: Phase diagram of Si-O system, experimentally assessed at temperatures below 1710°C. [27]	39
Figure 8: Si-O phase diagram computed by Hallstedt [28].	40
Figure 9: Oxygen solubility in silicon liquid solutions. Computed data and comparison with experimental works. References on the graph are from Hallstedt [28].	40
Figure 10: Calculated Si-O phase diagram at 1 bar, at high (a) and low (b) oxygen content. [29]	41
Figure 11: The Gibbs energy of SiO(am) compared to that of a mixture of 1/2 (Si+SiO ₂ (L)) and to SiO(g) at two different pressures [29].	42
Figure 12: The five possible configurations assumed in the RM-model and their probability of existence as a function of x [41].	44
Figure 13: Schematic illustrations of obtaining initial configurations from the periodic model of amorphous Si: a) amorphous SiO ₂ ; b) RB-model of SiO _x ; c) RM-model of SiO _x [50]	45
Figure 14: ICM model (left) and atomic bond configurations of SiO _x at different interfaces (right) [47].	46
Figure 15: (SiO) _N nanoclusters ground states, and segregation into Si-area and silica-area. Element key: Red = Oxygen; Grey = Silicon [49].	47
Figure 16: Si atoms belonging to the silica-zone Si _n O _N (blue), intermediate zone (green) and Si _m group (orange). Case for the SiO cluster with N=10. Revised after Bromley et al. [49].	47
Figure 17: Invariant point computation for the SiO ₂ -C-SiC-gas system [1].	48
Figure 18: Invariant point computation for the SiO ₂ -SiC-Si-gas system [1].	49
Figure 19: Invariant point assessment and p _{SiO} (T) in the Si-C-O system [1].	49
Figure 20: Crusts overview in silicon furnaces. Revised after Tranell et al. [56].	50
Figure 21: Positions of Si-SiO ₂ (brown) and SiO ₂ -SiC (white) samples in literature. Positions estimated from [4],[7], [9], [55]–[57].	51
Figure 22: Sample 1, brown condensate pilot scale sample, magnification x300 [4].	51
Figure 23: Sample 1 from Wacker furnace 1 [55] 1,6 = epoxy; 2,7 = SiO ₂ ; 8 = Si	52
Figure 24: Macroscopic (a) and microscopic SEM pictures (b,c) of Si-SiO ₂ sample from loose charge zone [57].	52
Figure 25: Microstructure of brown SiO ₂ condensate [7].	53
Figure 26: Stoking crust containing molten quartz and condensate, extracted from a FeSi75 furnace [56].	53
Figure 27: SEM analysis of sample 1[55]. Point 1: Epoxy; Point 2:SiC+SiO ₂ .	54

Figure 28: Overview of sample 2: visual inspection (a), mixture of SiC and SiO ₂ (b), carbon material converted to SiC (c), cracks in SiO ₂ matrix (d). [55]. Point 1: epoxy; Points 2,5: SiO ₂ ; Points 3,4,6: SiC; Point 7: carbon.....	55
Figure 29: (a) Appearance of sample 7; (b,c) cracked matrix embedding carbon materials converted to SiC; (d) SiC particles in cracked SiO ₂ matrix [55]. Points 2,6,8: SiO ₂ ; Points 3,5: SiC from coal; Point 4: Epoxy; Point 7: SiC in SiO ₂ matrix.....	56
Figure 30: SiC web structure surrounded and filled by SiO ₂ in the original pores of a carbon material, sample 7 [55].....	56
Figure 31: Different microstructures of SiC: porous (a), needles (b), flakes (c) and islands (d). Revised after [7].	57
Figure 32: SiC crater crust from a FeSi75 furnace. Revised after Tranell et al. [56]	58
Figure 33: Samples in the crater crust. Estimated positions from [55].	58
Figure 34: Sample 1, visual inspection and microstructure [55]. Points 4,8: Epoxy; Points 5,7,9: Si; Points 6,10: SiO ₂	59
Figure 35: Sample 2: slag and condensates [55]. Points 1,4,7: Epoxy; Points 2,6,9: impurity; Points 3,5,8: SiO ₂ ; Point 10: FeSi droplet.	59
Figure 36: Sample 3, physical appearance and microstructure. [55]. Points 1,5: Epoxy; Points 2,3,4,6: SiO ₂ +Si; Point 7: Si droplet.	60
Figure 37: Side crust [2]; Material zones observed in the furnace during excavation. Electrode 1 is visible in the middle of the picture, and SiC, slag and metal zones are indicated [60].	61
Figure 38: Side crust sample (P75c) from furnace excavation. The sample has a slag matrix with some SiC particles and some metal particles. [60].....	61
Figure 39: Shape of the gas spaces around the electrodes in a 16.5 MVA furnace used for melting FeSi75. a) Furnace not rotated; b-e) Furnace rotated at different speeds. The numbers close to the electrode are times for a single revolution, in hours.	62
Figure 40: Shapes of cavities and cross sections of furnaces producing different ferrosilicon alloys [62].	63
Figure 41: a): Ferrosilicon furnace excavation after smelting. Legend: 1=Ferrosilicon; 2= Coarse SiC crystals with voids filled with FeSi; 3=Cavity; 4=Green layer made of melted quartz, green lumps of (SiC+SiO ₂ +C), ferrosilicon drops covered by brown condensate; 5=Brown condensate (more abundant close to the electrode), unreacted charge; 6=Graphite electrode. [1] b): Proposed inner structure of a submerged arc furnace [1].	64
Figure 42: Excavation of pilot scale furnace, revised after Müller et al. [64]	64
Figure 43: Mechanism of formation of the cavity in industrial furnaces, according to Otani et al. [3].....	65
Figure 44: Time evolution of cavity in laboratory scale experiments [59].	65
Figure 45: Cavity formation mechanism proposed by Vangskäsen [15].	66
Figure 46: Zones in silicon furnace at Thamshavn [7].....	66
Figure 47: SiC deposits with gas channels [7].	67
Figure 48: Excavation of three silicon furnaces: Wacker 1 (a), Elkem ASA Thamshavn (b) and Wacker 4 (c) [2].	68
Figure 49: Zones in pilot scale furnace excavation [59].	69
Figure 50: Inner structure of a silicon furnace after pilot scale experiment [3]	70
Figure 51: a,b: Brown crust condensate from Tangstad and Ksiazek [53] compared to the ICM model [47]; c,d): Microstructure and appearance of condensate powder produced by Ksiazek et al. [12].	72

Figure 52: a) Charge before condensation (1450°C); b) Brown condensate formation at 1600°C; c) Molten quartz surrounding SiC particle (1760°C). [68].....	72
Figure 53: Brown Si-SiO ₂ condensate, ≈1610°C [68].	73
Figure 54: Sessile drop tests on brown condensate. The top line sketches the evolution of brown condensate, whereas the bottom line shows actual instants collected during the test. (a): Brown condensate before any transformation, 1600C; (b) softening of silica matrix, 1650°C; (c) production of SiO(g) and movement of Si, 1750°C; (d) silicon droplet separated from the brown condensate, leaving a grey silica matrix, 1850°C. Revised after Vangskåsen [15].	74
Figure 55: White-brown condensate transition zone [15] and compositional line scanning along the red line.	74
Figure 56: Morphology of brown condensate collected from the chamber (left) and from the off-gas system (right) [12]......	75
Figure 57: a): Microstructure of brown condensate [12]; b): physical appearance [12]; c): Topography of brown condensate at 1760°C [54].	75
Figure 58: Nano scale treads in pale blue condensate at very high magnification. The diameter of the treads is varying in the range 10 - 30nm. [54]	76
Figure 59: White condensate at three different temperatures. a): 1311-1375°C; b): 1371-1434°C; c): 1370-1425°C [11]......	77
Figure 60: a): Spherical microstructure of the white condensate [12]; b): White condensate appearance [12]; c): Spherical microstructure detail [54]; d): SiC-SiO _x nanowires produced by Wang et al. [33]	78
Figure 61: SEM micrograph of whiskers grown in carbon monoxide from a briquette containing potassium silicofluoride [76].	78
Figure 62: Change of shape of white condensate under heating [59]......	79
Figure 63: Green condensate [11].	79
Figure 64: a): Spherical black condensate microstructure; b): Tube-shaped black condensate [54].	80
Figure 65: Grey condensate [54].	80
Figure 66: Sketch of oxide assisted growth mechanism for SiC-SiO _x nanowires [35]	83
Figure 67: Conditions for growth of LXO sheath. Legend: 1=X _n Y _m species; 2= HXO droplet; 3= LXO; 4=X _n Y _m large cluster; 5=X _n Y _m small cluster [78]	84
Figure 68: Shapes of wires grown with the OAG mechanism [78]	84
Figure 69: Decrease in melting temperature of a spherical gold particle as a function of its radius [80].	86
Figure 70: Experimental variables analyzed during the experiments: substrate composition and size, gas temperature, pellets composition, time exposure and inert gas flow added.....	88
Figure 71: Work structure of experimental method and characterization.	89
Figure 72: Particles size distribution of SiO ₂ and SiC powders in the SiO ₂ -SiC pellets.	90
Figure 73: Pellets characterization. The red rectangle corresponds to the zoomed area of the picture on the right. Zones with SiC are lighter than zones with silica.	91
Figure 74: Calcined SiO ₂ -SiC pellets.	91
Figure 75: Particles size distribution of SiO ₂ and Si powders in the Si-SiO ₂ pellets.	92
Figure 76: Characterization of Si-SiO ₂ calcined pellets at x90 (left) and x700 (right) magnification, BSE-SEM images.....	92
Figure 77: a): Appearance of Quartz A (top) and SiC (bottom) particles chosen as substrates; Right: Section of carbon tube before the experiment. The ruler refers as scale to both pictures.	93

Figure 78: a) LOM image of surface irregularities of SiC substrate; b) SEM micrograph of inclusions in SiC substrate.....	94
Figure 79: Cumulative particle size distribution of SiC substrates used in the condensation and gas production zones.	94
Figure 80: LOM picture of a Quartz A particle.	95
Figure 81: Topography (left) and porosity (right) picture of the graphite part before the experiment.	95
Figure 82: Graphite tube furnace (Thermal Technology model 1000-3560-FP20) [22].....	96
Figure 83: Schematic overview of the graphite tube furnace setup. (a) Condensation crucible and offgas system; (b): Gas production chamber. The condensation chamber is mounted on top of the SiO production chamber; (c) Crucible overview and gas flow paths for He, Ar, SiO(g) and CO(g).....	97
Figure 84: Example of thermal history (a) and corresponding extrapolated temperature gradient (b), Exp. R19a.	98
Figure 85: Left: Large-scale setup; Right: Large-scale setup for lateral temperature gradient computation.	101
Figure 86: Thermal history (a) and computed temperature gradient (b) of experiment IF1b.	102
Figure 87: Temperature gradient in large-scale setup computed by modelling [82].....	103
Figure 88: Sample location in Elkem Fiskaa plant (Kristiansand, Norway)	104
Figure 89: Fragments of industrial samples from Elkem Kristiansand. Examples of compounds of different colors are highlighted by the circles in the figure.	105
Figure 90: Estimated position of samples S.22, S.23 and S.36. Revised from Ksiazek [84].	106
Figure 91: Overview of samples analyzed from Wacker 1 excavation. Revised after Ksiazek et al. [2]	107
Figure 92: Overview of Wacker 4 furnace and sample positions, revised after [55], [57].	108
Figure 93: A black and white SEM picture before (a) and after (b) a contrast threshold is applied on ImageJ®.	112
Figure 94: Samples from Experiment IF10, T = 1370-1650°C. a) 1) SiC particle without condensate; 2) SiC covered in white and blue condensate; 3) SiC covered in white condensate. 4) SiC covered in grey condensate. B) Top: Quartz A covered in white condensate; Bottom: Quartz A without deposition of condensate.	115
Figure 95: Blue condensate on SiC (Exp. R2a, estimated 1390-1500°C); Right: Blue condensate on Quartz A (Exp. R12a, estimated 950 - 1050°C).....	115
Figure 96: Left: White condensate on SiC (Exp. R2a, estimated 1390 - 1700°C) ; Right: White condensate on Quartz A (Exp. R8a, estimated 900-1200°C).....	116
Figure 97: Left: Orange condensate on SiC (Exp. R1a); Right: White condensate on SiC (Exp. IF1a).....	116
Figure 98: Left: Nodules on nanowires, organized in a necklace structure. White condensate, Exp. IF1a. Right: Necklace structure and disordered nanowires, white condensate from Exp. R4c, estimated 1150-1580°C.	117
Figure 99: Characterization of white and orange SiO ₂ -SiC condensates from different temperatures. Samples from experiment R4a and R1a. The bars show uncertainties at one standard deviation. Samples in R1b are collected between 1020 - 1725°C.	118
Figure 100: Dimension of core and shells in nanowires of blue condensate, Exp. R4c, T = 1250-1450°C.	119
Figure 101: Tip of a nanowire from Exp. R4c, T = 1250-1450°C. Left: Line scanning of blue condensate nanowire tip. Elemental analysis of silicon (grey), oxygen (blue) and carbon (green); Right: Zoom on a nanowire tip and diffraction pattern of the picture. Stacking faults between atomic planes can be seen in the core-phase.	120

Figure 102: EDS mapping of Si, O and C of a nodule and incoming wire, from TEM analysis of white condensate. Sample from Exp. R4c, T = 1450-1550°C.	121
Figure 103: Bead structure (left) and stacking faults in SiC nanowire (right). White condensate from Exp. R4c, T = 1450-1550°C.	122
Figure 104: Left: Wetting between shell and core phases. White condensate, Exp. R4c, T = 1450-1550°C. Right: Measurement of contact angle on a nodule in white condensate. The supplementary angle is measured, and the contact angle is then calculated.	122
Figure 105: a) Blue condensate on Sample 1; b) Sample 2, positions of points 2.1 and 2.2.	123
Figure 106: Survey spectra of blue condensate a) sample 1 and b) sample 2, point 2.1 and white condensate c) sample 2, point 2.2. The O 1s, C 1s and Si 2p core level regions are indicated.	124
Figure 107: a) Si 2p, b) C 1s and c) O 1s core level spectra of blue condensate (sample 1).	125
Figure 108 a) Si 2p and b) C 1s core level spectra of i) blue condensate (sample 2, point 2.1) and ii) white condensate (sample 2, point 2.2).	125
Figure 109: Grey and white condensate on a SiC particle. Sample from experiment R4c, T=1583-1706°C....	127
Figure 110: Grey condensate, SE-image from Experiment R4c; Building blocks of grey condensate, Experiment R4c, T=1583-1706°C.....	128
Figure 111: Brown condensate layer generated between SiC particles, white condensate and white scale. Sample from Exp. R4a., T = 1665 - 1800°C.	128
Figure 112: Left: Spheres and wires from experiment R1b, T = 1340 - 1570°C; Right: Top view of brown condensate embedding spheres inside the matrix. Sample from experiment R4a, T = 1665 - 1800°C.	129
Figure 113: EPMA mapping of brown condensate, Experiment R4a, wt. % on the colored scales.	130
Figure 114: Final aspect of the FIB-TEM sample of brown condensate. Left: Frontal view; Right: Cross section thickness. FIB sample.	131
Figure 115: Details of spheres borders. FIB sample.	131
Figure 116: Original TEM bright field picture (a). Mapping of Si (b), C (c) and O (d).....	132
Figure 117: Left: Silicon sphere from Experiment 1b used for diffraction pattern. Center: Diffraction pattern with twinning; Right: Diffraction pattern without twinning, indexed.....	132
Figure 118: Twin grain boundary in silicon.	133
Figure 119: Left: brown condensate XPS sample; Right: SE picture from the area chosen for the analysis.	134
Figure 120: Survey spectrum of brown condensate from experiment R4a.	134
Figure 121: XPS spectra for C-1s (left) and Si-2p (right) electrons in brown condensate from experiment R4a.	135
Figure 122: Line scanning of Sample 1: Increasing particle size towards sample external edge.....	137
Figure 123: Si spheres at x = 0 μm (a), x = 300 μm (b) and x = 600 μm (c), sample 1.	137
Figure 124: Sample 1, ImageJ® analysis results on average size (blue) and counted particles per picture (orange).	137
Figure 125: Line scanning of sample 3.	138
Figure 126: Sample 3, ImageJ® analysis results on average size (blue) and counted particles per picture (orange).	138
Figure 127: Silicon spheres in sample 3 at x = 0 (a), x = 120 μm (b), x = 210 μm (c), x = 240 μm (d). All pictures have the same magnification (x6000).....	138
Figure 128: Layer configuration at x220 (left) and x3000 (right) magnification, sample 8.	139
Figure 129: Line scanning of Sample 2.....	139
Figure 130: Sample 2, average area (blue), average size (blue) and counted particles per picture (orange).	139

Figure 131: Layer particle sizes in sample 2: $x = 0 \mu\text{m}$ (a), $x = 270 \mu\text{m}$ (b), $x = 450 \mu\text{m}$ (c)	140
Figure 132: Layer thicknesses in sample 3 (a) and 7 (b).....	140
Figure 133: Pore and silicon sphere size in sample 9	140
Figure 134: Nanofibers from sample W1-31.....	143
Figure 135: a) Bead structures in sample REC 3.1; b)Nanowires (right) deposited on SiC substrate (left), sample W1-38.	143
Figure 136: EDS analysis of nanowires from the surface of sample W1-38.....	144
Figure 137: Nanowires on sample W1-31.....	144
Figure 138: Nodules on nanowires from Sample REC 1.3, x250 magnification; Right: Nanowires with nodules from sample REC 3.1, x12k magnification.....	145
Figure 139: Thick whiskers with nodules, sample W4-29.	145
Figure 140: Brown condensate on black and pale green carbon materials, eventually covered with white condensate. Sample REC 3.1.	146
Figure 141: a,b): Si spheres in sample S.23; c): Interconnected Si islands in sample W1-40.....	147
Figure 142: Change in pore size in silica, sample S.36 (left) and S.22 (right).	147
Figure 143: porous silica from Sample S.36.	148
Figure 144: Spherical blocks on grey layer, sample W1-38 (a), W1-40 (b) and W4-29 (c).....	149
Figure 145: Condensation profiles of Experiment R7b (Quartz A) and R9b (SiC). Constant parameters: Target T = 1900°C, holding time = 1 hour, He flow 0.1 l/min, Substrate size 5-8 mm.....	151
Figure 146: Left : Condensation profiles for Experiments R3a (t=30 min), R4a (t=60 min), R5a (t=240 min). Constant parameters : Target T 2000°C, SiC substrates, Ar flow 0.02 l/min, substrate size 3-5 mm ; Right : Condensation profiles for Experiments R14a (t=30 min), R17a (t=60 min), R20a (t=240 min). Constant parameters : Target T 2000°C, SiC substrates, He flow 0.10 l/min, substrate size 3-5 mm.....	152
Figure 147: Variation in the lowest temperature of formation for blue condensate in the experiments from Figure 146. Error bars on temperature are $\pm 10^\circ\text{C}$, as described in Appendix C.	153
Figure 148: Condensation profiles for Experiments IF12 (t=10 min), IF10 (t=30 min) and IF5b (t=120 min), group with $p_{\text{SiO}_2,\text{in}} = 1.0$. Constant parameters : Target T 1890°C, SiC substrates, substrate size 3-10 mm, $p_{\text{SiO}_2,\text{in}} = 1.0$	154
Figure 149: Condensation profiles for Experiments IF11 (t=10 min), IF9 (t=30 min) and IF1b (t=120 min), group with $p_{\text{SiO}_2,\text{in}} = 0.75$. Constant parameters : Target T 1890°C, SiC substrates, substrate size 3-10 mm, $p_{\text{SiO}_2,\text{in}} = 0.75$	154
Figure 150: Variation in the lowest temperature of formation for condensates in the experiments from Figure 148 and Figure 149. The width of the error bars is the value of the deviation obtained at the nearest temperature measurement point during the temperature gradient assessment (see Appendix C, Table 53).	155
Figure 151: Effect of inert gas addition on condensation profile, experiments R4a (0.02 l/min), R2a (0.05 l/min), R17b (0.10 l/min) and R1b (0.4 l/min). Temperature gradients in the chamber depend also on the gas flow. Constant parameters : Target T 2000°C, SiC substrates, substrate size 3-5 mm, holding time 1 h.....	156
Figure 152: Variation in the lowest temperature of formation for condensates in the experiments from Figure 151. Error bars on temperature are $\pm 10^\circ\text{C}$, as described in Appendix C.	156
Figure 153: Partial pressure effect on different PSD groups. The SiO+CO experiment has grey pellets on the bottom, whereas the SiO(g) experiments have brown pellets. The experiments collected are IF1b and	

IF5b (3-10 mm), IF2a and IF6a (5-8 mm), IF3 and IF7a (12-20 mm), IF4 and IF8 (8-14 mm). Constant parameters : Target T 1890°C, SiC substrates, holding time 2 h.....	157
Figure 154: Variation in the lowest temperature of formation for condensates in the experiments from Figure 153. The width of the error bars on temperature is the value of the deviation obtained at the nearest temperature measurement point during the temperature gradient assessment (see Appendix C, Table 53).	158
Figure 155: Partial pressure effect at short times. The SiO+CO experiment has grey pellets on the bottom, whereas the SiO(g) experiments have brown pellets. Experiments IF11 and IF12 (10 min), IF9 and IF10 (30 min). Constant parameters : Target T 1890°C, SiC substrates, substrate size 3-10 mm.	158
Figure 156: Condensation profiles sorted by decreasing A_{cm} , experiments IF1b (3-10 mm), IF4 (8-14 mm) IF3 (12-20 mm) and IF2a (5-8 mm). Experiments with SiO ₂ -SiC pellets. Constant parameters : Target T 1890°C, SiC substrates, holding time 2 h, $p_{SiO,in} = 0.75$	159
Figure 157: Condensation profiles sorted by decreasing PSD broadness, experiments IF5b (3-10 mm), IF8 (8-14 mm), IF7a (12-20 mm) and IF6a (5-8 mm). Experiments with Si-SiO ₂ pellets. Constant parameters : Target T 1890°C, SiC substrates, holding time 2 h, $p_{SiO,in} = 1.0$	160
Figure 158: Variation in the lowest temperature of formation for condensates in the experiments from Figure 156 and Figure 157. The bubble size shows the PSD broadness qualitatively. Constant parameters : Target T 1890°C, SiC substrates, holding time 2 h. The width of the error bars on temperature is the value of the deviation obtained at the nearest temperature measurement point during the temperature gradient assessment (see Appendix C, Table 53).	160
Figure 159: Variation in the lowest temperature of formation for condensates in the experiments from Figure 156 and Figure 157. The bubble size shows the PSD broadness. Constant parameters : Target T 1890°C, SiC substrates, holding time 2 h, $d_{avg} = 6.5$ mm.	161
Figure 160: Condensation profiles for experiments R19a (1-3 mm, $d_{avg} = 2$ mm), R20a (3-5 mm, $d_{avg} = 4$ mm) and R21a (5-8 mm, $d_{avg} = 6.5$ mm). Constant parameters : Target T 2000°C, SiC substrates, holding time 240 min, $p_{SiO,in} = 0.71$ (He flow 0.10 l/min).	161
Figure 161: Condensation profiles for experiments R13a (1-3 mm, $d_{avg} = 2$ mm), R14a (3-5 mm, $d_{avg} = 4$ mm) and R15a (5-8 mm, $d_{avg} = 6.5$ mm). Constant parameters : Target T 2000°C, SiC substrates, holding time 30 min, $p_{SiO,in} = 0.71$ (He flow 0.10 l/min).	162
Figure 162: Variation in the lowest temperature of formation for condensates in the experiments from Figure 160 and Figure 161. The bubble size shows the PSD broadness qualitatively. Error bars on temperature are $\pm 10^\circ\text{C}$, as described in Appendix C.	162
Figure 163: Condensation profiles for experiment R9a (1900°C), R1b (2000°C) and R6a (2200°C). Constant parameters : SiC substrates, holding time 60 min, He flow 0.40 l/min., substrate size 3-5 mm.	163
Figure 164: Thermal history and CO(g) production, temperature effect.....	164
Figure 165: Thermal history and CO(g) production for setups R3 (30 min) and R4 (60 min).	164
Figure 166: Excavation of the crucible at Y = 18 cm, T = 1485°C. SiC charge before (left) and after poking (right), experiment IF2a.	169
Figure 167: Left: Stoking point Y = 21 cm, T=1420°C, Exp IF75-7a. Right: Brown condensates at Y = 18 cm, T = 1580°C for experiment IF75-7a.....	169
Figure 168: Variation of stoking point position as a function of target temperature. Constant parameters : SiC substrates, holding time 60 min, He flow 0.40 l/min., substrate size 3-5 mm.	172
Figure 169: Effect of holding time at different Ar/He flows on the stoking point in the small-scale setup. Constant parameters for blue and green lines: Target T 2000°C, SiC substrates, Ar flow 0.02 l/min,	

substrate size 3-5 mm; Constant parameters for orange and grey lines : Target T 2000°C, SiC substrates, He flow 0.10 l/min, substrate size 3-5 mm. Error bars on temperature are $\pm 10^\circ\text{C}$, as described in Appendix C.173

Figure 170: Effect of holding time at different pellets composition (starting gas composition) on the stoking point in the large-scale setup. Constant parameters for blue and green lines: Target T 1890°C, SiC substrates, substrate size 3-10 mm, $p_{\text{SiO}_2,\text{in}} = 0.75$; Constant parameters for orange and grey lines : Target T 1890°C, SiC substrates, substrate size 3-10 mm, $p_{\text{SiO}_2,\text{in}} = 1.0$. The width of the error bars on temperature is the value of the deviation obtained at the nearest temperature measurement point during the temperature gradient assessment (see Appendix C, Table 53).174

Figure 171: Effect of average particle size on the stoking point in the small-scale setup, at different holding times. The bubble size is qualitatively expressing the PSD broadness. Constant parameters : Target T 2000°C, SiC substrates, $p_{\text{SiO}_2,\text{in}} = 0.71$ (He flow 0.10 l/min). Error bars on temperature are $\pm 10^\circ\text{C}$, as described in Appendix C.175

Figure 172: Effect of average particle size on the clogging interval in the small-scale setup, at different holding times. The bubble size is qualitatively expressing the PSD broadness. Constant parameters : Target T 2000°C, SiC substrates, $p_{\text{SiO}_2,\text{in}} = 0.71$ (He flow 0.10 l/min).175

Figure 173: Effect of average particle size at different partial pressure on the stoking point in the large-scale setup. Constant parameters : Target T 1890°C, SiC substrates, holding time 2 h. The width of the error bars on temperature is the value of the deviation obtained at the nearest temperature measurement point during the temperature gradient assessment (see Appendix C, Table 53).176

Figure 174: Effect of average particle size at different partial pressure on the clogging interval in the large-scale setup. Constant parameters : Target T 1890°C, SiC substrates, holding time 2 h.177

Figure 175: Effect of inert gas flow on the stoking point and stoking interval position in the small-scale setup. Constant parameters : Target T 2000°C, SiC substrates, substrate size 3-5 mm, holding time 1 h. Error bars on temperature are $\pm 10^\circ\text{C}$, as described in Appendix C.178

Figure 176: Clogging intervals and stoking point sorted by SiO(g) partial pressure. Experiments from the IF75 large-scale setup. Constant parameters : Target T 1890°C, SiC substrates.179

Figure 177: Brown partially reacted pellets leftovers, Exp. IF5a (left) and IF6a (right).186

Figure 178: Left: BSE-image of Si-SiO₂ partially reacted pellets, Experiment IF6a. Right: Calcined Si-SiO₂ pellets.187

Figure 179: Left: Average condensation yield as a function of partial pressure, measurements including both setups (Blue = small-scale; orange = large-scale). Right: Total condensate mass (m_{cond}) against $p_{\text{SiO}_2,\text{in}}$ in small scale experiments. The setup name is written for each point. The value of m_{cond} is an average of the repetitions made. The error bars refer to one standard deviation. Constant parameters: Target temperature 2000°C, SiC PSD 3-5 mm, holding time 1h.188

Figure 180: Average Si-SiO₂ and SiO₂-SiC amounts in experiments at increasing partial pressure.189

Figure 181: Mass distribution of condensates with respect to temperature, Experiment IF2a. Left: Cumulative representation: Right: Distribution representation.189

Figure 182: Example of p_{SiO_2} vs T diagram for Reaction 2, experiment R1b.193

Figure 183: p_{SiO_2} -T curves for SiO₂-SiC condensation, small scale setup.194

Figure 184: p_{SiO_2} -T curves for Si-SiO₂ condensation, small scale setup.194

Figure 185: p_{SiO_2} -T curves for SiO₂-SiC condensation, large-scale setup.195

Figure 186: p_{SiO_2} -T curves for Si-SiO₂ condensation, large-scale setup.195

Figure 187: Thermal history at the pyrometer (continuous line) compared to the corresponding CO(g) production for experiments at 1900, 2000 and 2200 °C target temperature (dashed lines).	199
Figure 188: Reaction rate as a function of reaction time.	201
Figure 189: Reaction rate as a function of temperature.	201
Figure 190: Reaction rate as a function of total condensation area.	201
Figure 191: Arrhenius equation plots for $k(T)$ values in mode 2b, 3b and 4. The slope of the curve is the activation energy E_a , and the intercept is the natural logarithm of the frequency factor k_0	203
Figure 192: (SiO) _N nanoclusters ground state for N = 14, segregation into silica, suboxide and silicon area. Element key: Red = Oxygen; Grey = Silicon. Revised after Bromley et al. [49].	205
Figure 193: Equilibrium composition of a mixture of 2 moles SiO ₂ and 1 mol SiC, between 1000°C and 6000°C.	207
Figure 194: Stage 1: Incubation: Formation of the seed for the SiC-SiO _x nanowire by SiC(s) (green) and SiO _x (l) (Orange) nanoclusters.	208
Figure 195: Stage 2: Nucleation of SiC (Green) and SiO _x (l) (Orange) on a SiC particle. Left: Final form of the nucleus, once the lateral growth is completed. Right: Formation of droplet, reaction zone and SiO _x coating (Red)	209
Figure 196: Defects in SiC core-phase, highlighted inside the red rectangle. TEM picture of blue condensate, Exp. R4c, T = 1250-1450°C.	210
Figure 197: Left: Stage 3: Growth and terminated nanowire. Green = SiC(s); Orange = SiO _x (l); Red = SiO _x (s). Right: TEM picture of nanowire tip, picture from Experiment R4c. Zones highlighted with colors corresponding to the picture on the left.	211
Figure 198: Nodules formation mechanism, revised after [39]. Green = solid SiC; Red = Liquid SiO _x ; black = stacking faults.	212
Figure 199: Temperature dependence of reaction enthalpies for Reactions 1-4 and 12.	214
Figure 200: Condensation profiles of experiments R3a (left) and R4a (right).	215
Figure 201: Stage 1: Formation of a liquid SiO ₂ (brown) and Si (grey) emulsion on a SiC surface.	216
Figure 202: Tones of dark and light brown in condensate sample, T = 1580-1706°C, Experiment R4c.	217
Figure 203: Sphere size distribution in a sample from Experiment 2a, T=1525-1745°C.	217
Figure 204: Pores of porous silica from experiment IF4, T = 1590°C.	218
Figure 205: Stage 1: emulsion of Si(grey) and SiO ₂ (brown) in Si-SiO ₂ condensate. Stage 2: Movement of Si in a SiO ₂ matrix containing Si spheres at different average size. Porous silica (light grey) is formed after Si depletion caused by prolonged exposition to high temperatures.	218
Figure 206: Sphere size distribution in the same sample. Experiment R2a, T=1525-1745°C (Sample 8 from Table 26).	220
Figure 207: Sketch of the layer evolution in brown condensate.	220
Figure 208: Brown condensate from Experiment R1b. Left: Cracks in FIB sample; Right: Junction wire-sphere in FIB sample	221
Figure 209: Elemental EDX mapping of a sphere collected from the FIB-sample: survey area (a). Silicon (b), Carbon (c) and Oxygen (d) mapping.	222
Figure 210: SiC-SiO ₂ condensation (Reaction 1): p_{SiO_2} -T lines for the large-scale setup experiments compared to the equilibrium curves for the reactions in silicon production.	224
Figure 211: SiC-SiO ₂ condensation (Reaction 1): p_{SiO_2} -T lines for the small-scale setup experiments compared to the equilibrium curves for the reactions in silicon production.	225

Figure 212: Si-SiO ₂ condensation (Reaction 2): p _{SiO} -T lines for the large-scale setup experiments compared to the equilibrium curves for the reactions in silicon production.....	226
Figure 213: Si-SiO ₂ condensation (Reaction 2): p _{SiO} -T lines for the small-scale setup experiments compared to the equilibrium curves for the reactions in silicon production.....	226
Figure 214: Driving force as a function of injected inert gas flow. Left: SiC-SiO _x condensation (Reaction 1); Right: Si-SiO ₂ condensation (Reaction 2).	230
Figure 215: Correspondence between mass distribution (top) and condensation rate (bottom) vs temperature and clogging interval. The clogging interval is written in the graph below. Experiments IF2a (red), IF4 (green) and IF5b (blue). Error bars on mass percentage are ±5%.....	231
Figure 216: Condensates distribution as a function of temperature, related in experiments at different total condensates mass m _{cond} . Constant parameters: PSD 3-10 mm, p _{SiO,in} = 1.0. Error bars on mass percentage are ±5%.....	232
Figure 217: Condensation yield as a function of particle diameter and p _{SiO,in} in large-scale experiments. The sphere size is related to the broadness of the chosen PSD. Experiments considered: R19-R21 (green), IF1,2,4 (orange), IF5,8 (blue).	232
Figure 218: Preferential paths for the gas flow: narrow PSD (left) and broad PSD (right).....	233
Figure 219: Solution of the leading-order model for a = 1.5 mm, at t = 24 min (left) and t = 2 h (right). The white region depicts the brown Si-SiO ₂ condensate layer [114], whereas the colored region shows the local concentration of SiO(g) in the channel.	234
Figure 220: Clogging interval for experiments with changing p _{SiO,in} . The values of the maximum condensation rate are written in correspondence of each point, in g/min.	235
Figure 221: Left: external scales on crucibles; Center: : Microstructure of blue scale from external walls of the crucible, experiment R3c; Right: Traces of orange powder in the offgas system, experiment R2a.....	240
Figure 222: Conversion (left) and partially reacted pellets (right) as a function of time for SiO ₂ +SiC and Si+SiO ₂ reactions at 1890°C.	241
Figure 223: Comparison of conversion rates of pellets from this work (continuous lines) with results from Ni (dashed lines) [111] and Tangstad et al. [97].	242
Figure 224: Reaction chamber, crucible and graphite gas lance covered in green layer.	253
Figure 225: SE images of green SiC layer (a,b) and BSE image of penetration depth into the top gas distributor of Experiment 4b (d).....	254
Figure 226: Left and center: Grey condensate on graphite at x400 and x2500 magnifications; Right: Si areas (light grey) in SiC matrix (dark grey). White areas are impurities coming from graphite.	255
Figure 227: Left: Gas production chamber before Exp. 3a; Center: Top view of green layer on gas production chamber, Exp. 1a; Right: Top view of green and grey layer on gas production chamber, Exp. IF2a.....	255
Figure 228: a) Si droplets and SiC particles on gas production chamber, Experiment IF5a; b) Side view of gas production chamber after Exp. IF1a.	256
Figure 229: Pillar whiskers from experiments R6a (left) and IF1a (right)	257
Figure 230: Droplet SiC whiskers from experiment R6a.	257
Figure 231: Blue condensate at high temperatures, Exp. R6a.....	258
Figure 232: SiC nanowhiskers at x2200 (a) and x35000 (b) magnification, Exp. R6a	258
Figure 233: Left: Green layers in sample W1-34; Right: White areas on sample W1-43.....	259
Figure 234: Whiskers in sample REC1.2 ; Right: SiC Whiskers deposited on charcoal particle converted to SiC, embedded in SiO ₂ matrix, sample REC 1.3.....	260
Figure 235: Whiskers and nanowires from sample REC 1.1 (left) and REC 1.2 (right).....	260

Figure 236: Whiskers with spherical cap, sample REC 3.1 (left) and W4-30 (right).	260
Figure 237: EDS overview of whiskers from sample REC 3.2.	261
Figure 238: Graphite tube protecting the thermocouple in the large-scale setup, Experiment IF2a.	262
Figure 239: Graphite tube protecting the thermocouple in the large-scale setup, Experiment IF3a.	262
Figure 240: Tube overview and numbering of sections from 1 to 6. The values of Y are given in cm; b) Thin white and blue layer generated outside of the small-scale crucible, Exp. R3c.	263
Figure 241: Blue scale (left) and white scale (right) on Section 4 of the graphite tube.	264
Figure 242: Grey condensate from Section 5. Left: Finger structure; Center: Oriented wires on grey scale; Right: Building blocks of grey scale.	264
Figure 243: Grey scale on Section 5, top view.	264
Figure 244: EDS overview for the scale on graphite, section 5.	265
Figure 245: a) SiC production in graphite tube; b) SiC crystals on graphite tube, Section 6.	266
Figure 246: Individuation and definition of the sample on the surface substrate.	267
Figure 247: Extraction of the sample. The sample is ready for welding to the grid.	268
Figure 248: Insertion onto the dedicated TEM grid.	268
Figure 249: Final aspect of the TEM lamella of brown condensate. Front view (left) and lateral view (right).	268
Figure 250: Thermal histories of pyrometer temperature and thermocouples in setups 1c,1d,1e (left) and setups 4d-4e (right).	270
Figure 251: Temperature gradients computed in small scale setup: Temperature interval within time during different experiments.	270
Figure 252: Temperature profile and CO production in setups 3,4 and 5.	270
Figure 253: Thermal history of Experiment R7b at the furnace pyrometer and at Y = 0 mm.	271
Figure 254: Lateral and central temperature gradient in experiment IF6a.	275
Figure 255: Driving force proportional to the reaction stoichiometries.	285
Figure 256: Driving force for experiments with $p_{SiO} = 0.75$ and $p_{SiO} = 1$.	286
Figure 257: Comparison of driving forces for mode 3b (concentration of SiO) and mode 4 (distance from equilibrium), experiment IF5b. Driving force = Blue line; $k(T)$ = Orange line.	286
Figure 258: Thermodynamics of reaction at 1 (dashed lines) and 1.5 atm (continuous lines).	287
Figure 259: a) O-1s electron XPS spectrum; b) Si-2s electron XPS spectrum, sample 2.1.	295
Figure 260: XRD spectrum of Quartz A.	295
Figure 261: XRD spectrum of SiC substrate.	296
Figure 262: XRD spectrum of brown condensate from experiment R4a.	297
Figure 263: XRD spectrum of brown condensate sample for XRD analysis (IF7a, T = 1580-1750°C).	297
Figure 264: XRD spectrum of white condensate sample 1 (IF7b, T = 1250-1480°C).	298
Figure 265: XRD spectrum of white condensate sample 2 (IF7b, T = 1480-1720°C).	298
Figure 266: XRD spectrum of white condensate sample 3 (IF12, T = 1530-1710°C).	298
Figure 267: Condensation profiles of experiments with SiC substrates, small scale setup.	301
Figure 268: Condensation profiles for Quartz A experiments. Experiments R7b, R8a, R-P4011a, R12a.	301
Figure 269: Temperature profiles and colors of condensates formed in experiments of large-scale setup.	303

List of tables

Table 1: Reactions in the Si-O system, revised after [28].	39
Table 2: p(n) computed by the RB-model [45]	43
Table 3: Chemical analysis of sample P75c from furnace excavation. The table shows an average of the position numbers listed [60].	62
Table 4: Cavity size and thickness of charge layer around electrode in three different pilot scale FeSi furnaces [62]	63
Table 5: Condensates properties, revised after [12], [15], [53].	81
Table 6: Composition of starting materials detected by XRD (Quartz B) and XRF (SiC)	90
Table 7: XRD spectrum of SiC substrate.	93
Table 8: Overview of experimental conditions: time, holding temperature and condensation substrate type	99
Table 9: Overview of experimental conditions: time, pellets compositions and condensation substrate type.	103
Table 10: Overview of samples extracted from sample A, REC Solar.	105
Table 11: Overview of samples analyzed from Salten furnace n°2.	106
Table 12: Overview of samples analyzed from Wacker 1.	107
Table 13: Overview of samples analyzed from Wacker 4.	107
Table 14: Reference values chosen for peak fitting in XPS [86].	111
Table 15: Composition of XRD samples analyzed with the internal standard method.	112
Table 16: Characterization of SiO ₂ +SiC mixture (at. % ± st.dev.) and comparison with theoretical composition.	117
Table 17: Atomic concentration of oxygen, carbon and silicon as determined from the O-1s, C-1s and Si-2p regions of the XPS survey spectra.	123
Table 18: Condensates analyzed during XRD	126
Table 19: Relative amount of each polytype for silica and SiC, calculated by TOPAS v5. The composition is defined in wt.%. The theoretical SiO ₂ /SiC ratio is 3.00.	127
Table 20: TOPAS v5 fitting of XRD spectra for samples with white condensate. The composition is expressed in wt.%.	127
Table 21: Characterization of grey SiC-SiO ₂ mixture (at. %)	128
Table 22: Characterization of brown Si-SiO ₂ mixture (at. %).	129
Table 23: XPS analysis of brown condensate, survey spectrum	133
Table 24: Relative amount of each polytype for silica and SiC, calculated by TOPAS v5 for brown condensate. The composition is defined in wt.%.	136
Table 25: TOPAS v5 fitting of XRD spectra for the sample with brown condensate. The composition is expressed in wt.%.	136
Table 26: Samples used for Si spheres analysis.	136
Table 27: Overview of compounds in the samples analyzed. A cross marks the presence of the compound in the sample.	142
Table 28: Composition detected at the points from Figure 136.	144
Table 29: EDS analysis of points from Error! Reference source not found. (at. %).	147
Table 30: Composition detected by EDS in the points from Figure 143; (at. %)	148
Table 31: Temperatures of formation of condensates on different substrates and setups.	151

Table 32: Values of A_{cm} and d_{avg} for experiments in Figure 156 and Figure 157. Details on the PSD are collected in the experimental section.	159
Table 33: Summary of the effect of experimental parameters on condensation temperature.	165
Table 34: Stoking point (positions and temperatures), clogging intervals and temperatures at $Y = 0$ mm.	168
Table 35: Clogging intervals in large-scale setups.	170
Table 36: Comparison of clogging results between small and large-scale setup.	171
Table 37: Comparison between an experiment with quartz substrate (R11) and SiC substrate (R10)	180
Table 38: Summary of the effect of experimental parameters on condensation temperature.	181
Table 39: Condensates mass and phase distribution (wt. % in parenthesis), average value over all the experiments performed.	184
Table 40: Condensation yield and condensates mass in large-scale setup.	185
Table 41: Weight of partially reacted pellets at the end of the experiments.	186
Table 42: Comparison of mass balance and condensation yield between small and large-scale setups.	187
Table 43: Distribution of SiO ₂ -SiC condensate in temperature intervals of the large-scale setup. The temperature intervals written in bold are included in the clogging intervals.	190
Table 44: Values of t_r for large-scale setup experiments.	198
Table 45: Reaction rate values in different experiments and condensation intervals (highlighted in bold).	200
Table 46: Activation energy and frequency factor for mode 2b, 3b and 4.	202
Table 47: Comparison of activation energies in silicon production reactions and nanowires production	228
Table 48: Values of E_a , k_0 and R^2 for model 3b and model 4 in different temperature ranges.	229
Table 49: Composition found at the points from Figure 237 (at. %).	261
Table 50: EDS analysis at the points of Figure 244 and compound present at each point	265
Table 51: Overview of condensates temperature of formation on graphite, large and small-scale setups.	267
Table 52: Regression function for small scale setup experiments	269
Table 53: Experimental data and variation of temperature through time for each experiment performed in the large-scale setup. T_{min} , T_{max} and T_{Avg} are the minimum, maximum and average temperature over the experiment history (in °C). The deviation is the width of the temperature interval from T_{Avg} to T_{max} (or T_{min}), expressed in K.	272
Table 54: Temperature gradient computed for experiment IF6a.	276
Table 55: p_{SiO} values used for modeling in small scale setup.	277
Table 56: Temperature values and line regression coefficients used for modeling in small scale setup	278
Table 57: Values of d_p , A_p , $m_{SiC, before}$, V_{tot} , A_{tot} , A_{cm} for every experiment.	279
Table 58. Values of A in each temperature interval, for each experiment.	280
Table 59: k values for the models with the highest R^2 (Modes 2b, 3b) and Mode 4.	281
Table 60: Driving force values for Mode 3b and Mode 4	282
Table 61: Values of k for the remaining models (Modes 1a, 1b, 2a, 3a).	283
Table 62: Activation energies (kJ/mol) for experiments considered for the SiC-SiO _x modeling, for models 3b and 4.	284
Table 63: ImageJ® analysis results on number of particles and particle area, sample 1.	288
Table 64: ImageJ® analysis results on number of particles and particle area, sample 2.	289
Table 65: ImageJ® analysis results on number of particles and particle area, sample 3.	289
Table 66: ImageJ® analysis results on particle size parameters, sample 1.	290
Table 67: ImageJ® analysis results on particle size parameters, sample 2.	291
Table 68: ImageJ® analysis results on particle size parameters, sample 3.	291

List of reactions

$3 \text{SiO}(\text{g}) + \text{CO}(\text{g}) \rightarrow 2 \text{SiO}_2(\text{s,l}) + \text{SiC}(\text{s})$	Reaction 1
$2 \text{SiO}(\text{g}) \rightarrow \text{Si}(\text{s,l}) + \text{SiO}_2(\text{s})$	Reaction 2
$\text{SiO}(\text{g}) + 2 \text{C}(\text{s}) \rightarrow \text{SiC}(\text{s}) + \text{CO}(\text{g})$	Reaction 3
$\text{SiO}(\text{g}) + \text{SiC} \rightarrow 2 \text{Si}(\text{l}) + \text{CO}(\text{g})$	Reaction 4
$\text{SiO}(\text{g}) + \frac{1}{2} \text{O}_2 \rightarrow \text{SiO}_2(\text{s})$	Reaction 5
$\text{CO}(\text{g}) + \frac{1}{2} \text{O}_2 \rightarrow \text{CO}_2(\text{g})$	Reaction 6
$\text{Fe}_2\text{O}_3(\text{s}) + 3 \text{CO}(\text{g}) \rightarrow 2 \text{Fe}(\text{l}) + 3 \text{CO}_2(\text{g})$	Reaction 7
$\text{C} + \text{CO}_2(\text{g}) \rightarrow 2 \text{CO}(\text{g})$	Reaction 8
$\text{Si}_{0.87}\text{C}_{0.13}(\text{l}) + \text{C}(\text{s}) = \text{SiC}(\text{s})$	Reaction 9
$\text{SiO}_2 + \text{C} \rightarrow \text{SiO}(\text{s}) + \text{CO}(\text{g})$	Reaction 10
$\frac{x+1}{x-1} \text{SiO}(\text{g}) + \text{CO}(\text{g}) = \frac{2}{x-1} \text{SiO}_x(\text{l}) + \text{SiC}(\text{s})$	Reaction 11
$3 \text{Si}(\text{l}) + 2 \text{CO}(\text{g}) \rightarrow 2 \text{SiC}(\text{s}) + \text{SiO}_2(\text{s,l})$	Reaction 12
$\text{SiO}_2(\text{s,l}) + 3 \text{C}(\text{s}) \rightarrow \text{SiC} + 2 \text{CO}(\text{g})$	Reaction 13

Abstract

Condensation of SiO(g) is the combination of two reactions in silicon production process. The first is the interaction between SiO(g) and CO(g). The second is the reaction between two molecules of SiO(g). The two reactions take place in the low temperature zone of the furnace. Condensation is spontaneous in industrial Si and FeSi furnaces between 1400-1800°C, according to thermodynamics and excavations at industrial and pilot scale. Both reactions are exothermic, and their products contribute to decrease the SiO(g) losses by keeping Si in the furnace. Condensation affects the furnace operation by influencing the charge permeability and the silicon yield. However, accumulation of condensates clogs the furnace and makes the operation difficult. Laboratory scale experiments on condensation gave SiC-SiO_x core-shell nanowires (with $x \approx 2$) and a Si-SiO₂ condensation as products. The Oxide-Assisted Growth mechanism can explain the mechanism of formation of the nanowires. On the other hand, no mechanism has been explained yet for the Si-SiO₂ condensate.

The main goals of this work are four. First, to characterize the condensates with new techniques such as XPS and TEM, make hypothesis on their mechanism of formation, and compare them to industrial samples. Second, to know their temperature of formation and their contribution to clogging, and how these intervals depend on the experimental parameters related to the industrial process. Third, to estimate the potential application of condensation as a SiO(g) capture method, by quantifying the condensation yield and the relative amount of each condensation product. Fourth, find the kinetic constant and the rate of reaction dependence on available surface, temperature and SiO(g) content in the gas phase.

Condensates are produced in two different setups, which differ in size but are based on the same principle. In the bottom zone of the crucible, a mixture of SiO(g) and CO(g) is produced by heating Si-SiO₂ or SiO₂-SiC pellets. The composition of the gas is changed by injection of an inert gas (He or Ar). The gas produced in this way flows upwards towards a condensation zone. Here, a particle bed will capture the condensates. The material and the particle size distribution of the substrates is changed in different experiments. Condensation continues for an established reaction time, while the gas temperature is fixed. In the smaller scale setup, the offgas is also collected for qualitative compositional analysis, to detect the time during which gas production and condensation occurred. In the larger scale setup, the gas composition is calculated after a mass balance.

Two main condensates are produced. The first is a SiC-SiO_x compound, which assumes a blue or white color on the substrates. EDX, SEM and TEM revealed entangled SiC-SiO_x core-shell nanowires. TEM and XRD revealed the presence of 3C-SiC in the core, and amorphous silica in the shell. The condensation substrate and the temperature do not affect the composition of the nanowires. The condensates generate between 900 and 1810°C and $p_{\text{SiO}} = 0.53-0.99$. Blue layers tend to form at lowest (900-1200°C) and highest temperatures (1750-1810°C). White layers are richer in SiO_x nodules on the nanowires. The mechanism of formation proposed is based on the Oxide-Assisted Growth theory. First, SiC and SiO_x islands form a seed on the substrate. The lateral growth of the seed is terminated by the formation of the shell layer and the droplet at the top of the nanowire. Once the lateral growth is finished, the nanowire grows vertically, along the (111) direction typical of 3C-SiC. During vertical growth, the SiO_x coating might change from a uniform coating to a bead-like structures. SiO_x is liquid thanks to the exothermic reaction heat of condensation, which locally increases the temperature, and the melting point depression of the nanometric system. Finally, the growth continues until the temperature is too low, or SiO(g) is not reaching the droplet.

The other condensate is a thick, brown and strong crust, generated between 1350-1800°C and $p_{\text{SiO}} = 0.58-0.99$. SEM and TEM analysis revealed micrometric silicon spheres dispersed in a silica matrix. XPS, XRD and TEM revealed 3C-SiC nanocrystals, located at the sphere borders. The separation into Si and SiO₂ starts already in the gas phase, while SiO(g) molecules interact to produce (SiO)_n molecular clusters with Si-Si and Si-O-Si domains.

The interaction with the surface breaks the unstable Si-Si-O bonds, producing Si, SiO₂ and SiO_x. Si interacts with CO(g) to form SiC nanocrystals at the sphere's borders. The reaction is spontaneous for the largest and coldest Si spheres, according to thermodynamic calculation. Prolonged heating of brown condensates will push Si out of the condensate, leaving a porous grey layer containing porous silica. While cooling, Si spheres dilate and crack, creating nanometric-sized cracks filled with liquid silicon. Part of the silica matrix recrystallizes from amorphous into cristobalite during cooling.

The experimental parameters influence the temperature of condensation and the clogging of the crucibles. The condensation substrate does not affect the condensation and clogging intervals, unless it melts and creates further clogging. This is the case for quartz substrates, which soften from ≈1600°C and above. A longer holding time will transform the condensates located at higher temperature (1750-1800°C) into SiO(g) and CO(g), while clogging the system at lower temperatures. Condensates clog the furnace at lower temperatures when increasing the added He(g) or Ar(g) gas flow, or by producing a gas richer in SiO(g). The temperature of the produced gas affects the position of the temperature gradient and the clogging crust thickness, but it is believed to not affect the temperature of formation of condensates. A narrow particle size distribution makes the gas flow easier through the charge bed, clogging the system at lower temperatures and developing a larger condensation interval, at longer times. Most of the condensate are distributed in the temperature interval 1400-1700°C, in correspondence of the clogging intervals.

A mass balance was computed for the experiments for both setups. Only ≈20% of the initial gas producing pellets turns into condensate. The rest is lost by interaction with the graphite crucible or escapes the system as off-gas. The SiC-SiO_x condensates make between 60-100% of the total condensates weight. The partial pressure decreases slowly through the condensation zone, because of the low amount of condensates produced. A gas richer in SiO(g) tends to produce more Si-SiO₂ condensate, as the driving force for condensation is higher with increasing SiO(g) content in the gas. Metallic Si can make up to 16% of the condensates mass. It was concluded that condensation does not occur at equilibrium, after comparing the p_{SiO}-T conditions of the experiments with the p_{SiO}-T equilibrium conditions for condensation reactions.

The reaction rate was modelled for the white SiC-SiO_x condensate, to find the activation energy and the frequency factor for the reaction. The rate is assumed to be directly proportional to three terms: the available surface for condensation (*A*), the kinetic constant *k*(*T*) and the driving force. *A* is estimated from the charge bed particle size distribution. The kinetic constant *k*(*T*) follows the Arrhenius equation. The driving force is defined as the difference in p_{SiO} during the experiments minus the p_{SiO} at equilibrium conditions (p_{SiO} – p_{SiO,eq}). The frequency factor and the activation energies for *k* are respectively between 10³-10⁷ g cm⁻² s⁻¹ and 250-300 kJ/mol, between 1315-1750°C.

The rate of reaction increases with temperature until it reaches a maximum at ≈1600°C. This temperature corresponds to the zone where most of the white condensate is produced. After 1600°C, the gas production reaction starts to prevail, and less condensates are produced. Above 1810°C, the gas is stable, and the condensation rate drops to zero. The same trend is followed by the driving force for condensation. The rate is faster in the earlier stage of condensation, as the substrate is irregular and accommodates more SiO_x and SiC nanoclusters. The maximum rate is obtained in correspondence of the clogging intervals (1400-1700°C).

Sammendrag

Kondensasjon av SiO(g) er kombinasjon av to reaksjoner i silisiumprosessen. Den første er interaksjonen mellom SiO(g) og CO(g). Den andre er reaksjonen mellom to SiO(g) molekyler. Disse to reaksjonene foregår i lavtemperatursonen i silisium- og ferrosilisiumovner. Kondensasjon er spontan i disse industrielle prosessene mellom 1400-1800°C, ifølge termodynamikk, industrielle utgravinger og pilotforsøker. Begge reaksjonene er eksotermiske, og produktene deres bidrar til en lavere SiO-tap, med å holde Si i ovnen. Kondensasjon påvirker ovndriften ved å endre tetthet til råmaterialer og silisiumutbytte, men akkumulering av kondensat tetter ovnen opp og gjør at ovndriften blir mer vanskelig. På labbforsøk ble det fant to kondensater: det ene består av SiC-SiO_x core-shell nanotråder (med $x \approx 2$), mens det andre er et Si-SiO₂ kondensat. Den Oxide-Assisted Growth mekanismen kan forklare dannelsen av nanotråder, men mekanismen til Si-SiO₂ kondensat har ikke blitt forklart ennå.

Denne avhandlingen vil greie fire hovedmål. Første, å karakterisere kondensater med nye teknikker, som XPS og TEM, å lage hypoteser om deres dannelsesmekanismer, og å sammenligne prøvene fra forsøker med forskjellige industrielle kondensatprover. Andre, å måle temperaturområder hvor kondensatene dannes i, å finne hvor mye kondensater påvirker oppetting av silisiumovnen, og hvordan disse temperaturområdene endrer seg i forhold til viktige industrielle parametre. Tredje, å beregne potensialet til kondensasjon som gassfangstmetode med å kvantifisere kondensasjonutbytte og mengde av dannet kondensat. Fjerde, å beregne kinetiske konstanter og sammenhengen mellom reaksjonshastigheten og overflate, temperatur og SiO(g) partielltrykk i gassfasen.

Kondensater ble produserte i to forskjellige oppsett, som har to forskjellige størrelser, men som fungerer med den samme prisippelen. I det nedre rommet i digelen blir SiO(g) og CO(g) produsert ved å varme Si-SiO₂ eller SiO₂-SiC pellets. Sammensetningen av gassen er justert med å tilsette en inertgass (He eller Ar). Gassblandingen flyter oppover mot kondensasjonsområdet i det øverste rommet i digelen. Her kondenserer gassen på en partikkelbed. Materialen til partiklene og partikkelstørrelsen i partikkelbed endres mellom forskjellige forsøk. Forsøker fortsetter på en bestemt tid, mens temperaturet til gassen ble fikset over hele forsøket. Sammensetningen til gassen er analysert i det mindre oppsettet, for å estimere hvor langt gassproduksjonen og kondensasjon har foregått. I det største oppsettet skal sammensetningen til gassen beregnes etter en massbalanse.

To kondensater ble produsert. Den første er en SiC-SiO_x blanding, som har et blått eller hvitt farge. EDX, SEM and TEM viste et innviklet nett av SiC-SiO_x core-shell nanotråder. TEM og XRD viste 3C-SiC i core, og amorf silika i shellfasen. Verken kondensasjonoverflaten eller temperature påvirker sammensetningen til nanotrådene. Kondensatene ble funnet mellom 900-1810°C og $p_{\text{SiO}} = 0.53-0.99$. Det blå kondensatet dannes på de laveste (900-1200°C) og de høyeste temperaturene (1750-1810°C). Det hvite kondensatet inneholder mer SiO_x nodules enn det blå. Den foreslåtte dannelsesmekanismen er basert på Oxide-Assisted Growth teorien. Først, SiC og SiO_x islands danner en seed på substratet. Seeden gror i diameter fram til shell-fasen dekker core-fasen, og et dråpe dannes på toppen av nanotrådet. Når seeden er grodd horisontalt, gror nanotrådet vertikalt, langs den typiske retningen (111) for 3C-SiC. Under vertikal vekst kan SiO_x fasen omformes fra en uniform belegg til en bead-like struktur. SiO_x kan flyte på grunnen av den eksotermiske reaksjonen, som øker temperaturet lokalt, sammen med en reduksjon i smeltepunktet, som er typisk for nanometriske systemer. Til slutt, nanotrådet fortsetter å gro fram til at temperature er altfor lavt, eller til at gassen ikke inneholder nok SiO(g).

Det andre kondensatet er tjukt, brunt og sterkt, og ble fant mellom 1350-1800°C og $p_{\text{SiO}} = 0.58-0.99$. SEM og TEM viste mikrometriske silisiumsfærer spredt i en silikamatrikse. XPS, XRD og TEM viste 3C-SiC nanokrystaller, plassert på grensene til sfærene. Separasjonen i Si og SiO₂ kunne allerede begynt i gassfasen, mens SiO(g) molekyler danner (SiO)_n clusters med silisium og silika områder. Samspillet med overflattet bryter de ustabile Si-

Si-O forbindelser og danner Si, SiO₂ og SiO_x. Si reagerer med CO(g) og danner SiC nanokrystaller ved sfærenes grenser. Reaksjonen er spontan for de største og kaldeste sfærene, ifølge termodynamiske beregninger. Hvis brun kondensat varmes videre, skal Si fjernes av kondensatet, og grå porøs silika forblir. Mens kondensatet avkjøles, kan Si utvide og danne nanometriske sprekker, som blir fylt med flytende silisium. Silikamatriksen skal delvis omkrystalliseres til kristobalitt under avkjøling.

De eksperimentelle parametrene påvirker temperaturområdene for kondensasjon og opptetting i diglene. Materialen i partikkelbed påvirker verken temperaturområdene eller opptetting, med mindre materialen smelter seg og tetter diglene videre. Dette skjer for kvarts partikler, som mykgjøres over ≈1600°C. Med en lengre reaksjonstid skal kondensatene i de høyeste temperaturene (1750-1800°C) reagere til SiO(g) og CO(g) og tettes diglene ved lavere temperaturer. Kondensatene tetter diglene ved lavere temperaturer også når mengde tilsatt inert gass øker, eller med å produsere en gass som inneholder mer SiO(g). Temperaturen til gassen påvirker temperaturgradienten i digelen og tjøkkelse til det tette området, men den antas å ikke påvirke temperaturområdene for kondensasjon. En smal størrelsesfordeling gjør at gassen strømmer raskere gjennom partikkelbed. Diglen blir derfor tettet på lavere temperaturer og i et breiere temperaturområde, men senere i tid. Mesteparten av kondensater finnes i temperaturintervallet 1400-1700°C, der diglene vanligvis tettes opp. Massbalansen ble beregnet for alle forsøker i begge oppsetter. Bare ≈20% av pellets i gassproduksjonsområdet omformer seg til kondensat. Gasstap skyldes av reaksjonen mellom SiO(g) og grafittdigelen, eller med SiO tap fra digelen som avgass. Det SiC-SiO_x kondensatet gjør opp til 60-100% av kondensatene. SiO-partielltrykket minker sakte med temperatur, siden mengde kondensater er lavt. En gass som inneholder mer SiO(g) produserer mer Si-SiO₂ kondensat, siden den drivende kraften for kondensasjon øker med mengde SiO i gassfasen. Metallisk Si kan gjøre opp til 16% av kondensater. Etter å ha sammenlignet p_{SiO}-T betingelser for forsøker og likevekt for kondensasjon, ble det fant at kondensasjon ikke foregår på likevektsbetingelser.

Reaksjonshastigheten ble beregnet for det hvite SiC-SiO_x kondensatet, for å finne aktiveringsenergi og frekvensfaktor til reaksjonen. Reaksjonshastigheten antas å ha en direkte sammenheng med tre parameter: den tilgjengelige overflaten for kondensasjonen (*A*), den kinetiske konstanten *k*(*T*) og den drivende kraften. *A* er beregnet etter partikkelstørrelsen til partikkelbed. Den kinetiske konstanten *k*(*T*) antas å følge Arrhenius-lov. Den drivende kraften er forskjellen mellom p_{SiO} i forsøkene og p_{SiO} på likevektsbetingelser (p_{SiO} - p_{SiO,eq}). Frekvensfaktoren og aktiveringsenergien ble henholdsvis beregnet til 10³-10⁷ g cm⁻² s⁻¹ og 250-300 kJ/mol, i temperaturintervallet 1315-1750°C.

Reaksjonshastigheten øker med temperatur fram til en maksimum på ≈1600°C, der mesteparten av kondensater ble produsert i hver forsøk. Etter 1600°C er gassdannelse fremhersket, og en mindre mengde kondensat blir produsert. Når temperaturet går over 1810°C, blir gassen stabil, og både reaksjonshastigheten og den drivende kraften går mot null. Reaksjonshastigheten er høyere tidligst i forsøkene, siden partiklene i partikkelbed har en uregelmessig overflate. Den høyeste reaksjonshastigheten finnes der diglene er mest tette (1400-1700°C).

Introduction

General background

Si production process

Silicon is found in nature as quartz, which is ≈99% pure silicon oxide. The affinity between silicon and oxygen makes the Si-O bond stable. The aim of the reduction reaction is to break the Si-O bonds, to form elemental silicon. To do so, carbon is added to the process as coke, charcoal or woodchips. Despite carbon sources act as a reductant, silicon and carbon atoms will also interact easily, forming Si-C bonds. Solid bonds are involved in the process. The production of silicon is therefore energy demanding.

The demand of silicon in the global market is increasing, together with the variety of applications. Silicon is mostly used as an alloying element in steel and aluminum production. Norway has a strong silicon industry, because of high amounts of available energy. Energy in this country is easily available, since it comes from accessible and cleaner sources such as hydropower and natural gas. Therefore, other energy-consuming metallurgical processes, such as Al and Mn production, are also a consistent part of the industry of this country. Silicon is also used in the chemical, solar and electronic industry.

Nowadays silicon is extracted from the ore by a metallurgical process, shown in Figure 1. In the process, there are six compounds involved. SiO₂ (quartz) and C (coal, charcoal, woodchips) are the starting raw materials. Si(l) and CO(g) are the final main products. SiO(g) and SiC are the intermediates of Si production. An industrial furnace can be divided into a low temperature zone and a high temperature zone.

In the low temperature zone, between 1400 and 1800°C, SiO(g) and CO(g) act as reactants [1]–[9]. Reaction 1 involves both the two gas species, giving silica and silicon carbide as products. Reaction 2 is called disproportionation of SiO(g), which will form silicon and silica [10]–[13]. Both reactions are strongly exothermic (as calculated by the software HSC Chemistry®). At 1700°C, it was calculated that ΔH°₁=-1406 kJ/mol, whereas ΔH°₂=-620 kJ/mol. The products of Reaction 1 and 2 are referred to as condensates, according to industrial terminology.



In the same temperature interval as for Reaction 1 and 2, the ascending SiO(g) meets the carbon-containing particles. The result is the conversion of carbon to SiC and CO(g) (Reaction 3).



In the high temperature zone, Reactions 1 and 2 are reversed. Reaction -1 and -2 are called gas production reactions. Their products are SiO(g) and CO(g). Reaction -2 is also called synproportionation of SiO(g). Most of the produced SiO(g) will react with SiC, to produce Si(l) and CO(g), according to Reaction 4. Part of the gas mixture will however ascend to the colder areas and trigger Reaction 1-3. Reaction 4 is the actual silicon production reaction. The temperature should be at least 1810°C for Reaction 4 to occur [1], [14]. Normally the silicon production reaction temperature is around 2000°C in industrial furnaces. The purity of metallurgical grade silicon (MG-Si) lies between 96-99 wt. %.

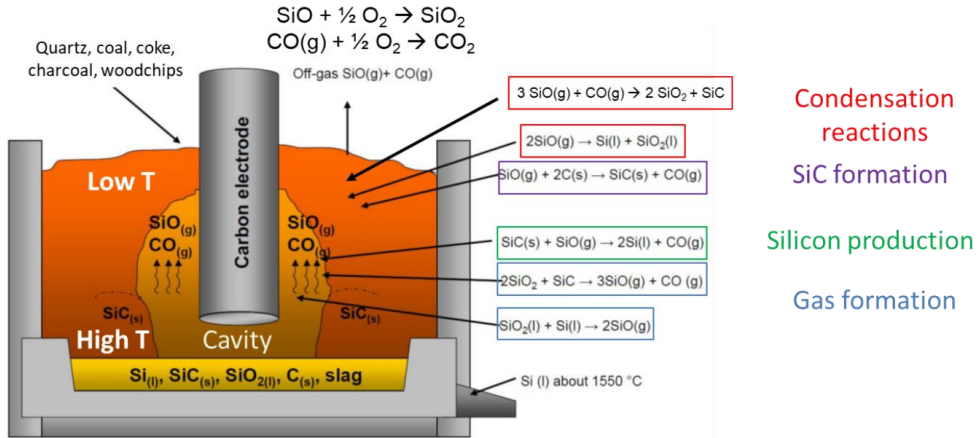


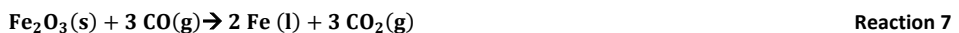
Figure 1: Overview of reactions involving SiO(g) and CO(g) in a silicon furnace. Revised after Ringdalen [13].

A dedicated microsilica production unity is located outside of the furnace, at temperatures lower than those in the low temperature zone. A portion of the gas would not be involved neither in condensation, nor in SiC or Si production, and hence leave the furnace as SiO(g) and CO(g). These residual gases are collected in the offgas system after oxidation with ambient air. SiO(g) will be oxidized to solid SiO₂ in micrometric-sized spheres (Reaction 5). Due to this peculiar microstructure, such product is commercially called Microsilica®. Microsilica is a by-product of silicon production. It is used as a filler material for concrete, or in refractory materials [1], [14]. CO₂(g) emissions will come from CO(g) oxidation (Reaction 6).



FeSi production process

For the FeSi process, the reactions are the same, but an iron source is added to a desired extent. The amount of iron source in the raw materials controls the final composition of the alloy produced. The iron is added to the process either as steel scrap or mill scale. The amount of iron in the metal is regulated by the following reaction (Reaction 7):



The CO₂ produced by Reaction 7 reacts with the carbon materials above 1000°C (Reaction 8). The product of this synproportionation reaction is CO(g). Reaction 8 is called Boudouard reaction. This is a strongly endothermic reaction, which influences the energy balance in the FeSi process.



The main difference between the FeSi and Si process is the addition of iron oxide in the process. The FeSi process is known to have lower SiO(g) losses [1], [14]. In fact, the addition of iron to the charge increases the charge mass flow per unit silicon. Condensation reactions are enhanced at the low temperature zone. The furnace might experience clogging issues, but SiO(g) is retained more effectively in the furnace. Besides, the activity of silicon in the melt is reduced, thanks to the presence of elemental iron. Silicon reduction can be carried out at lower temperatures. Despite iron reduction is an endothermic process, the addition of iron gives a lower energy consumption compared to the silicon process [1].

Condensation in industrial furnaces

The term **condensation** is used in the industrial world, for Reactions 1 and 2. The word is chosen to give a simple description of the event, but it does not sound correct from a physical point of view. It was thought that condensation would occur the same way as dew forms on grass, in winter times. In fact, “condensation” typically defines a phase transition. However, it was found that “condensation of silicon monoxide” consists of chemical reactions between different gas species. From now on, the reactions between SiO(g) and CO(g), or between SiO(g) molecules, will be referred to as “condensation reactions”.

One cannot overlook gas condensation when thinking about the mass balance of the silicon process. The mass of condensates in an industrial system can be estimated with the help of thermodynamics and mass balance calculations. Such equilibrium calculations would not be accurate for two reasons. First, condensation reactions occur out of equilibrium conditions. Second, the temperature gradients inside a furnace are very steep and difficult to control. It would be great to know how much, why, how and when SiO(g) condenses, but quantifying the mass of condensation products is unfeasible in an industrial furnace.

The offgas mixture contains high amounts of energy and silicon. SiO (g) and CO(g) will move upwards to colder temperatures, and trigger Reactions 1-3. The products of Reactions 1-3 will be a part of the descending raw materials. They will be recirculated in the process, by descending to the high temperature zone. These three reactions prevent Si losses to the offgas, giving a higher silicon yield. Energy will also be saved, as the reactions are strongly exothermic. To minimize energy and silicon losses, the gases should not leave the high temperature zone.

SiO condensation glues the descending raw materials into a crust, which will surround a cavity in the high temperature zone. Excessive condensation enhances the mechanical properties of the crust, which might result in a decreased silicon yield. If the crust blocks the descending charge, no silicon can be produced. In addition, the constrained gas in the cavity will increase its pressure and pierce the cavity roof by creating channels, leading to hot gas blows through the outer zone. Such blows lead to lower reactivity between the gas and the charge. The main detrimental effect of the blows is the direct loss of SiO(g) and energy. The off-gas temperature is higher when channeling occurs, because the gas comes straight from the high temperature zone without being cooled through the colder raw materials. It is required to regulate the charge permeability, to adjust the silicon yield and the mechanical property of the crust.

Three strategies have been proposed by the industrial process and by literature, to tune the mechanical properties of the crust:

- **Tune the particles size distribution and composition of the charge**, which affects channeling and permeability. Permeability defines how much free space there is between the charge lumps. Unreacted molten quartz will also decrease the charge permeability, and lead to the creation of gas channels. Woodchips are added to increase charge permeability. Their quantity is limited, as they have a great effect on charge permeability. A charge containing a low amount of fines is preferred, to enhance the silicon yield due to increased channeling.

- **Annihilating the temperature gradients in the furnace** minimizes condensation, by keeping temperatures at which condensation would not occur. This could be done by setting a temperature above 2000°C in the whole furnace. However, the process will not be convenient because of the high electricity cost. An industrial furnace measures 4 m in height and about 10 in diameter. Such temperature conditions in a large space need high amounts of energy.
- **Changing the furnace design.** Vangskåsen [15] suggests to implement a taller furnace design to promote a wider temperature gradient. However, the stoking procedure will be difficult to carry out.

To “stoke” means to poke the crusts in the low temperature zone, to favor the charge flow to the high temperature zone. Figure 2 shows where and how stoking is performed in a silicon furnace. Stoking is a necessary operation in industrial production. It is an inevitable cost in terms of human resources, money and time, as condensation and crust formation always occur. By stoking, an operator can influence condensation, gas composition, crater temperature, chemical reactions in the process and durability of the furnace [1]. Many specialized operators perform stoking several times daily, by using an automatic or manual stoking machine. Stoking is performed every 30-75 minutes [1]. According to Schei et al., one must not perform stoking at fixed times during his own shift, but rather observe continuously how the furnace operates before acting. An operator can stoke either too much or too little. These situations are called overstoking and understoking respectively. Both show advantages and disadvantages.

When overstoking, the charge permeability is increased. The main consequence will be the loss of SiO(g) and energy. Despite silicon-containing materials would flow downwards to the high temperature zone, a higher amount of SiO(g) is lost. The other disadvantages of overstoking are the higher electrode position and energy consumption. A higher amount of solid materials will accumulate at the bottom of the furnace. The electrode will shift to a higher position. Some minor electric arcs will be located higher in the furnace, interacting with the crust instead of the silicon pool, for example. In other words, the electric power is not applied where it is supposed to be applied.

Understoking would also create problems to the process. If the permeability is not reduced enough, materials would not access the furnace inner zone. Lack of SiC in the high temperature zone will reduce the extent of the silicon production reaction (Reaction 4). The cavity roof is mechanically strong, but the gas pressure increases quickly thanks to Reactions -1 and -2. High SiO(g) pressure would pierce the cavity roof by creating hot gas blows. Gas blows correspond to a local increase in pressure between charge pieces. Johansen et al. [16] measured an overpressure up to 50 mbar in a submerged arc furnace, at the crater zone. This is only 5% higher than the atmospheric pressure, but enough to trigger sudden, dangerous and unpredictable gas losses.

It can be concluded that condensation is:

- **Fundamental**, for the energy and mass balance. Condensation plays an important role in keeping energy and Si inside the furnace;
- **Detrimental**, since it causes clogging problems, if not controlled properly;
- **Unavoidable**, since it occurs in the temperature and pressure ranges typical of the Si and FeSi production process. The only way to avoid condensation would be to change the thermodynamics of the system by changing the chemistry of the raw materials (for instance, by choosing a raw material that does not contain oxygen).

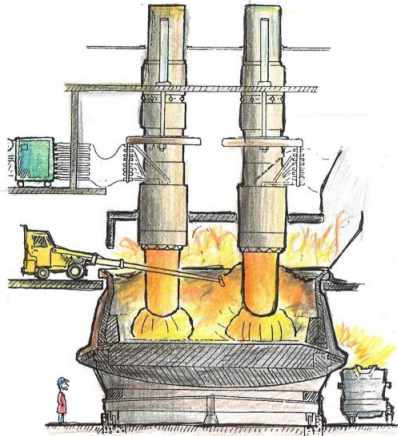


Figure 2: Stoking procedure in silicon furnaces [17].

Objective for the thesis

This thesis is a part of a larger project, in collaboration with industry. The research project is called “SiNoCO₂” (EnergiX program of the Research Council of Norway, project nr. 269431). The name stands for “Silicon process without direct CO₂ emissions”. The project owner is Elkem Technology ASA, with NTNU, SINTEF and NORCE as partners. The technology developed from this project can be integrated soon in the Norwegian industry, hopefully giving more benefits to both cost and environment.

The project works simultaneously on two different goals. The first main goal of the process is to create a closed silicon process, which is potentially CO₂-negative. CO(g) is consumed in one of the condensation reactions, therefore the gas emissions can potentially disappear. On the other hand, SiO(g) would either condensate, or react completely with the carbon charge. The second aim of the project is to verify if the open process can be operated at 100% silicon yield. In this way, the energy losses related to the offgas will disappear, and the process can be more energy and cost efficient.

The main aim of the research is spreading light in the black box of the silicon furnace, regarding the condensation process. The research works on this event are limited. There are discrepancies between the theories formulated on the results at laboratory, pilot and industrial scale. For example, when extracting samples from an industrial scale furnace, it is difficult to determine exactly if we are looking at a condensate, or at a piece of reacted charge mixed with SiC. The objectives covered by this thesis will be:

- **Identify** the condensates, and characterize them
- **Compare** the laboratory results of the characterization with the industrial samples
- Recognizing the **temperature of formation** and **partial pressure ranges** where the condensates form
- Set up a **mass balance** for condensation reactions
- Estimate the temperature intervals where **clogging** occurs.
- Analyze the **effect of experimental parameters**, related to the silicon production process, through a laboratory scale setup.
- Find out more about the **kinetics** of the condensation reactions, from proposing mechanisms of formation, to calculating activation energy and frequency factors.

Thesis outline

The thesis is divided into four parts.

Part 1 describes the background knowledge. Thermodynamic analysis is fundamental to understand how the Si-C-O system works. Two literature reviews on condensation will follow. The first will cover the condensation phenomena in industrial and pilot scale systems, whereas the second will show the results of characterization, mostly coming from laboratory scale experiments. Finally, the last section will cover previous hypothesis on mechanisms of reactions and thermodynamic surface effects.

Part 2 will analyze the experimental techniques used and the evolution of the experimental setup. A detailed plan will discuss the evolution and the choices taken while developing the experimental method. It was decided to use two different setups. The first setup was optimized for measurements of temperature of formation, mass balances and partial pressure calculations. Condensates were also extracted for characterization by different techniques. The analysis on the second setup focused on the effect of particle size distribution and clogging, besides confirming the previously measured temperatures of formation and partial pressure calculations.

Part 3 and 4 collects the results from the experiments and modelling. The first two sections are dedicated to microstructural and compositional characterization of each condensation product. The third section will collect microstructural characterization of samples from industrial Si and FeSi plants. The fourth and fifth section gives an overview of the temperature of formation and clogging, and the effect of the experimental parameters on these two events. The last section will quantify how much condensate was produced in each experiment and present the results of the reaction rate modelling. The modelling of reaction rate and the calculation of the p_{SiO} in the crucible is explained in part 4.

Part 5 links the laboratory data with the introduction knowledge. The mechanisms of formation are theorized, based on the microstructural changes and hypotheses from previous literature. Thermodynamic calculations will estimate the variation in partial pressures of SiO(g) after condensation has occurred. There is a relationship between condensation yield, condensates distribution in the sample, driving force for condensation and condensation rate. The other reactions occurring in the crucible are shortly discussed to make an overview of the mass balance. It is also discussed how to deal with condensation during industrial practice.

1. Theoretical background

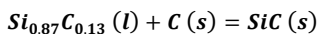
A. Thermodynamics and kinetics

Now that the silicon production process has been analyzed and explained, it is time to understand how thermodynamics work in the Si-O-C system. The sub-systems present are C-O, Si-O and Si-C. C(s) and CO(g) are the only two compounds relevant for silicon production in the C-O system. When it comes to the FeSi process, some CO₂ may however be present for the iron oxide reduction. O₂(g) is often assumed to be present in small amounts in the industrial process, below the charge level. In the Si-C system, a specific focus will be given on the solubility of C in Si and to the polytypes of SiC. The Si-O system will also inquire the solubility of Si and O, as well as the interaction between Si and SiO₂. A large scientific debate has been open on the existence of solid SiO since the beginning of 20th century. Thermodynamics can explain why SiO cannot exist in a stable solid state, but only as a metastable mixture of Si and SiO₂. The equilibrium diagrams will describe the formation of Si, SiC, SiO₂, CO(g) and SiO(g) at equilibrium. The thermodynamics of the Si-C-O system will clarify when and where the reactions of the silicon process can occur and define the phase spaces in silicon production.

Si-C system

Phase diagram

Kleykamp and Schumacher [18] assessed the Si-C system, between 1400 and 3000°C (Figure 3). After confirming that the crucibles were not influencing the results of the gas measurement by producing other vapor species than CO(g) and CO₂(g), DTA and X-ray diffraction and microanalysis were carried out on samples at different compositions. SiC is the only intermediate solid compound in the system. A eutectic point is found between Si and SiC at 1413°C and 0.02 at. % C. A peritectic reaction is present at 2830°C and can be associated to Reaction 9 [18]



Reaction 9

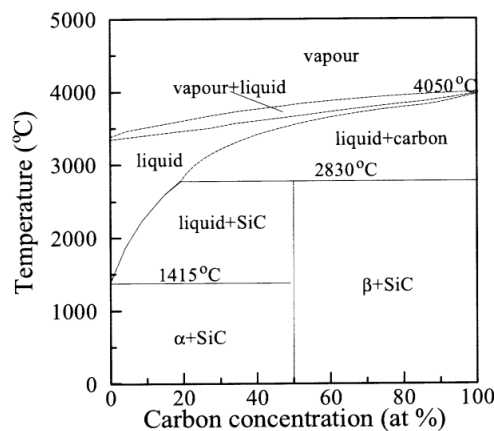


Figure 3: Si-C phase diagram at atmospheric pressure. α and β stand for solid solutions [18].

Olesinski and Abbaschian [19] assessed a phase diagram with different results from Kleykamp and Schumacher [18] (Figure 4). There is a eutectic point at 1404±5°C. The solubility limit of C in Si (s) in the temperature range

from 1200 to 1400°C is 10^{-3} to 10^{-4} at. % C, and C dissolves substitutionally in Si. At the eutectic temperature, the dissolved carbon is between 7-18 ppm, and up to 190 ppm if the sample is slowly cooled [20]. They also discussed the peritectic point found at $2545 \pm 40^\circ\text{C}$. The peritectic transition involves SiC and liquid containing 27 at. % C. SiC and C will always be two separated phases below the peritectic point, so their activities can be assumed to be equal to 1 ($a_{\text{C}}=a_{\text{SiC}}=1$). This is also a common assumption in industrial furnace conditions, even though C and SiC are not at their standard state. The atmospheric boiling point of Si is 3227°C , and the sublimation of C at 3798°C .

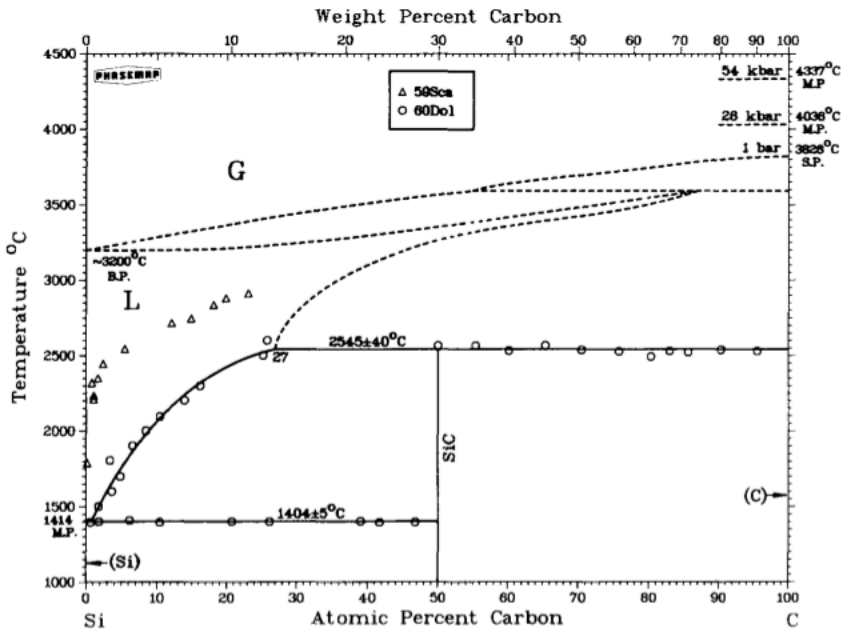


Figure 4: Si-C phase diagram at atmospheric pressure [19].

SiC polytypes

SiC is a very important solid intermediate in silicon production. Its crystalline structure has been studied thoroughly, since it changes often with temperature and pressure. Specific temperature and pressure ranges define the existence of different crystalline structures. Such structures have been called polytypes, and up to now there have been found about 250 different ones. Different polytypes of SiC differ only in the number of distinct basic units, i.e. the number of layers per unit cell, and the way these connect to each other. A basic unit is a Si_4C (or CSi_4) tetrahedron, shown in Figure 5.

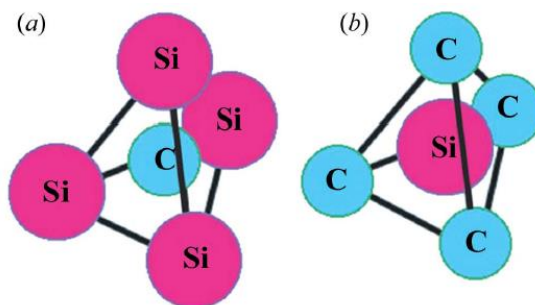


Figure 5: Simple tetrahedral coordination of Si and C atoms: (a) Si_4C tetrahedron, C atom located at the tetrahedrons centroid and Si atoms at its vertices and (b) C_4Si tetrahedron, Si atom located at the tetrahedrons centroid and C atoms at its vertices. [21]

Different SiC polytypes can be considered as the modification of the piling up of layers of SiC_4 (or CSi_4) tetrahedra. These tetrahedra are arranged in such a way that all the atoms lie in parallel planes on the nodes of regular hexagonal networks. Figure 6 shows the stacking sequences of tetrahedron layers for the four most common SiC polytypes, and the respective unit cell of each polytype described. At atmospheric pressure, these modifications can be simplified into two main structures, known as α -SiC and β -SiC [19], [21]. A specific polytype is identified by a number and a letter. The number stands for the number of tetrahedra layers in the unit cell, whereas the letter identifies the type of symmetry (C = cubic, H = Hexagonal, R = Rhombohedral).

A cubic structure can be generated by stacking tetrahedron layers with the same relative orientation. This polytype is called 3C-SiC (a) and belongs to the β -SiC group. The lattice parameters are $a_0 = b_0 = c_0 = 4.359 \text{ \AA}$. A unit cell contains four Si and four C atoms, and its theoretical density is $3.216 \times 10^3 \text{ kg m}^{-3}$. The structure resembles the diamond-type structure of carbon, but every other carbon atom is replaced by silicon atom. Each carbon atom is tetrahedrally bonded to the four nearest carbons with adjacent tetrahedral bonds in a 60° -staggered conformation. The 3C-SiC has a face centered cubic (FCC) lattice but an asymmetric unit cell. In fact, the unit is constituted by one Si atom placed at the fractional coordinates $(0, 0, 0)$ and one C atom at $(\frac{1}{4}, \frac{1}{4}, \frac{1}{4})$, as for the lattice arrangement in the diamond structure.

When every second tetrahedral layer is antiparallel to the preceding layer, the polytype belongs to the α -SiC group. The two main SiC polytypes with hexagonal symmetry are named 4H-SiC (b) and 6H-SiC (c). The 4H-SiC polytype crystallizes in the hexagonal system with a wurtzite-type crystal structure. Its lattice parameters are $a_0 = b_0 = 3.073$, $c_0 = 10.053 \text{ \AA}$. The two Si atoms placed at the fractional coordinates constitute the asymmetric unit $(0, 0, 0)$ and $(\frac{1}{3}, \frac{2}{3}, \frac{1}{4})$, as well as two C atoms at $(0, 0, 0.1875)$ and $(\frac{1}{3}, \frac{2}{3}, 0.4375)$. Therefore, the primitive hexagonal cell consists of four Si and four C atoms (total of eight atoms), resulting in a density of $3.239 \times 10^3 \text{ kg m}^{-3}$.

The 6H-SiC polytype differs from the 4H in the number of layers in the unit cell, but both have the same symmetry. The lattice parameters are $a_0 = b_0 = 3.073$ and $c_0 = 15.079 \text{ \AA}$ respectively. The asymmetric unit consists of three Si atoms located at $(0, 0, 0)$, $(\frac{1}{3}, \frac{2}{3}, \frac{1}{6})$ and $(\frac{1}{3}, \frac{2}{3}, \frac{5}{6})$, whereas the three C atoms located at $(0, 0, \frac{1}{8})$, $(\frac{1}{3}, \frac{2}{3}, 0.29167)$ and $(\frac{1}{3}, \frac{2}{3}, 0.95833)$. In this case the primitive hexagonal cell contains six Si and six C atoms (total of 12 atoms), resulting a density of $3.213 \times 10^3 \text{ kg m}^{-3}$.

Finally, a rhombohedral polytype 15R-SiC is stable after subsequent packing of 15 SiC tetrahedra layers (d). The lattice parameters of the cell are $a_0 = b_0 = 3.073$, $c_0 = 37.700 \text{ \AA}$ respectively. A unit cell is made of three primitive cells. Each primitive cell contains five Si atoms located at $(0, 0, 0)$, $(0, 0, 0.1333)$, $(0, 0, 0.4)$, $(0, 0, 0.6)$ and $(0, 0, 0.8667)$ and five C atoms at $(0, 0, 0.05)$, $(0, 0, 0.1833)$, $(0, 0, 0.45)$, $(0, 0, 0.65)$ and $(0, 0, 0.9167)$. Thus, the

rhombohedral unit cell contains 15 Si atoms and 15 C atoms (total of 30 atoms), with density of $3.220 \times 10^3 \text{ kg m}^{-3}$.

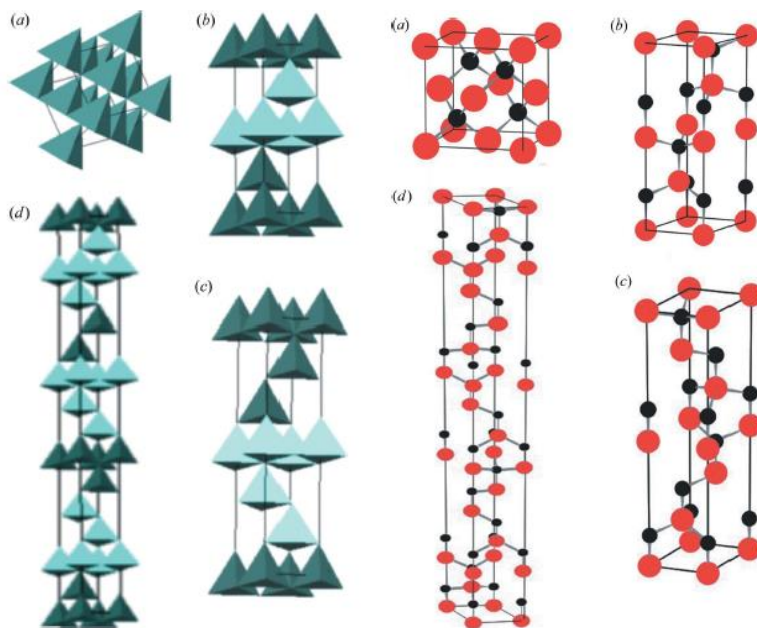


Figure 6: Left: Stacking sequences of tetrahedron layers of four most commonly occurring SiC polytypes at atmospheric pressure: (a) 3C-SiC; (b) 4H-SiC; (c) 6H-SiC; (d) 15R-SiC [21]. Right: unit cell of four SiC polytypes: (a) 3C, (b) 4H, (c) 6H and (d) 15R. Si atoms = red, C atoms = black [21].

3C-SiC is the most stable polytype at temperatures below 2500°C [22], [23]. β -SiC can decompose at atmospheric pressure to C and liquid Si at 3076°C , if the nonmixing of C and Si is assumed, i.e. if their entropy of mixing is equal to zero. The transformation of SiC to a mixture of Si and C occurs however at lower temperature because of positive entropy of mixing [19]. Concerning the stability of α -SiC, some authors claimed to observe the transformation from β -SiC to α -SiC at temperatures above 2000°C [22], [23], implying that α -SiC is more stable at higher temperatures.

The Si-O system

The compounds of interest for this system are Si, SiO(g) and SiO₂. The main aim of the silicon process is to convert SiO₂ into Si. The temperatures in the furnace environment are high, and often trespass the melting point of silicon ($\approx 1417^\circ\text{C}$ [24], [25]) or silica ($\approx 1723^\circ\text{C}$ [25], [26]). The behavior of Si and SiO₂ above the melting point of silicon is of fundamental importance in silicon production. Si and SiO₂ are generally immiscible, but small amounts of oxygen can be dissolved in silicon.

Johnson and Muan [27] assessed the phase diagram of the Si-O system. The result is shown in Figure 7. Si and SiO₂ were mixed at different ratios, and heated at temperatures between 1375°C and 1710°C . Silicon was found in liquid state between 1409 - 1415°C . The eutectic point is located at 1405°C , after extrapolating the experimental data and plotting a phase diagram. Tridymite is already stable at 1375°C and transforms into cristobalite at about 1470°C . However, the actual presence of the tridymite structure is debated nowadays. Cristobalite and the liquid will stay stable until 1700°C . Two immiscible liquids will form above 1700°C . Si and

SiO₂ were the only stable phases found during the experiments. According to Johnson and Muan [27], when the mixtures were quenched from molten state, the silicon-rich liquid was evenly distributed in the silica phase. In this work, many equilibrium curves are dashed, meaning that further experimental work was needed to explore the boundaries of the phase spaces. The authors assume that a SiO(s) phase could disproportionate into Si and SiO₂ during sample quenching.

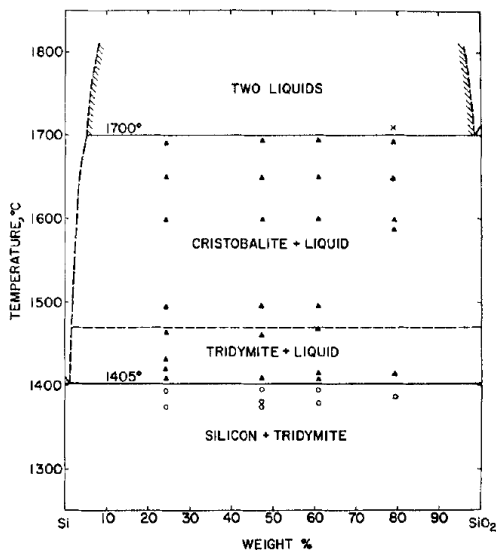


Figure 7: Phase diagram of Si-O system, experimentally assessed at temperatures below 1710°C. [27]

Hallstedt [28] assessed the thermodynamic model for the Si-O system by CALPHAD, when investigating the phase space above 1700°C. The phase diagram is computed after the Gibbs energies for (Si), SiO₂ and SiO(g) (Figure 8). (Si) stands for a solid solution of Si and O. Table 1 summarizes the reactions occurring in the system. L1 represents a silicon liquid solution, which has an oxygen molar fraction in the order of $\chi_o = 10^{-5}$. L2 is the silica-rich liquid phase. Figure 9 shows the calculation proposed by Hallstedt. The results fit well with the experimental data on oxygen solubility from various authors [28].

Table 1: Reactions in the Si-O system, revised after [28].

Reaction	Type	Temperature (K)	Mole fraction of O in each phase		
L1 → (Si) + Tridymite	Eutectic	1687	$6.3 \cdot 10^{-5}$	$4.5 \cdot 10^{-5}$	0.66667
L2 → L1 + Cristobalite	Monotectic	1994	0.66664	$2.6 \cdot 10^{-4}$	0.66667
Gas → L1 + L2	Gas Disproportionation	2130	0.5	$4.1 \cdot 10^{-4}$	0.66662

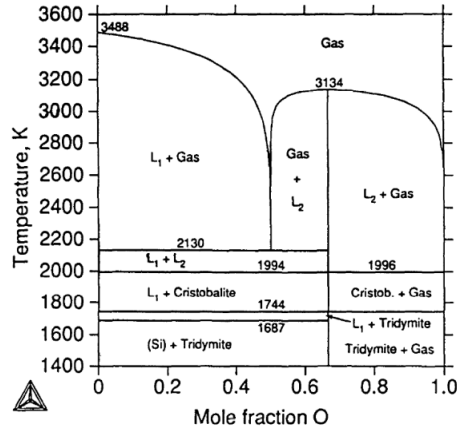


Figure 8: Si-O phase diagram computed by Hallstedt [28]

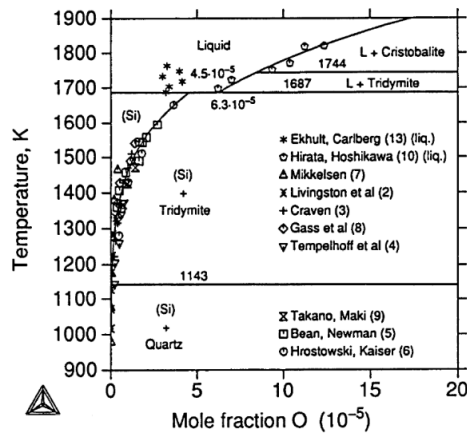


Figure 9: Oxygen solubility in silicon liquid solutions. Computed data and comparison with experimental works. References on the graph are from Hallstedt [28].

Schnurre et al. [29] studied also the Si-O phase diagram and oxygen solubility. The results are shown in Figure 10. At 1687 K (1413°C), solid silicon transforms into a liquid solid solution with oxygen. A eutectic phase appears at 1686.997 K, with $X_O^{(Si)} = 4.73 \cdot 10^{-5}$ and $X_O^{liquid} = 5.42 \cdot 10^{-5}$. Cristobalite also becomes liquid at 1998 K (1725°C). The “eutectic” point at 2134 K (1861°C) will have $X_O = 6.2 \times 10^{-4}$. At this composition, the stable phases are liquid silicon, gas and solid silica.

Figure 10a was developed by Schnurre et al. [29] after computation of the diagram from the Gibbs energy data. The compositional range of the oxygen solubility fits well with experimental points from previous works (Figure 10b). A eutectic point is located 0.007 K above the melting point of pure silicon. As the oxygen content increases, oxygen is both dissolved in the Si-rich phase as well as creating SiO₂ molecules or vacancies. The liquid silicon-rich solution will be in equilibrium with solid silica.

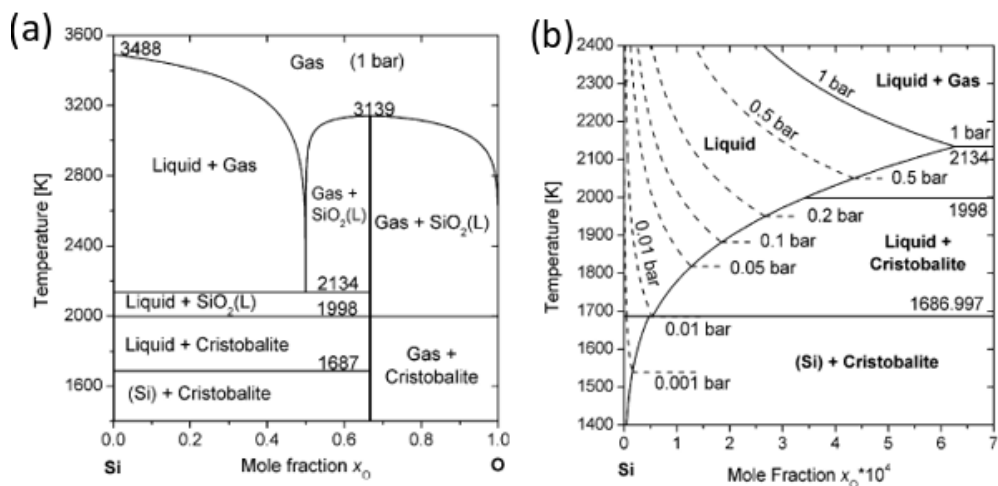


Figure 10: Calculated Si-O phase diagram at 1 bar, at high (a) and low (b) oxygen content. [29]

Thermodynamics stability of silicon monoxide

The scientific debate on the stability of solid SiO

Most papers postulate that SiO₂ is the only stable solid phase containing oxygen in the Si-O system (if excluding that Si can also dissolve ppm levels of oxygen). Other elements in Group 14 have stable oxide species with different oxidation states than +4 for the cation (e.g.: GeO, SnO, Pb₃O₄). There is hence a large disagreement in the scientific world about the existence of a solid SiO phase.

Mabery reported the existence of a solid compound with composition SiO, in 1887. He observed condensation products in an electric arc furnace [30]. Mabery states that SiO came as a greenish-yellow vitreous substance at the interface between the charcoal and silica particles. Reaction 10 was proposed as the SiO(s) generating reaction.



Reaction 10

In 1907, Potter claimed to have performed the first laboratory synthesis of SiO(s) [31]. A mixture of Si and SiO₂ was heated at 1700°C. The condensed material disproportionated into Si and SiO₂ after annealing. Potter recognized the compound from X-ray spectroscopy and electron diffraction analysis. The main clue was a characteristic diffraction ring corresponding to a spacing of 3.6±0.05 Å in the SiO electron diffraction analysis, which stands in the middle between Si (3.12 Å) and cristobalite (4.04 Å) [32]. According to Potter [31], the ring is quite broad and alone, so it should be easy to spot. The material produced by Potter had insulating properties, both electrically and thermally. Potter's work was not yet an evidence proving the existence of a bulk SiO crystalline phase.

Schnurre et al. [29] inspected a commercial SiO powder by X-ray diffraction (XRD), condensation experiments and annealing, to assess ΔG° for amorphous solid SiO. XRD gave a spectrum similar to that of silica glass, but slightly shifted to higher 2θ values. After annealing between 1000°C and 1450°C, the characteristic peaks of Si and cristobalite showed higher intensities than before. It was not possible to define a specific SiO peak that does not belong to neither Si nor SiO₂, after annealing.

From a thermodynamic point of view, a solid phase with composition SiO is less stable than a phase containing Si and SiO₂. Schnurre et al. [29] inquired the thermodynamic stability of SiO, assuming it to be amorphous. Amorphous SiO (SiO(am)) is not a homogeneous phase, because it is made of Si, SiO₂ and SiO_x nanometric domains. The subscript x is used, since the stoichiometry of the oxide phase is uncertain at nanometric sizes. Previous works also refer to SiO_x and not to SiO₂ [33]–[39]. SiO(am) cannot be classified as a heterogeneous mixture neither, since a large portion of atoms belongs to the intermediate phase domain, made of SiO_x suboxides.

Experimental evidence showed as well that a Si-SiO₂ mixture would be more stable than an amorphous SiO solid phase. This means that the Gibbs energy of SiO(am) must be higher than the average between the Gibbs energies of Si and SiO₂. Reference states for silicon is considered as the diamond solid structure, whereas liquid silica has its liquid state as reference. The inequality was assessed to be valid in the temperature range of 300-1723 K.

$$G_{SiO}^{am} > \frac{1}{2}(G_{Si}^{0,dia} + G_{SiO_2}^{0,L}) \tag{Equation 1}$$

The inequality was confirmed after calculation (Figure 11) and experimental measurements. The decomposition reaction of commercial SiO was analyzed between 300 and 1723 K. Condensation from the gas phase was observed at temperatures below 1652 K. Sublimation of SiO(am) occurs at 2070 K.

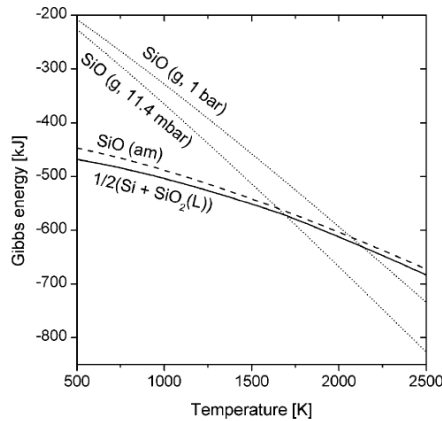


Figure 11: The Gibbs energy of SiO(am) compared to that of a mixture of 1/2 (Si+SiO₂(L)) and to SiO(g) at two different pressures [29].

SiO(s) is a well-known compound for the industrial world. A commercial product called “solid SiO” is widely used in glass and metallurgical industry. Its applications cover optical coatings and semiconductor device. To produce SiO(s), a Si-SiO₂ mixture is heated until it produces a vapor. Then the vapor is condensed on a substrate, and the black SiO powder is collected. The production process of SiO(s) is similar to the disproportionation reaction of SiO(g) shown in the industrial silicon process chapter.

Alternative and simple characterization techniques are used to identify SiO and distinguish it from a simple Si-SiO₂ mixture. Looking at the melting point can help to identify SiO [40]. If a lower melting point is registered, solid SiO might be present, instead of a Si-SiO₂ mixture. Acid leaching by HF can also help in distinguishing the two compounds, according to the extent of leaching [40]–[42], since SiO₂ dissolves in HF. The density of the compounds does not really help at distinguishing SiO from the mixture [40].

SiO(s) decomposes after annealing at different times and temperatures. According to Brewer and Russell [40], metastable SiO disproportionates between 400 and 700°C. Hass [43] found that SiO films disproportionate by

annealing over 600°C. Besides, heating up solid SiO at 650-700°C for 2 hours can cause increase in weight due to oxidation [44].

We have seen that some authors claimed that SiO(s) could be generated in a similar range of temperatures as SiO(g) disproportionation [31], [32], [40], [42]–[44]. According to these works, a phase transition occurs instead of SiO disproportionation. However, thermodynamic assessment and advanced characterization technologies showed that SiO(s) is metastable, and that it consists of a nanometric scaled mixture of Si and SiO₂ [41], [45]–[48]. Segregation into nanoclusters of Si and SiO₂ already starts in the gas phase, and this reflects in the formed solid phase [49].

To conclude, a material which is called solid SiO cannot exist in its stoichiometric form. It would rather be a nanometric scale mixture of Si, SiO_x and SiO₂, resulting in a Si:O ratio very close to 1. The only stable phase in which SiO exists is as a gas phase. Thermodynamics of condensation should be evaluated at the light of this statement.

Atomistic modelling of SiO and the concept of suboxide

The common point between the works discussed so far is the lack of justification of the existence of the new oxidation state Si²⁺. All of them assume its presence from theoretical computations. Besides, the amorphous nature of SiO implies that diffraction techniques can be misleading, since they provide information about modelled crystalline structures. Characterization techniques such as Transmission Electron Microscopy (TEM) and electron diffraction have given a boost to the comprehension of SiO structure, helping at developing models including even the presence of Si⁺ and Si³⁺ valence states.

The concept of suboxide SiO_x must be introduced when debating the nature of SiO. The discussion should start from what happens at the atomic scale, by comparing the configuration of the Si-O and Si-Si bonds in Si, SiO_x (x: 0<x<2) and SiO₂. Three models have been computed so far, one continuously improving the other after constructive criticisms. They are called random-bonding (RB), random-mixing (RM) and interface-cluster mixture (ICM) model.

Philipp [45] proposed the random-bonding (RB) model after studying optical properties of non-crystalline SiO_x-films. The main assumption by the author is that each Si atom has a tetrahedral coordination to *n* oxygen atoms and (4-*n*) silicon atoms. Each value of *n* has its own statistical probability of existence *p*(*n*), which the model computes for different oxides and suboxides. This results into a random distribution of Si-O and Si-Si bonds in the material. Philipp uses absorption data to justify his model. Amorphous SiO films have 20 times lower absorptivity compared to amorphous silicon films. By assuming that absorption and Si coordination are related, the results match well with the model, where only one Si atom out of 16 (6.25%) is bond to four Si neighbors in solid SiO. The experimental results agree with the theory proposed. Table 2 resumes the computed values of *p*(*n*) for the RB-model.

Table 2: *p*(*n*) computed by the RB-model [45]

<i>n</i>	SiO ₂ (%)	SiO _{1.5} (%)	SiO (%)	SiO _{0.5} (%)	Si (%)
4	100	31.64	6.25	0.39	0
3	0	42.19	25.00	4.69	0
2	0	21.09	37.50	21.09	0
1	0	4.69	25.00	42.19	0
0	0	0.39	6.25	31.64	100

The RB-model cannot justify the missing characteristic peaks of SiO_2 and other sub-oxides, which appear in crystalline state, since each value of n has also its own probability of existence. Besides, the optical absorption varies with the annealing temperature of the film. Shifting of the absorption edges occurs if the extent of coordination between Si and O varies, i.e. based on the value of x in the SiO_x phases formed. Tempkin [41] includes these criticisms, formulating the random-mixture model.

The RM-model is based on calculation of peak areas for radial distribution functions (RDF) of SiO_x . The theory is compared with the calculations from Yasaitis and Kaplow [46]. Tempkin computes $p(n)$ by assuming tetrahedral Si coordination and absence of O-O bonds. The bond length and angles are based on properties of amorphous silicon and SiO_2 . Figure 12 resumes the five configurations T_i available for the Si-O-Si bonds. In this work, $p(n)$ is referred as C_i . i varies from 1 to 5 and has the same meaning as n . For example, $i=1$ equals $n=0$ (Si), and $i=5$ equals $n=4$ (SiO_2). Tempkin compares the RDF of commercial silicon monoxide and a microscopic Si+ SiO_2 mixture, finding consistency between them.

The model is inconsistent with an RB-model and a large-scale phase mixture. Yasaitis and Kaplow [46] showed that there should be two resolved peaks for Si and SiO_2 , if the material was a microscopic mixture into large clusters. A single peak is detected instead, justifying the mixture at the atomic level. Hydrofluoric acid leaching experiments on SiO presented by Holland [42] confirmed the nature of the mixture at atomic level. In fact, bulk SiO and SiO_2 are soluble in the acid, whereas Si is not. No criticism was moved to this model. However, it needs to be improved, since it does not justify why SiO does not react as a simple mixture of Si and SiO_2 , even if this is present at atomic scale.

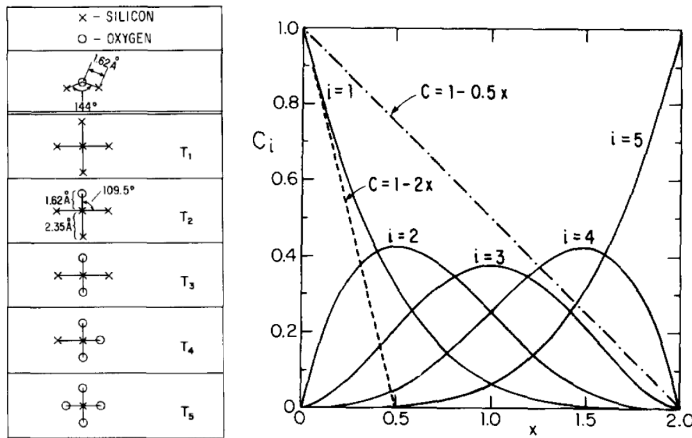


Figure 12: The five possible configurations assumed in the RM-model and their probability of existence as a function of x [41]

Ching [50] compares the random-network and random-mixture theories, by assessing atomic modelling calculation. The difference between the RM and RB-models is explained very simply in this paper. Starting from an amorphous-Si configuration, one can insert O atoms between each pair of Si atoms (Figure 13a). By rescaling the system to a cubic cell, the average density of the amorphous SiO_2 generated in this way should correspond to 2.20 g/cm^3 . Most likely, not all the available O sites can be occupied. In this way, SiO_x can be modelled. If the O sites are randomly taken, we are looking at an RB-model (Figure 13b). If they are not, we are computing a RM-model (Figure 13c).

The bond distortion creates a configuration, whose energy must be reduced by a potential function, which can minimize the energy. By changing the stoichiometry of Si and O, i.e. the value of x , it was seen that an RB-model gives closer results to the experimental, when $x=1$. This openly contrasts with Temkin's RM-model. Ching observes flaws in Temkin's theories. For example, Temkin assumes a constant ideal value of the O-Si-O and Si-O-Si angle (109.5° and 144° respectively). Besides, the G_i values are significantly different from a statistical prediction. Lastly, the radial distribution function computed by Ching correspond to other experimental results from other references, especially when the sample contains defect centers such as O-O bonds.

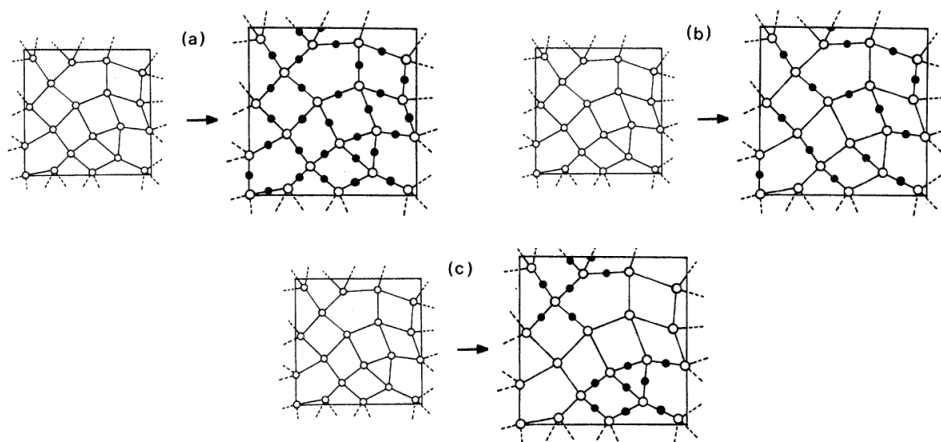


Figure 13: Schematic illustrations of obtaining initial configurations from the periodic model of amorphous Si: a) amorphous SiO₂; b) RB-model of SiO_x; c) RM-model of SiO_x [50]

Hohl et al. [47] investigated amorphous SiO utilizing diffraction, microscopy, spectroscopy and magnetometry methods. This allowed them to form a third model called interface cluster mixture model (ICM). The authors base their model mainly on the TEM analysis and pair distribution functions computed by Schulmeister and Mader [48], as well as from their own X-ray diffraction, TEM and XPS analysis. The interface cluster mixture model (ICM) states that SiO is a non-equilibrium state with three phases at different stoichiometry. Nanoclusters of amorphous SiO₂ (a-SiO₂) and amorphous Si (a-Si) are surrounded and connected by thin layers of SiO_x (Figure 14) The size of the nanoclusters ranges between 0.5 to 2.5 nm. Due to the small cluster size, the amount of SiO_x cannot be neglected. The interface layers can gather up to approximately 10 at. % of the total silicon involved. Siⁿ⁺ atoms in the lattice form the SiO_x. The authors tried to model the possible atomic interactions at the interface of two nanoclusters containing SiO₂-Si, SiO₂-SiO₂ and Si-Si. The generation of suboxides will give the atomic coordination schemes shown in Figure 14.

Since the existence of Si⁺ and Si³⁺ ions have not been widely discussed in the literature, no certain conclusions can be drawn about the efficacy of the proposed ICM model. So far, the ICM model looks like the most complete and exhaustive model for justifying the properties of solid SiO, but further confirmation in the experimental results is necessary.

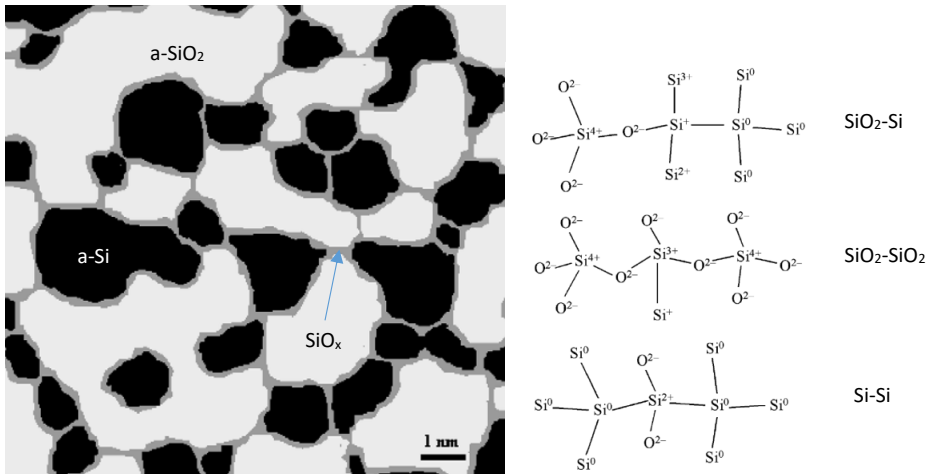


Figure 14: ICM model (left) and atomic bond configurations of SiO_x at different interfaces (right) [47].

Sugiyama et al. [51] studied the brown rims formed after exposing vitreous silica to silicon melts. They used Electron Spin Resonance (ESR) to analyze the bond types of the system. The spectra revealed the presence of dangling bonds $\bullet\text{Si}\equiv\text{Si}_3$, $\bullet\text{Si}\equiv\text{Si}_2\text{O}$ and $\bullet\text{Si}\equiv\text{SiO}_2$. The work suggests that the dangling bonds belong to the detected paramagnetic suboxide species in $\text{SiO}_{1.49}$. A sample of commercial silicon monoxide was analyzed. Its O/Si ratio is 1.04. The same signals were found for silicon monoxide. It was concluded that both the considered materials contain the same kind of dangling bonds, despite their different composition.

SiO_x clustering in the gas phase

According to the theories by Bromley et al. [49], it seems that Si, SiO_x and SiO_2 are already generated from segregation at atomic level in the gas phase. The authors studied a kinetic modelling for bottom-up growth of $(\text{SiO})_N$ nanocluster. This model could help understanding the mechanism of nucleation of nanostructured silicon materials, as well as $\text{SiO}(\text{g})$ nucleation in circumstellar conditions. They used classical nucleation theory (CNT) to inquire the ground states of nanoclusters at different values of N , with $N \leq 20$. They also obtained ranges of temperature and pressure for each isomer in the gas phase, and calculated nucleation rates. $\text{SiO}(\text{g})$ molecules can assemble into $(\text{SiO})_N$ clusters. The larger the value of N , the easier it will be to segregate.

Figure 15 shows the computed ground states for $N=1-20$ [49]. The red and grey atoms stand for oxygen and silicon respectively. Until $N=4$, the atoms are disposed only between Si-O-Si configurations, into ring structures. The ring structure is kept also for higher values of N . Above $N=4$, the structure becomes anisotropic. When $N=5$, the first Si-Si-O bond appears. Figure 16 shows the segregation phenomenon for $N=10$. Three regions will form in the molecule. The first will exclusively contain Si-Si bonds (orange). It will be called the Si-zone. An intermediate zone (green) will include Si-Si-O bonds. The last area is the largest, which includes Si-O-Si bonds (blue), typical of silica. It will be called silica-zone.

Segregation occurs into a Si_nO_n group and a Si_m group, with $N=n+m$. The Si_nO_n group comprehends both the silica and the SiO_x intermediate. In fact, the ratio between n and N is always smaller than 2. This ratio will tend to 2 as N increases. The molecular weight of the intermediate area will decrease with larger N . Silicon atoms would form tetrahedral structures by Si-Si or Si-O-Si bonds, rather than the more unstable Si-Si-O configuration. However, a certain number of Si-Si-O bonds is needed to dock the Si_m and the Si_nO_n groups.

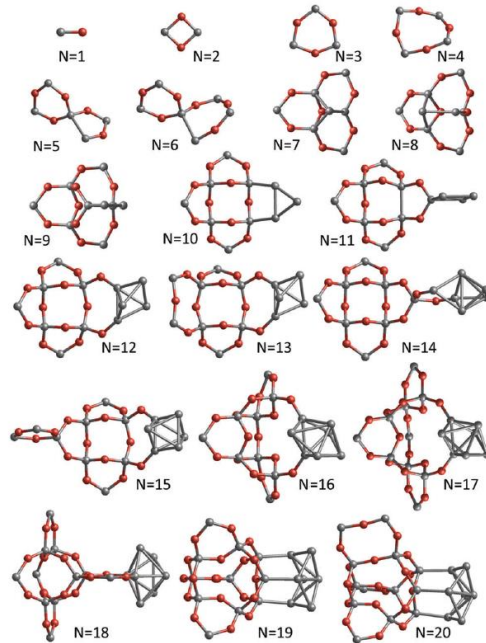


Figure 15: $(\text{SiO})_N$ nanoclusters ground states, and segregation into Si-area and silica-area. Element key: Red = Oxygen; Grey = Silicon [49].

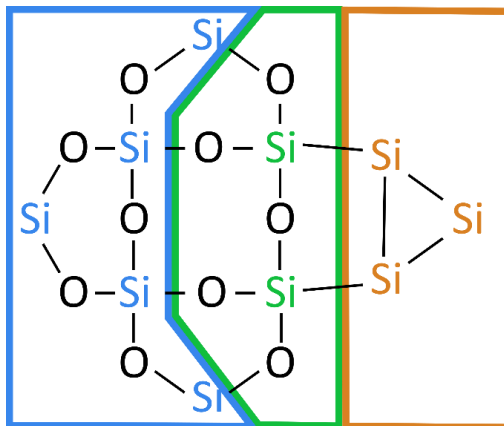


Figure 16: Si atoms belonging to the silica-zone Si_nO_n (blue), intermediate zone (green) and Si_m group (orange). Case for the SiO cluster with $N=10$. Revised after Bromley et al. [49].

Si-C-O system

A thermodynamic study of the Si-O-C system is assessed by discussing the coexistence of the following phases: gas, SiO_2 , SiC , Si and C. To define an invariant point, according to the Gibbs phase rule, four phases can be present at the same time at a constant pressure of 1 bar. Si and C cannot coexist, since SiC formation would be thermodynamically favored.

The equilibrium partial pressure of $\text{SiO}(\text{g})$ is useful to assess the gas composition at different temperatures in equilibrium with various phases. ΔG° for the reactions are available from the literature data of Schei et al. [1].

The gas is assumed to be made of SiO(g) and CO(g) only. The restrictions are applied on pressure ($p_{\text{tot}}=p_{\text{CO}}+p_{\text{SiO}}=1$). Temperature is the available degree of freedom. Once the equilibrium constants are found, the partial pressures of CO(g) and SiO(g) are calculated. The equilibrium constants are depending only on the pressure of the gas phase, since the activity of the solid phases is assumed close to 1. Solids are assumed to be pure, and the gas mixtures are considered ideal.

The Si-O-C system has two invariant points at equilibrium, with three condensed phases coexisting with the gas phase. SiO₂-C-SiC will coexist at 1512°C and $p_{\text{SiO}}=0.04$ atm (Figure 17). SiO₂-Si-SiC will coexist at 1811°C and $p_{\text{SiO}}=0.67$ atm (Figure 18). Experimental evidence of the invariant points is documented by Gjerstad [52]. The results are scattered. Therefore they should be interpreted as an approximate indication of equilibrium [1].

The invariant points are set in an equilibrium diagram, as shown in Figure 19. Below 1512°C, SiC formation will take place (Reaction 3). However, Reaction 1 and 2 can also occur below this temperature value, according to experimental results both at laboratory and industrial scale [1], [2], [5]–[8], [11]–[13], [53], [54]. Between the two invariant points, the SiO(g) will either react with CO(g) to produce SiC and SiO₂, or disproportionate to Si and SiO₂. Above 1811°C, SiO(g) and SiC will react to form Si(l) when p_{SiO} is larger than 0.67. A higher temperature gives lower equilibrium partial pressure of SiO(g) ($p_{\text{SiO,eq}}$). Silicon production can occur at lower SiO(g) partial pressures, if the temperature is larger than 1811°C.

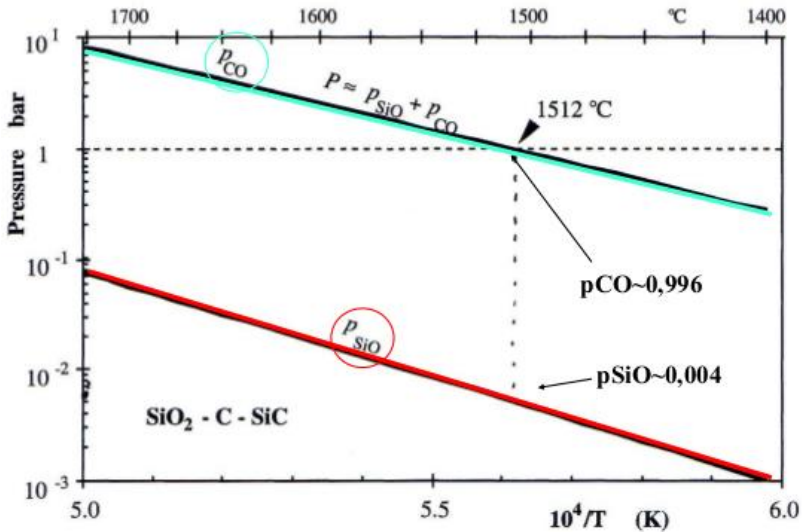


Figure 17: Invariant point computation for the SiO₂-C-SiC-gas system [1].

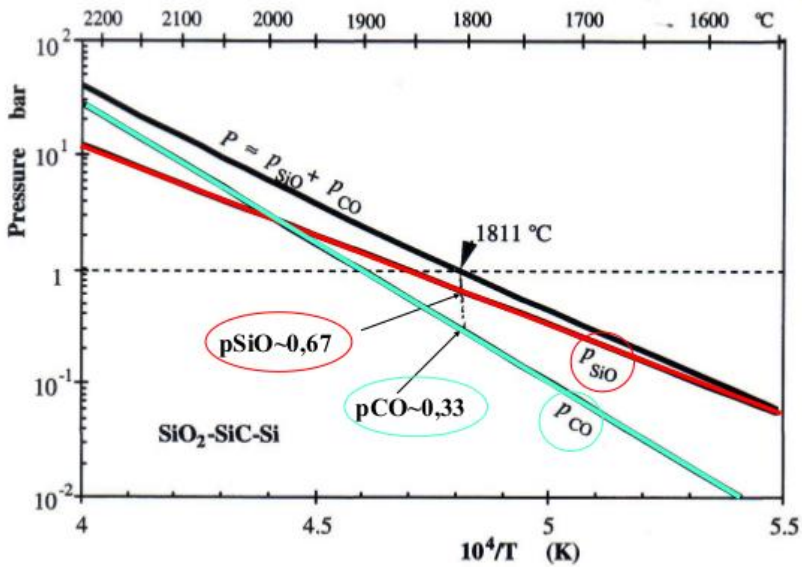


Figure 18: Invariant point computation for the $\text{SiO}_2\text{-SiC-Si-gas}$ system [1].

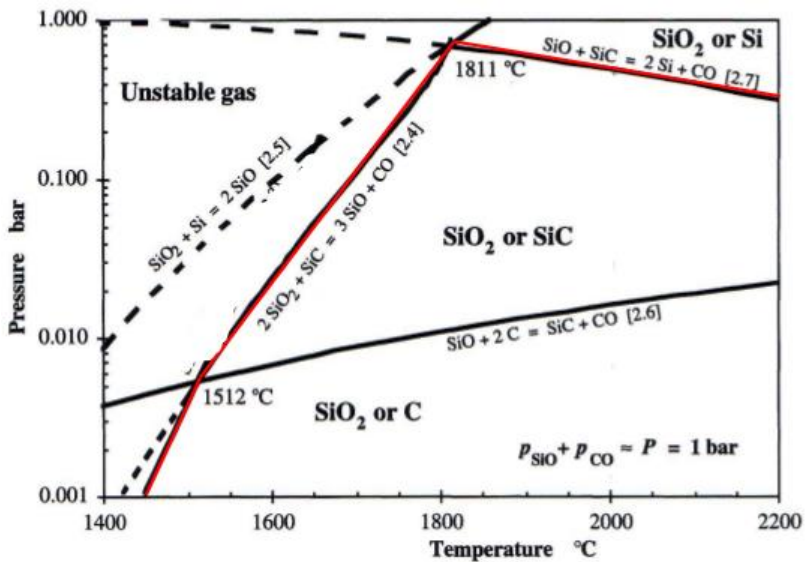


Figure 19: Invariant point assessment and $p_{\text{SiO}}(T)$ in the Si-C-O system [1].

B. Industrial and pilot scale condensates

In the industrial Si and FeSi processes, the furnace can be divided into a stoking crust, a crater crust and a side crust. The materials accumulated in the furnace take different names, according to their position and composition. Figure 20 shows their position inside a furnace. The stoking crust is located at the charge top. The crater crust is concentrated mostly at the center of the furnace, and at the cavity walls. The side crust covers the internal furnace walls, and it can extend sometimes up to the charge level. All these crusts contain condensates

of different kind. Most of the condensates are usually found in the stoking crust, but some of them have been recognized in zones above the crater crust or in the side crust.

There are two main types of condensates: the brown Si-SiO_2 and the white $\text{SiO}_2\text{-SiC}$ crust. The first one is typically brown or grey, whereas the second is white. Brown condensates are located outside the crater wall, and sometimes in the low temperature zone as well. The Si-SiO_2 mixture is generated in larger quantities in industrial silicon furnaces. The white condensate covers the zone below the charge top, usually at lower temperatures than the brown. A green mixture containing slag, SiO_2 and SiC is always detected in the side crust, and is often called “green condensate” [2], [7], [55]. It is however still unknown if this is really a condensate. The white and brown areas in Figure 20 show the results of the positions of the condensates in the excavation by Tranell et al. [56], with respect to the previously mentioned crusts.

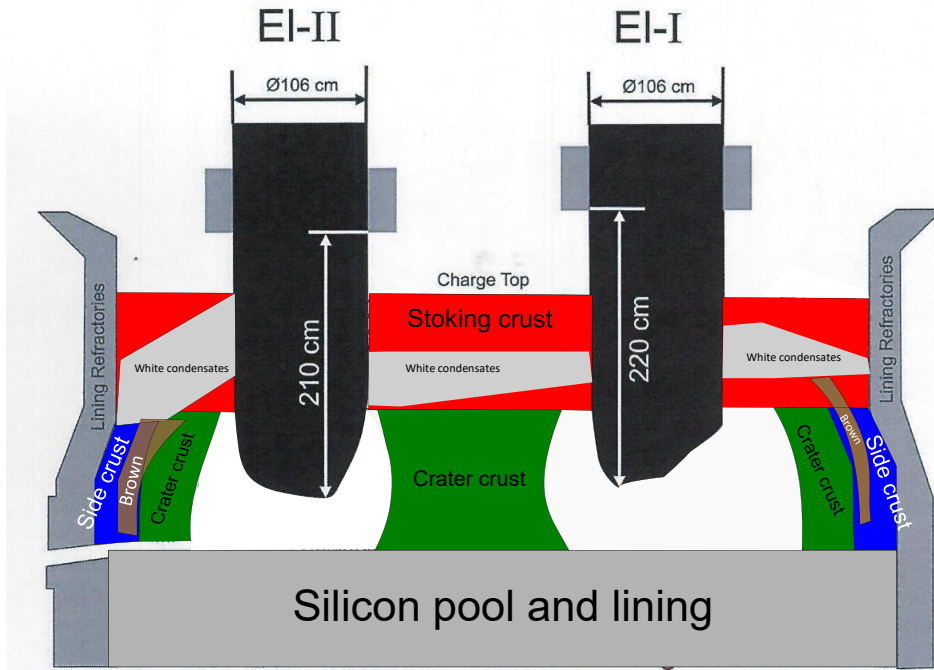


Figure 20: Crusts overview in silicon furnaces. Revised after Tranell et al. [56].

The condensation reactions occur in similar ways in both the FeSi and Si process. This section collects samples from both FeSi and Si furnaces. The temperature in the gas production zone in the FeSi furnaces would be slightly lower in FeSi furnaces, compared to the Si process. Moreover, the production of CO_2 by reduction of iron oxide will slightly reduce the content of SiO(g) in the chosen Si-C-O system. As a consequence, the gas composition and the invariant triple point (see the sub-chapter on the Si-C-O systems) do not change much while producing a FeSi75 alloy, rather than MG-Si. Therefore, it is expected that the amount of condensate would be lower in a FeSi furnace, but the composition of the condensates is similar between FeSi and Si furnaces.

Stoking crust

The stoking crust is a layer present at the top of the furnace. As the name suggests, this crust is placed where stoking occurs. This crust is rich in condensation products, unreacted charge and SiC . Its thickness ranges around 1 m from the charge top. Some stoking crust is also found close to the furnace walls. The numbers in Figure 21

refer to the samples described in this section. Brown numbers refer to Si-SiO₂ crusts, and white numbers to SiO₂-SiC crusts.

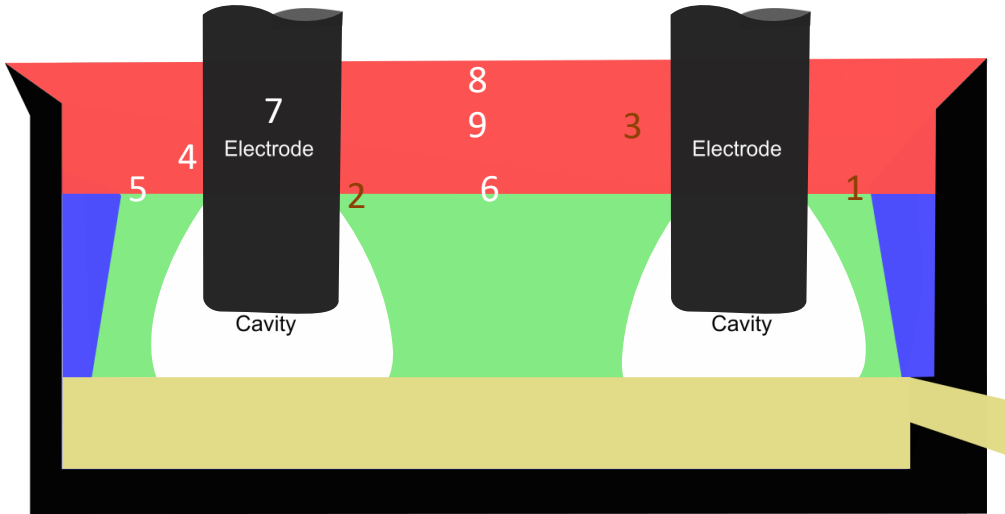


Figure 21: Positions of Si-SiO₂ (brown) and SiO₂-SiC (white) samples in literature. Positions estimated from [4],[7], [9], [55]–[57].

Si-SiO₂ mixtures

Sample 1 [4]. Figure 22 shows the typical microstructure of Si-SiO₂ condensates. Si spheres are spread in a SiO₂ matrix. The Si spheres size influences the color of the condensate. Smaller Si spheres are usually contained in brighter brown condensates. Most of the silicon is found at the edge of the sample. It is believed that Si was abandoning the SiO₂ matrix. Similar compounds were found in similar positions, among the charge lumps in the low temperature zone. [3], [9], [58].

Figure 22 shows also that some of the spheres are interconnected by small treads, also made of Si. The size of the spheres changes drastically in the sample. Two areas were formed, with different sphere sizes. The separation between Si and SiO₂ started earlier where the Si spheres are smaller.

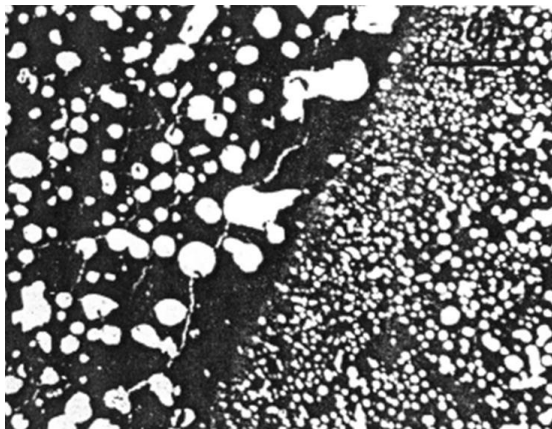


Figure 22: Sample 1, brown condensate pilot scale sample, magnification x300 [4].

Sample 2 [55]. This sample was collected close to the electrode. The sample was analyzed by Light Optical Microscopy (LOM), SEM and EPMA. LOM images reveal droplets dispersed in a matrix (Figure 23a). Points 1 and 6 correspond to the epoxy, 2 and 7 gave the composition of SiO_2 , and 8 showed high silicon content and no oxygen. This implies that the lighter phase is silicon, the grey phase is SiO_2 and the black is the epoxy (Figure 23b). The droplets size range between 1-20 μm . Few mm away from this area, the sample contained homogeneous silica with numerous cracks (Figure 23c).

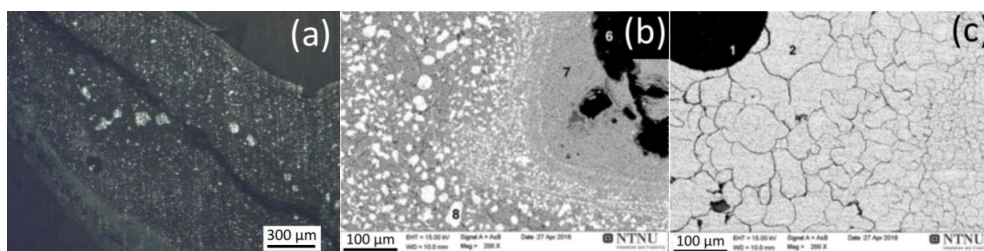


Figure 23: Sample 1 from Wacker furnace 1 [55] 1,6 = epoxy; 2,7 = SiO_2 ; 8 = Si.

Sample 3 [57]. A porous sample from the loose charge zone in Wacker furnace 4 contained Si and SiO_2 . Quartz is partially melted and covered by condensates, which are rich in silicon and FeSi droplets. The brown compound is easy to notice macroscopically. Silica is porous and rich in cracks, slag and Si/FeSi droplets (Figure 24).

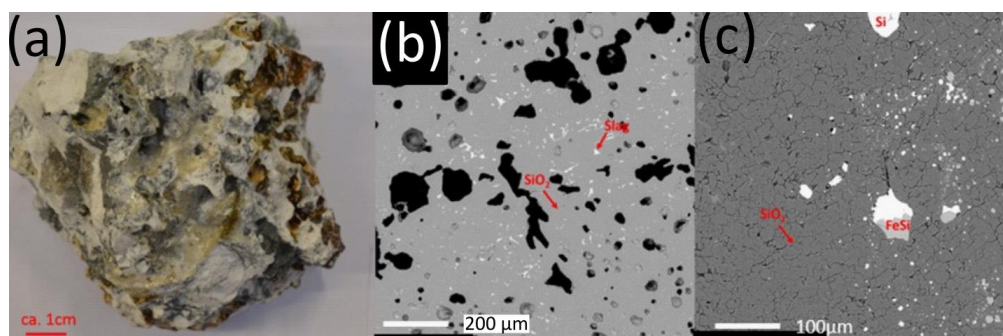


Figure 24: Macroscopic (a) and microscopic SEM pictures (b,c) of Si- SiO_2 sample from loose charge zone [57].

Elkem Thamshavn excavation [7]. Two more sample were extracted from the stoking crust zone. However, their position was not recorded. Both sample 5.1 and 16.2 show a brown SiO_2 -Si condensate layer deposited on a SiC particle. Si fills a minor portion of the SiC pores. A similar microstructure was also noticed by Vangskåsen [59], where Si has been formed in the SiC particles high up in the furnace.

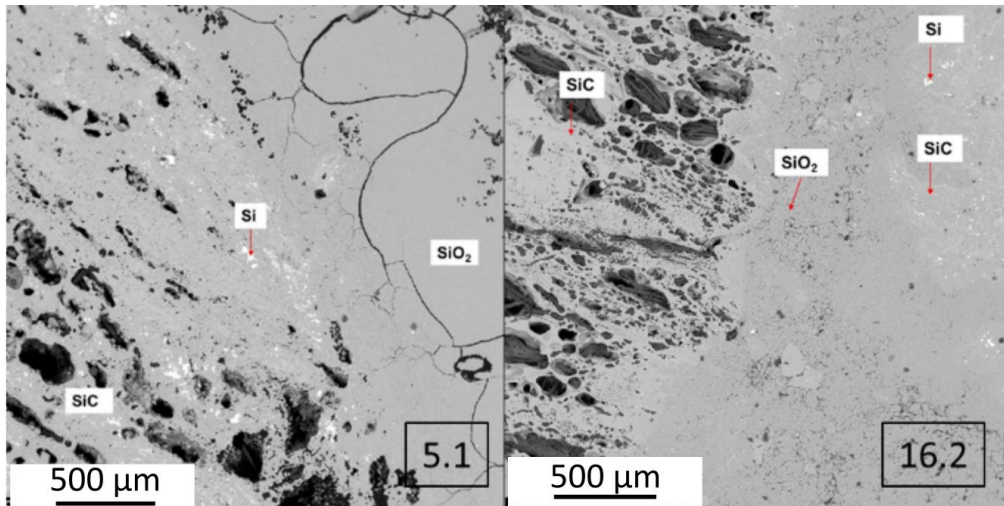


Figure 25: Microstructure of brown SiO_2 condensate [7].

SiO_2 -SiC mixtures

The SiO_2 -SiC mixtures consist of a SiO_2 matrix with SiC particles embedded in them. Their color is either white, blue or green. Tranell et al. [56] claimed the finding of a white crust close to the charge top. The SiO_2 matrix is often cracked. The size and the shape of the SiC phase changes according to the sample analyzed and the area. Schei [6] believed that the SiC particles in green condensates come from reaction between Si in the brown condensate and CO(g) . Figure 26 shows a piece of white stoking crust. It must be however remembered that it is not always easy to separate white condensate and molten quartz during excavation. The two compounds look very similar and can be easily mistaken.



Figure 26: Stoking crust containing molten quartz and condensate, extracted from a FeSi75 furnace [56].

Sample 4 [9]. A SiO_2 -SiC cotton-like, pale blue and white material occasionally covered the samples located in the low temperature zone of the furnace, at a height of 60-90 cm from the charge top [9]. Kurosawa et al. state that this compound contains cristobalite and SiC. The analysis could not confirm which SiC polytype is present, but β -SiC is supposed to be the main one. SiC is believed to be formed by sublimation and recrystallization from the gas phase.

Sample 5 [55]. Sample 1 and Sample 5 are different zones of the same sample. They are shown on the opposite side of Figure 20, to avoid misunderstandings. Figure 27 shows the SEM image collected from the sample. The coal was totally transformed to SiC at this position in the furnace. The black area in the picture is epoxy (point 1), and the grey is SiC and SiO₂ (point 2). The samples was a porous carbon piece originally, and SiO₂ has filled partially its pores as well [55].

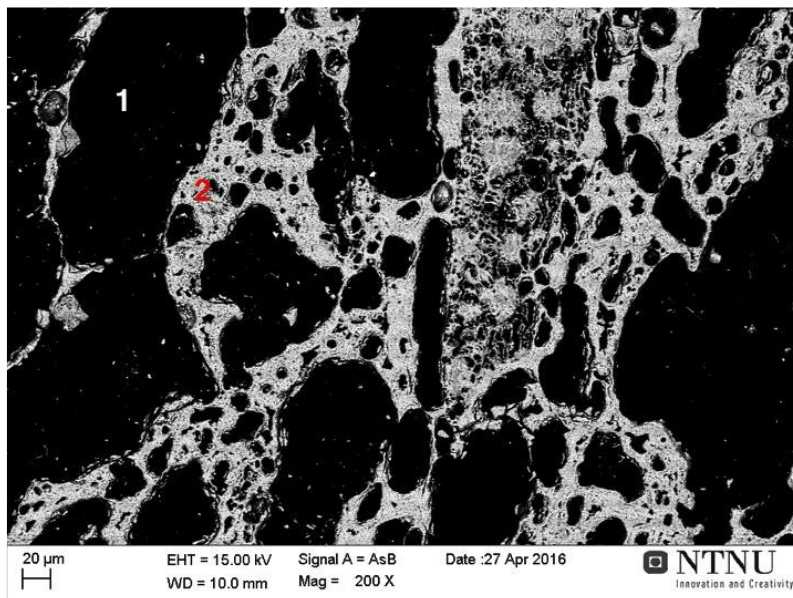


Figure 27: SEM analysis of sample 1[55]. Point 1: Epoxy; Point 2:SiC+SiO₂

Sample 6 [55]. This sample looks as a piece of partially reacted charge, at visual inspection (Figure 28a). The sample was collected in the electrode track zone. One can still distinguish the two different phases in the sample (Figure 28b). Bø assumes that the sample could have stayed at high temperatures for long times, hence favoring crystal growth of SiC. A piece of carbon material in this sample was not totally converted to SiC. The web structure in Figure 28c shows small amounts of SiO₂ between partially converted carbon (black). Another zone close to the carbon piece was rich in cracked SiO₂ (Figure 28d). The points on the figures mark the presence of epoxy (1), SiC (3,4,6) SiO₂ (2,5) and carbon (7).

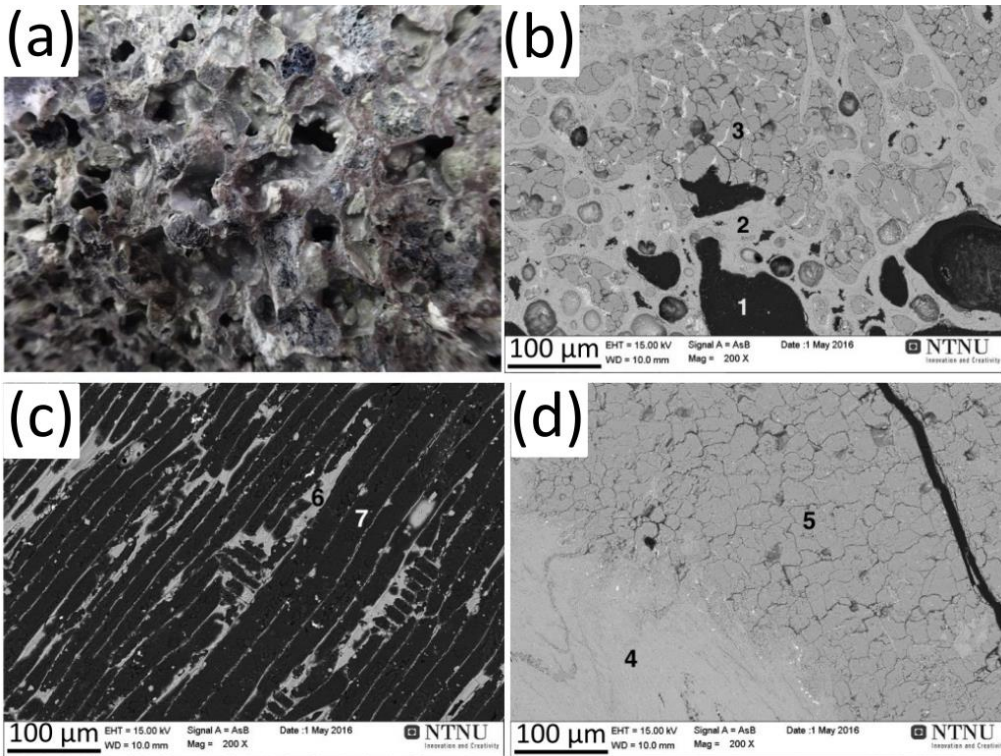


Figure 28: Overview of sample 2: visual inspection (a), mixture of SiC and SiO₂ (b), carbon material converted to SiC (c), cracks in SiO₂ matrix (d). [55]. Point 1: epoxy; Points 2,5: SiO₂; Points 3,4,6: SiC; Point 7: carbon.

Sample 7 [55]. This sample comes from the area around the electrode of Wacker furnace 4. Its appearance is white, therefore it was assumed that it contained white SiO₂-SiC condensate at visual inspection. EPMA confirmed that the sample consists of SiO₂ and SiC. The author states that might originally have contained Si-SiO₂ condensate, and that Si precipitated out of the Si-SiO₂ condensate. However, no Si is shown in the EPMA analysis of this sample.

SiC comes from conversion of coal (points 3, 5). SiO₂ is melted and embeds the SiC phase. The SiO₂ phase is rich in cracks (points 2, 6 and 8). SiC particles are eventually present in the SiO₂ matrix (point 7). Figure 29 shows how SiO₂ fills the pores in the carbon materials converted to SiC web structure. The lighter grey phase on the right side is SiC, whereas the darker phase with cracks is SiO₂. This structure surrounds a SiC particle laying on the left side of Figure 30.

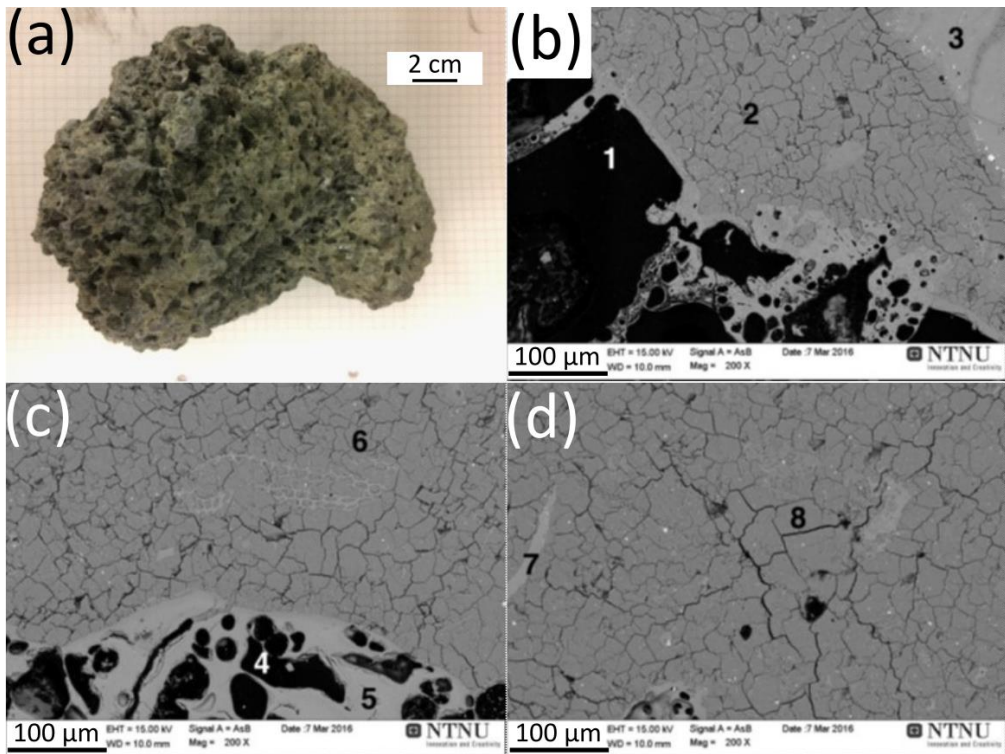


Figure 29: (a) Appearance of sample 7; (b,c) cracked matrix embedding carbon materials converted to SiC; (d) SiC particles in cracked SiO_2 matrix [55]. Points 2,6,8: SiO_2 ; Points 3,5: SiC from coal; Point 4: Epoxy; Point 7: SiC in SiO_2 matrix.

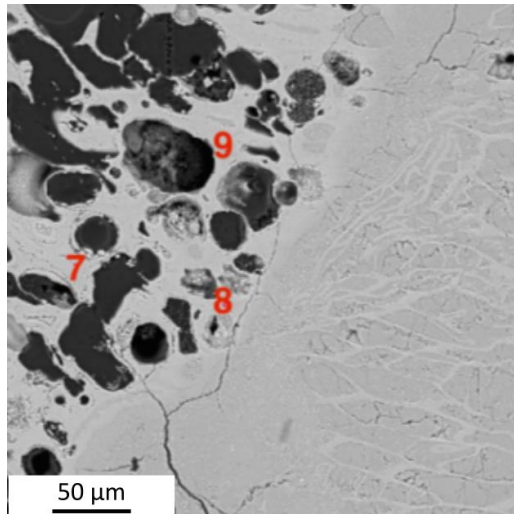


Figure 30: SiC web structure surrounded and filled by SiO_2 in the original pores of a carbon material, sample 7 [55].

Sample 8 [7]. The layer of condensates and charge materials found at Elkem Thamshavn was about 50 cm thick. SiO₂ embeds the pores left by SiC in the structure. SiO₂ appeared as cristobalite in these samples, implying that the temperature enhanced the transition from α-quartz to cristobalite over time. However, a large fraction of amorphous silica is detected by XRD. 6H and 15R-SiC were the predominant polytype in samples collected from the condensate layer.

SiC microstructure affects the green color of the sample. Porous SiC is formed by conversion from carbon from Reaction 3 [7] (Figure 31a). SiO₂ will fill the remaining voids of the converted carbon material. On the other hand, it is believed that SiC is coming from condensates, when it assembles into needles (Figure 31b), flakes (Figure 31c) or islands (Figure 31d).

Sample 9 [9]. The needle structure was also found 90 cm deep in the furnace, in the electrode track zone. The sample was easy to brake, brittle and white. Plate SiC crystals are found in the SiO₂-rich phase, close to a Si particle. The sample was extracted in the electrode track zone, 90 cm down from the charge top. SiC has a similar shape of recrystallized SiC from a high temperature melt [9].

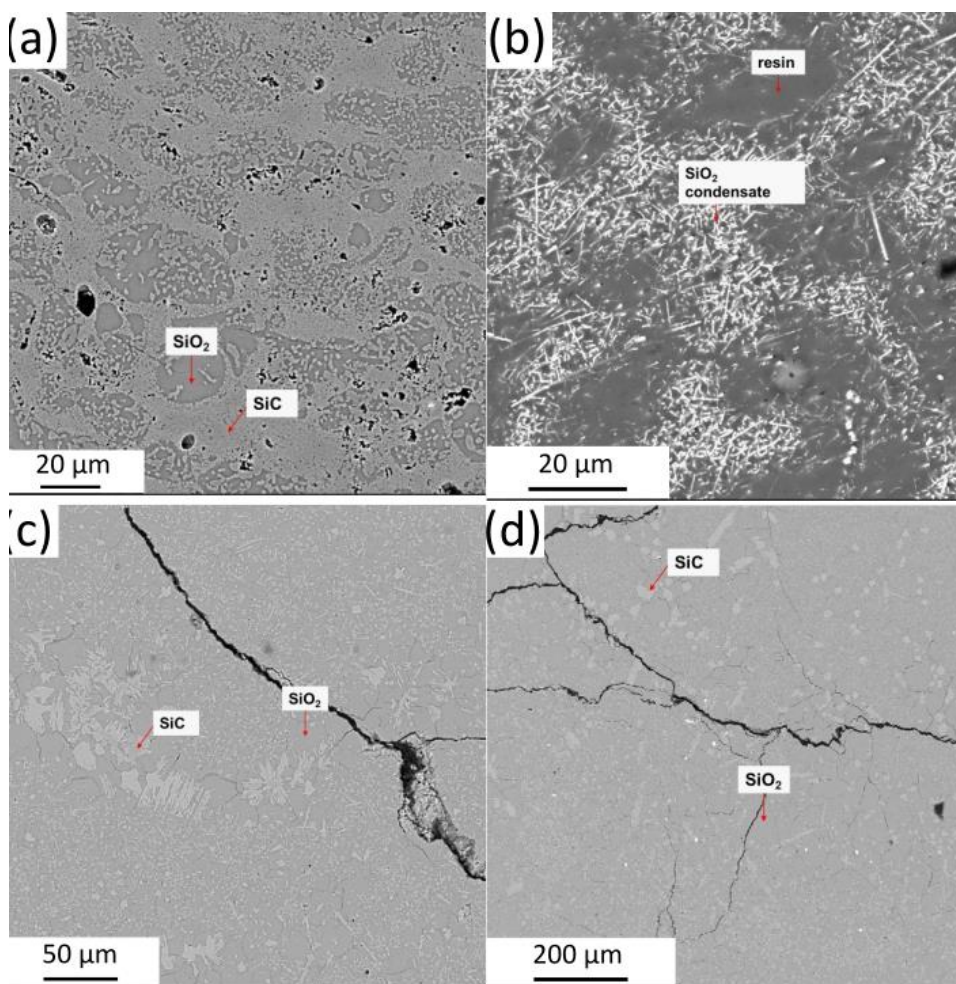


Figure 31: Different microstructures of SiC: porous (a), needles (b), flakes (c) and islands (d). Revised after [7].

Crater crust

The crater crust is located below the stoking crust. It generates in the proximity of the crater area, or where a crater is expected, if not found. The cavity is not always found during industrial excavations. It can depend on the geometry and the loading history of the furnace, as well as the gas production reactions occurring when the SiO(g) products are heated [2].

The crater crust consists mainly of SiC . This crust is formed at relatively high temperatures. It will not be surprising to notice silicon droplets in it [56]. In fact, SiC and ascending SiO(g) are in contact. Silicon production reaction can occur at the cavity roof. Eventual liquid silicon formed in the colder areas of the crater crust will flow downwards, thanks to gravity. Traces of quartz or Si-SiO_2 condensates can be present in this crust. There has been no evidence of white $\text{SiO}_2\text{-SiC}$ condensates in the crater zone. At the crater crust, gas channeling occurs to a wide extent. Figure 32 shows a piece of crater crust extracted from a Norwegian FeSi furnace [56]. Figure 33 shows the position of the three samples described in this section.

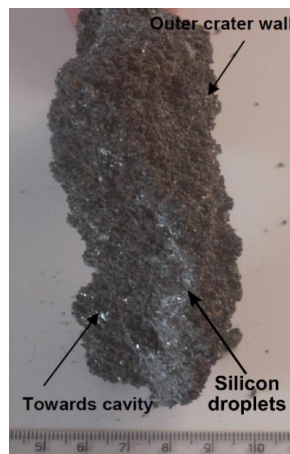


Figure 32: SiC crater crust from a FeSi75 furnace. Revised after Tranell et al. [56]

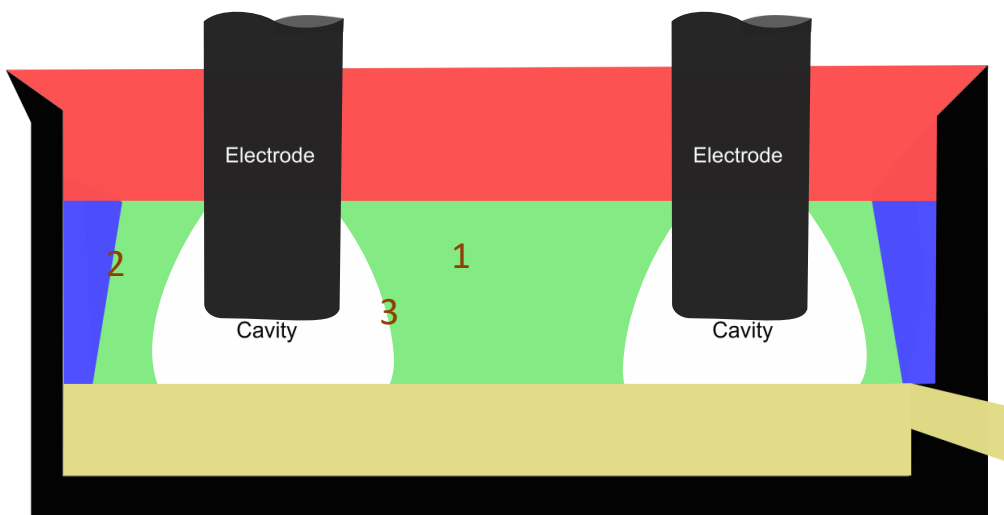


Figure 33: Samples in the crater crust. Estimated positions from [55].

Sample 1 [55]. Sample 1 was extracted in the central zone. By visual inspection, sample 1 looks like brown Si-SiO₂ condensate mixed with SiC [55]. The composition was confirmed by BSD, EDS and EPMA. Elemental Si is dispersed in the SiO₂ matrix, with a much broader size compared to other brown condensate samples from the stoking crust. Sometimes Si can even reorganize into pearls, which are already noticed at visual inspection (Figure 34). Similar samples were noticed by Vangskåsen [59] and Tangstad et al. [7]. The microstructure of sample 1 is shown in Figure 34. EPMA detected the presence of epoxy (points 4 and 8), Si (points 5,7,9) and SiO₂ (points 6 and 10). The sample contained a CaO-Al₂O₃-SiO₂ slag in another portion of the sample. [55]

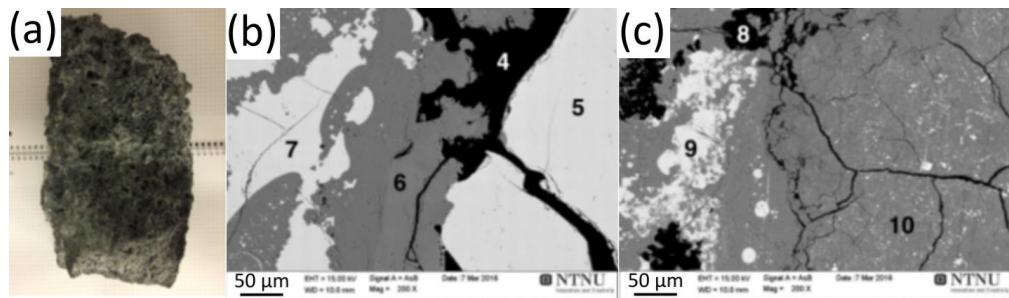


Figure 34: Sample 1, visual inspection and microstructure [55]. Points 4,8: Epoxy; Points 5,7,9: Si; Points 6,10: SiO₂.

Sample 2 [55]: In Wacker 4, a sample was collected at the edge of the crater, close to the slag accumulated at the side of the furnace. The sample contained slag, SiO₂ and FeSi. The typical brown color of the condensate is seen in Figure 35. SEM analysis revealed the slag microstructure: a bright phase (points 2,6,9) containing Mg, Fe, Ni, Al, Si and O, surrounding SiO₂ (points 3,5,8). Large spherical FeSi droplets (ca. 250 µm diameter, point 10) were noticed in the sample.

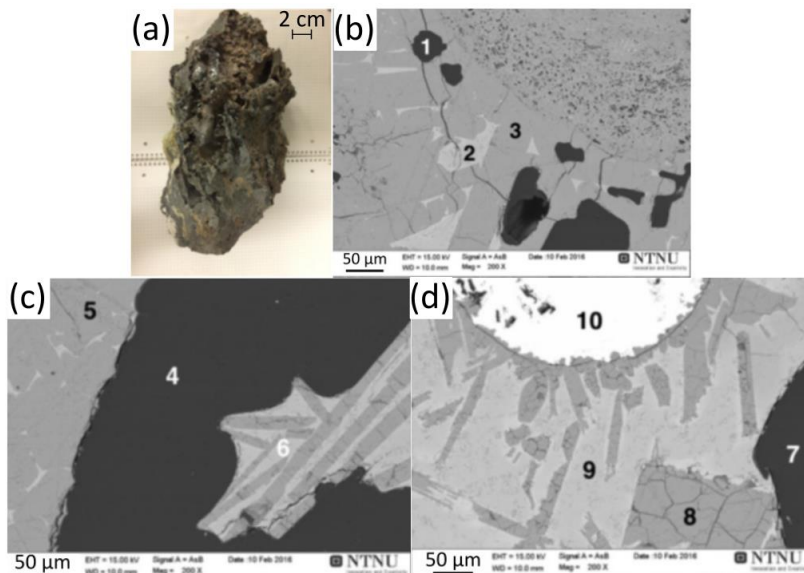


Figure 35: Sample 2: slag and condensates [55]. Points 1,4,7: Epoxy; Points 2,6,9: impurity; Points 3,5,8: SiO₂; Point 10: FeSi droplet.

Sample 3 [55]. Sample 3 was extracted close to the bottom of an electrode, in the crater crust. The sample is made of a SiO_2 matrix (points 2,3,4,6) embedding Si. A large silicon droplet was found at the edge of the sample (point 7). The porous zone in Figure 36b is SiC embedded by SiO_2 .

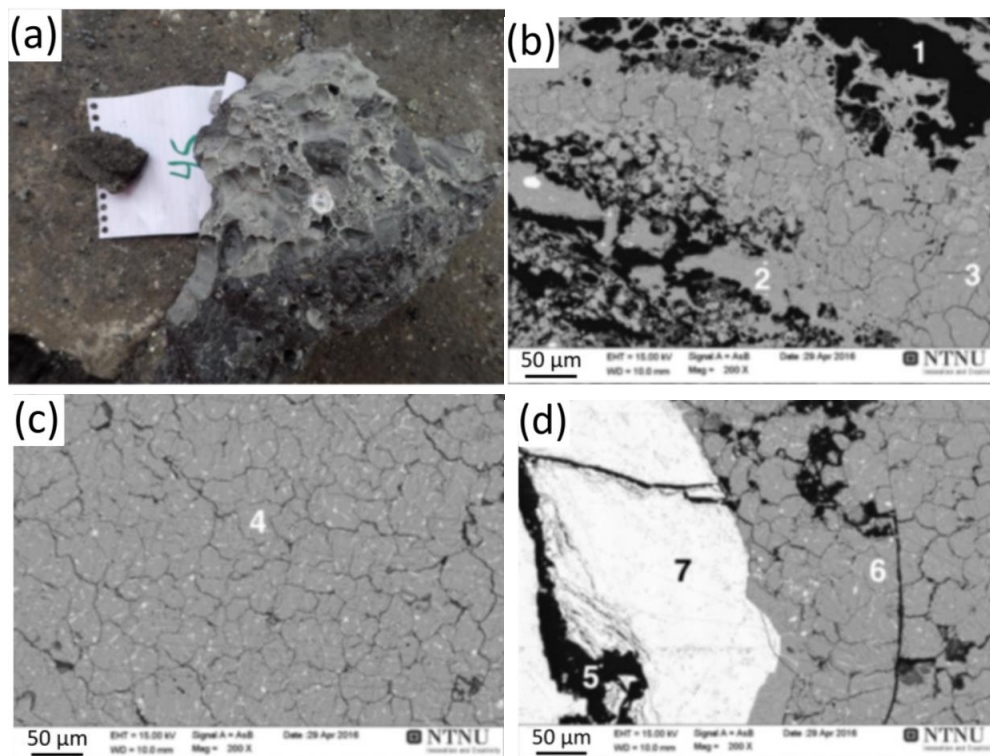


Figure 36: Sample 3, physical appearance and microstructure. [55]. Points 1,5: Epoxy; Points 2,3,4,6: SiO_2+Si ; Point 7: Si droplet.

High temperature condensates from gaseous species [58]. Müller observed a powdery dark-green substance in the crater wall, in a FeSi furnace. The exact position of the sample in the furnace is not specified. The material contained about 50% FeSi. The rest was SiO_2 and SiC in a molar ratio 2:1.

It is believed that FeSi came from evaporation of the metal at the high temperature zone. Due to the low activity of Fe in the liquid, the gas would be quickly depleted in Fe when condensation starts. By going towards lowest temperatures, the condensates should contain less Fe. If this theory was true, the gas would have a temperature of 2500-2800°C. At this temperature range, vapor species like Si(g) , $\text{Si}_x\text{C}_y(\text{g})$ and Fe(g) should be stable [58]. However, if it is considered that the partial pressure of Fe(g) is lower than the partial pressure of SiO(g) , a condensate generated from the gas should contain low amounts of Fe.

Side crust

The last kind of crust is called side crust (Figure 37a) and is located in the lateral portion of the furnace inactive zone [56]. As the name suggests, the side crust is developed close to the furnace refractory walls, from the same height of the crater crust down to the furnace bottom. In this zone, SiC is mixed with oxides in a green oxide

slag. Another constituent of the side crust can be the inactive charge, which does not enter the reaction zones. Sometimes condensates are also found [2].

The side crust is very difficult to remove. Its mechanical properties are strong thanks to the presence of slag and partially melted quartz, and its position is difficult to reach. The accumulated slag can narrow the effective furnace size, if not controlled properly. Figure 37b shows where the green side crust is located in an industrial excavation [60]. Slag accumulation on the furnace sides is a very common event in silicon and ferrosilicon processes.

The side crust may contain FeSi metal droplets, which can be found at very low temperature, at the top charge level. Jusnes [60] analyzed a sample was extracted from the slag zone and analyzed by EPMA (Figure 38). The sample came from the slag zone in the top right-side of Figure 37. The compositional analysis reported the presence of slag, SiC and FeSi particles. The results of the chemical analysis are reported in Table 3.

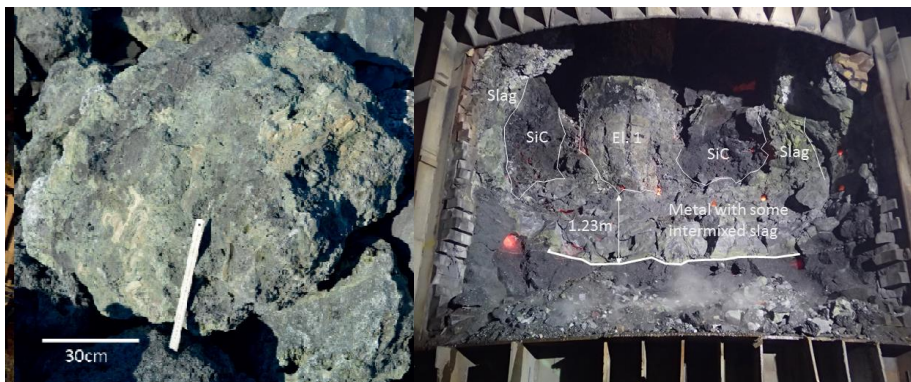


Figure 37: Side crust [2]; Material zones observed in the furnace during excavation. Electrode 1 is visible in the middle of the picture, and SiC, slag and metal zones are indicated [60].

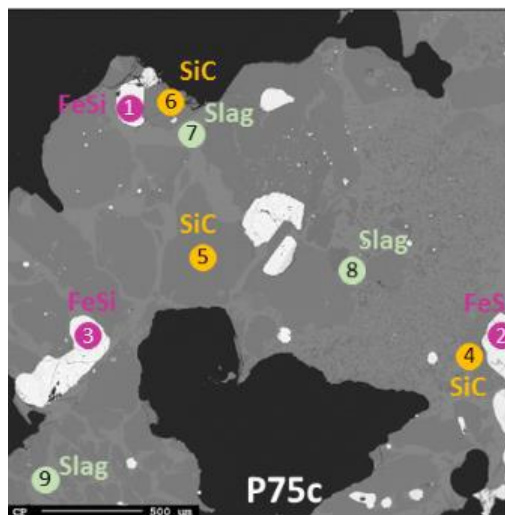


Figure 38: Side crust sample (P75c) from furnace excavation. The sample has a slag matrix with some SiC particles and some metal particles. [60].

Table 3: Chemical analysis of sample P75c from furnace excavation. The table shows an average of the position numbers listed [60].

Position no.	Element analysis (wt.%)									Phase
	Si	O	C	Fe	Ca	Al	K	Na	Mg	
1,2,3	54.0	0.2	0.6	48.1	/	/	/	/	/	FeSi
4,5,6	68.8	0.4	29.0	/	/	/	/	/	/	SiC
7,8,9	28.7	40.2	0.5	/	11.0	12.0	0.4	/	2.2	Slag

Formation of the cavity

The cavity size and shape can change by tuning the furnace parameters. Zherdev et al. [61] carried out five excavations in furnaces rotated at different revolution speeds, and compared the profiles to a static furnace (Figure 39a). A slow rotation speed (Figure 39b) does not alter relevantly the cavity size. A shorter revolution time (Figure 39c) gives a smaller cavity close to the electrode, as well as a distortion and loss in symmetry. Higher rotation speeds (Figure 39d) displace the high temperature zones into the furnace bath. The highest rotation speed (Figure 39e) gave the smallest cavity, but the difference between 70-hours and 50-hours revolution time was not large.

The movement of the furnace increases the temperature in the space around the electrode path. The electrical current distribution is altered if the furnace rotates too fast, but rotation is necessary to avoid clogging and enhance the mixing of the charge. Rotating over a critical speed will give an asymmetric, shorter, wider cavity. This practice is not recommended, as it may affect the electrode position.

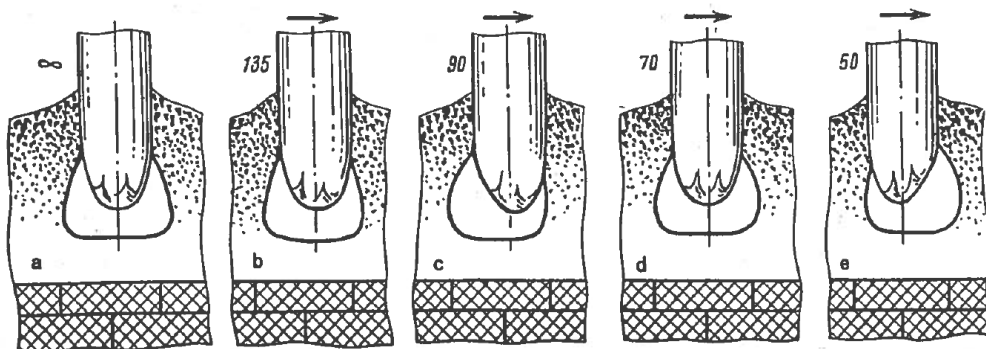


Figure 39: Shape of the gas spaces around the electrodes in a 16.5 MVA furnace used for melting FeSi75. a) Furnace not rotated; b-e) Furnace rotated at different speeds. The numbers close to the electrode are times for a single revolution, in hours.

Another study from Zherdev et al. [62] showed that the shape of the cavity changes by tuning the alloy composition (Figure 40). Table 4 gathers the measurements made by Zherdev et al. in three different FeSi furnaces, producing FeSi45, FeSi75 and FeSi90 respectively. Each of them has a power of 9 MW. If the alloy produced is richer in silicon, the cavity and the distance between electrode and crater walls will increase.

An alloy richer in silicon gives a smaller charge layer thickness. Such a process dissipates high amounts of heat, and higher amounts of SiO(g) can reach the offgas system. When this occurs, the process is not economically profitable, as massive amounts of Si are lost through the offgas.

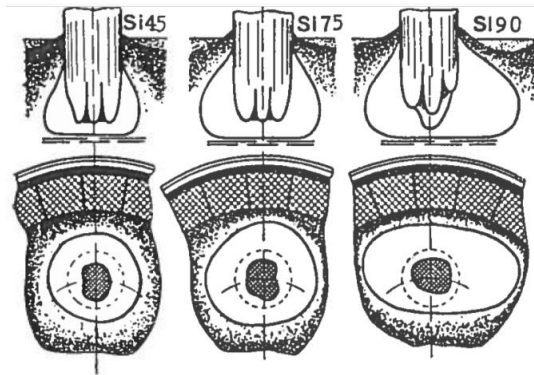


Figure 40: Shapes of cavities and cross sections of furnaces producing different ferrosilicon alloys [62].

Table 4: Cavity size and thickness of charge layer around electrode in three different pilot scale FeSi furnaces [62]

Furnace alloy	Max. distance between electrode and crater walls (m)	Max. height of cavity (m)	Thickness of charge layer in contact with the electrode (m)
FeSi 45	0.20	1.20	0.50
FeSi 75	0.60	1.40	0.32
FeSi 90	1.20	1.70	0.06

Figure 41a provides a schematic view of the furnace excavation results by Schei and Sandberg [4] and Schei [1], [6]. The sketch in Figure 41b looks correct qualitatively, and it has been accepted for long in the silicon industry community as a good examples of a typical silicon furnace cross section. However, there is a major flaw in the dimension of the arc.

If we could scale this picture to real size, the arc would be about 50 cm long. The arc size influences the size of the cavity. On the other hand, Sævarsdóttir [63] modelled the arc size in silicon furnaces to be maximum 15 cm long. Besides, one should not forget that the cavity size is depending on the history of each furnace, as shown in the previous chapter.

Muller et al. [58], [64] excavated two pilot scale furnaces at 150 kW power, producing FeSi67 and FeSi75. When stoking a pilot scale furnace with 150 kW power, they found a top cavity as well as a secondary bottom cavity (Figure 42). Where condensates form, and quartz is not melted yet, secondary cavities would form. Stoking a furnace has the purpose to break the roofs of these cavities. If secondary cavities are not stoked, the materials below will flow down, but new materials would accumulate at the top. This was also the case in the experiments by Myrhaug [65] and Tangstad et al. [7]. These cavities are generated by the materials consumed below the stuck charge, which leaves empty space below.

A double cavity was found also at laboratory scale experiments. In the works by Tangstad and Ksiazek [53] and Myrhaug [65], one cavity is located up in the furnace, and the other in the inner zone. At the end of the experiment the two cavities have collapsed on each other at some point during the process. The authors explain that these cavities are formed by the consumption of raw materials below the condensation temperature. It can be acknowledged that the geometry of the cavity formation is strongly dependent on the experimental setup and furnace operation condition.

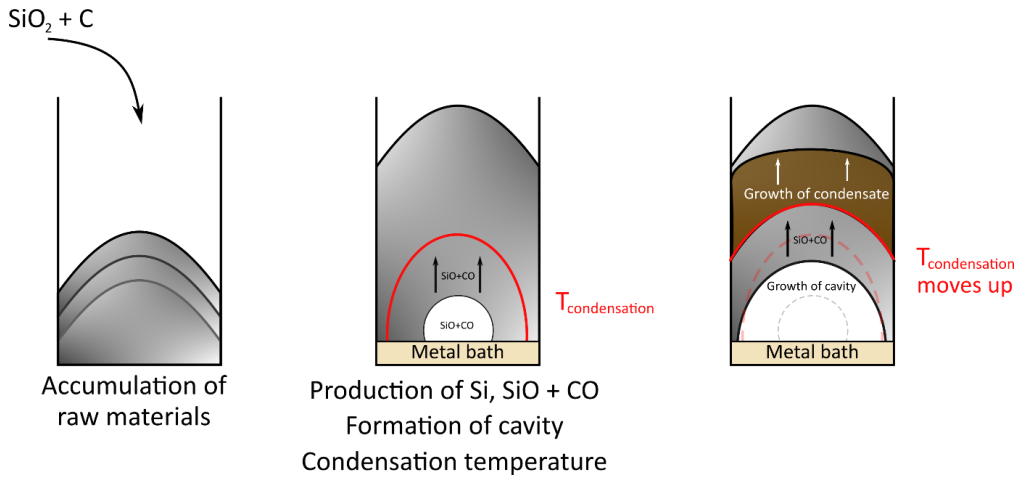


Figure 43: Mechanism of formation of the cavity in industrial furnaces, according to Otani et al. [3]

Vangskåsen [59] used a laboratory scale furnace with a temperature gradient, to estimate the temperature of formation of a cavity in a static heated charge. If a SiO₂-SiC charge is heated, it will react to SiO(g) and CO(g). Vangskåsen demonstrated that cavity roof is positioned always at the same temperature, even by changing the thermal history and the charge composition [15].

Figure 44 shows sections of laboratory scale crucibles after 10, 30, 40 and 60 minutes at 2000°C. The dimension of the cavity increases drastically between 10 and 30 minutes as the bottom raw materials are producing gases, as well as the amount of condensate in the top charge layer increases. Some charge materials are still at the bottom of the crucible after 30 and 40 minutes. These can either be unreacted charge, or lumps fallen from the cavity roof.

After these experiments, Vangskåsen suggested that the cavity grows downwards. A sketch of Vangskåsen's cavity formation mechanism is proposed in Figure 45. Above a critical temperature, gas formation will dominate, whereas the charge would remain unreacted and fixed with condensates at the colder zone. The point where the cavity roof is located is now fixed in the system. The charge will start reacting to SiO(g) and CO(g), and the cavity will grow downwards from the critical temperature.

Otani and Vangskåsen propose similar mechanisms. Both state that a certain isotherm will determine the position of the cavity roof. The difference between Vangskåsen and Otani is that Otani thinks that the isotherm will move upwards, and Vangskåsen does not.

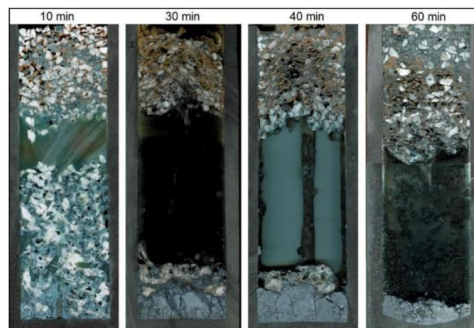


Figure 44: Time evolution of cavity in laboratory scale experiments [59].

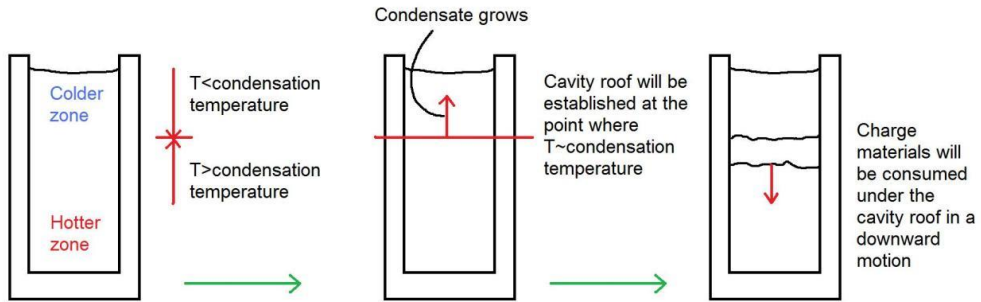


Figure 45: Cavity formation mechanism proposed by Vangskåsen [15].

Condensates position in industrial excavations

The excavation of Elkem Thamshavn in 2013 by Tangstad et al. [7] gave an interesting view of the furnace cross section. The furnace could be divided into four concentric areas. Each area has its own vertical cross section, with different compounds distributed through the height of the furnace (Figure 46). Condensates are found in the low temperature parts of the furnace, between the reacted charge (or together with it) and the black SiC.

The first one is the inactive zone. It is the outer ring of the furnace, closer to the lining. This area contained unreacted charge raw materials. The second zone is called SiC zone. The condensates are located at the top. A large SiC deposit is found below the condensates. The SiC zone is rich in gas channels, with dimensions between 5-10 cm. Below the SiC layer, slag is also present. The third area is the electrode track zone, which corresponds to the area covered by the rotation of the electrodes. Here it is possible to find black SiC at the highest temperatures. The low temperature portion of zone 3 contains mostly unreacted charge. Condensates were also noticed before the black SiC. The last is the mid-SiC zone (Zone 4), consisting mostly of accumulated black SiC. The zone is located at the center of the furnace, among the three electrodes. Condensates and reacted charge occupy only the top of the central part of the furnace.

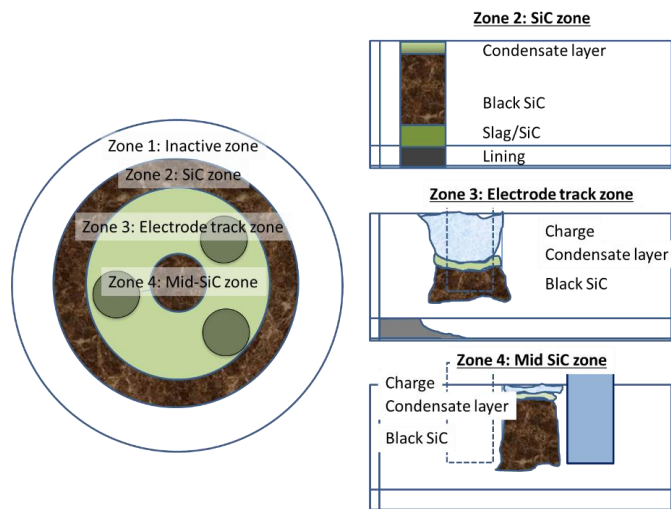


Figure 46: Zones in silicon furnace at Thamshavn [7].

Poch and Dietzel [8] were the first to hypothesize that condensation of $\text{SiO}(\text{g})$ and $\text{CO}(\text{g})$ has a determinant role in the production of silicon. The cavity roof was made of sintered charge, and condensates of different colors covered the charge according to their position (green at the bottom, brown with a greenish layer in the middle and brown only at the top). At the top of the charge, the condensates consist of Si and SiO_2 .

Brynjulfson and Bjerring [66] and Andersson [67] analyzed samples extracted from furnace 2 in Elkem Thamshavn. The condensates in the high temperature zone are found together with SiC and Si droplets, and eventually coal. Green slag and condensates are detected in the low temperature zone, close to the electrode. A large portion of the low temperature zone contained partially reacted charge and condensates.

In Bjølvefossen's excavation, condensates are found mostly in the low temperature zone, close to the furnace walls [2]. In a lump from this area, a sample revealed a large amount of FeSi spheres in a slag matrix. FeSi droplets in SiO_2 matrix were also found in other places surrounding the electrode. A sample containing SiC , FeSi and an oxide phase was covered with a layer of white fibers. The layer was close packed as a carpet [67].

Each furnace has its own history of operation, and crusts generate in different conditions. Ksiazek et al. [2] looked into five silicon furnaces, respectively two furnaces at Wacker chemicals (furnaces 1 and 4, operated at 13 and 33 MW respectively) and one furnace at Elkem ASA Thamshavn (40 MW). This is the first work that compares similarities between different industrial furnaces. Figure 48 sketches the sections of the three furnaces. Each color identifies a specific kind of compound or mixture. The extension of the zone is varying strongly from a furnace to another, but there are many similarities.

At the top of each furnace, the raw materials are loosely packed (blue). A green slag covers the furnace side walls, from the bottom lining up to the very top (green). Below the loose charge layer, quartz and condensates hold together a transformed charge material layer for Wacker furnace 1 and Elkem Thamshavn (red). The quartz is partially melted, and the carbonaceous materials are converted to SiC . SiC was also present in larger amounts in furnace 4 (Figure 48c). The amount of quartz increases towards the side walls or by going to lower temperatures.

The zone close to the electrode is filled by a SiC crust (dark grey). SiC crust is present on the outside of the electrode track zone or at the height of the electrode tip. The SiC crust contains large gas channels, from 5-10 cm diameter (Figure 47), which show the paths taken by $\text{SiO}(\text{g})$ and $\text{CO}(\text{g})$ while escaping from the inner zone. Below the electrode tip, a cavity can generate (purple), however this can be hard to see due to the excavation technique used (Figure 48a,b). The cavity was not found in Wacker furnace 4 (Figure 48c). Samples containing SiC , Si and melted quartz were collected around the electrode tip area. A metal bath is always located below the electrode. It contains Si (yellow), or both Si and SiC (light grey).

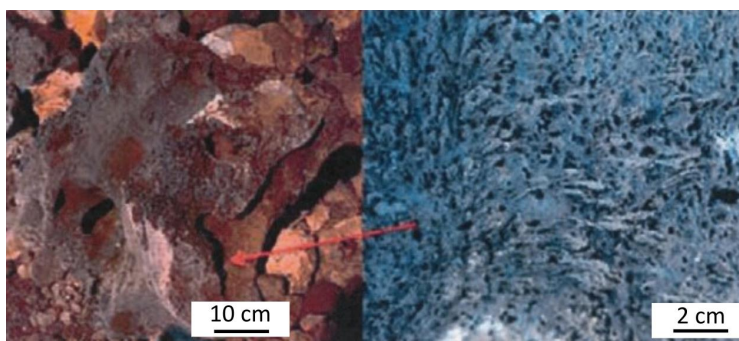


Figure 47: SiC deposits with gas channels [7].

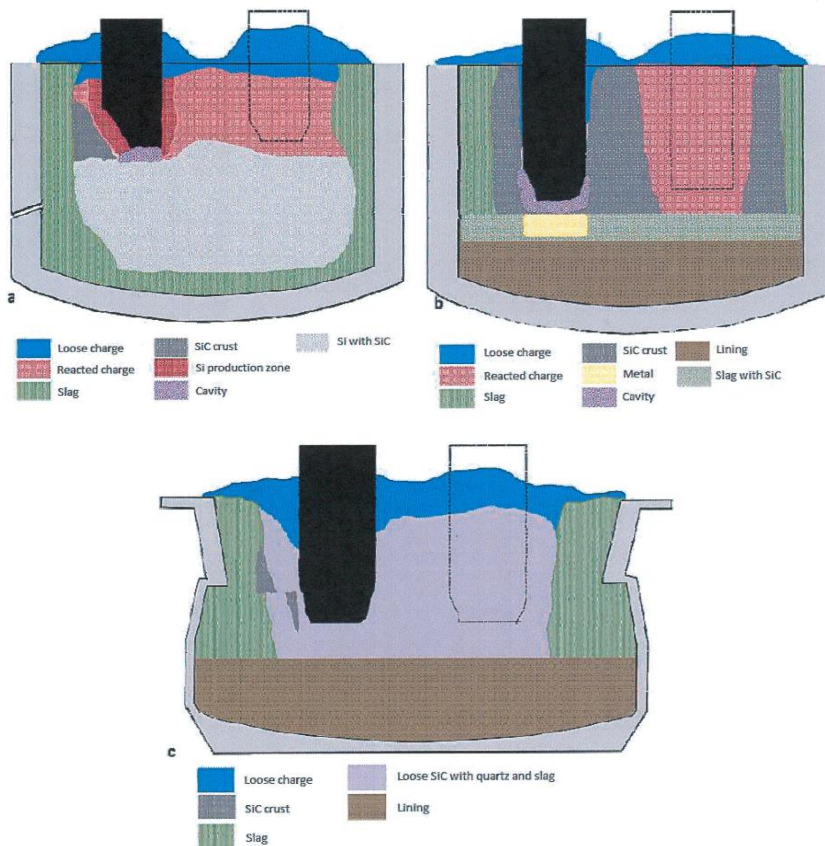


Figure 48: Excavation of three silicon furnaces: Wacker 1 (a), Elkem ASA Thamshavn (b) and Wacker 4 (c) [2].

Condensates in pilot-scale excavations

A pilot scale furnace should be easier to control than a regular industrial furnace. The system is simpler and smaller. It will be easier to make hypothesis on cavity and crust formation mechanisms, and to recognize temperature intervals in the system. All the experiments carried out at pilot scale gave similar products to those seen at industrial scale, and in similar zones.

Vangskåsen analyzed samples from a pilot scale experiment [59]. The zones are pointed out in Figure 49. Zone 1 at the top corresponds to the loose charge zone in the industrial systems. This zone was stoked every 200 minutes during the experiment. Part of the stoked charge fell, on the top of zone 4.

Zone 2 is located at the side of the furnace. It contains sintered quartz, carbon and condensate. Its high charge content can remind of the reacted charge area seen in Wacker 1, Thamshavn, Finnfjord and Bjølvefossen [2]. However, in this experiment, the crust contained also white and brown condensates. The crust in zone 2 is a mixture which is hard to remove and causes the previously discussed clogging problems in silicon industrial furnaces.

Zone 3 consists mainly of condensate and SiC. It is believed that gas production started in the cavity area, and that the gas condensed at the edges of zone 1 and 3. The size of zone 3 is affected by temperature. Zone 3 can

disappear, thanks to the formation of $\text{SiO}(\text{g})$ and $\text{CO}(\text{g})$. Alternatively, the crust in zone 2 will grow at the expense of zone 3, when the temperature at the side decreases. A secondary cavity is generated between zone 1 and 3. Finally, Si and SiC fill up zone 4, at the bottom of the furnace.

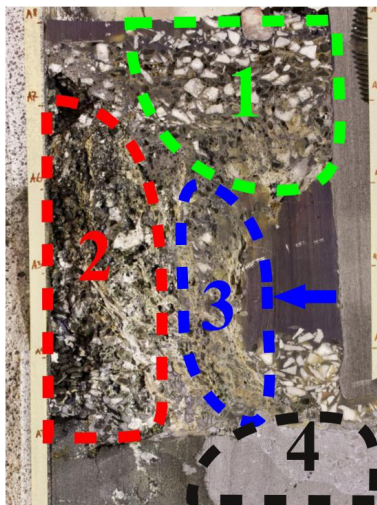


Figure 49: Zones in pilot scale furnace excavation [59].

Myrhaug [65] describes the inner structure of the furnace after a pilot scale experiment. Figure 50 represents the cross section of the furnace after the experiment. Si and SiC precipitated just below the tip of the electrode. A coarse crystalline SiC matrix embeds Si just above the bottom lining (Zone 2). This mixture was present at the arc crater wall as well (Zone 3). At this level, the amount of Si in the mixture increases. Zone 5 is filled with charcoal converted into SiC by $\text{SiO}(\text{g})$, which shows a typical green color. Molten quartz appears in zone 6 together with a brown material, identified as condensate from $\text{SiO}(\text{g})$. The side of the furnace are filled with unreacted charge (7). Some quartz fell while excavating, from the unreacted charge (Zone 8). The molten quartz holds the charge up, generating a secondary cavity. In the laboratory scale work by Tangstad et al. [68] explain that secondary cavities are caused by condensation, in the temperature range between 1700-1800°C. The materials below the roof are converted to $\text{SiO}(\text{g})$ and $\text{CO}(\text{g})$, leaving room for the cavity. The condensates give mechanical stability to the cavity roof, together with the molten quartz when the temperature is above the softening point.

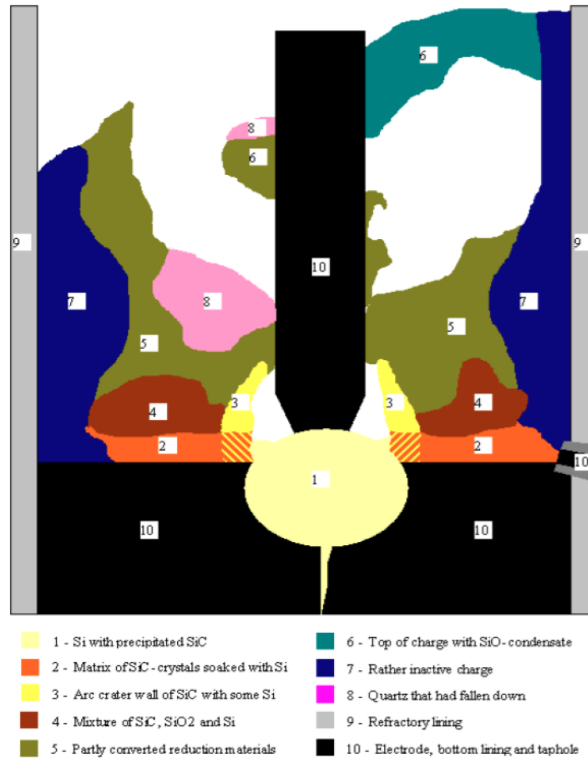


Figure 50: Inner structure of a silicon furnace after pilot scale experiment [3]

Schei [6] and Schei and Sandberg [4] excavated silicon and ferrosilicon furnaces operating at 50 kW with one electrode and bottom contact. The brown condensate was abundant between the charge lumps, above the cavity, on the electrode and in the areas around it. The authors believe that the presence of a Si-SiO₂ mixture confirms the thermodynamic metastability of solid SiO.

When the color of the compound tends to grey, the microstructure is similar to the brown condensates, but no Si is detected. Si could have separated from the SiO₂ matrix, when heated. This event was confirmed by one of the main findings of Vangskåsen's sessile drop furnace tests [59], discussed in the next section.

C. Laboratory-scale condensates

Condensates can be recognized by their microstructure, composition, partial pressures and temperature of formation. Some authors computed hypothesis on the mechanism of formation. This chapter is divided into three units that will go through condensates found in laboratory scale experiments.

The first group consists of mixtures containing Si and SiO₂. These condensates are generated in high quantity in industrial systems, but the knowledge on them is limited. Some authors tried to investigate their composition and their transformation at temperatures typical of the high temperature zone. The second group is including the SiC-SiO_x nanowires. A specific section will cover the mechanism of formation of core-shell nanowires. The last group includes all the other condensates, which were noticed in small amounts and specific conditions. At the end of the chapter, a table will summarize the main results of characterization of laboratory scale condensates.

Si-SiO₂ condensates

Brown condensate

Vangskåsen and Tangstad [15], [53], [54] found a brown crust condensate from a gas with a starting temperature of 2000°C. The gas moves upwards and condenses in colder furnace areas. In fact, some gas blows were noticed at the top of the furnace, implying that SiO(g) is present in high amounts. The SiO(g) production rate is high, since the gas temperature is higher than the melting point of SiO₂ [54]. Spherical droplets of Si are located into a SiO₂ matrix (Figure 51a). It is thought that the spherical microstructure of the crust is obtained by a slower cooling with respect to the brown powder condensate [54]. The microstructure revealed by Vangskåsen and Tangstad is similar to the industrial condensates [7], [55], as well as the presence of gas blows in a laboratory scale setup.

Despite the similar colors, the difference from the brown powder condensate mainly lies into the mechanical properties, which are strictly related to the microstructure. Figure 51a,c shows the microstructure and topography of the brown condensate. Vangskåsen proposes an analogy with the interface cluster model (ICM-model) proposed by Hohl et al. [47] (Figure 51b). The model represents the structure of SiO(s) at nanometric scale. SiO_x layers are located between clusters of amorphous Si and SiO₂. However, Si domains are three orders of magnitude larger in diameter compared to the ICM-model. The authors hypothesize that the areas around the Si spheres could be covered in SiO_x. It can be that amorphous SiO is formed from the gas phase, and then it disproportionates into Si and SiO₂.

In lab scale experiments, an Ar flow is typically added to SiO(g) and CO(g). Its purpose is to simulate different partial pressures of SiO(g) and tune the condensation temperature gradient. According to the laboratory scale experiments from Ksiazek et al. [12], a porous, brownish crust appears at high Ar flows (Figure 51d). This crust adheres strongly to the crucible walls but breaks easily. Temperatures of detection of the crust correspond to the interval between 1476 and 1643°C [12]. This compound is referred as brown crust or brown condensate, due to its similarity with the industrial product.

A supplementary Ar(g) flow can be added to the initial gas mixture. This will alter the gas velocity and its initial partial pressure. The temperature of formation of the brown condensate will also change. Ksiazek et al. [12] tuned the Ar flow from 0.1 to 3 l/min in different experiments. The brown condensates form at 1650°C in the experiment with the lowest Ar flow, and between 1476-1587°C at the highest flow. The brown condensates formed into intervals, located at progressively lower temperatures at increasing Ar flow.

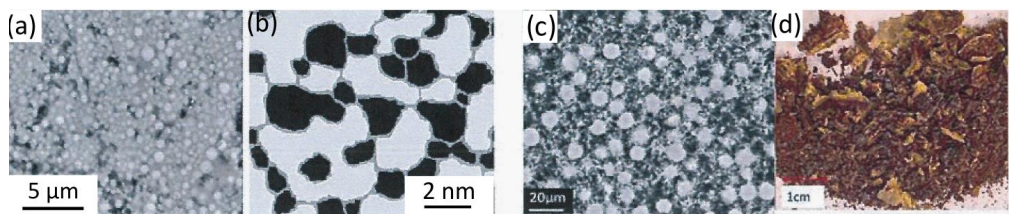


Figure 51: a,b: Brown crust condensate from Tangstad and Ksiazek [53] compared to the ICM model [47]; c,d): Microstructure and appearance of condensate powder produced by Ksiazek et al. [12].

Tangstad et al. [68] mixed industrial quartz and MG-Si at the bottom of a graphite crucible, in an induction furnace. Quartz and silicon produced almost pure SiO(g), which ascended through a mixture of industrial-sized quartz lumps and SiC. The aim of the experiments is to form condensates through a temperature gradient, characterize the condensates and understand the position and formation of the cavity.

The brown condensate occurs around 1600-1700°C (Figure 52b), above a cavity under which the charge material is consumed. A sample of brown condensate was extracted at the position corresponding to ≈1610°C. The condensate surrounds the SiC particles and contain Si droplets in SiO₂ matrix (Figure 53).

The white condensate appears as a thin coating inside the cracks and pores. In the colder portion of the crucible (1450°C, Figure 52a), the charge preserves its original shape. Above ≈1700°C (Figure 52c), the quartz in the charge melts.

No condensates are noticed above 1800°C. The authors explain that the partial pressure of SiO(g) is too low above 1800°C, for having a considerable driving force for condensation. At the same time, the condensates could also be too difficult to be noticed, since they could be mistaken with molten quartz. The driving force is defined as the difference between the experimental p_{SiO} and the equilibrium p_{SiO} . A gas richer in SiO(g) should promote condensation, according to Tangstad et al. [68].

The partial pressure and temperature at which the condensates form depends on the temperature. Tangstad et al. [68] estimated that the brown condensate could generate at a temperature of 1500°C and a p_{SiO} of 0.9, without adding any gas [68]. Vangskåsen and Høgsand [54] state that if the partial pressure of SiO is equal to 0.5, no crust condensate is found at temperatures below 1780°C [54].



Figure 52: a) Charge before condensation (1450°C); b) Brown condensate formation at 1600°C; c) Molten quartz surrounding SiC particle (1760°C). [68].

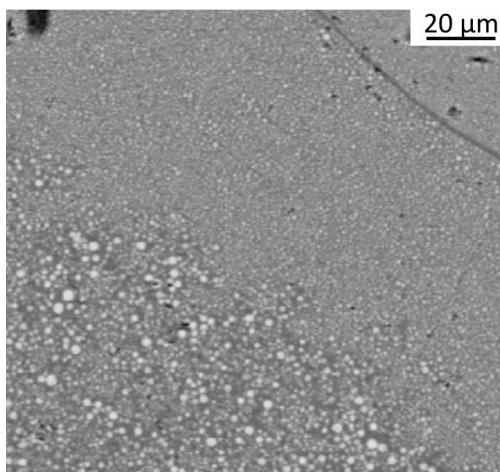


Figure 53: Brown Si-SiO₂ condensate, ≈1610°C [68].

Vangskåsen [15] discovered that the external color depends on the size of the silicon spheres in the condensate. Smaller silicon droplets ($\phi=100-200$ nm) in the matrix correspond to lighter external color, whereas larger droplets ($\phi=500-1000$ nm) are related to darker colors. This would help in recognizing which mixture is locally richer in silicon, since the overall Si/SiO₂ ratio is always close to 1 in brown condensate. Darker condensates are located closer to the substrate on which the condensate grew.

It took a long time to demonstrate that the Si-SiO₂ condensate would rather separate into its components, rather than transforming into SiO(g) upon heating. This hypothesis made by Schei [6] and Müller et al. [58] was confirmed during the wetting tests made by Vangskåsen, about 50 years later [59].

The results of the wettability tests are shown in Figure 54. The target temperatures were chosen between 1450-1850°C and held for 0-30 minutes. Before 1600°C, no relevant variation in microstructure is observed (Figure 54a). At 1650°C, the sharp edges of the sample become round, as if the material was softening. At 1750°C, liquid silicon detaches from the main condensate. Small droplets accumulate at the bottom of the sample and at its borders. The color of the condensate starts to shift to grey as this will be mainly SiO₂ (Figure 54c). At 1850°C, all the elemental silicon is expelled from the condensate, and the original sample assumes a grey color and a porous texture. Vangskåsen concluded that the color changed from brown to grey due to silicon perspiring from the silica matrix.

Silicon leaves empty spaces in the compound, which will be porous at the end of the test. Hence, when heated, the mixture does not react back to SiO(g) to a relevant extent. The phase separation happens first. The low wettability between the two compounds decreases the surface area available for the reaction. SiO(g) might however be produced in small quantities. Increasing the holding temperature enhances the separation of silicon from the brown condensate [59]. In fact, the rate of SiO production from Si and SiO₂ decreases above the melting point of SiO₂, as confirmed by Andersen [69] and Bao et al. [70]. This fact, however, is contradicted by Sindland [71], who only noticed a continuous increase in reaction rate between 1650-1950°C.

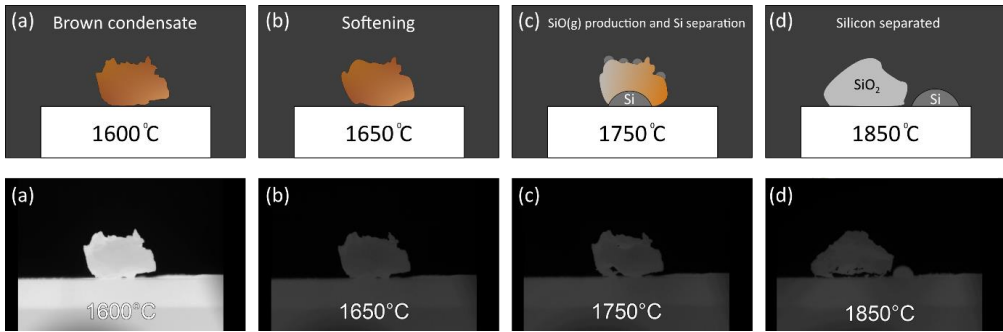


Figure 54: Sessile drop tests on brown condensate. The top line sketches the evolution of brown condensate, whereas the bottom line shows actual instants collected during the test. (a): Brown condensate before any transformation, 1600°C; (b) softening of silica matrix, 1650°C; (c) production of SiO(g) and movement of Si, 1750°C; (d) silicon droplet separated from the brown condensate, leaving a grey silica matrix, 1850°C. Revised after Vangskåsen [15].

The brown condensate may be sandwiched between two SiO₂-SiC white condensates layers at high temperatures. This happened during one of the experiments by Vangskåsen [15]. Figure 55 shows an EPMA line-analysis. The path starts from a SiC particle, passes through a white condensate layer, then through a brown, and finally to a white layer again [15]. An increase in O and a drop in Si and C were noticed in correspondence of the transition area from SiC particles to white condensates (distance = 20 μm). At the interface between the white and the brown layer, there was a decrease in C concentration (distance = 50 μm). The thickness of the first white layer (White 1) ranges between 20-30 μm. Further oscillation in composition in this interval are caused by the cracks crossed by the red path in Figure 55. The brown crust has a constant concentration over its whole 20-45 μm thickness. The external white layer (White 2, in the coordinate distance 100-140 μm) contains lower amounts of Si and higher amounts of C than the inner layer.

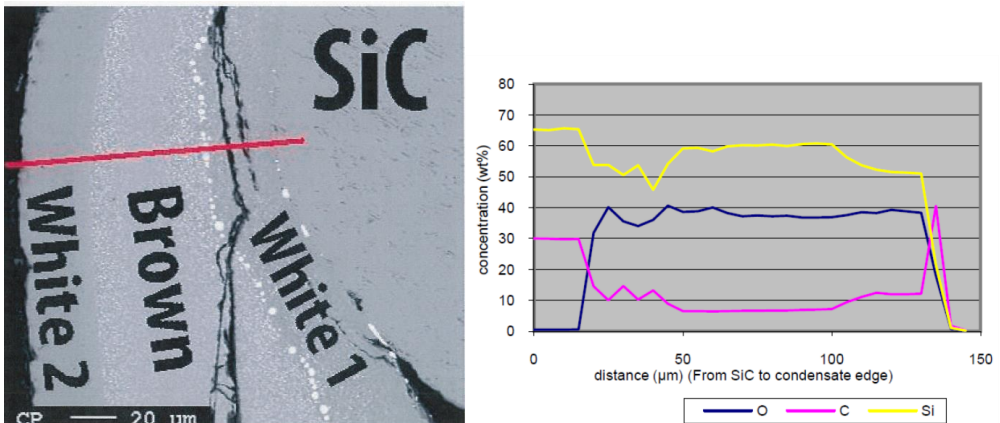


Figure 55: White-brown condensate transition zone [15] and compositional line scanning along the red line.

Brown powder

The brown powder consists in a mixture of Si and SiO₂ [12]. The compound coexists with white condensate or molten silica. Brown powders were collected between 1710-1760°C. The color is attributed to the optical effect of Si spheres in the SiO₂ matrix. The layer accumulates outside of the gas production crucible in laboratory scale

experiments, as well as in the off-gas tube or in the ventilation system [12]. The particle size distribution of the powder in the experiment from Ksiazek et al. [12] ranges between 7-250 μm . The powder appears as small spherical aggregates closely attached to each other. The scattered aggregates give a spongy, cotton-like structure. The microstructure of the brown condensate is shown in Figure 56.

In the experiment of Vangskåsen and Høgsand [54], the brown powder condensate shows a thin tread structure (Figure 57). Similar condensate compositions were seen at 1760°C, but the oxygen concentration was higher. The Si content increases in samples located towards the chamber walls. Longer time exposures give larger Si aggregates. The authors state that the agglomeration of Si depends on the exposure time to high temperature [54].

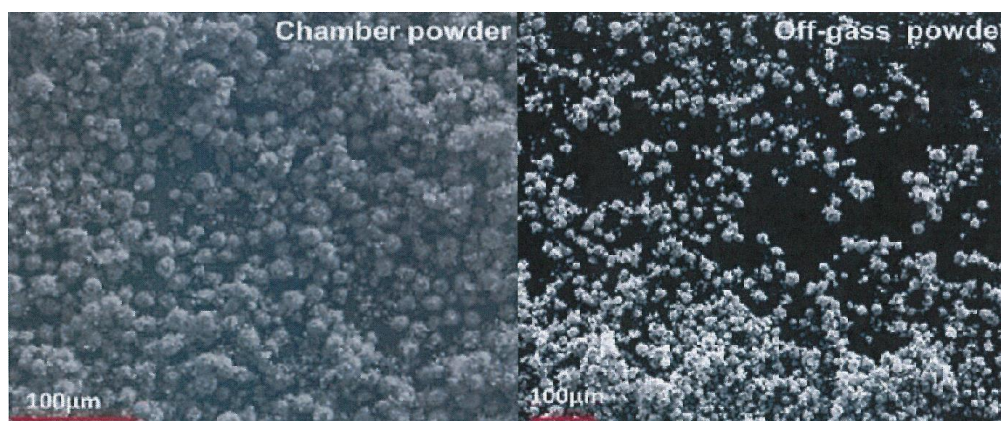


Figure 56: Morphology of brown condensate collected from the chamber (left) and from the off-gas system (right) [12].

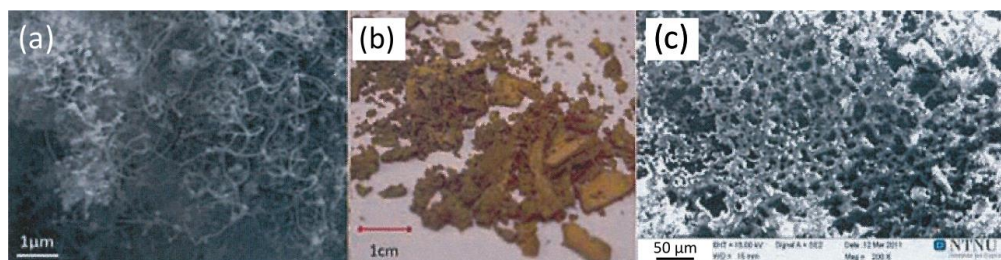


Figure 57: a): Microstructure of brown condensate [12]; b): physical appearance [12]; c): Topography of brown condensate at 1760°C [54].

SiC-SiO_x condensates

Blue condensate

The blue condensate generates typically in the coldest parts of the crucible in lab scale experiments. Mølnås [11] observed a thin pale-blue layer on the SiC particles below 1580°C, but mostly on the inside and outside of the graphite crucible walls. At visual inspection, it shows a cotton-like, porous structure.

The blue condensate appears together with white and brown condensate. According to Vangskåsen and Høgsand [54], the blue condensate disappears as going into the crucible warmer areas. Morphological analysis

at SE-SEM reveals nanosized treads with diameters of 10-30 nm [54], as those shown in Figure 58. Compositional analysis on a blue-whitish solid found by Pultz and Hertl [72] revealed a SiO_2 -SiC mixture in a molar ratio of 2:1. The very small diameter makes the local composition detection challenging. No interface is seen between SiO_2 and SiC in this compound after BSE-SEM analysis. Khrushchev [73] found a blue condensate containing cristobalite, SiC and Si on the top of the brown condensate at 1400-1500°C.



Figure 58: Nano scale treads in pale blue condensate at very high magnification. The diameter of the treads is varying in the range 10 - 30nm. [54]

White condensate

The white condensate is an important compound also in the industrial silicon process. It was found in relevant quantities in all the furnace excavations. It consists of SiO_x and SiC. It can appear as a porous, foamy layer of entangled wires on a surface. Many laboratory scale experiments report the presence of white condensates as well, but industrial white condensates were never analyzed thoroughly by SE or BSE-SEM analysis.

Mølnås [11] produced white condensate in the temperature region between 950 and 1440°C. X-ray diffraction on condensates produced at 1100°C revealed the presence of SiC and SiO_2 , 50% of which is crystalline. The wires are often together with nodules, with diameter ranging around 200 nm. Treads have diameters around 50 nm. The crystal structure of the substrate might influence the final structure. Carbon substrates do not favor formation of nodules, whereas SiC does [11].

Figure 59 underlines that higher condensation temperatures should increase the nodules concentration [11]. Higher temperatures in the proposed setup should correspond to higher p_{SiO} . Mølnås hypothesizes that the nuggets form first, and then the wires come out from them. However, the wires become locally thicker at higher temperatures. EDS analysis was directly performed on the nodules. Since the surface is not flat and regular, scattering might alter the quantitative signal received by the detector. Qualitatively, the nodules contain Si and O, and almost no C. It was deduced that the nodules are made of SiO_2 and Si.

The white SiC- SiO_x condensate originates at lower temperatures than the brown Si- SiO_2 mixture [11], [15], [54], [59]. This implies a lower partial pressure of SiO(g) while the white condensate is forming. Once the white and brown condensates have clogged the system, the pressure is built up in the cavity. The gas jets will become powerful and suddenly pierce the cavity. Vangskåsen [15] detected a higher p_{CO} when the first violent jet occurred. Since the white condensate has a higher content of C compared to the brown, the author states that the violent jets can be associated to the white condensate formation.

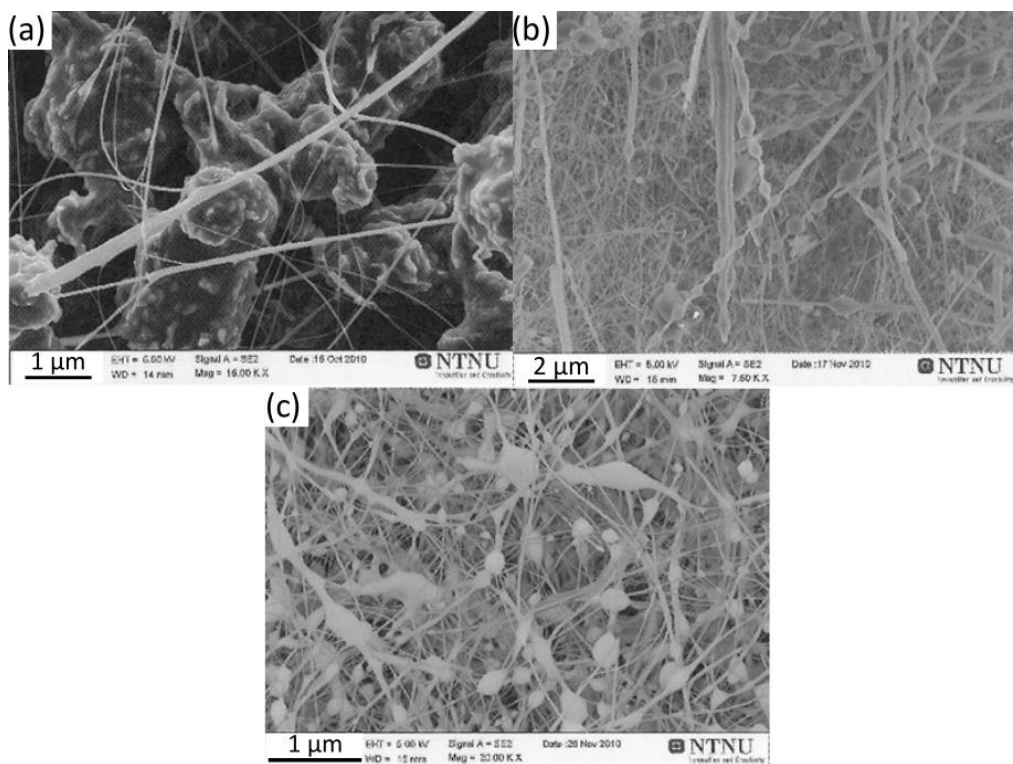


Figure 59: White condensate at three different temperatures. a): 1311-1375°C; b): 1371-1434°C; c): 1370-1425°C [11]

The nanowires and nodules generated in Figure 59 are not only typical of Si production. SiC-SiO_x nanoscaled composites have the same microstructure. This gives them excellent mechanical resistance and field emission properties.

Wang et al. [33] characterized white SiC-SiO_x nanostructured compounds by TEM-analysis (Figure 60d). The mixture was generated from reaction between quartz and carbon. The results showed stacking faults in high amounts, which are “*typical of SiC whiskers obtained by solid-gas reaction between C and SiO(g)*” [33]. The whiskers show a core-shell structure. Each 3C-SiC whisker is embedded into an external thin layer of amorphous SiO_x [33], [39], [73], [74]. High Resolution TEM (HR-TEM) and HF leaching demonstrate that the nodules and the wires surfaces are made of SiO_x [37], [38], [75].

The thickness of each layer depends on the temperature and time chosen for the heat treatment, and the partial pressures of Ar(g) and CO(g). Dhanalaban et al. [34] analyzed the effect of CO(g) concentration on the wires composition. They assumed that CO(g) is absorbed by SiO₂, and then diffuses through it, forming SiC. An increase in CO(g) concentration is proportional to the diffusion rate of CO(g) through the wire, hence a larger SiC core is obtained.

Spherical nodules and nanowires appear in the experiments of Ksiazek et al. [12] and Vangskåsen [15]. The condensate in Figure 60a,b is detected below 1615°C. Spheres start then to appear in considerable amounts, until 1790°C (Figure 60c). The white condensate forms a thin layer on the top of the brown condensate, or a sandwich structure enclosing the brown deposit. Spheres have higher Si concentration than wires. Their diameter ranges from 0.4 to 1 μm, whereas the wires size ranges between 40 and 100 nm [54].

Alkali impurities can affect the shell phase conformation, according to Pickles and Toguri [76]. Potassium silicofluoride was added to the system to inquire the effect of the impurities on the growth. Potassium was present at the tip of the whisker. Alkali impurities favor formation of liquid phases on SiC nanowhiskers [76]. This leads to formation of bead-like structures (Figure 61).

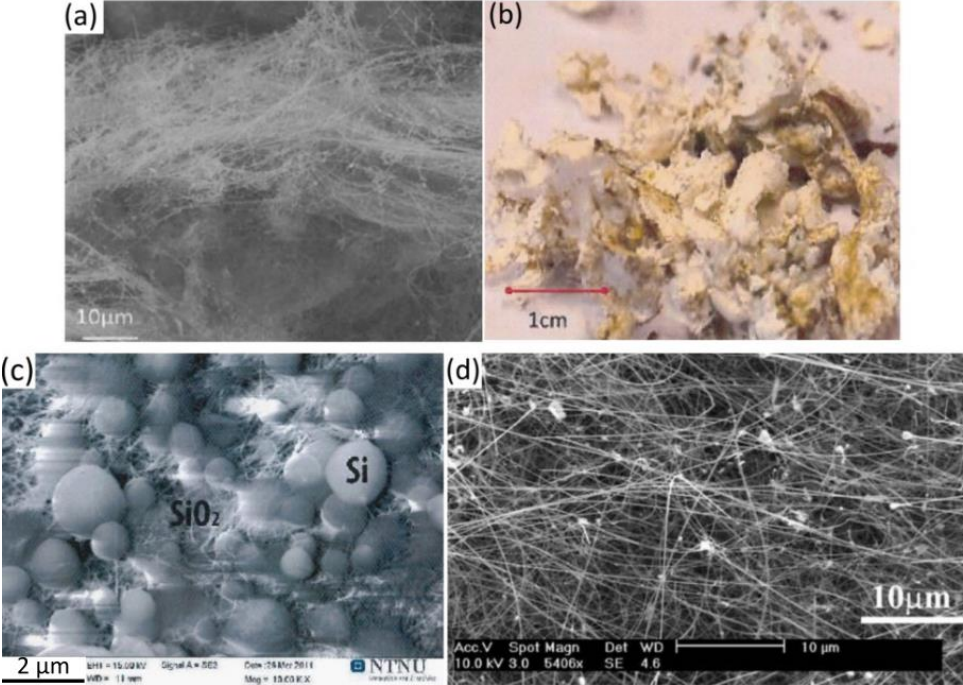


Figure 60: a): Spherical microstructure of the white condensate [12]; b): White condensate appearance [12]; c): Spherical microstructure detail [54]; d): SiC-SiO_x nanowires produced by Wang et al. [33]

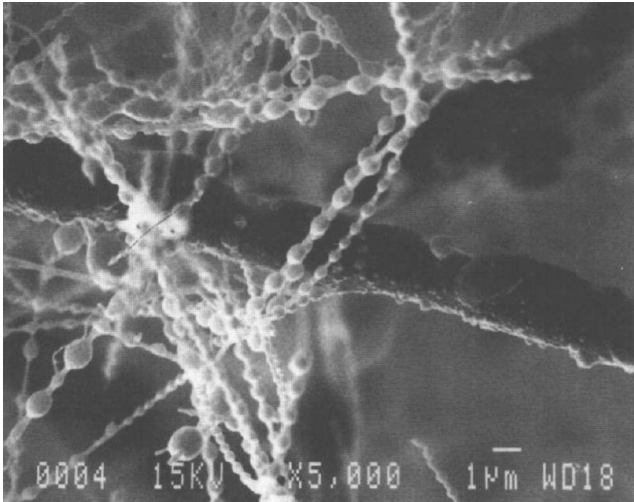


Figure 61: SEM micrograph of whiskers grown in carbon monoxide from a briquette containing potassium silicofluoride [76].

Vangskåsen [15] studied the behavior of white condensate when heating the condensate up to a target temperature between 1500 and 1850°C. He found that the compound starts softening between 1600-1650°C. Afterwards, the melting rate increased, and the shape of the sample begins to alter. This phenomenon is explained by softening of silica. At 1740°C, the sample begins to shrink. The SiC-SiO_x mixtures reacted back to SiO(g) and CO(g). The gas production reaction is seen in the picture at 1800°C, where the sample becomes bigger than it was at 1700°C. A round lump appeared at 1850°C. The surface energy effect will drive the sample form towards a spherical shape. Silicon was not found at the side of the sample, as it happened for the brown condensate. Figure 62 shows samples in the instant when the maximum target temperature was reached.

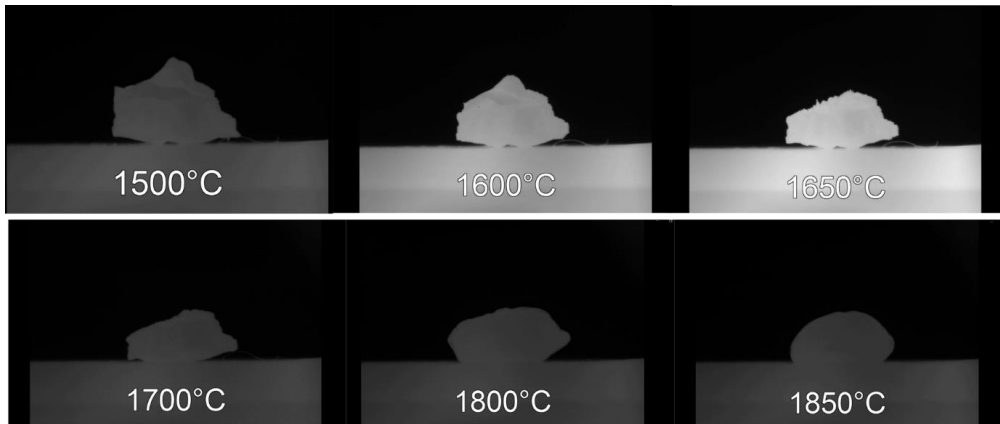


Figure 62: Change of shape of white condensate under heating [59].

Other condensates

Vangskåsen and Høgsand [15] found a green compound on the surface of the brown condensate at 1570-1580°C. It consists of SiC particles dispersed in a SiO₂ matrix (Figure 63). It was thought that Si and SiO₂ may separate at high temperatures, or that Si can react with CO and form SiC. Pultz and Hertl [72] found a green-grey condensate containing SiO₂, SiC and Si. The green condensate color is coming from the dispersion of SiC into the SiO₂ matrix [1], [11]. Mølnås [11] expects that the green condensates also follow the ICM-model [47].

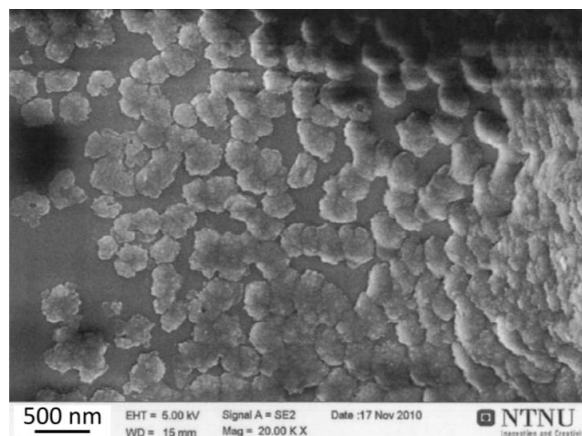


Figure 63: Green condensate [11].

The black condensate composition was not analyzed [54], so it remains unknown for now. It can come as continuous spheres with 15 μm diameter, but it can also be tube-shaped (Figure 64). A spherical type structure is a sign of the presence of a vapor-solid reaction. The compound would be noticed together with brown condensate if a $\text{SiO}_2+\text{Si}+\text{SiC}$ charge was heated at 2000°C for 40 minutes. It is thought that this could be carbon black.

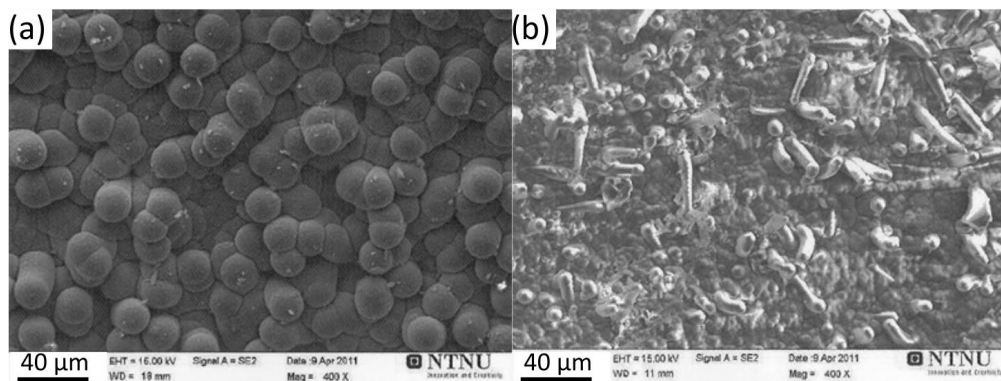


Figure 64: a): Spherical black condensate microstructure; b): Tube-shaped black condensate [54].

The grey condensate shows a needle-like structure, with length of the order of magnitude of 1 μm [54] (Figure 65). Its composition is unknown. As for the black condensate, it can form at holding a $\text{SiO}_2+\text{Si}+\text{SiC}$ charge at 2000°C for at least 40 minutes.

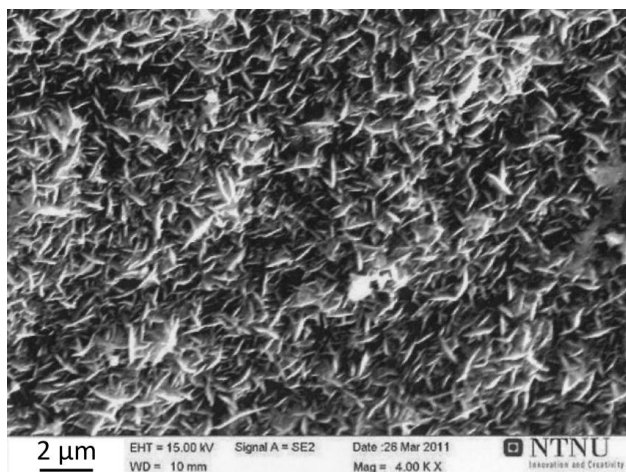


Figure 65: Grey condensate [54].

Summary

Table 5 resumes all the features of the condensates reviewed in this report.

Table 5: Condensates properties, revised after [12], [15], [53].

Color	Microstructure	Temperature	Substrate	Appearance	Compounds
Brown	Si clusters in SiO ₂ matrix. Spongy, cotton-like structure	1700-1780°C	Offgas, ventilation system, tube walls, SiC and SiO ₂ charge	Fine powder PSD ϕ : 7-250 μ m Not firmly attached to equipment	Si + SiO ₂ Elemental composition (wt. %) [15] Si = 57% O = 37% C = 6%
	Si spheres in SiO ₂ matrix Larger clusters with increasing temperature	1476-1643°C	Alumina crucible walls	Firmly attached Porous, easily brakes	SiO ₂ , Si, SiC
White	Needle structure. Can have thick or fine wires	950°C-1780°C	Below crucible for SiO production	Can sandwich the brown condensate between two layers	SiO ₂ , Si, SiC
	Si spheres in SiO ₂ wires		Found into cracks and pits. Parts protected from gas flow	Dense layer of whiskers on surface Easy to remove, flexible, foamy	Composition (wt. %) [15] Si = 52% O = 38% C = 10%
Blue	Cotton-like structure Nanosized treads of ϕ =10-30 nm	900-1580°C	SiC Inside and outside crucible walls	Together with white and brown	SiO ₂ (cristobalite), Si and SiC. Might be same composition as white
Green	SiC dispersed in SiO ₂ matrix	1570-1580°C	Brown condensate	Colored layer	SiC, SiO ₂
Black	Spheres with 15 μ m average diameter Tube shaped	1730-1760°C	White and brown condensate	Can be mistaken with the crust	Unknown, but from gas-solid reaction [54]
Grey	Needle structure with L=1 μ m	1760-1790°C	White and brown condensate	Together with white, brown and black	Unknown

D. The oxide assisted growth of nanowires

Introduction

In the previous section, it was seen that SiC-SiO_x core-shell nanowires are one of the products of the interaction between SiO(g) and CO(g). Numerous studies have tried to explain the reaction mechanism in the gas phase. Zhang et al. [77] proposed the Oxide Assisted Growth (OAG) as a mechanism of reaction. The mechanism was widely revised by other authors [35], [36], [78], [79]. Understanding the mechanism of formation of nanowires can help in controlling the SiO(g)-CO(g) interaction.

The OAG model can explain the generation of core-shell nanowires from a gas phase, without using a catalyst. The starting materials to produce nanowires are the gas species. They are generalized in the model as HXO(g), O(g) and YO(g). In our case, HXO stands for "High temperature oxide", i.e. there is no hydrogen in this compound. In the white condensates nanowires, the HXO compound will correspond to SiO(g). O(g) is monoatomic oxygen, and YO(g) is CO(g).

OAG-grown nanowires consist of a X_nY_m species in the core, and an oxide phase at the shell. The X_nY_m core phase will be SiC. Either *n* or *m* can be equal to zero. In fact, both Si-SiO₂ and SiC-SiO₂ nanowires can be associated to this mechanism [37]. The outer shell phase is made of SiO_x. The oxide is a combination of (SiO)_x nanoclusters, and consequent segregation into Si and SiO₂ domains. The suboxide phase is molten unless the tip size is large than 10-100 nm. Such small dimensions will favor size-dependent melting point depression. The theory behind this phenomenon is explained at the end of this section.

Mechanism

Hu et al. [35], [36] carry out a broad discussion about the mechanism of formation of SiC-SiO_x nanowires. SiO(g) and CO(g) are produced from a mixture of Si, SiO₂ and C powders. Si and C react with a low concentration of O₂(g) and generate SiO(g) and CO(g). The minimum concentration needed to trigger these reactions is very low [36]. Si powders adsorb oxygen at room temperature during milling. The poor tightness of the experimental setup chosen favors also air leakages in the setup.

It was assumed that the gas mixture consists of mainly SiO(g) and CO(g), with traces of CO₂(g) and O₂(g). Carbon dioxide is believed to form as an intermediate, confirming the theoretical discussion carried out by Schei [1] for SiC formation. Boudouard reaction is also considered responsible for CO₂ formation by Hu et al. [35], [36].

Once the gas mixture is produced, the nanowires generation occurs in three stages (Figure 66).

Stage I: Incubation (Production of nanoclusters). SiO(g) and CO(g) will deposit on the surface of a substrate, to produce SiC and SiO_x nanoclusters. SiC is solid and does not react easily with the oxide, unless the temperature is increased to favor the gas producing reaction (Reaction -1). SiO_x is liquid, and it will deposit as a separate phase, thanks to its low miscibility with SiC [15].

Stage II: Nucleation (Lateral growth). The oxides deposition at the sides will define the lateral growth of the core phase, and the final diameter of the nanowire. The external phase is made of suboxides that bind to the core phase, thanks to their dangling bonds. The dangling bonds facing the vapor phase will entrap more suboxides, thus favoring diffusion of silicon to the nanowire core. Eventual oxygen dissolved in the core will diffuse to the edge, thus balancing the stoichiometric composition of the external layer. Once the shell is completely formed and surrounds the core phase, the lateral growth of the wire stops.

The final product of this step is called seed. It consists of a SiC core, surrounded by a SiO_x shell, and a droplet at the top. The droplet is rich in liquid SiO_x. The formation of SiC and SiO_x on the top of the seed is always spontaneous, as well as exothermic.

Stage III: Growth and termination. The droplet is the point where SiC and SiO_x are further produced from this moment. Being the material at the droplet in molten state, the adsorption of gases at the surface and their diffusion to the core are favored. During the vertical growth, the suboxide phase (SiO_x) will also collect more molecules from the vapor phase, thanks to its dangling bonds. Silicon carbide nanoclusters can precipitate and further act as new available nuclei for nanowires.

SiC-SiO_x nanowires grow along a fixed axis during Stage III. The vertical growth will continue along a preferential direction. The amount of impurities in the core is reduced but stacking faults and other crystallographic defects are inevitable. This explains the irregular orientation of the nanowires, according to Hu et al. [35], [36].

Growth continues until the nanowires stop receiving SiO(g) and CO(g) at the droplet. At this point, termination occurs. The exothermic reaction producing SiC and SiO_x stops. The temperature decreases, and the droplet solidifies.

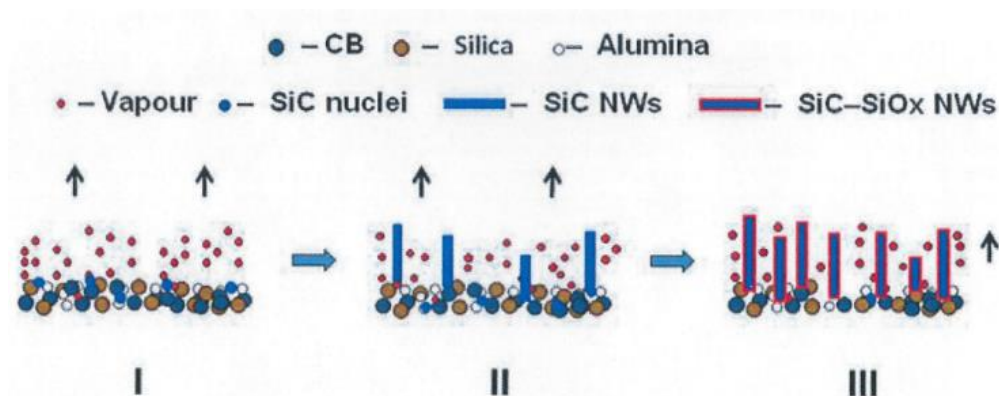


Figure 66: Sketch of oxide assisted growth mechanism for SiC-SiO_x nanowires [35]

Final configurations

The different thermodynamics and growth environments are responsible for different nanowires microstructure, according to Noor Mohammad [78]. Noor Mohammad makes a general discussion for any nanowire having a core-phase with composition X_nY_m, surrounded by an oxide layer. However, the discussion in this section is carried out, assuming that the nanowires produced are made of SiO_x and SiC.

Four situations may arise during growth. Figure 67 resumes the final appearances. TEM images from other works are also collected in Noor Mohammad's work (Figure 68).

Case a: SiO_x segregates to the droplet's periphery while being in liquid state (Figure 67a and Figure 68a). Oxygen atoms diffuse through the liquid-solid interface, at the nanowire tip. Supersaturation and nucleation of SiC at the tip brings to nanowire vertical growth, but lateral segregation of SiO_x to the periphery creates a shell. The core and the shell grow continuously, producing SiC and liquid SiO_x.

Case b: Liquid SiO_x eventually has not enough mobility to segregate at the contours (Figure 67b and Figure 68b). The core species becomes surrounded by liquid SiO_x at the droplet. SiC concentration increases thanks to the reactions with the gas phase and SiC nanoclusters will generate.

The larger the clusters, the more stable they will be. Consequently, it will be easier for them to expel SiO_x from the surroundings. The periphery will be richer in SiO_x, whereas SiC nanoclusters will pile up at the core. This is how the small clusters in the nanowires (Number 5 in Figure 67b) are created.

Case c: The vapor phase species land on the droplet surface (Figure 67c and Figure 68c). The core and the shell species will not be distributed uniformly on the surface top, regardless of the uniformity of the vapor phase

deposition. Thermodynamic conditions change continuously at the droplet surface during growth, resulting in a discontinuous core species diffusion in the droplet. The conclusion is that liquid SiO_x separates easily, by flowing to the periphery. The surface energy will also be uneven, thus causing highly disordered nanowires, with non-uniform SiC clusters.

Case d: the vibrations or oscillation of the droplet will be stronger than in case c. The deposition of the gas species is strongly non-uniform. This might result in a wavelike nanowire (Figure 67d and Figure 68d).

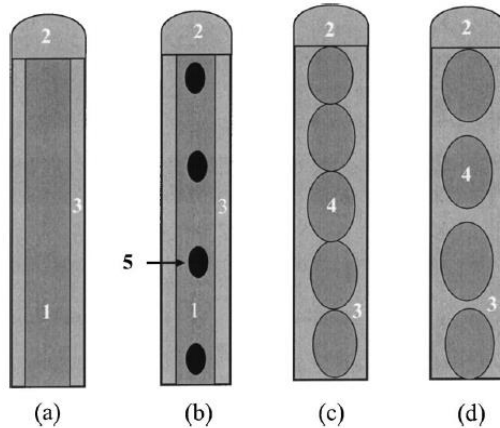


Figure 67: Conditions for growth of LxO sheath. Legend: 1= X_nY_m species; 2= HxO droplet; 3= LxO; 4= X_nY_m large cluster; 5= X_nY_m small cluster [78]

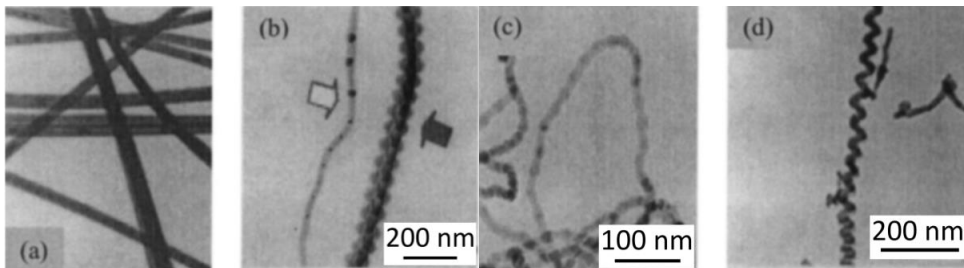


Figure 68: Shapes of wires grown with the OAG mechanism [78]

Melting point depression theory

When dealing with small particles, the curvatures of small surfaces play a key role in the thermodynamics. The surface energy is not negligible, and its contribution enters the energy balance of a system. One of the properties affected by the change of size and curvature is the melting point. Small particles may have a melting point depression of several hundred degrees.

Stølen and Grande [80] analyze the surface effect on the melting point, one should start by analyzing the equilibrium between a solid and a liquid droplet, having the same mass. The solid and the liquid are made of the same substance, to simplify the calculation. The chemical potentials μ of the liquid and the solid droplet are equal:

$$\mu^s(T, p^s) = \mu^l(T, p^l)$$

Equation 2

The equilibrium conditions require equal temperatures, but different pressures. The superscript * refers to the reference phase, “s” for solid and “l” for liquid. The previous equation can be rearranged in the form below, after the chemical potential as a power series, and by deriving partially with respect to temperature and pressure.

$$\mu_l^*(T^*, p^*) - \mu_s^*(T^*, p^*) + (S^l - S^s)(T - T^*) + \frac{M}{\rho_l}(p^l - p^*) - \frac{M}{\rho_s}(p^s - p^*) = 0 \quad \text{Equation 3}$$

In this equation, the first two terms are the chemical potential of the chosen reference states at the temperature and pressure T^* and p^* . They are both assumed to be zero. The third term contains the difference in the entropy in the solid and liquid. It corresponds, by definition, to the enthalpy of fusion $\Delta_{fus}H_m$, with changed sign, and divided by the reference temperature T^* . The fourth and the fifth term are the partial derivative of the chemical potential with respect to pressure, multiplied by the difference in pressure from the reference state. ρ_l and ρ_s are densities, whereas p_s and p_l are the pressure in the solid and in the liquid droplet respectively.

The equation can be rearranged to

$$-\frac{\Delta_{fus}H_m}{T^*}(T - T^*) + \frac{M}{\rho_l}(p^l - p^*) - \frac{M}{\rho_s}(p^s - p^*) = 0 \quad \text{Equation 4}$$

From the Laplace equation on pressure, p_s and p_l can be calculated by knowing the gas pressure, the surface tension with the gas and the radius of curvature. The equation can be rearranged to

$$\frac{\Delta_{fus}H_m}{T^*}(T - T^*) + \frac{M}{\rho_l} \frac{2\sigma^{lg}}{r^l} - \frac{M}{\rho_s} \frac{2\sigma^{sg}}{r^s} = 0 \quad \text{Equation 5}$$

The mass of the liquid and the solid are assumed to be the same. It follows that the curvature of the liquid and the solid particles are related by $\rho_l V^l = \rho_s V^s$, where V^i is the volume of a sphere with radius r^i . One can find a relation between r^s and r^l . By inserting it, the final equation will be

$$1 - \frac{(T_{fus})_r}{(T_{fus})_{r=\infty}} = \frac{2M}{r^s \rho_s \Delta_{fus}H_m} \left[\gamma^{sg} - \sigma^{lg} \left(\frac{\rho_s}{\rho_l} \right)^{\frac{2}{3}} \right] \quad \text{Equation 6}$$

With $(T_{fus})_{r=\infty} = T^*$ and $(T_{fus})_r$ are the melting temperature of a bulk material and a particle with radius r^s , respectively. The melting point decreases with decreasing size of a particle. Figure 69 shows an example for gold nanoparticles. The effect of the size starts becoming relevant in the order of magnitude of 10 nm. A particle of 1 nm diameter has reduced its melting point by more than 400 degrees. The trends of variation depend on every material, but this theory is applicable for all materials, even when solids and liquid differ in composition and amounts.

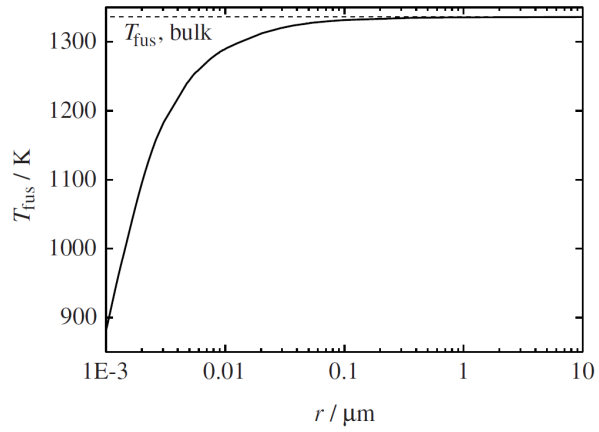


Figure 69: Decrease in melting temperature of a spherical gold particle as a function of its radius [80].

2. Experimental method

The main aim of this work is to investigate the type and structure of the condensates and to find the variables affecting their features. To do so, we have to produce a SiO(g)-CO(g) mixture, make it condensate, isolate the condensation products and analyze them. SiO₂-SiC and Si-SiO₂ pellets are the raw materials used for SiO(g) and CO(g) production. Two different equipments, differing in scale, are used to produce the condensates. Inert gases such as Ar(g) or He(g) could be added to tune the SiO(g) concentration and the gas velocity. Substrates of carbon, quartz or SiC collected the condensing gas.

After the experiments, the condensates microstructure and composition will be analyzed with different characterization techniques. In addition, the crucibles are excavated, to record the points where clogging occurs. Samples of condensates are extracted during excavation, and analyzed with optical microscopy, SEM, TEM, XPS and XRD. The analysis is compared to condensates samples extracted during excavation or operation. Finally, from the condensate weight and the experimental conditions, a kinetic model calculates the reaction rate and the activation energy for one of the condensation reactions.

A. Experimental method overview

Figure 70 resumes the experimental parameters analyzed during the research. The main thought of the setup is that the SiO-CO gas mixture is the raw material for the research. The gas could be produced from two mixes of powders, a Si-SiO₂ or a SiO₂-SiC mixture. According to the size of the two setups chosen, the amount of pellets was either 20 g or 200 g. The other parameters related to the pellets were kept constant, to avoid variations in the gas production reaction kinetics. For example, size, composition, raw materials, pellets size and calcination were kept constant for each batch.

The other parameters analyzed in this work are the gas temperature, the holding time, the substrate composition and its size, and the added inert gas flow. The gas temperature was fixed for each experiment at a constant value of either 1890, 1900, 2000 or 2200°C. The target gas temperature was kept at times between 10 minutes and 4 hours. The graphite of the crucible walls, together with SiC and quartz particles, were chosen as surfaces for condensate deposition. Different substrate sizes may influence the effect of clogging given by condensation. The substrates particle sizes chosen were 3-5, 5-8, 3-10, 8-14 and 12-20 mm for SiC, and 3-5, 5-8 mm for Quartz A. The partial pressure of SiO(g) and CO(g) could be tuned by adding an inert gas. He(g) or Ar(g) were added at different flows, to tune the gas speed and the partial pressure of SiO(g). Some experiments were performed also without adding any gas, as this would be similar to the industrial process.

Figure 71 shows a sketch of how each experiment was handled. The final weight of condensates, the initial moles of gas and the temperature measurements through the condensation chamber are measured. They were used to compute the temperature of formation, the partial pressures of SiO(g) in the system, and as basis for calculation of reaction rate and kinetic constants.

Characterization techniques are used to investigate the features of different condensates. The main techniques used for compositional purposes were EPMA, EDS, EDX and XPS. EPMA and XPS are quantitative, whereas EDS and EDX are semi-quantitative. Microstructure was inquired by TEM and SEM, with the help of FIB-preparation when needed. SiC polytypes were found by peak fitting of XRD spectra.

Samples from industrial plants were collected from other projects or previous works. The samples were analyzed in SEM and EDS. The places from which the samples were collected are the following:

- REC Solar (Kristiansand, Norway), Furnace 11, samples extracted during operation in 2019.
- Wacker Chemicals (Kyrksæterøra, Norway), Furnace 1, excavated in 2016 [55]

- Wacker Chemicals (Kyrksæterøra, Norway), Furnace 4, excavated in 2016 [55]
- Elkem Salten (Straumen, Norway), Furnace 2, excavated in 2018. [81]

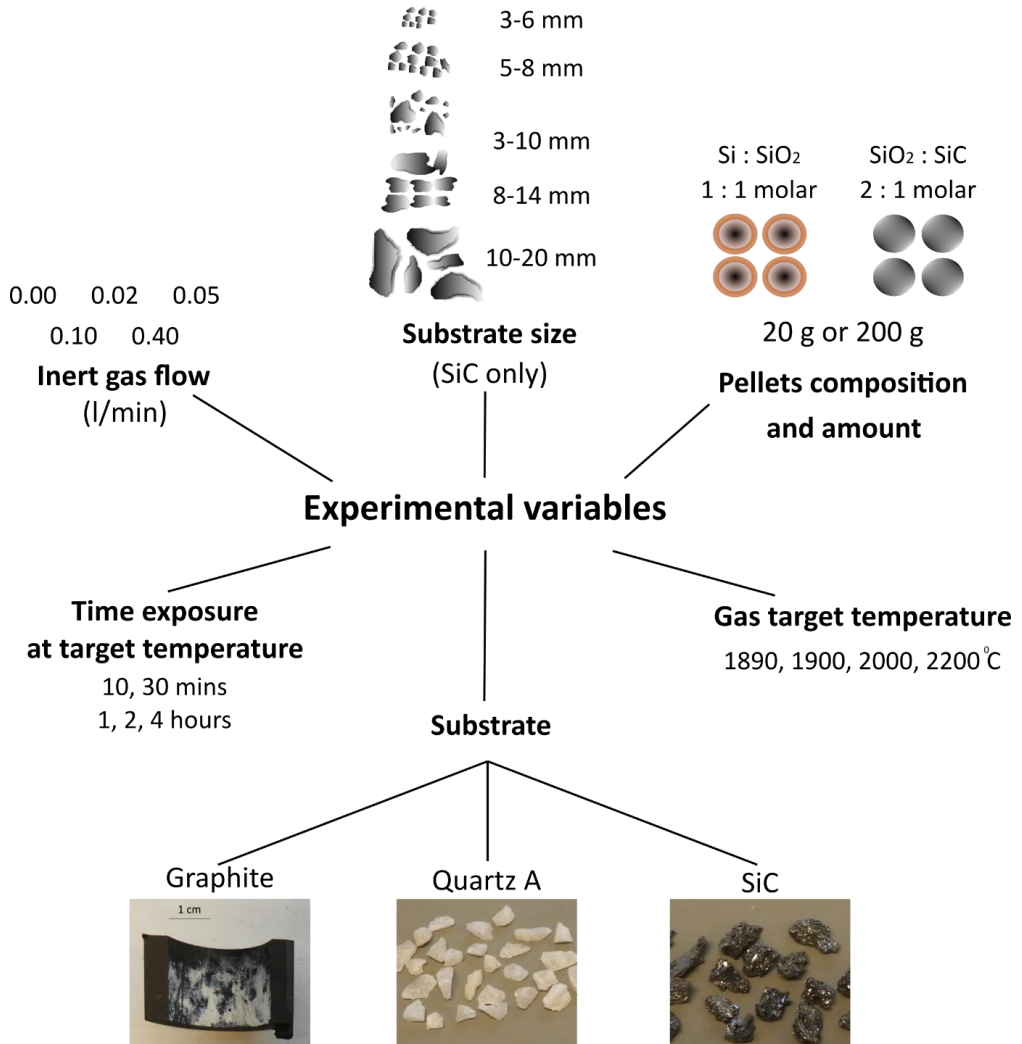


Figure 70: Experimental variables analyzed during the experiments: substrate composition and size, gas temperature, pellets composition, time exposure and inert gas flow added.

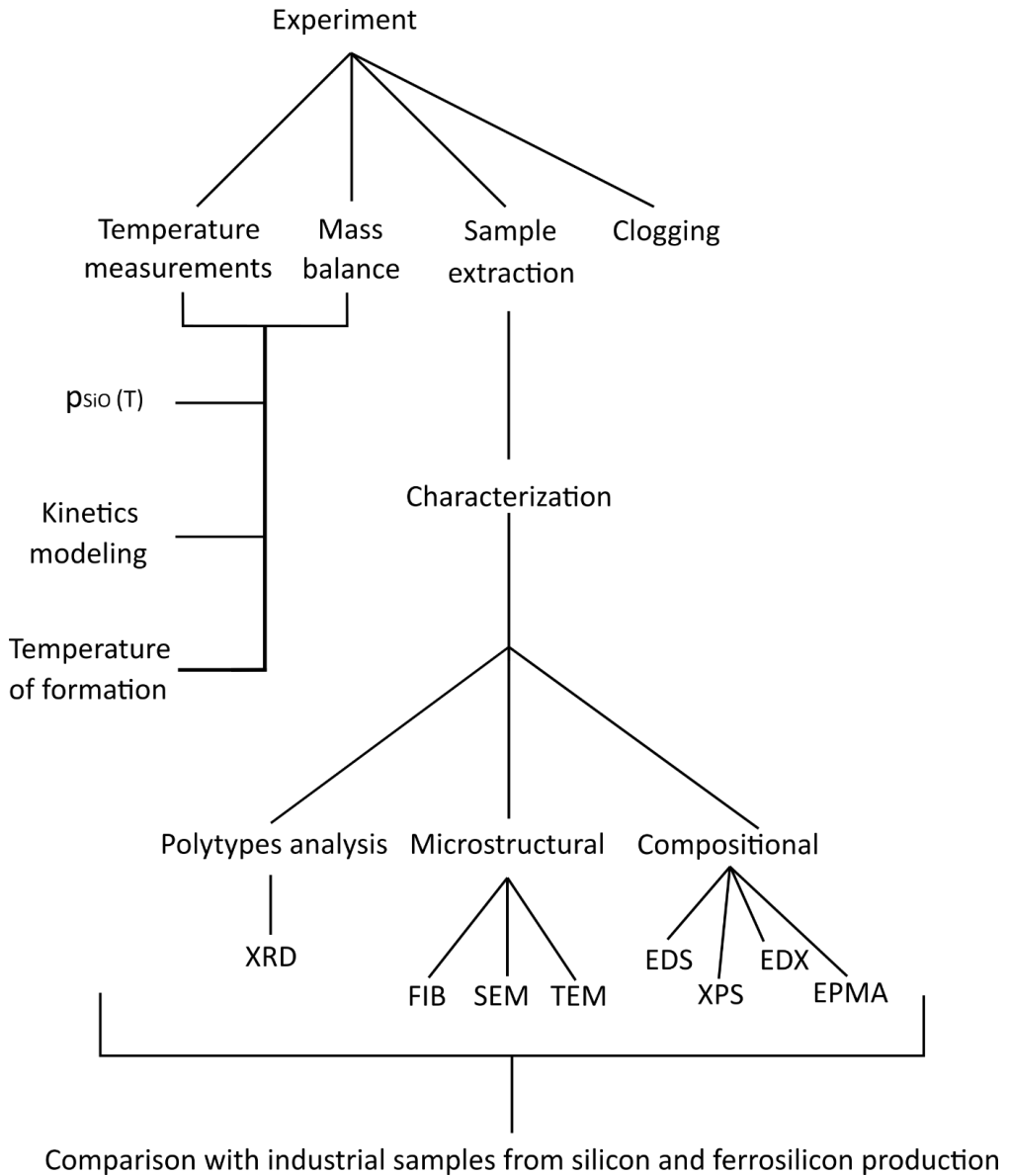


Figure 71: Work structure of experimental method and characterization.

B. Pellets characterization

SiO₂-SiC pellets

The raw materials are commercial quartz provided by Elkem ASA, which will be called Quartz B, and SiC from Washington Mills. The composition of the starting SiC was provided by Washington Mills, whereas the Quartz B analysis were performed by SINTEF Molab by using a Tiger 4 kW X-ray spectrometer. By XRD and XRF analysis

(Table 6), it was found that the quartz percentage in Quartz B is $\approx 99\%$. SiC powders are at least 95% pure. The XRD spectrum is shown in Appendix H.

Table 6: Composition of starting materials detected by XRD (Quartz B) and XRF (SiC)

Composition (wt. %)	Quartz B	Composition (wt. %)	SiC
SiO ₂	98.9	SiC	>95
Fe ₂ O ₃	0.58	SiO ₂	1.6
Al ₂ O ₃	0.17	Al	0.05
K ₂ O	0.02	Fe	1.8
CaO	0.02		

Most of the SiC powder size distribution ranges between 0.1 and 10 μm , whereas SiO₂ particles are mostly between 1 and 100 μm size. Figure 72 compares the powder diameters of SiO₂ and SiC. The average particle size for SiC is 0.953 μm . Quartz B powders were ground by using a Retsch RS200 grinding machine, equipped with a tungsten carbide grinding disc. The grinding time is 70 seconds, and the rotation speed is set at 1200 rpm. The mean particle dimension is reduced to 10.39 μm .

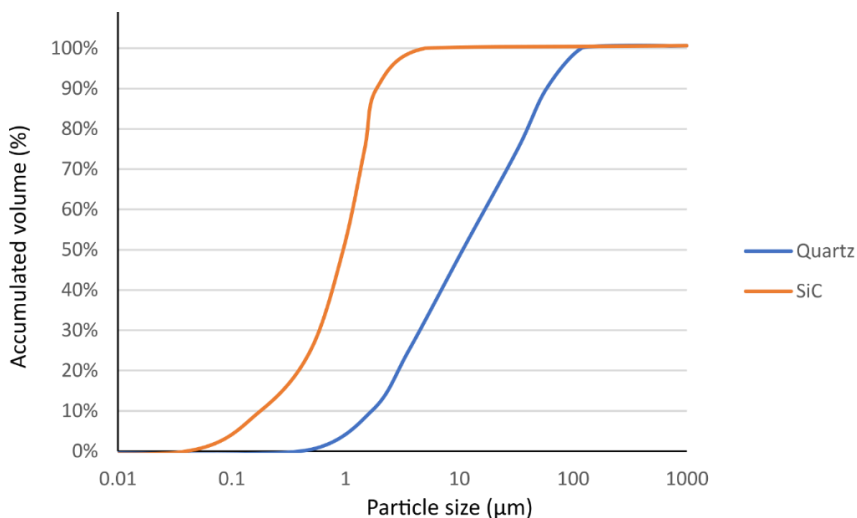


Figure 72: Particles size distribution of SiO₂ and SiC powders in the SiO₂-SiC pellets.

SEM analysis of pellets showed the final aspect of the particle size distribution (Figure 73). As demonstrated by the particle size distribution test, some large SiO₂ particles are present in the sample. SiC surrounds them effectively and fills the voids together with small SiO₂ particles.

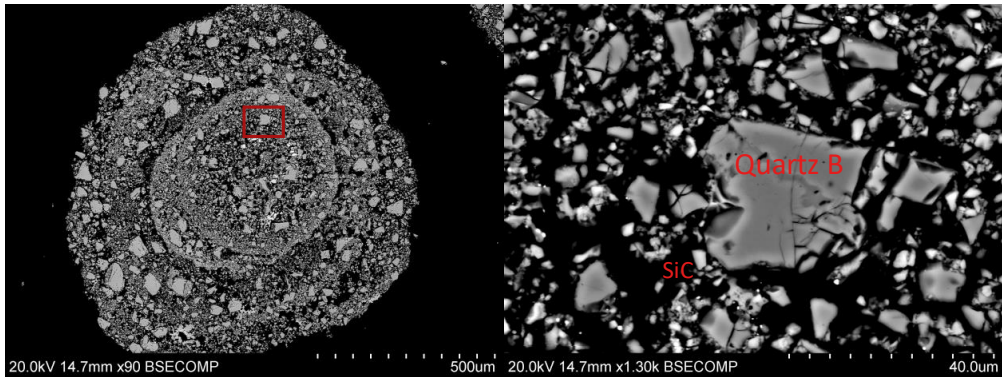


Figure 73: Pellets characterization. The red rectangle corresponds to the zoomed area of the picture on the right. Zones with SiC are lighter than zones with silica.

The powders were mixed for two hours starting from a molar ratio $\text{SiO}_2 : \text{SiC} = 2:1$ (75 wt. % SiO_2 and 25 wt. % SiC), and then pelletized at room temperature, with water as binder. The pellets final diameter ranges between 1 and 2 mm. The pellets underwent drying for 6 hours at 120°C and calcination for 30 minutes at 1200°C . Before feeding the pellets into the experiments, a 600- μm size sieve separated the fines. Figure 74 illustrates the final aspect of the pellets.

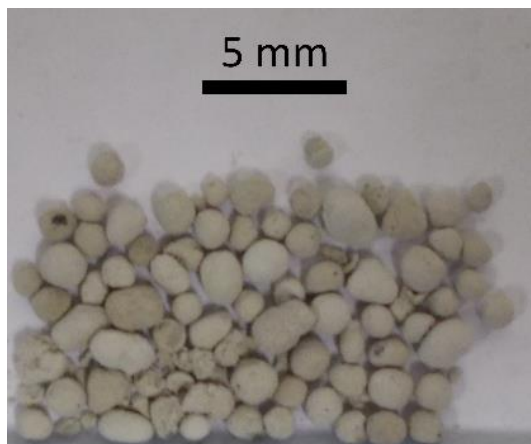


Figure 74: Calcined SiO_2 -SiC pellets.

Si- SiO_2 pellets

Si- SiO_2 pellets are made of 50 mol. % silicon and 50 mol. % Quartz B. The weight composition is therefore 68 wt. % quartz and 32 wt. % silicon. Metallurgical grade silicon (MG-Si) lumps were provided by Elkem ASA. The composition is 99 wt. % Si, with impurities of Fe, Ca, Ti and Al. For further calculation, the composition of MG-Si is assumed to be 100 wt. % Si.

Silicon lumps were hammered down to 10-20 mm size. Afterwards, the material was ground with a Retsch RS200 grinding machine, equipped with WC grinding disc. The grinding time was set at 70 s and the rotating speed at 1100 rpm. The grinding procedure is repeated twice. MG-Si lumps were ground down to an average size of 20.97 μm . The final particle size of the silicon and quartz powders is shown in Figure 75.

The pellets were dried for 6 hours at 120°C and calcined at 1000°C for 30 minutes. The final aspect of the pellets is shown in Figure 76.

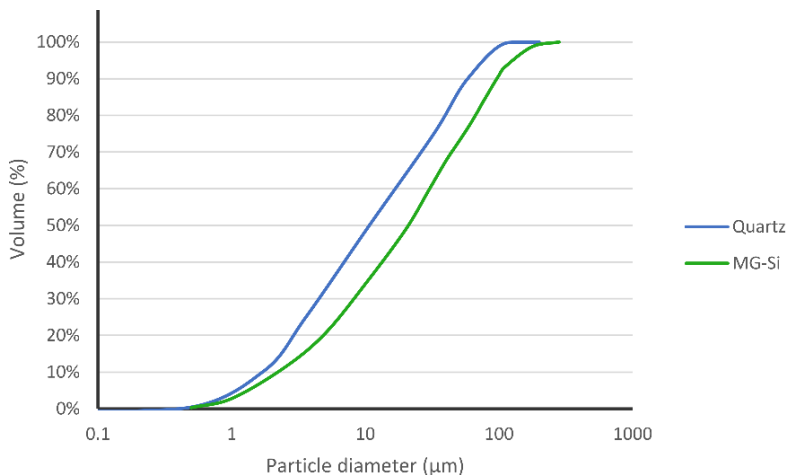


Figure 75: Particles size distribution of SiO_2 and Si powders in the Si- SiO_2 pellets.

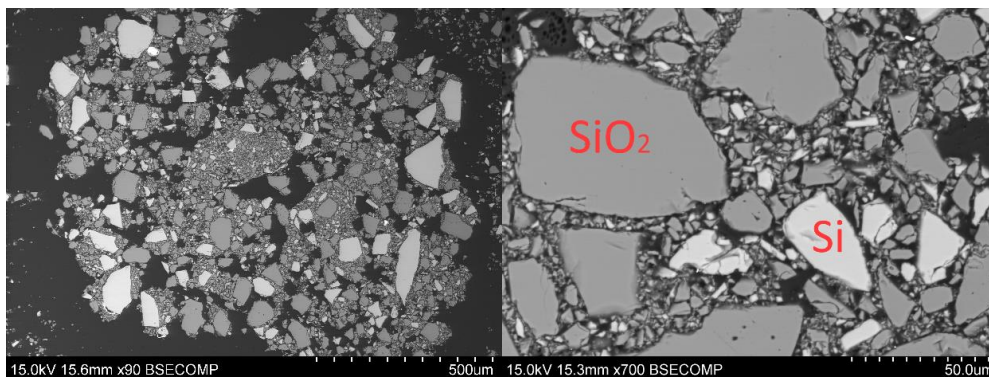


Figure 76: Characterization of Si- SiO_2 calcined pellets at x90 (left) and x700 (right) magnification, BSE-SEM images.

C. Characterization of substrates

SiC, quartz and graphite were chosen as materials for the deposition of the condensates. Figure 77 shows the appearance of the substrates before the experiments. Quartz and SiC were used as particles, whereas graphite comes from the walls of experimental setup. Quartz comes as particles, which are either opaque grey, white or transparent. SiC particles are shining grey or black. Graphite is opaque black.

This section collects the characterization of the substrates before the experiments. The substrates were characterized by XRD, SEM and Light Optical Microscope (LOM). The XRD spectrum was analyzed with TOPAS®. This software can recognize the characteristic peaks of a chosen crystalline structure, after modeling a curve which fits the experimental data. The crystalline parameter of SiC polytypes 3C, 4H and 6H were considered. The 15R-SiC polytype was found in traces during the analysis, therefore its contribution was neglected.

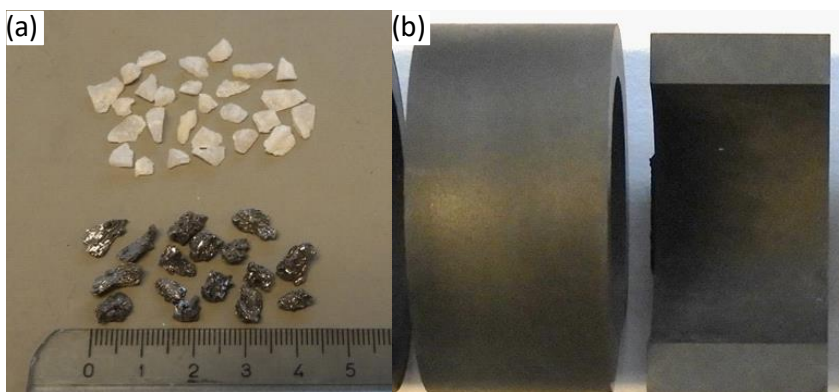


Figure 77: a): Appearance of Quartz A (top) and SiC (bottom) particles chosen as substrates; Right: Section of carbon tube before the experiment. The ruler refers as scale to both pictures.

SiC

SiC substrates are provided by Washington Mills. They have the same composition as the SiC powders used for the SiO₂-SiC pellets. The XRD spectrum revealed the presence of α -SiC in the substrate. Table 7 shows the quantitative results of an XRD spectrum from a ground SiC substrate. The XRD spectrum is shown in Appendix H. The polytypes 6H and 4H, belonging to the α -SiC group, make up to 88% of the substrate. The rest is 3C-SiC.

Table 7: XRD spectrum of SiC substrate.

Polytype	at. %
3C	11.86
4H	12.73
6H	75.41

Visual inspection and LOM showed surfaces rich in drifts and cracks. The crystals on the surface are visible with bare eyes. It is difficult to focus properly on the surface with LOM, as the profile is irregular. Figure 78a shows a picture of a corner of a particle at LOM.

The porosity of the material is very low, despite SEM analysis also revealed some cracks. The compositional analysis revealed inclusions containing Fe, elemental Si, Ti, V and Cr. The inclusions are located both at the core and on the cracks of the particles. Figure 78b shows a SEM picture of a SiC particle, with a crack and an inclusion.

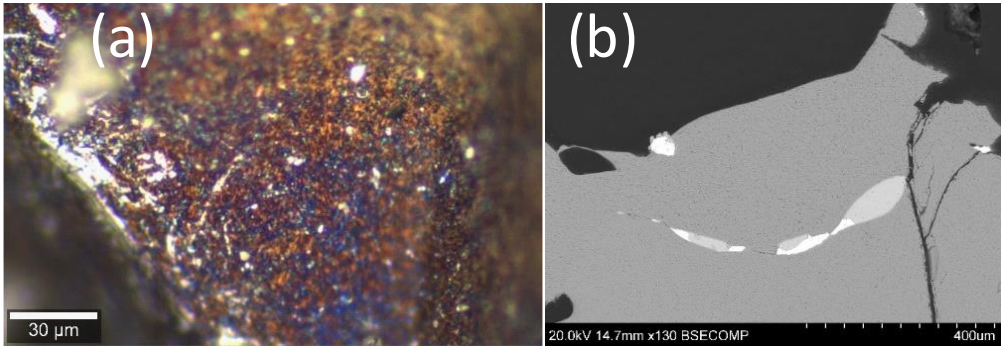


Figure 78: a) LOM image of surface irregularities of SiC substrate; b) SEM micrograph of inclusions in SiC substrate.

The particles were sieved by the following size: 1-3-5-6-8-10-12-14-16-20 mm. A particle size distribution analysis was carried out on the batches 1-3 mm, 3-5 mm and 5-8 mm.

The materials sieved were used to customize the batches called 3-10 mm, 8-14 mm and 12-20 mm shown in Figure 79. The 8-14 mm charge batch consists of 33 wt. % SiC with size 8-10 mm, 33 wt. % SiC with size 10-12 mm, and 34 wt. % SiC with size 12-14 mm. The 3-10 mm charge batch consists of one third of 3-5 mm, one third of 5-8 mm, and one third of 8-10 mm sieved particles. The same applies for the 12-20 mm batch, divided between 12-14, 14-16 and 16-20 mm particles.

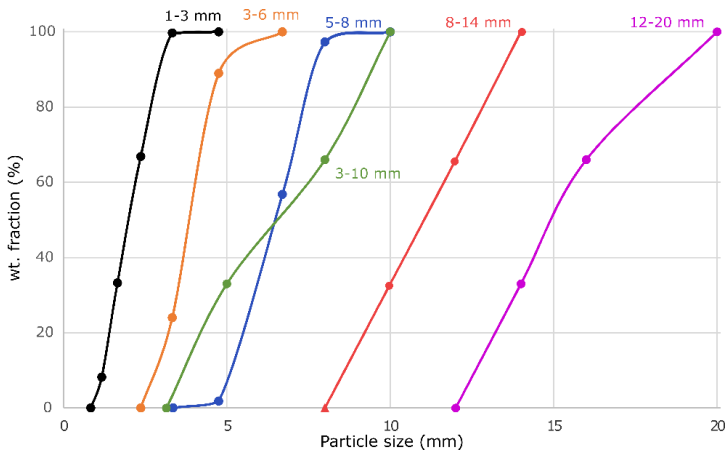


Figure 79: Cumulative particle size distribution of SiC substrates used in the condensation and gas production zones.

Quartz A

The quartz used as a substrate for this work was previously analysed by Jusnes, and called Quartz A [60]. This material is a gravel quartz, originating from a hydrothermal metamorphic vein. The material is inhomogeneous, therefore the results of the characterization analysis could vary locally. The amount of amorphous phase is below 10%, according to the XRD analysis [60]. The formation of amorphous phase could be attributed to milling of the

charge lumps [60]. Jusnes believes that the amount of amorphous phase before milling would be even lower, but still present.

The surface is irregular and can sometimes contain recrystallized materials [60]. The surface of quartz at LOM is shown in Figure 80. Small superficial impurities from the surroundings can accumulate on the surface. The transparent and opaque grey colors are seen with LOM as well. The particle size of Quartz A ranges either between 3-5 or 5-8 mm, according to the chosen experiment.

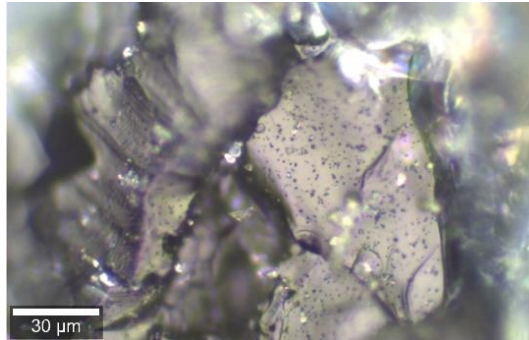


Figure 80: LOM picture of a Quartz A particle.

Graphite tube

The surface of graphite is smooth and regular, as the part was finely grinded for the setup. The material is porous and light. A black powder comes off the surface when scratched.

Figure 81 shows two SEM pictures from the section of the tube, shown previously in Figure 77. The SE-SEM picture (left) reveals the typical structure of graphite, with small compacted graphite crystals. The BSE-SEM shows that the porosity size of graphite lies in the order of magnitude of 10 μm or below.

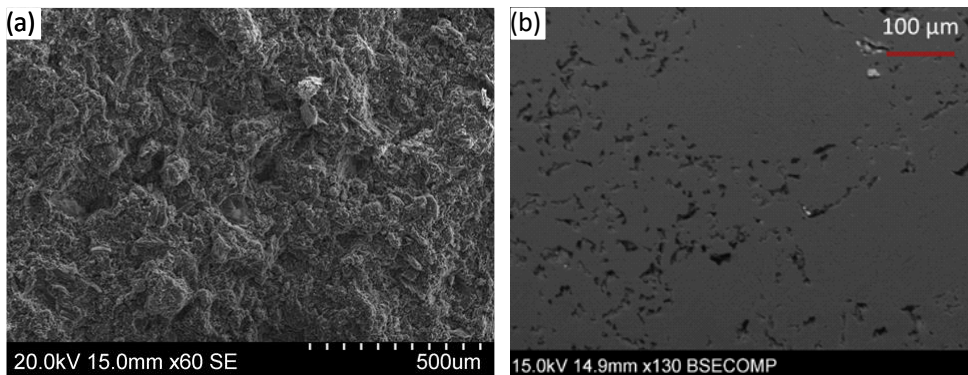


Figure 81: Topography (left) and porosity (right) picture of the graphite part before the experiment.

D. Experimental setups

Closed graphite tube (smaller scale)

Description

A graphite tube furnace is used to heat the pellets and produce a temperature gradient, through which the gas mixture reacts at lower temperatures. Figure 82 shows an overview of the system. The furnace chamber contains a graphite holder, surrounded by graphite heating elements. Water at room temperature circulates in copper tubes and removes heat from the system. The holder outer dimensions are 265 mm height and 95 mm diameter. An alumina tube protects the inlet gas flow and carries it down to the bottom of the graphite cylinder. The alumina tube is assumed inert to SiO(g) reaction at the temperature ranges present in the condensation chamber. The alumina tube is glued to a graphite lance with pure alumina paste. The junction is set at a position where the temperature would not be higher than 1700°C . At higher temperature, alumina would evaporate or sag.

The graphite holder consists of two parts: a condensation chamber mounted at the top, and a SiO(g) production chamber at the bottom. The two chambers can be screwed together into a single piece.

The condensation chamber has an inner diameter of 25 mm and a height of 150 mm (Figure 83a). At the bottom of the condensation chamber, another gas distribution ring homogenizes the gas mixture flow. Solid particles fill the condensation chamber with a height of 130 mm from the bottom of the condensation chamber. This is the place where the condensates are collected, and where the temperature gradient is measured.

The inner dimensions of the SiO(g) production chamber (Figure 83b) are 150 mm diameter and 65 mm height. A smaller crucible of 40 mm diameter and 60 mm height holds 20 g of pellets. A graphite gas distribution ring is placed at the bottom of the smaller crucible. In this zone, the SiO-CO-He mixture composition is controlled by changing the pellets composition and the inert gas flow.



Figure 82: Graphite tube furnace (Thermal Technology model 1000-3560-FP20) [22].

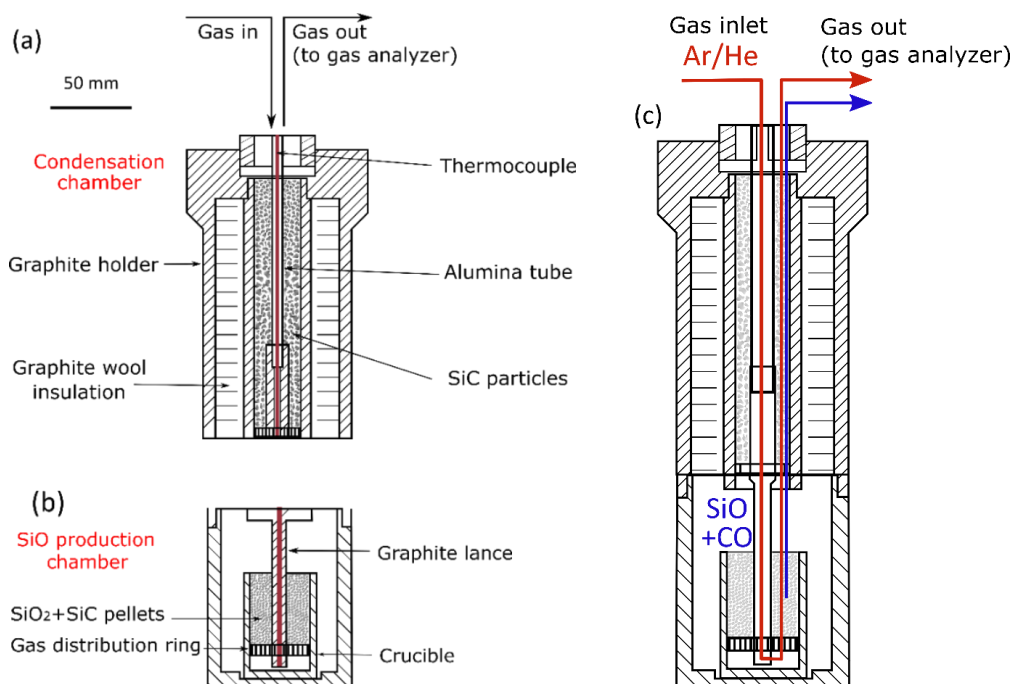


Figure 83: Schematic overview of the graphite tube furnace setup. (a) Condensation crucible and offgas system; (b): Gas production chamber. The condensation chamber is mounted on top of the SiO production chamber; (c) Crucible overview and gas flow paths for He, Ar, SiO(g) and CO(g).

Procedure

The experiments undergo a preliminary preparation procedure, to reduce the oxygen content in the graphite holder and in its surroundings. First, the chamber is purged with Ar for 15 minutes. Then, air is evacuated down to 180 mbar. Afterwards, the chosen input gas is injected in the system. He or Ar act also as protective gases over the whole setup, preventing oxidation of graphite.

The experiment starts after air evacuation. The inlet gas flows between the pellets, and the system is heated. SiO(g) and CO(g) develop from the pellets, according to Reaction -1. SiO(g) and CO(g) are pushed up towards the upper condensation crucible with the incoming inert gas. The temperature in the gas production chamber follows the chosen thermal history, generating a temperature gradient in the condensation chamber. The gas mixture flows through a particle bed, with variable particle size distribution, according to the chosen setup.

After the gas has travelled through the condensation chamber, the outlet gas undergoes compositional analysis. An ABB gas analyzer records the percentage of CO(g). He(g) and Ar(g) percentages in the collected offgas are calculated based on the remaining percentage, as a function of time and temperature. The data collected are only qualitatively reliable.

At the end of the experiment, all the condensates substrate particles are weighted. About 5-10 g of particles are extracted each time, until the crucible is empty. Substrates covered with significant amounts of condensates are selected for characterization. The position intervals of each group of particles is tracked, after each weighing step.

Other relevant positions recorded are the point where the system is clogged and where the particles change their color. The position coordinate is called Y . Y is equal to zero at the bottom of the condensation chamber,

where the temperature is highest. Y is equal to 13 cm when it reaches the top of the chamber, i.e. close to the offgas system.

The condensates also formed on the graphite surface tube. The tube is sectioned and the condensates on its surface were analyzed. Condensates on the condensation chamber graphite walls are partially removed by using SiC sandpaper. After performing the experiments in the order 1a, 2a, 5a, 4a to 4e, 3a, 1b, 1c (see Table 8), the condensation chamber was extracted from the system, for characterization.

Temperature gradients in condensation chamber

The holding temperature is set at temperatures between 1800 and 2200°C, according to the pyrometer located outside of the gas production chamber. The average heating and cooling rates are fixed at 50°C/min and 35°C/min respectively. A change in the target temperature influences the temperature gradient in the condensation chamber.

The temperature gradient is measured in the condensation chamber, by using C-type thermocouples. A single thermocouple is inserted for experiments 1c,d,e and 4c,d,e at a stable position, to monitor the thermal history at a fixed point. For experiments between 13a and 21a, a three-point thermocouple measures the temperature simultaneously in three positions, during the same experiment (Figure 84a).

An average temperature is computed over a time period for every thermocouple. The time period lasts from when the pyrometer reaches the target temperature, until the cooling process starts. The average temperatures are linked to the positions they were recorded at. For experiments 1c-e and 4c-e, each experiment gave an average temperature at a fixed position. The three points were used for a polynomial regression, to compute a temperature gradient specific for setup condition 1 or 4. For experiments 13a-21a, the thermocouple gave three average temperatures. The obtained gradients are characteristic of every experiment. However, it was assumed that other experiments followed the measured temperature gradients. More information can be found in Appendix C.

The temperature in the crucible increases slightly over the time period. The error bars in the picture show the temperature interval at the specific coordinate. The temperature gradient of experiment R19a is used as example (Figure 84b).

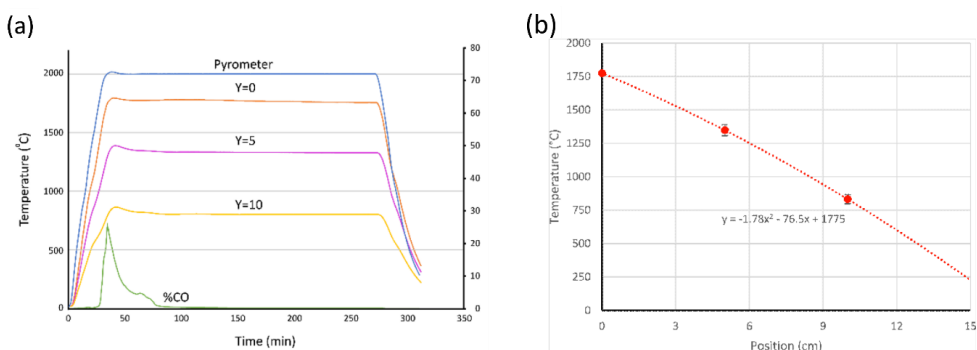


Figure 84: Example of thermal history (a) and corresponding extrapolated temperature gradient (b), Exp. R19a.

List of experiments

The setup variables are the target temperature, holding time, inert gas flow, substrate size distribution and substrate type. Table 8 collects an overview of the different conditions of the experimental setups. Each experiment is marked with “R”, to specify that the small-scale setup was used. Afterwards, a number specifies

the setup condition. Finally, a letter from *a* to *e* defines each experiment repetition. In the experiments marked with “P40”, 40 g of pellets were added to the crucible, instead of 20 g. For Setup R12, SiC filled the chamber between Y=0-30 mm, to avoid melting of Quartz A, which would clog the system. A total of 39 experiments were performed with this setup.

Table 8: Overview of experimental conditions: time, holding temperature and condensation substrate type

Setup	Target Temperature (°C)	Time (h)	Gas flow (l/min)	Substrate composition	Size (mm)
R 1 (a-e)	2000	1	0.4 a: Ar; b-e: He	SiC	3-5
R 2 (a-c)	2000	1	0.05 a: Ar; b-c: He	SiC	3-5
R 3 (a-c)	2000	0.5	0.02 a: Ar; b-c: He	SiC	3-5
R 4 (a-e)	2000	1	Ar 0.02	SiC	3-5
R 5 (a)	2000	4	Ar 0.02	SiC	3-5
R 6 (a)	2200	1	He 0.4	SiC	3-5
R 7 (a-b)	1900	1	He 0.4	Quartz A	3-5
R 8 (a)	1800	2	He 0.4	Quartz A	3-5
R 9 (a,b)	1900	1	He 0.4	SiC	5-8
R P40 10 (a)	2000	1	He 0.1	SiC	5-8
R P40 11 (a)	2000	1	He 0.1	Quartz A	5-8
R 12 (a)	2000	1	He 0.1	Quartz A+SiC	3-5
R 13 (a)	2000	0.5	He 0.1	SiC	1-3
R 14 (a-c)	2000	0.5	He 0.1	SiC	3-5
R 15 (a)	2000	0.5	He 0.1	SiC	5-8
R 17 (a-c)	2000	1	He 0.1	SiC	3-5
R 19 (a)	2000	4	He 0.1	SiC	1-3
R 20 (a)	2000	4	He 0.1	SiC	3-5
R 21 (a)	2000	4	He 0.1	SiC	5-8
R 22 (a)	2000	5 min	He 0.05 CO 0.25	SiC	3-5
R 23 (a)	2000	10 min	He 0.1 CO 0.1	SiC	3-5

Open induction furnace (larger scale)

Setup description

The large-scale setup is an induction furnace, containing a graphite crucible. The setup is sketched in Figure 85. The furnace crucible is cylindrical. The graphite crucible is 400 mm high (outer height) and 150 mm wide (outer diameter). The internal walls of the crucible are 35 mm thick on the bottom, and 20 mm thick on the sides. The crucible is divided into a gas production zone and a condensation zone.

The gas production zone is located at the bottom of the crucible, at the highest temperatures. The SiO(g) producing pellets are placed into a smaller graphite crucible, called pellets chamber. The pellets chamber has a circular base of 100 mm inner diameter and is 70 mm high (outer height). Its walls are 4 mm thick. The carbon surface on top of the pellets chamber was drilled with 128 concentric holes of 3 mm diameter, to let the gas escape from the chamber. A larger hole (25 mm diameter) is drilled at the center of the pellets chamber roof. This allows a shielding graphite tube to enter the pellets chamber. The chamber is placed at the bottom of the graphite crucible, with the drilled surface facing up. The crucible in the gas production zone was designed to separate the gas production materials from the condensation zone.

The space around the pellets chamber is filled with SiC particles, with size between 1-3 mm. Such particles fill the graphite crucible up to 70 mm from the crucible bottom, which is the same height as the height of the pellets chamber.

The condensation zone is the remaining space above the gas production zone. This area is 310 mm high. SiC particles at different size fill the crucible up to the top. The particles size distribution chosen were 5-8 mm, 3-10 mm, 12-20 mm and 8-14 mm, as described in the chapter about characterization of substrates. Condensation chambers were reused, when possible.

A shielding graphite tube protects a multi-point C-type thermocouple. C-type thermocouple wires were soldered at the desired measuring point before each experiment and inserted in the same alumina tube. The alumina tubes chosen are designed to provide up to five temperature measurement points. Temperature was measured every 70 mm, starting from $Y = 1$ cm (i.e. 1 cm from the bottom of the graphite crucible).

One of the experiments (IF6a) was used to check if there is a horizontal temperature gradient within the condensation zone. IF6a has a slightly different setup than the other experiments. The gas production chamber was moved to the edge of the crucible. Two graphite tubes were used in this experiment. The first was inserted in the gas production chamber, whereas the second was placed close to the opposite border of the chamber. Each tube protected a multi-point C-type thermocouple. The first thermocouple is close to the center, and measures the temperature at all the 5 available positions ($Y = 1, 8, 15, 22$ and 29 cm), whereas the second one has 4 available measuring points located at the crucible edge, at $Y = 8, 15, 22$ and 29 cm.

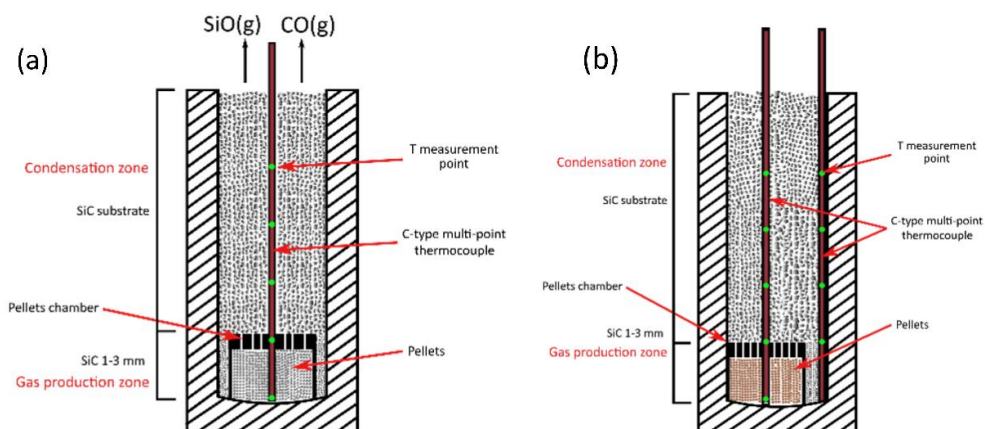


Figure 85: Left: Large-scale setup; Right: Large-scale setup for lateral temperature gradient computation.

Running experiments in a larger setup allows to analyze better some parameters which are difficult to inquire in the small-scale setup. In the larger scale setup, the effects of the particle size distribution could be investigated easier, pictures of the crusts are easier to be taken, and the amount of condensates produced will be larger. In addition, this will simulate the industrial furnace better, as no inert gas is added.

Procedure

The gas production zone is first assembled. The pellets chamber is inserted in the graphite crucible. Then, the desired pellets mixture is inserted in the pellets chamber with a funnel. Afterwards, the same funnel is used to fill the surroundings of the pellets chamber, with SiC particles with size 1-3 mm. The SiC particles must not enter the pellets chamber, nor the pellets should come out from the bottom of the pellets chamber itself. Finally, the graphite tube is inserted in the central hole of the pellets chamber.

For the condensation zone, the mounting procedure consist simply in placing the SiC particles and the thermocouple in the crucible. First, the desired SiC particles are poured in the condensation chamber to fill the crucible to the top. Their amount is usually around 3 kg. Then, the thermocouple is inserted in the graphite tube and connected to the temperature measurement software.

The thermal history of each experiment is controlled at the second measurement point from the bottom of the crucible ($Y = 80$ mm). This point is located slightly above the gas production zone. It is assumed that the gas came out of the gas production zone at the temperature measured at the top of the pellets chamber, i.e. at 80 mm from the bottom of the graphite crucible. The temperature is recorded continuously during the experiment. The experiment is aborted if the thermocouple at $Y = 80$ mm brakes.

The induction furnace is turned on and the experiment is carried out with the chosen temperature and time conditions. The power supply history was kept constant for each experiment, giving a heating rate of $40^{\circ}\text{C}/\text{min}$. The target temperature was fixed for all the experiments at $1890 \pm 10^{\circ}\text{C}$. The temperature at $Y = 80$ mm oscillated by 10 degrees, since the power was supplied manually to the furnace. When the target temperature is reached, the oscillation period lasted for ca. 20 minutes. An oscillation period is the time used for an increase from 1880°C to 1900°C , or vice versa.

Once the experiments were finished, the SiC charge is analyzed by excavating the crucible. The material is extracted with the help of a spoon. When the system is clogged, a steel pin is used to poke the charge. Partially reacted pellets are collected from the pellets chamber, then weighted and characterized.

The pellets chamber is cleaned from SiC and Si residues stuck on its surface. The extraction and cleaning procedure of the pellets chamber needs often the use of a hammer, and the pellets chamber could be damaged. If that happens, a new chamber is used the next experiment. This is always the case for experiments containing Si-SiO₂ pellets.

List of experiments

The parameters varied in the large-scale setup are the pellets composition, the holding time and the SiC substrate particle size distribution. The pellets are either the SiO₂-SiC or the Si-SiO₂ mixture. The holding time was fixed at 10, 30 or 120 minutes, since the instant when the target temperature was reached. The particle size distributions are those represented earlier in Figure 79. Table 9 gives an overview of the setup conditions. The letters “IF” indicate that the large-scale setup was used. The numbers identify a setup, whereas the letters label repetitions of each experimental setup.

As for the small-scale setup, a temperature gradient develops in the condensation chamber. The average temperatures are computed as described in the procedure section of the small-scale setup. An average value is computed and related to its position. After polynomial regression, the temperature gradient in the system is obtained. The thermal history and related temperature profile of experiment IF1b is shown in Figure 86. The relation between position and temperature follows a similar trend to a model previously computed by Kennedy [82], as shown in Figure 87. Appendix C contains all the polynomial expression for the temperature as a function of position in every experiment. The results of the horizontal temperature gradient computation (Experiment IF6a) are also collected in Appendix C.

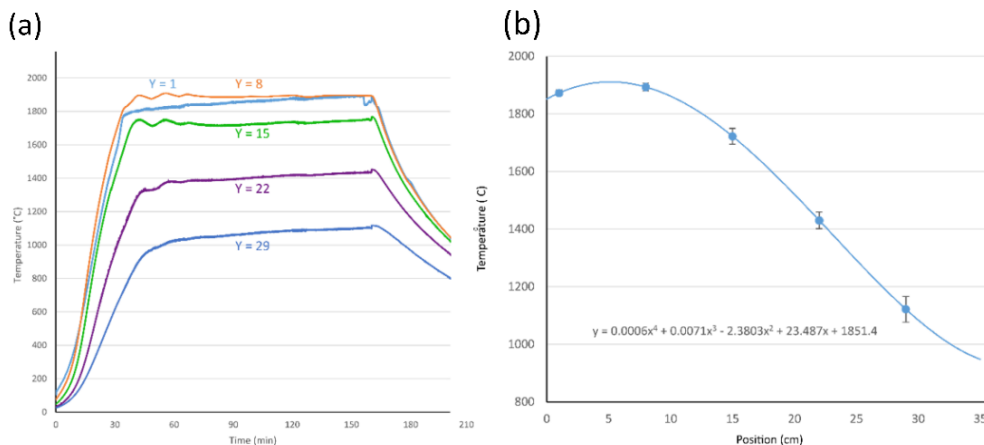


Figure 86: Thermal history (a) and computed temperature gradient (b) of experiment IF1b.

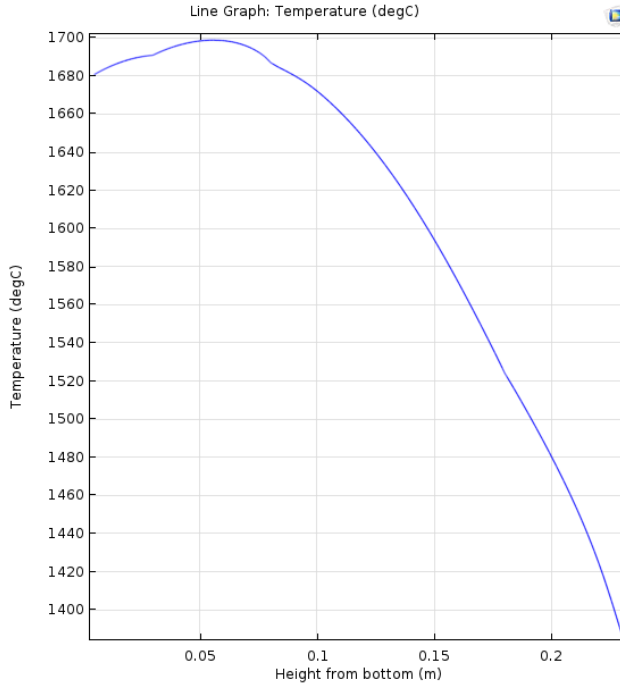


Figure 87: Temperature gradient in large-scale setup computed by modelling [82].

Table 9: Overview of experimental conditions: time, pellets compositions and condensation substrate type.

Setup name	Pellets used	SiC substrate size	Holding time (h)
IF 1 (a,b)	SiO ₂ -SiC	3-10	2 hours
IF 2 (a,b)	SiO ₂ -SiC	5-8	2 hours
IF 3	SiO ₂ -SiC	12-20	2 hours
IF 4	SiO ₂ -SiC	8-14	2 hours
IF 5 (a,b)	Si-SiO ₂	3-10	2 hours
IF 6 (a,b)	Si-SiO ₂	5-8	2 hours
IF 7 (a,b)	Si-SiO ₂	12-20	2 hours
IF 8	Si-SiO ₂	8-14	2 hours
IF 9	SiO ₂ -SiC	3-10	30 min
IF 10	Si-SiO ₂	3-10	30 min
IF 11	SiO ₂ -SiC	3-10	10 min
IF 12	Si-SiO ₂	3-10	10 min

E. Industrial samples

REC Solar

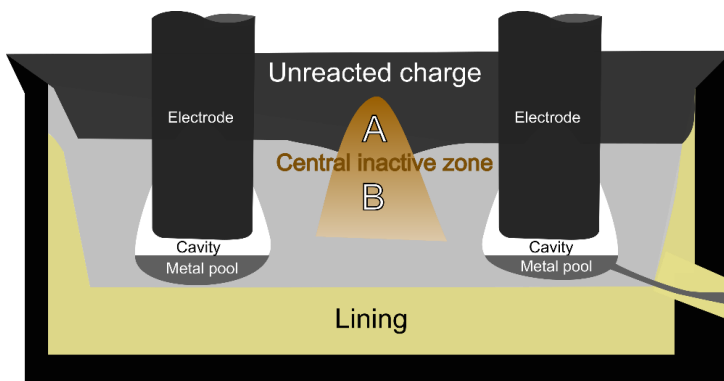


Figure 88: Sample location in Elkem Fiskaa plant (Kristiansand, Norway)

Two condensates samples were extracted from Furnace 11 at REC Solar in Fiskaa, Kristiansand (Norway), where the furnace is used for the production of solar grade silicon. The central inactive zone is located at about 1 meter from the top of the furnace. During operation of the furnace, the operators managed to push out the top of the inactive accumulated material, by using the stoking car. Thus, sample A and B were extracted from the position represented in Figure 88.

Samples A and B are shown in Figure 89. Sample A consists mostly of quartz and carbon particles, tied to each other by different materials. A brown, solid layer is present in large portions of the sample. Some areas have a grey color. Green and white layers cover and bind the charge. The white layers are easier to brake than the brown ones. Some charge pieces are also transparent. Sample A was broken with a hammer, and smaller samples were chosen according to their different colors, as marked in Figure 89. Ten samples were collected from sample A.

Sample B is a solid, black compound with shining grey droplets. This was a clear hint of the presence of SiC and silicon. SiC formation goes out of the scope of this thesis, therefore the sample was analyzed by Sethulakshmy Jayakumari (NTNU – Department of Materials Science and Engineering, Trondheim, Norway) [22].

Table 10 resumes the results of the visual inspection. Samples coming from this furnace will be identified with a prefix "REC" before the sample number. Samples were divided into three groups. Samples from Group 1 contains mostly the green and white compounds. Group 2 gathers samples with high amounts of the transparent compound, which is thought to be molten quartz. Group 3 consists of 5 lumps with high concentration of brown and grey materials. The "Expectation" columns collects the expectations made by Wegge [83] on the content of the samples.

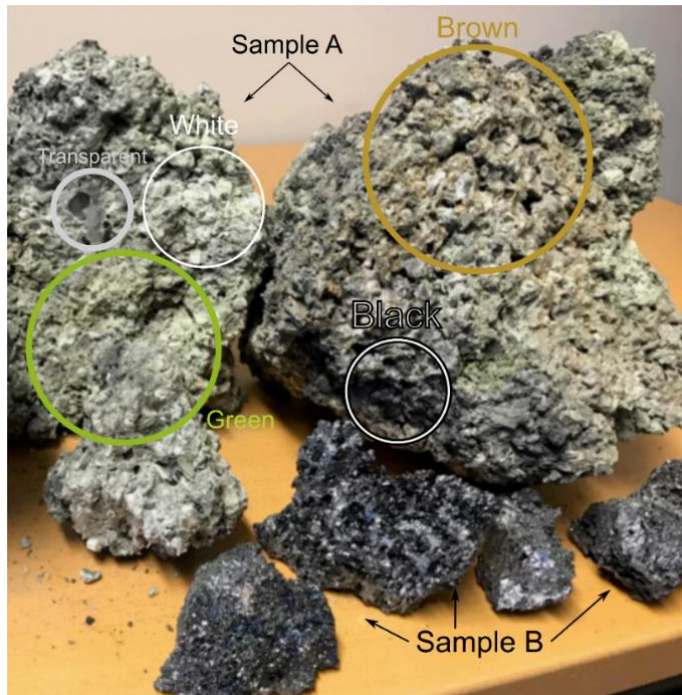


Figure 89: Fragments of industrial samples from Elkem Kristiansand. Examples of compounds of different colors are highlighted by the circles in the figure.

Table 10: Overview of samples extracted from sample A, REC Solar.

Sample number	Visual inspection	Expectation [83]
REC 1.1	Green and white particles	Molten quartz and SiC
REC 1.2	Green and white particles	Molten quartz and SiC
REC 1.3	Black and green particles	Carbon, SiC, quartz
REC 2.1	Transparent and black particles	Quartz, carbon, (SiC, quartz in minor amounts)
REC 2.2	Transparent material	Quartz
REC 2.3	Black particles and transparent material	Carbon, SiC, quartz.
REC 3.1	Brown and grey compounds	Brown condensate, porous and molten silica, quartz, silicon carbide
REC 3.2	Grey and white particles, small amounts of brown	
REC 3.3	Brown and grey compounds, mixed	
REC 3.4	with white particles	

Salten

The samples analyzed from furnace n°2 in Elkem Salten (Norway) come from the excavation performed by Ksiazek in 2018 [81] (Figure 90). Samples coming from this excavation will be identified with a prefix “S” before the sample number. Samples S.22 and S.23 were located between port 1 and electrode 2. They have fallen from the furnace top, as the top of the charge was being removed while the samples were being extracted. Sample S.22 is white and pale green. Sample S.23 is orange and white and disintegrates easily into crumbs when handled. Sample S.36 was found behind the refractory wall of the furnace, between port 4 and 5. The sample is made of a grey-brown compound which embeds green and white particles. Table 11 contains the sample details at visual inspection.

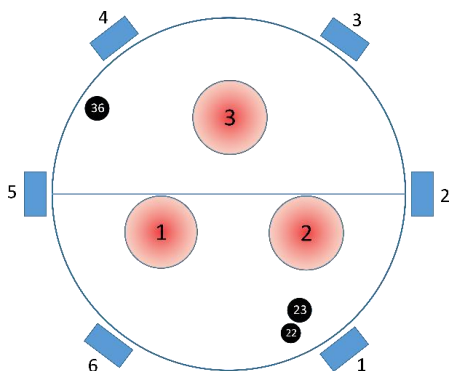


Figure 90: Estimated position of samples S.22, S.23 and S.36. Revised from Ksiazek [84].

Table 11: Overview of samples analyzed from Salten furnace n°2.

Sample number	Visual inspection
S.22	White-green solid lump
S.23	Orange porous compound
S.36	Grey-brown compound binding green and white particles

Wacker 1

Samples extracted from Wacker furnace n°1 come mostly from the electrode zone and upper charge areas. The furnace was excavated by Ksiazek et al. [2], and the samples come from the same study. Samples coming from this excavation will be identified with a prefix “W1” before the sample number.

Figure 91 shows an overview of the samples analyzed, and their position in the furnace. Sample W1-31 was extracted close to the electrode area, at a height of 1.7 m above the taphole. A part of the sample is green and contains mostly SiC and charge. The sample surface has also a soft white and blue coating, easy to remove, which is expected to be white condensate. Sample W1-34 consists of charge bound by green condensate. It is located slightly above sample W1-31, but on the other side of the electrode. Sample W1-43 was taken from the center of the furnace, on the border between loose charge and reacted charge. It is located near sample W1-34, but closer to the furnace core. Samples W1-38, W1-39 and W1-40 were extracted at heights between 1.5-2 m from the taphole level, at the furnace walls. Sample W1-43 comes from the low T central zone.

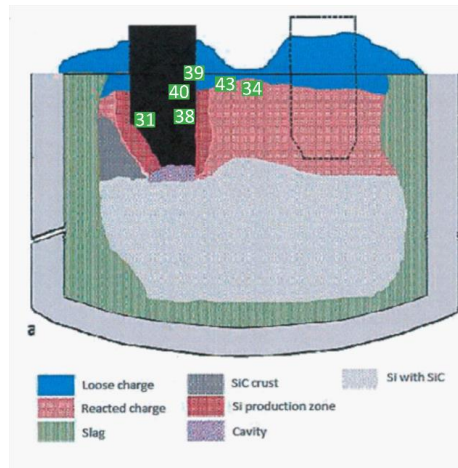


Figure 91: Overview of samples analyzed from Wacker 1 excavation. Revised after Ksiazek et al. [2]

Table 12: Overview of samples analyzed from Wacker 1.

Sample number	Visual inspection
W1-31	White-blue wool coating
W1-34	Brown/greyish condensate
W1-38	Porous white compound
W1-39	Porous white and green compound
W1-40	Porous grey compound
W1-43	White layer on charge lump

Wacker 4

The furnace was excavated earlier by Ksiazek et al. [2] and some samples were also analyzed by Bø [55]. The samples chosen from the excavation of Wacker 4 were taken in proximity of an electrode (Figure 92). Samples coming from this excavation will be identified with a prefix “W4” before the sample number. Samples W4-29 and W4-30 are white, and they come from the area where the charge particles start sticking to each other. Sample W4-34 comes from the loose charge area. Both Bø and Ksiazek identify it as a condensate at visual inspection. Sample W4-42 comes from the furnace bottom. The sample was identified as a slag, but some portions of it could contain Si-SiO₂ condensate .

Table 13: Overview of samples analyzed from Wacker 4.

Sample number	Visual inspection
W4-29	White
W4-30	White
W4-34	White/grey lump
W4-42	Black and white lump

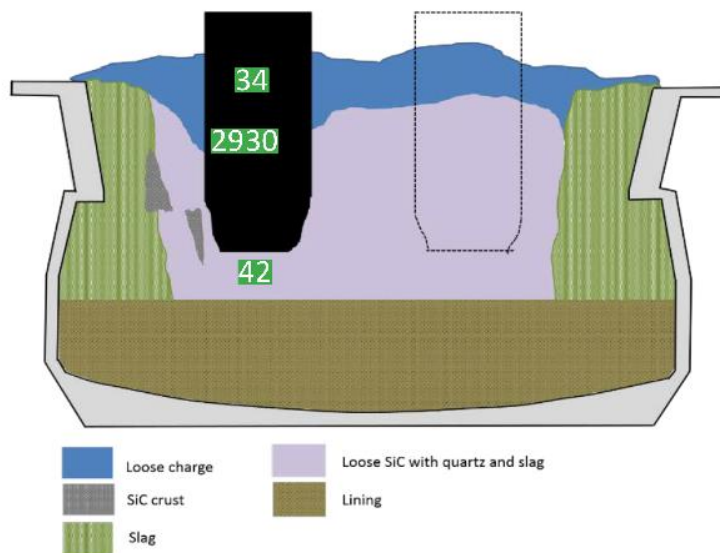


Figure 92: Overview of Wacker 4 furnace and sample positions, revised after [55], [57].

F. SEM (Scanning-Electron Microscopy) and EPMA (Electron Probe Micro-Analysis)

Sample preparation

Many samples were collected from each experiment and for some of the temperature intervals, to undergo SEM analysis. Some samples are analyzed to check the topography on the condensates deposited on their surfaces (SE-images). Some particles are mounted in traditional epoxy, to analyze phase distribution and composition (BSE-images). Other particles are mounted in an iodoform-containing epoxy, which enhances the contrast for carbon-containing materials (BSE images). Thanks to its higher conductivity, the epoxy was used when condensates were deposited on graphite or SiC.

The iodoform-containing epoxy was made by a custom-made experimental procedure, revised after Gomez [85]. For the creation of this resin, 10 wt. % iodoform is dissolved at room temperature into the remaining 90 wt. % resin precursor, after stirring thoroughly. Then, the mixture is cooled down to 10°C. The hardener is added in the proportions specified by the resin producer. The temperature is kept at 10°C for 3 hours, after having added the hardener. The sample is then ready for extraction, after hardening. The epoxy will turn dark orange. Once the resin has solidified, the application of a carbon coating grants the conductivity of the epoxy, which is necessary for SEM analysis.

SEM and EPMA tools

Back-scattered (BSE) and secondary-electron (SE) images are taken with a Hitachi SU-6000 FE-SEM. The working distance is set at 15 mm and the voltage between 5 and 20 kV.

EPMA (Electron Probe Micro-Analysis) is carried out on the samples used for the metallographic analysis by using a JEOL JXA-8500F. The work has been performed with Morten Raanes at the Department of Material Science

and Technology at NTNU. Points showing different contrasts are selected to detect the relative mass percentage of Si, O and C.

EPMA analysis is not quantitatively precise for light elements, such as C and O. However, assuming the technique is quantitative, the counts per second are proportional to the atomic percentage. In this way, the phase composition within 1 μm radius can be estimated. A mapping is performed on condensate samples from experiment R4a and R4c.

G. Transmission Electron Microscopy (TEM) and Focused-Ion Beam (FIB) preparation

TEM analysis can visualize details at a higher resolution and smaller scale than SEM. Qualitative elemental analysis and mapping are based on Electron Energy Loss Spectroscopy (EELS) data. Pictures collected from TEM analysis were scanned by High Angle Annular Dark Field Scanning Transmission Electron Microscopy (HAADF-STEM) and Selected Area Diffraction Analysis in Bright Field (SADA-BF).

TEM analysis is performed with a double Cs corrected coldFEG JEOL ARM 200F, operated at 200kV and equipped with a large solid angle (0.98 sr) Centurio SDD detector for X-ray energy dispersive spectroscopy (EDS) and a Quantum ER GIF for Electron Energy Loss Spectroscopy (EELS).

There are two possible ways to prepare TEM samples, according to the texture of the analyzed compound. The first one is specific for thin and soft layers, whereas the second for thick and hard compounds. In both cases, it is possible to perform HHADF-STEM, SADA-BF for topographic analysis, as well as EDS and EELS for compositional analysis.

Thin layers analysis

The condensates can appear as thin layers, which can be scratched away from the condensation substrates and analyzed in the TEM microscope. The removed fine material is mixed in an isopropanol solution. A droplet is extracted and placed on a copper TEM grid. The TEM substrate is dried at room temperature. The sample preparation and analysis were carried out by Ragnhild Sæterli (NTNU). Samples are collected from experiment 4c.

FIB preparation for thick condensate layers

Other compounds appear as continuous, dense layers, with a complex structure at nanometric level. The sample needs a special preparation procedure called FIB (Focused Ion Beam) preparation. The FIB preparation and the TEM analysis was done in collaboration with Per Erik Vullum (SINTEF). A step-by-step description of the FIB procedure is given in Appendix B.

A bulk piece of material is collected from experiment R1b, and a slice of desired extension was etched from the surface. An ion beam etches the surface of the sample in controlled places, in order to create a slab. The slab is collected and welded with tungsten to a dedicated TEM grid. The whole apparatus is controlled in a SEM chamber. A well-made FIB slab should be thin enough to allow the TEM signal to be transmitted through it, therefore it should not exceed 100 nm in thickness. The final slice dimensions were approximately 30 μm x 30 μm x 100 nm.

H. XPS analysis

Technique description

X-ray Photoelectron Spectroscopy (XPS) is a characterization technique that identifies the chemical environment of surface atoms of a sample. The technique is based on the photoelectric effect, where electrons are emitted from the materials when illuminated with X-rays. The electrons stemming from different elements and orbitals have their own characteristic energy. These binding energies further depend on the chemical environment. XPS is a surface sensitive technique, with an analysis depth ranging around 5-10 nm. The analysis area is approximately 200x200 μm .

The surface roughness is a possible error source in XPS. An even surface assures a more precise signal. The SiC substrates are not flat. Some of the reflected signal from a corrugated surface can go outside of the dedicated area of the sensor capturing the signal. When a surface is not perfectly flat, the analysis can be considered at least semi-quantitative.

The XPS technique is sensitive to the carbon content, i.e. the data about the chemical environment of carbon atoms should be interpreted qualitatively. Carbon signals may come from bonds to the surface as an organic impurity, which are belonging to what is called *adventitious carbon*. C-C bonds may belong to organic impurities, as well as the remaining peaks for the bonds involving C, H and O. Quantification of small quantities is challenging with XPS, since the dissolved carbon is present in very low amounts. The condensate was separated from the SiC substrate before XPS analysis, therefore any carbide signal is merely caused by the condensate itself.

Procedure

White and brown condensates were manually separated from the SiC particles and the graphite parts for XPS chemical analysis. The particles were extracted from Experiment R4c, in the temperature area between $T = 1580\text{-}1706^\circ\text{C}$. Each sample measures about 5 mm size.

The X-Ray source used is an aluminum monochromatic source K_{α} at $h\nu = 1486.6\text{ eV}$. Pass energy of 160 eV was used for survey scans and 40 eV for the individual core levels. The XPS analysis was performed by Ingeborg-Helen Svenum at the Department of Materials Physics at SINTEF, on a Kratos Axis Ultra.

For each sample analyzed, a survey spectrum and the core level regions of the elements present were recorded. The noise signal ratio is similar between the samples. The survey spectrum acts as a quantitative analysis. The element sub-spectra can quantify the relative amount of electrons involved in a specific bond. The amount of bonds is quantified by the counts per second.

The analyses of the spectra were performed using the software CasaXPS®. The spectrum collected is fitted by assessing the bond's contribution to the spectrum. Charge compensation is used during acquisition. The energy of the bonds used for peak fitting are collected in Table 14.

Table 14: Reference values chosen for peak fitting in XPS [86].

Si-2p core level spectra	Binding Energy (eV)
Si-C (SiC)	100.4
Si-O-C (fitted with three equally distanced peaks)	101.2 – 102.8
Si-O (SiO ₂)	103.6
Si-Si (elemental silicon)	99.4
C-1s core level spectra	Binding Energy (eV)
C-Si (SiC)	282.8
C-C , C-H (Adventitious carbon)	284.9 – 285.0
C-OH , C-O-C	286.3 – 286.4
C=O	287.4 – 287.6
C-O=C	289.1 – 289.3

I. X-Ray Diffraction (XRD)

To investigate SiC polytypes in the samples, X-ray diffraction (XRD) analyses are carried out by the internal standard method, suggested by Jusnes [60]. This method consists in adding a known amount of a crystalline material with a similar mass and mass absorption coefficient as the sample, in order to quantify the amount of amorphous phase in the sample. The analysis was performed in collaboration with Sethulakshmy Jayakumari (NTNU, Department of Materials Science and Engineering).

The SiC particles covered in condensates are brushed with a steel brush, to remove the white and brown layers. The powders obtained are dried at 250°C for 6h, then at 150°C for 4 hours and finally kept at 120°C. The sample is weighted and then mixed with α -Al₂O₃ (99.9% purity, see Appendix H for XRD analysis), so that the final sample consists of 20 wt.% Al₂O₃. SiC from the substrate is also coming into the sample. The dried sample is crushed manually with a mortar and mixed with acetone while crushing, until acetone is completely evaporated. Finally, the powder is loaded into back-loading sample holders, for the analysis. Table 15 collects the sample compositions for the internal standard method samples.

The X-ray diffractograms (XRD) from each sample are collected using a Bruker D8 Focus X-ray diffractometer running in Bragg-Brentano collection mode with Cu-K α radiation.

Quantitative analysis of phases is first performed with the software Diffract.Eva, to check the content of Si, SiO₂, SiC and Al₂O₃. Then, the quantitative analysis of diffraction patterns (i.e. the polytypes of SiC and SiO₂) was analyzed using the software Topas V5. The structures polytypes included in the models are 2H, 3C, 4H, 6H and 15R for SiC, and cristobalite and quartz for SiO₂. Corundum (Al₂O₃) and elemental silicon are also saved as structures. Since the amount of corundum is known in advance, the software can also calculate the amount of amorphous phase. To make a good fit with the calculated curve, unit cell parameters and sample displacement were refined for each sample. The Chebyshev order was kept at 4 for all the measurements, and the instrument had a 2 θ angular range of 3, and a fix divergent slit (FDS) angle of 0.3.

Table 15: Composition of XRD samples analyzed with the internal standard method.

Sample name	Sample weight (g)	Corundum weight (g)	Corundum percentage (wt.%)
White 1	0.4369	0.1126	20.49
White 2	1.7950	0.4518	20.11
White 3	0.8164	0.2041	25.00
Brown	1.5803	0.4069	20.48

J. ImageJ®

Software description

ImageJ® is an image-processing software. One of its functions can isolate areas of the pictures with different contrasts, for black and white pictures. This software is useful to analyze the particle size distribution of a compound inside a matrix, when the two phases have different colors. ImageJ® was used to quantify the size of silicon spheres in the Si-SiO₂ condensates, and their evolution in the sample.

Figure 93 shows how ImageJ® works. After setting a size scale on the original picture (Figure 93a), a contrast threshold will transform the picture into a black and white image. The picture is marked in red where the picture is darker than the threshold. The rest of the picture keeps its original color (Figure 93b). At this point, ImageJ® can collect information about relevant geometrical parameters of the white areas, for example aspect ratio, particle area, particle diameter and number of particles per picture.

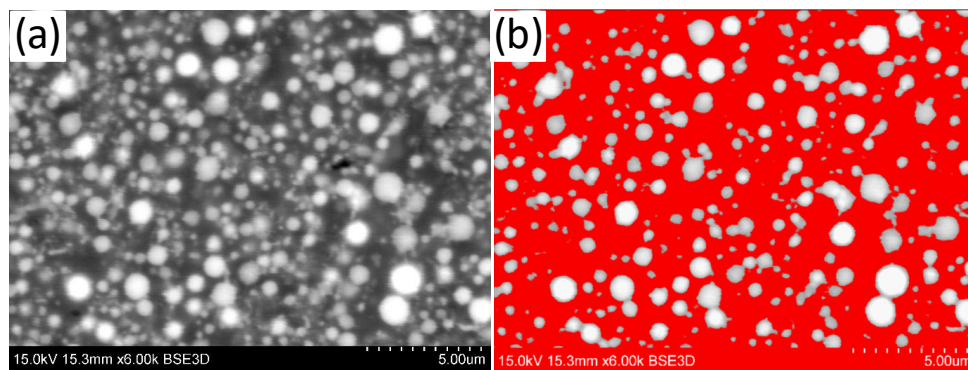


Figure 93: A black and white SEM picture before (a) and after (b) a contrast threshold is applied on ImageJ®.

Procedure for particle size analysis on brown condensate

The size distribution analysis was carried out through different pictures, taken at different positions on a coordinate x . Once chosen a starting point (placed at $x = 0 \mu\text{m}$) on a metallographic sample, a series of BSE-SEM pictures is taken along a fixed direction, until the external surface of the sample is reached. Every picture is taken at $30 \mu\text{m}$ from the previous one. All the pictures from the same sample have the same contrast, magnification and working distance. A series of images was taken either at $\times 4000$ or $\times 6000$ magnification.

ImageJ® cannot recognize merging spheres, therefore three filters were applied to spot merging particles, based either on area or circularity.

- **Filter 1:** a **maximum area** limit was set after measuring the largest particle in the picture. This area filter could spot merged particles which give areas larger than the largest particle in a picture.
- **Filter 2:** particles with **aspect ratio below 1.5** were considered. This filter was very useful to spot particles merging, as the merged areas are not circular anymore. The merged particles spotted by these two filters were separated by a thin black line. Then, the size distribution analysis was repeated.
- **Filter 3:** a **resolution filter** should be applied, to disregard particles which are too small to be resolved. Particles with areas below 50 pixels (7500 nm² with magnification x4000, or 3300 nm² with magnification x6000) were not considered.

ImageJ® collects the values of the major and minor axis of a circumscribed ellipse over every particle. When the particles almost circular, these two values are very similar. It is more convenient to define a new parameter as the average between the major and the minor axis of a sphere. This value will be called “average sphere diameter”. After collecting data on every sphere in a picture, the average sphere diameter, particle area and aspect ratio are computed. Appendix D collects numeric values for all the parameters and their standard deviations.

The contrast threshold is not enough to separate two phases during an ImageJ analysis. Sometimes a brighter phase particle would either merge or overlap with other particles, thus creating errors in evaluating their size. Besides, a small variation in the contrast threshold influence the detected particle size. This can happen to particle emitting a weaker signal, for example particles laying below the external surface, whose signal is partially hindered by the darker matrix.

3. Results

This section will gather all the analysis carried out on the condensation products. The main topics of this section will be characterization, analysis of industrial samples, temperature of formation, clogging, mass balance and reaction rates.

Sections A and B are the characterization chapters. Here the findings from visual inspection, micrographs and spectrographic techniques are collected. The characterization sections are two, one for each type of condensate. Section A describes the white, blue and grey SiC-SiO_x mixtures, consisting of nanowires or micrometric oriented fibers. Section B focuses on the brown Si-SiO₂ mixture, which appears to be an emulsion of Si and SiO₂ when formed from the gas phase. Elemental silicon in Si-SiO₂ mixture can flow inside the condensate, if heated at prolonged times above the melting point of silicon.

Section C analyzes the similarities between industrial samples and condensation products from this study. SEM analysis showed that industrial samples are rich in SiC-SiO_x nanowires, Si-SiO₂ condensates, porous silica and SiC whiskers (which are not considered as condensates and are further analyzed in Appendix A). Few of the samples also show the grey condensate. The samples are located in the low temperature zone of the furnaces, where the temperature is comparable to the lab-scale experiments.

Section D uses the correspondence between a position in the crucible and temperature, to identify the temperature intervals where the condensates are formed. The temperature in the crucibles ranges between 200 and 2000°C. SiC-SiO_x mixtures were found in a broader temperature interval (920-1810°C) than Si-SiO₂ condensates (1400-1810°C).

Section E focuses on clogging of crucibles at laboratory scale. The substrates stick to each other between ≈1300-1700°C. A crucible is more clogged when the particle size distribution is broad, or the average diameter is small. Besides, the higher temperature in the high temperature zone shifts the clogging intervals to higher position in the condensation zone, whereas a gas richer in SiO(g) creates thicker condensates crusts. Longer time make the crust build up over a larger interval. Smaller crucibles clog easier than large crucibles.

Section F studies the mass balance between the gas and condensates phase, and the condensation reaction rate. This section collects the condensates weights and the amounts of gas-producing materials reacted. From the initial mass of gas-producing materials, only 5-25% becomes a condensate. The rest is either lost to the off-gas system or reacted with graphite to produce SiC and Si. A dedicated section on Si and SiC formation on graphite is collected in Appendix A. Condensate weights, reaction times and temperatures are the basis for calculation of reaction rates. The rate increases between 1400-1700°C, in correspondence of the clogging intervals, and then decreases at about 1800°C. The rate is higher in correspondence of the clogging intervals, i.e. clogging will occur when more condensate is formed.

A. SiC-SiO_x mixtures characterization

Nanowire condensates

Visual inspection and SEM analysis

The blue condensate (900-1500°C) covers the SiC and quartz particles with a thin, wool-like layer. However, the condensate can be removed easily by manual scratching, especially for Quartz A. The appearance is the same for both the small and the large-scale setup. Figure 94a shows how the condensates look when deposited on SiC-substrates.

In SEM, the layer appears as a thick web of disordered nanowires which are several hundred μm long. Blue condensate on quartz tends to develop thinner nanowires than on SiC. In fact, Figure 95a and Figure 95b are similar, but the first is taken on SiC at x13k magnification, whereas the second is taken on a quartz substrate at x20k magnification.



Figure 94: Samples from Experiment IF10, $T = 1370\text{-}1650^\circ\text{C}$. a) 1) SiC particle without condensate; 2) SiC covered in white and blue condensate; 3) SiC covered in white condensate. 4) SiC covered in grey condensate. B) Top: Quartz A covered in white condensate; Bottom: Quartz A without deposition of condensate.

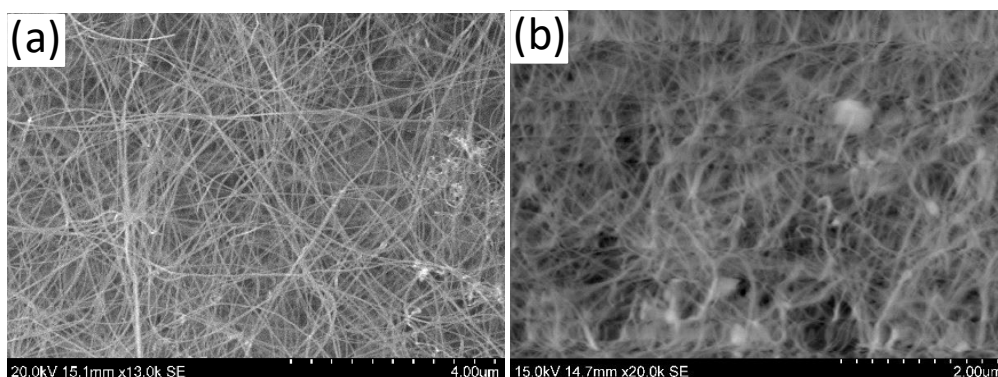


Figure 95: Blue condensate on SiC (Exp. R2a, estimated $1390\text{-}1500^\circ\text{C}$); Right: Blue condensate on Quartz A (Exp. R12a, estimated $950\text{-}1050^\circ\text{C}$)

The **white condensate** appears as a thin, opaque layer on both Quartz A and SiC (Figure 94). The condensate sticks to the surfaces better than the blue condensate. When scratched, layers of blue condensate often appear below the white.

In SEM analysis, the white condensate also consists of an intricate web of nanowires (Figure 96). The white condensate is therefore strictly related to the blue condensate, in terms of microstructure. However, the main difference from the blue condensate is the presence of **nodules in white condensate**, found either as large nodules covering several wires, or as small beads on a single wire. Blue condensates are poor of nodules and form generally at lower temperatures ($900\text{-}1500^\circ\text{C}$) than the white ($1100\text{-}1810^\circ\text{C}$). Areas with a large amount of nodules may assume an orange color, which has the microstructure of Figure 97. The nodules size ranges between $0.25\text{-}1.0\ \mu\text{m}$.

Nodules can either merge into a larger nodule or form a scale which embeds the wires. When they form on a single wire, nodules can be organized into “necklace structures”, as they are called in previous works [87], [88]. Necklace structures are found in samples from Experiments R1b, R4c and IF1a (Figure 98). Nanowires and necklace structures are found together also with SiC whiskers. Due to the resolution limitations of SEM, the nodules and nanowires are further analyzed in the TEM characterization chapter, at nanometric scale.

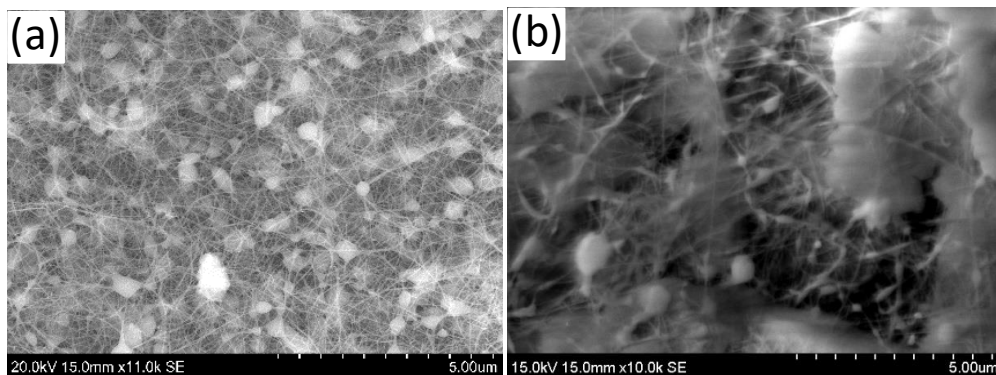


Figure 96: Left: White condensate on SiC (Exp. R2a, estimated 1390 - 1700°C) ; Right: White condensate on Quartz A (Exp. R8a, estimated 900-1200°C).

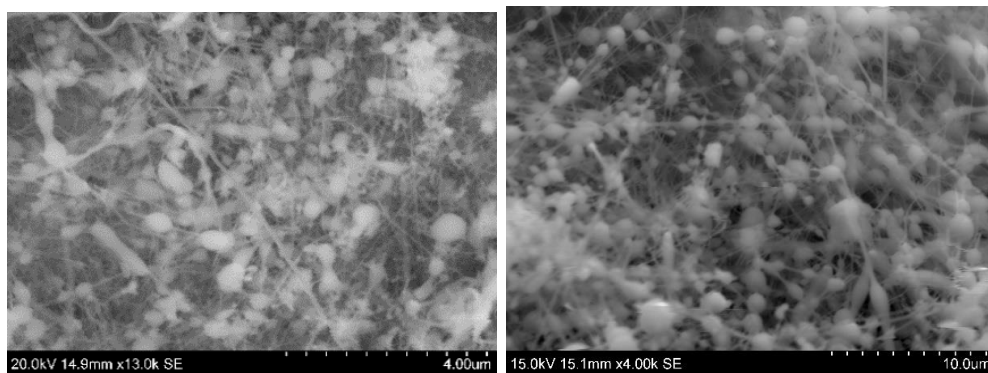


Figure 97: Left: Orange condensate on SiC (Exp. R1a); Right: White condensate on SiC (Exp. IF1a).

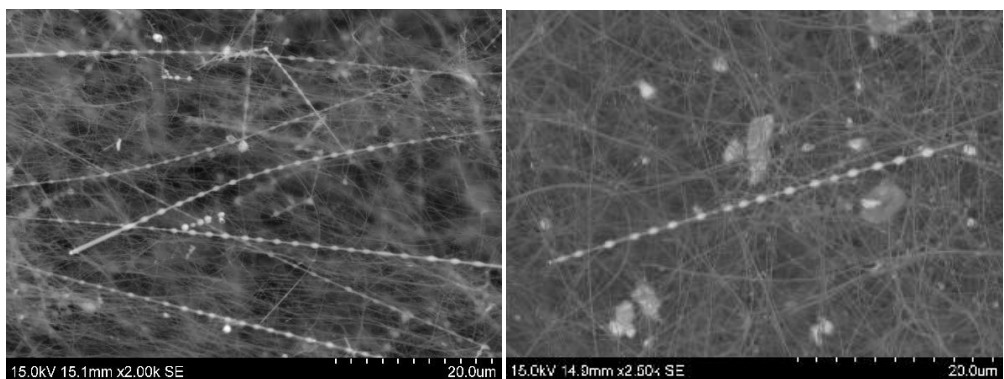


Figure 98: Left: Nodules on nanowires, organized in a necklace structure. White condensate, Exp. IF1a. Right: Necklace structure and disordered nanowires, white condensate from Exp. R4c, estimated 1150-1580°C.

EPMA

EPMA was useful to analyze the quantitative compositional features of the sample. This results in a higher precision in determining the condensates composition. The main results of this analysis are two.

First, the white and orange condensate compositions are similar. The compositions are also comparable to a mixture of SiO₂ and SiC in a molar ratio 2:1, called *theoretical composition*. The theoretical composition is calculated based on the stoichiometry of the products of Reaction 1. Table 16 summarizes the results of the characterization by EPMA, for orange condensate from Experiment R1a, and white condensate from experiment R1a, R1b and R4a. The values shown are the average of all the point analysis collected.

Table 16 shows also that condensates contain higher percentages of C and lower of O and Si, with respect to the theoretical composition. This is believed to occur for two main reasons:

- 1) The pores between the entangled nanowires web are filled with epoxy. The spaces between the nanowires are in the order of magnitude of nanometers. An EPMA point measurement involves an area in the order of magnitude of 1 μm^2 . Porosity is inevitable in an entangled nanowires web. The epoxy resin contributes to the carbon signal, as it is made mainly of C.
- 2) Carbon layers of the order of magnitude of 10 nm thickness are used to enhance the electrical conductivity of the sample under EPMA analysis. This contribution is corrected by a calibrated normalization, which is set before the analysis. However, the thickness of the deposition may vary during sample preparation, and the carbon signal may be altered slightly.

Second, the composition of white condensate does not change significantly over temperature, or between different experiments. The white condensate covers a wide temperature range in the crucibles (1100-1800°C), so the composition was studied in different temperature intervals for the same experiment. Figure 99 shows the number of points analyzed by EPMA in each temperature interval (or sample). As noticed previously in Table 16, the detected composition differs slightly from the theoretical composition.

Table 16: Characterization of SiO₂+SiC mixture (at. % \pm st.dev.) and comparison with theoretical composition.

Element	Theoretical (SiO ₂ :SiC 2:1 molar)	EPMA (White, Exp. R4a, 22 points)	EPMA (White, Exp. R1a, 4 points)	EPMA (White, Exp. R1b, 20 points)	EPMA (Orange, Exp R1a 6 points)

Si	37.5%	(34.3 ± 1.3)%	(34.4 ± 0.8)%	(36.4 ± 1.0)%	(35.3 ± 2.7)%
O	50,0%	(47.7 ± 1.7)%	(45.6 ± 1.2)%	(48.3 ± 1.2)%	(44.7 ± 2.3)%
C	12.5%	(18.0 ± 2.5)%	(20.1 ± 1.7)%	(15.3 ± 1.1)%	(20.1 ± 4.4)%

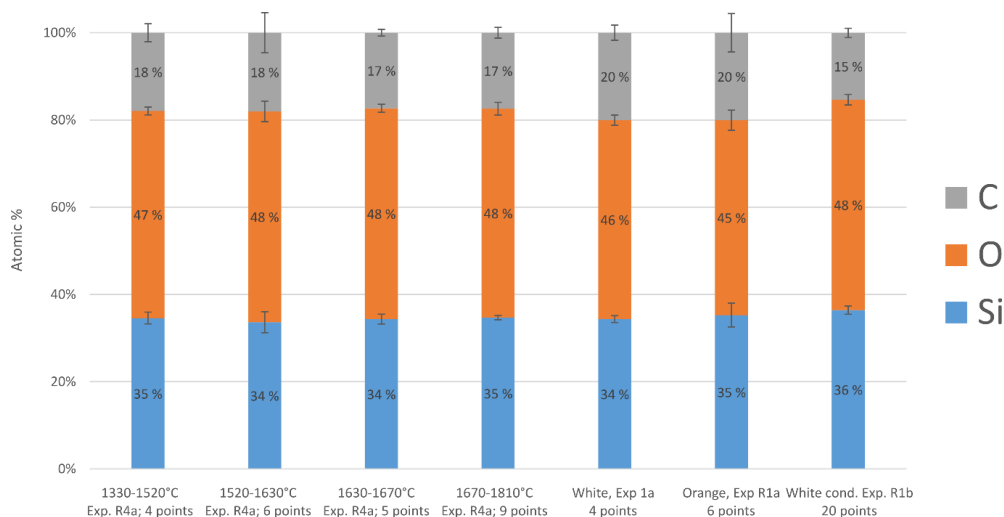


Figure 99: Characterization of white and orange $\text{SiO}_2\text{-SiC}$ condensates from different temperatures. Samples from experiment R4a and R1a. The bars show uncertainties at one standard deviation. Samples in R1b are collected between 1020 - 1725°C.

TEM characterization

Some of the features of the nanowires could not be noticed by SEM analysis. For example, the resolution for SEM is too low to estimate the nanowires or the nodules diameter. Besides, it would not be possible to check if the nanowires are hollow or if they have a defined crystallographic orientation. On the other hand, TEM analysis allows to distinguish the crystallographic planes, and give a higher resolution with respect to SEM analysis.

Samples of blue and white condensates were collected for the TEM topographic and EDX-EELS compositional analysis. Blue condensates were extracted in the position zones corresponding to 1250-1450°C, whereas white condensate sample was collected in the temperature zone corresponding to 1450-1550°C. Both samples come from Experiment R4c.

First, it was seen that the wires are made of an external phase called *shell*, embedding a nanowire made of a *core* phase. This first finding is shown in Figure 100. The core diameter ranges around 10-20 nm, and the shell layer gives a final thickness of 60-100 nm. The shell may coat many wires at the same time (Figure 100a). The external phase becomes sensibly thicker and assumes the shape of a nodule, where many wires cross their paths. The nodules are seldom present in blue condensate, as it was also observed in the SEM analysis. The dimension of the nodules in the blue condensate can reach up to 200 nm in diameter.

In the white condensate sample, the core-shell structure is still present, but some of the wires did not show any shell layer. Nodules are present in higher amounts than in the blue condensate. The total diameter of the wires reaches up to 80-100 nm.

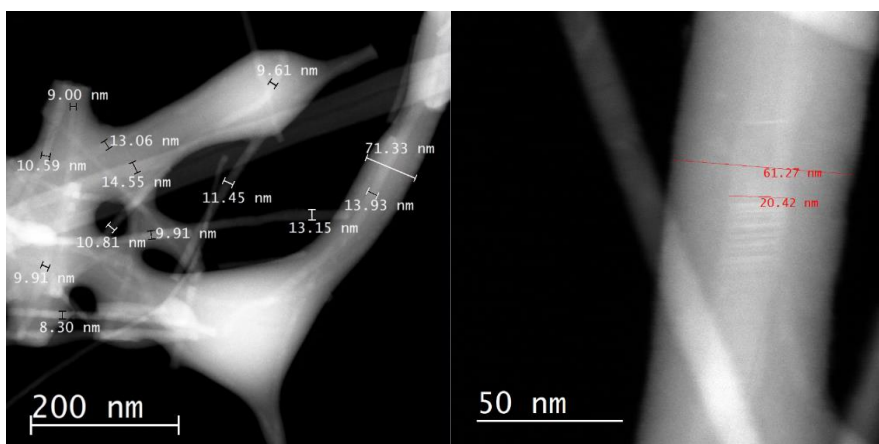


Figure 100: Dimension of core and shells in nanowires of blue condensate, Exp. R4c, T = 1250-1450°C.

Second, the core is richer in Si and C, and the shell are richer in Si and O. Hence, it was concluded that the core phase is made of SiC, and the shell-phase is made of SiO_x. This result of TEM analysis comes from the EDX-EELS line compositional scanning of a single wire (Figure 101). The core and the shell phase have different levels of Si, O and C. In fact, the counts per second for Si increase by going towards the core (Figure 101a). The same happens to C, whereas O follows the opposite trend. Some O signal is also revealed at the core, as the analysis is tridimensional, and part of the shell-phase contributes to the signal. The substrate for the analysis is made of Cu, so it was not interfering with the results.

The same conclusion can be reached by looking at an elemental mapping taken in proximity of a nodule (Figure 102). The scanned image can be divided into two parts. The first is the small portion of a wire left uncovered by the shell phase, on the right side of the picture. This area does not give a significant O signal. The wire is visible only in the Si and C mapping. The second zone is a triangular area in the center (a nodule). The intensity of the C signal is lower than Si and O. It can be concluded that the shell phase contains Si and O, and the core phase contains Si and C. Again, the shell and core phases can be identified as SiO_x and SiC respectively.

Third, the core phase has the crystalline structure of 3C-SiC. The third result from the TEM analysis concerns crystallinity, but also confirms the previous conclusion from the compositional analysis. The direction (111) predominates in the diffraction pattern of the core phase. The plane spacing was measured to be between 2.2-2.5 Å, which corresponds to the results from Hu et al. [35], [36]. It can be understood that the composition of the core-phase is 3C-SiC, also known as β-SiC. It can be concluded that the core of SiC-SiO_x nanowires is made of 3C-SiC, as noticed in other previous works [35], [36], [89]. The external borders of the core phase may not be crystalline.

For the shell phase, it is not possible to make crystallographic studies on the atomic plane spacings. In fact, SiO₂ can turn into its amorphous phase when irradiated by X-ray radiation [90].

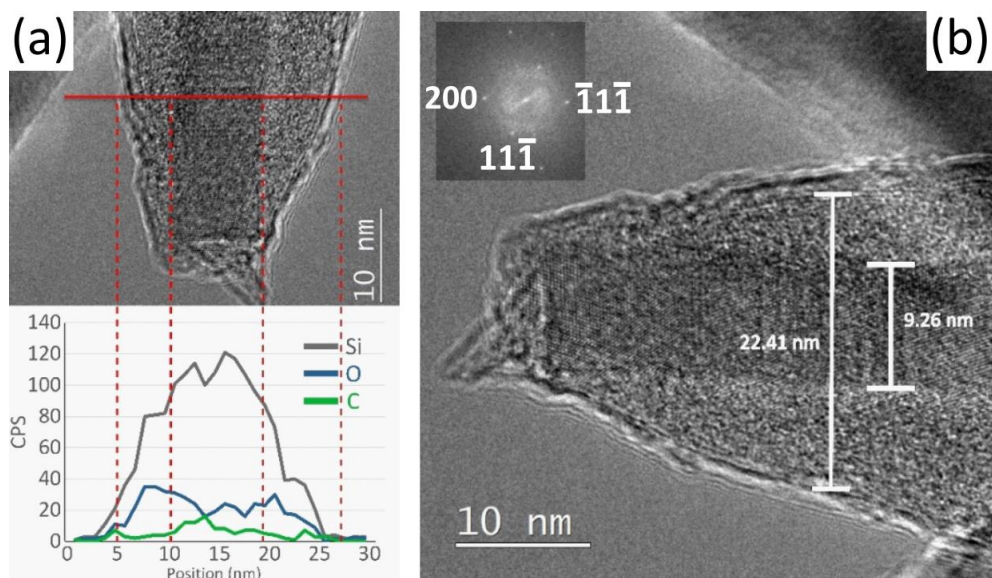


Figure 101: Tip of a nanowire from Exp. R4c, T = 1250-1450°C. Left: Line scanning of blue condensate nanowire tip. Elemental analysis of silicon (grey), oxygen (blue) and carbon (green); Right: Zoom on a nanowire tip and diffraction pattern of the picture. Stacking faults between atomic planes can be seen in the core-phase.

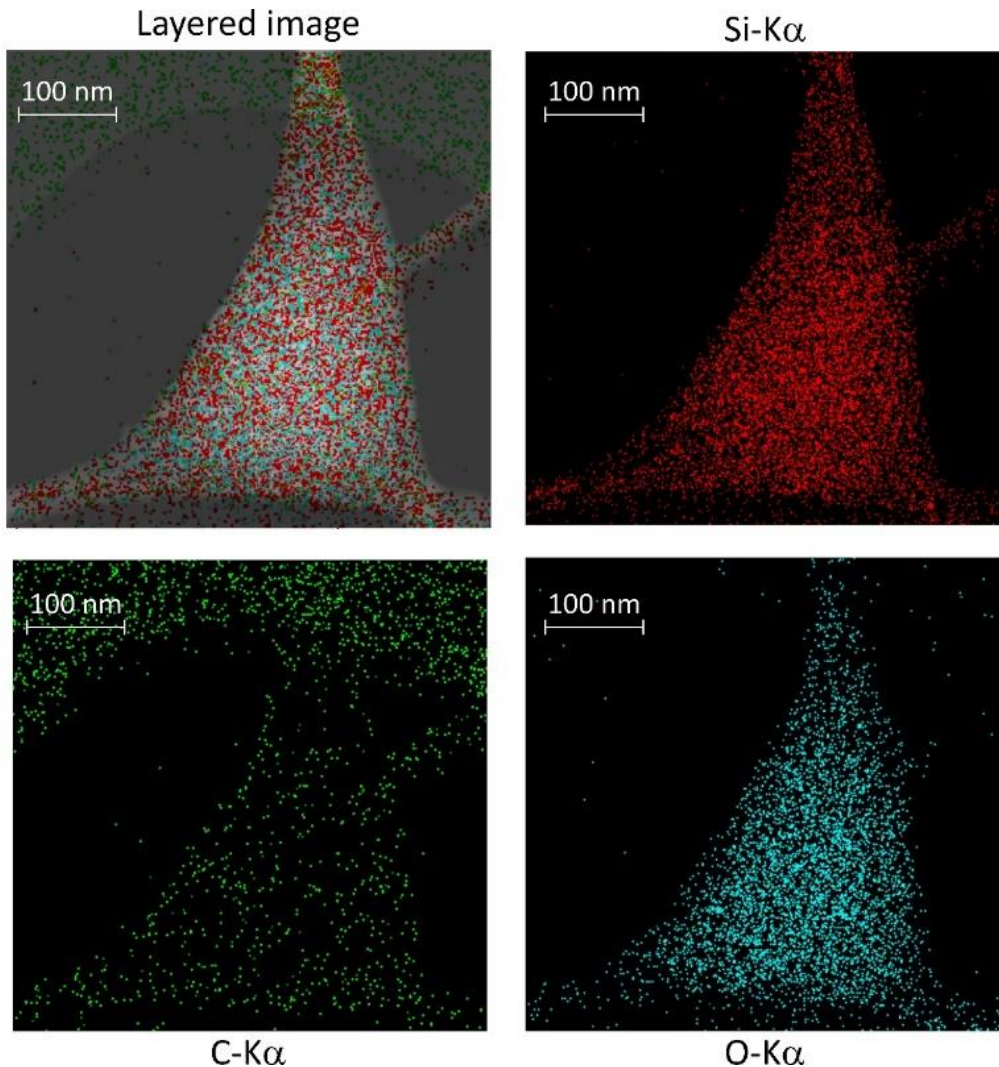


Figure 102: EDS mapping of Si, O and C of a nodule and incoming wire, from TEM analysis of white condensate. Sample from Exp. R4c, T = 1450-1550°C.

Finally, the core phase is rich in stacking faults. Despite that, the presence of stacking faults does not influence the contact area between the core and the shell phase. The last finding of TEM analysis concerns the presence of crystal defects in the core-phase, and the contact area between the core and the shell phases. These are visualized in Figure 103b and Figure 104a as shaded “slices”. The stacking faults are spread in the core phase, regardless the position and microstructure of the shell-phase. Similar configurations were found multiple times in the same sample.

Figure 104 takes a closer look at the interface between the core and the shell phase. The shell-layer is formed as a bead on a string, while keeping a continuous thin layer on the core phase. A well-defined interface is present between the SiC core and the amorphous SiO_x nodules. The shell phase presents a relatively good wetting to the core phase. In fact, the wetting angle was measured over 41 contact angles, giving an average value of 44.1±10.1° for blue and 43.6±9.9° for white condensate.

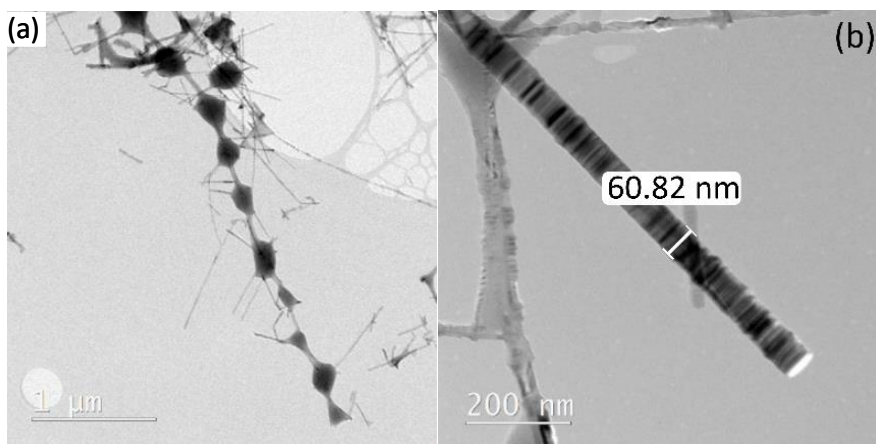


Figure 103: Bead structure (left) and stacking faults in SiC nanowire (right). White condensate from Exp. R4c, T = 1450-1550°C.

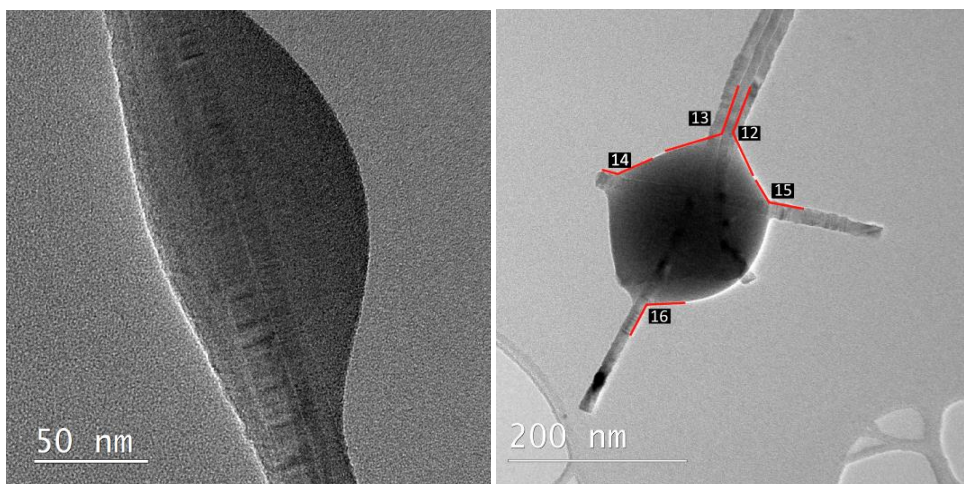


Figure 104: Left: Wetting between shell and core phases. White condensate, Exp. R4c, T = 1450-1550°C. Right: Measurement of contact angle on a nodule in white condensate. The supplementary angle is measured, and the contact angle is then calculated.

XPS

Two samples were collected for the XPS analysis, from Experiment R4c, between T = 1580-1706°C. Sample 1 is a SiC particle covered in blue condensate (Figure 105a). Sample 2 is scale detached from a SiC particle. Sample 2 has both blue and white color, therefore the analysis was carried out on each color zone (2.1 and 2.2 in Figure 105b).

By XPS, it was noticed that the blue and white condensates have similar compositions, which are also close to the theoretical composition previously shown in Table 16. Figure 106 shows the XPS survey spectra collected for the three inquired points, whereas Table 17 shows the numeric results. All the spectra show the presence of silicon, carbon and oxygen in similar percentages.

The position of the peaks is also similar for the three XPS measurements. Si-2p are revealed at ≈ 100 eV respectively. C-1s electrons are revealed at ≈ 285 eV. Peaks in the 530-eV area are coming from O-1s electrons. The position of these peaks correspond to those from references [86], [91]. Other peaks revealed in the spectrum are the Si-2s electrons (≈ 150 eV). Finally, the oxygen auger peaks (≈ 1000 eV) appear when using Al-K α radiation as X-ray source [86].

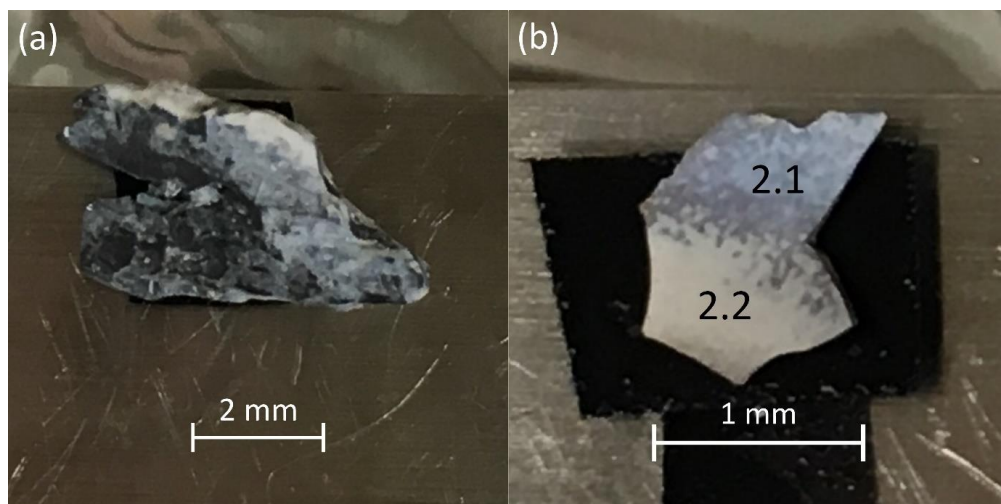


Figure 105: a) Blue condensate on Sample 1; b) Sample 2, positions of points 2.1 and 2.2.

Table 17: Atomic concentration of oxygen, carbon and silicon as determined from the O-1s, C-1s and Si-2p regions of the XPS survey spectra.

Sample	Name	Position	At. %
Sample 1	O 1s	532.96	51
	C 1s	284.96	22
	Si 2p	103.66	27
Sample 2.1	O 1s	532.99	55
	C 1s	284.99	18
	Si 2p	103.69	27
Sample 2.2	O 1s	532.79	47
	C 1s	284.89	26
	Si 2p	103.59	27

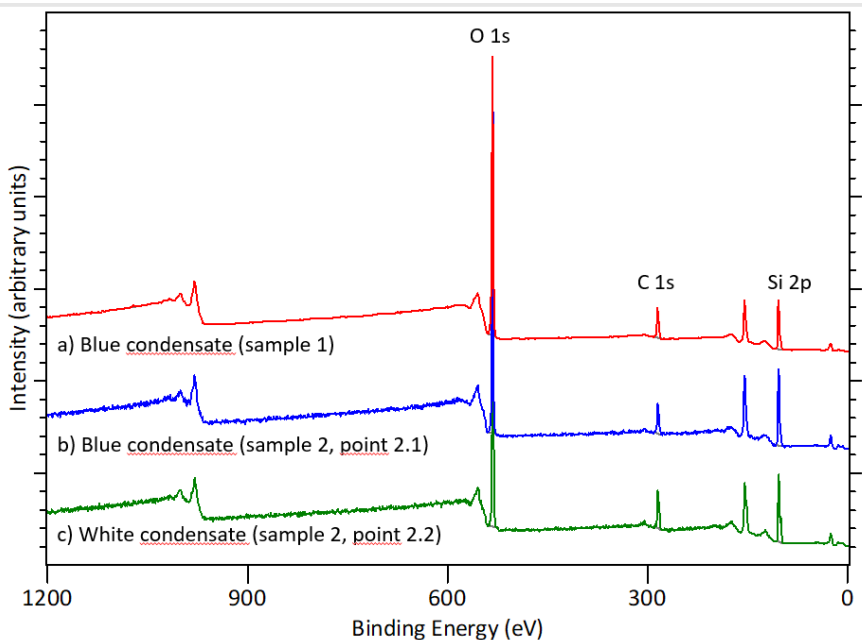


Figure 106: Survey spectra of blue condensate a) sample 1 and b) sample 2, point 2.1 and white condensate c) sample 2, point 2.2. The O 1s, C 1s and Si 2p core level regions are indicated.

The Si-2p and C-1s core level spectra are shown in Figure 107-Figure 108. A core level spectrum shows the XPS signals in a shorter binding energy interval. The electrons involved in Si-O, Si-Si and Si-C bonds belong to the Si-2p and C-1s groups, whose peaks were all previously revealed in the survey spectra. Si-2s and O-1s electrons are presented in the Appendix H, as they only belong to the Si-O bonds.

The Si-2p spectrum shows two major peaks. The first is located at 103.5 eV (Si-O), and the second between 101 and 102 eV (Si-O-C). In the C-1s group, the most present bonds are C-C and Si-C (carbide). The carbide signal in the C-1s localized spectrum is relatively strong (C-Si peak). The Si-O-C bonds can be explained by the presence of SiO_x and SiC at nanometric scale [86]. Other minor peaks such as C-O-C, C=O, C-OH and C=O=C were detected. They are usually associated to organic impurities and adventitious carbon deposited on the surface.

From the XPS results, it can be concluded that there are similarities between the chemical environments of blue and white condensate samples. A “carbide” peak is noticed for every sample, despite the contribution of the surface impurities and adventitious carbon. The profile of the Si-O and Si-C bonds in the Si-2p spectrum appears similar. There are, however, three empirical errors, which can influence the spectra. They are caused from three sources:

- 1) **Some signal from the SiC substrate could perturbate the C-1s and the Si-2p peaks intensities.** The nanowires are entangled in a thick web, with small free spaces between them. A small part of the XPS signal would come from the substrate, as the incoming radiation will encounter many obstacles on its way towards the substrate surface. The Si-C bonds are contained both in SiC-substrate and in the condensates, and one cannot separate the two.
- 2) **The contribution of the Si-2p electrons should be modelled on two contributions, instead of one.** When applying the fitting in the Si-2p electrons, the Si 2p_{3/2} and Si 2p_{1/2} electrons are combined in the spectra for visualization. Both these peaks are needed to fit the data for one chemical contribution. The ratio is fixed between them and the splitting depends on the element. For Si, this splitting is about 0.6

eV [92], [93]. However, in some cases in the literature only one peak is used to fit the data depending on resolution due to the low splitting [94]–[96].

- 3) **The presence of adventitious carbon.** Most samples exposed to air will have an adventitious carbon layer (typically 1-2 nm), consisting of mainly C-C, C-H species in addition to some oxygenated carbon species. This carbon overlayer is generally not detectable with other techniques. The amount of adventitious carbon is unfortunately impossible to quantify, therefore the C-1s analyses can be considered only to a qualitative level.

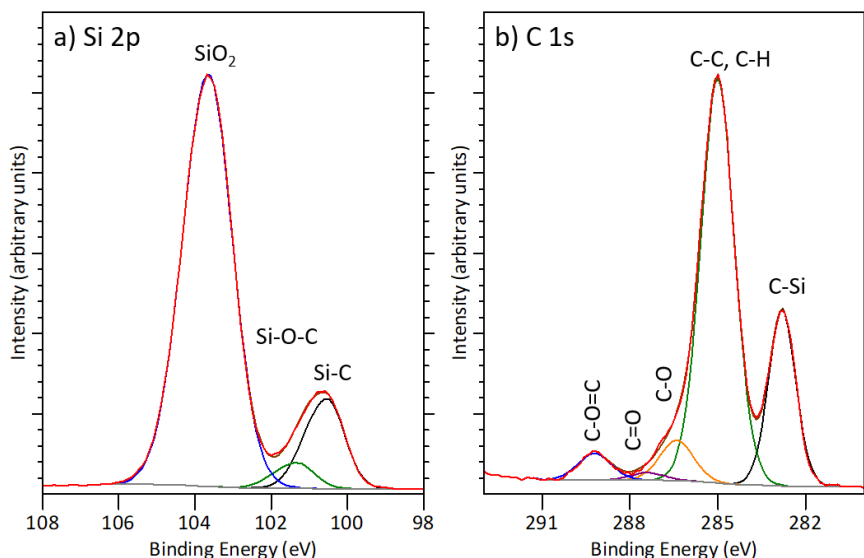


Figure 107: a) Si 2p, b) C 1s and c) O 1s core level spectra of blue condensate (sample 1).

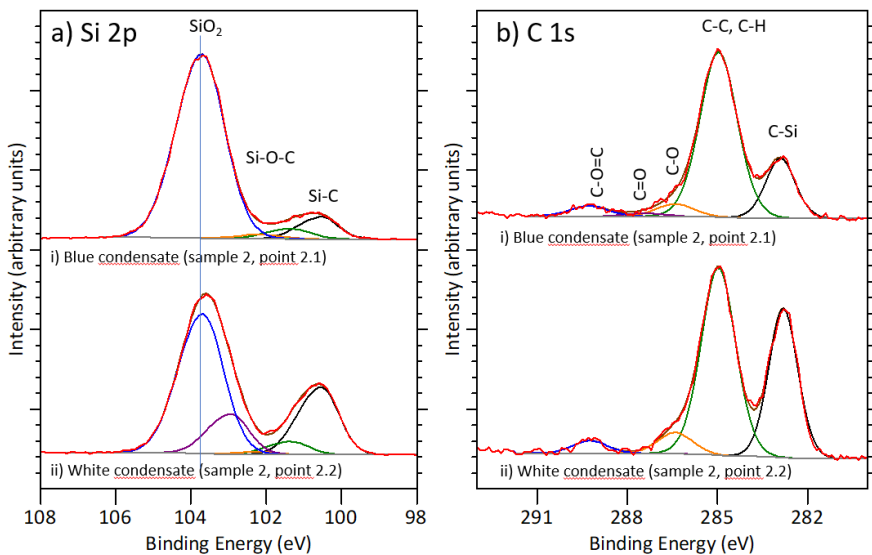


Figure 108 a) Si 2p and b) C 1s core level spectra of i) blue condensate (sample 2, point 2.1) and ii) white condensate (sample 2, point 2.2).

XRD polytypes analysis

Three samples were extracted from the large-scale setup experiments IF7b and IF12. All these experiments are run with Si-SiO₂ gas producing pellets ($p_{\text{SiO}_2} = 1.0$), exposed at 1890°C for 2 hours. The temperature and position intervals of the samples are listed in Table 18. The samples are chosen to check if the composition changes within the temperature gradient in the same experiment (Sample 1 vs 2) and with time at the same temperature (Sample 2 vs 3).

Table 18: Condensates analyzed during XRD

Sample	Condensate	Experiment	Holding time	Position (cm)	T interval
1	White	IF7b	2 h	12-17	1250 – 1480 °C
2	White	IF7b	2 h	17-23	1480 – 1720°C
3	White	IF12	10 min	19-23	1530 – 1710°C

The results of the XRD analysis is shown in Table 19 and Table 20, whereas the spectra are collected in Appendix H. The main results from the XRD analysis are the following:

1. The sample consists mainly of SiO₂ and SiC. These two compounds are the constituent of the condensate as demonstrated from the previous compositional characterization. However SiC may also come from the substrate. According to the XRD analysis of the substrate, the α -SiC contribution is believed to come from the scratched SiC substrates. Hence, the percentage of SiC is higher than expected, and the SiO₂:SiC ratio is slightly lower from the expected condensate composition (3:1 weight).

2. β -SiC makes ≈ 90 wt.% of the available SiC. This SiC polytype was also found in TEM analysis on nanowires. The SiC polytypes are distributed into α -SiC (2H and 6H-SiC) and β -SiC (3C-SiC). α -SiC may come from the SiC substrate used for condensation, which were scratched together with the sample. The amount of SiC is higher in Sample 3 compared to the other samples, but the α -SiC amount is not so high. Hence, the SiC amount is believed to be influenced by the presence of whiskers. Such whiskers are therefore made of β -SiC, as described in Appendix A.

3. Amorphous silica makes most of the present quartz polytypes. Silica might be amorphous due to the nanometric size of the system. However, a fraction of the nanowires is still made of cristobalite, especially in samples 1 and 2. The contribution of quartz is negligible at temperatures above 1200°C.

4. The amount of amorphous phase increases with temperature. Sample 1 is located at 1250-1480°C, whereas sample 2 is from 1480-1720°C. Both samples come from the same experiment. The amorphous phase increases from 80% to 90% in the silica polytypes composition. On the other hand, cristobalite decreases from 17% to 9%. Hence, the amorphous phase transforms gradually into cristobalite while cooling.

5. The amount of cristobalite increases with time. The cristobalite percentage at similar temperatures increases from 1% to 9%, between Sample 3 ($t = 10$ min) and Sample 2 ($t = 2$ h). On the other hand, the amount of amorphous phase decreases. Hence, at longer time the amorphous phase transforms into cristobalite by recrystallization.

Table 19: Relative amount of each polytype for silica and SiC, calculated by TOPAS v5. The composition is defined in wt.%. The theoretical SiO₂/SiC ratio is 3.00.

Sample	Silica polytypes			SiC polytypes		Total SiO ₂	Total SiC	SiO ₂ /SiC ratio
	Quartz	Cristobalite	Amorph.	α-SiC	β-SiC			
1	3%	17%	80%	12%	88%	71%	29%	2.47
2	1%	9%	90%	10%	90%	75%	25%	3.08
3	3%	1%	96%	7%	93%	59%	41%	1.43

Table 20: TOPAS v5 fitting of XRD spectra for samples with white condensate. The composition is expressed in wt.%.

Sample	Quartz	Cristobalite	Amor.	α-SiC	β-SiC	Si	Total
1	2.25	11.78	56.89	3.35	25.35	0.38	100
2	0.81	6.78	67.69	2.46	21.99	0.27	100
3	1.87	0.65	56.27	2.85	38.18	0.19	100

Grey condensate

A grey, thick layer is formed close to the highest temperature ranges of the white condensate (1320 – 1800°C). This condensate generates together with, or above, the white layers. This was noticed both at visual inspection (Figure 94) and SEM analysis (Figure 109). This layer consists of oriented wires of length ≈500-800 μm and diameters between 1-4 μm (Figure 110a). These wires are made of spherical building blocks piled up on each other (Figure 110b).

Table 21 shows the results from the characterization of a sample from Experiment R4c. The composition is close to the SiO₂-SiC nanowires previously analyzed, and therefore also to the theoretical composition with respect to Reaction 1. It is believed that grey condensate is also a product of Reaction 1.

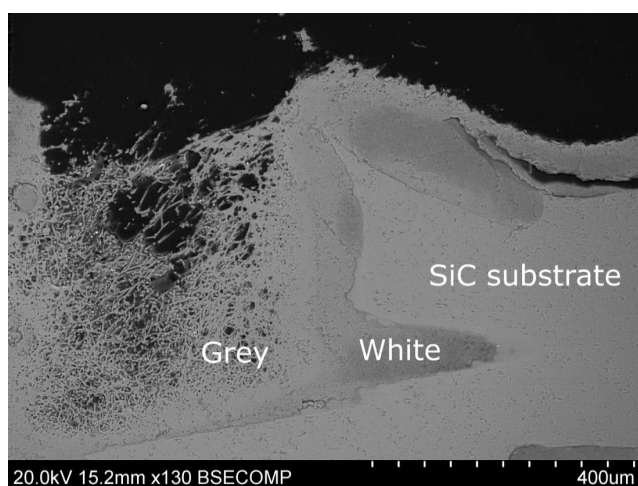


Figure 109: Grey and white condensate on a SiC particle. Sample from experiment R4c, T=1583-1706°C.

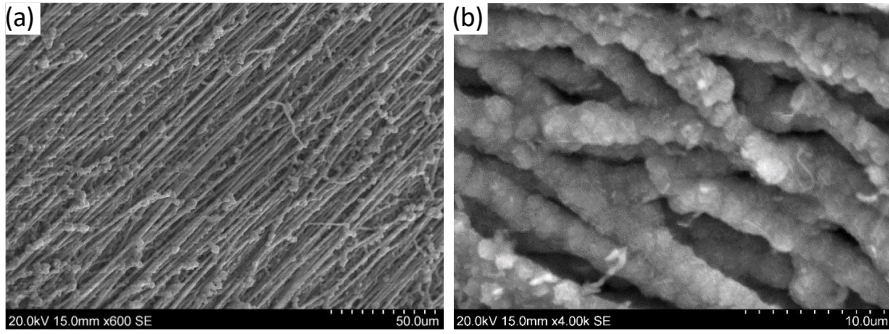


Figure 110: Grey condensate, SE-image from Experiment R4c; Building blocks of grey condensate, Experiment R4c, T=1583-1706°C.

Table 21: Characterization of grey SiC-SiO₂ mixture (at. %)

Element	Theoretical composition (SiO ₂ :SiC= 1:2 molar)	EPMA (Exp. R4c 11 points)
Si	37.5%	(36.1 ± 0.6)%
O	50,0%	(52.7 ± 0.4)%
C	12.5 %	(14.8 ± 0.9)%

B. Si-SiO₂ condensate characterization

Visual inspection and SEM analysis

A brown, glassy material glues the SiC substrates, as it happened to the sample from Experiment R4a shown in Figure 111. The brown condensate covers particles which are already covered in white condensate. The substrates stick together as if the brown compound was molten during the experiment. Different shades of brown appear at different temperatures. In particular, the color shifts from dark brown to grey while going downwards in the crucible, i.e. towards high temperatures. The brown condensate sticks to the graphite parts. When removed, the brown condensate is still attached to the white condensate removed from the graphite parts.

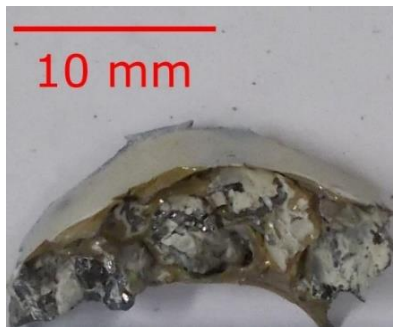


Figure 111: Brown condensate layer generated between SiC particles, white condensate and white scale. Sample from Exp. R4a., T = 1665 - 1800°C.

As far as microstructure is concerned, SE-SEM pictures reveals a matrix, which contains spherical inclusions (Figure 112). The spheres are interconnected by treads. The spheres diameter ranges in the order of magnitude of 0.5-1 μm . The sample would charge under SEM analysis, implying that the compound should contain a considerable amount of an oxide.

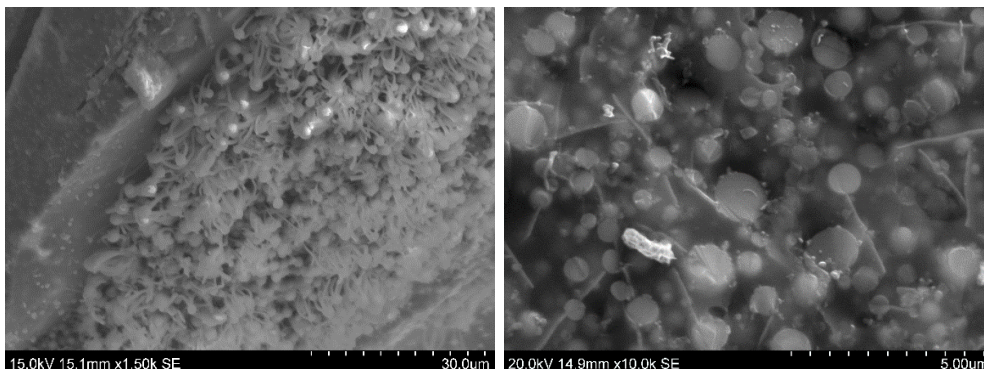


Figure 112: Left: Spheres and wires from experiment R1b, T = 1340 - 1570°C; Right: Top view of brown condensate embedding spheres inside the matrix. Sample from experiment R4a, T = 1665 - 1800°C.

EPMA

The EPMA point analysis gave almost equivalent atomic percentages of Si and O, but also a carbon signal up to 10 at. % (out of 14 points analyzed in a sample from experiment R4a, with an analysis radius of 10 μm). Hence, if carbon was neglected, the brown condensate composition can be approximated to a mixture of Si spheres in a SiO_2 matrix, in a molar ratio 1:1 (Table 22). This is the *theoretical composition* for the Si- SiO_2 condensate, which neglects the contribution of carbon. However, the empirical error caused by the carbon layer (previously discussed for EPMA analysis in the SiC-SiO_x mixture) is also present for the Si- SiO_2 mixture.

Table 22: Characterization of brown Si- SiO_2 mixture (at. %).

Element	Theoretical composition (Si: SiO_2 1:1 molar)	EPMA (Exp. 4a, 14 Points)
Si	50.0%	(43.1 \pm 2.6)%
O	50.0%	(49.4 \pm 0.4)%
C	0 %	(7.5 \pm 2.6)%

Element mapping showed that the spheres contain more than 90 wt. % silicon, whereas the matrix composition corresponds to SiO_2 . The EPMA was also performed as an area mapping over the same sample, which analyses the distribution of Si, C and O over an area. Figure 113 shows elemental mapping of brown condensate from Experiment R4a, for the elements Si, C and O. Carbon signal is also present where the spheres are located. Carbon concentration in the spheres can be up to 8 wt. %. However, C measurement are semi-quantitative, and a carbon coating is applied during sample preparation, therefore it is believed that the carbon content is lower.

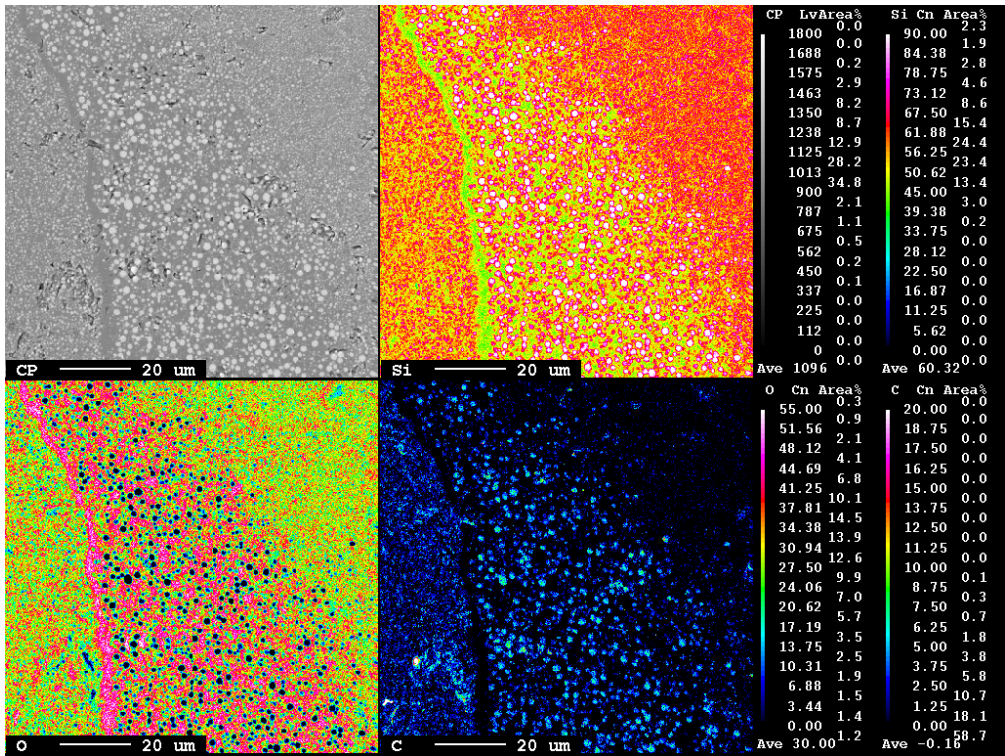


Figure 113: EPMA mapping of brown condensate, Experiment R4a, wt. % on the colored scales.

TEM characterization

The elemental mapping in Figure 113 shows numerous spots giving a carbon signal, especially close to the silicon spheres. However, the SEM resolution was not high enough to identify if this carbon signal was caused by a carbon-containing phase, or by empirical errors. Therefore, the Si-SiO₂ condensate is characterized with a technique at a higher resolution. Since brown condensate is a thick and dense material, a thin slab could be extracted through FIB preparation, and used for TEM analysis.

The FIB sample was collected from Experiment R1b. Figure 114 shows how the FIB sample looked like before undergoing TEM characterization. The borders of the spheres are not perfectly smooth. The light glance at the particle borders is caused by the charging effect of the silica surface (Figure 114 and Figure 115). Appendix B shows the process used for preparing the sample by FIB. The final sample size is about 30 x 30 x 0.1 μm.

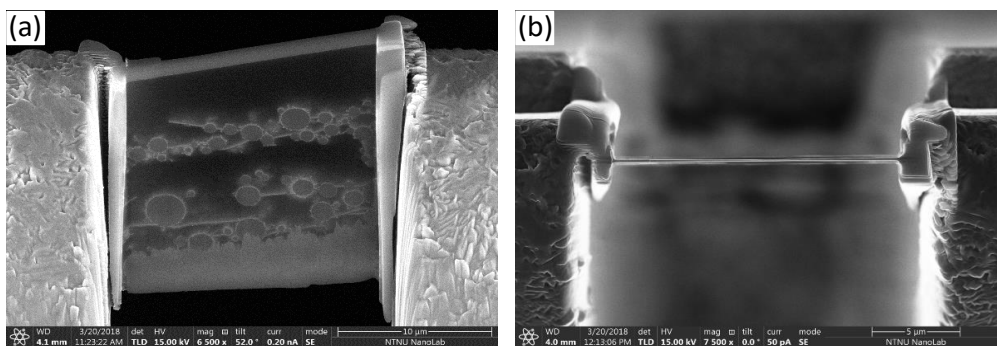


Figure 114: Final aspect of the FIB-TEM sample of brown condensate. Left: Frontal view; Right: Cross section thickness. FIB sample.

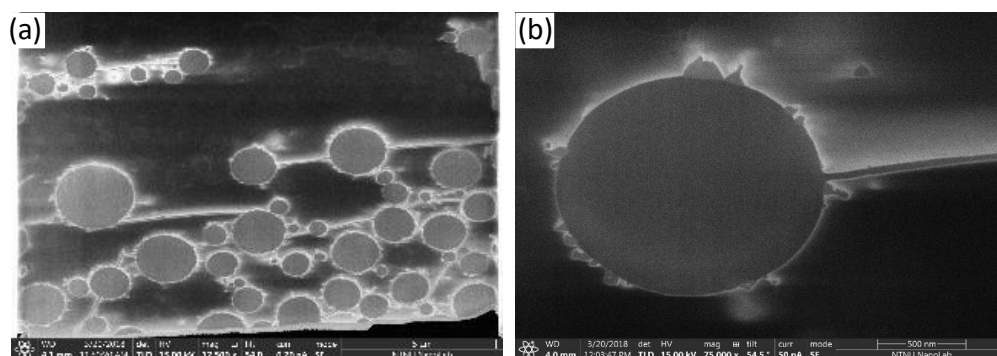


Figure 115: Details of spheres borders. FIB sample.

As for SEM analysis, elemental mapping can be performed also at TEM resolution. EDX area mapping visualizes the qualitative concentration of Si, O and C in a sample. EDX was carried out on a portion of the FIB sample, which contained both large and small silicon spheres. A brighter color corresponds to a stronger concentration of the detected element. The results are summarized in Figure 116.

The first thing noticed was that the Si signal is stronger inside the spheres and a lower outside. This confirms the previous results from the area mapping in the SEM characterization. **However, it can be added that the wires interconnecting the spheres are also made of elemental silicon.** The oxygen mapping shows, as expected, a low signal from the spheres and a stronger outside them. Again, it can be stated that the Si-SiO₂ condensate consists of Si spheres embedded in a SiO₂ matrix.

The second result is that both Si and C are present around the spheres. Therefore, it is believed that there are SiC crystals located around the spheres. By looking at the C elemental mapping (Figure 116c), it can be noticed that the C signal on the spheres borders is more intense than inside the spheres. At the same time, in the Si mapping, the signal at the spheres borders is represented by an orange zone, i.e. the concentration of Si is lower than inside the spheres, but higher than in the matrix. The size of the SiC protuberances ranges between 50-150 nm. Only the largest spheres show relevant amounts of carbide on their boundaries.

The very low C solubility of the two phases is also noticed in the elemental mapping. The SiO₂ matrix can dissolve low amounts of carbon (in the order of magnitude of ppb). In fact, the matrix appears dark blue in the C mapping. The Si spheres are dark blue in both the C and O mappings and is only dissolving O and C on a ppm level.

Many of the large spheres show SiC nanocrystals, whereas the smallest ones do not. The small spheres might not be large enough to react with CO(g) to a sufficient extent.

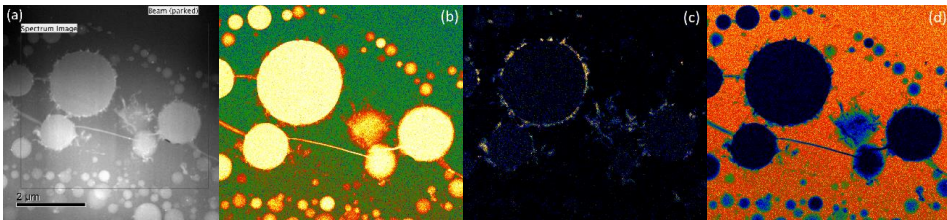


Figure 116: Original TEM bright field picture (a). Mapping of Si (b), C (c) and O (d).

Finally, it was seen that crystallographic defects are widely spread both in the spheres and wires. The most common defects are twin grain boundaries. The structure is not monocrystalline. Figure 117a displays the twin grain boundaries inside a sphere of 2 μm diameter. There are differences in the diffraction pattern between the bulk and the twinning pattern (Figure 117b,c), but the overall pattern is similar. Figure 118 illustrates a close view of the twinning defect. The bulk diffraction pattern of the sphere coincides with a reference diffraction pattern of pure Si [90]. The pattern at the twinning is typical of a $\Sigma 3$ {111} grain boundary.

As is happened for the SiC-SiO_x condensates, it is not possible to comment the crystallographic structure of the SiO₂ matrix, since it may change to amorphous under X-Ray radiation [90].

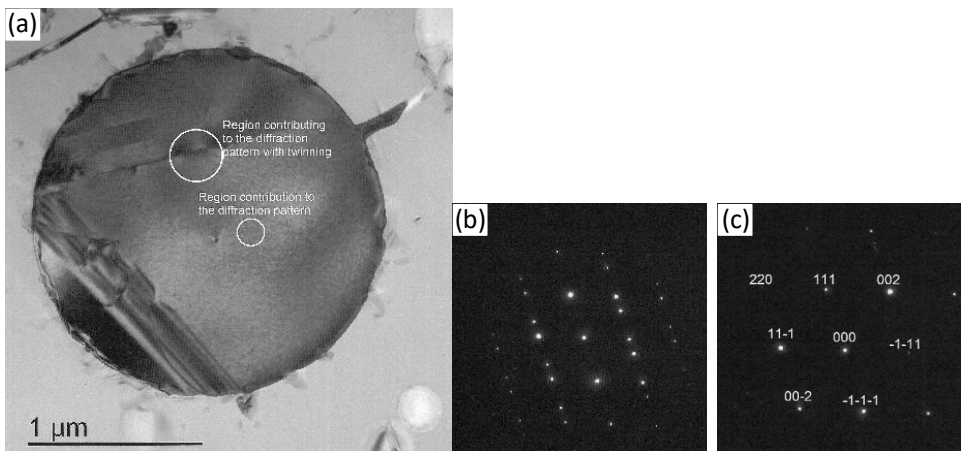


Figure 117: Left: Silicon sphere from Experiment 1b used for diffraction pattern. Center: Diffraction pattern with twinning; Right: Diffraction pattern without twinning, indexed.

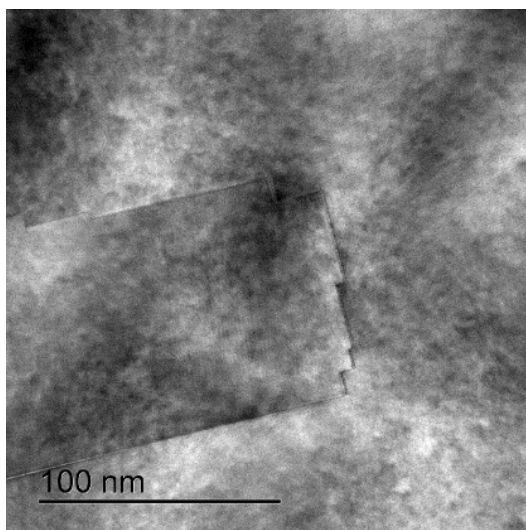


Figure 118: Twin grain boundary in silicon.

XPS

Samples from experiment R4a were used for XPS analysis (Figure 119a). The survey spectrum from Figure 120 shows that the amount of carbon is significant, due to surface contamination of adventitious carbon. Some of the C signal comes also from SiC in the brown condensate. The Si:O ratio is close to 1, as the overall composition of brown Si-SiO₂ condensate.

The position of the peaks, their areas and FWHM are collected in Table 23. F, N and Na are coming from organic impurities. Again, the positions of the peaks in the survey spectrum correspond to those from references [86], [91], as well as to those found in the SiC-SiO_x condensates (see Table 17).

Table 23: XPS analysis of brown condensate, survey spectrum

Name	Position	At. %
O 1s	532.77	37
C 1s	284.77	28
Si 2p	103.77	34
N 1s	399.77	0.5
F 1s	689.27	<0.5
Na 1s	1071.27	<0.5

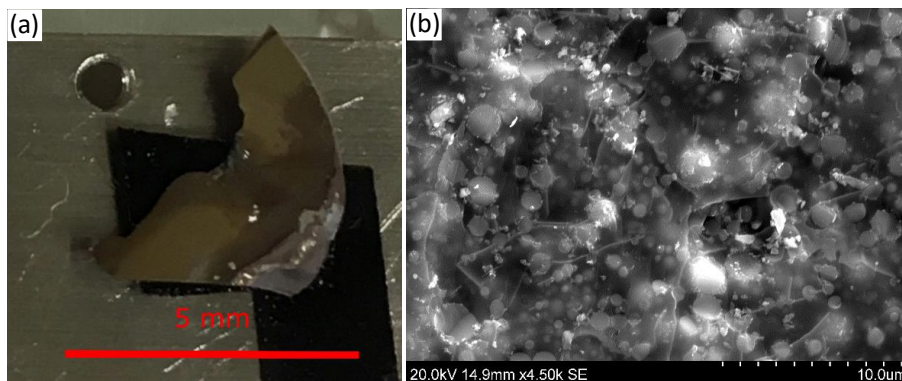


Figure 119: Left: brown condensate XPS sample; Right: SE picture from the area chosen for the analysis.

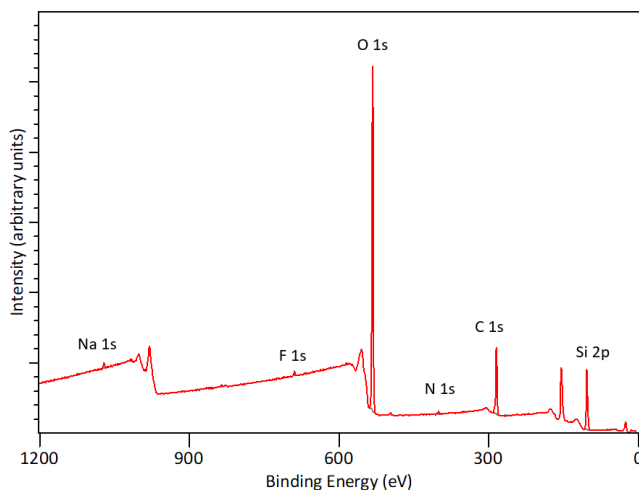


Figure 120: Survey spectrum of brown condensate from experiment R4a.

As far as the localized spectra are concerned, the Si-2p core level spectrum gave also two peaks at 101 and 103.5 eV (Figure 121a). The latter is related to Si-O bonds. Elemental silicon should give its own peak at ≈ 100 eV, but the Si-Si peak might be overlapping with Si-C (≈ 101 eV). The Si-Si peak is lower than the Si-O peak. The shape of the Si-Si peak is distorted because of the overlapping with the Si-C peak, as it happened for the SiC-SiO_x condensate.

When it comes to the C-1s core level spectrum (Figure 121b), the Si-C signal is lower in this sample, compared to the SiC-SiO_x condensates. The carbide signal (282.88 eV) is low, but not negligible. XPS is a surface technique, therefore some of the carbide signal comes from the spheres exposed at the surface shown in Figure 119b. Contamination of the substrate is negligible, as the sample was detached from the SiC substrate.

The experimental errors discussed for the SiC-SiO_x condensates (i.e. SiC contribution to the signal, single peak fitting for Si-2p electrons and adventitious carbon) are also valid for the Si-SiO₂ condensate analysis.

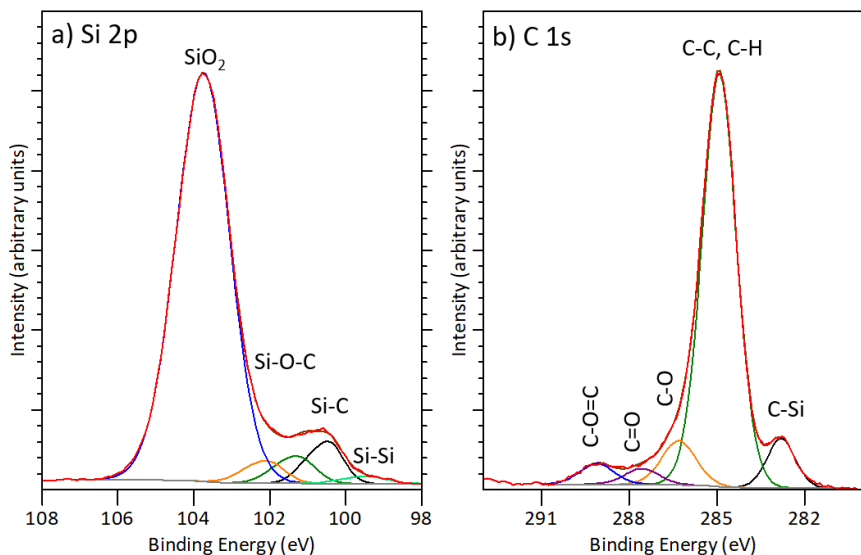


Figure 121: XPS spectra for C-1s (left) and Si-2p (right) electrons in brown condensate from experiment R4a.

XRD polytypes analysis

For the SiO₂ polytypes distribution, a sample from experiment IF7a was extracted. The sample comes from the temperature interval 1580 – 1750°C. The experiment used Si-SiO₂ pellets for gas production ($p_{\text{SiO}} = 1.0$), exposed at 1890°C for 2 hours. The amount of polytypes was inquired by TOPAS by peak fitting with the internal standard method. The results are shown in Table 24 and Table 25. The main results are three:

1. The Si/SiO₂ ratio is higher than expected. This value is still comparable to the theoretical Si:SiO₂ ratio expected from Reaction 2 (1:1 molar, 32:68 weight). The silicon content could be higher than expected, as the condensate layer was scratched for the outer portion of the sample. The model was also not very precise in quantifying the amount of silica polytypes, as described in Appendix H. Some of the amorphous phase might come also from the crystallographic defects in SiC and Si. Other causes for contamination are those who reduce the SiO₂ content (e.g. presence of SiC from the substrate).

2. The percentage of SiC is higher than expected (≈20%), due to contamination from the scratched SiC substrates. β-SiC may come from SiC crystals embedded in the Si spheres, as shown during TEM analysis. The amount of β-SiC (14%) is in the order of magnitude of the estimated amount by TEM (5-10%). The contamination from of α-SiC from the substrate is small (≈5%).

3. Most of the silica is amorphous (64 wt.%). The cristobalite phase makes 26 wt.% of the sample, and quartz is present at 10 wt.%. There is less amorphous phase compared to the SiC-SiO_x condensate. Therefore, the sample has partially undergone a recrystallization process under cooling.

Table 24: Relative amount of each polytype for silica and SiC, calculated by TOPAS v5 for brown condensate. The composition is defined in wt.%.

Silica polytypes			SiC polytypes		Total SiO ₂	Total Si	Si/SiO ₂ ratio	Expected ratio (1:1 molar; 32:68 weight)
Quartz	Cristobalite	Amorph.	α-SiC	β-SiC				
10%	26%	64%	23%	77%	48.83	32.83	0.67	0.47

Table 25: TOPAS v5 fitting of XRD spectra for the sample with brown condensate. The composition is expressed in wt.%.

Quartz	Cristobalite	Amor.	α-SiC	β-SiC	Si	Total
5.02	12.73	31.07	4.29	14.05	32.83	100

Silicon spheres size distribution

The size distribution of silicon spheres changes within sub-millimetric distances in a sample. A metallographic analysis was carried out on 9 brown condensate samples, to understand how the silicon phase changes its microstructure through a brown condensate deposited layer. Table 26 lists the samples considered for the study. The temperature interval corresponds to the position in the condensation chamber where the sample was extracted from. All the samples were analyzed by BSE-SEM. Sample 1-3 showed the clearest contrast between the spheres and the matrix and were analyzed with Image J®. Samples 4-7 do not show good contrast between Si and SiO₂, but a qualitative analysis by visual inspection shows similar results collected for samples 1-3. Samples 8-9 contain representative overview pictures of microstructural configurations at smaller magnification (x100).

Table 26: Samples used for Si spheres analysis.

Sample	Experiment name	T interval (°C)	Number of pictures
1	P40 R10a – sample a	1420-1590°C	23
2	R2a – sample a	1525-1745°C	23
3	R4a	1665-1810°C	9
4	P40 R10a – sample b	1420-1590°C	20
5	R1b	1450-1550°C	7
6	R4c	1575-1705°C	12
7	R17a	1470-1680°C	15
8	R2a – Sample b	1525-1745°C	3 (overview only)
9	R23	1420-1700°C	2 (overview only)

Figure 122 shows how **the sphere size increases while getting closer to the outer surface of the sample**. The white rectangles show the dimension of each picture taken during line scanning. At the point closest to the SiC substrate ($x = 0 \mu\text{m}$), the average silicon sphere size is 256 nm. At $x = 300 \mu\text{m}$, the size has already increased to 475 nm. The growth continues again towards the edge, where an average size of 555 nm was calculated at $x = 660 \mu\text{m}$. While the average size increases, the counted particles in every picture decrease, from 415 ($x = 0 \mu\text{m}$) to 104 ($x = 660 \mu\text{m}$). The counted spheres and the average sphere diameter are plotted in Figure 124.

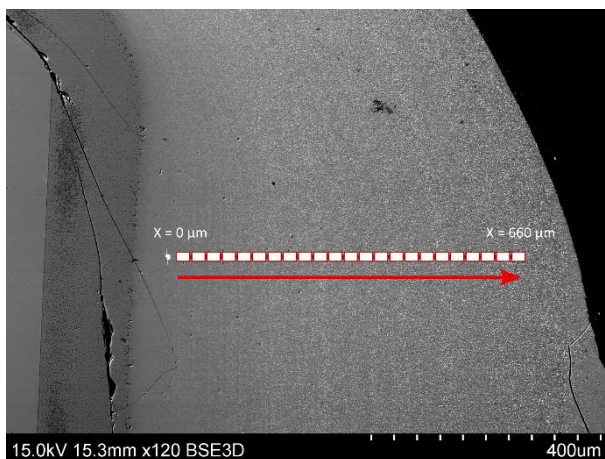


Figure 122: Line scanning of Sample 1: Increasing particle size towards sample external edge

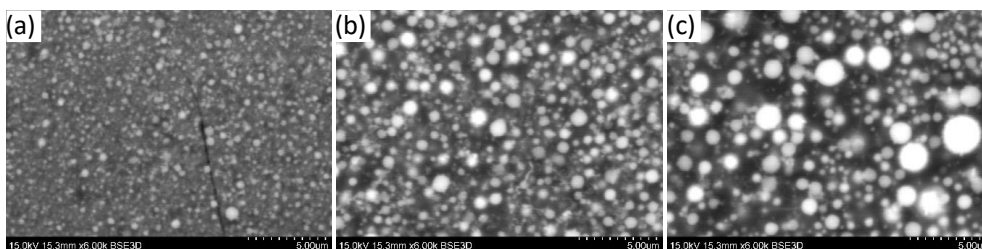


Figure 123: Si spheres at $x = 0 \mu\text{m}$ (a), $x = 300 \mu\text{m}$ (b) and $x = 600 \mu\text{m}$ (c), sample 1.

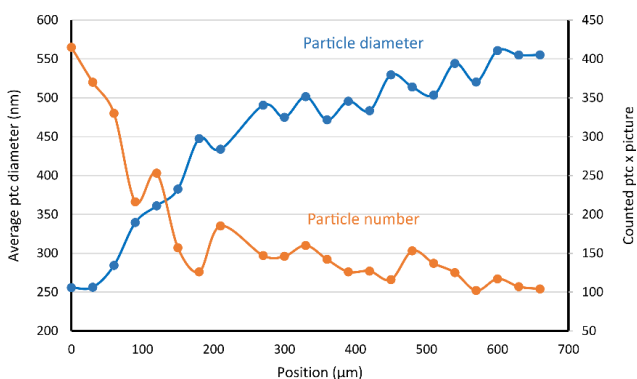


Figure 124: Sample 1, ImageJ® analysis results on average size (blue) and counted particles per picture (orange).

Also in sample 3 (Figure 125 and Figure 126), the particle size grows progressively while going towards the outer surface (Figure 127a,b). The average particle area will increase while going towards the edge of the sample. The sphere diameter increases 2.75 times within $180 \mu\text{m}$, from 228 nm to 627 nm . At $x = 240 \mu\text{m}$, a new layer starts, with a different Si sphere size (Figure 127c) Within $30 \mu\text{m}$, the number of spheres increases 5 times and the size decreases from 527 nm to 194 nm (Figure 127d).

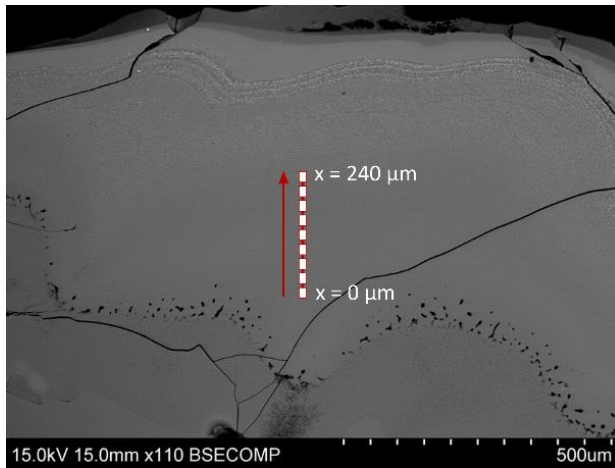


Figure 125: Line scanning of sample 3.

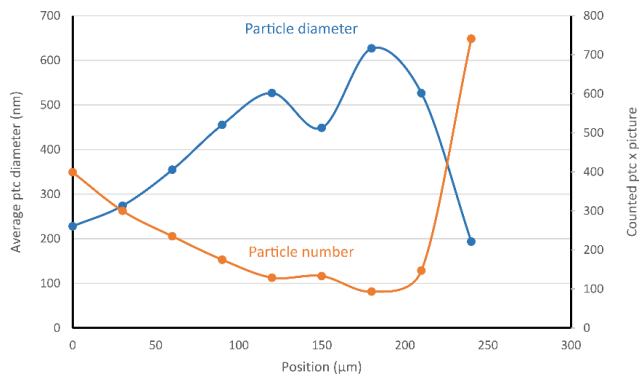


Figure 126: Sample 3, ImageJ® analysis results on average size (blue) and counted particles per picture (orange).

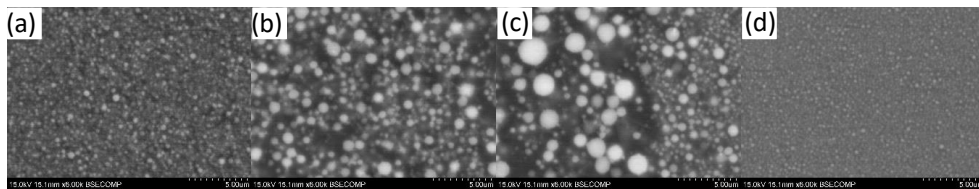


Figure 127: Silicon spheres in sample 3 at $x = 0$ (a), $x = 120 \mu\text{m}$ (b), $x = 210 \mu\text{m}$ (c), $x = 240 \mu\text{m}$ (d). All pictures have the same magnification ($\times 6000$).

Another typical feature of brown condensate is the **layered structure** (Figure 128 and Figure 129). Layers have variable thicknesses between 10-50 μm . In each layer, the average sphere size changes, alternating smaller and larger particles. There is no correlation between layer size and silicon sphere size. Figure 130 show how the particle number and size can change drastically from a layer to the next one, in sample 2. The layer thickness is thinner than the SEM-picture. This affects the particle average size, which oscillates between 805 nm ($x = 270 \mu\text{m}$, Figure 131b) and 463 nm ($x = 450 \mu\text{m}$, Figure 131c). The number of particles also oscillates between 125 and 239. Where the particle size increases, the number of particles decreases.

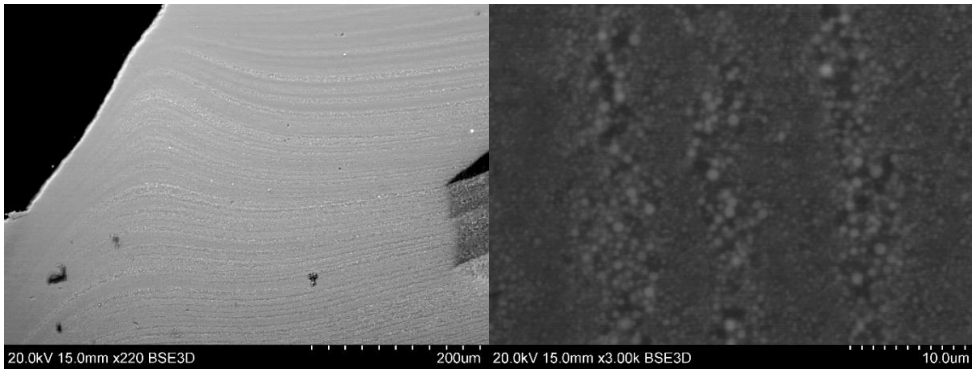


Figure 128: Layer configuration at x220 (left) and x3000 (right) magnification, sample 8.

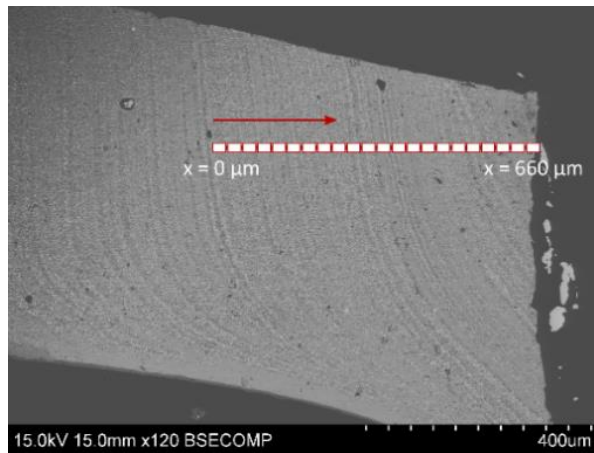


Figure 129: Line scanning of Sample 2.

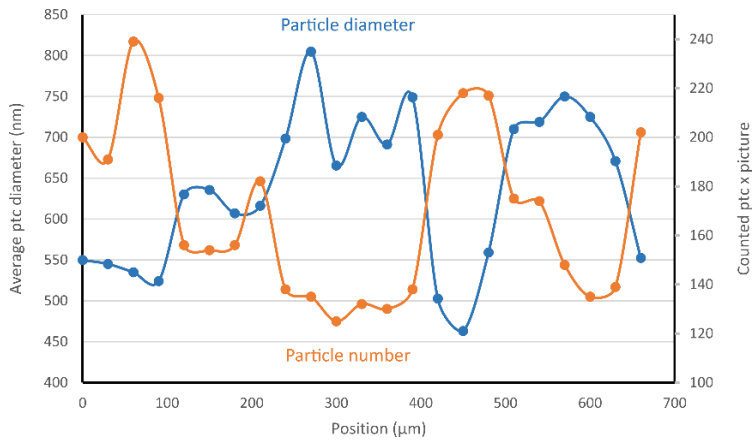


Figure 130: Sample 2, average area (blue), average size (blue) and counted particles per picture (orange).

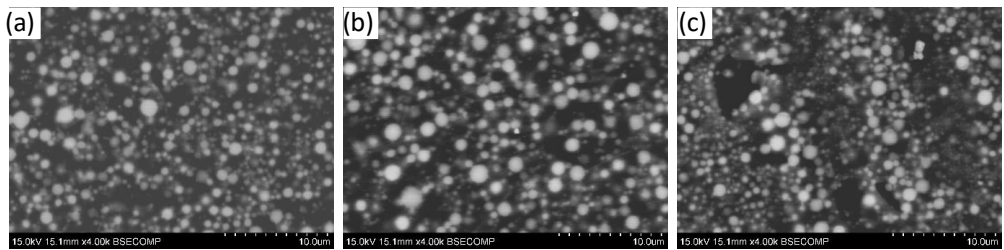


Figure 131: Layer particle sizes in sample 2: $x = 0 \mu\text{m}$ (a), $x = 270 \mu\text{m}$ (b), $x = 450 \mu\text{m}$ (c)

Silicon spheres are smaller, while going towards the white-brown condensate interface. While moving towards this interface, the silicon spheres gradually get smaller and disappear, and only a porous silica matrix is left. The porous silica layers were found in samples 3, 7 and 9 (Figure 132). Porous silica layers are located between brown and white condensate. The interface between porous silica and white condensate is sharp (Figure 132a,b). Pore size ranges between 0.5-20 μm . At the interface with brown condensate, the pores and the silicon spheres size are similar (Figure 133). Porous silica layers can sometimes contain silicon spheres with size below 100 nm.

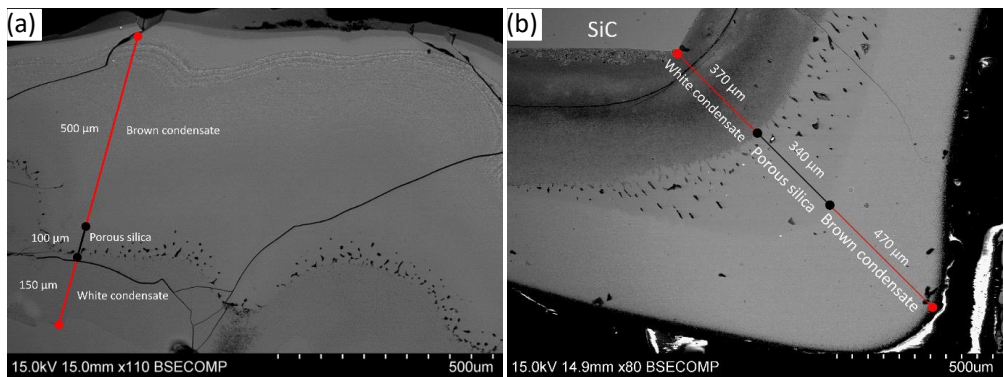


Figure 132: Layer thicknesses in sample 3 (a) and 7 (b).

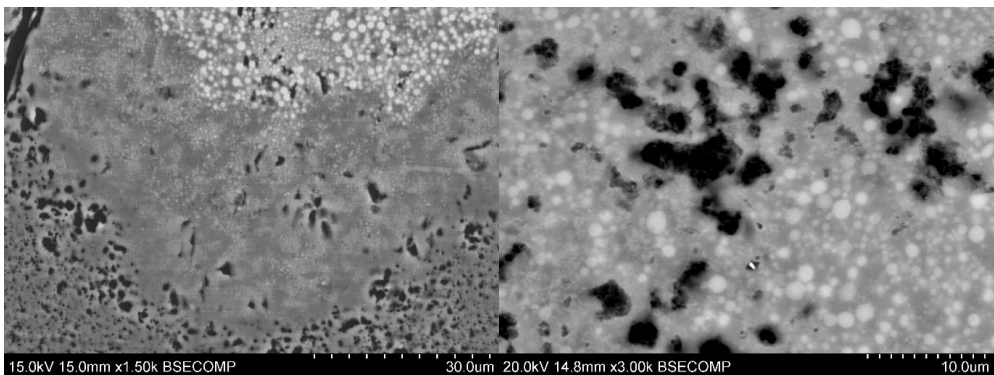


Figure 133: Pore and silicon sphere size in sample 9.

C. Industrial samples

This chapter will investigate the industrial sample microstructure and appearance. A special focus will be on the similarities and differences between the industrial and laboratory samples, analyzed previously in sections A and B. The microstructure found at laboratory scale show many similarities with the industrial samples. SiC comes as whiskers on most of the samples. SiC-SiO_x condensates appear also as wool-like layers, made of nanowires forests. Sometimes the nanowires have the same dimensions of the laboratory scale, and sometimes their size is 20 times larger. Si-SiO₂ condensates are also found as mixtures of Si and SiO₂. Grey condensate is also made of oriented wires, made of spherical blocks. Samples contain also porous silica, with pores with similar dimensions of the Si spheres.

Summary

Concerning the sample position in the furnace, it can be said that most of the industrial samples come either from the central inactive zone (all the REC samples), or from the zone close to the electrode (W1 and W4 samples). The only sample located at the high temperature zone is sample W4-42. The three samples from Salten are further from the electrode than the others, as they were extracted just behind the lining. However, the Salten samples are also located in the low temperature zone of the furnace.

Table 27 collects the compounds found on the surfaces of the samples by SE-SEM and EDS analysis. Samples REC 2.2 and 2.3 are not reported in the table, as they contained silica only. It was not possible to collect SE-SEM pictures, as the samples was strongly charging even after the application of the carbon coating. SiC whiskers are inserted anyways in this table, despite they are not considered as condensates. Further information on SiC whiskers are collected in Appendix A.

Table 27: Overview of compounds in the samples analyzed. A cross marks the presence of the compound in the sample.

Sample	Position in the furnace	SiO ₂ -SiC Nanowires	Si-SiO ₂ mixture	Porous silica	Grey condensate	SiC whiskers
REC 1.1	Central inactive zone					X
REC 1.2			X			X
REC 1.3		X				X
REC 2.1			X			
REC 3.1		X	X			X
REC 3.2						X
REC 3.3						X
REC 3.4				X		
S.22	Low T zone, close to the furnace lining			X		X
S.23			X			X
S.36			X	X		X
W1-31	Electrode zone (1.7 m above taphole)	X				X
W1-34		X				X
W1-38	Furnace walls, 1.5-2.0 m above taphole	X	X		X	X
W1-39			X			
W1-40				X	X	
W1-43	Low T zone					X
W4-29	Low T zone (stoking crust)	X			X	X
W4-30						X
W4-34	Loose charge zone		X			
W4-42	Furnace bottom		X			

Samples containing SiC-SiO_x condensates

The visual appearance of industrial white and blue condensate is shown in Figure 134. The samples seen in this chapter have some portions covered in a fluffy compound. Sample W1-31 is shown in the figure, as it was the sample with the highest amount of condensate on its surface. Other industrial samples containing nanowires have a thinner and more fragile white layer. The samples also contained quartz and reacted carbon materials, such as sample REC1.3.



Figure 134: Nanofibers from sample W1-31.

The microstructure of the condensate consists of nanowires and nodules (Figure 135-Figure 138), as noticed for the laboratory scale sample. However, the laboratory scale sample might sometimes differ in size compared to the industrial samples. The main differences were noticed in the size of nodules and nanowires.

Case 1: SiC-SiO_x nanowires, with nodules of comparable size to the laboratory scale nanowire. In the nanowires of sample REC 3.1, the nodules are either distributed randomly on the nanowires, or on necklace structures (Figure 135a), which resemble the results of TEM and SEM characterization from laboratory scale experiments (Chapter 3A, Figure 98 and Figure 103).

The BSE-appearance is shown in Figure 135b. BSE-SEM analysis on sample W1-38 reveals intricate nanometric treads embedded in SiO₂ and deposited on a SiC substrate. EDS on the nodules was collected during SE-SEM analysis, in the points shown in Figure 136. The composition consists of Si, O and C (Table 28). The two points with the largest C amounts (points 3 and 6) are far from large nodules.

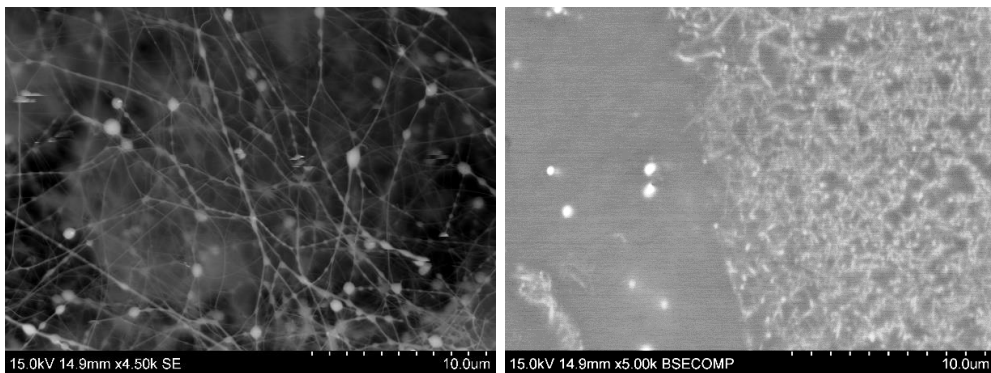


Figure 135: a) Bead structures in sample REC 3.1; b) Nanowires (right) deposited on SiC substrate (left), sample W1-38.

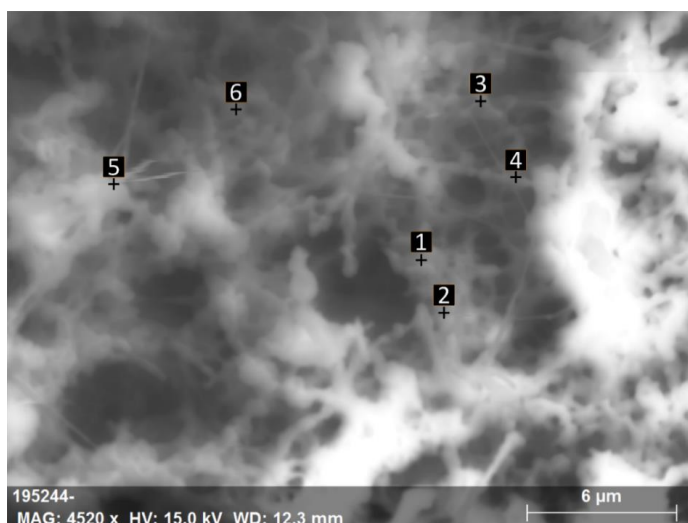


Figure 136: EDS analysis of nanowires from the surface of sample W1-38.

Table 28: Composition detected at the points from Figure 136.

Point	Si (at. %)	O (at. %)	C (at. %)
1	43%	39%	18%
2	41%	43%	16%
3	34%	43%	23%
4	44%	38%	18%
5	47%	41%	12%
6	45%	36%	19%

As it happened for the blue condensates from the laboratory scale, some nanowires forests have lower amount of nodules. This is the case of the blue condensate of sample W1-31 (Figure 137), which does not contain as many nodules as the REC samples. This microstructure is more typical of a blue condensate, with low amount of nodules and thin, long nanowires. In fact, the magnification of the picture corresponds to the blue and white condensates picture at laboratory scale (x10k) (see Figure 95).

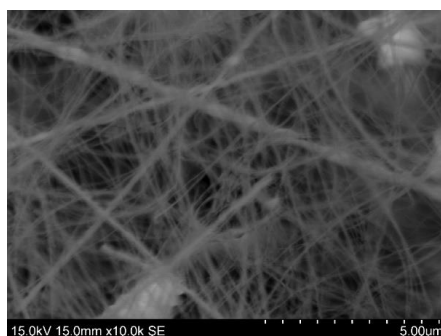


Figure 137: Nanowires on sample W1-31.

Case 2: SiC-SiO_x nanowires, with nanowire size larger compared to the laboratory scale nanowires. The samples REC 1.3 and W1-34 showed nanowires with a length, number of nodules and wires shape similar to the results from the SiO₂-SiC nanowires characterization. However, the thickness of the nodules and nanowires is 20 times larger than the ones found in lab-scale experiments, despite the same appearance. In fact, Figure 138 compares the size of nanowires in sample REC 1.3 (magnification x250) to those previously seen in sample REC 3.1 (magnification x7.5k and x12k). The figures look almost identical, but the magnification is different.

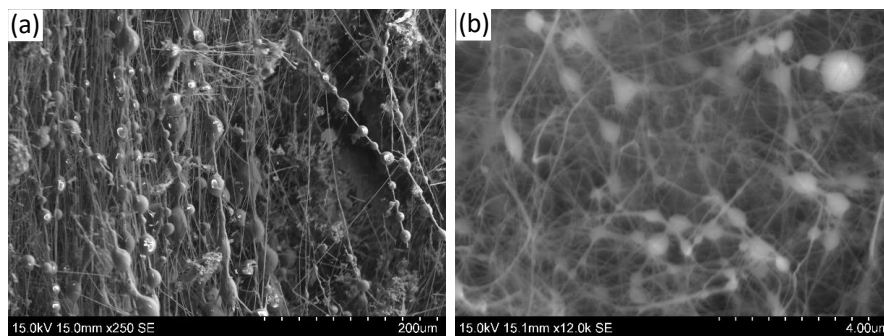


Figure 138: Nodules on nanowires from Sample REC 1.3, x250 magnification; Right: Nanowires with nodules from sample REC 3.1, x12k magnification.

Case 3: SiC-SiO_x nanowires and SiC whiskers covered in nodules, with same size compared to laboratory scale samples. Figure 139 shows the peculiar microstructure noticed on sample W4-29. There are short nanowires and whiskers. The similarity with the SiO_x nodules can be appreciated by looking at the droplet-like shape of the white layer. These are thought to be either SiC whiskers covered in SiO₂ or SiO₂ nanometric whiskers. However, the image is not blurry due to charging, so there should be at least another compound in proximity which is not an oxide. This compound could be either embedded in the white layer or making the substrate on which the nanowires are deposited.

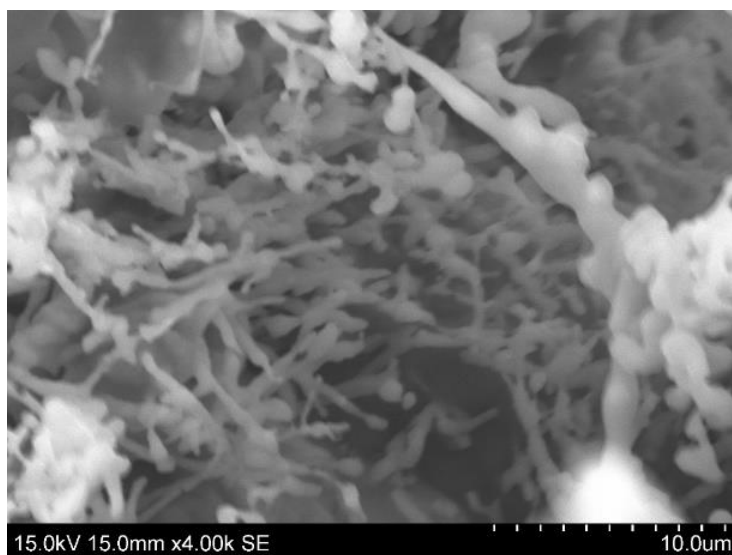


Figure 139: Thick whiskers with nodules, sample W4-29.

Samples containing Si-SiO₂ condensates (and porous silica)

Some of the samples extracted from industrial furnaces contain also massive amounts of brown layers on carbon materials converted to SiC. These are samples REC 1.2, 2.1, 3.1, 3.4, S.23, S.36, W1-38-39-40, W4-34, W4-42. The color of the brown zones from these samples is very similar to the brown condensate from laboratory scale samples. An example is shown in Figure 140. The brown compound is rigid and has stronger mechanical properties, compared to the previously seen SiC-SiO_x condensates.



Figure 140: Brown condensate on black and pale green carbon materials, eventually covered with white condensate. Sample REC 3.1.

In SEM analysis, these samples showed a thick layer with Si and FeSi spherical islands deposited on a carbon material particle converted to SiC. Table 29 lists the results of the EDS point analysis in sample S23, from the zone in Figure 141b. The white areas are Si droplets. SiC may come from a converted carbon material. SiO₂ fills the voids left by the SiC phase. The microstructure comparison brought to three main conclusions:

- 1) **The largest spheres are usually located towards the sample edges (Figure 141a).** The silicon spheres dimension ranges between 1-10 μm (Figure 141b), which is comparable to what was seen during the experimental findings on brown condensate characterization. Si islands are usually spread within the SiO₂ matrix, but also close to carbonaceous materials converted to SiC. The shape of the silicon islands tends to be circular in most of the samples analyzed.
- 2) **The silicon droplets are interconnected by treads.** This also happened in the laboratory scale samples. However, the threads are larger than the Si-SiO₂ laboratory scale condensate. Figure 141c shows the microstructure of the brown condensate in sample W1-40.
- 3) **The Si droplets may be some order of magnitude larger than in the laboratory scale samples.** For instance, in sample W1-39, Si inclusions have a diameter of 500 μm , and could almost be seen with bare eye. Sample W1-40, S.23, W4-34, and W4-42 have also large silicon inclusions, with size between 30 -100 μm (Figure 141b). However, such droplets are present only in small portions of the samples.

It can be said, after SEM analysis on the samples, that the microstructure is similar at laboratory and industrial scale, but the size of the silicon droplets and threads might be different. FeSi inclusions are sometimes present instead of Si inclusions, according to the raw materials composition and the alloy produced in the furnace.

Table 29: EDS analysis of points from Error! Reference source not found. (at. %).

Zone color	Si	O	C	Phase
White spheres	78%	5%	17%	Si on SiO ₂
Grey matrix	60%	40%	0%	SiO ₂

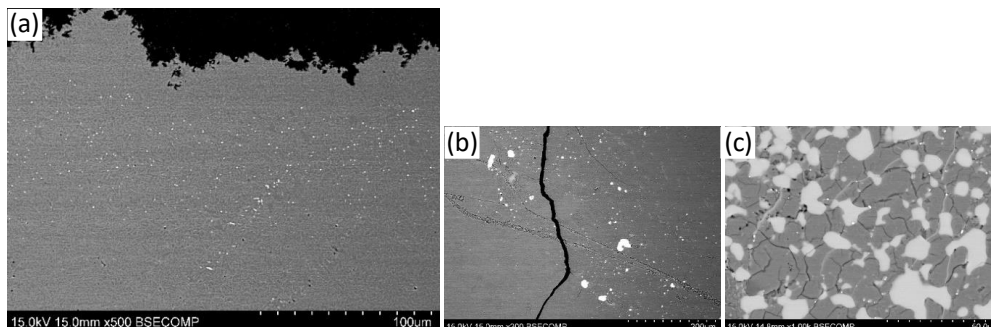


Figure 141: a,b): Si spheres in sample S.23; c): Interconnected Si islands in sample W1-40

Samples containing porous silica

Sample S.22 and S.36 are porous and easy to brake. It was seen during SEM characterization that the samples also contain Si-SiO₂ condensates, as shown in the previous section. However, while going towards the center of the sample, the silicon spheres gradually decrease in number, leaving empty spaces. The SiO₂ matrix becomes full of pores and cracks.

Figure 142 shows how the pore size increases from 1-10 μm to 30-50 μm, while going from right (sample core) to the left (sample edge). The interface between phases with different porosity is quite sharp. Cracks and voids may become larger while going away from the center of the sample, until the silicon spheres are found again.

EDS analysis confirmed the presence of silica in sample S.36 (Figure 143). Table 30 shows the compositions detected in the points. The composition does not change, even in areas with different size of the pores. The pores tend to be circular, and have a similar size compared to the Si droplets seen in Figure 141, or in the laboratory scale samples.

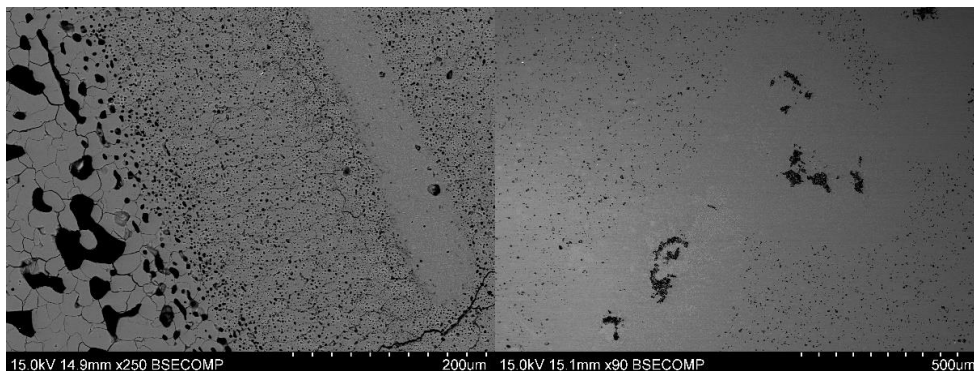


Figure 142: Change in pore size in silica, sample S.36 (left) and S.22 (right).

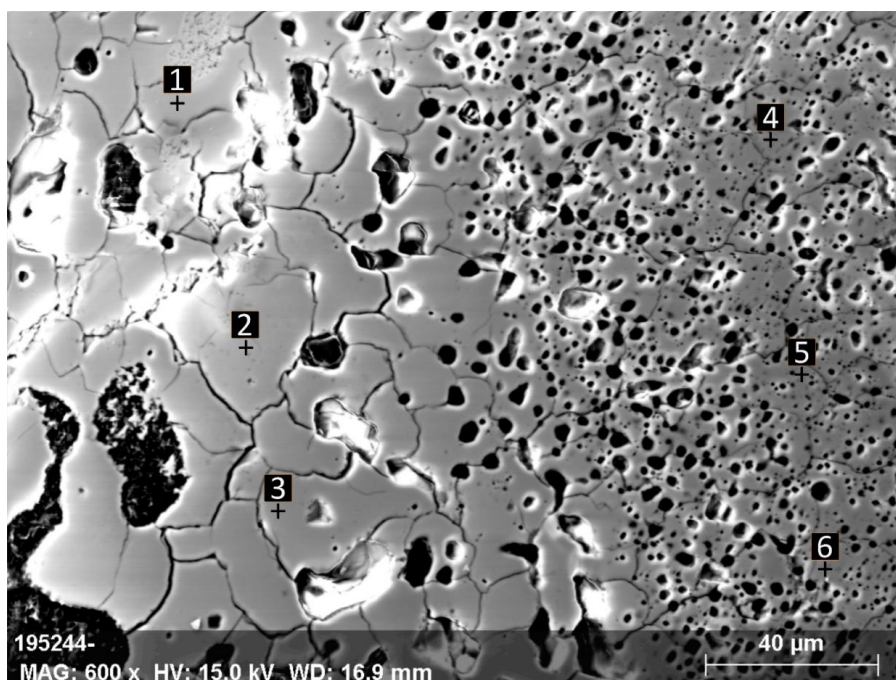


Figure 143: porous silica from Sample S.36.

Table 30: Composition detected by EDS in the points from Figure 143; (at. %)

Point	Si	O	Al	Compound
1	54%	44%	1%	SiO ₂
2	55%	44%	1%	SiO ₂
3	54%	45%	1%	SiO ₂
4	54%	45%	1%	SiO ₂
5	55%	44%	1%	SiO ₂
6	55%	45%	0%	SiO ₂

Samples containing grey condensate

Samples W1-38, W1-40 and W4-29 revealed the presence of grey and white layers with features similar to the grey condensate scales. The samples have also similar color to the grey scale on the carbon tubes.

The microstructure is shown in Figure 144. The figure shows the condensate in SEM analysis, at two different level of magnification. Three comparisons can be made with the laboratory scale samples:

- 1) **Small islands are distributed over the sample surface**, at magnification x1000 and x1500. The oriented wires are not found, as in grey condensates from laboratory scale experiments.
- 2) **Nanowires and small whiskers can appear** close to the islands (Figure 144a). Their diameter is nanometric, but it cannot be quantified due to resolution limitations.
- 3) **The islands are made of accumulated spherical blocks (Figure 144c)**. A picture at x5000 magnification, shows blocks of similar dimensions to those found on the graphite tube substrate from the small-scale setup (see Figure 110).

It is theorized that grey layers could either contain porous silica, or grey condensates resembling those found at laboratory scale.

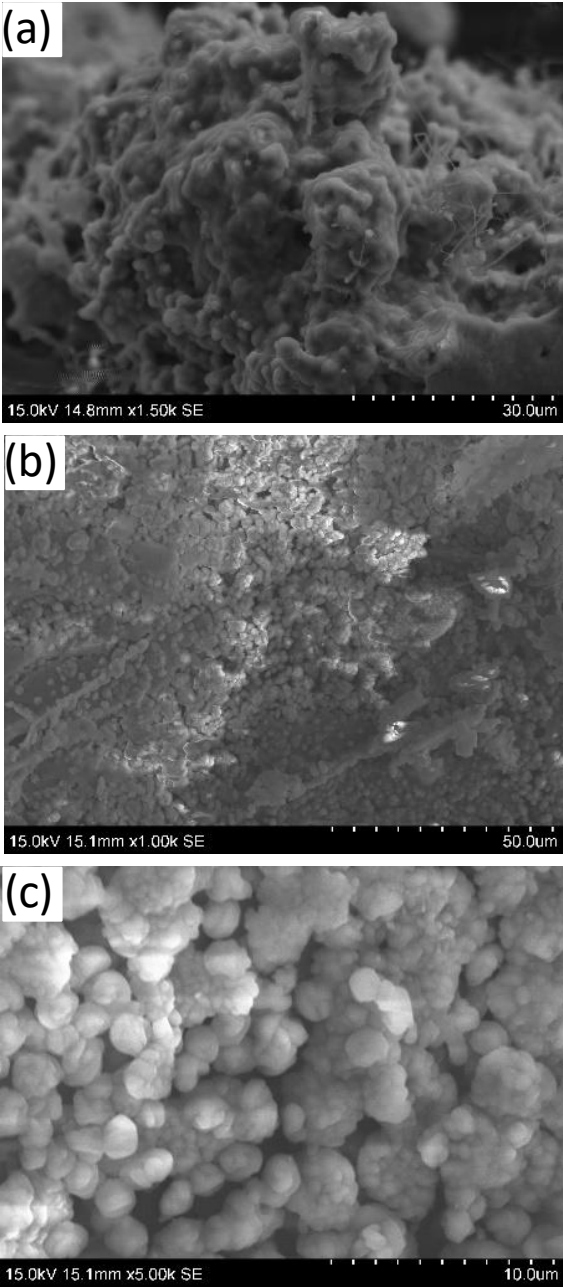


Figure 144: Spherical blocks on grey layer, sample W1-38 (a), W1-40 (b) and W4-29 (c).

D. Temperature of formation

The aim of this chapter is to analyze how the experimental parameters influence the condensates temperature of formation in the crucible. First, all the results are collected in an overview section. Then, specific chapters will analyze the parameters chosen, i.e. holding time, holding temperature, pellets amount, substrate composition, particle size and calculated gas composition ($p_{SiO,in}$) (see the “Modeling – p_{SiO} -T calculation” chapter for further details about calculation of this parameter). Each part of this section focuses on a single parameter, while keeping the others constant (unless specified). The results from the small-scale and large-scale setups are analyzed into two separate sections. Finally, the results and the correlations found from the two setups are compared.

To visualize the results of the temperature measurements and crucible excavations, the **condensation profiles** are used. These profiles show which condensate is generated in a position and temperature interval in the condensation zones. They were collected for all the experiments, with few exceptions. In fact, a total of 52 condensation profiles was collected, out of the 55 experiments performed (36 experiments out of 39 from the small-scale setup, and all the 16 experiments from the large-scale setup).

A condensation profile shows the cross section of the condensation zone. The experiment number is written on the top of each condensation profile. When two condensates are present in the same position, both colors are represented by transversal lines. The thicker the transversal lines, the higher the relative amount of condensate in that temperature interval. Where no color is shown, the substrate did not capture any condensate. The temperature and the positions where the condensates appear are shown on the side of each picture. The temperature gradient was not assessed for all the setups, therefore some profiles miss the temperature-position correlation. Appendix C summarizes the calculation of temperature gradient for the experiments, whereas Appendix J shows all the condensation profiles and the legend for illustration of the condensates colors.

Effect of experimental parameters

Comparison between small and large-scale setup

Table 31 resumes the temperature of formation for each condensate, comparing the condensation substrates and the setups chosen. The temperature intervals include all the experiments, regardless of the experimental parameters.

The condensates temperatures of formation extend in similar ranges, regardless of the setup chosen. The main difference is that the large-scale setup produces negligible amounts of blue condensate, compared to the small-scale experiments. The small-scale setup produces condensates at lower temperatures, especially in the experiments with longer holding time (240 min).

Table 31: Temperatures of formation of condensates on different substrates and setups.

Condensate type	SiC	Quartz
Si-SiO ₂	Small scale: 1400 - 1780°C Large-scale: 1420 - 1810°C	Not formed
SiO ₂ -SiC	<p>Blue layer Small scale: 900 – 1500°C; 1600 – 1810°C Large-scale: 1135 – 1370°C ; 1720-1810°C (traces)</p> <p>White layer Small scale: 910 – 1800°C Large-scale: 1135 – 1810°C</p> <p>Grey layer Small scale: 1320 – 1800°C Large-scale: Together with Si-SiO₂</p>	<p>Blue and white condensates appear</p> <p>Up to 1673°C: White condensate</p> <p>Highest temperature measured in melting area is 1673°C at Y=0</p>

SiC and quartz substrates

Changing the condensation substrate from SiC to Quartz A did not affect the temperature of formation of the condensates significantly. Figure 145 shows the condensation profiles for experiments R7b and R9a, which look almost identical. Softened quartz can often be mistaken by quartz particles with white condensate on it, as they both get opaque at the end of the experiments.

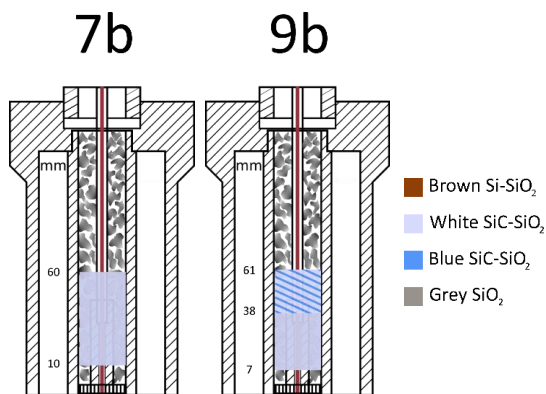


Figure 145: Condensation profiles of Experiment R7b (Quartz A) and R9b (SiC). Constant parameters: Target T = 1900°C, holding time = 1 hour, He flow 0.1 l/min, Substrate size 5-8 mm.

Effect of holding time (small-scale)

A longer holding time gives a wider condensation temperature interval for brown Si-SiO_2 condensate. One can compare profiles for setup R3a, R4a and R5a (Figure 146), which have a starting $\text{SiO}(\text{g})$ fraction $p_{\text{SiO},\text{in}} = 0.74$ (He flow at 0.02 l/min). The brown condensate layer at $t = 30$ min (Exp. R3a) is constrained in a small temperature interval. At $t = 60$ min (Exp. R4a) or $t = 240$ min (Exp. R5a), the brown condensate is located at a similar $T_{\text{SiO},\text{R2,start}}$, but it covers a larger interval. These temperature intervals are similar in extension ($1665\text{-}1800^\circ\text{C}$ at $t = 60$ min; $1710\text{-}1780^\circ\text{C}$ at $t = 240$ min).

Longer holding times shift condensation of the grey condensates to lower temperatures or in a wider temperature range. However, the temperature of formation changes mostly between 30 – 60 minutes, rather than between 60 – 240 min. It was seen that the grey condensate has its temperature of formation from $1670 - 1800^\circ\text{C}$ at 30 min (R3a), then between $1520 - 1665^\circ\text{C}$ at 1h (R4a), and finally to $1520 - 1710^\circ\text{C}$ at 4 h (R5a). For the experiments R14a, R17a and R20a, ($p_{\text{SiO},\text{in}} = 0.71$, He flow at 0.1 l/min), the position of white condensate also shifts upwards: $1305 - 1710^\circ\text{C}$ at 30 min (R14a), then $1090 - 1700^\circ\text{C}$ at 60 min (R17a), and finally between $1040 - 1630^\circ\text{C}$ after 240 min (R21a). The variation of the lowest temperature of condensation for the compounds and experiments described are collected in Figure 147.

The lowest condensation temperatures for brown condensate does not change much between the experimental set R3-5, their interval widens out between 30 minutes and 1 hour, and there are not many changes between 1 hour and 4 hours holding time. It is believed that at the beginning the Si-SiO_2 brown condensate form where the temperature is lowest. Then most of these condensates will form between $1650\text{-}1800^\circ\text{C}$. The brown condensate will remain in a similar temperature area at different experiments, whereas the SiC-SiO_x condensate form higher up, since the gas can flow between the SiC -substrates.

Finally, it can be concluded that condensates do not change their position after the gas production reaction has stopped. In fact, the gas production ends between 30- and 60-minutes holding time. As described, the major changes in lowest condensation temperature occur between 30- and 60-minutes holding time.

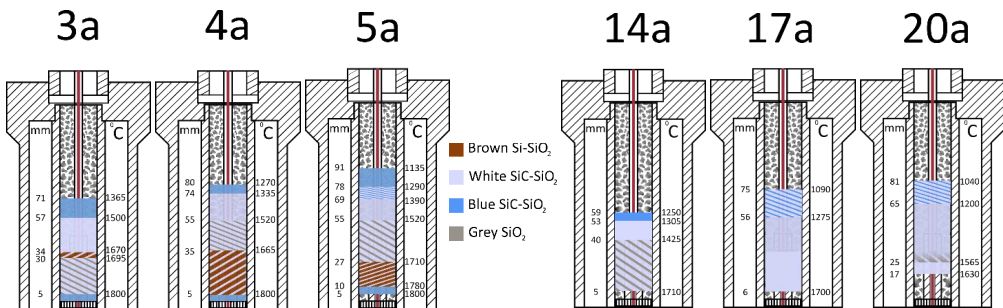


Figure 146: Left – Condensation profiles for Experiments R3a (t=30 min), R4a (t=60 min), R5a (t=240 min). Constant parameters : Target T 2000°C, SiC substrates, Ar flow 0.02 l/min, substrate size 3-5 mm ; Right : Condensation profiles for Experiments R14a (t=30 min), R17a (t=60 min), R20a (t=240 min). Constant parameters : Target T 2000°C, SiC substrates, He flow 0.10 l/min, substrate size 3-5 mm.

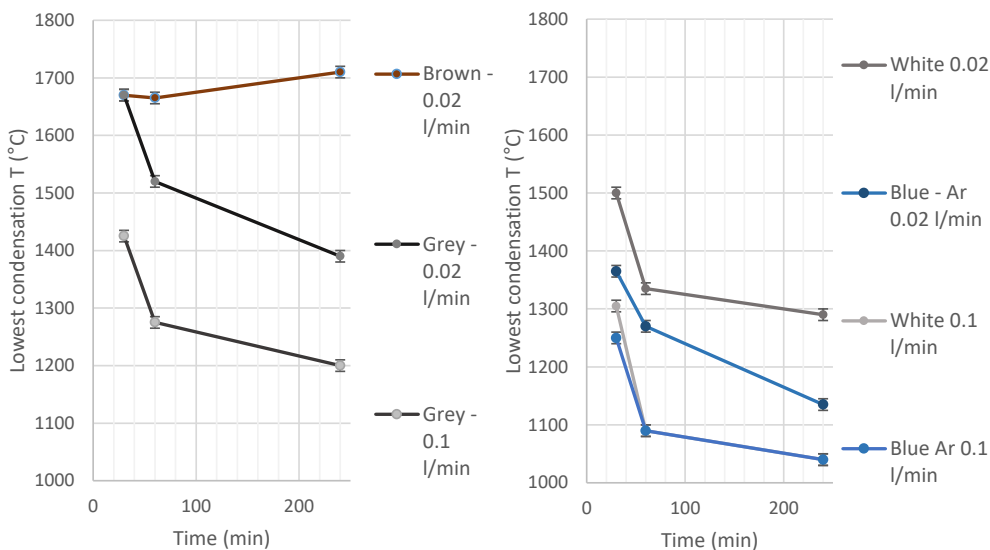


Figure 147: Variation in the lowest temperature of formation for blue condensate in the experiments from Figure 146. Error bars on temperature are $\pm 10^\circ\text{C}$, as described in Appendix C.

Effect of holding time (large-scale)

As for the small-scale setup, a longer holding time shifts the condensation front of white condensate upwards, to colder positions. The starting temperature for condensation of white condensate does not move much in neither Figure 148 or Figure 149. On the other hand, the condensation finishes at 1390°C (10 min, IF12a) or 1370°C (30 min, IF10), whereas it moves to 1240°C (120 min, IF5b) at longer times, when $p_{\text{SiO}_2, \text{in}} = 1.0$. However, in experiments IF11, IF9 and IF1b, ($p_{\text{SiO}_2, \text{in}} = 0.75$) the white condensate develops in similar temperature intervals, regardless of the holding time chosen. The variation of the lowest temperature of condensation for the compounds and experiments described are collected in Figure 150. The temperatures decrease more for setups with higher $p_{\text{SiO}_2, \text{in}}$.

The brown condensate temperature interval does not change much by varying the holding time. However, in experiment IF1b ($t = 120$ min), brown condensate was noticed between 1565 - 1650°C , whereas in the experiment at shorter holding times ($t = 30$ min and $t = 10$ min) no brown condensate was found.

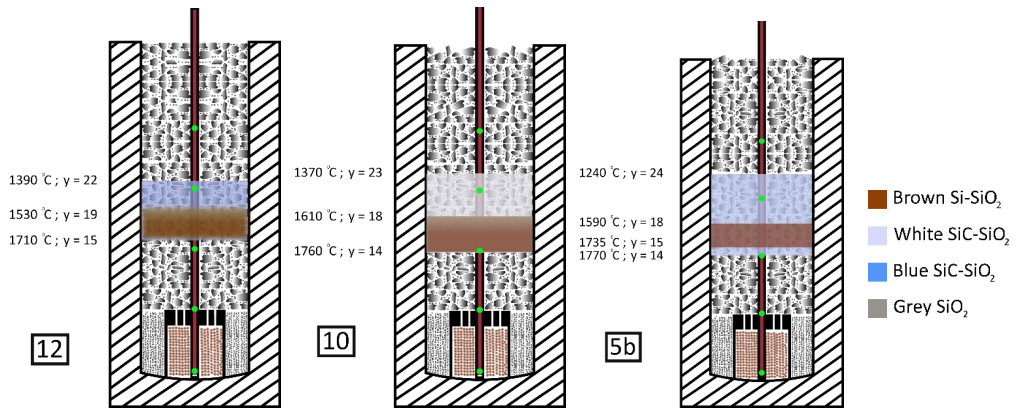


Figure 148: Condensation profiles for Experiments IF12 (t=10 min), IF10 (t=30 min) and IF5b (t=120 min), group with $p_{\text{SiO}_2, \text{in}} = 1.0$. Constant parameters : Target T 1890°C, SiC substrates, substrate size 3-10 mm, $p_{\text{SiO}_2, \text{in}} = 1.0$

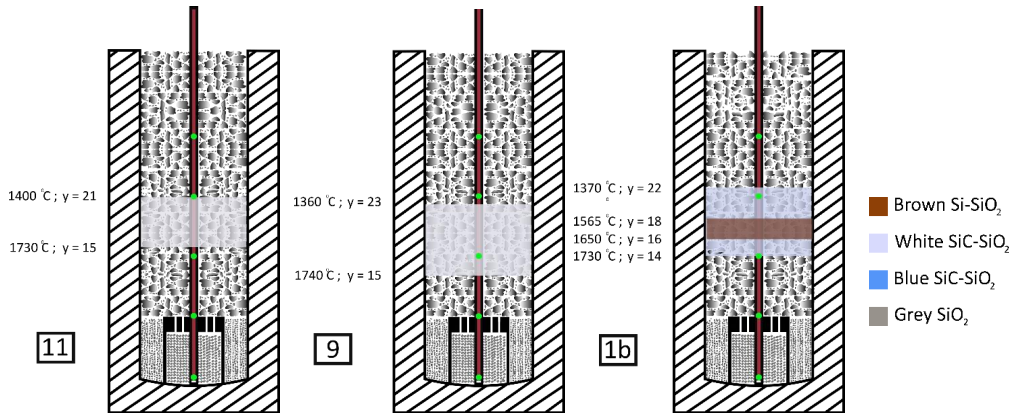


Figure 149: Condensation profiles for Experiments IF11 (t=10 min), IF9 (t=30 min) and IF1b (t=120 min), group with $p_{\text{SiO}_2, \text{in}} = 0.75$. Constant parameters : Target T 1890°C, SiC substrates, substrate size 3-10 mm, $p_{\text{SiO}_2, \text{in}} = 0.75$

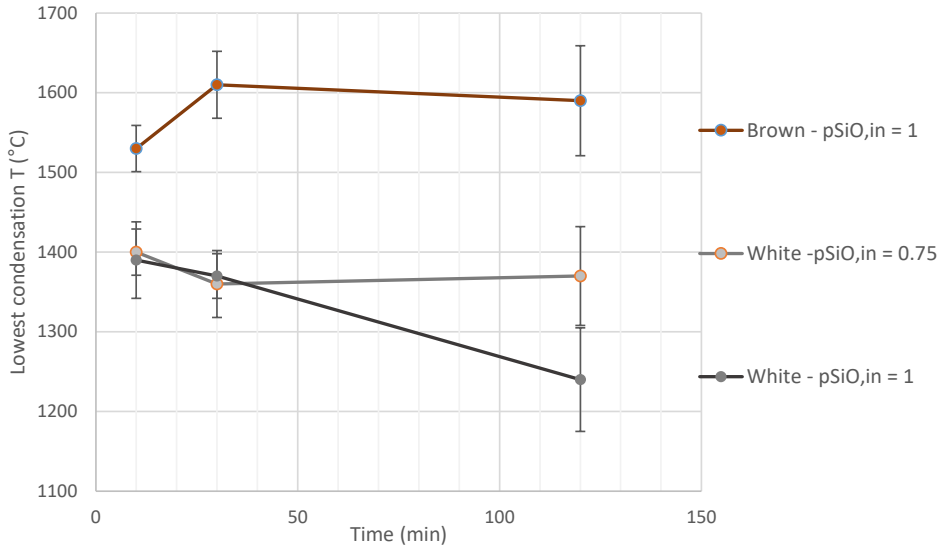


Figure 150: Variation in the lowest temperature of formation for condensates in the experiments from Figure 148 and Figure 149. The width of the error bars is the value of the deviation obtained at the nearest temperature measurement point during the temperature gradient assessment (see Appendix C, Table 53).

Effect of partial pressure in small-scale setup (gas flow)

The addition of Ar and He give similar condensation profiles. This can be seen by comparing the repetitions of setups R4. R4a (with Ar) does not differ much from the repetitions R4c-e (with He). However, R4b looks slightly different when it comes to the temperature of formation of brown condensate and can be considered an outlier. Increasing added gas shifts also blue and white SiO₂-SiC condensates to lower temperatures and higher up in the crucible, and in a wider temperature range (Figure 151). The blue condensates move from 1270 - 1335°C (Ar 0.02 l/min, p_{SiO,in}=0.74) to 910 - 1020°C (Ar 0.40 l/min, R1b, p_{SiO,in}=0.62). However, the condensate was found at higher temperatures in setups R2a and R17b. The white condensate also shifts from 1335 - 1800°C (Ar 0.02 l/min, R4a, p_{SiO,in}=0.74) to 1220 - 1700°C (He 0.1 l/min, R17b, p_{SiO,in}=0.71) and finally to 910 - 1725°C (He 0.4 l/min, R1b, p_{SiO,in}=0.62). Finally, the brown condensate moves from 1665°C-1800°C (R4a), to 1470 - 1700°C (R17b), then to 1340-1570°C (R1b), by increasing the inert gas flow from 0.02 to 0.10 and then to 0.4 l/min. The positions of the brown condensates in experiments R4a and R2a (Ar 0.05 l/min) are also similar. It can be concluded that the inert gas flow must be increased, to decrease the temperature of formation of the condensates.

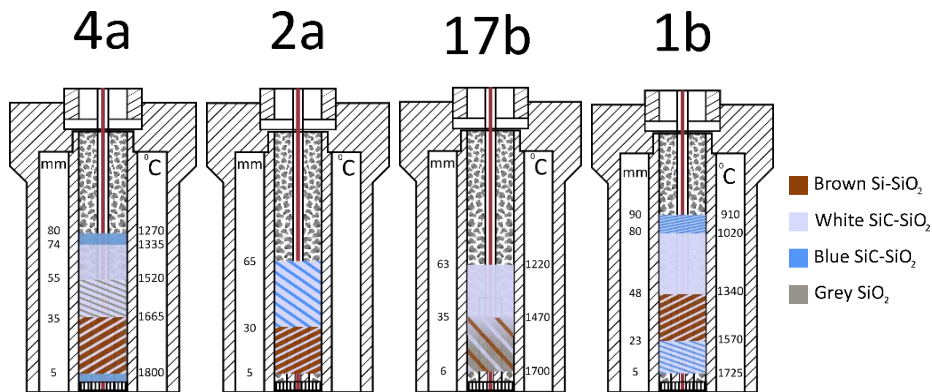


Figure 151: Effect of inert gas addition on condensation profile, experiments R4a (0.02 l/min), R2a (0.05 l/min), R17b (0.10 l/min) and R1b (0.4 l/min). Temperature gradients in the chamber depend also on the gas flow. Constant parameters : Target T 2000°C, SiC substrates, substrate size 3-5 mm, holding time 1 h.

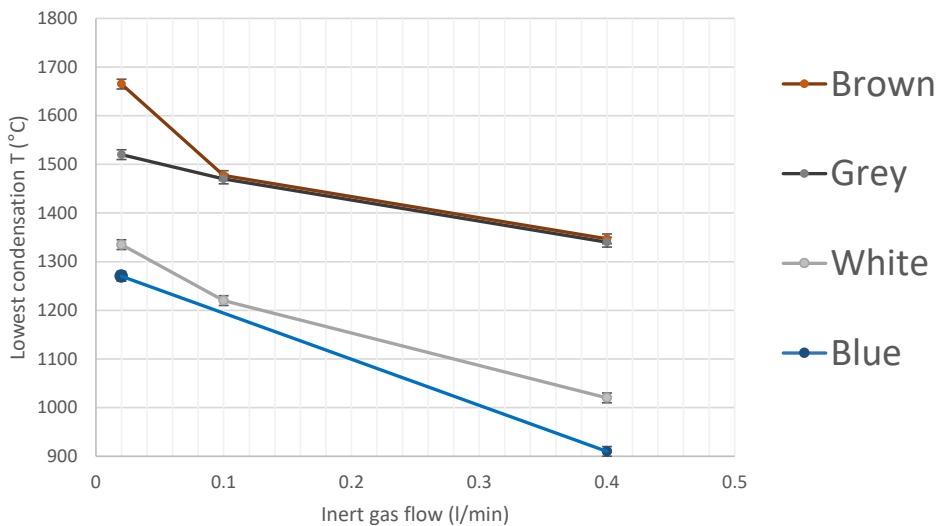


Figure 152: Variation in the lowest temperature of formation for condensates in the experiments from Figure 151. Error bars on temperature are $\pm 10^\circ\text{C}$, as described in Appendix C.

Effect of partial pressure in large-scale setup (pellets composition)

There are slight differences in the condensates position when changing the pellets composition, in the large-scale setup (Figure 153 and Figure 155). In Figure 153, experiments are divided into four groups, made of two experiments each, one with SiC-SiO₂ pellets (grey) and one with Si-SiO₂ pellets (brown) in the gas production zone. The former pellets give a starting $p_{\text{SiO}_2, \text{in}}$ of 0.75 (in experiments IF1b, IF2a, IF3 and IF4), whereas the latter give a starting $p_{\text{SiO}_2, \text{in}}$ of 1 (in experiments IF5b, IF6a, IF7a and IF8). Figure 154 shows the variation in the lowest temperature of condensation for brown and white condensates, in experiments at differing starting gas composition $p_{\text{SiO}_2, \text{in}}$. The diameter of the dots is proportional to the width of the particle size distribution, i.e. the distance from the average and the maximum diameter present in the particle size distribution of the SiC particles in the condensation chamber.

The lowest temperature for white condensate formation tends to decrease while switching from SiO₂-SiC ($p_{\text{SiO},\text{in}}=0.75$) to Si-SiO₂ ($p_{\text{SiO},\text{in}}=1$) pellets. For example, it will decrease from 1370°C to 1240°C between experiments IF1b and IF5a, or from 1320°C to 1240°C from experiments IF4 to IF8. However, the change is less relevant in the large-scale crucible, when comparing IF2a and IF6a, or IF3 and IF7a.

An increase in the partial pressure of the SiO-gas will give larger temperature of formation intervals for brown condensate or will form brown condensate in those experiments where it was not noticed at $p_{\text{SiO},\text{in}} = 0.75$. This can be noticed in the groups IF11+IF12 and IF9+IF10 (Figure 155). The same occurs between experiments IF3 to IF7b, where the brown condensate is absent in the first case and present between 1420 - 1750°C in the second, or again the formation between 1740 - 1810°C in experiment IF6a. The experiments at short time (IF4 and IF8) and with a wide particle size distribution (IF1b, IF5b) show similar temperature of formation for brown condensate.

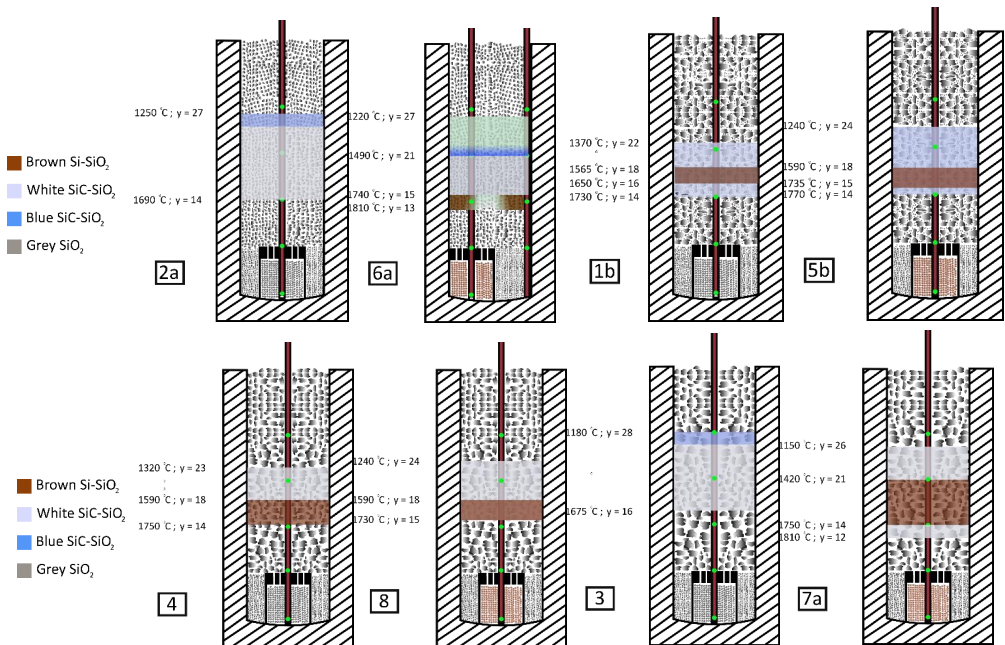


Figure 153: Partial pressure effect on different PSD groups. The SiO+CO experiment has grey pellets on the bottom, whereas the SiO(g) experiments have brown pellets. The experiments collected are IF1b and IF5b (3-10 mm), IF2a and IF6a (5-8 mm), IF3 and IF7a (12-20 mm), IF4 and IF8 (8-14 mm). Constant parameters : Target T 1890°C, SiC substrates, holding time 2 h.

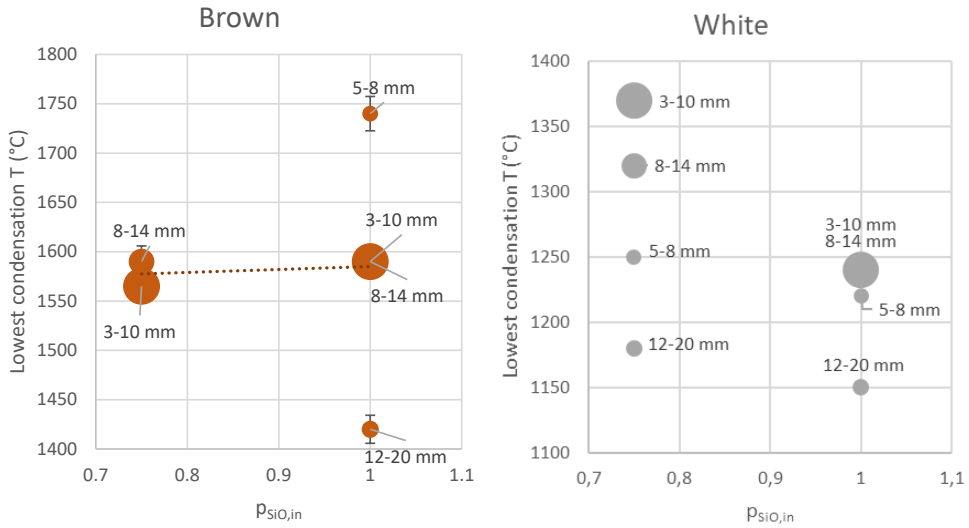


Figure 154: Variation in the lowest temperature of formation for condensates in the experiments from Figure 153. The width of the error bars on temperature is the value of the deviation obtained at the nearest temperature measurement point during the temperature gradient assessment (see Appendix C, Table 53).

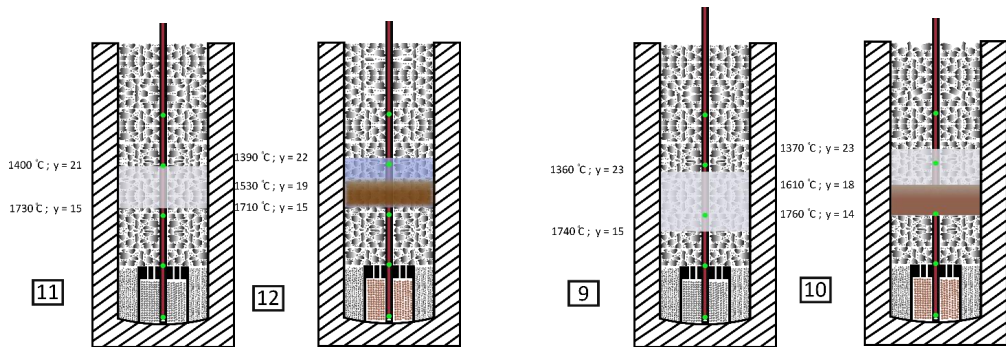


Figure 155: Partial pressure effect at short times. The SiO+CO experiment has grey pellets on the bottom, whereas the SiO(g) experiments have brown pellets. Experiments IF11 and IF12 (10 min), IF9 and IF10 (30 min). Constant parameters : Target T 1890°C, SiC substrates, substrate size 3-10 mm.

Effect of substrate particle size (large-scale)

A narrow size distribution means a higher void fraction in the crucible, and therefore a low available surface and a more permeable charge. The parameter A_{cm} estimated available area per cm height in the crucible. If the distribution is broad, the smallest particles fill the voids, giving a higher available surface for condensation. For instance, changing from a 3-10 mm (IF1b and IF5b) to 5-8 mm (IF3a and IF7a) decreases A_{cm} by 7%. The calculation of A_{cm} in different experiments are listed in Table 32. These values are calculated in the Chapter 4 (Modeling), and are also collected and described in Appendix D and G. The parameter was not calculated for experiment IF6a.

A decrease in the available surface A_{cm} gives usually a larger condensation interval. The condensation interval for white condensate increases from 8 cm in IF1b to 13 cm in IF2a. The two experiments share the same d_{avg} of the particles, i.e. only the PSD broadness contributes. The same can be said by comparing IF5b to IF6a.

At the same time, even if d_{avg} is slightly different between IF4 and IF3a, the condensation interval increases from 9 to 12 cm. Experiment IF3a contains larger particles compared to IF4. The same can be noticed while comparing experiments IF8 (9 cm) and IF7a (14 cm).

The brown condensates tend to appear (or be spread in wider intervals) in experiments with broader PSD. In fact, Experiments IF1b and IF4 have brown condensate, whereas IF2a and IF3 do not. Brown condensate keeps a thickness of 2-3 cm between IF5b and IF6a, but it increases its thickness from 3 to 7 cm by comparing experiments IF8 and IF7a.

A broad PSD favors condensation over a small temperature range, probably due to a low gas permeability. A larger d_{avg} has the same effect on A_{cm} . Large particles leave larger voids between each other, and the broadness of the distribution must be compensated by a higher number of fines. The available surface area decreases strongly (63% decrease in A_{cm} from exp. IF1b to IF3a; 50% decrease IF5b to IF8).

Table 32: Values of A_{cm} and d_{avg} for experiments in Figure 156 and Figure 157. Details on the PSD are collected in the experimental section.

Exp.	Size distribution	d_p (cm)	A_{cm} (cm ² /cm)
IF1b	3-10 mm	0.65 (broad PSD)	323
IF2a	5-8 mm	0.65 (narrow PSD)	303
IF4a	8-14 mm	1.10 (broad PSD)	169
IF3a	12-20 mm	1.60 (narrow PSD)	119
IF5b	3-10 mm	0.65 (broad PSD)	339
IF6a	5-8 mm	0.65 (narrow PSD)	n.p.
IF7b	12-20 mm	1.60 (broad PSD)	123
IF8	8-14 mm	1.10 (narrow PSD)	169

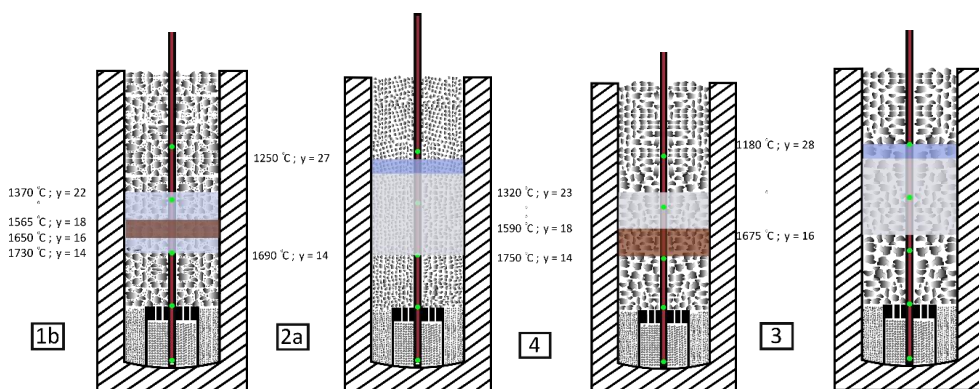


Figure 156: Condensation profiles sorted by decreasing A_{cm} , experiments IF1b (3-10 mm), IF4 (8-14 mm) IF3 (12-20 mm) and IF2a (5-8 mm). Experiments with SiO₂-SiC pellets. Constant parameters : Target T 1890°C, SiC substrates, holding time 2 h, $p_{SiO_2,in} = 0.75$

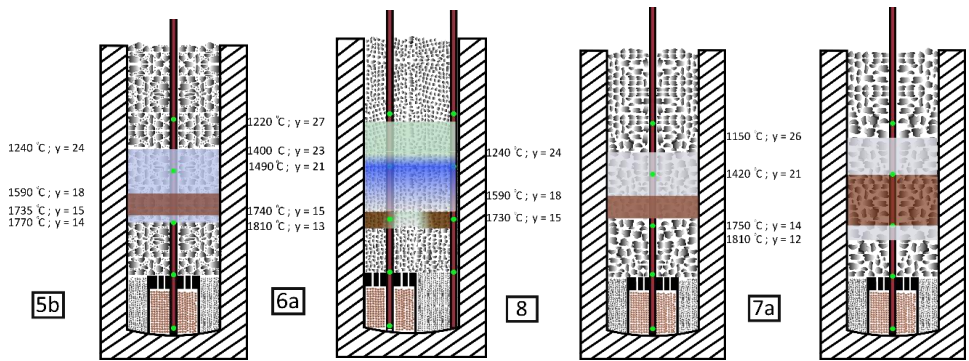


Figure 157: Condensation profiles sorted by decreasing PSD broadness, experiments IF5b (3-10 mm), IF8 (8-14 mm), IF7a (12-20 mm) and IF6a (5-8 mm). Experiments with Si-SiO₂ pellets. Constant parameters : Target T 1890°C, SiC substrates, holding time 2 h, $p_{\text{SiO}_2, \text{in}} = 1.0$.

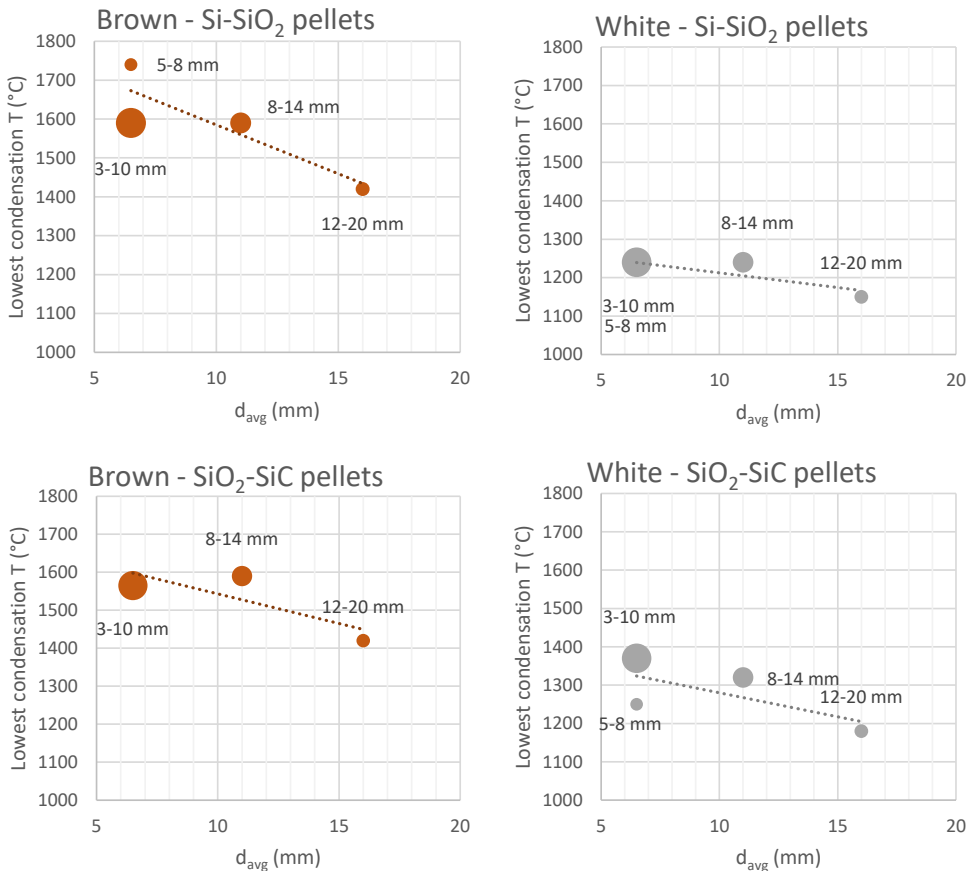


Figure 158: Variation in the lowest temperature of formation for condensates in the experiments from Figure 156 and Figure 157. The bubble size shows the PSD broadness qualitatively. Constant parameters : Target T 1890°C, SiC substrates, holding time 2 h. The width of the error bars on temperature is the value of the deviation obtained at the nearest temperature measurement point during the temperature gradient assessment (see Appendix C, Table 53).

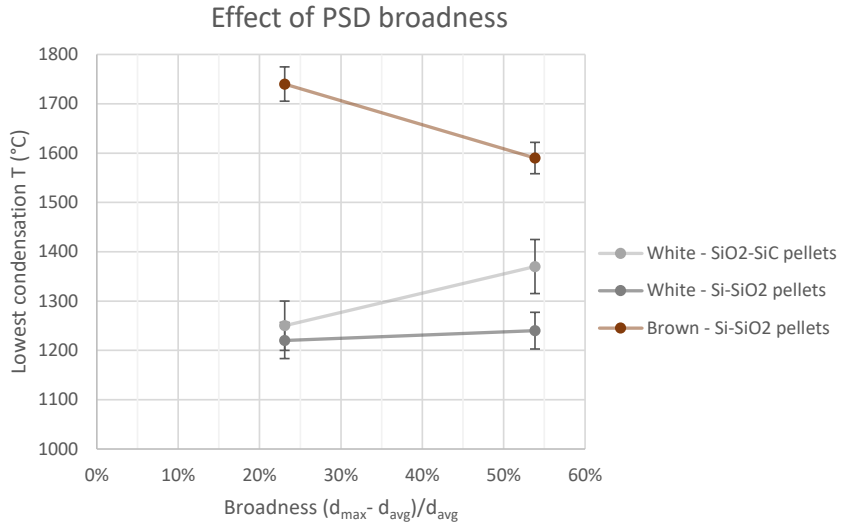


Figure 159: Variation in the lowest temperature of formation for condensates in the experiments from Figure 156 and Figure 157. The bubble size shows the PSD broadness. Constant parameters : Target T 1890°C, SiC substrates, holding time 2 h, $d_{avg} = 6.5$ mm.

Effect of substrate particle size (small-scale)

The SiC particles permeability decreases while increasing the PSD broadness, while condensates are produced in a wider space interval and at lower temperatures. Figure 160 compares experiments R19a, R20a and R21a. The thicknesses of condensation intervals are 62 mm for R19a ($d_{avg} = 2$ mm), 64 mm for R20a ($d_{avg} = 4$ mm), 77 mm for R21a ($d_{avg} = 6.5$ mm). The blue condensate moves from 1180 - 1290°C ($d_{avg} = 2$ mm, R19a) to 1040 - 1200°C ($d_{avg} = 4$ mm, R20a) to 1000 - 1080°C ($d_{avg} = 6.5$ mm, R21a).

Experiments R13-15 have also an increasing d_{avg} and decreasing broadness (Figure 161). However, these experiments are carried out at short holding times. The effect at long times is stronger compared to $t = 30$ mins. However, condensates are kept at high temperatures compared to Figure 160. A broader PSD allows development of other condensates, such as blue and grey SiC-SiO_x condensates.

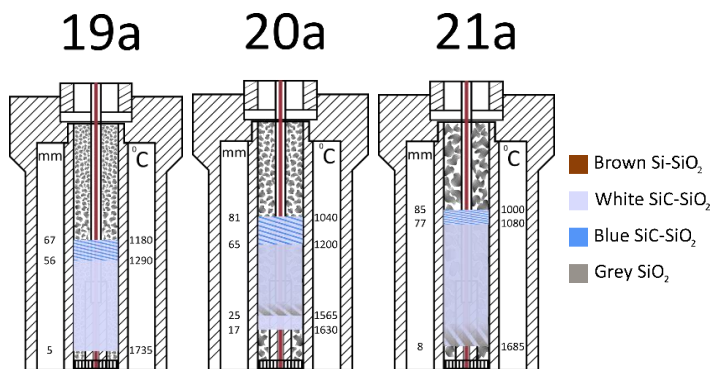


Figure 160: Condensation profiles for experiments R19a (1-3 mm, $d_{avg} = 2$ mm), R20a (3-5 mm, $d_{avg} = 4$ mm) and R21a (5-8 mm, $d_{avg} = 6.5$ mm). Constant parameters : Target T 2000°C, SiC substrates, holding time 240 min, $p_{SiO, in} = 0.71$ (He flow 0.10 l/min).

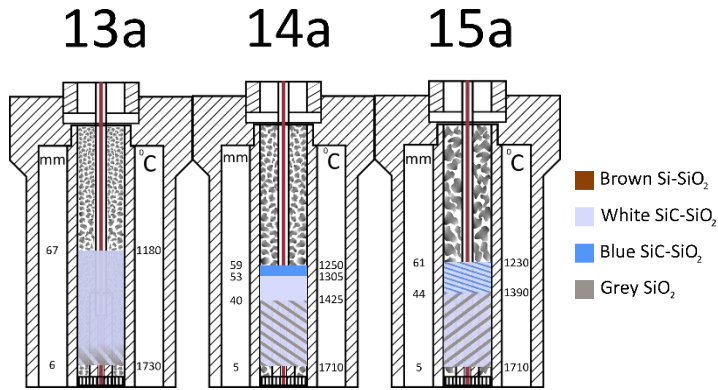


Figure 161: Condensation profiles for experiments R13a (1-3 mm, $d_{avg} = 2$ mm), R14a (3-5 mm, $d_{avg} = 4$ mm) and R15a (5-8 mm, $d_{avg} = 6.5$ mm). Constant parameters : Target T 2000°C, SiC substrates, holding time 30 min, $p_{SiO, in} = 0.71$ (He flow 0.10 l/min).

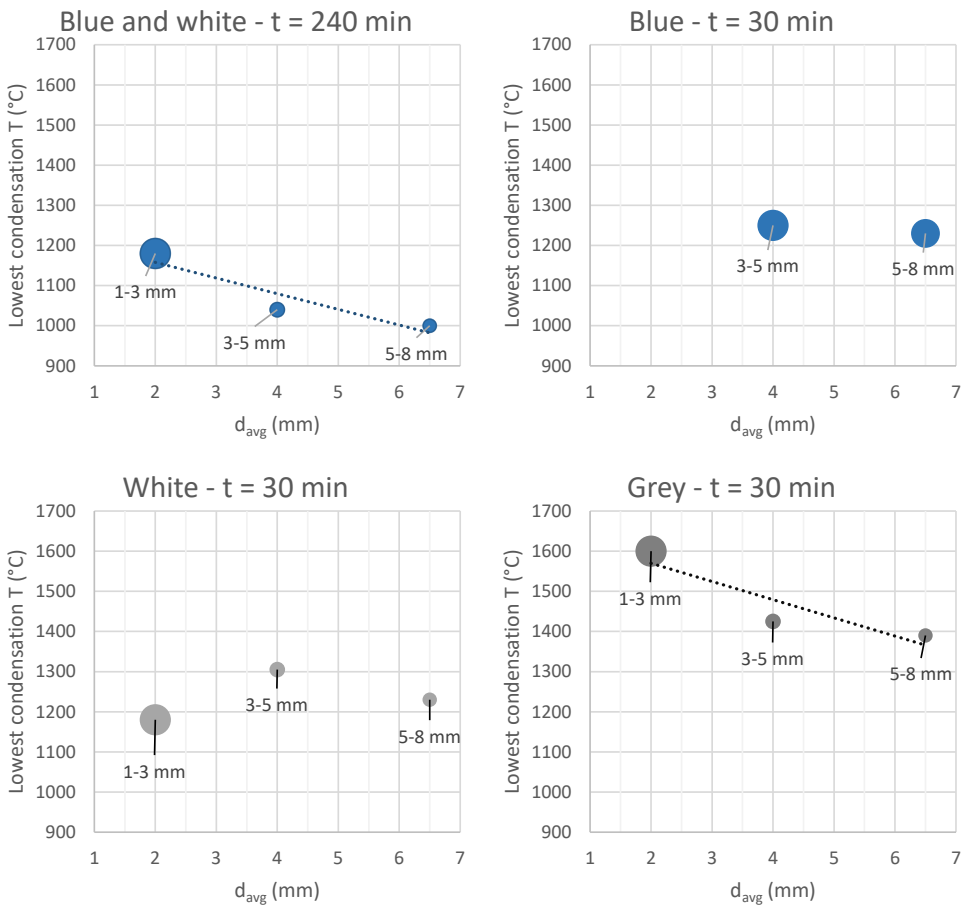


Figure 162: Variation in the lowest temperature of formation for condensates in the experiments from Figure 160 and Figure 161. The bubble size shows the PSD broadness qualitatively. Error bars on temperature are $\pm 10^\circ\text{C}$, as described in Appendix C.

Effect of target temperature and thermal history

An increase in the target temperature (i.e. the temperature at which SiO is produced) favors the formation of condensates higher up in the crucible. Figure 163 compares the cases of Exp. R9a, R1b and R6a, where the target temperatures were set at 1900°C, 2000°C and 2200°C respectively. The thickness of the condensation interval increases for blue and white condensate. The temperature gradients were not computed, but the white condensate extends for 69 mm, 85 mm and 84 mm in the three cases. Experiment R9a is carried out with a different substrate size distribution (5-8 mm), but despite that, the position remains still below Exp. R1b. Since the temperature increases by about 10°C/mm (see Appendix C), the temperature profile can be estimated to be shifted 10 mm upwards from experiment R9b to R1b, and 20 mm upwards from R1b to R6a. It can be concluded that a higher target temperature can also increase the thickness of the condensation interval.

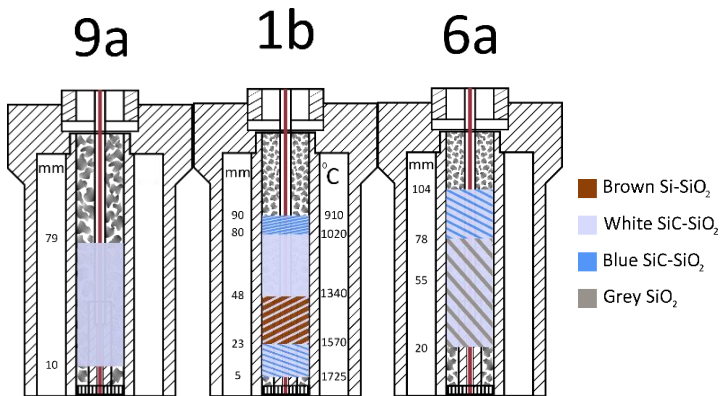


Figure 163: Condensation profiles for experiment R9a (1900°C), R1b (2000°C) and R6a (2200°C). Constant parameters : SiC substrates, holding time 60 min, He flow 0.40 l/min., substrate size 3-5 mm.

An increase in the holding temperature leads to faster SiO(g) production, as predicted by kinetic studies of the SiO+CO production reaction [69], [70], [97]. The gas production increases significantly above 1770°C, few minutes before the target temperature of 2000°C is reached (Figure 164). Then the CO% decreases around 30-40 minutes. However, when the temperature is set at 1900°C (blue line in Figure 164), some pellets do not react, and the gas production rate decreases smoothly compared to the cases at T = 2000°C and 2200°C. The sharp decrease of the dashed blue line at t≈95 min corresponds to when the furnace is shut down, and to the interruption of the SiO(g) production reaction. A similar interruption occurs when comparing Setup R3 and R4 (Figure 165). The production of CO(g) is similar between experiments at short and longer times, but the CO(g) production is still ongoing for short times, when the experiment is terminated.

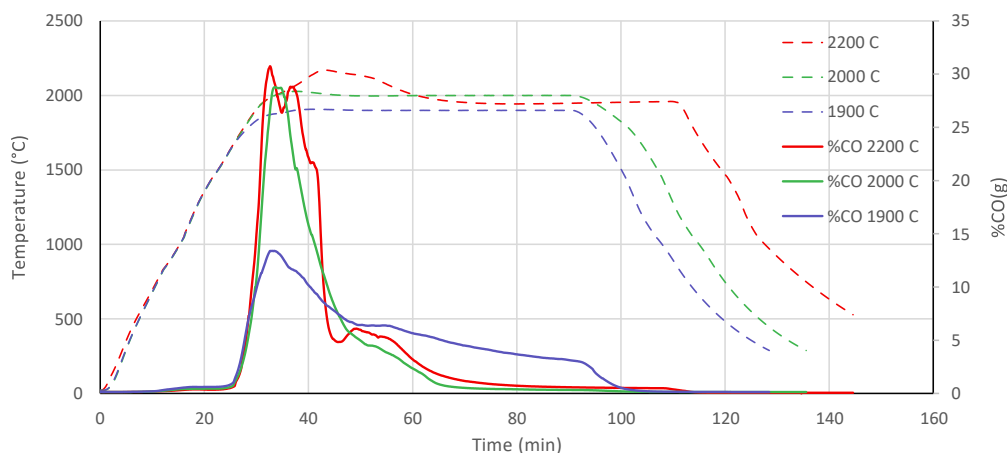


Figure 164: Thermal history and CO(g) production, temperature effect.

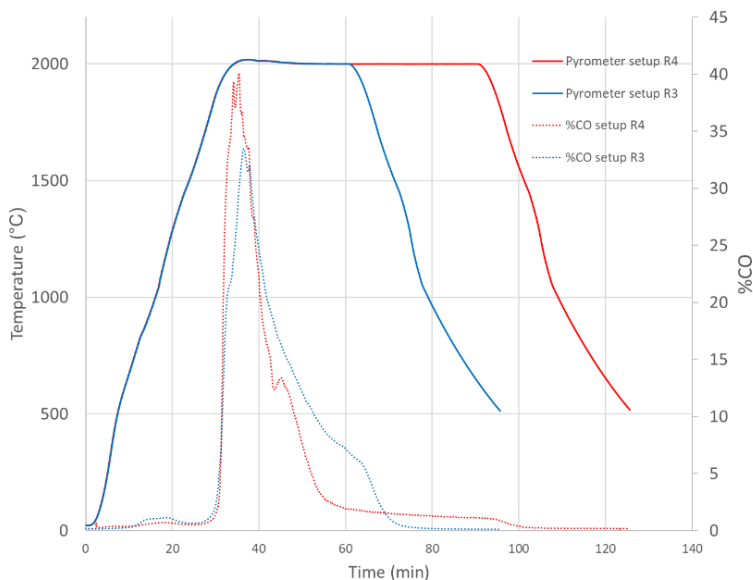


Figure 165: Thermal history and CO(g) production for setups R3 (30 min) and R4 (60 min).

Summary

Effect of parameters

Table 33 summarizes the effects of experimental parameters on condensation temperature. Having already seen that the setups give equivalent results in terms of temperature of formation intervals (see chapter “SiC, quartz and graphite substrates in small and large-scale experiments”), and after seeing from the table below that the small and large-scale experiments have given similar results in the trends, it can be concluded that both setups arrive to the same conclusions, and their results can be comparable.

Table 33: Summary of the effect of experimental parameters on condensation temperature.

Parameter (increasing)	Small scale		Large-scale		Further comments
	Condensation T broadness	Condensation temperatures	Condensation T broadness	Condensation temperatures	
SiC vs quartz	No effect	No effect	n.p.	n.p.	
Target gas T	Broader intervals	Shifted to higher position	n.p.	n.p.	
Holding time	Broader intervals*	Shifted to lower T**	Broader intervals	Shifted to lower T**	*especially at t<60 min ** brown condensate might not appear
Partial pressure (pellets composition)	n.p.	n.p.	Broader intervals	Shifted to lower T*	*small shift for white condensate; does not affect brown condensate
He vs Ar (added inert gas type)	No effect	No effect	n.p.	n.p.	
Added inert gas flow	Broader intervals	Shifted to lower T*	n.p.	n.p.	*relevant variations from 0.1 to 0.4 l/min
Particle size (d_{avg})	Broader intervals	Shifted to lower T	Broader intervals*	Shifted to lower T	*for grey condensate only
PSD broadness	Broader intervals*	Shifted to lower T**	Broader intervals**	Shifted to lower T	* blue and grey condensate form **small effect on brown condensate

Condensation on SiC (small-scale setup)

Appendix J collects all the condensation profiles of the SiC substrates experiments. There are 4 compounds formed on the SiC substrates.

Blue condensate generates both at the lowest and highest temperature intervals in an experiment. This happens regardless of the intensity of the inert gas flow, time and SiC size. Temperature measurements show that the blue condensate appears between 900-1500°C and 1600-1810°C. Blue particles appear often together with clean SiC particles or white condensate. In fact, blue condensate appears after scratching particles covered in white condensate, as mentioned in section A.

White condensate is the compound that covers the widest temperature range in the condensation chamber (910-1800°C). It appears together with grey, blue and brown condensate. Blue condensates are generated either below the white condensate, or at lower temperatures.

Brown condensate generates between 1400-1780°C. A layer of white or grey condensate is placed between the brown condensate and the SiC substrate. Small amounts of white condensate can cover the brown mixture. The

system is strongly clogged by this compound. Experiments carried out at shorter times develop brown condensate in a smaller temperature interval. The experiments from R13 to R21 developed negligible quantities of brown condensate together with grey condensate. The chamber could not be sealed properly, and the gas losses from the crucible could have been greater than expected.

Grey condensate develops together with white or brown condensate. Grey condensate appears mostly between 1275-1800°C.

Condensation on SiC (large-scale setup)

The main compounds formed on the substrates are three: white, brown and grey condensates. Green layer appeared only in one experiment.

White condensate extends for the largest condensation space interval. It could be noticed over 15 cm length for experiment IF5a, between 1135-1720°C. The condensate was found up to 1810°C (IF7b). Blue condensate is found in traces in the particles at the top of the white condensate layer.

Brown condensate generates occasionally in experiments with SiO₂-SiC pellets (IF1-4, 9, 11), but the Si-SiO₂ pellets experiments reveal higher presence of brown Si-SiO₂ condensate, in wider temperature intervals (IF4-8, 10, 12). The brown layer is present between 1420-1810°C. **White condensate is always present where brown condensate is found.**

A green layer appeared in Experiment IF6 between 1220-1400°C. In this temperature interval, white and blue condensate were also detected in minor amounts.

Condensation on quartz (small-scale)

The main condensate appearing in these experiments are the white and blue condensates, together with molten and glassy quartz particles. Brown condensate was not noticed during experiments with quartz substrates.

Blue condensate is present only at the top of the condensation chamber, between Y = 69 – 89 mm. The blue condensate fades away while moving towards higher temperatures. Blue condensate was not found during experiments R8a and R7b. Instead, for experiment R11a, blue condensate was present through a large portion of the crucible, together with white condensate.

Glassy and molten quartz particles showed up at Y = 0 – 20 mm in experiment R8a, and at Y = 0 – 10 mm in experiment R7b. Glassy quartz comes together with quartz covered in white condensate. The amount of molten quartz increases in experiment R11a (Y = 0 – 29 mm). This caused clogging of the system, and the experiment was aborted few minutes before the holding time was supposed to end. In experiment R12a, between Y = 20 – 30 mm, some of the SiC particles were embedded in molten quartz. SiC was assumed inert while being in contact with SiO₂ in the condensation chamber.

White condensate covers, again, the largest temperature intervals in every experiment. Due to the similar color, clean quartz particle cannot be distinguished easily from particles covered in white condensate. The condensates cover the whole crucible area, between Y = 20 – 89 mm. Some of the molten quartz zones may embed white condensates as well.

While experiments R7b and R8a have a holding temperature of 1800 and 1900°C respectively, experiment R11a, has a holding temperature of 2000°C, to involve all the pellets in the gas production reaction. The amount of pellets was also increased from 20 g to 40 g. To avoid clogging of the system by molten quartz, Experiment R12a was filled with 30 mm of SiC at the bottom of the condensation crucible. Experiments R7a is not shown, as it was interrupted earlier than expected and therefore considered not representative.

When the molten quartz clogs the system, the pressure inside the system reaches the safety limit. Experiment R11a was aborted 15 minutes before the cooling procedure was supposed to start. All the pellets were already consumed. However, condensation still glued the particles at lower temperatures.

A temperature of 1673°C was measured at the bottom of the condensation chamber during experiment R7b, and the quartz had probably started to melt. Appendix B shows the thermal history measured during experiment R8a at $Y = 0$ mm.

E. Clogging

The purpose of this section is to compare the effect of the experimental parameters on the temperature and position of clogging of the crucibles. The experimental parameters inquired are the gas target temperature (i.e. the temperature at which SiO is produced), the holding time, the substrate type, the amount of gas producing materials, the substrate particle size distribution and the composition of the incoming gas ($p_{\text{SiO},\text{in}}$ – see the “Modeling – $p_{\text{SiO}}-T$ calculation” chapter for further details about calculation of this parameter).

A crucible is **clogged** from a certain position, i.e. the material in the crucible does not flow out of the condensation chamber when the crucible is flipped upside down. That position is called **stoking point**. This point corresponds to a temperature, called **stoking temperature**. The crucible is clogged by a crust, made of condensates and condensation substrates. The thickness of this crust is called **clogging interval**. The term “stoking point” is chosen to recall the industrial procedure, where stoking carts are used to poke the raw material charge and allow its flow towards the bottom of the furnace.

The figures and graphs in this chapter show the clogging intervals and the stoking points for different experiments, sorted by a chosen increasing experimental parameter. Some figures emphasize the starting and end points of the clogging crust, whereas others focus on the thickness of the stoking interval.

Clogging at the stoking point is always characterized by high amounts of white SiO₂-SiC condensate, binding the condensation substrates. However, the Si-SiO₂ condensate can also glue the particles to each other. Its mechanical properties are stronger than the SiO₂-SiC condensates. When the Si-SiO₂ condensate compound is present, the SiC particles are held together so tight that it is sometimes necessary to break the whole condensation chamber in order to free the substrates. This was the case for experiments where the condensation profiles and the mass balance were not traced.

Overview of results

Clogging in small-scale experiments

Table 34 lists the stoking temperatures and positions for the different setups. For the experiments with multiple repetitions, the stoking point varies between a minimum and a maximum position.

The stoking temperature is located between 1060°C (setup 12) and 1630°C (setup 3), whereas the corresponding position covers an interval between $Y = 25$ mm (setup 2) and $Y = 78$ mm (setup 12). All the crucibles are clogged from the stoking point to a lower position in the chamber, usually located at $Y = 5-10$ mm. For most of the experiments, this is at about 1700°C.

Table 34: Stoking point (positions and temperatures), clogging intervals and temperatures at Y = 0 mm.

Experiment	Stoking point position (mm)	End of clogging interval (mm)	Clogging interval thickness (mm)	Volume % occupied by stoking crust	Stoking point position (°C)	Highest T of clogging interval (°C)	Clogging interval thickness (K)
1	48 – 64	5	51	39 %	1260	1725	465
2	25 – 30	5	22.5	17 %			
3	40 – 49	5	39.5	30 %	1600	1800	200
4	47 – 55	5	46	35 %	1550	1800	250
5	69	5	64	49 %	1390	1800	410
6	49	20	29	22 %			
7	48	10	38	29 %			
8	50	0	50	38 %			
9	48 – 62	7 – 10	46.5	36 %			
10	56	21	35	27 %	1260	1580	320
11	69	0	69	53 %			
12	78	20	58	45 %	1060	1590	530
13	61	6	55	42 %	1230	1730	500
14	53 – 58	5	50.5	39 %	1280	1710	430
15	51	5	46	35 %	1325	1710	385
17	45 – 56	6	44.5	34 %	1330	1700	375
19	65	5	60	46 %	1200	1735	535
20	65	17	48	37 %	1200	1630	430
21	77	8	69	53 %	1070	1685	615
22	48	5	43	33 %			
23	40	5	35	27 %			
Average values and st.dev.	56±12	8±6	48±12	37±9 %	1290±160	1710±70	420±120

The last line of the table reports the average position and temperature of the stoking points, and the average thickness of the stoking crusts. Overall, it can be said that:

- 1) **The charge gets clogged at around 1300°C.** The lowest temperatures are reached in setups with high gas flow (setup 1), long holding times (setup 5, 19-21) or containing quartz with a holding temperature of 2000°C (setup 11-12)
- 2) **The materials are clogged to a temperature of about 1710°C.** The particles are free to flow from about 5-10 mm from the bottom of the chamber. Few exceptions are made by experiments R6a, R10, R12 and R20.
- 3) **The thickness of the clogging interval covers about 420°C.** In terms of space coordinate, clogging occurs from an average position of Y = 56 mm downwards. Considering that a condensation chamber is 130 mm high, this corresponds to approximately 40% of the volume of the condensation chamber

occupied by a condensation crust. The setups with a clogged volume of $\approx 50\%$ or more are setups 5,11,12, 19-21.

Experiments with Quartz A substrates (R8a, R9a, R11a, R12a) are also clogged by molten quartz between $Y = 0 - 30$ mm. When the molten quartz clogs the system, the pressure inside the system reaches the safety limit. Experiment R11a was aborted 15 minutes before the cooling procedure was supposed to start. All the pellets were already consumed. However, condensation still glued the particles at lower temperatures.

Clogging in large-scale experiments

Pictures of crusts were collected only from the large-scale setup. Figure 166 shows the crust appearance before and after poking the charge at the stoking point. *At the stoking point, the SiC the particles are well stuck to each other.* It is enough to poke the charge to separate the particles glued by these compounds. However, it is more difficult to detach the brown condensate from the particle surface. Figure 167 shows the brown and white condensates in two different experiments, gluing even large SiC particles (the PSD of experiment IF7a is 12-20 mm). The particles are abundantly covered in white or brown condensates just below the stoking point.



Figure 166: Excavation of the crucible at $Y = 18$ cm, $T = 1485^\circ\text{C}$. SiC charge before (left) and after poking (right), experiment IF2a.



Figure 167: Left: Stoking point $Y = 21$ cm, $T=1420^\circ\text{C}$, Exp IF75-7a. Right: Brown condensates at $Y = 18$ cm, $T = 1580^\circ\text{C}$ for experiment IF75-7a.

Table 35 lists the stoking intervals in large-scale setup experiments. Crucibles are clogged between $1270-1810^\circ\text{C}$. Some particles below the crust are still covered with condensates (usually white, and small amounts of brown).

However, the condensation did not give enough mechanical stability in these zones, and the particles are free to flow at positions located below the stoking interval. As for the small-scale setup, the white condensate is clogging the crucible at lowest temperatures, and the brown condensate gives higher mechanical stability at higher temperature.

The last line of the table reports the average position and temperature of the stoking points, and the average thickness of the stoking crusts. Overall, it can be said that:

- 1) **The charge gets clogged at around 1450°C.** The lowest temperatures are reached in setups with the broadest PSD (setup 5), long holding times (setup 1-8 compared to 9-12) or small average diameter (setups 2,5). The average clogging temperature is higher compared to the small-scale setup.
- 2) **The materials are clogged up to a temperature of about 1710°C.** The experiments with the lowest clogging temperatures have both a small average diameter, a narrow PSD and a $p_{SiO_2, in} = 0.75$ in the starting gas composition (IF2a,IF3a).
- 3) **The thickness of the clogging interval covers about 260°C.** In terms of space coordinate, clogging occurs from about 15 to 21 cm. Considering that the condensation zone is 31 cm high, and the average clogging interval is 6 cm thick, it can be concluded that approximately 20% of the volume of the condensation chamber is occupied by a condensation crust. The most clogged setups are IF5a and IF6a, whose stoking crust occupies 10-11 cm of the condensation zone (approximately 30% of the volume of the condensation zone).

The excavation was not performed for Experiments IF2b and IF6b, as the two crucibles were cast into epoxy once the experiment was done. All the other experiments were carried out regularly.

Table 35: Clogging intervals in large-scale setups.

Experiment	Stoking point position (cm)	End of clogging interval (cm)	Clogging interval thickness (cm)	Volume % occupied by stoking crust	Stoking point position (°C)	Highest T of clogging interval (°C)	Clogging interval thickness (°C)
IF1b	14	20	6	19 %	1470	1730	260
IF2a	18	23	5	16 %	1380	1550	170
IF3a	16	21	5	16 %	1480	1675	195
IF4	14	20	6	19 %	1490	1750	260
IF5a	14	25	11	35 %	1270	1720	450
IF5b	14	21	7	23 %	1420	1770	350
IF6a	13	23	10	32 %	1400	1810	410
IF7a	18	21	3	10 %	1420	1580	160
IF7b	15	21	6	19 %	1480	1720	240
IF8	15	21	6	19 %	1420	1730	310
IF9	16	20	4	13 %	1520	1700	180
IF10	14	21	7	23 %	1470	1760	290
IF11	15	18	3	10 %	1580	1730	150
IF12	15	20	5	16 %	1490	1710	220
Average values and st.dev.	15±1	21±2	6±2	19±7%	1450±70	1710±70	260±90

Comparison between large and small-scale setup

Table 36 compares the results of the small and large-scale setups. The four results compared in the table are an average over all the experiments performed.

The first result analyzed is the volume occupied by the stoking crust, with respect to the condensation zone. This value can be used to compare the setups, regardless of their different sizes. The second value is the stoking point temperature, i.e. the temperature below which the charge is not clogged anymore. The third column compares the highest temperatures of the clogging interval, i.e. where condensation starts. Finally, the last column compares the clogging interval thickness, in terms of “temperature coordinates” inside the crucible.

The main conclusion of the table is that the small-scale setup is clogged more than the large-scale setup, i.e. a larger portion of the condensation zone is obstructed by the glued substrates. In fact, the volume occupied by the stoking crust grows from 10-35% in the large-scale, to 20-55% of the small-scale setup. Hence, a smaller scale setup gives lower stoking point temperatures (from 1450 to 1290°C) and thicker clogging intervals (from 260 to 420°C). This is probably due to the sticking effect to the chamber walls, and hence a smaller set up will clog more easily, that is at lower temperatures and higher part of the chamber. However, the two setups have the average end temperatures for the clogging interval of 1710°C.

Table 36: Comparison of clogging results between small and large-scale setup.

Setup	Occupied volume (%)	Stoking point position (°C)	Highest T of clogging interval (°C)	Clogging interval thickness (K)
Large-scale	10-35	1450±70	1710±70	260±90
Small-scale	20-55	1290±160	1710±60	420±120

Effect of experimental parameters

Effect of target temperature (small-scale)

A higher holding temperature does not affect much the stoking point position, but rather its stoking temperature. Figure 168 shows the variation in position for the stoking point between experiments with holding temperatures at 1900 (R9a), 2000 (R1) and 2200°C (R6a) respectively. The position shifts slightly downwards, by about 5-7 mm.

However, two experiments with different holding temperatures will have different temperature gradients. When the position is fixed, the experiment with the highest holding temperature will give a higher temperature compared to another experiment with a lower temperature. For example, if for R1 it was estimated to have $T = 1260^{\circ}\text{C}$ at $Y = 56$ mm, we can estimate the temperature at $Y = 46$ mm in experiment R9. The target temperature in experiment R9 was approximately 100°C lower in the gas production zone (giving a deviation of -100°C), and the stoking point was measured 5 mm below (which gives a deviation of $+50^{\circ}\text{C}$), giving an estimated temperature of $\approx 1210^{\circ}\text{C}$. For experiment R6, the target temperature was 200°C higher ($+200^{\circ}\text{C}$), but the stoking point is recorded 7 mm below (which give a deviation of $+70^{\circ}\text{C}$). The three stoking points are therefore located at 1210, 1260 and 1430°C , which confirm that a higher holding temperature increases the temperature of the stoking point.

A higher target temperature decreases the thickness of the clogging interval. In fact, the estimated upwards shift in the temperature gradient would give a great difference between the temperatures. As mentioned in the temperature of formation chapter, the temperature profile can be estimated to be shifted 10 mm upwards from

experiment R9b to R1b, and 20 mm upwards from R1b to R6a. This leads to thinner clogging intervals at higher target temperatures.

A higher target temperature will create the condensates in similar temperature intervals, but just shifted upwards. However, most of the condensates produced at high temperature ($T > 1800^\circ\text{C}$) will transform back into SiO and CO. Hence, clogging would occur, but condensates will disappear during the experiment, giving a thinner clogging interval thickness in experiment with higher target temperature. This can also explain why the stoking point does not change much, as only the condensates at higher temperatures should be consumed.

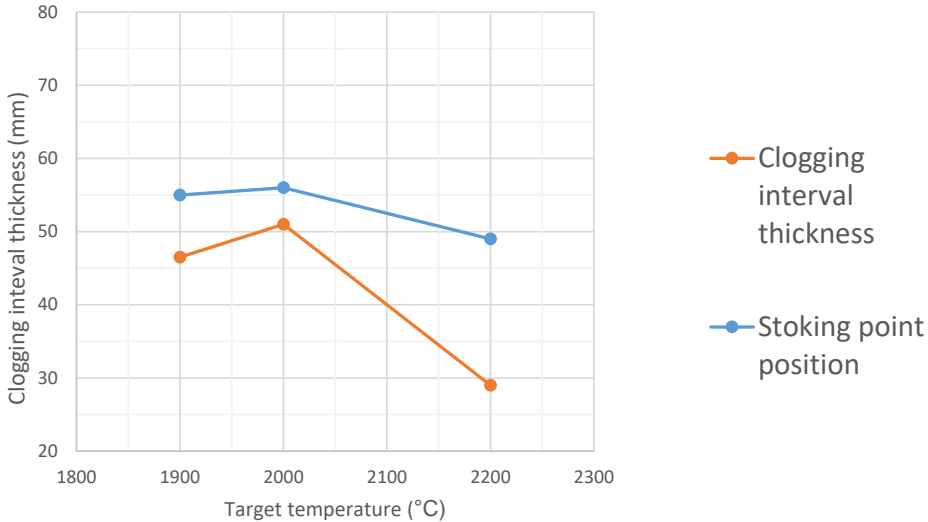


Figure 168: Variation of stoking point position as a function of target temperature. Constant parameters : SiC substrates, holding time 60 min, He flow 0.40 l/min., substrate size 3-5 mm.

Effect of holding time (small-scale)

A longer holding time shifts the stoking point towards lower temperatures. Figure 169 shows the decrease of the stoking point position over time, in two different in Ar and He flow. The decrease is sharper for the group with the highest partial pressure ($p_{\text{SiO}_2, \text{in}} = 0.74$ when Ar flow is 0.02 l/min, setups 3-5, blue line) compared to the group with the highest inert gas flow ($p_{\text{SiO}_2, \text{in}} = 0.69$ when He flow is 0.1 l/min, setups 14,17,20, orange line).

The clogging interval thickness follows an opposite trend, i.e. it increases with increasing time. Again, the thickness increases more in the group with the lowest added gas flow (setups 3-5, green line) compared to the highest inter gas flow (setups 14,17,20, grey line).

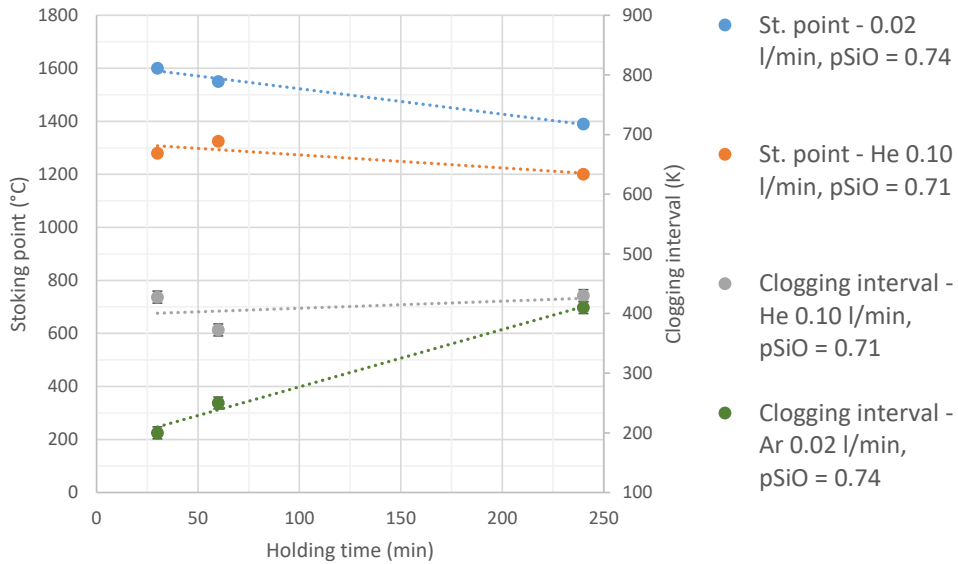


Figure 169: Effect of holding time at different Ar/He flows on the stoking point in the small-scale setup. Constant parameters for blue and green lines: Target T 2000°C, SiC substrates, Ar flow 0.02 l/min, substrate size 3-5 mm; Constant parameters for orange and grey lines : Target T 2000°C, SiC substrates, He flow 0.10 l/min, substrate size 3-5 mm. Error bars on temperature are $\pm 10^\circ\text{C}$, as described in Appendix C.

Effect of holding time (large-scale)

As it happened for the small-scale setup, a longer holding time shifts the stoking point to a lower temperature. Figure 170 shows the effect of time on the stoking point and on the clogging interval. Two groups of experiments are shown in the graphs, differing in the initial gas producing pellets mixture. The first one is the group with SiO₂-SiC pellets (IF11, IF9 and IF1b, respectively at 10, 30 and 120 min holding time), and the second one is the group with Si-SiO₂ pellets (IF12, IF10 and IF5b, respectively at 10, 30 and 120 min holding time). The stoking point decreases by 100-200°C, from 10 to 120 min holding time. The steepness of the line is higher for the Si-SiO₂ pellets ($p_{\text{SiO}_2, \text{in}}=1$), compared to the SiO₂-SiC pellets ($p_{\text{SiO}_2, \text{in}}=0.75$).

The clogging interval increases its thickness by increasing the condensation time. However, experiments at shorter holding times consume less gas producing pellets, so there would be less condensates and hence a thinner condensation interval. Again, the steepness of the line is higher for the group of experiments with the highest starting $p_{\text{SiO}_2, \text{in}}$. The clogging interval almost doubles its thickness between 10 and 120 min, regardless of the chosen gas composition.

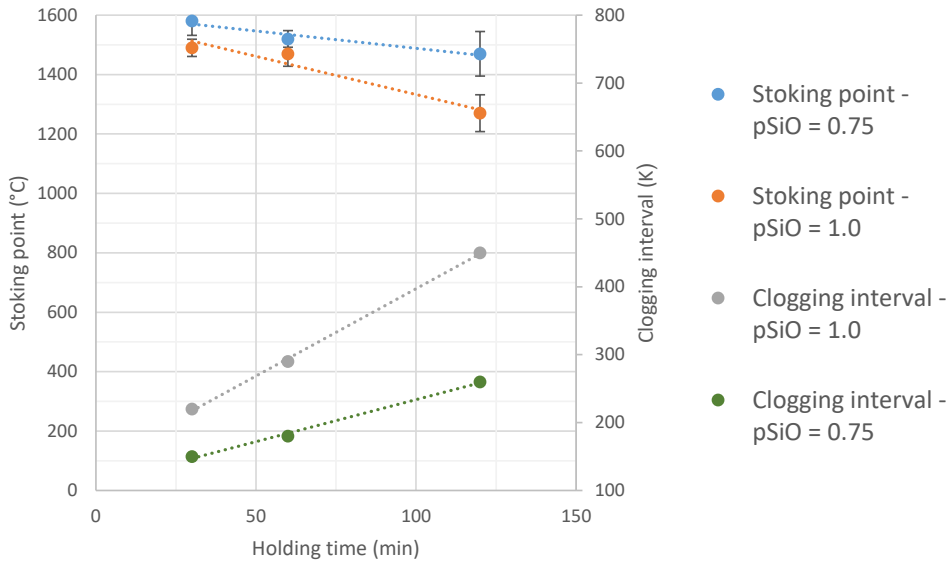


Figure 170: Effect of holding time at different pellets composition (starting gas composition) on the stoking point in the large-scale setup. Constant parameters for blue and green lines: Target T 1890°C, SiC substrates, substrate size 3-10 mm, $p_{\text{SiO},\text{in}} = 0.75$; Constant parameters for orange and grey lines : Target T 1890°C, SiC substrates, substrate size 3-10 mm, $p_{\text{SiO},\text{in}} = 1.0$. The width of the error bars on temperature is the value of the deviation obtained at the nearest temperature measurement point during the temperature gradient assessment (see Appendix C, Table 53).

Effect of substrate particle size (small-scale)

Two groups of experiments are chosen to study the effect of the substrate particle size. The first group is performed at $t = 30$ min (R13-15) and the second at $t = 240$ min (R19-21). The average diameter increases from $d_{\text{avg}} = 2$ mm (R13 and R19) to $d_{\text{avg}} = 4$ mm (R14 and R20), and finally to $d_{\text{avg}} = 6.5$ mm (R15 and R21), while the PSD broadness decreases, as shown by the bubble diameter in the graphs.

An increase in the average diameter shifts the stoking point to higher temperatures at short times, and to lower temperatures at long times. Figure 171 shows the difference between the two groups. In the group at short holding times, the stoking temperature shifts upwards by about 100°C. However, in the long holding times group, the stoking point decreases by 130°C. The same can be said in terms of position coordinate, which decreases by 10 mm between R13 and R15, and increases by 12 mm between experiment R19 and R21. However, the position coordinate does not vary from experiment R19 to R20.

The effect of the PSD broadness is the opposite compared to the average diameter. At short times, the clogging interval thickness decreases by 20% in narrower PSD with large average particle size. On the other hand, the thickness increases by about 10% at long holding time. It can be concluded that the time effect can interfere with the substrate particle size distribution, in the small-scale setup.

In the beginning of the experiments ($t = 30$ min), when the amount of condensates is small, smaller particles will clog the condensation zone easier. This means that it will be easier to get the gas between the larger particles with a narrow PSD. However, after longer times ($t = 240$ min), the larger particles will slip more gas through and hence lead to a lower stoking temperature, and hence a larger stoking interval.

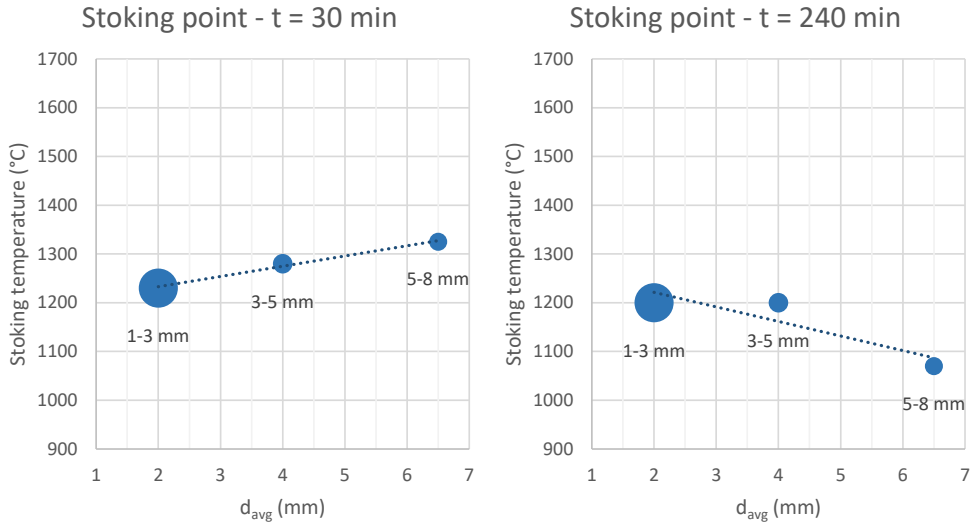


Figure 171: Effect of average particle size on the stoking point in the small-scale setup, at different holding times. The bubble size is qualitatively expressing the PSD broadness. Constant parameters : Target T 2000°C, SiC substrates, $p_{\text{SiO}_2, \text{in}} = 0.71$ (He flow 0.10 l/min). Error bars on temperature are $\pm 10^\circ\text{C}$, as described in Appendix C.

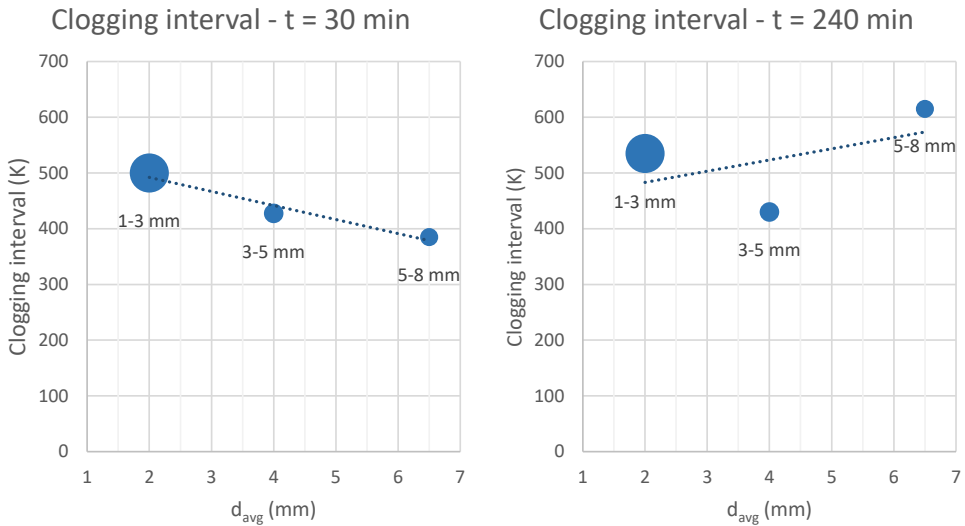


Figure 172: Effect of average particle size on the clogging interval in the small-scale setup, at different holding times. The bubble size is qualitatively expressing the PSD broadness. Constant parameters : Target T 2000°C, SiC substrates, $p_{\text{SiO}_2, \text{in}} = 0.71$ (He flow 0.10 l/min).

Effect of substrate particle size (large-scale)

Figure 173 visualizes the effect of the particle size distribution in the large-scale setup. The experiments are divided into two groups, according to the initial pellets composition. The first group (grey graph) is including setups IF1-4, whereas the second group (blue graph) includes the setups IF5-8. Repetitions are also included.

An increase in the average diameter and a decrease in the PSD broadness will move the stoking point to higher temperatures. The coordinate position stays between 14-18 cm for the first group, and between 13-18 for the second group. The narrow PSD experiments (12-20 mm) give the highest stoking temperatures, at about 1500°C. Experiments with the highest d_{avg} and a narrow PSD have a smaller clogging interval. *Figure 174* shows that the clogging interval decreases by 50°C from experiment IF1b (3-10 mm) to IF 3a (12-20 mm). However, the clogging interval decreases by about 300°C, by comparing experiment IF5b (3-10 mm) to IF7a (12-20 mm). In fact, the volume occupied by the clogging crust remains constant between 16-19% in the group at $p_{SiO, in} = 0.75$, but increases by 3 times (from 10 to 35%) in the group of experiments with $p_{SiO, in} = 1$. It can be concluded that the gas composition also plays a role in the clogging of the crucibles.

By increasing the average diameter, the system is clogged through a smaller temperature interval. Larger particles leave larger channels in the system, and the crust becomes less stable. By increasing the broadness of the particle size distribution, the voids are filled easier by the smallest particles, and the condensate layers will glue the charge.

According to the two repetition of experiment IF5 (3-10 mm, $p_{SiO} = 1.0$), the uncertainty is at 50-200 K, which means that the change with the diameter may not be significant. However, a linear interpolation of the graphs shows a decreasing trend for the clogging interval, and an increasing trend for the stoking point, which coincide to what was seen in the small-scale setup at short times.

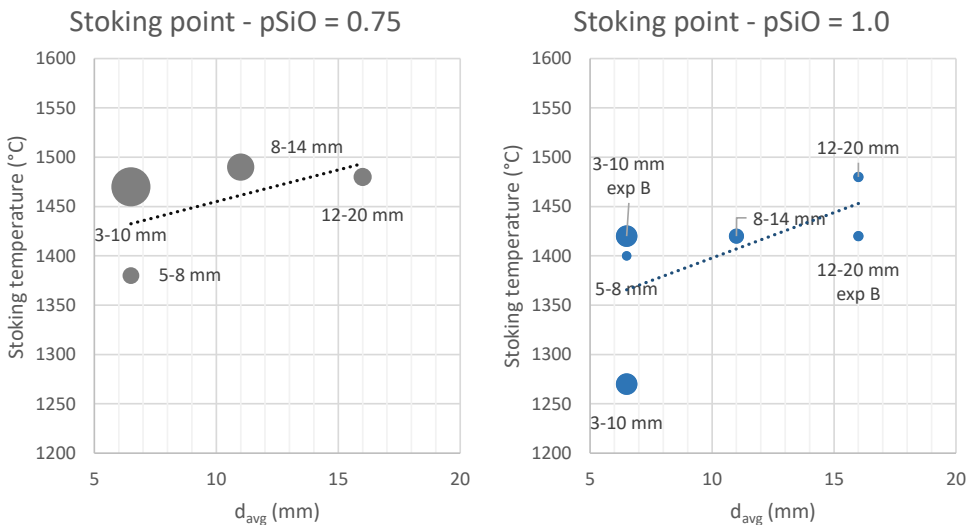


Figure 173: Effect of average particle size at different partial pressure on the stoking point in the large-scale setup. Constant parameters : Target T 1890°C, SiC substrates, holding time 2 h. The width of the error bars on temperature is the value of the deviation obtained at the nearest temperature measurement point during the temperature gradient assessment (see Appendix C, Table 53).

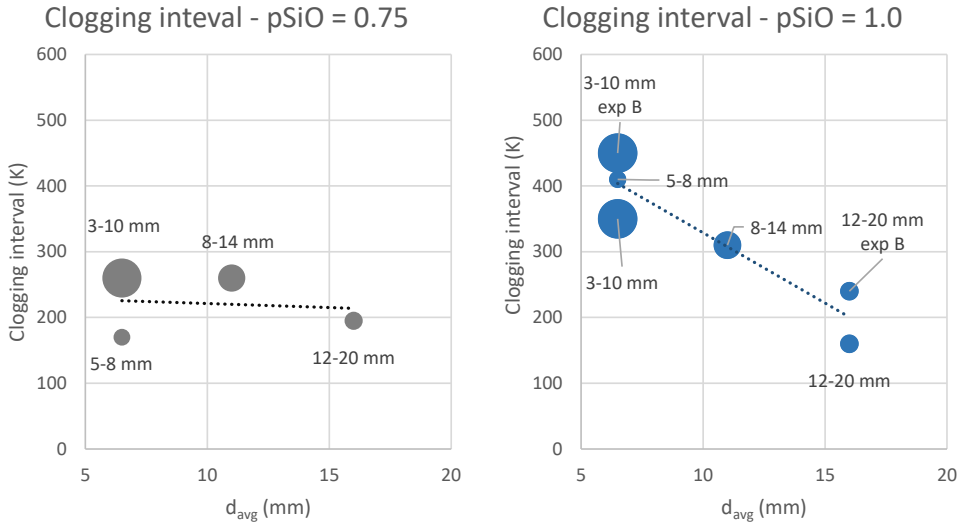


Figure 174: Effect of average particle size at different partial pressure on the clogging interval in the large-scale setup. Constant parameters : Target T 1890°C, SiC substrates, holding time 2 h.

Effect of partial pressure in small-scale setup (gas flow)

The effect on clogging by choosing Ar or He as an inert gas is negligible. Considering the experiments in setup 4, the repetitions vary the position in the stoking point in a considerably small range, i.e. 8 mm. The deviation could be attributed to experimental intrinsic errors or by the stoking point surface, which is not flat.

A higher $p_{SiO,in}$ in the gas moves the stoking point to higher temperatures, while giving thinner clogging intervals. Figure 175 compares the results of the experiments R4 (Ar/He, 0.02 l/min, $p_{SiO,in} = 0.74$), R17 (He, 0.1 l/min, $p_{SiO,in} = 0.71$) and R1 (He, 0.4 l/min, $p_{SiO,in} = 0.62$). The concentration of SiO(g) in the gas is inversely proportional to the injected Ar flow. The stoking point increases by 300°C by increasing the partial pressure by 0.12 (or by decreasing the inert gas flow by 20 times). At the same time, the coordinate position of the stoking point decreases from 56 to 51 mm. On the other hand, the clogging interval decreases by 200°C, when increasing $p_{SiO,in}$ by 0.12 (or by decreasing the inert gas flow from 0.40 to 0.02 l/min). Besides, the occupied volume in the chamber decreases from 39 to 34%.

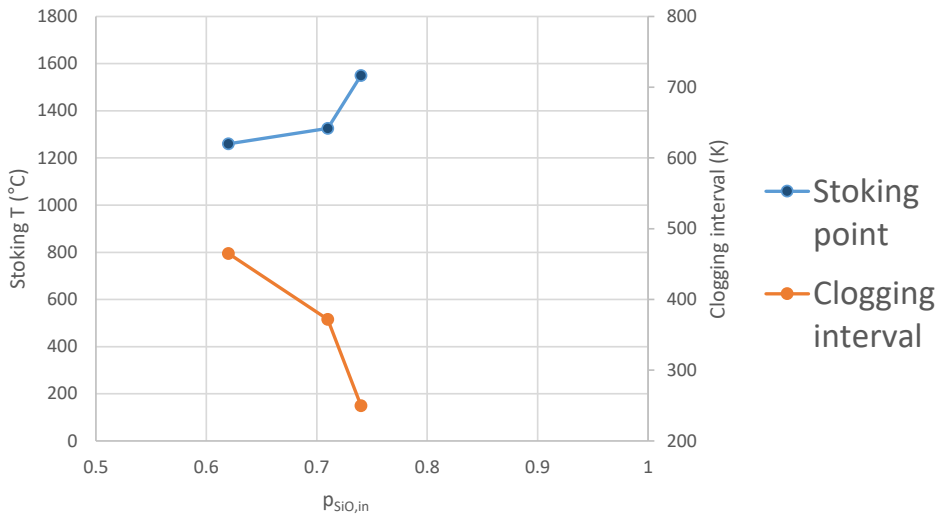


Figure 175: Effect of inert gas flow on the stoking point and stoking interval position in the small-scale setup. Constant parameters : Target T 2000°C, SiC substrates, substrate size 3-5 mm, holding time 1 h. Error bars on temperature are $\pm 10^\circ\text{C}$, as described in Appendix C.

Effect of partial pressure in large-scale setup (pellets composition)

Figure 176 shows the effect of the partial pressure on clogging, in the large-scale setups. The experiments colored in brown are those which had SiO(g) only in their starting gas composition ($p_{SiO,in} = 1$), whereas the grey ones are those containing both SiO(g) and CO(g) in the starting gas composition ($p_{SiO,in} = 0.75$). The figure is divided into four areas. In the top area, the experiments at 3-10 mm are also sorted by increasing holding time. The three areas below compare the experiments with the same PSD, but at different starting gas compositions. The reported $p_{SiO,in}$ in the picture defines the concentration of SiO in the gas coming from the gas production zone. The thickness of the interval is in °C, and it is placed inside the corresponding colored bar. The number on the left of the colored bar is the temperature at which clogging ends, i.e. the stoking point.

A gas richer in SiO(g) gives a lower stoking point temperature. The stoking point decreases by 50-200°C when increasing $p_{SiO,in}$ from 0.75 to 1. The only experiments making an exception are the 5-8 mm experiments (IF2a and IF6a), where the stoking point increases by only 20°C when increasing the partial pressure. In the 3-10 mm group (setups 1, 5, 9-12), the variations are larger compared to the other groups. In fact, the stoking point can decrease by 200°C by comparing experiments IF1b (3-10 mm, SiO+CO, 2h) and IF5a (3-10 mm, SiO, 2h).

The clogging interval becomes thicker by 30-240°C when increasing the partial pressure. Again, in the 3-10 mm the relative increase of the clogging interval is higher, compared to the other groups. The group with the lowest variations has the highest d_{avg} , i.e. 12-20 mm (IF3 and IF7).

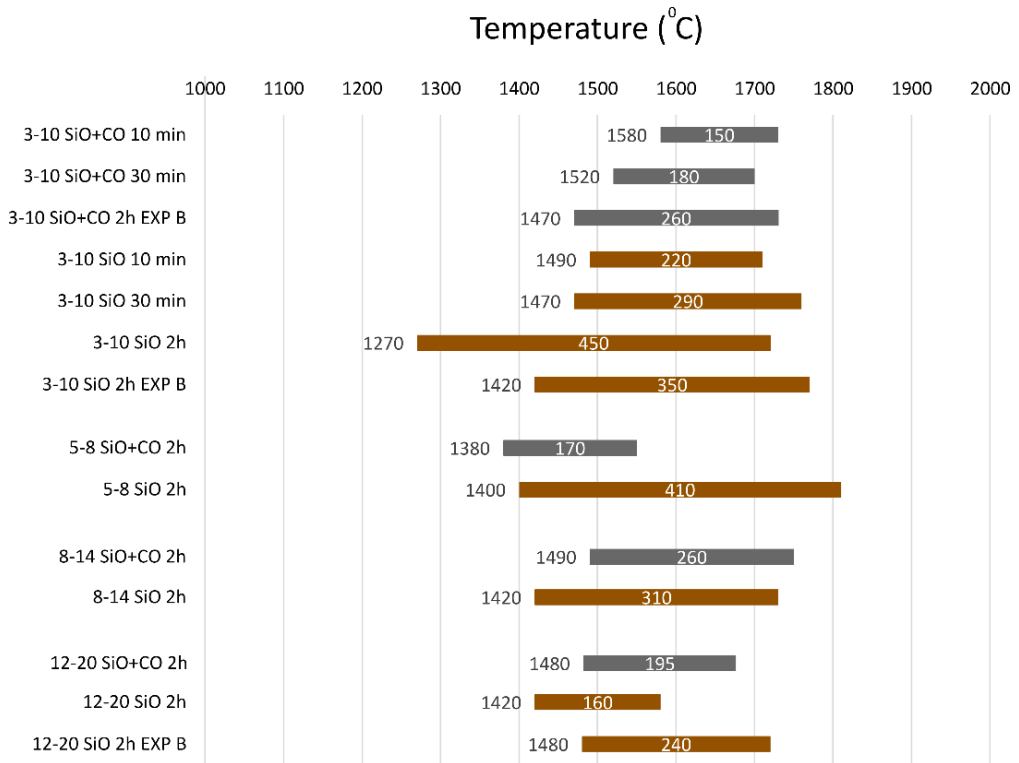


Figure 176: Clogging intervals and stoking point sorted by SiO(g) partial pressure. Experiments from the IF75 large-scale setup. Constant parameters : Target T 1890°C, SiC substrates.

Effect of substrate particle type (SiC vs Quartz)

The stoking point position does not shift its position when changing from SiC to Quartz A substrate (from 56 to 69 mm). A stoking point at 1260°C is estimated for experiment R10. Table 37 lists the results of two experiments, one with quartz substrate (R7b) and one with SiC substrate (R9). On the other hand, the thickness of the clogging interval increases by switching from SiC to quartz substrate.

However, when increasing the holding temperature to 2000°C, the stoking interval increases more. In fact, experiment R11 is also clogged down to Y = 0 mm by the partially molten quartz, located at the bottom of the condensation chamber. The volume occupied by the clogged charge is almost doubled between experiment R7 and R11.

In both experiments R7 and R11, part of the condensation chamber has overcome the softening point of quartz substrate. In fact, partially molten quartz was found between Y = 0-30 mm in experiment R11. To avoid clogging by molten quartz, SiC was inserted between Y = 0 – 30 mm in experiment R12, therefore less quartz undergoes softening, and the system will not be as clogged as R11. This change could affect the thickness of the clogging interval. Despite that, the volume occupied by the stoking crust is increasing by only 8%. It was estimated that the temperature was at least ≈1650°C at Y = 30 mm in both experiments R11 and R12, after having seen the results by Jusnes [60] on the softening point of the chosen quartz substrate.

Table 37: Comparison between an experiment with quartz substrate (R11) and SiC substrate (R10)

Experiment	Stoking point position (mm)	End of clogging interval (mm)	Clogging interval thickness (mm)	Volume % occupied by stoking crust
R7b (Quartz, T = 1900°C)	48	10	38	29 %
R9 (SiC, T = 1900°C)	48 – 62	7 – 10	46.5	36 %
R11 (Quartz, 40g pellets, T = 2000°C)	69	0	69	53 %
R12 (Quartz + SiC at bottom, 20g pellets, T = 2000°C)	78	20	58	45 %

Summary

Table 38 summarizes the effects of experimental parameters on clogging temperatures. Both setups arrive to the same conclusions, and their results can be comparable for most of the parameters chosen.

The only parameter which is not consistent between the two setups is the partial pressure. In the large-scale setup, the variation occurs between $p_{\text{SiO},\text{in}} = 0.75$ and $p_{\text{SiO},\text{in}} = 1$, whereas in the small-scale the parameter varies between 0.74 and 0.61. However, in the small-scale setup the pressure varies because a gas is injected with a higher velocity, compared to the large-scale setup, where the SiO(g) production occurs without any additional inert gas. It can be that the velocity of the injected gas flow plays a role in the position of the stoking point and in the thickness of the clogging interval.

Table 38: Summary of the effect of experimental parameters on condensation temperature.

Parameter (increasing)	Small scale		Large-scale		Further comments
	Clogging interval broadness	Stoking point	Clogging interval broadness	Stoking point	
Target gas T	Thinner intervals	Higher T ¹	n.p.	n.p.	¹ similar positions in the crucible, but different T due to thermal gradient
Holding time	Thicker intervals ¹	Lower T ¹	Thicker intervals ¹	Lower T ¹	¹ stronger effect at higher p _{SiO} in the gas (or lower inert gas flow, for small-scale setup)
PSD broadness	Thicker intervals at short times (t = 30 min) Thinner intervals at long times (t = 240 min)	Lower T at short times (t = 30 min) Higher T at long times (t = 240 min)	Thicker interval ¹	Lower T ¹	¹ stronger effect at higher p _{SiO} in the gas
PSD - d_{avg}	Thinner intervals at short times (t = 30 min) Thicker intervals at long times (t = 240 min)	Higher T at short times (t = 30 min) Lower T at long times (t = 240 min)	Thinner interval ¹	Higher T ¹	¹ stronger effect at higher p _{SiO} in the gas
He vs Ar (added gas)	No effect	No effect	n.p.	n.p.	
Added gas flow	Thicker intervals	Lower T	n.p.	n.p.	
SiO-partial pressure	Thinner intervals	Higher T	Thicker interval ¹	Lower T ²	¹ Small variations in broad PSD ² Strong variations in broad PSD
SiC vs quartz	Thicker intervals with quartz	Lower T with quartz	n.p.	n.p.	Partially molten quartz contributed to clogging

F. Mass balance

This chapter has two main objectives.

The first is making a mass balance of the two condensation reactions. The tables in this section will gather the amount of condensates produced in the experiments, together with the ratio between the weight of the starting gas producing materials and the condensates weight. The amount of unreacted gas producing pellets must be considered. In particular, the partially reacted Si-SiO₂ pellets will be characterized.

The condensates composition found from characterization will help to estimate how Si, SiO₂ and SiC are divided, starting from SiO(g) and CO(g). The data are collected for both setups and compared to verify that the setups are comparable.

Finally, the last section will show how SiC-SiO_x condensates are distributed over the temperature gradient. This calculation was carried out only for the large-scale setup and will be one of the bases for the calculation of the kinetic model described in chapter 4.

The second objective is to calculate the reaction rate r and its dependence on experimental parameters. The rate expresses the amount of reaction product over the reaction time. First, the reaction time is estimated. Then, the rate is calculated as a function of temperature in each experiment. Finally, all the reaction rates in the different experiments are plotted together, to find trends over the three experimental parameters which will enter the kinetic model: **temperature, available surface for condensation and reaction time.**

Condensate mass balance

Small-scale setup

Table 39 lists the amount of condensates collected from each experiment. The ratio between the mass of the reacted pellets and the amount of condensates produced is called *condensation yield*. This ratio reaches a maximum of 27% for experiment R4a and has an average value of 10±5%. The experiments with the highest condensation yield are generally those having the lowest injected inert gas flow, such as Series 2 and 4.

To quantify the weight of each condensate, the following procedure is used:

- 1) The SiC particles are weighted before the experiment
- 2) The experiment is run
- 3) The SiC particles are weighted after the experiment. The difference in weight before and after the experiment is the total amount of condensate
- 4) The Si-SiO₂ condensate is separated manually from the SiC substrate, and then weighted. The Si-SiO₂ only includes the brown condensate
- 5) The weight of the SiO₂-SiC condensate is calculated by subtracting the Si-SiO₂ mass from the total condensate weight. The SiO₂-SiC condensate weight is the sum between the white, blue, orange and grey condensates.

The left hand-side of the table shows that the SiO₂-SiC condensate is generally produced in higher amounts (86±14%), compared to the Si-SiO₂ condensate (14±14%). In some experiments, the Si-SiO₂ condensates were not even generated.

The right-hand side shows the amounts of Si, SiO₂ and SiC in the condensates. The composition for the condensates are assumed to be the theoretical compositions from Table 16 and Table 22. The amounts of Si, SiO₂ and SiC are calculated after assuming that all the Si goes to the Si-SiO₂ mixture, and all the SiC is contained

in the SiO₂-SiC condensates. SiC in the brown Si-SiO₂ condensate was neglected. The percentages in each line sum up to 100% and show the relative mass percentage of each compound.

It was estimated that the amount of metallic Si in the condensate is 5±4 wt. %, and it can reach up to 14 wt. % of the total condensates mass. There is more SiO₂ in the SiO₂-SiC condensate (64±11 wt. %) compared to the Si-SiO₂ condensate (10±10 wt. %), since the amount of the brown condensate is lower compared to the other. SiC takes 21±3 wt. % of the total condensate mass. The rest is SiO₂, which is mostly found in the SiO₂-SiC condensate. Some experiments did not undergo the mass balance procedure, such as experiments R1e, R6a, R7a, RP4011a and R22. These experiments were too clogged to extract the SiC (or Quartz A) substrates. It is impossible to detach manually and with precision all the condensate produced. Some of the layers will always remain stuck to the condensation substrates or to the graphite walls, and some small parts of the substrate might contaminate the condensate isolated. An uncertainty of ±0.05 g is expected for this reason, for both the brown and white condensate masses.

Large-scale setup

Table 40 collects the amounts of condensate for each experiment performed. The quantification of condensates and the calculation of phase compositions was carried out in the same way as for the small-scale setup. The condensation yield ranges between 10-22%, with an average of 16±4%. Up to 16 wt. % of the condensation product is elemental silicon (average 7±5 wt. %). SiC makes 20±4 wt.% of the total condensate weight. The rest is SiO₂, split between the SiO₂-SiC (61±11 wt. %) and the Si-SiO₂ condensate (11±9 wt. %).

Experiments IF2b and IF6b were cast into epoxy, therefore no other analysis than visual inspection was possible after the experiment was done. The mass balances for experiments IF1a, IF5a and IF9 were not computed, as the crucible were destroyed after the extraction, and it was not possible to quantify the partially reacted pellets in the gas production chamber.

The scale used for weighting the condensates has an error of 0.01 g, as specified in Appendix G. However, it was chosen to use only one decimal for the weight calculation, to include eventual experimental errors coming from contamination or errors in the measurements.

Table 39: Condensates mass and phase distribution (wt. % in parenthesis), average value over all the experiments performed.

Exp.	Condensation yield	Si-SiO ₂ (g)	SiO ₂ -SiC (g)	Si (g)	SiO ₂ (g)		SiC(g)
					SiO ₂ in Si-SiO ₂ (g)	SiO ₂ in SiO ₂ -SiC (g)	
1a	7%	0	1.43 (100%)	0	0	1.07 (75%)	0.36 (25%)
1b	10%	0.38 (18%)	1.71 (82%)	0.12 (6%)	0.26 (12%)	1.28 (61%)	0.43 (21%)
1c	13%	0.24 (10%)	2.27 (90%)	0.12 (3%)	0.16 (7%)	1.70 (68%)	0.43 (23%)
1d	5%	0	0.98 (100%)	0	0	0.74 (75%)	0.24 (25%)
1e	Not collected						
2a	20%	1.40 (35%)	2.61 (65%)	0.45 (11%)	0.95 (24%)	1.96 (49%)	0.65 (16%)
2b	13%	0.60 (23%)	1.97 (77%)	0.19 (7%)	0.41 (16%)	1.48 (57%)	0.49 (19%)
2c	15%	0.70 (24%)	2.25 (76%)	0.22 (8%)	0.48 (16%)	1.69 (57%)	0.56 (19%)
3a	5%	0.10 (10%)	0.88 (90%)	0.03 (3%)	0.07 (7%)	0.66 (67%)	0.22 (23%)
3b	8%	0.15 (9%)	1.51 (91%)	0.05 (3%)	0.10 (6%)	1.14(68%)	0.38 (23%)
3c	14%	0.35 (13%)	2.35 (87%)	0.11 (4%)	0.24 (6%)	1.76 (65%)	0.59 (22%)
4a	27%	1.65 (31%)	3.70 (69%)	0.53 (10%)	1.12 (21%)	2.78 (52%)	0.93 (17%)
4b	7%	0.10 (7%)	1.38 (93%)	0.03 (2%)	0.07 (5%)	1.03 (70%)	0.34 (23%)
4c	13%	0.70 (26%)	1.98 (74%)	0.22 (8%)	0.48 (19%)	1.49 (55%)	0.50 (18%)
4d	16%	1.28 (40%)	1.90 (60%)	0.41 (13%)	0.87 (27%)	1.42 (45%)	0.47 (15%)
4e	9%	0.12 (6%)	1.78 (94%)	0.04 (2%)	0.08 (5%)	1.34 (70%)	0.45 (23%)
5a	7%	0.20 (15%)	1.14 (85%)	0.06 (5%)	0.14 (10%)	0.85 (64%)	0.28 (21%)
6a	Not collected						
7a	Not collected						
7b	1%	0	0.24 (100%)	0	0	0.18 (75%)	0.06 (25%)
8a	8%	0	0.12 (100%)	0	0	0.09 (75%)	0.03 (25%)
9a	4%	0	0.89 (100%)	0	0	0.67 (75%)	0.22 (25%)
9b	10%	0.30 (16%)	1.52 (84%)	0.10 (5%)	0.20 (11%)	1.14 (63%)	0.38 (21%)
P40 10a	4%	0.68 (44%)	0.85 (56%)	0.22 (14%)	0.64 (42%)	0.46 (30%)	0.21 (14%)
P40 11a	Not collected						
12a	6%	0	1.18 (100%)	0	0	0.89 (75%)	0.29 (25%)
13a	11%	0	2.24 (100%)	0	0	1.68 (75%)	0.56 (25%)
14a	9%	0	1.73 (100%)	0	0	1.30 (75%)	0.43 (25%)
14b	15%	0.60 (20%)	2.41 (80%)	0.19 (6%)	0.41 (14%)	1.81 (60%)	0.60 (20%)
14c	5%	0.30 (31%)	0.66 (69%)	0.10 (10%)	0.20 (21%)	0.50 (52%)	0.17 (17%)
17a	13%	0.15 (6%)	2.37 (94%)	0.05 (2%)	0.10 (4%)	1.78 (71%)	0.59 (24%)
17b	15%	0.95 (31%)	2.10 (69%)	0.30 (10%)	0.65 (21%)	1.58 (52%)	0.53 (17%)
17c	9%	0.60 (32%)	1.25 (68%)	0.19 (10%)	0.41 (22%)	0.94 (51%)	0.31 (17%)
19a	7%	0	1.30 (100%)	0	0	0.98 (75%)	0.33 (25%)
20a	8%	0.10 (6%)	1.58 (94%)	0.03 (2%)	0.07 (4%)	1.19 (71%)	0.40 (24%)
21a	12%	0	2.38 (100%)	0	0	1.79 (75%)	0.60 (25%)
22a	Not collected						
23a	15%	0.47 (18%)	2.14 (82%)	0.15 (6%)	0.32 (12%)	1.61 (61%)	0.54 (20%)
Avg. ± st.dev	(10±5)%	(14±14)%	(86±14)%	(5±4)%	(10±10)%	(64±11)%	(21±3)%

Table 40: Condensation yield and condensates mass in large-scale setup.

Experiment	Condensation yield	Si-SiO ₂ (g)	SiO ₂ -SiC (g)	Si (g)	SiO ₂ (g)		SiC (g)
					SiO ₂ in Si-SiO ₂ (g)	SiO ₂ in SiO ₂ -SiC (g)	
IF1b	14%	0	27.0 (100%)	0	0	20.2 (75%)	6.8 (25%)
IF2a	18%	0	35.0 (100%)	0	0	26.2 (75%)	8.8 (25%)
IF3a	12%	6.2 (27%)	16.8 (73%)	2.4 (10%)	3.9 (17%)	12.6 (55%)	4.2 (18%)
IF4	21%	10.9 (28%)	28.1 (72%)	4.1 (11%)	6.8 (17%)	21.1 (54%)	7.0 (18%)
IF5b	11%	4.4 (21%)	16.7 (79%)	1.6 (8%)	2.7 (13%)	12.5 (59%)	4.2 (20%)
IF7b	12%	5.4 (23%)	18.6 (78%)	2.0 (8%)	3.3 (14%)	14.0 (58%)	4.7 (19%)
IF8	22%	11.0 (27%)	30.0 (73%)	4.2 (10%)	6.8 (17%)	22.5 (55%)	7.5 (18%)
IF10	15%	3.0 (15%)	17.0 (85%)	1.1 (6%)	1.9 (9%)	12.8 (64%)	4.3 (21%)
IF11	16%	0.2 (2%)	11.8 (98%)	0.1 (1%)	0.2 (1%)	8.8 (73%)	2.9 (24%)
IF12	19%	6.8 (43%)	9.2 (58%)	2.6 (16%)	4.2 (26%)	6.9 (43%)	2.3 (14%)
Average values and st.dev.	(16±4)%	(18±14)%	(82±14)%	(7±5)%	(11±9)%	(61±11)%	(20±4)%

Partially reacted pellets

Table 41 shows the amount of partially reacted pellets collected at the gas production chamber when the crucible was excavated. The experiments which are not listed in the table had no leftover pellets in the gas production zone. For Experiment R9a, 1.0-1.5 g of pellets leftovers were estimated. Some of them were weighted, whereas the rest was stuck on the gas production crucible.

Experiments IF1, IF9 and IF11 have the same experimental parameters, except the holding time. The same also happens for experiments IF5b, IF10 and IF11. More than 50% of the pellets is still in the chamber at the end of experiments IF11-12. After 30 minutes, the partially reacted pellets are about 30-40% of the initial value. Finally, at two hours the pellets have been consumed. It is possible that the pellets were completely consumed before the two hours have passed, for experiment IF1b. On the other hand, 3 g of partially reacted pellets were still found in Experiment IF5b. When leftovers are found in the gas production chamber, it is assumed that they have kept their initial composition.

Table 41: Weight of partially reacted pellets at the end of the experiments.

Setup name	Leftovers (g)	Holding time
R 3a	0.98	30 min
R 8a	4.17	1 hour (at 1800°C)
R 9a	1.0-1.5 (estimated)	1 hour (at 1900°C)
R 9b	1.08	1 hour (at 1900°C)
R 22a	3.64	5 min
R 23a	3.02	10 min
IF 5 (a,b)	0 (a); 3 (b)	2 hours
IF 8 (a)	15	2 hours
IF 9 (a)	83	30 min
IF 10 (a)	65	30 min
IF 11 (a)	125	10 min
IF 12 (a)	114	10 min

Brown crusts are also found in the pellets production zone, at the bottom of the large-scale crucible. The gas production chamber has been removed to reveal its content after Experiment IF5a and IF6a (Figure 177). The microstructure of the leftovers from these experiments is the same as it was seen earlier for the brown condensate. However, these are not condensates, but Si-SiO₂ partially reacted pellets. In fact, the silicon spheres have a similar size to the starting Si powder used to make the pellets (Figure 178). The Si spheres seen earlier in the condensate characterization are considerably smaller than in Figure 178. In fact, SEM pictures of the condensates are taken at x4000 magnification, whereas the magnification was at x220 for the partially reacted pellets. There are similarities in microstructure with the Si-SiO₂ condensates, which can suggest that Si and SiO₂ can behave as a mixture of solids heated above their melting points.

Figure 177 shows also that some of the silicon was separated from the matrix, forming droplets which stick to the borders of the gas production chamber. A grey, transparent compound would also appear in this zone this compound is believed to be porous silica.

SiO₂-SiC pellets leftovers were seen both in the large and small-scale setup. However, their microstructure is not of interest for the sake of this work.



Figure 177: Brown partially reacted pellets leftovers, Exp. IF5a (left) and IF6a (right).

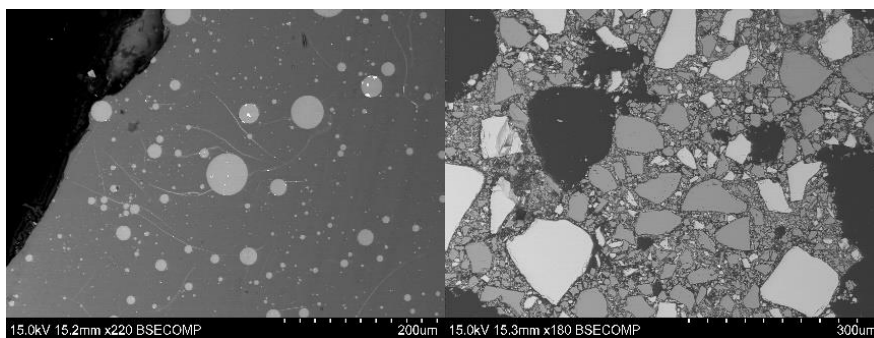


Figure 178: Left: BSE-image of Si-SiO₂ partially reacted pellets, Experiment IF6a. Right: Calcined Si-SiO₂ pellets.

Summary of mass balance

The main results from the mass balance experiments are presented in this section.

1. The condensation yield is low. Condensation is not the most effective way to recover SiO(g) and CO(g). The maximum yield was 22% (Experiment IF8). The gas was either lost to other reactions, such as SiC and Si production in the crucible (see Appendix A), however, it is believed that part of the gas left the condensation zone without reacting.

2. The large and the small-scale setups have comparable results. Table 42 compares the mass balance results between the small- and the large-scale setups. All the parameters found lie in similar ranges, despite the larger setup has a higher amount of Si-SiO₂ condensate and a higher condensation yield. Hence it can be said that the two setups are comparable.

Table 42: Comparison of mass balance and condensation yield between small and large-scale setups.

Setup	Condensation yield	Si-SiO ₂	SiO ₂ -SiC	Si	SiO ₂		SiC
					SiO ₂ in Si-SiO ₂	SiO ₂ in SiO ₂ -SiC	
Small scale	(10±5)%	(14±14)%	(86±14)%	(5±4)%	(10±10)%	(64±11)%	(21±3)%
Large-scale	(16±4)%	(18±14)%	(82±14)%	(7±5)%	(11±9)%	(61±11)%	(20±4)%

3. A higher SiO content in the gas before condensation ($p_{\text{SiO},\text{in}}$) tends to give a higher condensation yield, until a maximum of ≈25% is reached. Figure 179 relates the partial pressure of the produced gas mixtures with the condensation yield. When the gas flow is small (0.02-0.05 l/min, $p_{\text{SiO},\text{in}} = 0.74$ -0.73), the gas mixture will flow slowly through the chamber. The gas has more time to condensate. Hence, the gas is retained for a longer time at high temperatures. On the other hand, when the inert gas flow is high ($p_{\text{SiO},\text{in}} = 0.62$), the gas mixture flows will flow fast between the particles, covering a larger area in a short time.

As a consequence, **the total amount of condensates m_{cond} increase when the partial pressure of SiO(g) is higher and the injected flow is lower.** Figure 179 shows the condensate mass for experiments at small scale. Experiments at small scale are more sensitive to changes compared to the large-scale setups. In fact, the amount of condensate between experiments at $p_{\text{SiO},\text{in}} = 0.75$ and $p_{\text{SiO},\text{in}} = 1.0$ is almost the same for the large-scale setup (39 vs 41 g from IF4 to IF8, 23 vs 24 g from IF3b to IF7b).

The data do not look statistically significant, however there is an indication that the yield is higher in the small scale when p_{SiO} is increased (i.e. at lower He flow). In fact, a gas that goes slowly through the particle bed has more time to condense, hence more condensates can form. Fast flowing gases will not condensate and they will hence escape the chamber, as it happens during gas blows in industrial practice. On the other hand, the large-scale system is less sensitive to a change in condensation yield and mass.

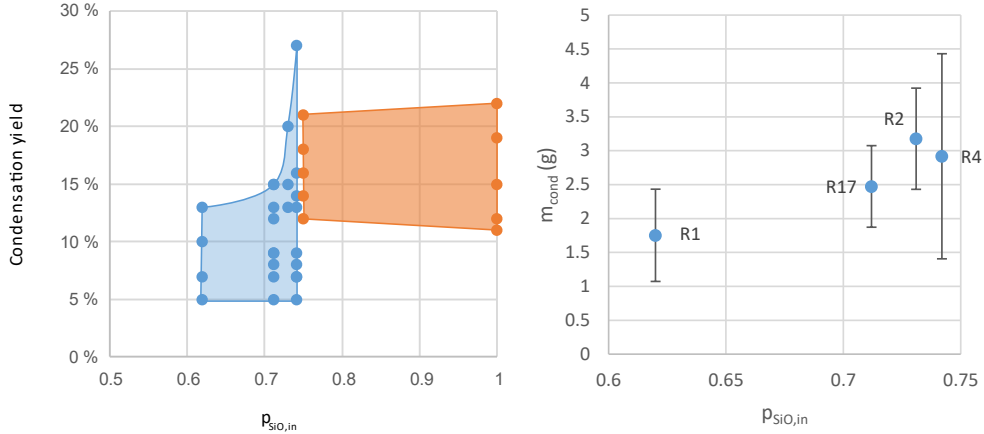


Figure 179: Left: Average condensation yield as a function of partial pressure, measurements including both setups (Blue = small-scale; orange = large-scale). Right: Total condensate mass (m_{cond}) against $p_{\text{SiO},in}$ in small scale experiments. The setup name is written for each point. The value of m_{cond} is an average of the repetitions made. The error bars refer to one standard deviation. Constant parameters: Target temperature 2000°C, SiC PSD 3-5 mm, holding time 1h.

4. The $\text{SiO}_2\text{-SiC}$ condensates make most of the condensates mass in both setups. The SiC-SiO_x mixture makes usually between 60-100% of the total condensates mass in the experiments. In fact, the Si-SiO₂ condensates do not even appear in some of the small-scale experiments, especially in those with short holding times or low target temperatures.

5. The relative amount of Si-SiO₂ condensates increases with the initial SiO(g) content in the gas (or decreases by adding an inert gas flow). Vice versa, the SiC-SiO_x condensate amount increases by adding an inert gas flow (or by decreasing the SiO(g) content in the gas).

Figure 180 shows the average amounts of SiO₂-SiC and Si-SiO₂ condensate at different gas flow, while keeping constant the other experimental parameters. The amount of Si-SiO₂ condensate tends to be higher when $p_{\text{SiO},in}$ increases, i.e. at lower inert gas flows. However, the mass of Si-SiO₂ condensate changes often between experiments at the same conditions.

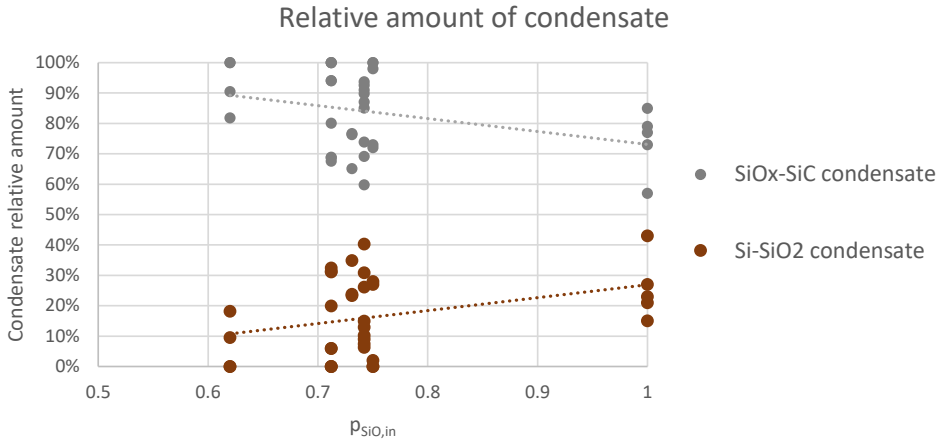


Figure 180: Average Si-SiO₂ and SiO₂-SiC amounts in experiments at increasing partial pressure.

Distribution of SiC-SiO_x condensate in large-scale setup

Figure 181 shows how the condensate is distributed in the four temperature intervals within experiment IF2a. The points and the error bars show respectively the average temperature and the temperature interval width. The condensates distribution follows a bell-like trend. A low amount of condensate is located at the lowest (1250-1380°C, Y = 27-23 cm, t = 4 cm) and highest temperatures (1550-1690°C, Y = 18-14 cm, t = 4 cm). Most of the condensates is in the stoking interval (1485-1550°C, Y = 20-18 cm, t = 2 cm).

Table 43 shows the estimated distribution of the mass of SiO₂-SiC condensate in each temperature interval, for every experiment. A small part of the condensates is located at the lowest and highest temperature interval, whereas the majority is in the middle, between 1400-1700°C. Table 44 shows the amount of SiC-SiO_x condensate collected, which is called m_{cond} .

The table compares the amount of condensates with the position of the clogging interval. Most of the condensates are found in temperature intervals similar to the clogging intervals. Hence, the more condensates are present in a temperature interval, the more clogged the system is.

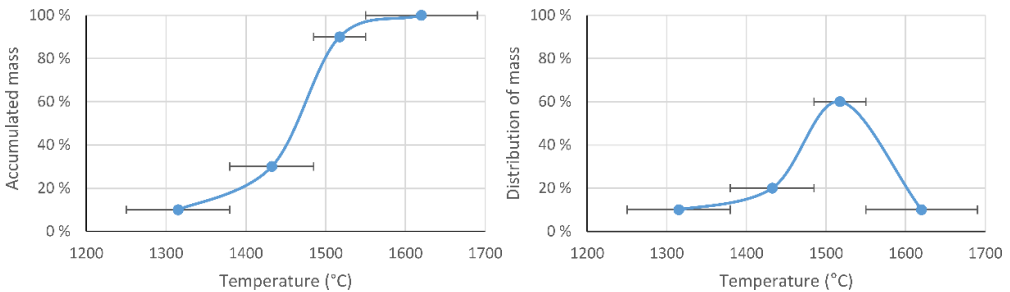


Figure 181: Mass distribution of condensates with respect to temperature, Experiment IF2a. Left: Cumulative representation: Right: Distribution representation.

Table 43: Distribution of SiO₂-SiC condensate in temperature intervals of the large-scale setup. The temperature intervals written in bold are included in the clogging intervals.

Experiment	T interval (°C)	Estimated fraction of SiO ₂ -SiC condensate (wt. %)	Estimated SiO ₂ -SiC condensate mass (g) (<i>m_{cond}</i>)
IF2a Clogging interval at 1380-1550°C	1250-1380	10	3.50
	1380-1485	20	7.00
	1485-1550	60	21.00
	1550-1690	10	3.50
IF3a Clogging interval at 1480-1675°C	1180-1480	10	1.68
	1480-1675	90	15.11
IF4 Clogging interval at 1490-1750°C	1320-1490	10	2.81
	1490-1590	20	5.62
	1590-1680	60	16.86
	1680-1750	10	2.81
IF5b Clogging interval at 1420-1770°C	1240-1420	5	0.83
	1420-1590	25	3.33
	1590-1735	65	9.99
	1735-1770	5	0.83
IF7b Clogging interval at 1480-1720°C	1250-1480	10	1.86
	1480-1570	10	1.86
	1570-1720	80	14.91
IF8 Clogging interval at 1420-1730°C	1240-1420	5	1.50
	1420-1590	25	7.50
	1590-1730	70	21.01
IF10 Clogging interval at 1470-1760°C	1370-1470	5	0.85
	1470-1610	20	3.41
	1610-1760	75	12.78
IF11 Clogging interval at 1580-1730	1400-1580	20	2.35
	1580-1730	80	9.41
IF12 Clogging interval at 1490-1710°C	1390-1490	10	0.92
	1490-1530	10	0.92
	1530-1710	80	7.36

4. Modeling

A. p_{SiO} -T calculation

Aim of the calculation

The first model computed through this work is called p_{SiO} -T model. Its aim is to relate the amount of SiO(g) in the gas phase with the temperature gradient in the condensation zones. This model includes both Si-SiO₂ and SiO₂-SiC condensation reactions. The initial temperature of the gas is highest where the gas is produced. The temperature gradually decreases by going upwards from the gas production zone. At a certain position, the gas is not condensing anymore. The partial pressure of SiO(g) changes through the condensation zone, since condensates develop through a temperature gradient.

The initial gas composition is known from the amount of gas-generating materials consumed, and the final composition is known from the amount of condensates generated. The compositional change of the gas phase through the condensation zone is caused by the condensation reactions, which consume SiO and CO in different proportions. If the initial and final T and p_{SiO} conditions are calculated, it is possible to track the partial pressure variation through the furnace temperature gradient. The p_{SiO} -T curves will estimate the partial pressure of SiO(g) at any temperature inside the condensation chamber.

Procedure

The p_{SiO} -T lines are traced for each experiment for which both the mass balance and temperature gradients were computed, and for each condensation reaction. To trace a p_{SiO} -T line, one must interpolate between two points in a p_{SiO} vs T diagram. The first point identifies the initial condition, i.e. the gas temperature and composition before condensation. The second point describes the final conditions, i.e. at the position where the last condensate is noticed. Hence, the edges of a p_{SiO} -T lines have coordinates ($T_{SiO,in}$; $p_{SiO,in}$) and ($T_{SiO,out}$; $p_{SiO,out}$).

$T_{SiO,in}$ is the temperature at which the gas mixture of SiO(g) and CO(g) (and He/Ar when added) enters the condensation zone. In the large-scale setup, $T_{SiO,in}$ is assumed to be constant at 1890°C. In the small-scale setup, $T_{SiO,in}$ was measured to be 1815°C for all the experiments with a target temperature of 2000°C. $T_{SiO,in}$ was measured 20 mm below the condensation chamber for setup R1b, R2a and R4e. The inert gas enters the gas production chamber at room temperature. The inert gas is assumed to be heated up to 1815°C in a short time. $T_{SiO,out}$ is the temperature at which the gas stops forming condensates of any kind. Above this point, the particles are not covered in any condensate.

Before calculating the partial pressures $p_{SiO,in}$ and $p_{SiO,out}$, the total pressure inside the system must be calculated. When it comes to the large-scale setup, the system is always exposed to atmospheric pressure, as the furnace is open. For the small-scale setup, the pressure is fixed at 1.5 atm. The overpressure is generated by the inert gas. The small-scale furnace is not equipped with a system recording the pressure continuously, so the pressure of the outgoing gas is measured in three different instants. In the small-scale setup, the pressure before the SiO(g) production reaction was 1.4 atm. Then the pressure increases up to 1.6 atm when the gas production reaches its maximum extent. Finally, the pressure stabilizes at around 1.5 atm few minutes after the CO(g) peak was reached. For simplicity, it was assumed that the pressure of the system is constant at 1.5 atm through the whole condensation process.

$p_{SiO,in}$ is computed according to the pellets composition, the stoichiometries of Reaction (-1) or (-2) and the amount of inert gas injected. SiO₂-SiC pellets will produce $n_{SiO,in}$ moles of SiO(g) and $n_{CO,in}$ moles of CO(g)

according to Reaction (-1), whereas Si-SiO₂ pellets will follow Reaction (-2) and produce $n_{\text{SiO},\text{in}}$ moles of SiO(g). Both $n_{\text{SiO},\text{in}}$ and $n_{\text{CO},\text{in}}$ consider only the portion of the pellets charge that has reacted.

The volume of injected inert gas n_{IG} is calculated by multiplying the gas production time t_r and the injected gas flow. The amount of inert gas moles added n_{IG} is computed with the ideal gas law. The gas phase contains n_{tot} moles of three compounds before condensation.

$$n_{\text{tot}} = n_{\text{IG}} + n_{\text{SiO},\text{in}} + n_{\text{CO},\text{in}} \quad \text{Equation 7}$$

In Si-SiO₂ pellets large-scale experiments (IF5-8, IF10, IF12), the theoretical partial pressure of CO(g) should be $p_{\text{CO}} = 0$. However, SiC-SiO_x condensates form anyways in the setup, implying that a certain amount of CO(g) should be present in the gas phase before condensation. The graphite parts are believed to be responsible for CO production, as they are covered with a SiC layer (see Appendix A). It is assumed that CO(g) is generated by the interaction with the graphite wall (Reaction 3). $n_{\text{SiO},\text{in}}$ should decrease by a number of moles corresponding to the CO moles generated in this way. To summarize, 0.1 mol CO are added to $n_{\text{CO},\text{in}}$, and 0.1 mol SiO are taken away from $n_{\text{SiO},\text{in}}$, in the mass balance of experiments IF5-8, IF10 and IF12.

The value 0.1 mol was estimated from the amount of SiC-SiO_x condensates found in these experiments, assuming that all the CO(g) generated from Reaction 3 is used for Reaction 1. The same correction was applied for the SiO₂-SiC pellets, and only for the large-scale setup experiments. After the correction, the number of moles is scaled to partial pressures (with respect to the total pressure of each setup), and $p_{\text{SiO},\text{in}}$ is found.

The value of $p_{\text{SiO},\text{out}}$ is found from the weight of Si-SiO₂ and SiO₂-SiC condensates collected from each experiment. It is possible to calculate the SiO(g) and CO(g) moles used during condensation, either by Reaction 1 (SiC-SiO_x condensates) or Reaction 2 (Si-SiO₂ condensate). These moles are called $n^{\text{R1}}_{\text{cond,SiO}}$, $n^{\text{R1}}_{\text{cond,CO}}$ and $n^{\text{R2}}_{\text{cond,SiO}}$, where the superscript specifies the condensation reaction, and the subscript the gas species considered. At this point, the mole balance is carried out by the equations below. n_{IG} remains constant through the experiment.

$$n_{\text{SiO},\text{in}} - n^{\text{R1}}_{\text{SiO},\text{cond}} - n^{\text{R2}}_{\text{SiO},\text{cond}} = n_{\text{SiO},\text{out}} \quad \text{Equation 8}$$

$$n_{\text{CO},\text{in}} - n^{\text{R1}}_{\text{CO},\text{cond}} = n_{\text{CO},\text{out}} \quad \text{Equation 9}$$

Finally, n_{IG} , $n_{\text{SiO},\text{out}}$ and $n_{\text{CO},\text{out}}$ are proportional to the partial pressures at the point where condensation ends. The value of $p_{\text{SiO},\text{out}}$ can be found, with respect to the total amount of moles in each setup. In particular, for the large-scale setup, p_{CO} is assumed to be $(1 - p_{\text{SiO}})$, as no other species are assumed to be present in the gas phase. Once the two points ($T_{\text{SiO},\text{in}}$; $p_{\text{SiO},\text{in}}$) and ($T_{\text{SiO},\text{out}}$; $p_{\text{SiO},\text{out}}$) are found for every experiment, a linear regression gives a $p_{\text{SiO}}-T$ curve with the form $p_{\text{SiO}} = \gamma T + \delta$. The graphs should be read from right to left, therefore the partial pressure of SiO(g) decreases linearly through the condensation chamber, according to the model. The points are united by a line, as shown in Figure 182.

Reactions 1 or 2 take place in the temperature interval [$T_{\text{SiO},\text{R1},\text{start}}$; $T_{\text{SiO},\text{R1},\text{stop}}$] (or with R2 subscript, in case Reaction 2 is considered). These temperatures can be related to the corresponding p_{SiO} on the linear interpolation, after having found γ and δ . In this way, the corresponding partial pressures $p_{\text{SiO},\text{R1},\text{start}}$ and $p_{\text{SiO},\text{R1},\text{stop}}$ can be calculated.

Figure 182 shows how the $p_{\text{SiO}}-T$ curve looks like for experiment R1b, considering Reaction 2. The interval between ($T_{\text{SiO},\text{R2},\text{start}}$; $p_{\text{SiO},\text{R2},\text{start}}$) and ($T_{\text{SiO},\text{R2},\text{stop}}$; $p_{\text{SiO},\text{R2},\text{stop}}$) is continuous, and represents the interval where the condensate was found. The dashed line represents the zone where the reaction is not occurring.

All the values of T , p_{SiO} , γ and δ discussed in this section, for all the experiments, are collected in Appendix D.

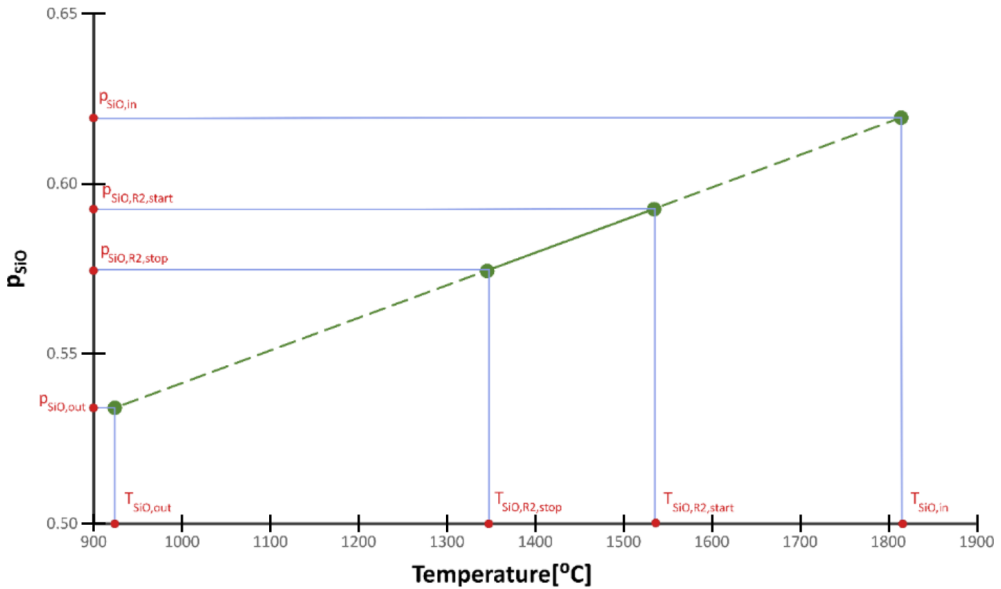


Figure 182: Example of p_{SiO} vs T diagram for Reaction 2, experiment R1b.

Results

This section shows all the p_{SiO} - T curves computed for the small- and large-scale setup experiments. The slope of the curves is very similar between experiments in different conditions and setups, whereas the intercept δ shifts to lower p_{SiO} by increasing the inert gas flow added. The partial pressure does not decrease dramatically through the condensation setup, according to the mass balance calculations performed.

In Figure 183 and Figure 184, experiments at the same inert gas flow have been collected in groups of lines with similar colors. A higher inert gas flow gives a lower $p_{SiO,in}$ and shifts condensation to temperature intervals located at colder positions. $p_{SiO,out}$ and $T_{SiO,out}$ decrease by adding a higher inert gas flow, whereas $T_{SiO,start}$ follows the same trend for Reaction 2 only. Experiments at longer holding times have wider gaps between $T_{SiO,start}$ and $T_{SiO,stop}$. For example, Experiments R3a, R4 and R5a have respectively 30, 60- and 240-min holding times, as well as R14a, R17a and R19-21.

In the large-scale setup (Figure 185 and Figure 186), every experiment has a different color. Experiments at shorter holding times (IF10, IF11, IF12) tend to have a higher $T_{SiO,stop}$ compared to their respective experiments at longer holding time (IF1b, IF1b and 5b). A broader particle size distribution has the opposite effect, as it happens between IF1b - IF2a - IF4 - IF3a and IF5b - IF8 - IF7b (each group is ordered by increasing particle size distribution broadness).

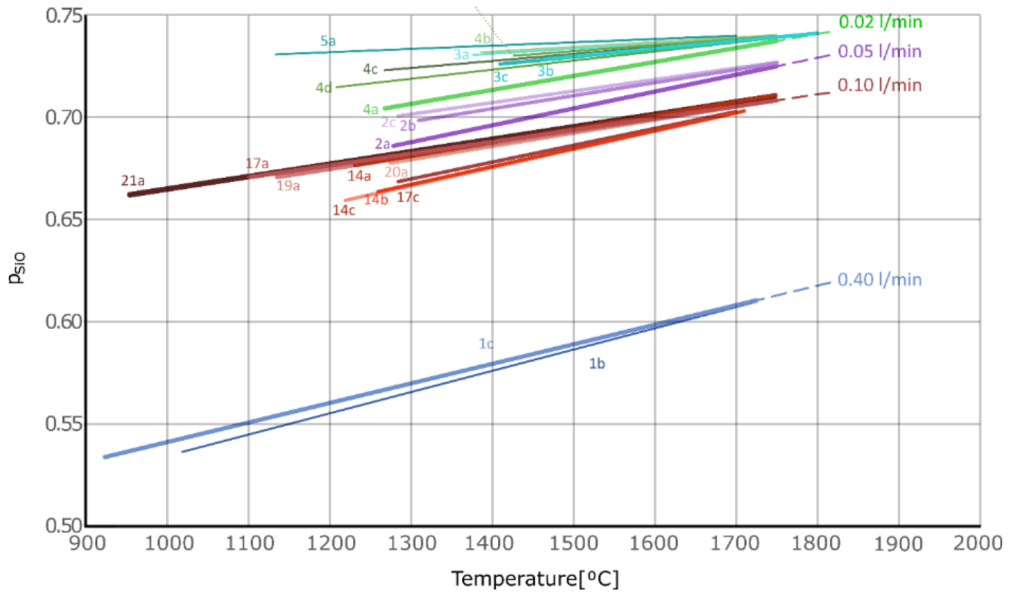


Figure 183: p_{SiO_2} -T curves for SiO_2 -SiC condensation, small scale setup.

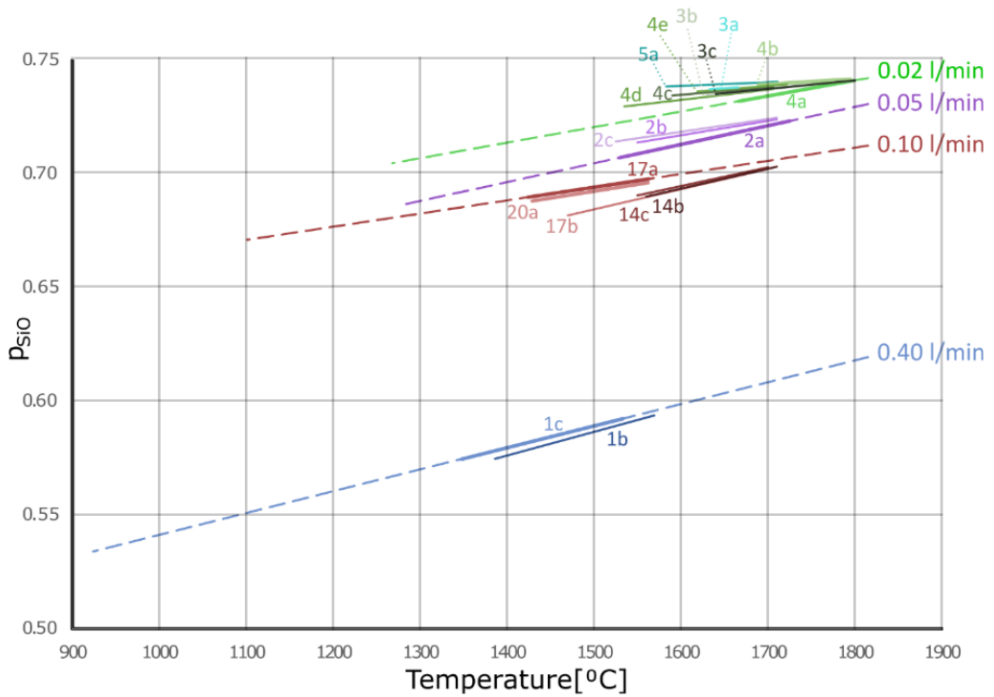


Figure 184: p_{SiO_2} -T curves for Si-SiO₂ condensation, small scale setup.

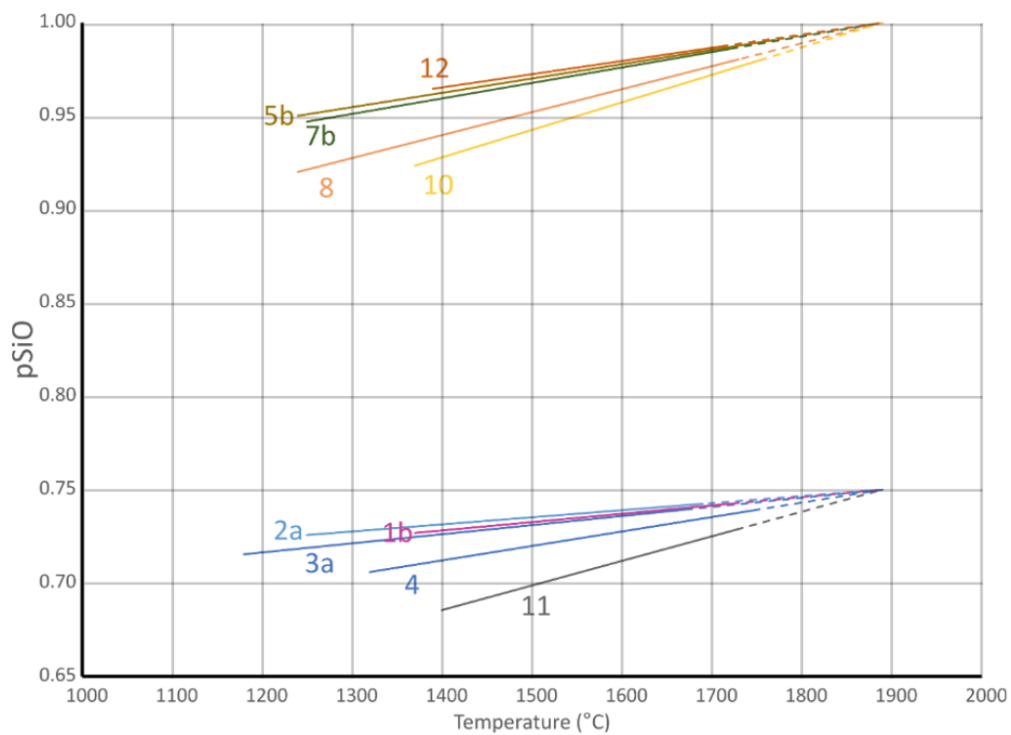


Figure 185: p_{SiO} -T curves for SiO_2 -SiC condensation, large-scale setup.

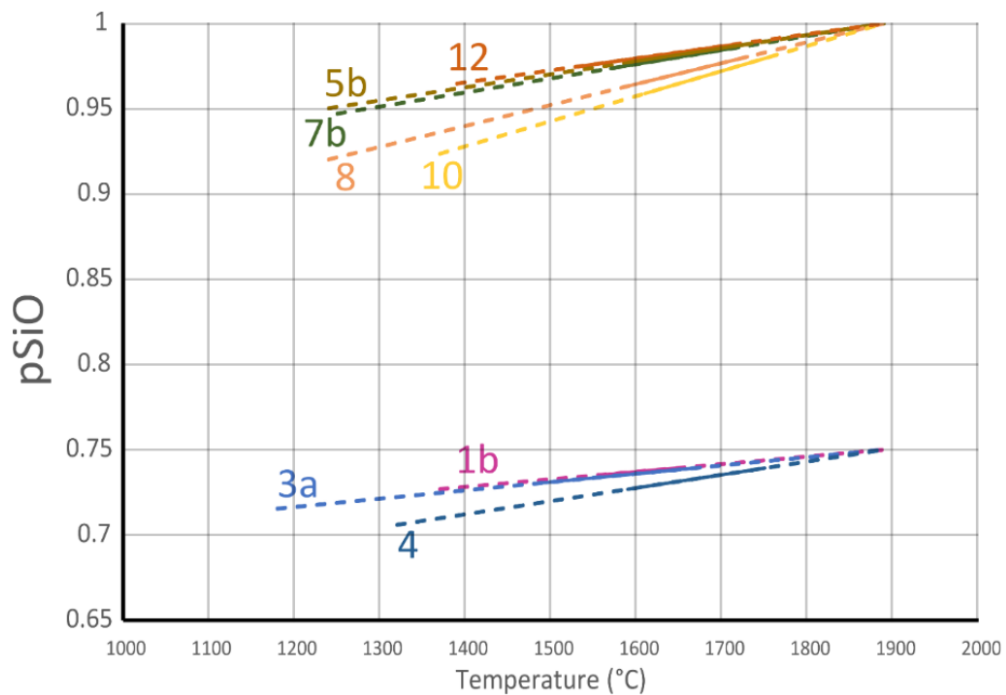


Figure 186: p_{SiO} -T curves for Si-SiO₂ condensation, large-scale setup.

B. Kinetic modelling for SiO₂-SiC condensates (Reaction 1)

Aim of the model

This model is a kinetic model for Reaction 1 only, i.e. production of SiO₂-SiC condensates. Its aim is to calculate the reaction rate constants E_a and k_0 . The activation energy E_a has a significant physical meaning. E_a can be interpreted as the minimum amount of energy required to activate a transformation of atoms or molecules, or their physical transport. This parameter is useful to compare the rate of different reactions.

With this kinetic model, one can estimate the rate of condensation at temperatures typical of the low temperature zone in industrial furnaces. The model is based on the large-scale setup experiments only, which have the conditions closer to the industrial furnaces. By knowing the temperatures where condensates form, and the partial pressure of the ascending gas from the high temperature zone, the model can be easily applied to industrial level, to estimate the mass of condensates produced over time. It must be however noticed that the variance is quite high for the experiments, based on the reaction rate calculation (Chapter 3F, Figure 188- Figure 190). However, it is still worthwhile to have a model that at least gives the correct order of magnitude for the activation energy and k_0 value.

Procedure

The rate of Reaction 1 (r_1) is modelled according to the following equation

$$r_1 = \frac{dm}{dt} \approx \frac{m_{cond,R1}}{t_r} = k(T) \cdot A \cdot f(p_{SiO})$$

Equation 10

with $m_{cond,R1}$ being the amount of SiC-SiO_x condensate produced over the reaction time t_r , $k(T)$ the kinetic constant, A the available area for the reaction and $f(p_{SiO})$ a function depending on the gas composition. The experimental data needed for the model are m_{cond} , t_r , T , A and p_{SiO} . The steps of this calculation are:

- 1) Find r , A and $f(p_{SiO})$,
- 2) Rearrange the formula above and find $k(T)$.
- 3) Assume an expression for $k(T)$
- 4) Find E_a and k_0

Step 1: r is found from the ratio between m_{cond} and t_r . These values are collected in the results section, in Table 43 and Table 44 respectively.

A is the surface available for condensation. To estimate A , it is assumed that the SiC particles inserted in the condensation chamber are spherical and have the same average size d_p . The average diameter is found by looking at the particle size distribution diagrams (Figure 79). For example, in experiment IF2a, where the PSD is 5-8 mm, d_p will be 6.5±1.5 mm. The available surface of a single particle A_p is easily found from the diameter.

$$A_p = \pi d_p^2$$

Equation 11

The total number of particles n_p is found from the total volume of SiC in the condensation zone V_{tot} . This volume is found by dividing the mass of SiC in the condensation zone before the experiment started ($m_{SiC,before}$), and the density of SiC ($\rho = 3.21 \text{ g cm}^{-3}$ [98]).

$$n_p = \frac{V_{tot}}{V_p} = \frac{m_{SiC,before}}{\rho \cdot \pi d_p^3} \quad \text{Equation 12}$$

Once the estimated number of particles has been found, it can be multiplied with A_p to find the total available area in the condensation chamber for the experiment A_{tot} .

$$A_{tot} = A_p \cdot n_p \quad \text{Equation 13}$$

By dividing A_{tot} by 31 cm, one can find the amount of area available in an interval which is 1 cm thick. This parameter is called A_{cm} . 31 cm is the height of the condensation chamber, filled with SiC particles substrates. Therefore, the value of A is calculated by multiplying A_{cm} and L for every temperature interval. L is the thickness of a condensation interval, which is found during the excavation of the crucible. Each experiment has up to 4 temperature intervals.

$$A = A_{cm} \cdot L = \frac{A_{tot}}{31} \cdot L \quad \text{Equation 14}$$

The values of d_p , A_p , $m_{SiC,before}$, V_{tot} , A_{tot} , A_{cm} , L and A for every experiment are collected in Appendix D. $f(p_{SiO})$ is the driving force term related to the SiO(g) content in the gas. 7 various expression of the driving force were proposed. Six of these models study the combination of molecules of SiO(g) and CO(g) at different ratio. The amount of moles involved for each molecule is the order of reaction of each species, i.e. the exponent to which the term is elevated. The last one considered the deviation from the equilibrium partial pressure for reaction 1. Each mode was also tested without including the proportionality with A in the equation. A total of 14 models were hence computed.

Mode 1: 1 SiO(g)	$\frac{dm}{dt} = k(T) \cdot A \cdot (p_{SiO})$
Mode 1b: 1 SiO(g) + 1 CO(g)	$\frac{dm}{dt} = k(T) \cdot A \cdot (p_{SiO}) (p_{CO})$
Mode 2: 2 SiO(g)	$\frac{dm}{dt} = k(T) \cdot A \cdot (p_{SiO})^2$
Mode 2b: 2 SiO(g) + 1 CO(g)	$\frac{dm}{dt} = k(T) \cdot A \cdot (p_{SiO})^2 (p_{CO})$
Mode 3: 3 SiO(g)	$\frac{dm}{dt} = k(T) \cdot A \cdot (p_{SiO})^3$
Mode 3b: 3 SiO(g) + 1 CO(g)	$\frac{dm}{dt} = k(T) \cdot A \cdot (p_{SiO})^3 (p_{CO})$
Mode 4: distance from equilibrium	$\frac{dm}{dt} = k(T) \cdot A \cdot (p_{SiO} - p_{SiO,eq})$

The value of p_{SiO} and p_{CO} in each interval is calculated by the procedure exposed in the $p_{SiO}-T$ model section.

Step 2: The value of r is computed at the average temperature T in every temperature interval, which has an interval width ΔT . Each experiment has up to 4 temperature intervals. The values of T and ΔT for every experiment are collected in Appendix C. At this point, the values of $k(T)$ can now be computed in each temperature interval.

Step 3: $k(T)$ is assumed to follow the Arrhenius equation

$$k(T) = k_0 \cdot \exp\left(-\frac{E_a}{RT}\right) \quad \text{Equation 15}$$

Step 4: A plot with coordinates $\ln k$ vs $-1/RT$ will give a linear function after regression. All the 27 values of k are taken from all the experiments. The curve will have E_a as slope and $\ln(k_0)$ as intercept.

$$\ln k(T) = \ln(k_0) + E_a \cdot \left(-\frac{1}{RT}\right) \quad \text{Equation 16}$$

Reaction rate

Reaction time

The time interval where the condensate is produced is called *reaction time* (t_r). In this section, the estimation of the reaction time is presented for the large and the small-scale setup.

Case 1: Large-scale setup. The value of t_r is the time during which the flames come out of the crucible. These flames are associated to CO(g) and SiO(g) burning at the crucible top, producing either blue or orange/white flames. The values of t_r are listed in Table 44, for different experiments. t_r is assumed to be the same for every temperature interval in the same experiment. In other words, it is assumed that the condensate is produced at the same time.

Table 44: Values of t_r for large-scale setup experiments.

Experiment	t_r (min)
IF2a	137
IF3a	131
IF4	95
IF5b	158
IF7b	98
IF8	127
IF10	61
IF11	15
IF12	20

Case 2: Small-scale setup. The gas production time (which is equal to the reaction time t_r) is \approx 30-40 minutes for every experiment. This time is estimated after comparing the CO(g) production over time in the gas detector. The time interval starts where the %CO in Figure 187 starts to increase and ends when the %CO graph is flat. The figure below shows three examples of CO(g) production over time detected by the gas analyzer, for Experiment R6a (red), R17a (green) and R9a (blue). Experiments with same holding temperatures and times show similar profiles. The inert gas flow changes only the height of the %CO detected by the gas analyzer, without affecting the reaction time.

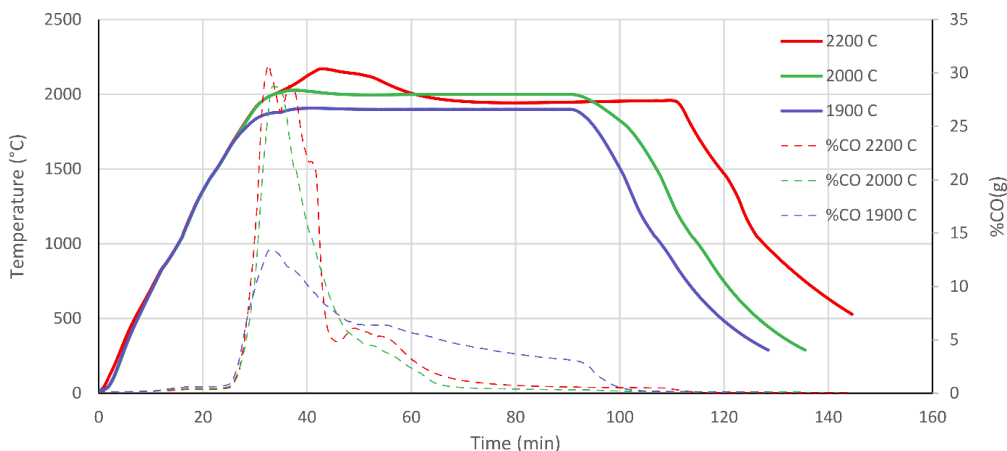


Figure 187: Thermal history at the pyrometer (continuous line) compared to the corresponding CO(g) production for experiments at 1900, 2000 and 2200 °C target temperature (dashed lines).

Calculation and analysis of reaction rate for SiC-SiO₂ condensation

The rates of reaction are plotted as a function of three parameters, which are the reaction time t_r , the temperature in the condensation zone T and the available area for condensation A (calculated in appendix D) The reaction rate increases with temperature from 1200°C (Figure 189). After reaching a maximum at about 1650°C, the reaction rate drops quickly.

The overall trend in Figure 189 is not statistically significant, but all the experiments follow the same behavior. The reaction rate increases smoothly with temperature, and reaches its maximum at about 1600°C. The rate is proportional to the driving force. After maximum rate, the rate decreases. This can happen because of the back reaction to SiO(g) and CO(g), which slowly begins to dominate above 1600°C. There are therefore three temperature regions, where the gas production reaction and the condensation reaction try to prevail:

- 1) $T = 1315 - 1600^\circ\text{C}$:** The condensation reaction dominates, and its rate increases with temperature. The maximum rate is reached between 1400-1700°C, according to the experiment.
- 2) $T = 1600 - 1810^\circ\text{C}$:** The gas production and the condensation reactions occur at the same time, giving a lower amount of condensate than in the previous temperature range. The gas production rate increases with temperature also in this temperature range. The gas production rates increases with temperature, but it decreases when going over the melting point of silica [69], [70], [97].
- 3) $T > 1810^\circ\text{C}$:** The gas production reaction is dominating, and the gas phase remains stable.

The experiments with the shortest times have faster reaction rates (IF11,12). Experiment IF5b is the slowest, but also the experiment with the longest reaction time. Figure 188 shows the dependence of the rate on the reaction time.

There is no clear dependence between the reaction rate and the available surface for condensation, in the experiments analyzed. The values of the reaction rate are listed in Table 45. There is a correspondence between the intervals with the highest rates, and the clogging intervals, which are highlighted in bold.

The values of the reaction rates have only been estimated for the small-scale setup. The value of m_{cond} is of course the total amount of white SiC-SiO_x condensate, whereas t_r is chosen as 30 or 40 minutes according to the holding time. That will give a rate value in the order of magnitude of 0.003 – 0.120 g/min. Most of the results

obtained in the large-scale setup are comparable to these numbers. This gives higher statistical significance to the calculation of the rate values.

Table 45: Reaction rate values in different experiments and condensation intervals (highlighted in bold).

Experiment	T interval (°C)	Rate (g/min)
IF2a	1250-1380	0.026
	1380-1485	0.051
	1485-1550	0.153
	1550-1690	0.026
IF3a	1180-1480	0.013
	1480-1675	0.115
IF4	1320-1490	0.030
	1490-1590	0.059
	1590-1680	0.177
	1680-1750	0.030
IF5b	1240-1420	0.005
	1420-1590	0.026
	1590-1735	0.068
	1735-1770	0.005
IF7b	1250-1480	0.019
	1480-1570	0.019
	1570-1720	0.152
IF8	1240-1420	0.012
	1420-1590	0.059
	1590-1730	0.165
IF10	1370-1470	0.014
	1470-1610	0.056
	1610-1760	0.209
IF11	1400-1580	0.157
	1580-1730	0.627
IF12	1390-1490	0.046
	1490-1530	0.046
	1530-1710	0.368

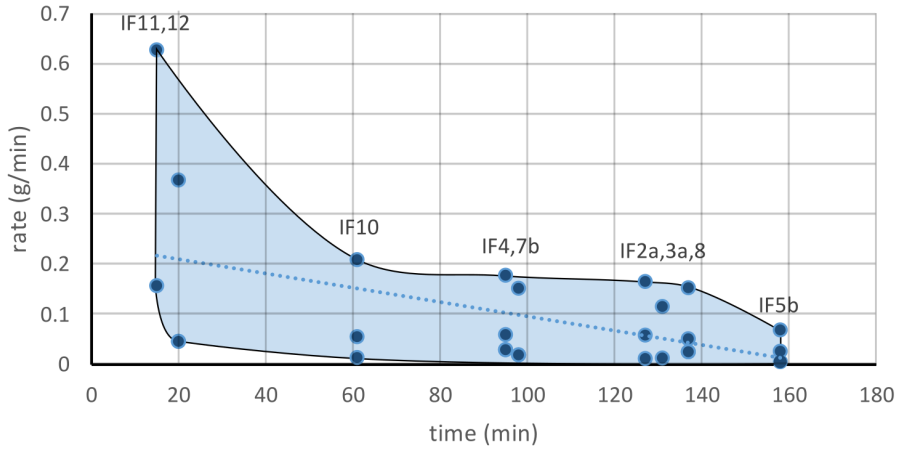


Figure 188: Reaction rate as a function of reaction time.

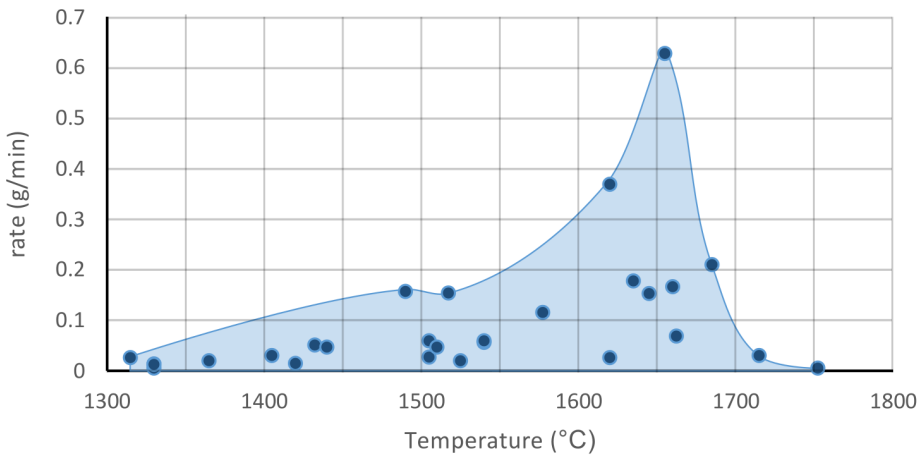


Figure 189: Reaction rate as a function of temperature.

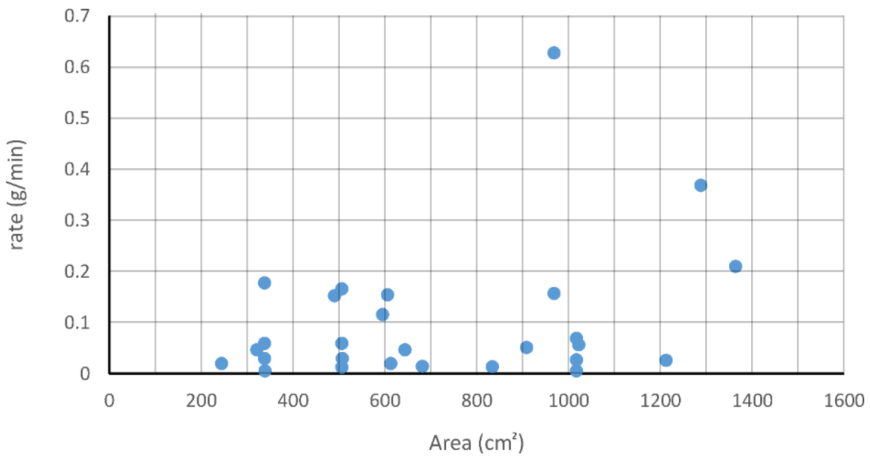


Figure 190: Reaction rate as a function of total condensation area.

Kinetic constants

The functions $k(T)$ were plotted for all the models, but only the two models with the highest R^2 parameter were chosen. R^2 is a statistical parameter called coefficient of determination, which defines how well the experimental points fit the Arrhenius equation curve proposed. The models chosen are the following ones:

$$\text{Mode 2b : } R^2 = 0.7752 \quad \frac{dm}{dt} = k(T) \cdot A \cdot (p_{SiO})^2 (p_{CO})$$

$$\text{Mode 3b : } R^2 = 0.8072 \quad \frac{dm}{dt} = k(T) \cdot A \cdot (p_{SiO})^3 (p_{CO})$$

Model 4 was also chosen for further study, since it is the only model that considers the distance from equilibrium. Its R^2 is somewhat lower than mode 2b and 3b.

$$\text{Mode 4 : } R^2 = 0.7100 \quad \frac{dm}{dt} = k(T) \cdot A \cdot (p_{SiO} - p_{SiO,eq})$$

The computed values of E_a and k_0 for the three models are reported in Table 46. The values of E_a stay within the same order of magnitude, but k_0 is two orders of magnitude smaller for model 4, compared to model 2b and 3b. Figure 191 shows the $\ln k$ vs $-1/RT$ diagrams plotted for each model. The error bars are computed with the help of the Gauss error propagation law. The three graphs show the expected increasing trend of $k(T)$ with temperature.

The temperature points are taken over the range 1315-1750°C, but not all the experimental points are used for the computation of the Arrhenius plots. The results of E_a and k_0 are computed using the points in the temperature range 1315-1685°C.

Table 46: Activation energy and frequency factor for mode 2b, 3b and 4.

Model	E_a (kJ/mol)	k_0 (g cm ⁻² s ⁻¹)
2b	283±33	3.35 · 10 ⁵
3b	279±29	3.05 · 10 ⁵
4	242±33	1.49 · 10 ³

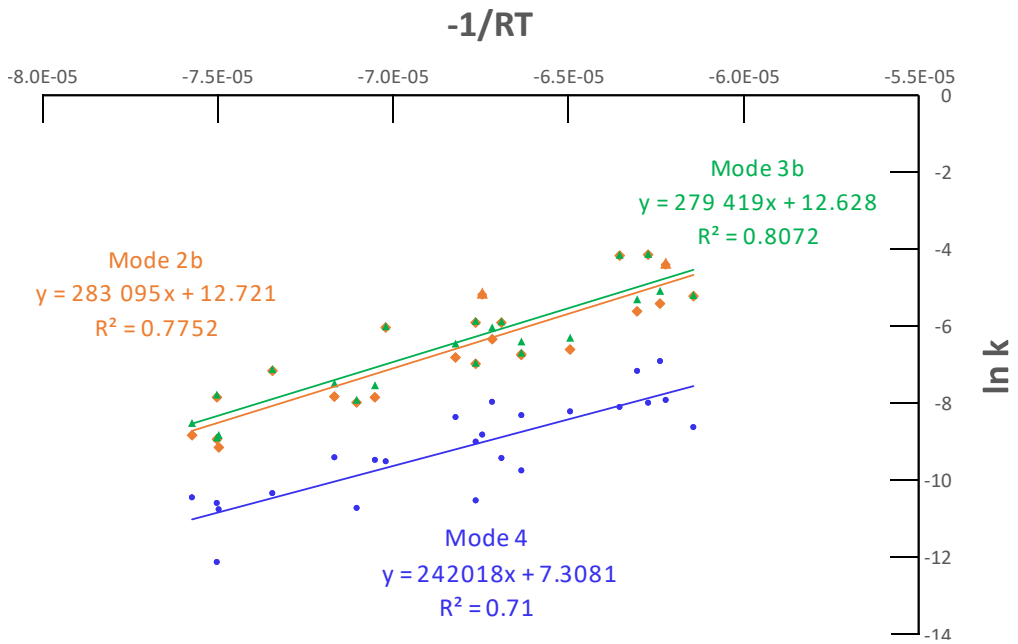


Figure 191: Arrhenius equation plots for $k(T)$ values in mode 2b, 3b and 4. The slope of the curve is the activation energy E_a , and the intercept is the natural logarithm of the frequency factor k_0 .

5. Discussion

The discussion section compares the knowledge from the experimental results, trying to find correlations between the investigated parameters. The results are also compared with the previous literature and the industrial experience. The mechanism of formation and transformation of condensates will be discussed, as well as the thermodynamic and kinetic calculations on the condensation rate. The chapter is divided into four sections.

Section A describes the formation and transformation of SiC-SiO_x core-shell nanowires. The mechanism consists of three steps: seed generation, nucleation and vertical growth. The diameter of the nanowires depends on the duration of the seed generation step. During growth, the shell-layer of the nanowires can transform its shape from a constant layer into a necklace structure and then into nodules, which become larger with increasing temperature and time. The transformation is driven by the exothermic reactions (which may develop a superheated temperature in a nanometric system), surface energy reduction and wettability between SiO_x and SiC. A large amount of localized heat may favor the back reaction to SiO(g) and CO(g). The segregation into Si, SiO_x and SiO₂ is believed to start already from the gas phase.

Section B covers the formation and transformation of the Si-SiO₂ condensate. The mechanism is divided into three stages. The first is the gas deposition, which forms a Si-SiO₂ emulsion at the surface. Then, the matrix solidifies, while Si is able to move. During this stage, three processes will occur: crack formation, formation of alternate layer structures and SiC development at the Si-SiO₂ interface. If cooled below 1400°C, Si will solidify, and the condensate will freeze into its final structure.

Section C analyses the relationship between mass balance, clogging of the crucibles, thermodynamics and kinetics of the experiments. These four aspects are those which have the highest industrial significance. First, the relationship between charge permeability (i.e. particle size distribution (PSD) of the charge bed), condensation yield and SiO(g) content is analyzed. Second, there is a correlation between condensates mass, gas composition, maximum condensation rate and clogging, which affects the distribution of condensates in the crucible. Third, the reaction time can affect the clogging interval and the condensates. A clogged particle bed builds up within 10 minutes in the large-scale setup. Finally, an increase in temperature can transform a fraction of condensates back into SiO(g) and CO(g), and reduce clogging. The industrial relevance is finally discussed.

Section D will discuss the production of SiO(g) and CO(g) during the experiments. The conversion parameter and the conversion rate are in the same order of magnitude as previous works. The gas composition and the gas producing reagents affects the quantity and the type of condensates produced.

A. Formation and transformation of SiC-SiO_x nanowires (Reaction 1)

SiC-SiO_x nanowires come as a blue, white or orange thin layer on the substrates. In SEM and TEM, SiC-SiO_x condensates look like intricated forests of nanometric wires, covered with “droplets” especially where white layers are present. It was demonstrated that the nanowires are made of a core phase, containing SiC, and a shell-phase made of SiO_x. This result confirms what happened in previous works concerning SiC-SiO_x nanowires [11], [35]–[37], [39], [54], [59], [79], [99]. Since there are no substantial microstructure differences between nanowires generated on SiC, graphite and quartz, it can be assumed that the mechanism of formation for SiC-SiO_x nanowires is the same, regardless of the substrate.

The mechanism proposed is based on the theory of the Oxide Assisted Growth (OAG) mechanism by Noor Mohammad [78], combined with results and theories from other works. The mechanism can be divided into three stages: seed generation, nucleation and vertical growth.

Stage 1: Seed generation (Figure 194). SiO(g) and CO(g) travel to the substrate surface and react. They produce SiC and SiO_x at the same time and close to each other, thanks to Reaction 11. For $x=2$, Reaction 1 and 11 are equal.



SiO(g) are formed in the gas phase as (SiO)_N molecules, which can disproportionate into Si, SiO₂ and SiO_x. Figure 192 shows the (SiO)_N nanocluster conformations as a function of the value of N. The configuration at N = 14 is considered as an example. In the molecule sketch, there are three distinct areas. The first is called *silicon area* (orange, on the right. O/Si ratio = 0). Only Si-Si bonds atoms are present in this zone. The second is called *silica area* (blue, on the left. O/Si ratio = 2). In this zone, the atoms are linked by Si-O-Si bonds, typical of silica. Such bonds were found in the XPS peak fitting analysis, as well as silica was found in the XRD analysis. The atoms connecting the silica and the silicon area are responsible for the formation of SiO_x, forming the *suboxide area* (green, center). There are Si-Si-O bonds in the suboxide area, which decrease the local O/Si ratio to 1.

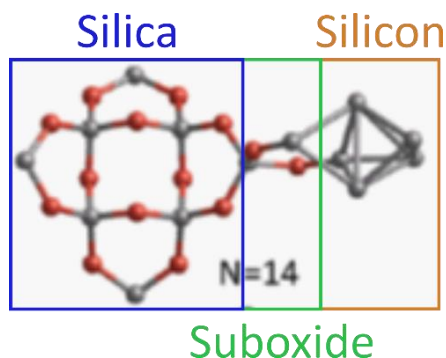


Figure 192: (SiO)_N nanoclusters ground state for N = 14, segregation into silica, suboxide and silicon area. Element key: Red = Oxygen; Grey = Silicon. Revised after Bromley et al.[49].

Suboxides are produced during the segregation of (SiO)_N molecular clusters into Si, SiO₂ and SiO_x. In fact, the O/Si ratio in the suboxide area is between 1 and 2. The nanowires have always been called SiC-SiO_x nanowires, despite the stoichiometry of the SiO(g)+CO(g) condensation reaction implies that SiO₂ is formed. As the

nanowires structure is defined at atomic level, the local Si:O atomic ratio in the oxide phase may not always be 1:2. Therefore the compositional characterization techniques at atomic scale mentions SiO_x rather than SiO_2 . It has been known for a long time that the oxidation number of Si may change between 0 and +4 at atomic scale, as described in the Random-Bonding (RB), Random Mixture (RM) and Interface Cluster Model (ICM) [41], [45], [47], [50], [51]. Ching showed as well that suboxides contain both Si-Si and Si-O bonds [50], as revealed by XPS analysis in this work. Only in recent times, kinetic models have explained the formation of suboxides and the segregation of Si and SiO_2 in the $(\text{SiO})_N$ gas nanoclusters [49].

The condensation reaction of Stage 1 occurs at atomic scale, and the reaction environment could be considered in nearly adiabatic (superheated) conditions in the immediate vicinity of the atoms reacting. This implies that some of the Si and SiO_2 formed may vaporize back to Si(g) and O(g), or $\text{Si}_x\text{O}_y(\text{g})$ gas species. Such species will recombine randomly into the nanowires shell phase, deviating from the expected SiO_2 composition.

The superheated temperature is somewhat below the adiabatic temperature. The adiabatic condition is a theoretical assumption. In fact, the adiabatic conditions require that the internal energy of the reactants is equal to the internal energy of the products, and no heat is lost to the surroundings. The adiabatic temperature of the nanowires formation reaction (Reaction 1) can reach $\approx 6000^\circ\text{C}$, according to calculation performed with HSC Chemistry 10[®]. This temperature can resist only for very short times, as there will be some heat losses. Hence it can be assumed that the superheated temperature is around the boiling point of SiO_2 (2230°C). In fact, at the boiling point, the temperature will not increase further until all the materials are evaporated. As there is not enough energy in the reaction to do this, only part of the SiO_2 have reacted, and the temperature could not be more than 2230°C .

At such temperature ($T > 2200^\circ\text{C}$), the previously mentioned Si(g) and O(g) species are stable at low concentrations, in equilibrium conditions. Figure 193 shows the equilibrium amounts of gas species obtained from a mixture of 2 kmol SiO_2 and 1 kmol SiC, heated between 1000°C and 6000°C . The calculation is computed by the software HSC Chemistry 10[®].

3 kmol of SiO are produced from the initial mixture, at 1850°C . Then, the SiO(g) concentration decreases at $\approx 3500^\circ\text{C}$, while Si(g) and O(g) start increase together. Si(g) and O(g) come from the decomposition of SiO(g), according to the software. However, the kinetic models by Bromley et al. [49] showed that these species can also form $(\text{SiO})_N$ nanoclusters at lower temperatures. These species are not included in the software species database. If the temperature rises locally above 3500°C due to superheated conditions, $(\text{SiO})_N$ nanoclusters may form.

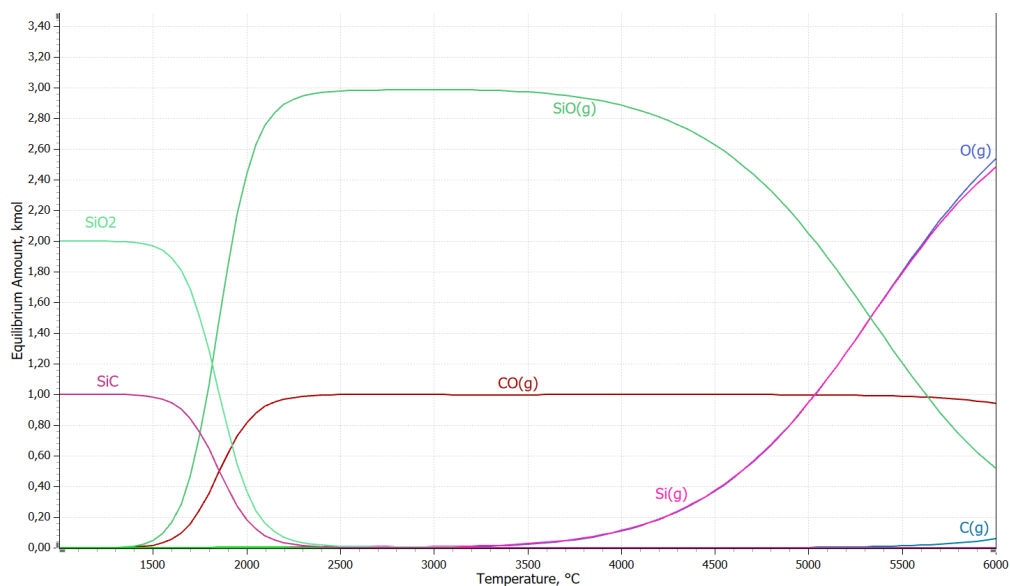


Figure 193: Equilibrium composition of a mixture of 2 moles SiO₂ and 1 mol SiC, between 1000°C and 6000°C.

Once produced, the SiC seeds are inert and solid, while the suboxides will either decompose into SiO₂, O and Si, or react with incoming gas species. These two scenarios will both give the same result, i.e. SiC and SiO_x seeds on the substrate surface.

Case a: SiO_x is unstable and decomposes into SiO₂, O and Si [35],[78]. SiO₂ creates a matrix containing Si islands, as the two compounds do not mix. This is demonstrated by the results of the microstructure of Si-SiO₂ condensates, as well as by literature studies of the Si-O system [27]–[29]. Then, Si attracts CO(g) to form SiO₂ and SiC (Reaction 12).

In other words, the Si islands contribute to seed formation for both the core and the shell phase, by attracting CO(g). Reaction 12 will also occur below 1500°C, as documented by Lim [100].



On the other hand, O may react with SiO(g) to form SiO_x or SiO₂ (Reaction 5). If SiO_x is formed in this way, it may disproportionate again, and the cycle repeats.

Case b: SiO_x does not decompose [78],[101]. Si seeds are created because of a chemical reaction between SiO_x and CO(g) (and not by SiO_x decomposition). SiO_x will attract SiO(g) and CO(g) from the vapor phase thanks to the dangling bonds. Accumulation of Si in SiO_x brings instability, and O atoms segregate at the periphery. This assertion is possible thanks to density functional calculation provided by Chu et al. [101]. Si seeds form when SiO_x is depleted in oxygen. The Si atoms react with incoming CO(g) to form SiC and SiO₂ (or SiO_x) in the reaction zone located around the SiC seed, as shown in Figure 194.

The lateral growth of the seed occurs also during Stage 1 [78]. SiO_x binds with the substrate surface and to the SiC seeds, thanks to its dangling bonds. SiO_x gradually embeds the SiC seed. The two compounds have a discrete wetting interaction. In fact, the contact angle between them is $\approx 45 \pm 10^\circ$, as measured during TEM. Once a shell is formed around the SiC seed, the suboxide prevents diffusion of the vapor species through the sidewalls. The

vicinity of SiC and SiO_x could be seen by XPS techniques as chemically bonded seeds, which result into the Si-O-C bond peak. Once the diameter of the nanowire is fixed, the seed generation step is over.

The lateral growth of nanowires can explain why blue condensate nanowires (diameter = 60-100 nm) may be thinner than white condensate (diameter = 80-100 nm), or why industrial nanowires may be larger than laboratory scale nanowires. In the industrial sample REC1.3 the nanowires are 1-2 μm thick, whereas at lab scale the diameter is 40-100 nm. A higher amount of gas molecules brings more molecules available for the reaction. The nanowire will grow thicker, as more oxide molecules will be needed to cover a larger SiC seed.

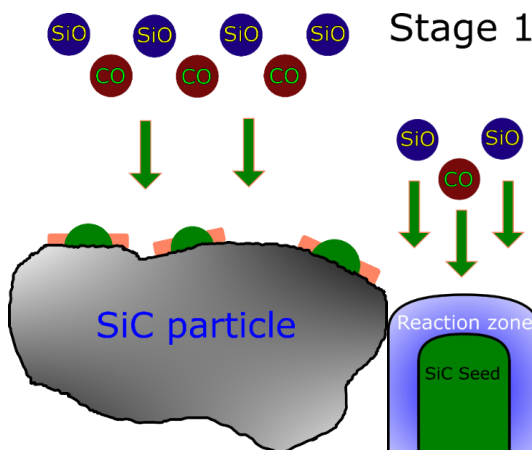


Figure 194: Stage 1: Incubation: Formation of the seed for the SiC-SiO_x nanowire by SiC(s) (green) and SiO_x(l) (Orange) nanoclusters.

Stage 2: Nucleation. Nucleation begins when the lateral growth of the seed is completed. During Stage 2, a droplet forms at the top of the SiC seed, by Reaction 11. In the meantime, the SiC seed remains solid. A *nucleus* is therefore a SiC seed, with a droplet on the top and covered laterally in SiO_x. Figure 195 visualizes the main features of nucleation.

The area above the seed can be divided into a droplet (or inner zone) and a reaction zone (or outer zone). The inner zone contains precipitated SiC in a liquid droplet of SiO_x(l). SiC and SiO_x are immiscible and separate, as it happened in the wettability tests performed by Vangskåsen on white condensate [15]. Hence, solid SiC tends to precipitate at the bottom of the droplet, precisely at the core of the nanowire.

The reaction zone is the interface between the droplet and the gas phase. This is where the condensation happens. The dangling bonds of SiO_x attract SiO(g) and CO(g), which diffuse slowly through the oxide [78]. As suggested by Zhong et al. [87], gas species can be easily absorbed on the SiC seed surfaces, thus reacting with many chemically active sites at high temperature. Here three chemical reactions take place:

- 1) **Reaction 11, i.e. the condensation reaction.** This reaction is hence responsible for both the seed formation and the droplet formation;
- 2) **The decomposition of SiO(g) into Si(l), SiO₂(l) and SiO_x(l)**, according to the interface cluster model and the segregation in the SiO(g) molecules predicted by Bromley et al. [47]–[49]. SiO₂ and SiO_x accumulate on the side of the SiC seed, while Si(l) will be involved in a reaction with CO(g);
- 3) After SiO(g) decomposition, **Si(l) will react with CO(g) to form SiC** (Reaction 12).

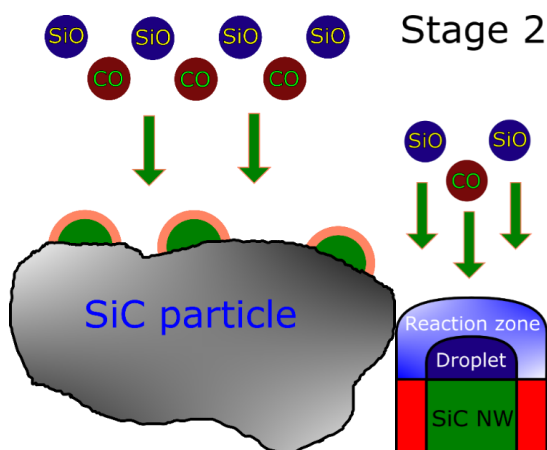


Figure 195: Stage 2: Nucleation of SiC (Green) and SiO_x(I) (Orange) on a SiC particle. Left: Final form of the nucleus, once the lateral growth is completed. Right: Formation of droplet, reaction zone and SiO_x coating (Red)

Stage 3: Vertical growth and termination. Thanks to the three reactions described in Stage 2, the nanowire will grow vertically in the preferential direction (111), found in 3C-SiC nanowires in this and other previous works [35], [39], [74], [88], [102]. Termination occurs when:

- 1) The SiO(g) and CO(g) partial pressures are low enough
- 2) The temperature is low enough to stop Reaction 11.

Once these conditions are not satisfied, the growth will stop, and the droplet will solidify at the top of the nanowire, as the exothermic reactions stop and the temperature will decrease locally.

Despite the crystallographic defects, branching is hindered by the formation of the SiO_x shell phase. The growth direction is forced towards a preferential direction (111). In fact, SiO(g) and CO(g) will form SiC and SiO_x either on the substrate surface, or at the reaction zone during Stage 2. Branching of the nanowire implies that the gas flows through the SiO_x shell walls. However, the diffusion rate is limited by the high molecular masses of SiO_x, SiC and SiO(g) itself [78]. The gas does not diffuse through SiO_x, therefore SiC can only precipitate by supersaturation at the droplet. The (111) preferential direction is typical of the 3C-SiC polytype. Previous works also analyzed the crystallinity of the nanowires and found this polytype in their XRD results [33]–[35], [37], [39], [87]–[89]. This confirms also that β-SiC is stable below 1800°C, as reported by Jayakumari [22], [103].

During growth, the nanowires do not grow into perfect crystals. **Crystallographic defects** (Figure 196) are caused by lattice mismatch and inclusion of oxygen atoms from the gas phase. Oxygen atoms may diffuse into the nanowire core [36]. Oxygen inclusions formation is possible also at low oxygen partial pressures, as suggested by Hu et al. [35]. In fact, the core phase still gives an oxygen signal during EDX line scanning. However, this signal may originate from oxygen scattering from the shell phase.

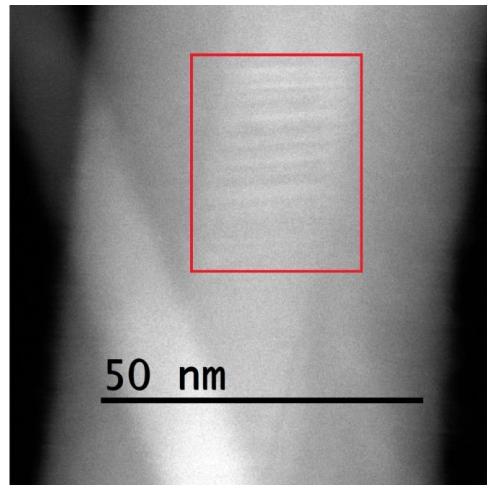


Figure 196: Defects in SiC core-phase, highlighted inside the red rectangle. TEM picture of blue condensate, Exp. R4c, T = 1250-1450°C.

Concerning the crystallinity of the shell phase, SiO_x is amorphous once condensed, and the cristobalite fraction increases with time and decreases with temperature. Silica is cooled down from high temperatures, hence the amorphous phase makes most of the sample at high temperatures and shorter times, when the condensates has just formed. The cristobalite content increases while cooling because of recrystallization. In fact, the opposite happens for Jusnes [60], who obtained an increase in amorphous phase and cristobalite by shock-heating quartz at 1500-1700°C. Another difference is that silica appears at nanometric size in this work and is therefore more likely to be amorphous. In both works, the quartz fraction disappears if the temperature is set above 1500° for at least 10-15 minutes. These temperatures and times are reached by all the three samples analyzed during XRD for this work.

The nanowire terminates with a tip. When the temperature decreases, the SiO_x in the droplet stops absorbing species from the gas phase, and the reaction zone ceases to be active. SiO_x forms at the tip of the wire and SiC precipitates on the seed. Surface tension effects causes the shape of the tip to be nearly spherical. Figure 197 sketches the growth and termination processes. The TEM picture highlights the tip of a nanowire collected from Experiment R4c.

Formation of grey condensate is believed to take place during growth, by piling of SiC and SiO_x seeds on top of each other. This was proposed due to the spherical shape of the blocks that make these nanowires, which are micrometric and oriented. EPMA revealed large presence of C within the grey condensate, therefore SiC is also contained in the condensate. The literature does not report a similar compound to be compared with the grey condensate.

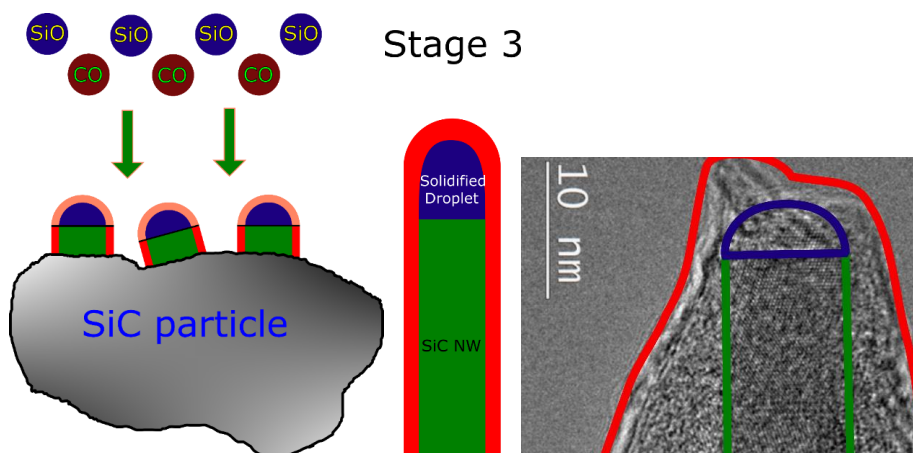


Figure 197: Left: Stage 3: Growth and terminated nanowire. Green = SiC(s); Orange = SiO_x(l); Red = SiO_x (s). Right: TEM picture of nanowire tip, picture from Experiment R4c. Zones highlighted with colors corresponding to the picture on the left.

Si, SiO₂ and SiC were the gas precursors used for this work. They produce mixtures of SiO(g) and CO(g) at different compositions. However, commercial carbon powders are preferred for laboratory scale experiments in other studies, since they are cheaper and easily available, compared to SiC. Carbon can also react with silica to produce SiO(g). In fact, in the industrial furnaces, we also find C as woodchips, coal or coke. SiO₂ can react with C to form SiC, through Reaction 13. Once SiC is generated, Reaction -1 would take place in the pellets crucible, above 1450°C [14], [22]. In other words, Reaction 13 can be “bypassed” by mixing SiO₂ and SiC in the pellets.



Despite the different mechanism of production of SiO(g), the physical appearance of blue and white condensate is comparable to what was seen during industrial excavations [55], [57] and pilot scale experiments [59], [65]. The final condensation product is similar in microstructure and composition to those from other laboratory scale works, when SiO₂ and C are used [33]–[38], [74]–[76]. The wires are forming a core-shell nanofiber structure, with a 3C-SiC core and a shell layer made of amorphous silica and cristobalite.

Generation and evolution of nodules

During vertical growth, the SiO_x shell-layer may coat the core phase uniformly or transform into droplets called *nodules* or the so-called *bead* or *necklace structure*. This term was used first by Hu et al. [88]. A mechanism for nodules evolution is proposed. The mechanism is sketched in Figure 198, and consists of five steps. The transformation from layer into nodules occurs during vertical growth.

Step 1: a uniform SiO_x layer is generated around the SiC-core phase. This occurs as described during the nucleation and growth steps of the nanowires formation mechanism. The uniform coating is typical of blue condensate, which is formed at low temperatures and/or small amounts. The heat of condensation is small, and the superheated temperature is relatively low.

Step 2: the uniform layer changes its shape to the bead structure. The shape can vary when the suboxide is liquid or viscous. The movement of SiO_x occurs for two main reasons:

1) *The superheated conditions and the melting point depression.* The bulk temperature measurements showed that SiO_x nodules are generated from $\approx 1300^\circ\text{C}$, which is $\approx 400^\circ\text{C}$ below the melting point of silica. However, the shape of the beads indicates that the oxide was locally close to liquid (or at least softened) state. The suboxides are in liquid state because of the melting point depression or local temperatures close to the superheated conditions due to exothermic condensation (discussed earlier), even when the bulk temperature is below the melting point of bulk silica.

2) *The presence of stacking faults in SiC* [35], [89], [104]. Stacking faults were detected during TEM analysis in this work. In some cases, stacking faults in the core phase were present in correspondence of nodules. The high density of stacking faults leads to a rough surface, with a high surface energy. The uniform coating transforms into beads where the concentration of stacking faults in the wires is high. SiO_x rearranges and obtain a lower energy system, as documented by Wu et al. [39]. However, other TEM pictures from this work also show that nodules can form also on defect-free nanowires. From this work it is hence showed that some nodules evolve at the stacking faults, but others have moved to other positions, as SiO_x is liquid.

Step 3: the beads merge into nodules. The surface energy can be further reduced by increasing the size, and the curvature, as Laplace law suggests for the equilibrium between a liquid and a gas [80]. For example, SiO_x beads can move, merge and create even larger nodules. The nodules are typical of white condensates, which are produced at higher temperatures and amounts. Nodules are the equilibrium state of the oxide on a single nanowire, i.e. the state of lowest surface energy. Due to melting point depression and exothermic energy produced, the SiO_x layer will be locally liquid even if the bulk temperature is below the melting temperature of SiO_2 , that is below 1700°C .

Step 4-5: Generation of larger nodules. Nodules can further reduce their surface energy by increasing the contact area with the SiC core. This can occur where the wires cross their paths, as the oxide can grip to a larger SiC surface. The result is the generation of larger nodules at the crossing paths (diameter = 200-500 nm). Nodules here are larger than those found on a single nanowire (diameter = 50-200 nm).

An increase in temperature causes a reduction of surface energy, and hence agglomeration occurs to a higher extent. SEM analysis at different positions showed that the number of nodules increases with temperatures in all the experiments, especially when switching from blue to white condensate. This is in good agreement with research done by Hu et al. [35], [36] and Mølnås [11].

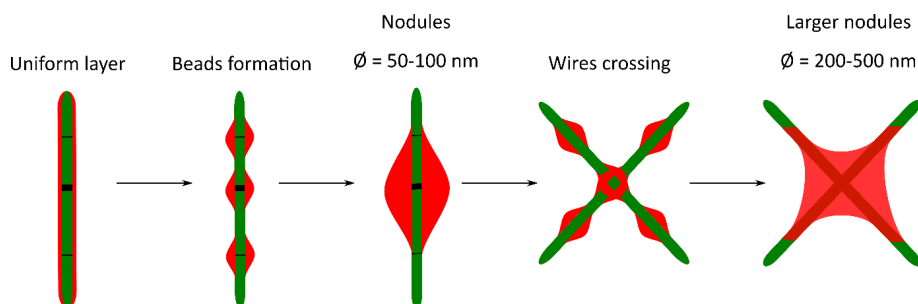


Figure 198: Nodules formation mechanism, revised after [39]. Green = solid SiC; Red = Liquid SiO_x ; black = stacking faults.

This mechanism is a layer-to-nodule mechanism, as the one described by Liu et al. [37]. However, the work by Wu et al. [39] proposes the mechanism as a nodule-to-layer transformation. The mechanism proposed by Wu et al. has a major flaw: the SiC nanowire grows first, and then follows the SiO_x deposition from the gas phase. This assertion does not respect the mass balance of Reaction 11. In fact, Wu et al. mention that the oxide molecules should deposit on SiC during growth, from the gas phase. However, the oxide should form at the substrate during seed generation, to respect the mass balance. Moreover, gas species have a low diffusivity through the oxide [78] and the SiC seed will always be covered either by the droplet or by the shell-phase.

Nodules are created during growth, above a certain temperature or SiO(g) partial pressure. In fact, they are not noticed in blue condensates, where the temperature and p_{SiO} are lower than for white condensate nanowires. The transition between blue and white condensates defines a temperature above which nodules formation is possible, which is located at about 1200-1300°C for most of the experiments carried out in this work. Longer holding times increase this temperature, as the exothermic condensation reaction is responsible for the superheated conditions. This favors formation of liquid suboxides below the bulk melting point of silica.

The whole mechanism assumes that SiO_x wets the SiC surface. This is confirmed by the contact angle measurements performed during TEM analysis. A contact angle of about 45±10° promotes wetting between SiO_x and SiC but avoids the formation of a uniform layer. The wetting between SiO₂ and SiC was also noticed in the sessile drop furnace tests on white condensate performed by Vangskåsen between 1500-1850°C [59]. Rather than separating into two different phases (as it happened instead for Si and SiO₂), the liquid SiO₂ and SiC will keep a good surface attraction and react back to SiO(g) and CO(g).

The transversal concept of the theories on nanowires growth is that SiO_x is liquid, and that it can rearrange. There are samples with clear signs of molten silicon oxides and suboxides, even at temperatures below the melting point of silica, for instance the bead structures found at 1500°C in the laboratory scale samples. The liquid state of SiO_x is also a very important point of the nodule evolution mechanism by Wu et al. [39]. SiO_x can still be present in liquid state for two possible reasons.

First, the condensation reactions are exothermic. The local temperature can increase above the melting point of silica, in the previously discussed superheated conditions. Condensation of SiO(g) and CO(g) releases a large amount of heat (Reaction 1, $\Delta H^\circ = -1393$ kJ/mol at 1700°C, according to HSC Chemistry 10®). Other condensation reaction can also contribute to a temperature rise, for example the Si-SiO₂ condensation reaction, carbide formation or solidification of Si and SiO₂ (see chapter 5B). The heat developed by the reactions can cause a temperature increase in the immediate surroundings of the nanowires, even if the measured bulk temperature is hundreds of degrees below the melting point of silica.

The heat of reaction ΔH° of the Reactions 1-4 and 12 are computed by using HSC Chemistry 10® (Figure 199). Reactions 1-3 and 12 are always exothermic in the temperature ranges typical of industrial furnaces (800-2000°C). Reaction 4 is the only endothermic reaction in the system. Steps in phase transitions occur at the melting point of silicon (1414°C) and silica (1720°C K).

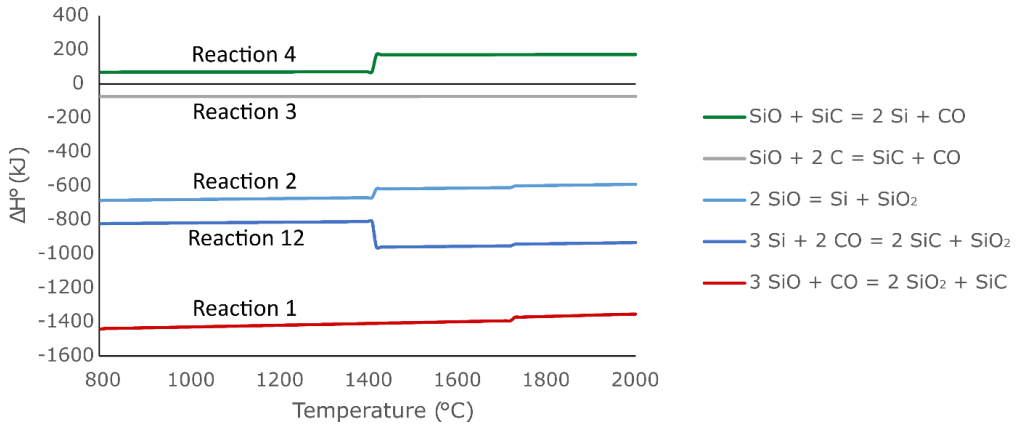


Figure 199: Temperature dependence of reaction enthalpies for Reactions 1-4 and 12.

Second, the melting point decreases in nanometric systems. This event is known as *size-dependent melting point depression* (MPD) in thermodynamics [78], [80], [105]. MPD consists in a decrease of the melting point, due to a surface energy contribution which is stronger in sub-micrometric systems. This event is not documented for silica nanoparticles, but it is considered by Noor Mohammad [78] when discussing the formation of core-shell nanowires with a core phase made of two different elements.

MPD was documented by Dick et al. [105] who report the variation of the melting point for gold nanoparticles encapsulated with silica, as a function of the diameter. The melting point decreases by approximately 100°C by decreasing the particle radius from 100 nm to 10 nm. The considered SiC-SiO_x system of this work is also nanoscaled in a similar order of magnitude, since the nanowires, beads and nodules radii range between 10-500 nm. Hence, the melting point depression effect may also be taken into consideration, as its thermodynamic theory is valid for every gas-liquid-solid system. Noor Mohammad [78] estimated that the melting point depression effect should start when the considered system is in the order of magnitude of 10-100 nanometers.

Hence, nodules transformation and liquid oxides below the melting point of bulk silica can be explained by the phenomena of melting point depression [80], [105], exothermic reaction heat and superheated conditions.

Back reaction to SiO(g) and CO(g)

Most of the SiC-SiO_x condensate is generated between 1400-1700°C. Between 1700-1800°C, the condensate amount decreases gradually, until the substrate is free from condensate deposition. Blue condensate, which is a compound found at low temperatures, may appear also at ≈1800°C. The exothermic reaction heat and superheated condition assumption could increase the temperature locally and be responsible for a back reaction to SiO(g) and CO(g). Figure 200 shows the condensation profiles of two experiments, which revealed blue condensate both at the top and at the bottom of the condensation zone. Blue condensate would form at ≈1800°C also after 1 hour holding time.

It is believed that the blue condensate at high temperatures is formed by the back reaction of the condensate to SiO(g) and CO(g). In fact, white condensate tends to react back to SiO(g) and CO(g) above 1500°C, as documented by Vangskåsen [59]. Since the reacting material is not much, the amount of SiO(g) and CO(g) should be low and condensation would happen in a short time. Hence, blue condensate formation is preferred at high temperatures, and the oxide layer cannot to reorganize into nodules.

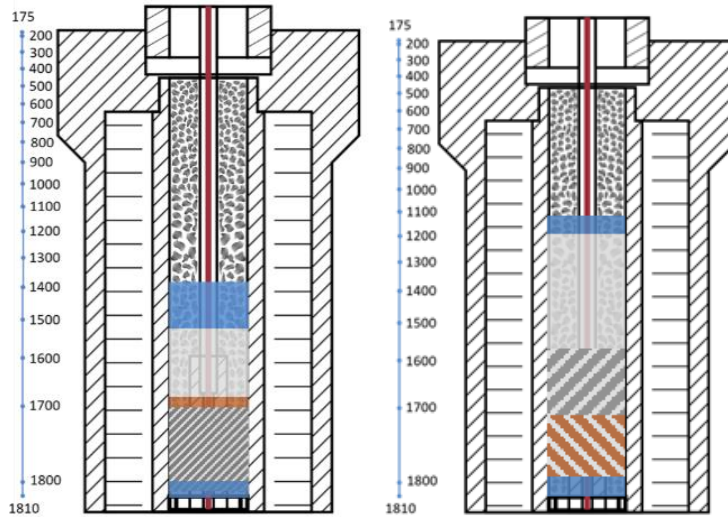


Figure 200: Condensation profiles of experiments R3a (left) and R4a (right).

The experiments in the large-scale setup show negligible amounts of blue condensate, both at the top and at the bottom of the condensation intervals. It can be that the partial pressure and temperatures were high enough to generate thick layers of nanowires. The amount of gas is higher in the large-scale setup, therefore blue condensate deposition is less likely to happen.

The gas does not condense above $\approx 1800^\circ\text{C}$. This also explains why some particles at the bottom of the condensation zone are free from condensates. The temperature at which condensation starts may be interpreted as the condensation front isotherm predicted by Otani et al. [3] and Vangskåsen [15],[59].

B. Formation and transformation of Si–SiO₂ condensate (Reaction 2)

The overall structure of the brown Si–SiO₂ condensate consists of silicon spheres immersed in a SiO₂ matrix. The morphology matches with previous works [2], [7], [11], [12], [15], [40], [53], [54], [59], [68]. The brown condensate generates at temperatures between 1400°C – 1810°C and p_{SiO} between 0.58–0.99. There is a small deviation in the expected condensate composition. The deviation is caused by the carbon content, which was detected to be between 5–10% during EPMA analysis, even if this number is uncertain. Carbon is not expected in the reaction products of the SiO(g) disproportionation ($2 \text{SiO}(\text{g}) \rightarrow \text{Si}(\text{l}) + \text{SiO}_2(\text{s,l})$) However, TEM revealed SiC nanocrystals in proximity of the Si spheres.

The formation for brown condensate was never discussed in previous works. However, a mechanism can be proposed from the results obtained both in this work and in literature. The temperature of formation of the condensate is high enough to allow both melting of silicon ($T_m=1414^\circ\text{C}$) and softening (or melting) of silica ($T_m=1723^\circ\text{C}$). These two temperatures can be considered the turning points between each mechanism step. The proposed mechanism of formation of Si–SiO₂ condensate can hence be divided into three stages.

Stage 1: Gas disproportionation and Si–SiO₂ emulsion. ($T > 1723^\circ\text{C}$). The segregation into Si and SiO₂ starts already in the gas phase, as discussed in chapter 5A. Once the (SiO)_N nanoclusters reach a surface, disproportionation into Si and SiO₂ will happen. SiO_x generates as well [47], [49], [78], despite this compound

was not clearly detected. Eventual SiO_x formed will either decompose into Si, O and SiO_2 , as described by Noor Mohammad [78]. The $(\text{SiO})_N$ ground states computed by Bromley et al. [49] must be considered to explain segregation into silicon, silica and suboxide. These were earlier discussed in chapter 5A.

Once formed, Si and SiO_2 will produce a Si- SiO_2 emulsion. In fact, both silicon and silica will be liquid, due to the local high temperature from the exothermic reaction (see chapter C). Silica and silicon are immiscible, as documented by previous works on the Si-O system [27]–[29]. Figure 201 sketches the evolution of brown condensate during Stage 1.

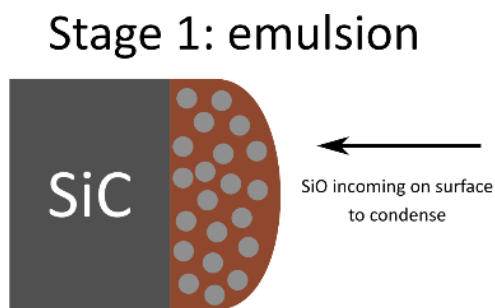


Figure 201: Stage 1: Formation of a liquid SiO_2 (brown) and Si (grey) emulsion on a SiC surface.

Stage 2: Liquid Si and solid SiO_2 ($T = 1414\text{--}1723^\circ\text{C}$). The silica matrix solidifies (or at least, becomes very viscous [60]), as the condensation heat is lost to the surroundings. The glassy appearance of the brown condensate, together with the temperature of generation, are a clear hint that the compound generated when SiO_2 was close to the softened state, and that it has cooled fast. This hypothesis was also made by previous works [11], [59], [65].

Most of the silica is in amorphous state. The compound develops cristobalite and amorphous phase at $1500\text{--}1700^\circ\text{C}$, as reported by Jusnes [60] and Sindland [71] during heating. While quartz was the starting point for Jusnes and Sindland, the liquid silica is the starting point in this work. Therefore, the partial recrystallization for brown condensate can explain the higher amount of amorphous phase in this work (64 wt.% amorphous phase, $T = 1580\text{--}1750^\circ\text{C}$ for 2 hours) compared to Jusnes (0-40 wt.% amorphous, $T = 1600\text{--}1700^\circ\text{C}$ for 0-2 hours [60]) and Sindland (12.9-24.7 wt.% $T = 1650^\circ\text{C}$ for 2 hours [71]). The conversion into a crystalline phase (i.e. cristobalite) is more efficient for brown condensate, rather than for white SiC- SiO_x nanowires (>90 wt.% amorphous phase from XRD analysis).

During stage 2, three events happen simultaneously.

Stage 2A: accumulation of Si at the outer condensate and formation of porous silica. A “fresh” brown condensate is rich in silicon and tends to have a dark brown color. Over time, the heated condensate tends to get a grey, lighter color. An exposure to high temperatures favors the separation of silicon from brown condensate. The change in the particle size distribution of the Si spheres will affect the condensate color, as hypothesized by Vangskåsen [59]. Figure 202 shows the different color tones of brown condensates in experiment R4c. The dark brown condensate comes at lower temperatures compared to the light brown sample.



Figure 202: Tones of dark and light brown in condensate sample, T = 1580-1706°C, Experiment R4c

When silicon in brown condensate is exposed to high temperatures, the largest spheres in the Si-SiO₂ emulsion would grow at the expense of the small ones, through an Ostwald-ripening mechanism. In fact, every liquid tends to reduce its surface energy by changing its shape, if exposed to high temperatures for long times. One way to reduce the surface energy is to increase the size, thus increasing the curvature [80]. The consequence of the surface energy reduction is a progressive accumulation of Si in the outer (and latest formed) condensate layers, i.e. larger Si spheres where the temperature is higher.

Figure 203 shows sphere sizes at different positions, in the same brown condensate sample. The smallest spheres are located closer to the SiC substrate (top right, black areas). The higher temperature in the external areas is maintained thanks to the exposition to the hot gas and exothermic reactions. Si droplets are repelled from the SiO₂ matrix and accumulate outside, as documented by the sessile drop furnace tests carried out by Vangskåsen [59]. In this work, however, silicon has not been found to come out from the silica matrix as visible droplets, as it happened to Ksiazek et al. [12]. Despite this difference, the comparison with Vangskåsen's results can justify the movement of silicon and its accumulation towards the external edge of the sample. As concluded by Vangskåsen [59], the driving force for the silicon migration is the surface repulsion from the silica matrix.

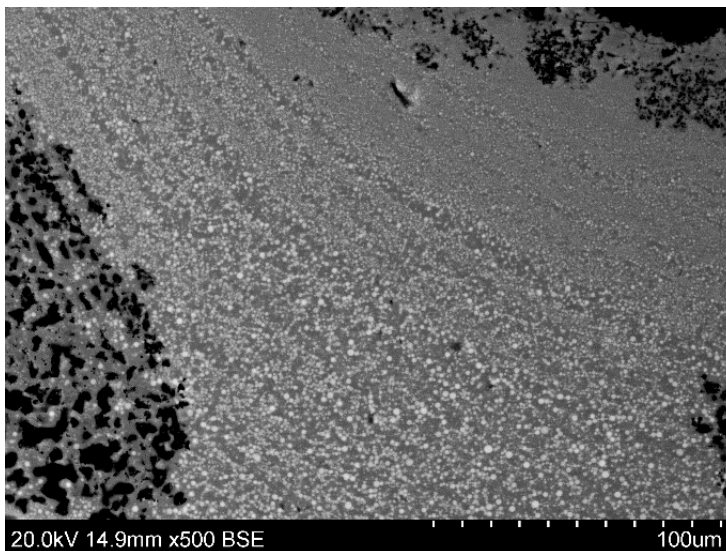


Figure 203: Sphere size distribution in a sample from Experiment 2a, T=1525-1745°C.

After the inner layers of condensate are depleted in silicon, a porous silica matrix is left. Porous silica was found in many brown condensates samples in this work, both an industrial and laboratory scale. The results showed also that the pores size and the silicon droplets size are comparable, both at laboratory and industrial scale. The transformation of brown condensate into porous silica is triggered by a prolonged exposure to temperatures around $\approx 1600^{\circ}\text{C}$ and above, which are reached in the condensation zone for both the small- and the large-scale setup. For example, porous silica was noticed at $T = 1590^{\circ}\text{C}$ in experiment IF4 (Figure 204). Hence, recognizing transformed brown condensate can be a useful method to trace the temperature evolution in an industrial furnace. Vangskåsen's sessile drop experiments [59] demonstrated that the brown condensate turns into porous silica when exposed at temperatures between $1750\text{--}1800^{\circ}\text{C}$ for 0-30 minutes. Figure 205 sketches the movement of Si in the silica matrix, and the transformation of brown condensate into porous silica.

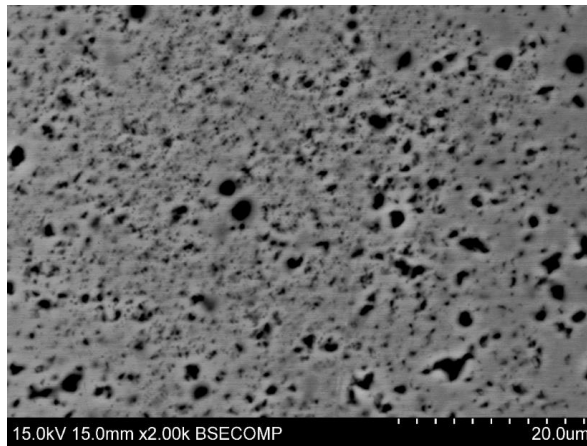


Figure 204: Pores of porous silica from experiment IF4, $T = 1590^{\circ}\text{C}$.

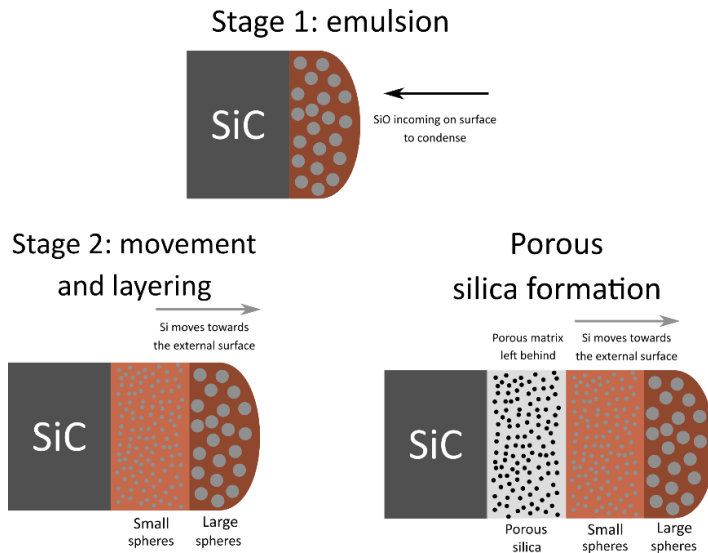
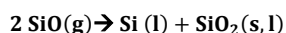


Figure 205: Stage 1: emulsion of Si(grey) and SiO₂ (brown) in Si-SiO₂ condensate. Stage 2: Movement of Si in a SiO₂ matrix containing Si spheres at different average size. Porous silica (light grey) is formed after Si depletion caused by prolonged exposition to high temperatures.

Stage 2B: Alternate layer structures. The alternate layer microstructure in Si-SiO₂ condensate is characterized by SiO₂ matrix domains with similar thickness (10-20 μm). A domain with small Si spheres (50-200 nm diameter) is alternated with another domain with large Si spheres (0.2-3.0 μm diameter) (Figure 206). This implies that the local temperature oscillated and changed often locally, as if a cyclic series of events were taking place. The cycle is believed to consist of two steps (Figure 207).

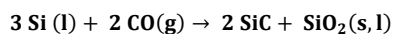
In the first step (2.1), the condensate deposits on the surface and heat is released to the immediate surroundings, i.e. Stage 1 occurs and condensation may stop for a short time. The gas around the condensate is heated by the reaction heat of four reactions and becomes stable again right after condensation. These reactions are:

- 1) **The condensation reaction itself (Reaction 2)**, ($\Delta H^\circ = -610\text{kJ/mol}$ at 1700°C). Part of the Si and SiO₂ may vaporize at the superheated temperature (above 2230°C), which may even produce Si and SiO₂ species. This could alter the gas composition, as Si(g) and O(g) species are more stable at this temperature range (see chapter 5A for a detailed explanation of the superheated conditions). The superheated temperature may be similar to the the SiC-SiO_x condensate, as part of the SiO₂ may also evaporate above 2200°C.



Reaction 2

- 2) **SiC formation from Si and CO(g)** (Reaction 12, $\Delta H^\circ = -980\text{kJ/mol}$, at 1700°C). This reaction releases a higher amount of kJ/mol compared to reaction 2, but Si-SiO₂ condensation occurs to a major extent, despite its lower amount of developed heat.



Reaction 12

- 3) **Solidification of silicon and silica** also release heat, but in minor amounts ($\Delta H^\circ = -50$ and -10 kJ/mol respectively [98]).

As condensation stops in step 2.1, step 2.2 takes place. The spheres can accumulate and move out of the matrix, while reducing their surface energy by merging. The spheres growth occurs faster at higher temperatures. Once the external surface has also cooled down by releasing heat, the gas becomes unstable again, and condenses on the cold surface. The stability of the gas during this cycle is discussed in detail in Chapter 5C, while presenting the p_{SiO}-T curves for brown condensate.

Step 2.3 and 2.4 correspond to 2.1 and 2.2, when the cycle is repeated. The difference is that steps 2.3 and 2.4 involve also the Si depletion from the inner layers, and the formation of porous silica.

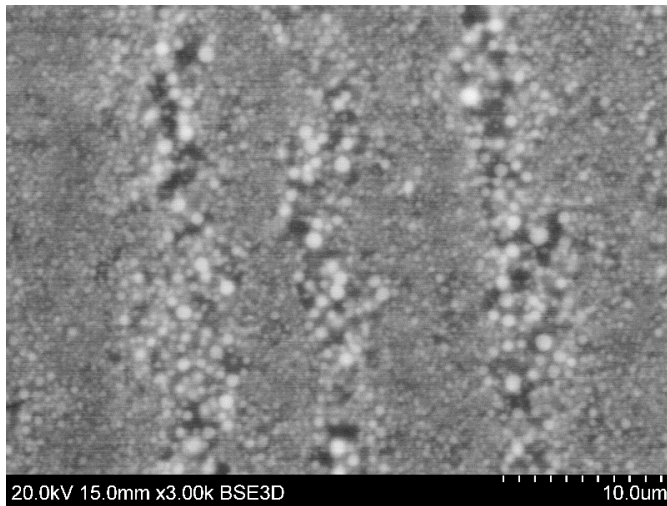


Figure 206: Sphere size distribution in the same sample. Experiment R2a, T=1525-1745°C (Sample 8 from Table 26).

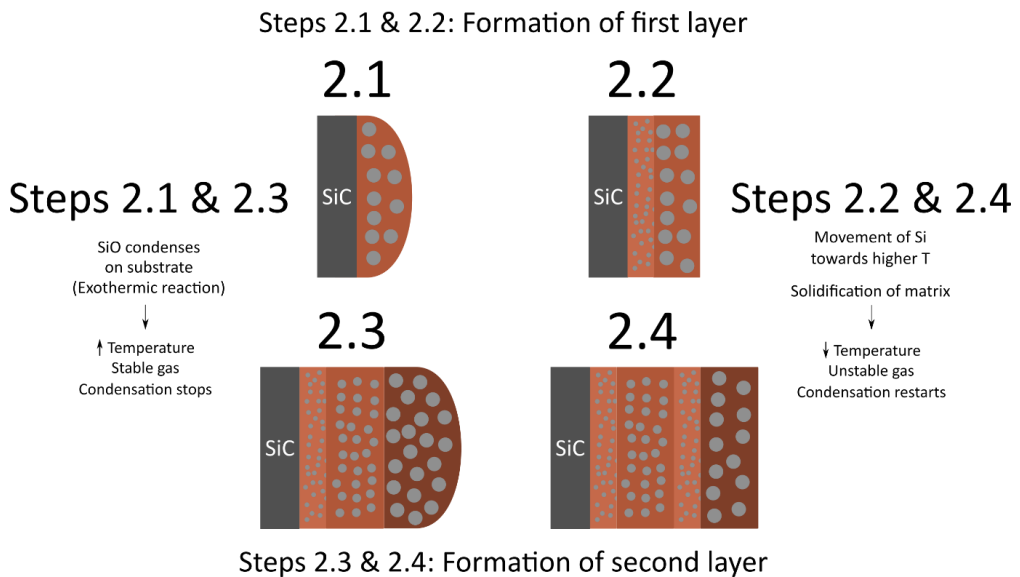


Figure 207: Sketch of the layer evolution in brown condensate.

Stage 2C: Formation of cracks. A temperature gradient will generate through the condensate, when generating alternate layer structures. The temperature difference will give thermal internal stresses, which could be one of the causes of crack formation (Figure 208a). Porous silica is an excellent insulator and can crack easily under thermal stress, in the temperature range typical of stage 2 [60]. Jusnes showed that thermal shock for quartz takes place after 10 minutes at 1500°C during heating.

Silicon expansion can be another cause for crack formation. Silicon expands under solidification. The internal stresses created in this way may be responsible for crack formation. If cracks are created, part of the Si from

another droplet could still flow through them. Figure 208b shows a silicon tread which connects two different silicon spheres. The solidification front is clearly visible on the left side of the wire.

A third cause for crack formation may be the back reaction to SiO(g) from (Reaction -2), or SiC formation from Si and CO(g). Since Si and SiO₂ are still in contact, the condensate can react back to SiO(g) between 1400-1700°C, as proposed by Andersen, Bao et al. and Sindland [69]–[71]. The same can be said when Si reacts with CO(g) to generate SiC nanocrystals [100]. The production of SiC nanocrystals is discussed in detail in the next subchapter. Finally, temperature oscillations can favor shock heating and crack formation in quartz, as demonstrated by Jusnes [60]. Brown condensate does not form at constant temperature, as described in Stage 2B. This event might be responsible for temperature oscillations, which could be the cause for crack formation in quartz.

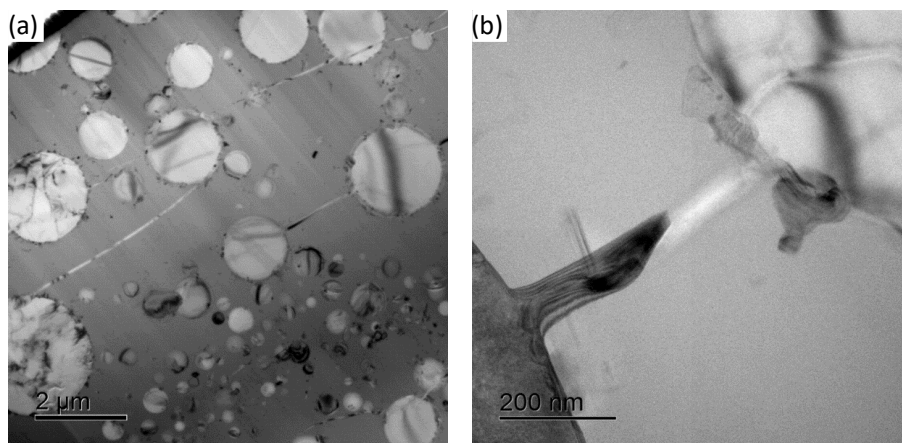


Figure 208: Brown condensate from Experiment R1b. Left: Cracks in FIB sample; Right: Junction wire-sphere in FIB sample

Stage 3: The microstructure freezes ($T < 1414^\circ\text{C}$). When the local temperature is below the melting point of silicon, the final microstructure cannot change anymore. However, the shock heating of quartz could still be present at 1300°C, as demonstrated by Aasly [106] and by thermal shock of industrial quartz between 700-1300°C [107].

Formation of SiC

FIB-TEM analysis of brown Si-SiO₂ condensate revealed nanometric SiC particles at the interface between Si and SiO₂ (Figure 209). This SiC makes 5-10 wt. % of the brown condensate mass, according to EPMA analysis. However, it must be remembered that C measurement is semi-quantitative for C. EPMA has a limited resolution, therefore the conclusion of EPMA is that the SiC *may* be present in the condensate.

On the other hand, TEM analysis clearly shows the presence of SiC nanocrystals. Traces of C with Si are detected by EDX-TEM mapping inside the silicon spheres, as shown in Figure 209c. Scattering effects of SiC nanocrystals can also be responsible of the weak carbon signals in the spheres. As the sample is a thin slice of condensate, SiC could be present on other positions of the sphere surface.

There is a deviation in the carbon content from the expected theoretical composition (50 mol. % Si, 50 mol. % O). In fact, all the used characterization techniques revealed the presence of carbon (or carbide, for TEM), which does not appear in the products of Reaction 2. This also happened in previous works [11], [54], but no clear explanation was given to explain the presence of carbon in brown condensate.

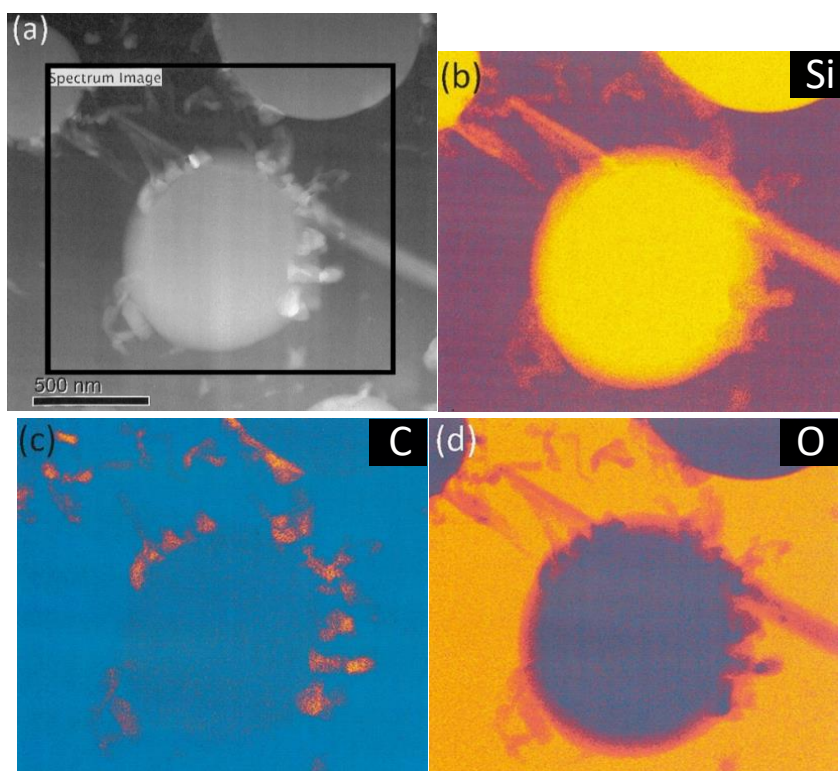
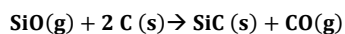


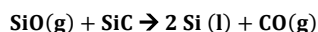
Figure 209: Elemental EDX mapping of a sphere collected from the FIB-sample: survey area (a). Silicon (b), Carbon (c) and Oxygen (d) mapping.

The presence of SiC can be explained by the interaction of CO(g) with the Si in the condensate. The main carbon source will be CO(g) ascending from the gas production zone. CO(g) can also be produced by ascending SiO(g) reacting with C on the graphite walls, which will give SiC and CO(g) (Reaction 3).

CO(g) cannot originate from SiC substrates, since they react scarcely with SiO(g) between 1400-1800°C. This can be verified from the experience in the industrial silicon process, where the temperature in the bottom zone is raised to 2000°C to produce Si and CO(g) from SiC and SiO(g) (Reaction 4).



Reaction 3



Reaction 4

Hence, CO(g) can react with Si to generate SiC by two different mechanisms:

Mechanism 1: Dissolution of carbon in liquid silicon and precipitation of SiC. C will dissolve into Si by interacting with CO(g). However, the C signal in TEM analysis is negligible and not quantitatively reliable. In fact, from the literature regarding carbon dissolution in Si, one can estimate that the order of magnitude of dissolved C in Si ranges between $10^{-2} - 10^{-4}$ at. % C [19]. An equation written by Durand and Duby [108] assesses that the molar fraction of carbon in liquid silicon X_C^L at a fixed temperature between 1414-2820°C is

$$\log(X_C^L) = 2.714 - \frac{10623}{T(K)} \quad \text{Equation 17}$$

Equation 17

The equation is valid when liquid silicon is in equilibrium with precipitated SiC and dissolved C. For example, at T= 1700°C, the theoretical amount of X_C^L is 0.002. This corresponds to a 0.2 at. % C dissolved in liquid silicon, before segregation starts. The value can be compared to an estimation made on Figure 209c, which is described in Appendix I. The figure analysis brought to an estimation of 5 at.% C. The amount of SiC generated at the sphere boundary is larger compared to Durand and Duby's results. This also supports the theory that condensation does not occur at equilibrium conditions, since Equation 17 is based on an equilibrium assumption. As silicon cools down (or while its temperature is constant), the value of X_C^L decreases and SiC precipitates. Silicon cannot dissolve more carbon unless the temperature increases again. Therefore Mechanism 1 should be relevant only when the temperature is oscillating.

Mechanism 2: Reaction between Si and flowing CO(g). Continuous dissolution and precipitation would be possible only when CO(g) can reach Si by flowing through the matrix, i.e. when both Si and SiO₂ were liquid. It is proposed that liquid Si interacts with CO(g) through Reaction 12



The SiC protuberances could also be the starting step of a nanowire's growth process, which stopped because of slow diffusion of the gas through the SiO₂ dense liquid matrix [78]. SiC would be incorporated in the Si-SiO₂ condensate over time and SiC growth would stop while cooling. The nanocrystals found in Figure 209c resemble small clusters, from which nanowires growth could be possible.

Previous works studied the interaction between Si(l) and CO(g). Lim [100] and Antipov [109] discovered that reaction between Si powders and CO(g) at 1300-1400°C can form SiO₂-SiC nanowires with diameters ranging between 50-100 nm. The nanocrystals diameter in this work are in the same order of magnitude as the nanowires, and the mechanism can be considered as a valid hypothesis. SiC and SiO_x nanoclusters are the basis for the growth of SiO_x-coated SiC nanowires [33], [35]–[37], [39], [77], [78]. Such nanowires grow as 3C-SiC crystals, as demonstrated by the XRD and TEM analysis, both in this work and in the listed references.

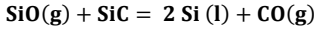
C. Mass balance, thermodynamics and kinetics

p_{SiO}-T curves and equilibrium conditions

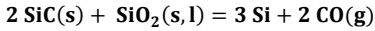
The p_{SiO}-T lines of the experiments are compared to the equilibrium SiO(g) partial pressures and temperature of some the reactions of the silicon production process. The reactions chosen are Reactions 1-4,12. The equilibrium constants K_{eq} for the reactions were calculated by the software HSC Chemistry 9®. The total pressure was set at 1.5 atm. Appendix E shows how the equilibrium curves shift by changing the total pressure from 1 to 1.5 atm. From these constants and their dependence on temperature, it is possible to obtain five curves, which will be called *equilibrium p_{SiO}-T curves* (or just equilibrium curves).

If the real p_{SiO} is lower than the p_{SiO} given by the curve, or at its left side, the reagents are stable. Vice versa, the products are stable if the real p_{SiO} is higher than the curve or is located on the right-hand side.





Reaction 4



Reaction 12

The equilibrium curves are compared with the p_{SiO} -T lines from the experiments in Figure 210-Figure 213. The straight lines are the experimental p_{SiO} values as a function of T, in the condensation zone. A line is continuous where the condensate forms and dashed where the reaction is not occurring. Figure 210 collects groups of the small-scale experiments according to their injected He flow, whereas in Figure 211 the large-scale experiments are grouped. The five main conclusions from these figures are:

1. The partial pressures of the system are far from equilibrium conditions, for both Reaction 1 and 2. This is not obvious, as the corresponding gas production reactions are believed to occur at equilibrium conditions according to previous works [40], [65], [69]. Condensation is hence added to the group of reactions which do not occur under equilibrium conditions in the Si process. This group includes SiC production [22] and the silicon production reaction itself. All of them are slow reactions, which clearly occur out of equilibrium conditions, according to industrial experience.

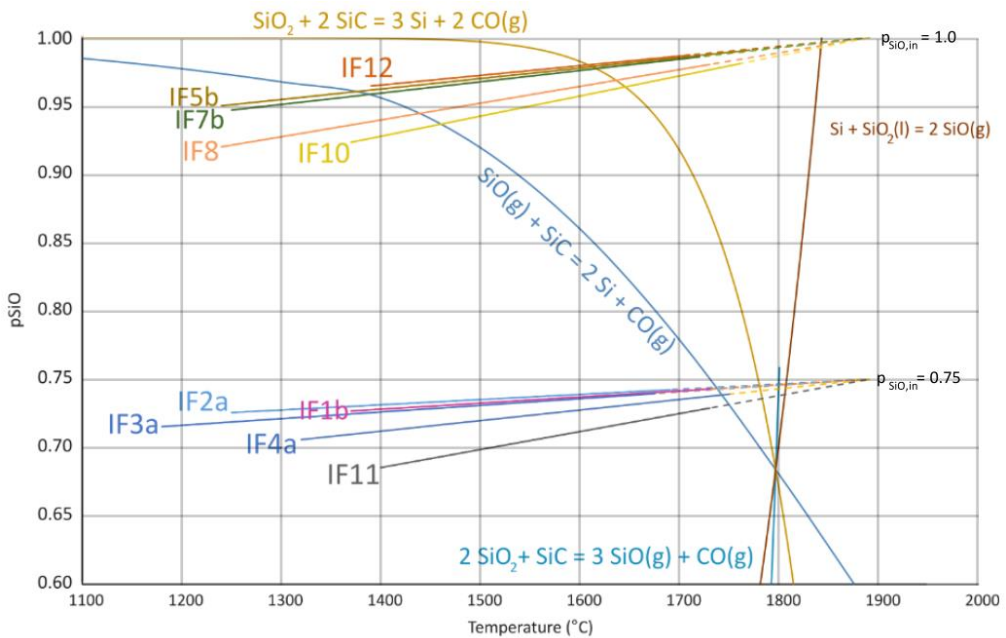


Figure 210: SiC-SiO₂ condensation (Reaction 1): p_{SiO} -T lines for the large-scale setup experiments compared to the equilibrium curves for the reactions in silicon production.

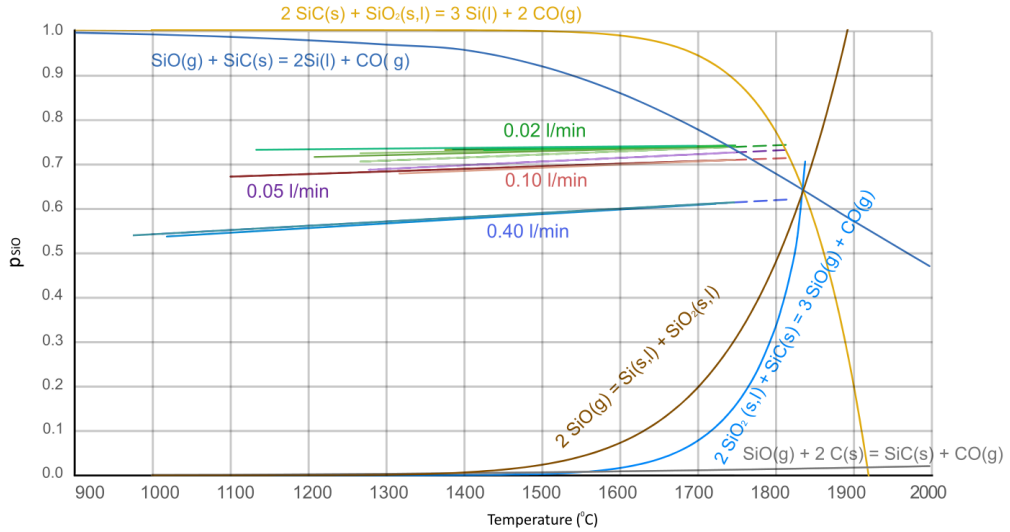


Figure 211: SiC-SiO₂ condensation (Reaction 1): p_{SiO₂}-T lines for the small-scale setup experiments compared to the equilibrium curves for the reactions in silicon production.

2. The superheated conditions can explain the formation of alternate layer structures and the back reaction to SiO(g) and CO(g). The curves for Si-SiO₂ condensation are collected in Figure 212 and Figure 213 and divided as before between the small- and large-scale setups. When the p_{SiO₂}-T lines lay on the right hand-side of the reaction curves, the gas mixture is thermodynamically stable. The exothermic condensation reactions need to increase the local temperature by at least 200°C, in order to make the gas stable. The temperature is expected to reach about 2500°C locally, as discussed earlier for the superheated conditions in the Si-SiO₂ condensation mechanism. The p_{SiO₂}-T line is shifted to higher T in the graph. Hence, the gas production reactions would stop for a short time, until the gas is cooled below the maximum temperature. This justifies the formation of layer structure in brown condensate. The same explanation can be done for SiC-SiO_x nanowires condensation (Reaction 1), where the effect shifts the local temperature up, favoring the back reaction to SiO(g) and CO(g).

3. The presence of SiC nanocrystals is depending on the local temperature of the Si spheres, according to thermodynamics. Reaction 12 ($3 \text{ Si} + 2 \text{ CO(g)} \rightarrow \text{SiO}_2 + 2 \text{ SiC}$) is happening at the silicon spheres borders, where SiC nanosized crystals are noticed. Only the largest Si spheres were surrounded by SiC nanocrystals in the FIB-TEM sample. The smallest Si spheres, which are newly formed from the exothermic condensation reaction, could be hot enough to hinder the formation of SiC. Hence, SiC nanocrystals are produced at low temperatures or in larger, colder Si spheres, i.e. only below the equilibrium curve for Reaction 12.

Consequently, SiC nanocrystals are expected to form spontaneously also from gases at lower p_{SiO₂}, as the concentration of CO(g) is higher and would push the reaction towards SiC production. This needs to be confirmed experimentally by TEM analysis on Si-SiO₂ condensate produced from a gas at p_{SiO₂}>0.75, as the effect of p_{SiO₂} on the SiC crystallite formation was not investigated.

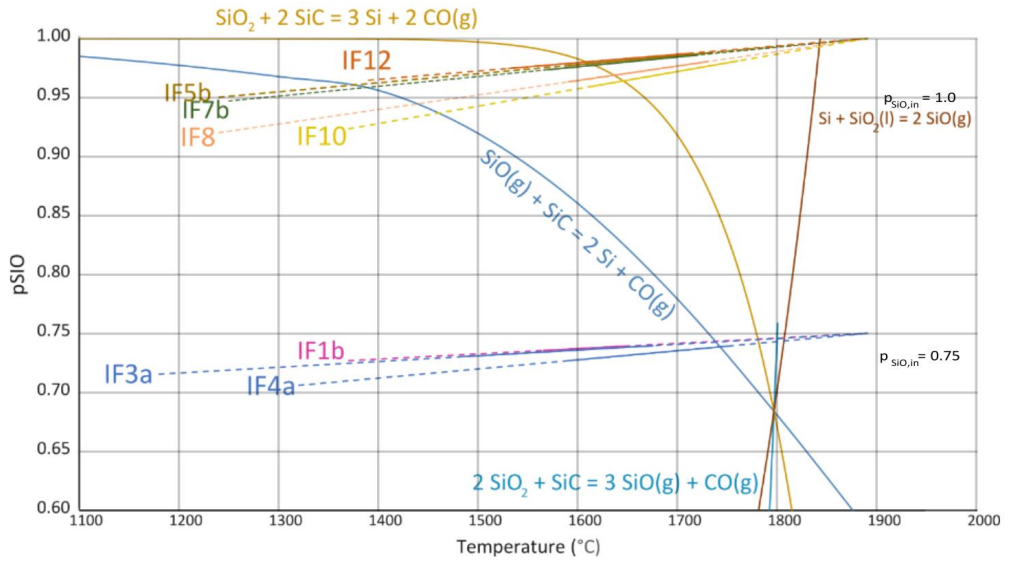


Figure 212: Si-SiO₂ condensation (Reaction 2): p_{SiO}-T lines for the large-scale setup experiments compared to the equilibrium curves for the reactions in silicon production.

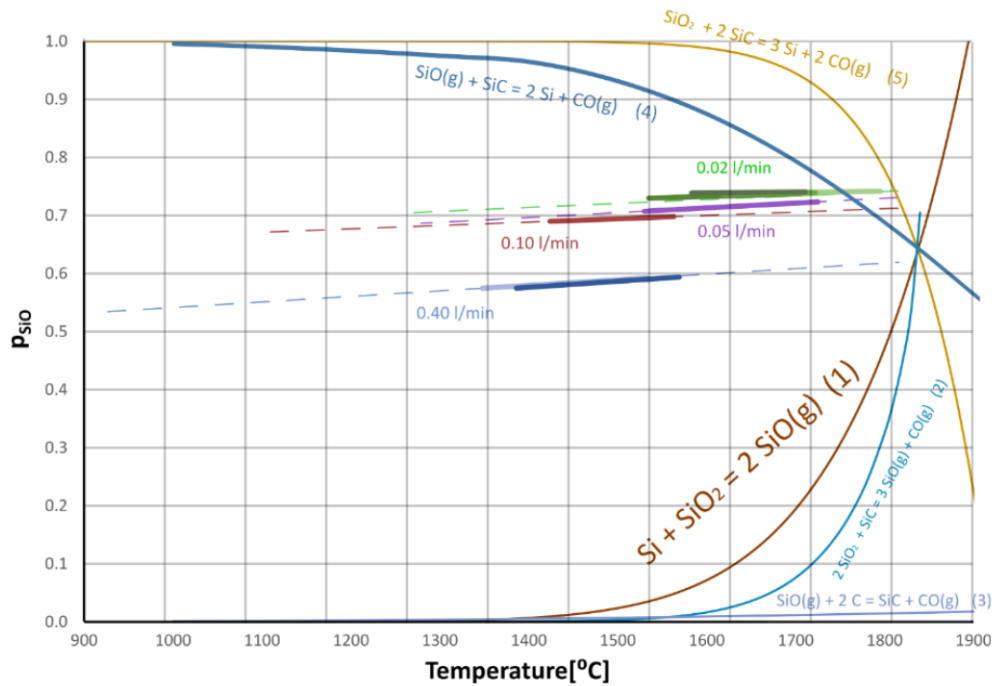


Figure 213: Si-SiO₂ condensation (Reaction 2): p_{SiO}-T lines for the small-scale setup experiments compared to the equilibrium curves for the reactions in silicon production.

4. By condensation only, the partial pressure of the gas decreases by 0.1 every ≈ 1000 K. The slope of the p_{SiO} -T lines expresses how the partial pressure decreases through the condensation chamber, by the combination of Reaction 1 and 2. The p_{SiO} -T lines are expressed by the equation $p_{SiO} = \gamma T + \delta$.

The slope γ is calculated only by considering the incoming and outgoing p_{SiO} in the system and based only on the gas involved in condensation. The slope is calculated by the formula

$$\gamma = \frac{p_{SiO,in} - p_{SiO,out}}{T_{SiO,in} - T_{SiO,out}} \quad \text{Equation 18}$$

The slope γ ranges between $1-15 \cdot 10^{-5}$ (K^{-1}) (the values are listed in Appendix D). The slope is hence a very small number, implying that the partial pressure decreases slowly through the crucible. The slope is small because the partial pressure difference is low, the temperature interval is broad, and the condensation is a slow reaction. A steeper slope means a higher drop in p_{SiO} through the chamber, i.e. more Si-SiO₂ condensates are produced.

The values of the slope of the p_{SiO} -T curves have the same order of magnitude in the large- and small-scale experiments. They could be used also in other setups, or even at industrial scale, to estimate the partial pressure variations caused by condensation in an industrial furnace. Other reactions, such as Si production and SiC production, would also contribute to the decrease in SiO(g) content in the gas, as described in the previous section "SiO losses due to other reactions".

5. The values of $p_{SiO,out}$ are higher than a typical off-gas from an industrial furnace. The intercept of the p_{SiO} -T lines expresses the value of $p_{SiO,out}$ if condensation ended at $T = 0$ °C. The intercept (called δ in Appendix D) ranges between 0.4-0.7, whereas industrial furnaces offgas at 700-1000°C [1], [14] with a calculated $p_{SiO,out} = 0.05-0.10$. The main reason of this difference is that condensation is a slow reaction. Again, other reactions contribute to the SiO(g) recovery more than condensation does, such as Si production and SiC production.

Activation energy and statistical significance

The activation energy for the condensation of SiC-SiO_x nanowires was calculated to be 250-300 kJ/mol, in the temperature range 1315-1750°C. Table 47 shows the activation energy found for SiC-SiO_x condensation, comparing it with nanowires formation and other reactions typical of the silicon production process. The values of this work are comparable to those found by Liu et al. and Wallis et al. [102], [104] for SiC nanowires formation, even if they were found in different temperature intervals. The other reactions listed in the table generally have a higher activation energy value.

Between the 7 kinetic models chosen, Model 3b and Model 4 gave the highest value of the coefficient of determination R^2 . However, the variance and the statistical significance of the model changes with temperature. If the kinetic constant $k(T)$ is divided into four temperature intervals (1300-1405°C; 1405-1505°C; 1505-1620°C; 1620-1685°C), the value of R^2 decreases from 0.48 to 0.19 (or from 0.43 to 0.06 for Model 4). The activation energy becomes negative in this last interval. The physical meaning of a negative activation energy can be interpreted as a tendency for the reaction to be hindered between 1620-1685°C. In fact, a lower amount of condensates is usually present in this temperature interval. However, a negative E_a value may also come from the low statistical significance of the interpolation ($R^2 = 0.19$ and 0.12). Hence, it is not simple to get a good fitting for the reaction rate models over the whole temperature interval.

$$\begin{aligned} \text{Model 3b} : R^2 = 0.8072 & \quad \frac{dm}{dt} = k(T) \cdot A \cdot (p_{SiO})^3 (p_{CO}) \\ \text{Model 4} : R^2 = 0.7100 & \quad \frac{dm}{dt} = k(T) \cdot A \cdot (p_{SiO} - p_{SiO,eq}) \end{aligned}$$

Table 47: Comparison of activation energies in silicon production reactions and nanowires production

Reaction / phase transition	Author	Temperature (°C)	E _a (kJ/mol)
$3 \text{ SiO(g)} + \text{CO(g)} \rightarrow 2 \text{ SiO}_2 + \text{SiC}$	This work	1315 – 1750	250 – 300
$\text{SiO(g)} + 2 \text{ C} \rightarrow \text{SiC (NW)} + \text{CO(g)}$	Liu et al. [104]	900 – 1100	345
	Wallis et al. [102]	1040 – 1550	254 ± 36
$\text{Si} + \text{SiO}_2 \rightarrow 2 \text{ SiO(g)}$ (Reaction -2)	Sindland [71]	1650 – 1950	557
	Andersen [69]	1450 – 1910	528
	Filsinger and Bourrie [110]	1410 – 1610	348
$2 \text{ SiO}_2 + \text{SiC} \rightarrow 3 \text{ SiO(g)} + \text{CO(g)}$ (Reaction -1)	Tangstad et al. [97]	1650 – 2000	424 – 464
	Ni [111]	1650 – 1700	15.9 – 195
	Andersen [69]	1450 – 2000	370 – 420
	Filsinger and Bourrie [110]	1460 – 1800	348
	Bao et al. [70]	1550 – 1820	351
	Khrushchev [73]	1800 – 1900	794 – 823
	Pultz and Hertl [72]	1270 – 1430	406 – 548
$\text{SiO(g)} + 2 \text{ C} \rightarrow \text{SiC} + \text{CO(g)}$ (Reaction 3)	Filsinger and Bourrie [110]	1460 – 1660	472
	Shimoo et al. [112]	1600 – 1700	429
$\text{SiO}_2 + 3 \text{ C} \rightarrow \text{SiC} + 2 \text{ CO(g)}$	Ono and Kurachi [113]	1500 – 1800	391
$\text{SiO(g)} + \text{SiC} = 2 \text{ Si} + \text{CO(g)}$	Filsinger and Bourrie [110]	1690 – 1800	505
$\text{SiO}_2 \text{ (quartz)} \rightarrow \text{SiO}_2 \text{ (amorphous)}$	Jusnes [60]	1550 – 1700	100 – 500
$\text{SiO}_2 \text{ (amorphous)} \rightarrow \text{SiO}_2 \text{ (cristobalite)}$	Jusnes [60]	1550 – 1700	100 – 1300

Despite the values for E_a in the four temperature ranges are in the same order of magnitude, the values of k₀ change between 10⁶ – 10⁷ g cm⁻² mol⁻¹, as shown in Table 48 for model 3b. The change for k₀ is stronger for model 4, where the value changes between 10⁶-10¹ g cm⁻² mol⁻¹. However, the strong decrease in R² in the temperature interval 1405-1505°C affects the statistical significance of the model. The reaction rate model is therefore complex, as four driving forces are interacting:

- **A**: its value does not depend on temperature, but on the measurement method. A change with the thickness of the selected temperature interval.
- **k(T)**: the reaction constant has the assumed Arrhenius dependence, implying that it increases exponentially with temperature.
- **p_{SiO}(T)**: the partial pressure increases linearly with temperature, as assumed during the p_{SiO}-T calculations.
- **Driving force (DF)**: this term is either almost constant or decreasing with temperature. The next section will focus on the DF term for model 4.

Table 48: Values of E_a , k_0 and R^2 for model 3b and model 4 in different temperature ranges.

Model 3b $r = k(T) \cdot A \cdot (p_{SiO})^3 (p_{CO})$				Model 4 $r = k(T) \cdot A \cdot (p_{SiO} - p_{SiO,eq})$			
T range (°C)	E_a (kJ/mol)	k_0 (g cm ⁻² mol ⁻¹)	R^2	T range (°C)	E_a (kJ/mol)	k_0 (g cm ⁻² mol ⁻¹)	R^2
1300 - 1685	$2.79 \cdot 10^5$	$3.05 \cdot 10^5$	0.80	1300 - 1685	$2.42 \cdot 10^5$	$1.50 \cdot 10^3$	0.71
1300 - 1405	$3.45 \cdot 10^5$	$4.43 \cdot 10^7$	0.48	1300 - 1405	$3.88 \cdot 10^5$	$8.04 \cdot 10^7$	0.44
1405 - 1505	$3.07 \cdot 10^5$	$1.91 \cdot 10^6$	0.42	1405 - 1505	$1.24 \cdot 10^5$	$3.77 \cdot 10^{-1}$	0.06
1505 - 1620	$3.65 \cdot 10^5$	$8.41 \cdot 10^7$	0.32	1505 - 1620	$3.45 \cdot 10^5$	$1.2 \cdot 10^6$	0.27
1620 - 1685	$-3.27 \cdot 10^5$	$1.22 \cdot 10^{-11}$	0.19	1620 - 1685	$-3.01 \cdot 10^5$	$2.64 \cdot 10^{-12}$	0.12

The driving force for condensation of SiC-SiO_x condensates

After modelling of Reaction 1, it was concluded that model 4 fits the experimental results best. In fact, model 4 can explain clogging, the distribution of condensates and the effect of the inert gas on the rate. However, model 3b has a higher value for R^2 compared to model 4. Appendix D presents a description of the driving force for model 3b and a comparison with mode 4.

The driving force for condensation in model 4 and the condensates distribution in the chamber have a similar dependence on temperature. This distance from equilibrium can be interpreted as a driving force for the reaction rate. The value of the driving force can be expressed as

$$DF = p_{SiO}(T) - p_{SiO,eq}$$

Equation 19

The driving force follows a bell-like trend, as shown in Figure 214a. DF increases slowly with temperature, then it reaches its maximum at around 1600°C for the SiO₂-SiC and 1400°C for the Si-SiO₂ mixture formation. Above ≈1650°C, the driving force decreases again, since $p_{SiO,eq}$ increases. It is expected that the driving force for Si-SiO₂ condensates will follow a similar equation, but with a steeper increase and decrease at the extremes of the condensation intervals.

The gas production reactions prevail from ≈1700°C. In fact, most of the condensate is found between 1400-1700°C, as it was seen for the distribution of condensates in the condensation zone. Besides, white condensate reacts back to SiO(g) and CO(g) above 1500°C, as found by Vangskåsen in the sessile furnace drop tests [15], [59]. There is a parallel between how the condensate reacts back to SiO(g) and CO(g), and how the driving force for condensation decreases, as the equilibrium p_{SiO} and T conditions get closer. The maximum in driving force coincides with the temperature intervals where most of the condensation occurs (1400-1700°C).

Moreover, Figure 214 shows that a higher injected He flow shifts the p_{SiO} -T curve to lower p_{SiO} values. A lower $p_{SiO,in}$ gives a lower condensation yield, and DF is lower for a higher injected He flow. In practical terms, if the gas flow is higher, the gas condenses at lower temperatures, as demonstrated in the analysis of the temperature of formation. SiC-SiO_x condensate is formed over a large temperature area 900-1810 °C, however the largest amount is formed between 1400-1700°C. Below 1400°C the reaction is too slow (i.e. $k(T)$ decreases quickly) and will not occur to a large extent, despite DF is still high. Above 1700°C the temperature is too high, and the driving force will be low.

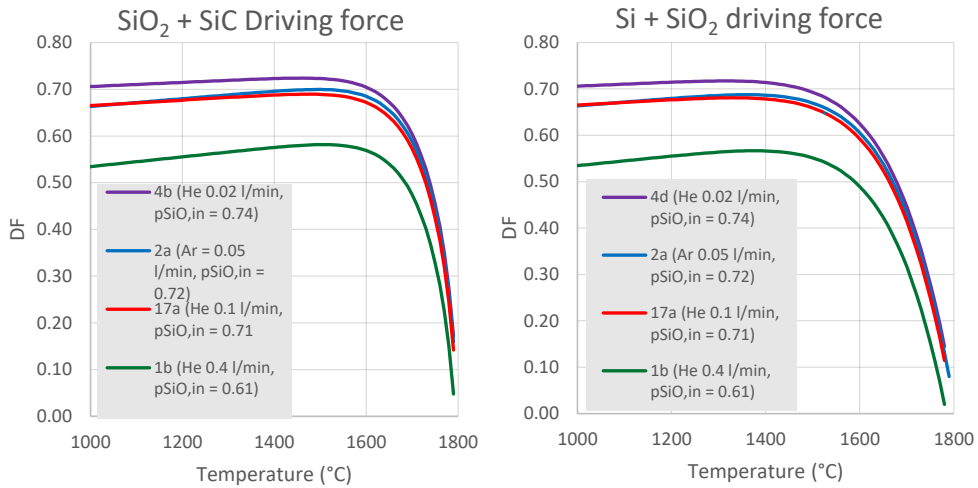


Figure 214: Driving force as a function of injected inert gas flow. Left: SiC-SiO_x condensation (Reaction 1); Right: Si-SiO₂ condensation (Reaction 2).

Condensation yield, mass distribution and clogging

The clogging intervals are located in correspondence of the maximum rate. By comparing the results of the kinetic modelling with the clogging intervals, it was seen that the maximum rate and condensate amount is reached in correspondence of the clogging intervals. Figure 215 shows the rate as a function of temperature, for the experiments IF2a (red), IF4 (blue) and IF5b (green). Both the rate and the condensates amount increase, then they reach a maximum, and finally decrease again. The increase occurs in correspondence of the clogging intervals, written in the graphs. It can be concluded that clogging intervals and the maximum condensation rate are related.

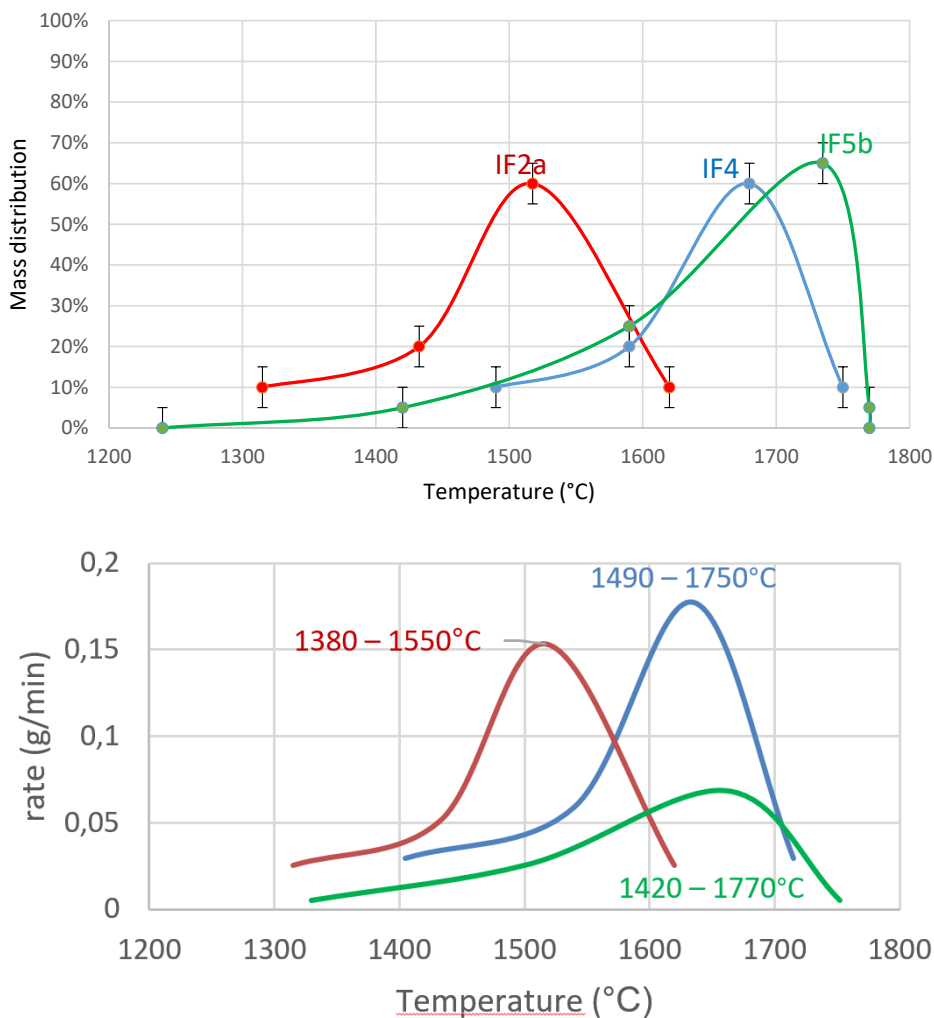


Figure 215: Correspondence between mass distribution (top) and condensation rate (bottom) vs temperature and clogging interval. The clogging interval is written in the graph below. Experiments IF2a (red), IF4 (green) and IF5b (blue). Error bars on mass percentage are $\pm 5\%$.

The condensates distribution in the chamber is not related to the amount of condensates produced (m_{cond}) and reaction time (t_r). Figure 216 shows that the experiments with different m_{cond} (and longest reaction times t_r) have similar mass distributions. The figure compares experiments IF5b ($t = 2\text{ h}$, $m_{cond} = 21\text{ g}$), IF 10 ($t = 30\text{ min}$, $m_{cond} = 20\text{ g}$) and IF 12 ($t = 10\text{ min}$, $m_{cond} = 16\text{ g}$). At short times (red line), however, most of the condensates are concentrated in a small temperature area. As time passes, the distribution keeps the same shape, and some of the condensates reaches the lowest temperature zones (orange line). As a result, the clogging interval width increases with time and condensates appear at lower temperatures, as demonstrated in section 3D and 3E.

Distribution of mass in condensation zone

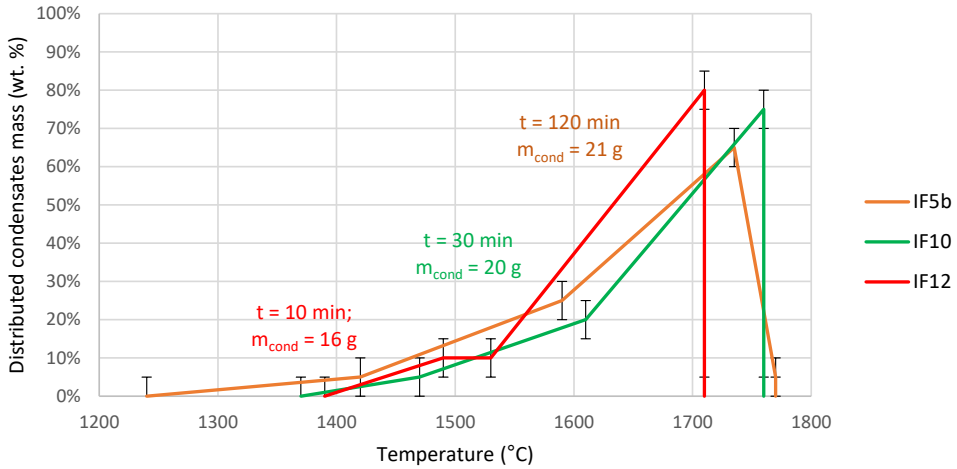


Figure 216: Condensates distribution as a function of temperature, related in experiments at different total condensates mass m_{cond} . Constant parameters: PSD 3-10 mm, $p_{\text{SiO}_2, \text{in}} = 1.0$. Error bars on mass percentage are $\pm 5\%$.

There is an indication that the condensation yield increases with a larger $p_{\text{SiO}_2, \text{in}}$, a narrow PSD, and a large diameter. Each of these effects can be analyzed separately by comparing this graph with the results obtained so far. Figure 217 shows the condensation yield as a function of particle size and width, at different gas pressures.

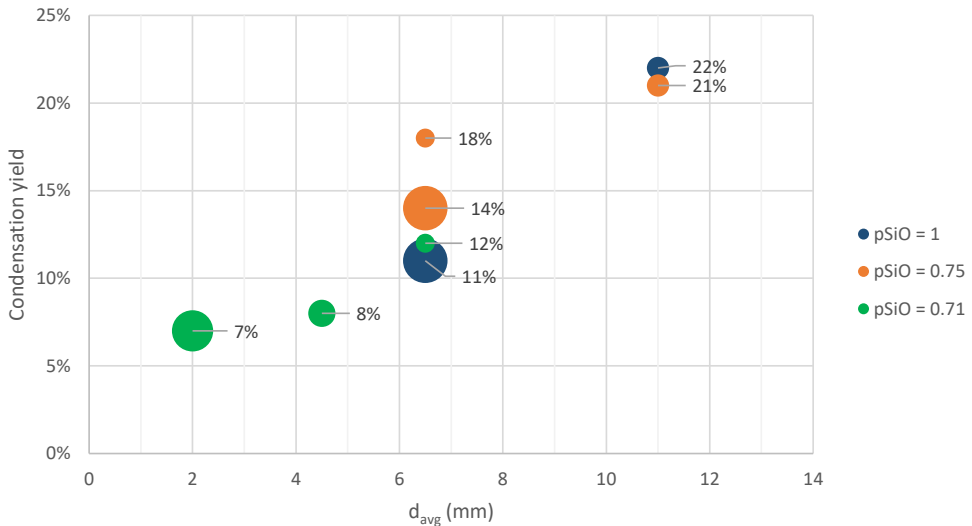


Figure 217: Condensation yield as a function of particle diameter and $p_{\text{SiO}_2, \text{in}}$ in large-scale experiments. The sphere size is related to the broadness of the chosen PSD. Experiments considered: R19-R21 (green), IF1,2,4 (orange), IF5,8 (blue).

A narrow PSD and a larger crucible increase the condensation yield. The smaller bubbles in Figure 217 represent the experiments with narrow PSD, which have a higher condensation yield compared to their respective experiments performed at the same gas composition. Figure 218 shows the preferential paths of the gas flow when flowing through a narrow (left) and a broad (right) PSD.

Case 1: A narrow PSD and a large average particle size gives a high charge permeability. This allows the gas to flow easily through the particle bed. A narrow PSD allows condensates to be produced higher up in the crucible, i.e. at lower temperatures. This corresponds to a higher available area, and therefore to a higher condensation yield, as demonstrated by the mass balance and modelling results. In fact, Metherall [114] suggested that the clogging time increases with a larger space between particles in the bed.

Case 2: a wide PSD (or a PSD with a smaller average particle size) will be easily clogged. The void fraction decreases, and the channel size decreases when the particle size distribution (PSD) is broad, since the particles can pack closer. The channel size is the average space between each particle in a charge. The small voids are quickly filled with condensates. As smaller channels are clogged, the particles that are packed better are glued easier by the condensate. This retains the gas in the temperature interval where the driving force for condensation is highest (1400-1700°C). In fact, experiments at small d_{avg} and broad PSD (3-10 mm in large-scale, 1-3 mm in small scale) will give more condensates in a smaller temperature interval (at long times). This was seen in the effect of the PSD on the temperature of formation.

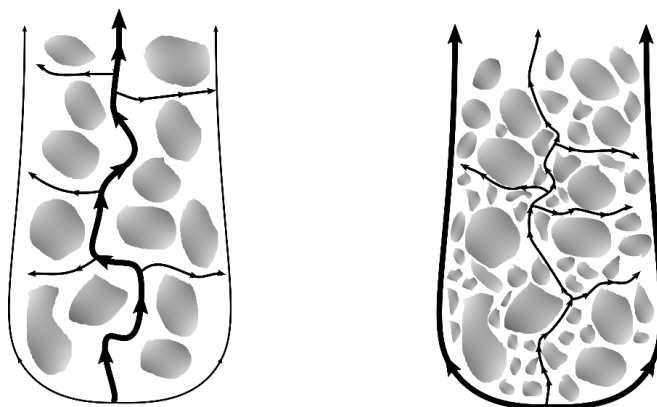


Figure 218: Preferential paths for the gas flow: narrow PSD (left) and broad PSD (right).

These results can be compared to the work by Metherall [114], who modelled clogging by Si-SiO₂ condensation in a channel at a chosen size. The sizes of the channels in this work and Metherall's model are comparable. The channels size in this work is the space between the SiC substrates, which should be close to the case of $a = 1.5$ mm for the 3-10 mm PSD cases (or even smaller).

It seems that the 8-14 mm PSD reaches the desired results for the industrial production: a high condensation yield (21-22%) and a relatively low thickness for the clogging interval (300 K). This prediction fits with the expectations of Metherall. In fact, he suggests that there is an optimal size for the channel, where the condensation yield is maximum, and the clogging is not critical yet. According to Metherall, a channel accumulates most condensate when its diameter reaches 6 mm, which is close to the space that an 8-14 mm charge would leave between spherical particles.

Clogging already occurs after 10 minutes of gas production reaction, and the differences of the clogging temperature intervals are not so large between 30- and 120-minutes holding time. In the beginning, the gas flows between the larger particles. Condensation starts from the highest temperature ($\approx 1800^\circ\text{C}$) and continues

upwards towards the lowest temperatures. The bed will slip more gas through and hence lead to a lower condensation temperature. Instead, if the particles are well packed and the gas runs quickly between the substrates, the crucibles are clogged quickly, and the differences between 30, 60- and 240-minutes holding time are not so large.

This result can also be compared to Metherall's prediction about the channel obstruction. Figure 219 shows the model's prediction at $t = 24$ and $t = 120$ min, for a starting $p_{\text{SiO}} = 1$ at the entrance of the channel. About 40% of the channel is partially obstructed from $t = 24$ min, but it will take about two hours to clog $\approx 65\%$ of the channel. Clogging by brown condensate is found in the experiments with high SiO(g) concentration, but the same concept should apply for clogging caused by white condensate. The only difference would be the values of the reaction rates and the activation energies input in Metherall's model, but the final effect at long times would always be the obstruction of the pipe.

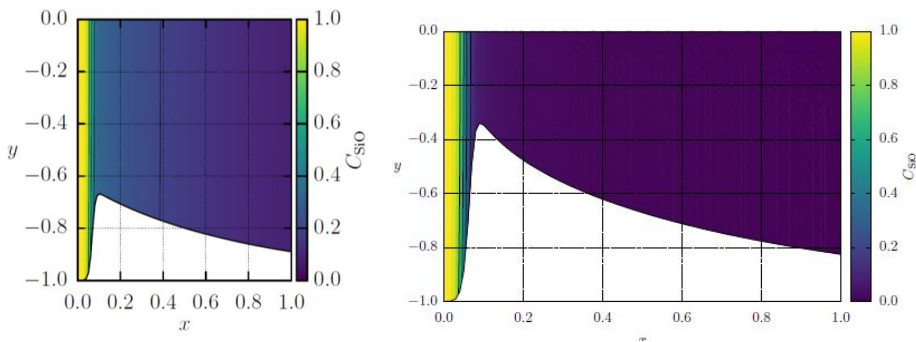


Figure 219: Solution of the leading-order model for $a = 1.5$ mm, at $t = 24$ min (left) and $t = 2$ h (right). The white region depicts the brown Si-SiO_2 condensate layer [114], whereas the colored region shows the local concentration of SiO(g) in the channel.

The experiments with the highest DF give larger clogging intervals. Figure 220 shows three couples of experiments (IF3b vs IF7b, IF4 vs IF8 and IF11 vs IF 12), which share all the experimental parameters except the starting $p_{\text{SiO,in}}$ ($p_{\text{SiO,in}} = 0.75$ for IF3b, IF4 and IF11; $p_{\text{SiO,in}} = 1.0$ for IF4, IF7b and IF12). The plot indicates that the maximum DF and the clogging interval width are related.

Experiments with a higher DF produce more condensates, which accumulate in a larger temperature interval. However, a faster rate may clog the system too early and decrease the thickness of the interval width. In fact, if we plot the driving force again the maximum condensation rate, the trend is opposite (i.e. thinner clogging intervals with larger condensation rate). This could mean that the system may be clogged quickly and in a thinner interval by the high condensation rates. However, we should also remember that the difference between the experiments is within the uncertainty of the measurements.

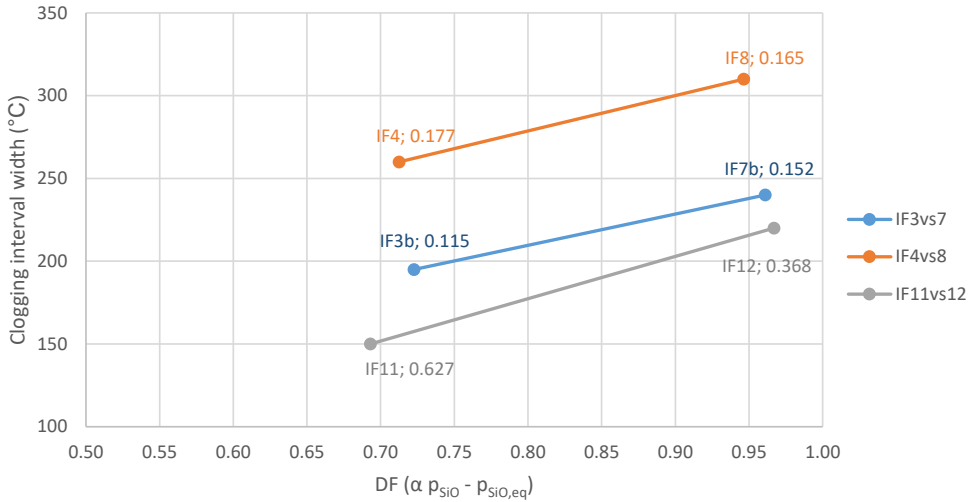


Figure 220: Clogging interval for experiments with changing $p_{\text{SiO,in}}$. The values of the maximum condensation rate are written in correspondence of each point, in g/min.

Since the system is progressively clogged with time, the available surface for condensation A should decrease as time passes. In fact, the voids between the particles get filled up with condensates. However, the kinetic model assumes a constant value of A over time. The constant area and spherical shape assumptions were also made by Sindland while studying the reactivity of $\text{SiO}_2\text{-SiC}$ and Si-SiO_2 mixtures [71]. According to the error calculations performed in Appendix G, the gauss propagation law gives an error on A of 10-25% (even 50% for some intervals). It is believed that the constant area assumption is reliable, despite the error in the value of A may be higher than expected, due to the geometric assumption on the particles shape.

The constant area assumption might be true for $\text{SiO}_2\text{-SiC}$ condensates, since they form thin layers with a similar thickness after 30 minutes. However, brown condensate fills up the voids more effectively than white condensate. The assumption of a constant A value is hence valid if the condensates form a thin layer around the particles, which does not affect the available area. Other effects that influence the value of A during the experiments are the surface roughness of the particles, which also changes due to the condensates deposited.

A system with a larger surface/volume ratio is more sensitive to changes in temperature of formation, clogging intervals and stoking points. The discussion on clogging and channel size can also be applied for a comparison between the small and the large-scale setups described in this work. It was seen that condensation yield is influenced by the available area in the system. The large- and small-scale setups can be compared in terms of surface/volume ratio. In fact, the small crucible system has a higher surface volume ratio (A/V_{tot}) compared to the large-scale crucible. The values of A/V_{tot} are respectively 1-3 for the large-scale ($A \approx 5000 - 10000 \text{ cm}^2$, $V_{\text{tot}} \approx 3000 \text{ cm}^3$) and 10-30 for the small scale ($A = 250 - 650 \text{ cm}^2$; $V_{\text{tot}} \approx 20 \text{ cm}^3$). The numbers consider also the effect of the graphite walls. If the crucible size is considered the channel size, it is possible to explain why the small-scale setup is clogged in a larger interval and at lower temperatures compared to the large-scale crucible.

A higher p_{SiO} is believed to increase the condensation yield. A gas which is pushed up by a He flow has a lower condensation yield for two reasons. First, the gas flows fast through the particle bed. The gas does not have enough time to condense, therefore the condensation yield will be lower. Second, the addition of other gases

reduces the partial pressure of SiO(g) in the system, and the driving force for condensation will be lower. This applies also when p_{SiO} is reduced by changing the gas production pellets composition from SiO₂-SiC ($p_{\text{SiO,in}} = 0.75$) to Si-SiO₂ ($p_{\text{SiO,in}} = 1.0$).

The condensation yield is higher with a higher p_{SiO} due to a higher condensation rate, however this is not verified in the conditions of these experiments. more work is needed to verify this assertion.

Industrial interpretation of the results

For the industrial practice, it is expected that SiO(g) decreases with temperature faster than in this work, and the $p_{\text{SiO,out}}$ value would be lower compared to the experiments performed in this work, by including Reaction 3 and 4 in the calculations. The industrial furnace has a condensation length in the range of meters, while the lab scale setups are in the length of cm. In this work, the $p_{\text{SiO,out}}$ value was higher than 0.5. On the other hand, the industrial offgas contains about 5-10% SiO(g) ($p_{\text{SiO,out}} = 0.05$ -0.10). These numbers can be calculated by computing the mass balance, assuming a furnace yield of 80-90%. The amount of gas recovered is therefore higher in the industrial process, and in fact the offgas is poorer in SiO(g).

The difference between this work and the industrial practice is that there are other reactions contributing to the SiO(g) recovery in the industrial process, such as SiO(g) capture by carbon materials [22]. As suggested by Jayakumari [22], one should pay attention to the carbon material reactivity, to recover as much SiO(g) as possible. Eventually, ascending SiO(g) can form elemental silicon, at the cavity roof in the industrial process, as described by Tranell et al. [56].

Heating the low temperature zone looks like a valid strategy to dissolve the condensate, but it is not applicable in an industrial furnace. According to the results of this work and previous literature, heating the SiC-SiO_x condensates zone gives SiO(g) and CO(g) production, which reduces the condensation crust thickness [1], [3], [7], [65],[69], [70], [72]. Even better, it is possible to recover elemental silicon from the Si-SiO₂ condensate [12], [59]. However, supplying extra energy in the low temperature zone of the furnace is what the industrial world wants to avoid, since it is expensive and affects the furnace operation. In fact, heating the low temperature zone melts the quartz and lifts the electrode position upwards, which are two strong disadvantages. The only positive effect is the formation and recovery of silicon at the cavity roof:

- Disadvantages: Smelting of quartz and high electrode position. Softening and melting of quartz contributes to clogging of the charge bed [60]. The experiments performed with quartz substrate showed that a quartz charge can aggregate when the softening temperature of quartz is trespassed. Translated into industrial terms, an increase in power would lift the electrode up, but quartz will be heated higher up in the furnace. An increase in thermal energy increases energy consumption and cost, and the silicon yield would decrease. In fact, the electrodes generate parasite electric arcs, which flow towards the condensate and not towards the silicon pool. This zone of the furnace will receive a lower amount of electrical energy, and the silicon production reaction will slow down.
- Advantage: Si formation on cavity roof. Traces of Si were detected at the cavity roof level during industrial excavations [56], [66], [67]. This reaction is supposed to happen at the metal pool, but Si from the cavity roof can be recovered, as it flows easily to the taphole. This favors a high Si yield.

To conclude, the best thing to do would be to stoke the clogged condensates, and just make them flow downwards in the high temperature zone ($T > 1800^\circ\text{C}$). This is exactly what is done in nowadays industrial practice. In industrial furnaces the condensates will be heated as the charge descends in the furnace. Heating the Si-SiO₂ condensates in the high temperature zone enhances the recovery of elemental Si. Large amounts of brown condensate were noticed in many industrial furnaces [2], [3], [7]–[9], [53], [55]–[58], [64], hence a

considerable amount of Si is extracted as the charge materials moves to higher temperatures. Vangskåsen [59] estimated from a pilot scale experiment that nearly 10-15% of the metallic Si from the raw materials was contained in the condensates. When the Si-SiO₂ condensate is exposed to temperatures of at least 1650°C, silicon separates from the condensate crust [12], [59]. Such temperatures are also reached at the boundary between the high and low temperature zones in an industrial furnace.

Condensation will be a limited factor in the increase in silicon yield, as only maximum 20-25% of the initial gas could be recovered. The industrial operation could take therefore two different approaches to obtain the highest silicon yield:

- 1) The first would be to maximize the silicon yield by maximizing condensation. In this way, the silicon yield would be improved, as the available surface and condensation times would be larger. However, this implies that the Si furnaces must be rebuilt. The furnaces would need to be taller and larger, in order to capture the outcoming gas and develop a temperature gradient through which condensation can occur. Together with condensation, a good carbon reactivity can approach the full SiO(g) recovery. However, one must deal with clogging in a larger space, and the operation will be more complicated.
- 2) The other approach would be to avoid condensation and make all the gas react in the high temperature zone. It is not possible to get all the SiO to react in the high temperature zone due to the equilibrium situation as you have shown above, but one could have a second chamber where the SiO in the off gas could be recycled (and of course after filtering eventual fines and microsilica, which would clog the system). All the off-gas would be forced to react in the high temperature zone. A gas richer in SiO(g) in the high temperature zone gives a faster and more efficient Si production reaction, as the silicon production reaction depends on the SiO(g) concentration in the gas production zone. However, with this setup the temperature in the furnace must be above 1500-1600°C in the whole furnace, to avoid condensation. This increases the energy consumption. Therefore, one should build a higher number of smaller furnaces to follow this strategy.

According to the results in this thesis, the injection of an inert gas (and the reduction of p_{SiO}) can reduce the condensates amount. This sounds as a valid action to decrease condensation and clogging in the system. However, the drawbacks in the industrial practice are more than the advantages. Let us think at what could happen if an inert gas flow system was integrated in the two different zones of the furnace. In both cases, the introduction of a gas flow reduces the p_{SiO} locally and decreases the Si yield of the furnace:

The inert gas is injected at the low temperature zone: The gas flows faster towards the off-gas system. Less condensates would form, since p_{SiO} is reduced and the time for condensation is lower. Therefore, the Si yield decreases, as less SiO(g) is recovered. Moreover, a lower p_{SiO} decreases also the reactivity with carbon materials. The only positive aspect is that the original charge permeability is kept, and the clogging interval decreases, as a lower amount of condensate is generated.

The inert gas is injected at the high temperature zone: Again, the addition of an inert gas decreases p_{SiO} . A lower p_{SiO} in the high temperature zone is what we do not want at all in the production nowadays, since the silicon production reaction might not take place at the desired efficiency. Hence the energy consumption will increase, as a higher temperature is needed to produce silicon when the p_{SiO} is lower. Another detrimental effect is the overpressure at the taphole, which would result in a dangerous working environment.

It can be estimated that p_{SiO} could be between 0.75 and 1 in the high temperature zone of the industrial furnaces. Equilibrium data and earlier industrial mass balance calculations estimate the inner zone conditions to be

between $T=1800-2000^{\circ}\text{C}$ and $p_{\text{SiO}} = 0.5-0.7$ [1]. p_{SiO} could even lie between 0.75 and 1 in industrial practice in the gas production zone, for these reasons.

1. The equilibrium conditions are not respected, as it has been documented in the thermodynamic calculation.

2. The fraction of brown condensate in industrial furnace is estimated to be high. A higher brown condensate fraction is obtained at experiments with $p_{\text{SiO}} > 0.75$, therefore this could be the case also in industrial excavations.

3. The experiments gave similar compounds compared to the industrial samples. The gas composition conditions and temperature may be similar in industrial and laboratory scale. However, **it is hard to say if there is a real correspondence, as the amounts of condensates in an industrial furnace was never clearly quantified. In fact, blue and white condensate were hardly noticed in the industrial excavations.** They could be easily mistaken with partial reacted quartz, or with oxide scales. The results from this thesis show that white condensate can create a scale which becomes thicker over time, as more gas condenses, creating stronger clogging effects. This makes the SiC-SiO_x condensate amounts difficult to quantify.

The blue and white condensates might be also difficult to detect because the brown condensate can embed the white [11], [54], [59]. Nucleation and growth of Si-SiO₂ mixture occurs in the same temperature and p_{SiO} range as the SiC-SiO_x condensate formation, as noticed in the results of this work. Vangskåsen [15], [54] also showed that the brown condensate is sandwiched between two layers of white SiO₂-SiC mixture.

Clogging is believed to be more intense in the industrial system compared to the laboratory scale crucibles.

The crucibles get clogged mainly between $1400-1700^{\circ}\text{C}$, and part of the top and bottom SiC charge could still flow. On the other hand, clogging and condensation in industrial furnace could occur from the charge top (700°C) to the cavity roof (1800°C) [4], [7], [9], [55]–[57]. In fact, the industrial charge contains quartz and carbon fines, which also contribute to the mechanical properties of the crust. The furnace can be clogged up to the charge top because of gas blows at $T > 1600^{\circ}\text{C}$, which melts the quartz fines generating during furnace loading [60], [115]. The industrial gas blows are believed to be faster than the gas flow analysed in the laboratory scale experiments, which means that SiO(g) and CO(g) can flow upwards and create condensates even at the charge top. Moreover, the industrial furnace could be clogged down to the bottom when a cavity is not generated [2].

Clogging is affected by the raw materials size distribution. The materials with low density (e.g. charcoal) or packing factor (e.g. woodchips) makes the charge descend faster and cause less clogging. The porosity of charcoal and woodchips affects the permeability of the gas, which is related to the void size between charge particles. The charge in the furnace should have a narrow particle size distribution to decrease the clogging interval thickness, as confirmed by the results of this work. The main drawback will be higher silicon losses and lower charge reactivity with SiO(g). Clogging occurs either because of condensation, or because the quartz fines melt and glue the charge bed [115]. In both cases the initial PSD of the raw materials is altered.

It was seen that clogging is a result of the condensation rate. However, it is also possible to interpret this result in the opposite way, i.e. the condensation rate increases due to increased clogging. In fact, a clogged system retains the gas in the high temperature zone, making the flow lower and giving more time for condensation. In the industrial furnaces, this may not always be the case when a clogged system causes gas blows. A gas blow corresponds to a SiO loss, which reduces the condensation rate. Therefore, the condensation rate and the clogging interval thickness may decrease as a consequence of complete clogging at high temperatures ($T > 1600^{\circ}\text{C}$).

Considerations on condensation substrates

Carbon: Condensation of nanowires takes place after formation of a SiC layer at the external surface of graphite. Hence condensation does not occur directly on elemental carbon. The condensation reaction is slower than SiC formation. SiC production and SiO condensation may occur at the same time. Once a SiC layer is developed on carbon after exposition to SiO(g) (Reaction 3, see Appendix A), the carbon substrates give the same SiC-SiO_x condensates on their surfaces.

Charcoal, coal and woodchips are used in silicon production rather than graphite. The porosity of graphite can be compared to the porosity of petroleum coke used by Jayakumari [22] (or even lower). Graphite has therefore a low reactivity with SiO(g). The reactivity with SiO(g) of graphite is limited to the external surface.

SiC substrates: The presence of SiC substrates allows a higher production of SiC-SiO_x nanowires, compared to an empty condensation chamber. A previous work by Tetlie [116] was carried out in the same closed tube furnace as this work. The main difference between Tetlie's work and this study is the presence of SiC particles in the condensation zone. Despite the microstructure of the condensate and the temperature of formation is the same, the condensation yield is lower in Tetlie's work (~5%). The condensation yield increases with the presence of a SiC charge in the condensation zone, since there is a higher available area for condensation. The SiC chosen for this work contains mostly α -SiC, which is not what is expected in the low temperature zone of an industrial furnace. In fact, the low temperature zone should be richer in β -SiC [1], [22]. Despite the nanowires have a 3C-SiC core crystalline structure, the nanowires grow anyways on an α -SiC crystalline substrate. It can be concluded that condensation is influenced by the amount of surface, rather than the composition of the surface.

Quartz: It was not possible to see brown condensate on quartz in these experiments, due to a low partial pressure and temperature in the setup. Previous works in the large-scale setup have shown that brown condensate can develop on quartz [117]. It is possible that a higher holding temperature could develop brown condensate in this setup, and that the quartz and the condensate would partially interact. Saadieh [117] showed that the interface between quartz and brown condensate remains quite sharp, despite they both contain silica. This also shows that the exothermic heat from the condensate may affect only the surface of quartz. Quartz and condensate do not blend, since a layer of white condensate might form on the substrate first, but also because the melting temperature of quartz has not been trespassed.

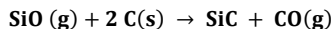
White condensate: Si-SiO₂ condensates can develop on top of white condensate in a sandwich structure. This was also noticed by Vangskåsen and Møltnås [11], [59]. Since white SiC-SiO_x condensate forms at lower temperature and higher up in the crucibles, it can be said that nanowires need a lower SiO(g) concentration in the gas to form, compared to brown Si-SiO₂ condensate. Si-SiO₂ condensate formation will take place on the top of the nanowires, eventually embedding them in a SiO₂ matrix.

SiO consumption by other reactions and SiO losses

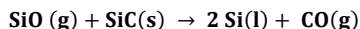
Condensation is not the only reaction that reduces p_{SiO} in the crucible. p_{SiO} becomes lower due to the SiO(g) interaction with the graphite or by leakages in the crucibles.

1. The interaction between SiO(g) and graphite. SiC and Si were found on the graphite walls of the gas production zone, thanks to Reactions 3,4,-12 [1], [14]. The reactions might be a cause of reduction of SiO(g)

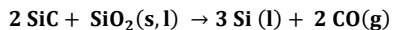
content in the system, making p_{SiO} lower than expected. More information about formation of Si and SiC in the graphite parts are collected in Appendix A.



Reaction 3



Reaction 4



Reaction -12

The diffusion of SiO(g) into the graphite parts of the setup forms a layer of SiC up to 400 μm thick. In the gas production chamber, the temperature is high ($T > 1815^\circ\text{C}$), and Si coexists with SiC generated on the graphite parts. Both the reactions consume some SiO(g) from the gas phase and produce CO(g). The volume of SiC generated is hard to compute precisely, but the estimations of the volume of SiC formed led to a consumption of 0.02 mol SiO(g) in the small-scale setup, and 0.1 mol SiO(g) in the large-scale setup, as explained in the “Results” chapter. Both these values are considered negligible losses for the mass balance, as they affect $p_{SiO,out}$ by only 0.01-0.05.

2. SiO(g) loss from off-gas system and crucibles leakages. In every small-scale crucible, the external walls were covered with a thin blue and white layer, whose microstructure is the same as the white condensate. The scale comes off easily while handling the cylinder. Condensate formation could occur also outside of the crucible, and that part of the gas leaked from the chamber. The condensates generated in this way were not considered relevant for the mass balance.

The loss of SiO(g) in the system could lead to less condensates capture on the chosen substrates. For example, brown condensate does not show up all the time in all the repetition experiments. It can be that SiO(g) has leaked through the setup to a larger extent, compared to the other cases. Minor amounts of white, blue and orange layers are deposited on the alumina tube at low temperatures, and in the offgas system walls. The mass of the tube was not affected by those deposits. Finally, the off-gas filters at the outlet contained often a brown-orange powder, which resembled what Ksiazek et al. [12] found. Figure 221 shows the appearance of the deposits.

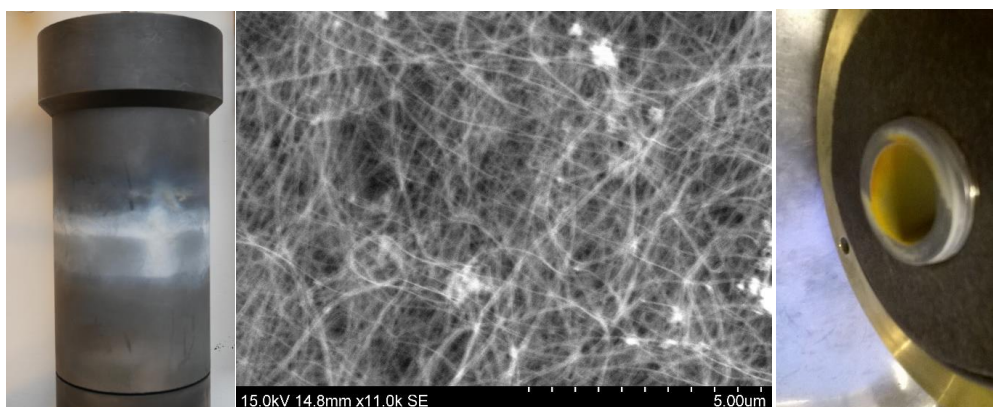


Figure 221: Left: external scales on crucibles; Center: : Microstructure of blue scale from external walls of the crucible, experiment R3c; Right: Traces of orange powder in the offgas system, experiment R2a.

D. Production of SiO and CO

The reaction time is influencing the conversion parameter α , which is defined as the *extent of reaction* (i.e. the fraction of pellets used in the gas production reaction, in our case). This section studies SiO+CO production at 1890°C, which give conversions between 40-100% in a time interval of 15-160 minutes. The relation between α and t_r for this work is plotted in Figure 222. The conversion α increases by increasing the reaction time t_r , as materials have longer time to react and to be consumed. The gas production pellets charge is consumed in around 100-120 min at 1890°C.

The conversion is similar for the SiO₂+SiC reaction, compared to the Si+SiO₂ reaction. Pellets are therefore consumed at the same rate, regardless of their composition. This is in contrast with the results by Sindland [71], who noticed that the SiO₂+SiC reaction is slower than the Si+SiO₂ reaction. It must be also considered that Sindland's reacting materials were crushed into pieces, instead of making pellets. This could have affected the conversion and the conversion rate, making the particle size more inhomogeneous in Sindland's work.

The values of the α in this work can be compared to the previous works on Si+SiO₂ and SiO₂+SiC reactions. Above 1700°C, the gas production reaction yield for the SiO₂+SiC mixture is above 65% for Andersen [69], while heating at 2 deg/min. Tangstad et al. [97] obtained eventually a \approx 100% conversion at 1900°C and above for a mixture of cristobalite and SiC, heated for 1 hour. In Ni's work [111], the conversion is lower compared to this work, due to the lower temperature chosen for the experiments. In fact, Ni carries out experiments at temperatures between 1400-1700°C for 60 min, getting conversions between 0 – 40%. In the experiments of Bao et al. [70] the temperature is maintained at 1820°C for 1 hour, but the extent of reaction reaches a maximum of \approx 70% for the Si+SiO₂ reaction and \approx 85% for the SiO₂+SiC reaction.

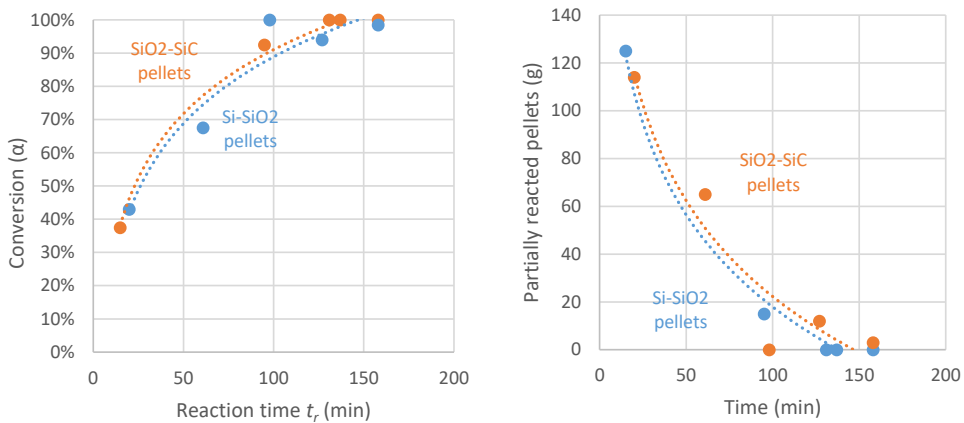


Figure 222: Conversion (left) and partially reacted pellets (right) as a function of time for SiO₂+SiC and Si+SiO₂ reactions at 1890°C.

The derivative of α with respect to time gives the values of the *conversion rate* (da/dt). The values of da/dt as a function of α are also shown in Figure 223. The conversion rates are in between 0.001 – 0.030 %/min.

Figure 223 collects also the results on the conversion rate found by Ni [111]. Ni gets a conversion rate of about 0.003%/min at \approx 0.3 conversion, in the temperature range 1400-1700°C, whereas in this setup the conversion rate is 0.002%/min at $\alpha \approx$ 0.4, at a fixed temperature of 1890°C. These values are higher compared to Ni's work,

but at least located in the same order of magnitude. The temperature increases the reaction rate, as confirmed by Tangstad et al. [97].

The method presented in this work gives a higher partial pressure in the system, compared to what is presented by Tangstad et al. [97], where the gas production reaction is also analyzed at 1900°C. While no inert gas is injected in the crucible, Tangstad et al. used a high flow of Ar(g) (1.7 NI/min), which reduce the SiO(g) concentration in the gas phase. The reaction rate obtained by this work is about 10 times lower than Tangstad et al. [97], which reaches a maximum of 0.11%/min at 0.32 conversion. This could suggest that the presence of an inert gas increases the gas production rate. This is expected, as the inert gas flow would take away SiO(g) and CO(g) from the reaction environment. Hence, the reaction moves towards the gas production, according to Le Chatelier's principle. This also agrees with the results by Ni, shown in Figure 223.

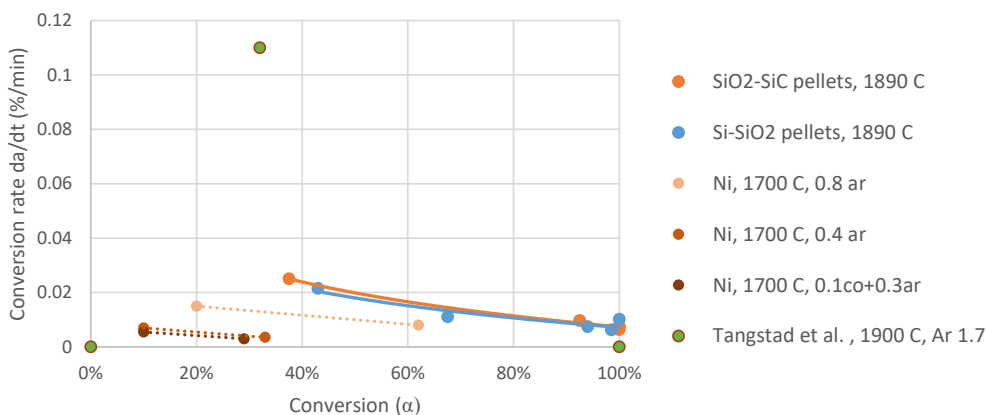
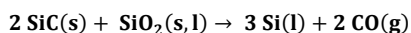


Figure 223: Comparison of conversion rates of pellets from this work (continuous lines) with results from Ni (dashed lines) [111] and Tangstad et al. [97].

When it comes to the effect of the gas production on condensation, it was seen that the gas production reactions do not affect the final microstructure, composition of the condensates. Condensation does not depend on how we produce the gas, but on how much gas is produced and how much SiO(g) it contains. The composition of the gas production materials affects the SiO(g) content in the gas and the amount of SiC-SiO_x and Si-SiO₂ condensates in the furnace. Therefore, the gas producing materials should be studied anyways, to estimate which condensate is produced in highest amounts.

The final composition of the partial reacted pellets should also be analysed in the gas production materials. Tangstad et al. [97] found that the SiO₂:SiC ratio in the pellets changes during the reaction, due to side-reactions in the gas production zone (e.g. Reaction -12). The results by Tangstad et al. show that there is a small difference in the amount of reacted SiO₂ in pellets with a SiO₂:SiC ratio of 1:1, 3:2 ad 3:1. However, in this work, the pellets composition was assumed to be constant throughout the reaction. The effect could bring a slight difference uncertainty in the calculation of p_{SiO}.



Reaction -12

6. Conclusions

In this work the condensation of SiO(g) and CO(g) was studied, and it was seen that the condensation products can be separated into two main groups. The first is the SiC-SiO_x condensate (with $x \approx 2$), while the second consists of Si and SiO₂ (Si-SiO₂ condensate). This work analyzed the condensates microstructures, temperature and partial pressure ranges of formation. The condensates clogged the crucibles in different zones according to the experimental parameters involved. After quantifying the condensates amounts, the reaction rate was modeled for the SiC-SiO_x condensate, to estimate the activation energy of the condensation reaction and explain the distribution of the condensates in the crucible.

SiC-SiO_x condensate

The SiC-SiO_x condensate is the product of the reaction between SiO(g) and CO(g). Its color changes with temperature between blue (900-1500°C; 1600-1810°C), white (910°C-1800°C) and grey (1275-1800°C). The SiC-SiO_x condensates are generated between $p_{\text{SiO}}=0.53-0.99$. The compounds appear at both industrial and laboratory scale as a cotton-like layer or scales.

SEM and TEM detected core-shell nanowires, which built up a few hundred- μm thick layer. The shell-phase is made of about 90% amorphous SiO_x and 10% cristobalite. The core-phase is made of β -SiC. The core-phase is rich in stacking faults, caused by lattice mismatch with the substrate or oxygen inclusions. In the shell-phase, the amount of amorphous phase increases with temperature, whereas the amount of cristobalite increases with time.

A mechanism of formation is proposed. First, molecular nanoclusters of (SiO)_n and SiC will form a seed on the surface, from SiO(g) and CO(g). Solid SiC accumulates at the core, while the oxides will flow accumulate at the shell. This event is called lateral growth, as it determines the nanowire diameter. Then, a nucleus is generated. A nucleus is a seed which can grow vertically. The reaction zone is located in a droplet and above the seed. The reactions occurring are the condensation reaction, the SiO(g) decomposition into Si, SiO₂ and SiO_x, and SiC production from Si and CO(g). Finally, the growth terminates with a tip, when the temperature or the partial pressure of SiO(g) are too low.

During growth, the SiO_x shell-phase changes its microstructure, from a uniform thin coating ($d = 10-20$ nm) to beads ($\phi = 50-200$ nm) and finally nodules ($\phi > 200$ nm). Nodules are typical of white condensates, whereas beads were also found in blue condensate. The nodules grow with time and temperature, to reduce their surface energy.

The transformation is driven by surface energy reduction. The oxide can flow even below the melting point of bulk silica, thanks to the melting point depression of nanometric systems, the heat freed by the exothermic condensation reaction, and thus the superheated conditions in the immediate vicinity of the reacting molecules. Superheated conditions are also responsible for the back reaction to SiO(g) and CO(g) during condensation, and for the formation of thin layers of blue condensate at high temperatures.

Si-SiO₂ condensate

The brown condensate is a glassy mixture of Si and SiO₂ distributed in a molar ratio 1:1. The condensate generates from SiO(g). The compound generates between 1400-1800°C and p_{SiO} between 0.58-0.99. The color is darker in condensates produced at highest temperatures, due to the size of the Si spheres. The colors are similar between the laboratory experiments and the industrial samples.

SEM detected silicon spheres embedded into a silica matrix. Si spheres are interconnected by silicon treads, and the size of silicon spheres increases while moving away from the condensation substrate. Silicon spheres are usually larger in industrial scale samples compared to laboratory scale. At the same time, the spheres are also distributed into a layered structure, which alternate a zone with small spheres (≈ 400 nm) to a zone with larger spheres (≈ 800 nm). Each layer is about 10-20 μm thick.

The proposed mechanism of formation begins with the separation into Si, SiO_x and SiO_2 domains from the $(\text{SiO})_n$ molecular clusters ($T > 1723^\circ\text{C}$). The molecular clusters are divided into areas at different Si/O ratio, which are believed to enhance segregation. The oxides and the elemental silicon generate an emulsion above the melting point of silica.

Between the melting point of silica and silicon (1414 - 1723°C), three phenomena occur. First, the silicon droplets grow and move out of the condensate, leaving a porous silica matrix close to the condensation substrate. In this way, elemental Si is recovered also at industrial scale. Second, the alternate layer structures generate, thanks to the cyclic release and absorption of heat of the gas during condensation and cooling. Third, cracks form in the SiO_2 matrix. The cracks get filled with Si. The main causes of crack formation are related to thermal stresses (oscillation in temperature and temperature gradient within the condensate) and mechanical stresses (SiC formation and back reaction between Si and SiO_2).

During cooling, the silica matrix recrystallizes from amorphous into cristobalite. Once the temperature is below 1414°C , the microstructure freezes.

TEM, XRD and XPS revealed 3C-SiC nanocrystals located at some of the silicon spheres borders. SiC makes 5-10 wt.% of the whole brown condensate mass. SiC could form after continuous dissolution and segregation of C in liquid silicon, or from interaction of $\text{CO}(\text{g})$ and liquid silicon. The SiC production reaction is spontaneous for the largest Si spheres and for condensates generated at low temperatures.

Temperature of formation and clogging

White SiC-SiO_x condensate is responsible for clogging, but brown Si-SiO₂ condensate gives higher mechanical properties to the condensates crust. White condensate generates in a larger temperature interval and glues more particles compared to the brown. Moreover, it can form in wider temperature and p_{SiO} intervals and in higher amounts compared to the brown.

A small-scale system is more sensitive to clogging compared to the large-scale setup. The clogged portion of the crucible increases from 20 vol.% to 40 vol.% by increasing the surface/volume ratio of the crucible by a factor of 10. The walls of the crucible affect clogging, as the condensates glue the charge to the walls. The crucibles are usually clogged between 1400 - 1800°C in the larger setup, or between 1150 - 1700°C in the small-scale setup.

The major changes in temperature of formation of the condensates occur up to 30-60 minutes. The experiments at short times tend to have less condensates, and hence a thinner condensation and clogging interval. The Si-SiO₂ condensate may not appear at short times. After $t = 60$ min, brown Si-SiO₂ condensate stabilizes between 1550 - 1800°C , whereas SiC-SiO_x nanowires form down to temperatures of $\approx 1050^\circ\text{C}$.

The addition of an inert gas reduces the p_{SiO} and increases the gas velocity through the substrates. A higher gas velocity shifts the condensates to lower temperatures and gives condensation in a wider temperature range.

The same effect was seen for clogging. Brown Si-SiO₂ condensate may not appear at low SiO(g) content in the gas, since the driving force for condensation may be too low.

A gas richer in SiO(g) develops condensates at lower temperatures and in wider temperature intervals. More condensates are produced if the p_{SiO} in the starting gas is higher. In fact, the crucible is more clogged in experiment with a higher SiO(g) concentration.

A narrow particle size distribution (PSD) of the substrate gives a charge with a higher permeability, which allows the gas to flow faster through the charge bed. The condensation interval becomes larger and the condensation temperatures become lower. On the other hand, the smaller voids of a broad PSD are quickly filled by condensates, therefore most the condensates develop at higher temperatures.

A higher gas temperature favors condensates formation higher up in the crucible and increases the thickness of the condensation interval. A higher initial gas temperature shifts the temperature gradient upwards. Moreover, the clogging interval thickness decreases, since some of the SiC-SiO_x condensates tend to react to SiO(g) and CO(g).

Mass balance, thermodynamics and industrial interpretation

Both condensation reactions occur out of equilibrium conditions for p_{SiO} and T. Condensation is a slow reaction, and p_{SiO} in the crucible maintains a high value ($p_{\text{SiO}} > 0.5$) even after condensation, which occurs down to $\approx 950^\circ\text{C}$. Equilibrium conditions state that p_{SiO} should be lower than 0.1 at around 1600-1700°C.

According to the mass balance computed in this work, condensation is not an effective method for SiO(g) and CO(g) recovery. From the initial pellets mass, only 1-20% is recovered as condensate in the small-scale setup, and 10-22% in the large-scale setup. Some gas is consumed by the SiC production in graphite, but most goes away as off-gas and oxidizes below 900°C. Some losses are also caused by leakages in the setup.

A gas richer in SiO(g) tends to give a higher condensation yield, because the gas flows slower between the particles, giving more time to condense. Moreover, a higher SiO(g) content implies a higher driving force for condensation. In fact, the amount of condensates increases with higher SiO(g) content in the gas.

Experiments with narrow PSD have higher condensation yield compared to the broad PSD experiments. A narrow particle size distribution captures more condensate in a larger space interval. The PSD with the best results was the 8-14 mm, which gave the highest condensation yield (21-22%) and a relatively low thickness of clogging interval (300 K).

About 60-100% of the formed condensate is SiC-SiO_x condensate, whereas the rest is Si-SiO₂ condensate. The amount of Si-SiO₂ condensate is higher with higher SiO(g) content in the gas. Elemental Si can make up to 16 wt.% of the condensates generated. After assuming that all Si goes to the Si-SiO₂ and all SiC goes to the SiC-SiO_x condensate, it was estimated that silica is contained mostly in the SiC-SiO_x condensate.

p_{SiO} decreases by 0.1 every 100-1000°C according to the chosen condition, since the condensates are produced in small quantities through a large temperature area. The partial pressure decreases with temperature, as SiO(g)

is consumed by condensation. The relationship between T and p_{SiO} in the crucible is assumed to be linear. The slope of this line is low because condensation is a slow reaction.

Most of the SiC-SiO_x condensates (80-95%) are distributed in correspondence of the clogging intervals, i.e. between 1400-1700°C. In this zone, both white and brown condensate can contribute to the mechanical properties of the stoking crust. Condensates are distributed in the chamber with a bell-like distribution regardless of the condensation yield and the condensates mass. The width of the bell distribution increases with time towards lower temperatures.

Reaction rate and kinetic model for SiC-SiO_x formation

The values of the condensation rates are in the order of magnitude of 10⁻³ – 10⁻¹ g/min for both the large and the small-scale setups. The reaction rate for the production of SiC-SiO_x nanowires was modelled between $T = 1300 - 1685^\circ\text{C}$. The relationship assumes a linear correlation with the available surface for condensation, the kinetic constant and a driving force term. The expression of the rate which fits the experimental results best is

$$r_1 = \frac{dm}{dt} = k(T) \cdot A \cdot f(p_{\text{SiO}}) = k(T) \cdot A \cdot (p_{\text{SiO}} - p_{\text{SiO,eq}})$$

The kinetic constant is assumed to follow the Arrhenius equation with temperature. $k(T)$ is an increasing exponential following the Arrhenius equation. The area changes with temperature according to the measurement technique used. p_{SiO} is increasing linearly with temperature and $p_{\text{SiO,eq}}$ resembles an increasing exponential. The value for the activation energy in the temperature interval 1315-1750°C range between 250-300 kJ/mol, whereas the frequency factor is $1.5 \cdot 10^3 \text{ g cm}^{-2} \text{ s}^{-1}$.

The condensation rate increases with temperature until $\approx 1650^\circ\text{C}$. At this point, there is a maximum rate, then the condensation rate decreases quickly to zero until 1810°C . The highest condensation rates are found in correspondence of the clogging intervals, where the condensate amount and the driving force are also highest. Above 1810°C , the gas production reaction prevails. This temperature corresponds to the cavity roof temperature in industrial furnaces, which is also the border between the stability of the gas and the condensates.

There is a parallel between the dependences of temperature for the condensate distribution in the crucible, the driving force and the reaction rate. The driving force for the model is the term $DF = [p_{\text{SiO}} - p_{\text{SiO,eq}}]$. DF increases slowly with temperature until 1600°C , where it reaches its maximum. Then DF decreases until it reaches zero at $\approx 1810^\circ\text{C}$. The maximum value of the driving force coincides with the clogging intervals and the temperatures where most of the condensates are found.

7. Further challenges

The effect of the gas composition can be further studied by adding CO(g) to the starting gas mixture, or by tuning the pellets composition. The intermediate values of $p_{\text{SiO}_2, \text{in}}$ between 0.75 and 1 can be inquired by adding CO(g) to a Si-SiO₂ pellets mixture. In this way, it will be easier to simulate the gas composition in the industrial furnace.

The reaction rate can be modelled for the Si-SiO₂ condensate as well. The experimental setup should be changed: one should either increase the amount of brown condensate or use an experimental setup with a smoother temperature gradient for the brown condensate temperature intervals.

In addition, the kinetic model for white condensate could be reproduced on another setup, to compare the activation energies and the reaction rate dependences on temperature, surface, p_{SiO_2} and time.

Carbon materials converted to SiC could be used as condensation substrates. In this work, condensation occurred on SiC obtained from the Acheson process. This material is different than the SiC generated from carbon materials during silicon production. Carbon materials could be first transformed into SiC in another setup. The converted SiC could be ground at the desired particle size distribution and used as substrate for condensation.

The nature and mechanism of formation of grey condensate should be further investigated. From this work, it was seen that the compound is made of SiO₂ and SiC. Grey condensate was found both at laboratory and industrial scale. However, literature does not provide examples of similar compounds. A compound with such a peculiar microstructure (oriented SiO₂-SiC wires) can surely find applications in micrometric scale technologies.

The surface roughness could affect the available area for condensation. In this work, the charge bed was assumed to be made of spherical particles. However, the SiC particles could have any shape. This parameter could therefore affect both clogging and the condensation yield. A more precise estimation of the available area can also influence the exact value of the condensation rate.

The extent of the melting point depression effect can be modeled with a similar theory to what was proposed by Stølen and Grande [80], but by starting from two substrates with different compositions. This model needs however the collection of other thermodynamic data, for instance the surface tension of liquid SiO₂ on SiC substrates. This value could be estimated by wettability experiments.

The rate of the condensation reaction is slow, but in reality the condensation reaction rate could be limited by mass or heat transfer. In fact, the exothermic reaction increases the temperature locally above 1700°C, which then decreases the condensation rate. Further studies should be made about modeling of the heat and mass transfer in the condensation reactions, as this work depicts only the rate of the overall reaction.

8. References

- [1] A. Schei, J. Tuset, and H. Tveit, *Production of high Silicon Alloys*, 1st ed. Trondheim, Norway: Tapir, 1998.
- [2] M. Ksiazek, E. Ringdalen, and M. Tangstad, "Five furnaces, five different stories," Kristiansand, Norway, 2016, pp. 33–42.
- [3] Y. Otani, M. Saito, K. Usui, and N. Chino, "The inner structure in submerged arc furnaces," in *6th International Congress of Electroheat*, Brighton, 1968, pp. 1–7.
- [4] A. Schei and O. Sandberg, "Back Reactions during production of silicon metal in a submerged arc electric furnace," in *Selected topics of high-temperature chemistry*, 1st ed., Oslo, Norway: Universitetsforlaget, 1966.
- [5] A. Schei, "Impurity distribution in silicon," in *Silicon for the Chemical Industry*, 1992, pp. 11–23.
- [6] A. Schei, "The chemistry of Ferro-Silicon Production," *Tidsskr Kjemi Bergves. Met.*, vol. 27, no. 8, pp. 252–258, 1967.
- [7] M. Tangstad, M. Ksiazek, and B. Faanes, "Zones and Materials in the Si furnace," in *Silicon for the Chemical and the Solar Industry XII*, Trondheim, Norway, 2014, pp. 19–28.
- [8] W. Poch and A. Dietzel, "The formation of silicon carbide from silicon dioxide and carbon," *Trans Nat Res Inst Met.*, vol. 14, no. 6, pp. 22–51, 1962.
- [9] T. Kurosawa, T. Yagihashi, S. Ochiai, and T. Naramura, "Several aspects on the products in a silicon-making Electric furnace," *Trans Nat Res Inst Met.*, vol. 14, no. 6, pp. 22–51, 1972.
- [10] L. Fei, "SiC production using SiO₂ and C agglomerates," Doctoral thesis, NTNU, Trondheim, 2017.
- [11] H. Mølnås, "Investigation of SiO-condensate formation in the silicon process," NTNU, Trondheim, Norway, Internal report, 2010.
- [12] M. Ksiazek, I. Kero, and B. Wittgens, "Challenges in transporting the off-gases from the Silicon process," in *Takano International Symposium on Metals and Alloys*, 2015, pp. 157–166.
- [13] E. Ringdalen, "Phase transformations in quartz and its effect on furnace operation," in *Silicon for the Chemical and the Solar Industry XIII*, Kristiansand, Norway, 2016, pp. 269–278.
- [14] M. Tangstad, *Metal production in Norway*, 1st ed. Trondheim, Norway: Akademika Forlag, 2013.
- [15] J. Vangskåsen, "Investigation of the cavity formation in the silicon process," NTNU, Trondheim, Norway, Internal report, 2011.
- [16] S. Johansen *et al.*, "Clogging of ferro-silicon furnace off-gas channels at high temperatures," *TJA Smith CJ Newman Miner. Met. Mater. Soc.*, pp. 7–18, 1991.
- [17] T. Hannesson, *The silicon process drawings*. Elkem Iceland, 2016.
- [18] H. Kleycamp and G. Schumacher, "The constitution of the silicon-carbon system," *Berichte Bunsenges. Für Phys. Chem.*, vol. 97, no. 6, pp. 799–804, 1993.
- [19] R. W. Olesinski and G. J. Abbaschian, "The C-Si system," *Bull. Alloy Phase Diagr.*, vol. 5, no. 5, pp. 486–489, 1984.
- [20] G. G. Gnesin, V. Kurdymov, and G. S. Oleinik, "X-ray diffraction investigation of the reaction of silicon with carbon," *Sov. Powder Metall. Met. Ceram.*, vol. 11, no. 5, pp. 402–404, 1972.
- [21] A. L. Ortiz, F. Sanchez-Bayo, F. L. Cumbreira, and F. Guibertau, "The prolific polytypism of silicon carbide," *J. Appl. Crystallogr.*, vol. 46, pp. 242–247, 2013.
- [22] S. Jayakumari, "Formation and characterization of β - and α -Silicon Carbide produced during Silicon/Ferrosilicon process," Doctoral thesis, NTNU, Department of Materials Science and Engineering, Trondheim, Norway, 2020.
- [23] A. R. Verma and K. Padmanabhan, *Polymorphism and polytypism in crystals*. New York, USA: New York, 1965.
- [24] O. Knacke, O. Kubachewski, and K. Hesselmann, *Thermodynamic properties of inorganic substances*. Berlin: Springer, 1991.
- [25] G. Belov, V. Iorish, and V. Yungman, "IVTANTHERMO - database on thermodynamic properties and related software," *Calphad*, vol. 23, no. 2, pp. 173–180, 1999.
- [26] I. Barin, *Thermodynamical Data of Pure substances*. Weinheim, Germany: VCH Verlags Gesellschaft, 1989.
- [27] R. E. Johnson and A. Muan, "Phase diagrams for the Systems Si-O and Cr-O," *J. Am. Ceram. Soc.*, vol. 51, no. 8, pp. 430–433, 1968.
- [28] B. Hallstedt, "Thermodynamic Assessment of the Silicon-Oxygen System," *CALPHAD*, vol. 16, no. 1, pp. 53–61, 1992.
- [29] S. Schnurre, J. Gröbner, and R. Schmid-Fetzer, "Thermodynamics and Phase stability in the Si-O system," *J. Non-Cryst. Solids*, vol. 336, no. 1, pp. 1–25, 2004.

- [30] A. Hirata *et al.*, "Atomic-scale disproportionation in amorphous silicon monoxide," *Nat. Commun.*, vol. 7, p. 11591, May 2016.
- [31] N. P. Potter, "Silicon Monoxide," *Ber Chem Ges*, vol. 23, pp. 191–214, 1907.
- [32] H. Erasmus and J. Persson, "Preparation and Properties of Silicon Monoxide," *J. Electrochem. Soc.*, vol. 95, no. 6, pp. 316–318, 1949.
- [33] X. J. Wang *et al.*, "Large Scale SiC/SiO_x nanocables: Synthesis, photoluminescence, and field emission properties," *J. Appl. Phys.*, vol. 102, no. 1, pp. 1–6, 2007.
- [34] S. C. Dhanalaban *et al.*, "Effects of growth parameters on SiC/SiO₂ core/shell nanowires radial structures," *Mater. Sci. Forum*, vol. 740–742, pp. 494–497, 2013.
- [35] P. Hu, S. Dong, K. Gui, X. Deng, and X. Zhang, "Ultra-long SiC nanowires synthesized by a simple method," *R. Soc. Chem.*, vol. 5, pp. 66403–66408, 2015.
- [36] P. Hu, R.-Q. Pan, S. Dong, K. Jin, and X. Zhang, "Several millimeters long SiC-SiO_x nanowires synthesized by carbon black and silica sol," *Ceram. Int.*, vol. 42, pp. 3625–3630, 2016.
- [37] H. Liu, Z. Huang, J. Huang, M. Fang, Y.-G. Liu, and X. Wu, "Thermal evaporation synthesis of SiC/SiO_x nanochain heterojunctions and their photoluminescence properties," *J. Mater. Chem. C*, vol. 2, pp. 7761–7767, 2014, doi: 10.1039/c4tc01391c.
- [38] J. Wei, K.-Z. Li, H.-J. Li, Q.-G. Fu, and L. Zhang, "Growth and Morphology of one-dimensional SiC nanostructures without catalyst assistant," *Mater. Chem. Phys.*, vol. 95, no. 1, pp. 140–144, 2006.
- [39] R. Wu, B. Zha, L. Wang, K. Zhou, and Y. Pan, "Core-shell SiC/SiO₂ Heterostructures in nanowires," *Phys. Status Solidi A*, vol. 209, no. 3, pp. 553–558, 2012, doi: 10.1002/pssa.201127459.
- [40] L. Brewer and R. Edwards, "The stability of SiO Solid and Gas," *J. Phys. Chem.*, vol. 58, no. 4, pp. 351–358, 1954.
- [41] R. J. Tempkin, "An analysis of the Radial Distribution Function of SiO₂," *J. Non-Cryst. Solids*, vol. 17, pp. 215–230, 1975.
- [42] L. Holland, *Vacuum Deposition of Thin Films*, 1st ed. Chapman & Hall, 1970.
- [43] G. Hass, "Preparation, structure and Application of Thin films of Silicon monoxide and Titanium Dioxide," *J. Am. Ceram. Soc.*, vol. 33, no. 12, pp. 353–360, 1950.
- [44] K. Kolobova, "Some Properties of silicon monoxide," *Union Inst. Refract.*, vol. 12, pp. 42–43, 1967.
- [45] H. R. Philipp, "Optical properties of Non-Crystalline Si, SiO and SiO₂," *J. Phys. Chem. Solids*, vol. 32, no. 8, pp. 1935–1945, 1971.
- [46] J. A. Yasaitis and R. Kaplov, "Structure of Amorphous Silicon Monoxide," *J. Appl. Phys.*, vol. 32, no. 8, pp. 1935–1045, 1972.
- [47] A. Hohl *et al.*, "An interface clusters mixture model for the structure of amorphous silicon monoxide (SiO)," *J. Non-Cryst. Solids*, vol. 320, no. 1–3, pp. 255–280, 2003.
- [48] K. Schulmeister and W. Mader, "TEM investigation of the structure of amorphous silicon monoxide," *J. Non-Cryst. Solids*, vol. 320, no. 1, pp. 143–150, 2003.
- [49] S. T. Bromley, J. C. Gómez Martin, and J. M. C. Plane, "Under what conditions does (SiO)_N nucleation occur? A bottom-up kinetic modelling evaluation," *Phys. Chem. Chem. Phys.*, vol. 18, no. 38, pp. 26913–26922, 2016.
- [50] W. Y. Ching, "Theory of amorphous SiO₂ and SiO_x. Part 1: Atomic structural models," *Phys. Rev. B*, vol. 26, no. 12, pp. 6610–6621, 1982.
- [51] Y. Sugiyama, M. Tamura, and A. Ikari, "Electron Spin Resonance Studies on Spots with Brown Rims on a Vitreous Silica Surface formed by a Silicon Melt," *Jpn. J. Appl. Phys.*, vol. 37, no. 12R, pp. 6390–6393, 1998.
- [52] S. Gjerstad, "Chemical metallurgical investigations concerning carbothermic reduction of alumina and silica," PhD thesis, NTNU, Department of Inorganic Chemistry, Trondheim, Norway, 1968.
- [53] M. Tangstad and M. Ksiazek, "Investigation of white and brown condensate," SINTEF, Trondheim, Norway, Internal report, 2010.
- [54] J. Vangskåsen and Ø. Høgsand, "Investigation of cavity and condensate formation in the silicon process," NTNU, Trondheim, Norway, Internal report, 2011.
- [55] S. M. Bø, "Phases and Zones in the Silicon Process," Master thesis, NTNU, Department of Materials Science and Engineering, Trondheim, Norway, 2016.
- [56] G. Tranell, "Reaction zones in a FeSi75 furnace - Results from an industrial excavation," in *Sustainable Future*, Helsinki, Finland, 2010, pp. 709–716.
- [57] M. Ksiazek, M. Tangstad, and E. Ringdalen, "The rapid Si-furnace excavation - an unique chance to investigate the interior of the furnace," Cape Town, South Africa, 2018.
- [58] M. B. Müller, S. E. Olsen, and J. Tuset, "Heat and mass transfer in the ferrosilicon process," *Scand. J. Metall.*, vol. 1, pp. 145–155, 1972.

- [59] J. Vangskåsen, "Metal-producing reactions in the Carbothermic Silicon process," Master thesis, NTNU, Department of Materials Science and Engineering, Trondheim, Norway, 2012.
- [60] K. F. Jusnes, "Phase transformations and thermal degradation in industrial quartz," PhD thesis, NTNU, Department of Materials Science and Engineering, Trondheim, Norway, 2020.
- [61] I. Zherdev, I. Polyakov, V. Semenov, I. I. Barashki, D. P. Moskovtsev, and E. R. Yaskov, "Critical rate of rotation for ferrosilicon furnace baths," *STAL Engl.-USSR*, vol. 5, p. 406, 1968.
- [62] I. Zherdev, D. P. Moskovtsev, and I. Polyakov, "Dimensions of the gas spaces in ferrosilicon furnaces," *Ferroalloys*, vol. 716–717, pp. 635–636, 1965.
- [63] G. Sævarsdóttir, "High-current AC arcs in silicon and ferrosilicon furnaces," Doctoral thesis, NTNU, Trondheim, Norway, 2002.
- [64] M. B. Müller, H. Mellegaard, H. Lynum, and S. E. Olsen, "Metallurgy of the ferrosilicon process [collection of 8 reports in Norwegian]," The Norwegian Council for Technical and Scientific Research, Oslo, Norway, 1971.
- [65] E. Myrhaug, "Non fossil reduction materials in the silicon process - properties and behaviour," Doctoral thesis, NTNU, Department of Materials Science and Engineering, Trondheim, Norway, 2003.
- [66] T. Brynjulfsen and O. K. Bjering, "Førsteutkast av rapport tilhørende sommerprosjekt i ROMA 2008," NTNU, Trondheim, Norway, Internal report, 2008.
- [67] M. Andersson, "Reaction mechanisms in the ferrosilicon production process - Results from a industrial furnace excavation," Master thesis, Luleå University of Technology, Minerals and Metallurgical Engineering Department of Chemical Engineering and Geosciences, 2009.
- [68] M. Tangstad, M. Ksiazek, V. Andersen, and E. Ringdalen, "Small scale laboratory experiments simulating an industrial furnace," in *Sustainable Future*, Helsinki, Finland, 2010, pp. 661–670.
- [69] V. Andersen, "Reaction Mechanism and Kinetics of the High Temperature reactions in the silicon process," Master thesis, NTNU, Department of Materials Science and Engineering, Trondheim, Norway, 2010.
- [70] S. Bao, M. Tangstad, K. Tang, and E. Ringdalen, "Production of SiO gas in the silicon process," presented at the INFACON, Almaty, Kazakhstan, 2013.
- [71] C. Sindland, "Production Rate of SiO Gas from Industrial Quartz and Silicon," Master thesis, NTNU, Department of Materials Science and Engineering, Trondheim, Norway, 2020.
- [72] W. Pultz and W. Hertl, "SiO₂+SiC reaction at elevated temperatures. Part 1 - Kinetics and mechanism," *Trans. Faraday Soc.*, vol. 62, no. 1, pp. 2499–2504, 1966.
- [73] M. S. Khrushchev, "Kinetics and Mechanism of Reaction between Silicon Carbide and Silica," *Inorg. Mater.*, vol. 36, no. 5, pp. 462–464, 2000.
- [74] J. Wang, S. Liu, T. Ding, S. Huang, and C. Qian, "Synthesis, characterization and photoluminescence properties of bulk-quantity β-SiC/SiO_x coaxial nanowires," *Mater. Chem. Phys.*, vol. 135, pp. 1005–1011, 2012.
- [75] M. Saito, S. Nagashima, and A. Kato, "Crystal growth of SiC whisker from the SiO(g)-CO system," *J. Mater. Sci. Lett.*, vol. 11, pp. 373–376, 1992.
- [76] C. A. Pickles and J. M. Toguri, "The Plasma Arc production of Si-based ceramic whiskers," *J. Mater. Res.*, vol. 8, no. 8, pp. 1996–2003, 1992.
- [77] R.-Q. Zhang, Y. Lifshitz, and S.-T. Lee, "Oxide-Assisted Growth of Semiconducting Nanowires," *Adv. Mater.*, vol. 15, no. 7–8, pp. 635–640, 2003.
- [78] S. Noor Mohammad, "Investigation of the oxide-assisted growth mechanism for nanowire growth and a model for this mechanism," *J. Vac. Sci. Technol. B*, vol. 26, no. 6, pp. 1993–2007, 2008.
- [79] K. Y. Cheong and Y. L. Chiew, "Advances of SiO_x and Si/SiO_x Core-shell Nanowires," in *Nanowire science and Technology*, 1st ed., IntechOpen, 2010.
- [80] S. Stølen and T. Grande, *Chemical Thermodynamics of Materials: Macroscopic and Microscopic Aspects*, 1st ed. John Wiley & Sons, 2004.
- [81] M. Ksiazek, "Excavation of Si-furnace 2 at Elkem Salten," SINTEF, Trondheim, Norway, Internal report, 2018.
- [82] M. Kennedy, "Modeling of IF75 temperature profile," Trondheim, Norway, 2018.
- [83] H. Wegge, *Private communication*. Kristiansand, Norway, 2020.
- [84] M. Ksiazek, *Private communication*. 2018.
- [85] Gomez, D. W. Strickler, and L. G. Austin, "An Iodized Mounting Medium for Coal Particles," *Microsc. Res. Tech.*, vol. 1, no. 3, pp. 285–287, 1984.
- [86] I. E. Svenum, *Private communication*. Trondheim, 2018.

- [87] B. Zhong, L. Kong, B. Zhang, Y. Yu, and L. Xia, "Fabrication of novel hydrophobic SiC/SiO₂ bead-string like core-shell nanochains via a facile catalyst/template-free thermal chemical vapor deposition process," *Mater. Chem. Phys.*, vol. 217, pp. 111–116, 2018.
- [88] Y. Hu *et al.*, "Bead-curtain shaped SiC-SiO₂ core-shell nanowires with superior electrochemical properties for lithium-ion batteries," *Electrochem. Acta*, vol. 190, pp. 33–39, 2016.
- [89] Z. Li, W. Gao, A. Meng, Z. Geng, and L. Gao, "Large-Scale Synthesis and Raman and Photoluminescence Properties of Single Crystalline b-SiC Nanowires Periodically Wrapped by Amorphous SiO₂ Nanospheres 2," *J. Phys. Chem.*, vol. 113, no. 1, pp. 91–96, 2009.
- [90] P. Vullum, *Private Communication*. 2018.
- [91] S. L. Katar *et al.*, "Silicon encapsulated carbon nanotubes," *Nanoscale Res Lett*, vol. 5, no. 1, pp. 74–80, 2010.
- [92] W. Zhang, S. Zhang, L. Yang, and C. Tupei, "Evolution of Si suboxides into Si nanocrystals during rapid thermal annealing as revealed by XPS and Raman studies," *J. Cryst. Growth*, vol. 311, no. 5, pp. 1296–1301, 2009.
- [93] F. J. Himpsel, F. R. McFeely, A. Taleb-Ibrahimi, and J. A. Yarmoff, "Microscopic structure of the SiO₂/Si interface," *Phys. Rev. B*, vol. 38, no. 9, pp. 6084–6096, 1988.
- [94] E. A. Dalchiale *et al.*, "XPS and electrochemical studies of ferrocene derivatives anchored on n- and p-Si(100) by Si-O or Si-C bonds," *J. Electroanal. Chem.*, vol. 579, no. 1, pp. 133–142, 2005.
- [95] M. Anwar, C. A. Hogarth, and R. Bulpett, "An XPS study of amorphous MoO₃/SiO film deposited by co-evaporation," *J. Mater. Sci.*, vol. 25, no. 3, pp. 1784–1788, 1990.
- [96] S. Yu, A. Ito, R. Tu, and T. Goto, "Dome-like and dense SiC-SiO₂ nanocomposite films synthesized by laser chemical vapor deposition using CO₂ laser," *Surf. Coat. Technol.*, vol. 205, no. 8–9, pp. 2818–2822, 2011.
- [97] M. Tangstad, J. Safarian, S. Bao, E. Ringdalen, and A. Valderhaug, "Reaction rates of 2SiO₂+SiC = 3SiO+CO in pellets at Elevated Temperatures," *Asp. Min. Miner. Sci.*, vol. 3, no. 2, pp. 1–11, 2019.
- [98] G. Aylward and T. Findlay, *SI chemical data*, 7th ed. Australia: John Wiley & Sons, 2014.
- [99] S. T. Lee, N. Wang, and C. S. Lee, "Semiconductor nanowires: synthesis, structure and properties," *Mater. Sci. Eng. A*, vol. 286, no. 1, pp. 16–23, 2000.
- [100] K. Lim, "Recovery and Utilisation of Kerf Waste from Silicon Wafering Process," Master thesis, NTNU, Department of Materials Science and Engineering, Trondheim, Norway, 2018.
- [101] T. S. Chu, R.-Q. Zhang, and H. F. Cheung, "Geometric and electronic structures of silicon oxide clusters," *J. Phys. Chem.*, vol. 105, no. 9, pp. 1705–1709, 2001.
- [102] K. L. Wallis, J. K. Patyk, and T. W. Zerda, "Reaction kinetics of nanostructured silicon carbide," *J. Phys. Condens. Matter*, vol. 20, no. 32, pp. 325216–325221, 2008.
- [103] S. Jayakumari and M. Tangstad, "Silicon carbide formation from coal in the silicon/ferrosilicon process," in *INFACON XV, International Ferro-Alloy Congress*, Cape Town, South Africa, 2018.
- [104] Y. Liu, M. Jing, W. Feng, L. Cheng, and L. Zhang, "Catalyst-free growth of SiC nanowires in a porous graphite substrate by low pressure chemical vapor infiltration," *Ceram. Int.*, vol. 40, no. 8, pp. 11889–11897, 2014.
- [105] K. Dick, T. Dhanasekaran, Z. Zhang, and D. Meisel, "Size-Depending Melting of Silica-Encapsulated Gold Nanoparticles," *J. Am. Chem. Soc.*, vol. 124, no. 10, pp. 2312–2317, 2002.
- [106] K. Aasly, "Properties and behavior of quartz for the silicon process," Doctoral thesis, NTNU, Department of Materials Science and Engineering, Trondheim, Norway, 2008.
- [107] S. Grådahl and et al., "Miljø og ovnprosesser. Del III," Trondheim, Trondheim, Norway, STF24 F00600, 2000.
- [108] F. Durand and J. C. Duby, "Carbon solubility in Solid and Liquid silicon - A review with Reference to Eutectic Equilibrium," *J. Phase Equilibria*, vol. 20, no. 1, pp. 61–63, 1999.
- [109] A. V. Antipov, R. G. Pavelko, V. G. Sevast'yanov, and N. T. Kuznetsov, "Thermodynamic and Experimental Study of the interaction of Silicon and Carbon Monoxide: Synthesis of Silicon carbide nanofibers," *Russ. J. Inorg. Chem.*, vol. 56, no. 10, pp. 1517–1524, 2011.
- [110] D. H. Filsinger and D. B. Bourrie, "Silica to Silicon: Key Carbothermic Reactions and Kinetics," *J. Am. Ceram. Soc.*, vol. 73, no. 6, pp. 1726–1732, 1990.
- [111] F. Ni, "Kinetics of the reaction between quartz and silicon carbide in different gas atmospheres," Master thesis, NTNU, Department of Materials Science and Engineering, Trondheim, Norway, 2015.
- [112] T. Shimoo, F. Mizutaki, S. Ando, and H. Kimura, "Mechanism of formation of SiC by reduction of SiO with graphite and CO," *Nippon Kinzoku Gakkaishi*, vol. 52, no. 3, pp. 279–287, 1988.
- [113] K. Ono and Y. Kurachi, "Kinetic studies on b-SiC formation from homogeneous precursors," *J. Mater. Sci.*, vol. 26, pp. 388–392, 1991.

- [114] B. Metherall, "Clogging of Charge in Silicon Furnaces," University of Oxford, Technical report for InFoMM CDT Mini-Project 1, 2020.
- [115] K. F. Jusnes, M. Tangstad, and E. Ringdalen, "Shock heating test of quartz for Si and FeSi production," Cape Town, South Africa, 2018.
- [116] P. Tetlie, "Private communication," 2018.
- [117] R. Saadieh, "To be published," PhD thesis, NTNU, Department of Materials Science and Engineering, Trondheim, Norway, 2021.
- [118] T. Lindstad, S. Gaal, S. Hansen, and S. Prytz, "Improved SINTEF SiO-reactivity test," New Delhi, India, 2007, pp. 414–423.

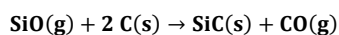
9. Appendix

A. Condensates, SiC and Si formation on graphite

SiC and Si formation in small scale setup

A fine, light-green layer deposited on the walls of the SiO(g) production chamber, the small crucible, the graphite gas lance (Figure 224) and the gas distributor ring located at the bottom of the condensation chamber. The gas production chamber and the small crucible walls are colored in green from the junction with the condensation chamber, until 44 mm from the bottom of the chamber (Figure 224a). At this point, the temperature is estimated to be 1850°C, after the regression of the gas temperature gradient. The graphite lance is covered with a green layer from the gas distribution bottom ring to the gas distribution ring at the bottom of the condensation chamber (Figure 224b). The green layer forms also at the junction between the condensation and the gas production chamber. This results in a challenging opening procedure, which lead once to the destruction of the gas production chamber (after experiment R1e). The layer position did not change relevantly between different experiments. The layer is removed by using SiC sandpaper. Once scratched, the graphite part takes the original appearance and color of graphite.

SE-images show well-organized and piled hexagonal crystals, in correspondence of the green areas (Figure 225). The crystal size range between 12-15 μm diameter. The smallest nanocrystals can reach down to 50 nm in diameter. The layer is around 50-400 μm thick over the gas distributor and the small crucible. EPMA showed that the layer generated contains only SiC. The SiO(g) produced at the bottom of the chamber might have diffused in the carbon by Reaction 3, as described by Lindstad et al. [118].



Reaction 3

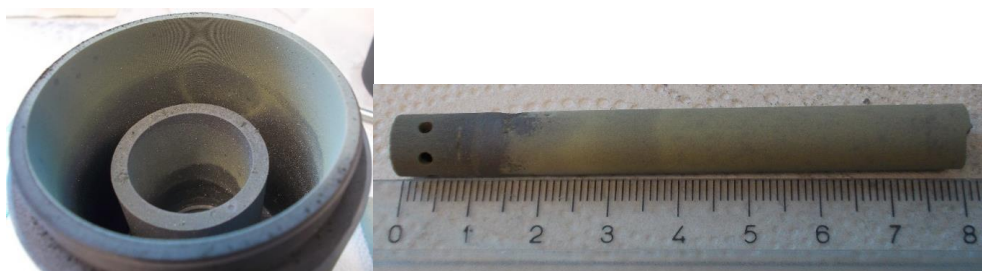


Figure 224: Reaction chamber, crucible and graphite gas lance covered in green layer.

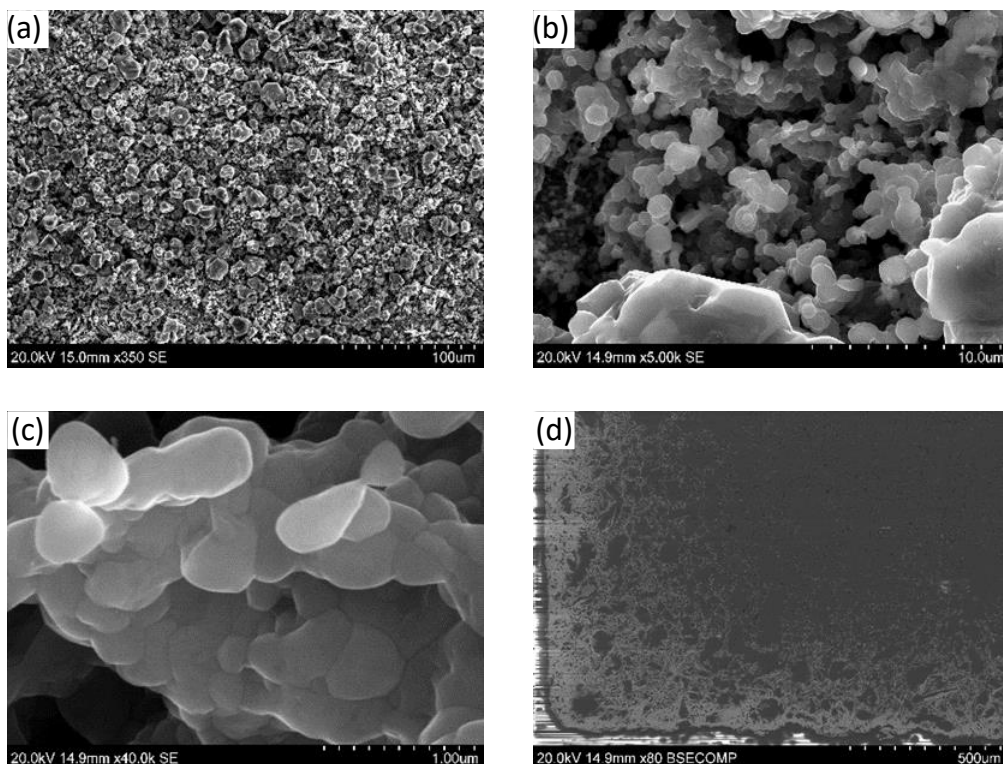


Figure 225: SE images of green SiC layer (a,b) and BSE image of penetration depth into the top gas distributor of Experiment 4b (d).

In Experiment R6a, the whole gas production chamber became silver grey. For the other experiments, the grey, shiny layer covered completely the gas distributor ring at the bottom of the SiO production chamber (Figure 226). The graphite part became stronger in mechanical properties after the experiment. The shining grey layer is also found at the bottom of the graphite gas lance and extends for 44 mm in height from the bottom of the condensation crucible and chamber. SE-images shows crystals with sizes ranging around 10-20 μm (Figure 226). The grey layer penetrates in the graphite for about 300-500 μm. The BSE-image of Figure 226 show Si domains in the SiC layer.

The change in color from green to silver grey is sharp. However, the grey layer has still some green tones in it. That should be a hint of a transition from SiC (green) to a SiC-Si mixture. The formation of the grey layer is believed to occur into two steps. First, the green SiC layer forms by Reaction 3. Then it reacts further with SiO(g) to produce Si by Reaction 4. This mechanism is described also by Lindstad et al. [118].



The partial pressure of SiO(g) in the gas production chamber is assumed to be the theoretical partial pressure coming from the gas mixture. It can be assumed that the partial pressure has the value of $p_{\text{SiO}, \text{in}}$ in the gas

production zone. The space coordinates (1850°C ; $p_{\text{SiO},\text{in}}$) lay well above the $p_{\text{SiO}}\text{-T}$ line for Reaction 4. Formation of Si from SiC and SiO(g) is thermodynamically favored.

Reaction 4 is triggered above the estimated temperature of 1850°C , which is surely trespassed at the bottom of the gas production chamber. SiO(g) diffusion in graphite should be the driving force for Reaction 4. This should also explain why Si formation occurs inside the SiC layer, as it happens for the C – SiC transition. However, Si formation does not occur at the interface between SiC and the atmosphere, but rather in islands inside the SiC domain (Figure 226c). This fact cannot still be explained, but once this passage is understood, the knowledge about the kinetics of Reaction 4 should be clearer.

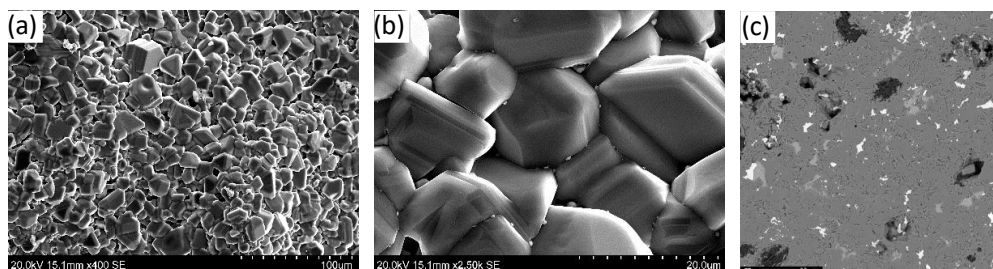


Figure 226: Left and center: Grey condensate on graphite at x400 and x2500 magnifications; Right: Si areas (light grey) in SiC matrix (dark grey). White areas are impurities coming from graphite.

SiC and Si formation in large-scale setup

In the large-scale setup, the gas production chamber is covered with the green layer and with silver grey spots at the end of every experiment, regardless of the pellets composition used. Some areas kept their original graphite color, as for Experiment IF1a. The holes drilled in the chamber top let the SiO(g) pass, without being clogged. However, their diameter decreases slightly due to formation of SiC. At the bottom of the chamber, silver grey droplets forms and glue the chamber to the crucible bottom. Some SiC particles are sticking to the chamber and the droplets (Figure 227). The first 7 cm of the graphite tube in the large-scale setup are also covered in a shining grey layer (Figure 228).



Figure 227: Left: Gas production chamber before Exp. 3a; Center: Top view of green layer on gas production chamber, Exp. 1a; Right: Top view of green and grey layer on gas production chamber, Exp. IF2a.

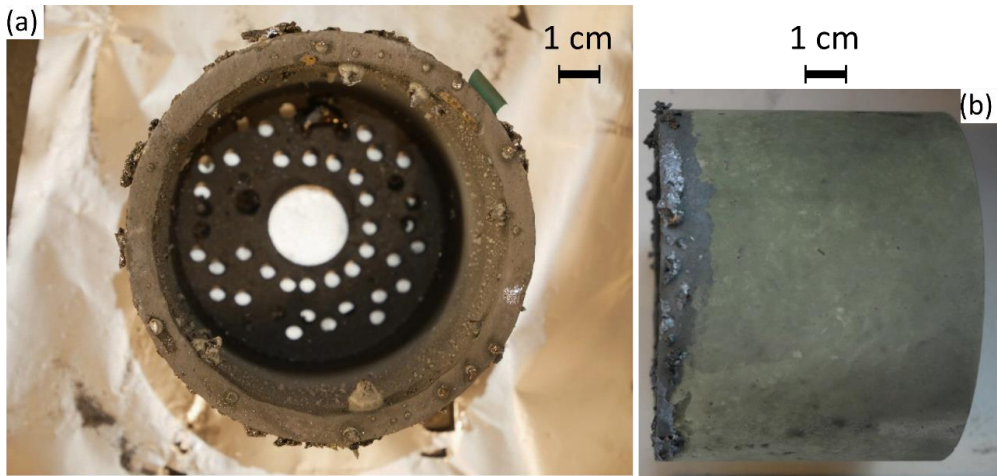


Figure 228: a) Si droplets and SiC particles on gas production chamber, Experiment IF5a; b) Side view of gas production chamber after Exp. IF1a.

The temperature in the gas production chamber range between 1794°C (Exp. IF2b) and 2008°C (Exp. IF7b) at $Y = 1$ cm, and between 1871°C (Exp. IF4) and 1933°C (Exp. IF6) at $Y = 8$ cm. Partial pressures of SiO(g) are either 0.75 or 1, according to the pellets type chosen. However, the corrections to $p_{\text{SiO},\text{in}}$ might already apply to the gas production chamber. The correction considers the consumption of SiO(g) due to the interaction with C and SiC, as explained in the $p_{\text{SiO}}-T$ model chapter. In other words, $p_{\text{SiO},\text{in}}$ should range between 0.71-0.75 for SiO₂-SiC pellets, or between 0.95-1.00 for Si-SiO₂ pellets.

Visual inspection reveals the same texture and color for both the green and grey layer in the small-scale setup. It is assumed that the mechanism of formation and the microstructure of green SiC and grey SiC-Si mixture is the same for both setups, i.e. Reaction 3 for the green layer, and the two-steps mechanism with Reactions 3 and 4 for the grey layer.

SiC whiskers in laboratory-scale experiments

SiC whiskers appeared as a green or white layer, on both graphite and SiC substrates. Their appearance is more frequent for the large-scale setup. They are formed together with SiC-SiO_x nanowires. Their diameter ranges between 1-3 μm in diameter. The whiskers have mainly two microstructures. The first one is a classical pillar microstructure (Figure 229), which can reach lengths up to 100 μm . The second one has a thinner diameter, but a characteristic droplet at the top (Figure 230). EDS on the droplets showed the presence of Al, Fe, Si, O, C and Ti.

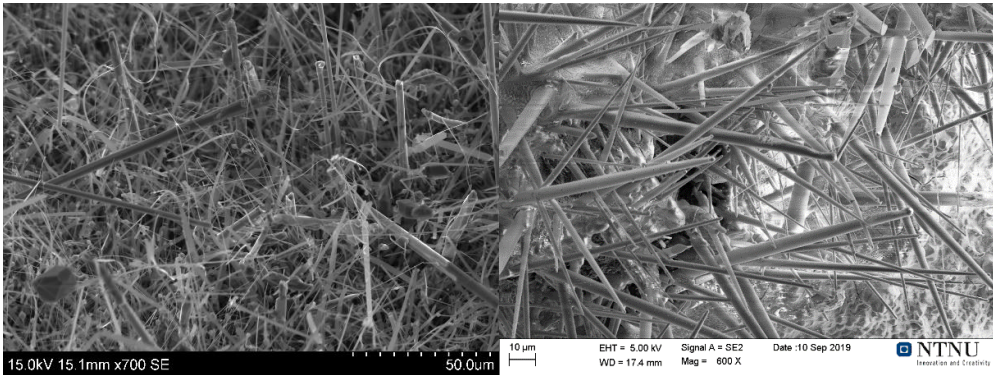


Figure 229: Pillar whiskers from experiments R6a (left) and IF1a (right)



Figure 230: Droplet SiC whiskers from experiment R6a.

Crystalline SiC nanowhiskers are generated in experiment R6a, together with blue condensate. Figure 231 and Figure 232 show the microstructure of the new product. SiC nanowhiskers were noticed only in this experiment and in the large-scale setup, together with white condensate. It can be that SiC whiskers are typical of gases at high temperatures. Fei [10] and Jayakumari [22] noticed the same type of whiskers in the temperature interval 1500-1600°C.

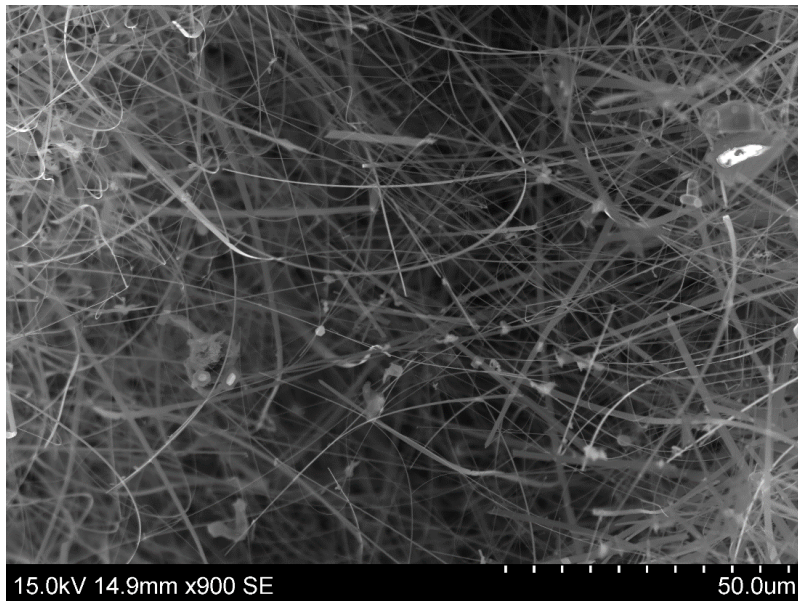


Figure 231: Blue condensate at high temperatures, Exp. R6a

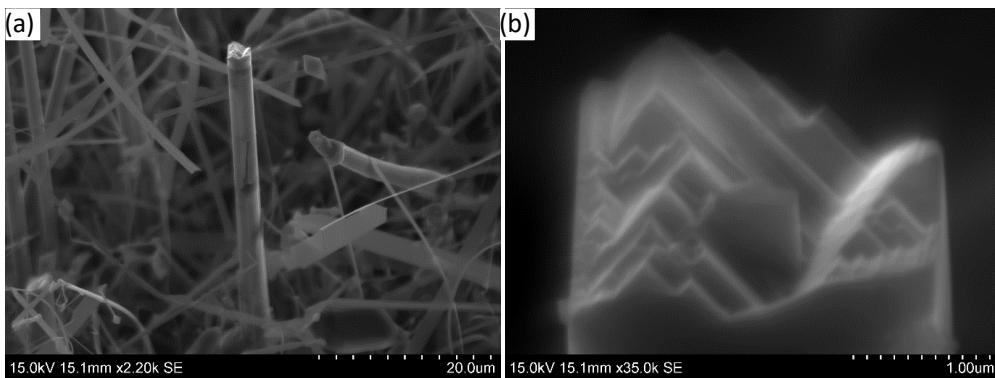


Figure 232: SiC nanowhiskers at x2200 (a) and x35000 (b) magnification, Exp. R6a

The SiC whiskers might have formed from the gas phase at high temperatures. In fact, the Si_xC_y gas species are more stable and increase their concentration above 2000°C , as documented by Jayakumari [22]. The pillar whiskers could form by Vapor-Solid (VS) growth, whereas the droplet whiskers could follow the Vapor-Liquid-Solid (VLS) growth mechanism. The main difference between the mechanism is the presence of impurities, which act as catalyst in a liquid phase. Both whiskers VS and VLS whiskers are also formed in the industrial samples. The whiskers are sometimes embedded into a matrix, made of SiO_2 and SiC. The matrix could form from condensation or from materials in the charge, which could have molten earlier. Hence, it can be said that the embedded whiskers form in two steps. First, the Si_xC_y species condense at high temperatures. Then, silica from raw materials or from condensates embeds them into a continuous layer.

SiC whiskers in industrial samples

Pale green and white areas were noticed on most of the samples. The pale green portions on sample W1-34 are shown as an example in Figure 233. The white areas, however, can be easily mistaken with nanowires at visual inspection. In fact, SEM analysis would be the only way to distinguish them. Besides, the mechanical property of whiskers and nanowire condensates are very similar. Both compounds are thin, opaque and easy to remove. Sample W1-43 is shown as an example of white layer containing SiC whiskers.



Figure 233: Left: Green layers in sample W1-34; Right: White areas on sample W1-43.

The SiC microstructures analyzed could be divided into two groups:

Group 1: SiC whiskers similar to the laboratory scale experiments. The whiskers are shorter and straighter than the nanowires. Most of these whiskers are sticking to SiC surfaces, which were originally made of carbonaceous materials (charcoal or woodchips).

Most of the times, SiC whiskers are immersed in a SiO₂ matrix. The matrix also embeds the charcoal particle surface of sample REC 1.2 and REC 1.3 (Figure 234). Similar microstructures were also revealed in Sample W1-38, REC 3.3 and S.22, S.23, S.36. Whiskers vary in size and shape according to the sample chosen. For example, sample REC 1.1 has thinner whiskers than REC 1.2 (Figure 235).

The whiskers found in sample W4-29 are not inserted in this category. In fact, the whiskers from Figure 139 are only covered in nodules, whereas here the whiskers are completely embedded into the SiO₂ matrix.

Group 2: Whiskers have a spherical droplet on the top. (Figure 236). These whiskers are very thin. Sample W1-31,34,43, REC 1.2,3.1, 3.2, W4-29,30 showed this microstructure on their white surfaces. EDS was performed on sample W1-31, in SE-mode (Figure 237). The analysis detected Si and C in large quantities, with minor amounts of oxygen (Table 49).

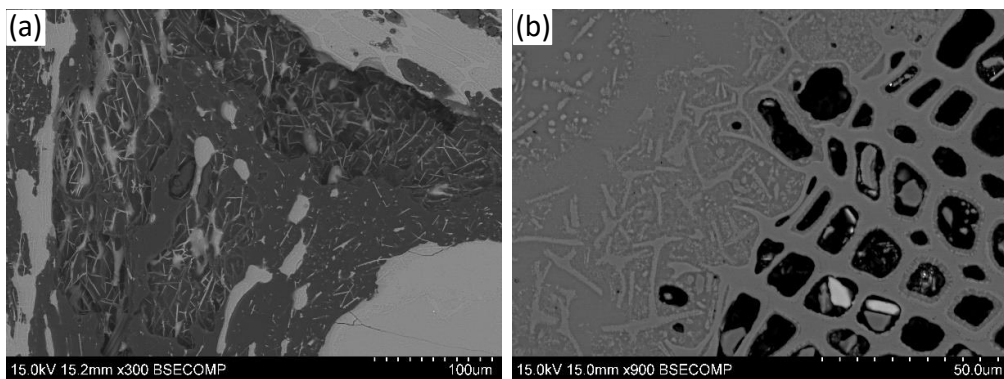


Figure 234: Whiskers in sample REC1.2 ; Right: SiC Whiskers deposited on charcoal particle converted to SiC, embedded in SiO₂ matrix, sample REC 1.3.

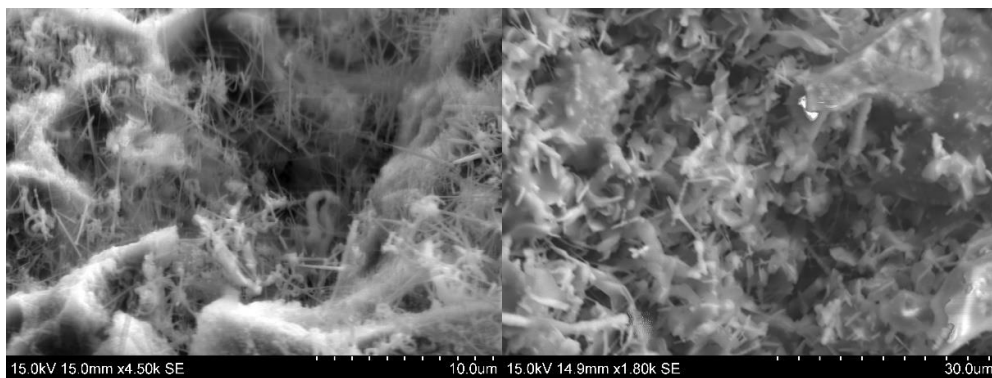


Figure 235: Whiskers and nanowires from sample REC 1.1 (left) and REC 1.2 (right).

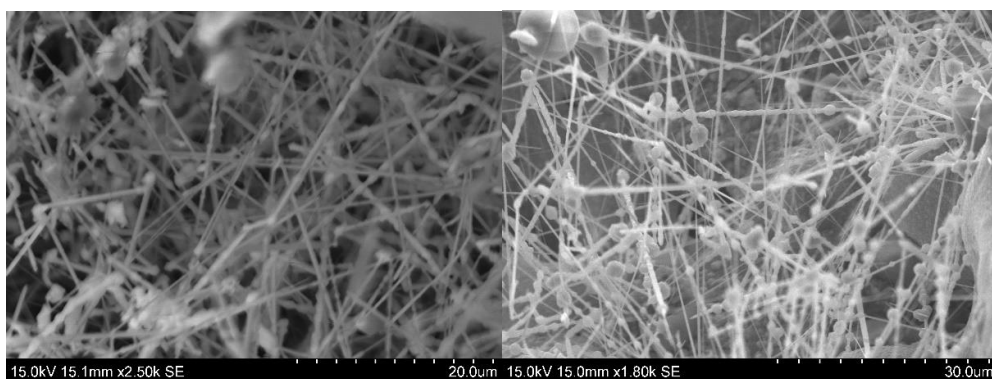


Figure 236: Whiskers with spherical cap, sample REC 3.1 (left) and W4-30 (right).

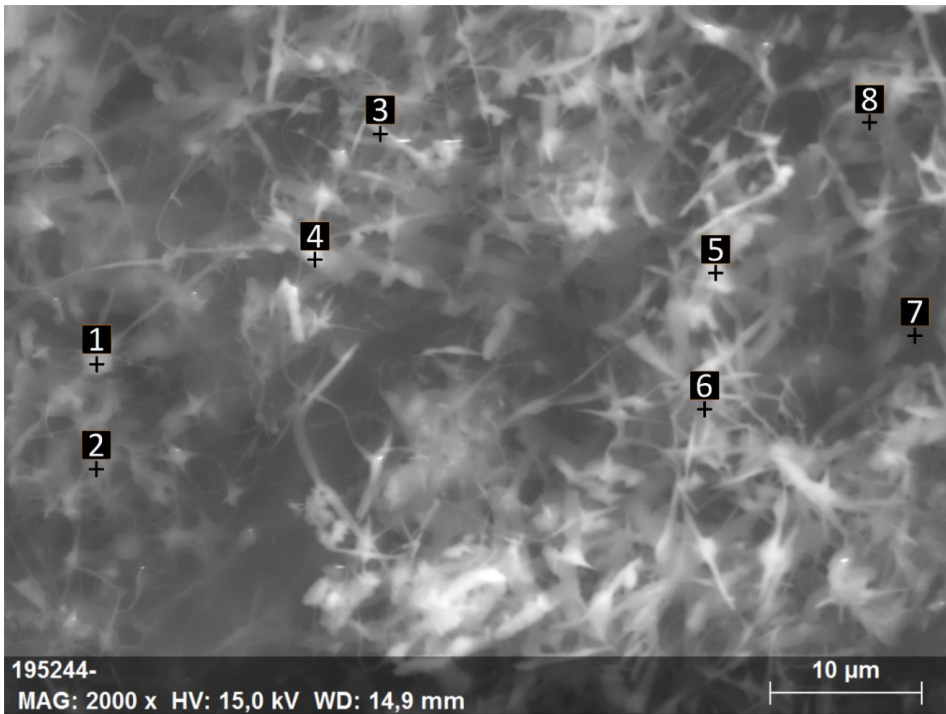


Figure 237. EDS overview of whiskers from sample REC 3.2

Table 49: Composition found at the points from Figure 237 (at. %).

Point	Si (at. %)	O (at. %)	C (at. %)
1	80%	6%	14%
2	85%	5%	10%
3	74%	9%	18%
4	79%	6%	15%
5	76%	5%	19%
6	67%	10%	23%
7	83%	4%	13%
8	85%	4%	11%

Condensates formation on graphite

Visual inspection: Large-scale setup

Condensates also cover the graphite tube of the large-scale setup. White, grey and green layers are formed in every large-scale setup experiment. Two examples are shown in Figure 238 and Figure 239. The ruler on the picture is showing the position coordinate from the bottom of the crucible.

The tube could be divided into four parts, according to the color of the condensate. The space coordinate Y is shown by the ruler in the figures.

Zone 1: Y = 0 – 7 cm ($\approx 1900^\circ\text{C}$): this part corresponds to the portion of the tube located in the SiO production zone. The tube has turned dark grey, and is covered in small, shining crystals. It is thought that the tube is covered in Si and SiC. For further information about Si and SiC production on graphite, see Appendix A.

Zone 2: Y = 7 – 15 cm ($1890 - \approx 1650^\circ\text{C}$): a pale-green and white coating forms. This color is associated to SiC formation, as described in Appendix A. The coating tends to a pale blue and white color while moving up, towards lower temperatures.

Zone 3: Y = 15 – 19 cm ($\approx 1650 - \approx 1500^\circ\text{C}$): Brown and grey layers form in proximity of those generated on SiC substrates (Figure 239). The tube is still pale-green when scratched from the layers.

Zone 4: Y = 19 – 24 cm ($\approx 1500 - \approx 1300^\circ\text{C}$): The coating gradually turns from white to blue, while keeping a pale green background.

Above 24 cm, the tube turns back to its original color and texture. The portion of the tube above the crucible ($Y > 31$ cm) is usually oxidized and vaporizes to CO_2 thanks to the oxygen in the surrounding air.

The condensation zone in the large-scale setup is 5 times wider than in the small-scale crucible. Therefore, the lateral temperature gradient in the large-scale setup is more significant, as described in Appendix C.



Figure 238: Graphite tube protecting the thermocouple in the large-scale setup, Experiment IF2a.



Figure 239: Graphite tube protecting the thermocouple in the large-scale setup, Experiment IF3a.

Visual inspection: Small scale setup

Condensates with different colors were found on the internal walls of the condensation zone in the small-scale setup. An analysis was carried out on different sections, to see how the condensate evolves through the temperature gradient. To do so, the condensation chamber was extracted and sectioned into six parts by a diamond blade with 2 mm thickness. The sections were numbered from 1 to 6, from the top to the bottom of the tube. Then each section was cut across into two. One cross-section was kept for topographic and morphological analysis (SE-SEM). The other was cast into epoxy for metallographic analysis (BSE-SEM). Figure 240 shows how the tube was sectioned, and how each cross section looked like.

The tube can be divided into four temperature areas: which eventually overlap:

- 1) **Clean crucible (up to 1470°C).** No interaction is noticed between SiO(g) and the graphite crucible at temperatures below 1470°C .
- 2) **Blue and white layers ($1470-1700^\circ\text{C}$).** These layers could be present also at lower temperatures. The cutting and handling procedure removed part of the accumulated scale.

- 3) **Grey and brown layers (1600-1700°C).** They come on the top of the white layer, or together with it. The grey scale is stronger and more difficult to remove than the white. It can be that part of the grey and brown scale was removed while handling the graphite tube.
- 4) **Pale green layer (above 1700°C).** The scale layers suddenly stop, and the tube assumes a pale green color. This color is associated to SiC formation, as described in Appendix A. SiC diffusion also occurs below 1700°C behind the scale deposition (1470-1780°C).

Condensates deposit also on the external walls of the graphite holder (Figure 240b). By assuming that the gradient is the same both inside the chamber and outside the holder, the blue and white layer is formed between ≈ 1000 - 1400°C ($Y = 60$ - 110 mm in experiment R3c). This layer is easily removed while handling the holder during the extraction of the substrates. Compared to the deposits on the SiC particles, this layer has lower mechanical strength, weight and thickness.

By comparing the profiles of the tubes with the condensation on SiC, it can be concluded that condensation on graphite follows a similar temperature profile compared to condensation on SiC.

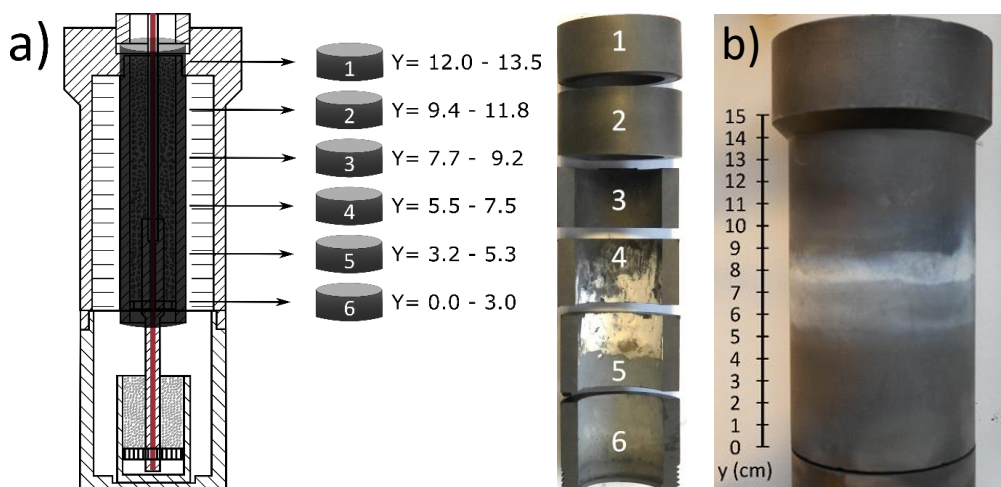


Figure 240: Tube overview and numbering of sections from 1 to 6. The values of Y are given in cm; b) Thin white and blue layer generated outside of the small-scale crucible, Exp. R3c.

Microstructure, composition and temperature of formation

It was seen that the condensates on graphite can assume either a white/blue color, or a grey/brown color. This happened for both the small-scale and the large-scale setup. This section focuses on the microstructural analysis of each scale found in the internal walls of the condensation chamber, i.e. in the small-scale setup only.

The white and blue condensate appear on carbon as a disordered nanowire web, as it happened for the SiC substrates (Figure 241). The nanowire size and length are comparable to what was found on the SiC substrates, especially for blue condensate. In fact, the SEM pictures look similar, and are taken at magnifications similar to Figure 97 and Figure 98. This microstructure is found on the thin blue and white layers of section 4 of the analyzed graphite tube (refer to Figure 240), but also on condensates located outside of the crucible walls.

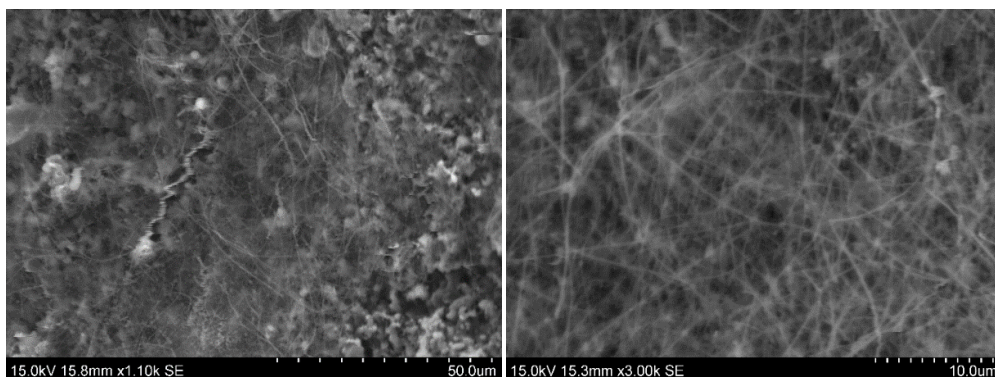


Figure 241: Blue scale (left) and white scale (right) on Section 4 of the graphite tube.

The grey condensate is organized into oriented wires. The microstructure is shown in the SE-SEM analysis in Figure 242. The figure is taken on the sample from section 5 ($Y \approx 4.0$ cm). The spheres are packed in finger-like structures (Figure 242a), which are made of oriented treads (Figure 242b). The oriented treads can be embedded in a matrix, at the top of the condensate (Figure 243a). At smaller scale, the deposit looks like a compact layer, made of packed small spheres (Figure 242c). Due to the similarities with the grey condensate formed on SiC, the two condensates were assumed to have the same composition.

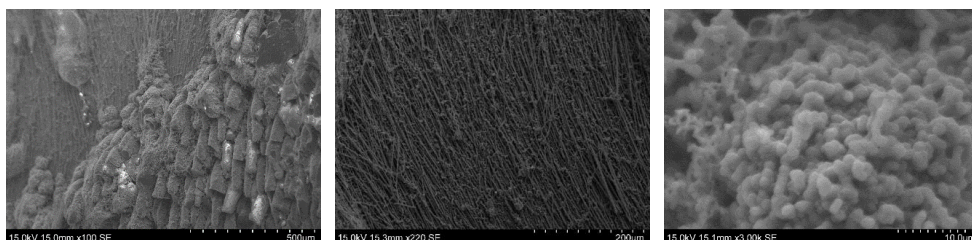


Figure 242: Grey condensate from Section 5. Left: Finger structure; Center: Oriented wires on grey scale; Right: Building blocks of grey scale.

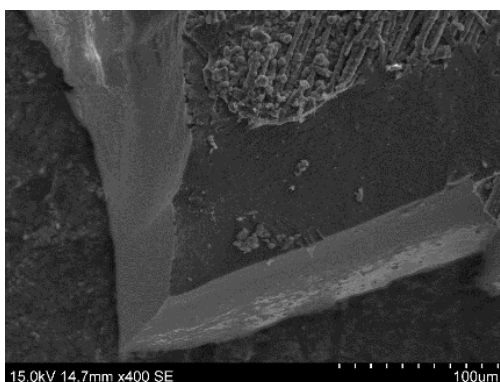


Figure 243: Grey scale on Section 5, top view.

EDS was performed on Section 5 of the condensation chamber ($Y = 3.2 - 5.3$ cm). The analyzed area is shown in Figure 244, and the results of the analysis are collected in Table 50. The picture can be divided into three areas:

- 1) The portion on the left is the epoxy where the samples are embedded.
- 2) The central white zone (points 4-6) corresponds to the white and grey scale on the graphite crucible. A higher C concentration corresponds to a higher porosity, since the signal would come from the embedding resin.
- 3) On the right side, there are two phases. SiC inclusions (points 4-5) are generated on the external edges of a graphite matrix (points 10-12).

After seeing the similarity in thickness, color and mechanical properties, it was concluded that the scales formed on the condensation chamber walls (small-scale setup) and the graphite tubes (large-scale setup) have similar microstructures and compositions.

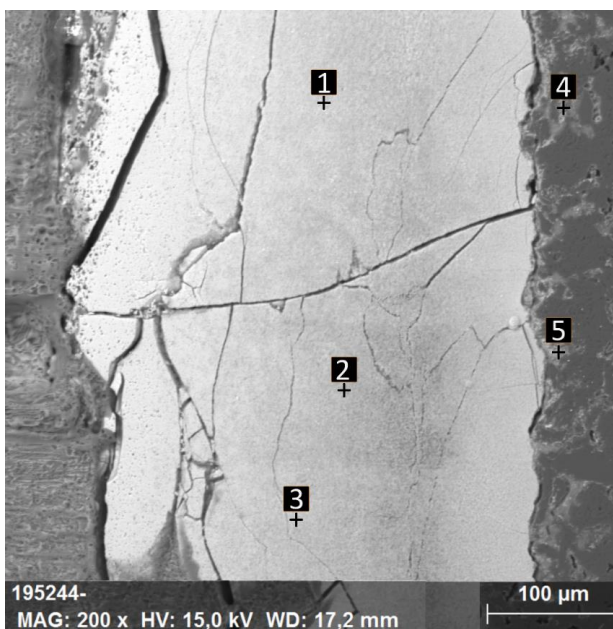


Figure 244: EDS overview for the scale on graphite, section 5.

Table 50: EDS analysis at the points of Figure 244 and compound present at each point

Point	Si	O	C	I	Material
1	61%	21%	16%	1%	White scale
2	48%	18%	32%	1%	White scale
3	56%	18%	25%	1%	White scale
4	21%	3%	75%	1%	Graphite and SiC
5	32%	2%	66%	0%	Graphite and SiC

The condensates do not generate directly on graphite, but on a produced SiC layer, located between the condensate and the graphite tube (Figure 245a). The thickness of the SiC layer ranges between 100-500 μm. SiC forms through Section 4 to 6, from the bottom of the tube to the coldest zones where condensation takes place on the SiC particles. Figure 245b shows SiC formation in section 6. SiC crystals are detected at SE-SEM analysis. Further information on SiC generation on graphite crucible is provided in Appendix A.

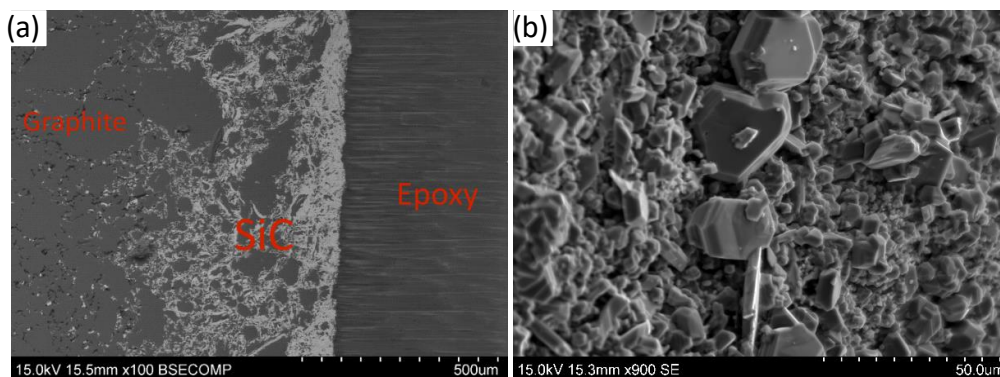


Figure 245: a) SiC production in graphite tube; b) SiC crystals on graphite tube, Section 6.

The condensates from this analysis are accumulated after different experiments, performed at different conditions. The condensate on graphite are stronger and harder to remove, compared to those generated on SiC. The thickness can range up to few hundreds of μm . Part of the scale is also removed while extracting the SiC substrates from the reaction chamber.

Since the tube in the small-scale setup was collected after performing experiments with SiC only, the temperature profile of the graphite tube was assumed to be the same as the one computed for SiC, in Setup 1. The tube chamber was assumed to be narrow enough to have the same temperature both at the center and at the graphite tube walls. The temperature difference from the center to the chamber walls should be negligible in a radius of 13 mm (in the small-scale setup).

The temperature on the graphite surfaces might be different however, since the graphite parts in both furnaces heat up during the experiments. The graphite walls act as heating elements, therefore they could be warmer than expected. However, the temperature measurements in the system have been taken anyways as starting points for temperature estimation of condensation on graphite.

Table 51 reports the condensates temperature of formation on graphite for the small and large-scale setups. Most of the temperature intervals are comparable between the setups, but also with SiC and quartz as substrates.

Table 51: Overview of condensates temperature of formation on graphite, large and small-scale setups.

Condensate type	Temperature
Si-SiO ₂	Small scale: 1600 - 1700°C Large-scale: Not formed
	Blue and white scales Small-scale: 1460-1600°C Large-scale: 1300-1650°C
SiO ₂ -SiC	Grey scale Small-scale 1600-1700°C Large-scale: 1500 - 1650°C
	Green layer (SiC formation by SiO(g) diffusion in graphite) Small scale: 1460-1810°C Large-scale: 1300 - 1890°C

B. FIB preparation

This section shows the FIB preparation step by step, with the help of the SEM pictures taken during operation. The surface was coated with carbon while being in the preparation chamber. The sample was inserted in the SEM chamber. Pictures were collected applying a 15 or 30kV voltage.

Once a suitable spot was individuated, the sputtering current and voltage at the carbon source were set to 750pA and 5kV (Figure 246). This was made in order to extract a sample with a thickness of about 1 μm.

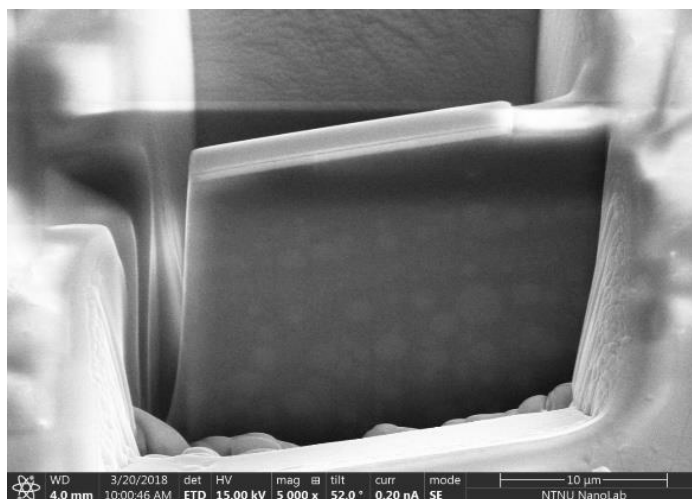


Figure 246: Individuation and definition of the sample on the surface substrate

A tungsten tip was put close to the sample and welded to the carbon deposited layer. The tip can be controlled from the SEM unit. The sample could be easily extracted, once it stuck to the substrate only by a thin face. Figure 247 shows the sequence of picture taken during extraction.

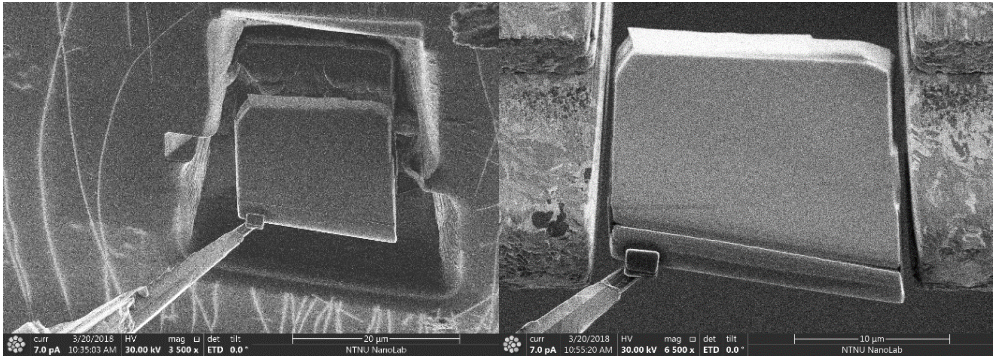


Figure 247: Extraction of the sample. The sample is ready for welding to the grid.

The tungsten tip was moved until it reached the dedicated TEM grid. The sides of the chosen sample were welded with tungsten and carbon to the TEM grid slot (Figure 248).



Figure 248: Insertion onto the dedicated TEM grid.

About 10 sputtering steps at 63pA and 5kV were performed, until the section reached a thickness of 100 nm. The surface damage is down to sub-nanometer scale, according to the instrument description. The final aspect of the lamella is shown in Figure 249.

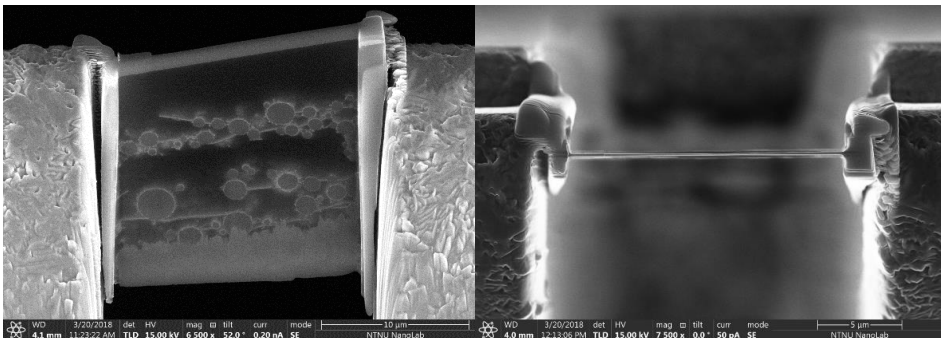


Figure 249: Final aspect of the TEM lamella of brown condensate. Front view (left) and lateral view (right).

C. Computation of temperature gradients

Small scale

Thermal histories were recorded during different experiments. Both the thermal history and the thermal gradient were computed for different setups. It was assumed that measurements from different experiments could be coupled to build up the temperature gradient. In fact, the condensation profiles were very similar between different replicas of the same setup. For each chosen point, the temperature was measured as a function of time.

Figure 250, Figure 248 and Figure 252 show how the temperature varies in time for different positions. The temperature reaches a plateau after ≈ 40 minutes from the beginning of the experiment. The pyrometer temperature rises above 2000°C for about 5 minutes before going back to the target temperature. The temperature at the thermocouples stabilizes into a plateau after slightly longer times, compared to the furnace pyrometer position. The temperature decreases while the pyrometer temperature is constant. The temperature difference experienced at each position is visualized in Figure 251a, by the error bars. The marker on the graph is not a value around which the temperature oscillates, but only the average temperature over the plateau. The broadness of the temperature interval increases while going towards lower temperature. The average temperature of each interval is taken as a point for the second-grade polynomial regression. The result of the regression is the temperature gradients computed and used for the temperature estimation in the crucibles (Figure 251b). The regression functions are collected in Table 52, together with the temperature values used for the polynomial regression and the experiment where these were measured.

For those experiments where the gradient was measured, the temperature changes by about $10^{\circ}\text{C}/\text{mm}$.

Table 52: Regression function for small scale setup experiments

Setups	Experiment	Measured value ($^{\circ}\text{C}$)	Position (mm)	Function
1	1b	1765	0	$T = -1.38y^2 - 82.19x + 1765$
	1c	1505	30	
	1d	1122	70	
3, 4, 5	4c	1810	0	$T = -5.89y^2 - 20.667y + 1810$
	4d	1695	30	
	4e	175	150	
10, 12, 13, 15	15a	1745	0	$T = -1.98y^2 - 72.70y + 1745$
	15a	1332	50	
	15a	820	100	
14	14a	1816	-20	
	14a	1566	30	
	14a	1046	80	
17,19	19a	1775	0	$T = -1.75y^2 - 76.50y + 1775$
	19a	1350	50	
	19a	830	100	
20,21	20a	1764	8	$T = -1.64y^2 - 75.98y + 1764$
	20a	1340	58	
	20a	840	108	

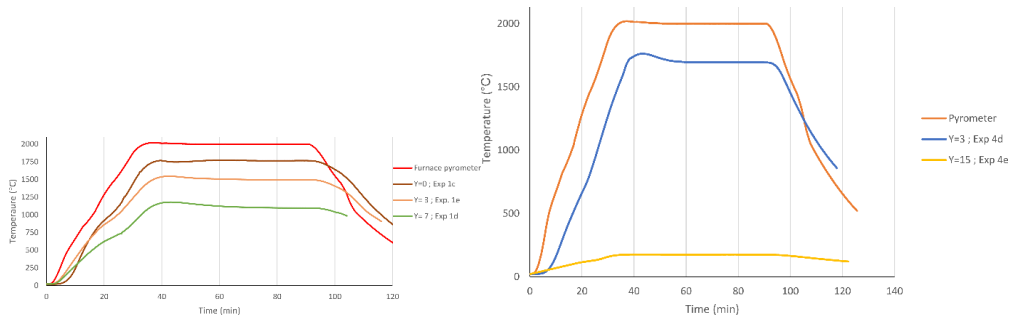


Figure 250: Thermal histories of pyrometer temperature and thermocouples in setups 1c,1d,1e (left) and setups 4d-4e (right).

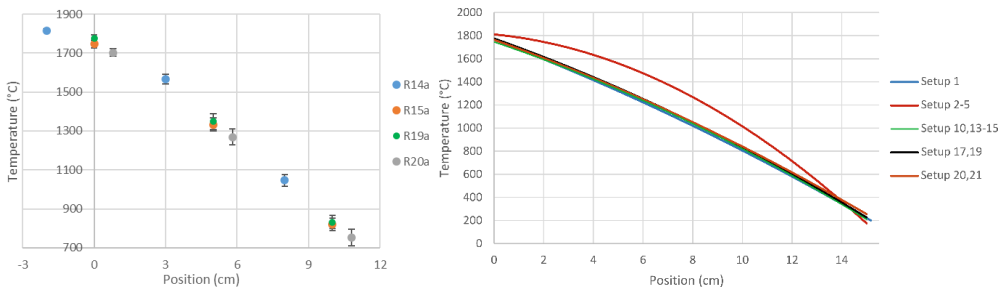


Figure 251: Temperature gradients computed in small scale setup: Temperature interval within time during different experiments.

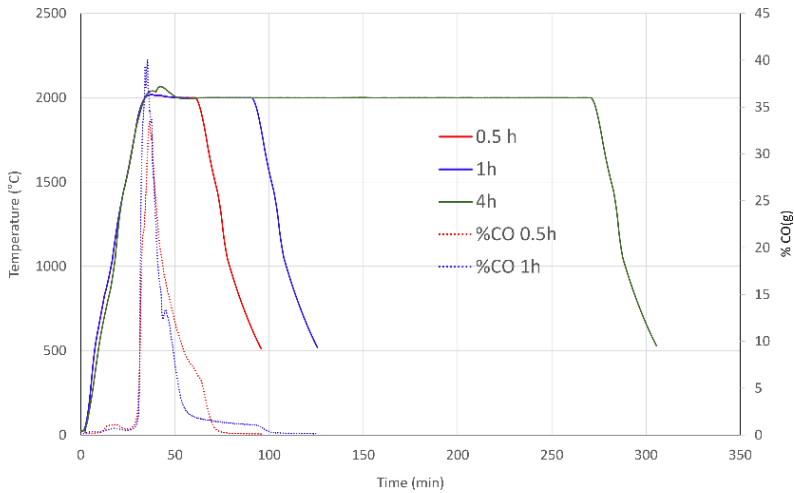


Figure 252: Temperature profile and CO production in setups 3,4 and 5.

Figure 253 shows the thermal history of experiment R8a. The logging position are the furnace pyrometer and a thermocouple at Y=0 in the condensation chamber. A temperature of 1673°C was measured during the plateau.

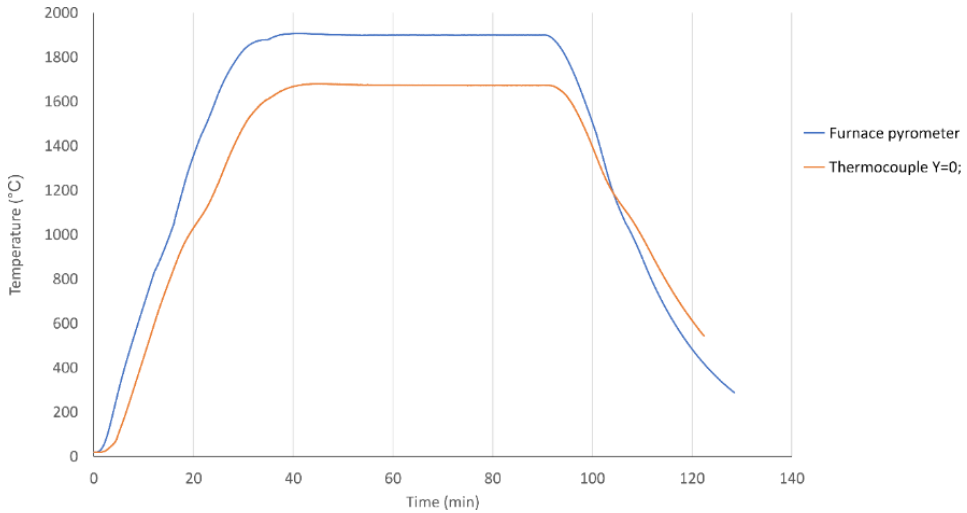


Figure 253: Thermal history of Experiment R7b at the furnace pyrometer and at Y = 0 mm.

The change in temperature during the experiments is always larger than the thermocouple measurement uncertainty. The error certified by the thermocouple wire producer is about $\pm 1\%$ of the measured value, i.e. 20°C at 2000°C.

Large-scale

Vertical gradient

Table 53 collects the regression function calculated for each experiment, together with the temperature's values used for the regression and the thickness of the temperature variation during the experiment. The table includes the coordinate at which the temperature history is measured, the maximum and minimum temperature registered, their average value and the thickness of the interval. The regression formula is computed by Microsoft Excel. Its grade depends on the amount of temperature points collected. For example, if all the five thermocouples were working, the regression would be a 4th-grade polynomial function.

The temperature changes by about 30-50°C/cm.

Table 53: Experimental data and variation of temperature through time for each experiment performed in the large-scale setup. Tmin, Tmax and TAvG are the minimum, maximum and average temperature over the experiment history (in °C). The deviation is the width of the temperature interval from TAvG to Tmax (or Tmin), expressed in K.

Experiment IF1b: $T = 0.00001y^4 + 0.0558y^3 - 3.6588y^2 + 33.252y + 1832.9$				
Y (cm)	Tmin	Tmax	TAvG	Deviation
1	1796	1929	1863	67
8	1880	1906	1893	13
15	1659	1728	1694	35
22	1298	1448	1373	75
29	937	1137	1037	100

Experiment IF2a: $T = -0.0272y^2 - 32.898y + 2154.4$				
Y (cm)	Tmin	Tmax	Avg	Deviation
8	1876	1903	1889.5	14
22	1377	1458	1417.5	41
29	1125	1230	1177.5	53

Experiment IF2b: $T = 0.0034y^4 - 0.1592y^3 + 0.385y^2 + 10.569y + 1850.7$				
Y (cm)	Tmin	Tmax	Avg	Deviation
1	1794	1929	1862	68
8	1880	1905	1893	13
15	1706	1760	1733	27
22	1279	1484	1382	103
29	891	1179	1035	144

Experiment IF3a: $T = 0.0379y^3 - 2.6698y^2 + 20.262y + 1878.4$				
Y (cm)	Tmin	Tmax	Avg	Deviation
8	1875	1903	1889	14
15	1671	1748	1709.5	39
22	1365	1506	1435.5	71
29	1060	1230	1145	85

Experiment IF4: $T = 0.018y^3 - 2.508y^2 + 25.617y + 1835.9$				
Y (cm)	Tmin	Tmax	Avg	Deviation
1	1799	1919	1859	60
8	1871	1908	1890	19
15	1680	1753	1717	37
22	1296	1458	1377	81

Experiment IF5a: $T = 0.0638y^3 - 3.7795y^2 + 31.355y + 1849.1$				
Y (cm)	Tmin	Tmax	Avg	Deviation
1	1807	1945	1876	69
8	1873	1914	1894	21
15	1615	1745	1680	65
22	1300	1483	1392	92
29	1035	1234	1135	100

Experiment IF5b: $T = 0.1076y^3 - 7.2515y^2 + 102.98y + 1484.7$				
Y (cm)	Tmin	Tmax	Avg	Deviation
8	1878	1921	1900	22
15	1699	1823	1761	62
22	1243	1530	1387	144
29	802	1193	998	196

Experiment IF6a (central): $T = 0.0007y^4 - 0.0021y^3 - 2.2252y^2 + 23.6385y + 1840.1$				
Y (cm)	Tmin	Tmax	Avg	Deviation
1	1795	1928	1861.5	67
8	1873	1904	1888.5	16
15	1682	1761	1721.5	40
22	1366	1476	1421	55
29	1023	1151	1087	64

Experiment IF6a (lateral): $T = 0.0753y^3 - 4.8790y^2 + 60.3416y + 1706.0$				
Y (cm)	Tmin	Tmax	Avg	Deviation
8	1897	1933	1915	18
15	1747	1788	1767.5	21
22	1434	1514	1474	40
29	1148	1231	1189.5	42

Experiment IF6b: $T = 0.0005y^4 + 0.0323y^3 - 3.2994y^2 + 29.315y + 1854$				
Y (cm)	Tmin	Tmax	Avg	Deviation
1	1795	1965	1880	85
8	1879	1913	1896	17
15	1500	1874	1687	187
22	1275	1464	1370	95
29	961	1220	1091	130

Experiment IF7a: $T = 0.0022y^4 - 0.0954y^3 - 0.3331y^2 + 5.6937y + 1910.2$				
Y (cm)	Tmin	Tmax	Avg	Deviation
1	1823	2008	1915.5	93
8	1880	1909	1894.5	15
15	1678	1739	1708.5	31
22	1276	1457	1366.5	91
29	895	1110	1002.5	108

Experiment IF7b: $T = 0.0006y^4 + 0.0071y^3 - 2.3803y^2 + 23.487y + 1851.4$				
Y (cm)	Tmin	Tmax	Avg	Deviation
1	1794	1951	1873	79
8	1873	1980	1893	87
15	1679	1765	1722	43
22	1359	1501	1430	71
29	1024	1219	1122	98

Experiment IF8: $T = 0.0046y^4 - 0.2204y^3 + 1.2418y^2 + 8.5998y + 1836.9$				
Y (cm)	Tmin	Tmax	Avg	Deviation
1	1797	1896	1847	50
8	1874	1908	1891	17
15	1710	1755	1733	23
22	1256	1443	1350	94
29	859	1108	984	125

Experiment IF9: $T = 0.0018y^4 - 0.0662y^3 - 1.316y^2 + 23.883y + 1810$				
Y (cm)	Tmin	Tmax	Avg	Deviation
1	1810	1855	1833	23
8	1873	1908	1891	18
15	1709	1775	1742	33
22	1397	1453	1425	28
29	1031	1136	1084	53

Experiment IF10: $T = 0.0008y^4 - 0.0047y^3 - 2.3499y^2 + 26.681y + 1832.7$				
Y (cm)	Tmin	Tmax	Avg	Deviation
1	1830	1884	1857	27
8	1881	1912	1897	16
15	1691	1764	1728	37
22	1372	1455	1414	42
29	997	1128	1063	66

Experiment IF11: $T = 0.0933y^3 - 6.6115y^2 + 90.907y + 1542.1$				
Y (cm)	Tmin	Tmax	Avg	Deviation
8	1884	1904	1894	10
15	1705	1761	1733	28
22	1288	1383	1336	48
29	829	958	894	65

Experiment IF12: $T = 0.0554y^3 - 3.852y^2 + 38.921y + 1805.6$				
Y (cm)	Tmin	Tmax	Avg	Deviation
1	1832	1853	1843	11
8	1878	1905	1892	14
15	1693	1748	1721	28
22	1351	1409	1380	29
29	1003	1092	1048	45

Horizontal gradient

Figure 254 shows the differences in the temperature gradient in experiment IF6a. The central thermocouple and the lateral thermocouple gradients are plot in the same graph, together with error bars. The temperature is higher in the lateral setup. The average temperature over time is highlighted with a marker in the setup. A temperature gradient is computed when the thermocouple recorded the temperature continuously in at least 3 points. The average temperature of the lateral setup is located outside of the temperature interval. The temperature difference due to the setup geometry is larger than the temperature variation over time.

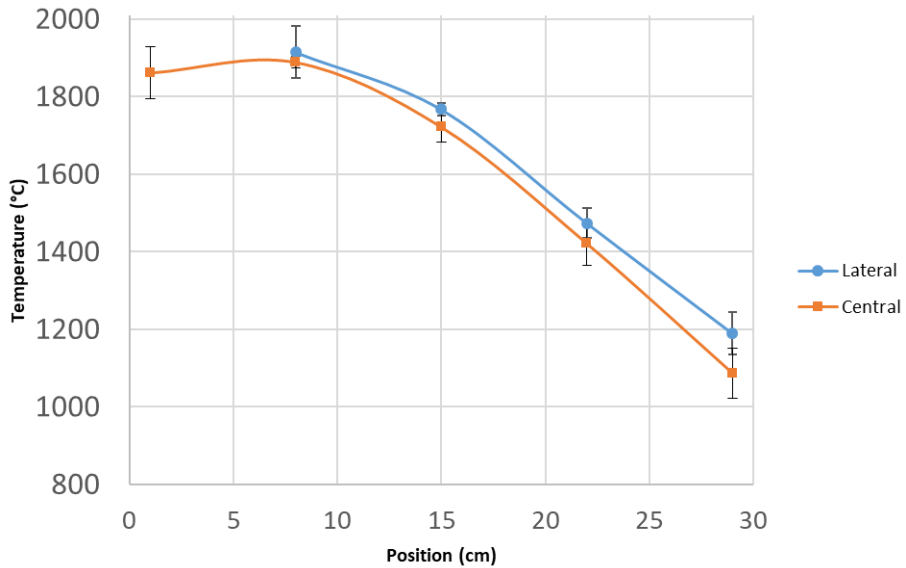


Figure 254: Lateral and central temperature gradient in experiment IF6a.

The values chosen for each position in experiment IF6a are listed in **Error! Reference source not found.**. To establish a temperature gradient for this experiment, a new average temperature is required. This is the average between the central and the lateral temperature. The deviation in **Error! Reference source not found.** expresses the difference of temperature from the center to the edges. The geometric temperature variation is larger than the temperature variation which occurred during the experiment.

Table 54: Temperature gradient computed for experiment IF6a.

Position (cm)	T central	T lateral	Avg T	Deviation
7	1915	1897	1906	9
8	1915	1888	1902	13
9	1909	1876	1892	17
10	1897	1859	1878	19
11	1880	1838	1859	21
12	1858	1814	1836	22
13	1831	1786	1809	23
14	1801	1755	1778	23
15	1768	1721	1744	23
16	1731	1685	1708	23
17	1692	1646	1669	23
18	1651	1604	1627	23
19	1608	1561	1584	24
20	1564	1515	1540	24
21	1521	1466	1494	28
22	1474	1421	1447	27
23	1429	1373	1401	28
24	1385	1324	1354	31
25	1342	1275	1308	34
26	1300	1226	1263	37
27	1261	1178	1220	41
28	1224	1132	1178	46
29	1190	1087	1138	51
30	1159	1044	1101	57
31	1132	1004	1068	64
32	1109	967	1038	71
33	1091	933	1012	79
34	1078	904	991	87
35	1070	879	975	96

D. Modeling calculation

psio-T model

The p-T functions are linear, but they should follow a similar trend to the SiO₂-SiC condensates mass distribution computed for the kinetic modeling (despite the trend was estimated for the white condensate only). The slope at the edges of the p-T curves should be lower at the edges, where less condensates are produced, and higher between 1300-1700°C. It was thought that a linear dependence would be a quick and effective way to estimate the p_{SiO} drop through the condensation chamber.

The values of p_{SiO,in} are computed after assumptions. For example, the gas is assumed to be produced instantly at 2000°C, and the partial pressure remains constant through the gas production time. However, the gas

production started earlier than 2000°C, and p_{SiO} is decreasing gradually through the experiment, as detected by the CO% analysis from the off-gas in the small-scale setup (Figure 164). $p_{SiO,in}$ is also time dependent in the system, and can be also lower than expected during the experiments.

Table 55 and Table 56 reports the values of partial pressures and temperatures relevant for the p_{SiO} -T model. The subscript R1 refers to the formation of SiO₂-SiC condensates, whereas the subscript R2 for the Si-SiO₂ condensate. Condensation start at highest temperatures, when the gas comes from the gas production chamber, and finishes at low temperatures.

Table 55: p_{SiO} values used for modeling in small scale setup.

Exp.	$p_{SiO,in}$	$p_{SiO,R2,start}$	$p_{SiO,R2,stop}$	$p_{SiO,R1,start}$	$p_{SiO,R1,stop} = p_{SiO,out}$
1b	0.619	0.594	0.575	0.610	0.537
1c	0.619	0.592	0.575	0.611	0.534
2a	0.731	0.723	0.707	0.725	0.686
2b	0.731	0.725	0.714	0.727	0.701
2c	0.731	0.724	0.714	0.727	0.699
3a	0.742	0.738	0.737	0.740	0.731
3b	0.742	0.741	0.735	0.741	0.729
3c	0.742	0.741	0.735	0.741	0.726
4a	0.742	0.741	0.732	0.738	0.705
4b	0.742	0.742	0.739	0.741	0.732
4c	0.742	0.738	0.734	0.740	0.723
4d	0.742	0.737	0.73	0.739	0.715
4e	0.742	0.739	0.736	0.740	0.731
5a	0.742	0.741	0.738	0.740	0.731
14a	0.712	n.p.	n.p.	0.706	0.676
14b	0.712	0.703	0.690	0.703	0.664
17a	0.712	0.698	0.69	0.709	0.671
17b	0.712	0.702	0.682	0.702	0.660
17c	0.712	0.703	0.691	0.703	0.669
19a	0.709	n.p.	n.p.	0.704	0.671
20a	0.709	0.696	0.690	0.699	0.669
21a	0.709	n.p.	n.p.	0.702	0.667
IF1b	0.750	0.739	0.736	0.743	0.727
IF2a	0.750	n.p.	n.p.	0.742	0.726
IF3a	0.750	0.740	0.730	0.740	0.715
IF4a	0.750	0.739	0.727	0.739	0.706
IF5b	1.000	0.988	0.977	0.991	0.950
IF7b	1.000	0.986	0.973	0.986	0.947
IF8	1.000	0.980	0.963	0.980	0.920
IF10	1.000	0.981	0.959	0.981	0.923
IF11	0.750	n.p.	n.p.	0.729	0.686
IF12	1.000	0.987	0.975	0.987	0.965

Table 56: Temperature values and line regression coefficients used for modeling in small scale setup

Exp.	T _{SIO,R2,start} (°C)	T _{SIO,R2,stop} (°C)	T _{SIO,R1,start} (°C)	T _{SIO,R1,stop} = T _{out} (°C)	$\gamma \cdot 10^5$ (K ⁻¹)	δ
1b	1569	1386	1725	1019	10.42	0.430
1c	1533	1348	1725	924	9.58	0.446
2a	1725	1530	1750	1279	8.27	0.581
2b	1710	1525	1750	1285	5.65	0.628
2c	1710	1550	1750	1310	6.36	0.615
3a	1800	1670	1750	1377	2.47	0.697
3b	1800	1640	1800	1465	3.74	0.674
3c	1800	1630	1800	1410	3.86	0.672
4a	1798	1666	1750	1268	6.84	0.618
4b	1795	1689	1750	1387	2.32	0.7
4c	1706	1590	1750	1268	3.42	0.68
4d	1706	1535	1750	1209	4.46	0.661
4e	1722	1619	1750	1427	3.00	0.688
5a	1711	1583	1700	1134	1.61	0.713
14a	n.p.	1250	1710	1250	6.49	0.595
14b	1710	1560	1710	1260	8.76	0.553
17a	1563	1424	1750	1101	5.80	0.607
17b	1700	1470	1700	1220	8.88	0.551
17c	1700	1550	1700	1285	8.24	0.563
19a	n.p.	n.p.	1735	1180	5.95	0.601
20a	1565	1450	1630	1040	5.20	0.615
21a	n.p.	n.p.	1685	1000	5.16	0.615
IF1b	1650	1565	1730	1370	4.46	0.666
IF2a	n.p.	n.p.	1690	1250	3.80	0.678
IF3a	1675	1480	1675	1180	4.87	0.658
IF4a	1750	1590	1750	1320	7.73	0.604
IF5b	1735	1590	1770	1240	7.67	0.855
IF7b	1720	1570	1720	1250	8.28	0.843
IF8	1730	1590	1730	1240	12.29	0.768
IF10	1760	1610	1760	1370	14.72	0.722
IF11	n.p.	n.p.	1730	1400	13.16	0.501
IF12	1710	1530	1710	1390	7.08	0.866

Kinetic model for Reaction 1

Table 57 and Table 58 collect the relevant values for the kinetics model for Reaction 1. Table 59 lists the values of k computed for every temperature interval, for mode 2b, 3b and 4.

This section collects also all the driving forces, the kinetic constant values and the activation energies computed for all the experiments (Table 60 – Table 62).

Table 57: Values of d_p , A_p , $m_{\text{SiC, before}}$, V_{tot} , A_{tot} , A_{cm} for every experiment.

Exp.	d_p (cm)	A_p (cm ²)	$m_{\text{SiC, before}}$ (g)	V_{tot} (cm ³)	n_p	A_{tot} (cm ²)	A_{cm} (cm ² /cm)
IF1b	0.65	1.327	3290	1025	7500	9955	322.77
IF2a	0.65	1.327	3269	1018	7028	9461	303.24
IF3a	1.60	8.042	2983	929	459	3695	119.20
IF4a	1.10	3.801	3028	943	1382	5253	169.47
IF5b	0.65	1.327	3290	1025	7500	9955	339.31
IF7b	1.60	8.042	3071	957	473	3804	122.72
IF8	1.10	3.801	3017	940	1377	5234	168.85
IF10	0.65	1.327	3307	1030	7539	10006	341.06
IF11	0.65	1.327	3311	1031	7548	10018	323.16
IF12	0.65	1.327	3300	1028	7523	9985	322.10

Table 58. Values of A in each temperature interval, for each experiment.

Experiment	T interval (°C)	A (cm ²)
IF2a	1250-1380	1213
	1380-1485	910
	1485-1550	606
	1550-1690	1213
IF3a	1180-1480	834
	1480-1675	596
IF4	1320-1490	508
	1490-1590	339
	1590-1680	339
	1680-1750	339
IF5b	1240-1420	1018
	1420-1590	1018
	1590-1735	1018
	1735-1770	339
IF7b	1250-1480	614
	1480-1570	245
	1570-1720	491
IF8	1240-1420	507
	1420-1590	507
	1590-1730	507
IF10	1370-1470	682
	1470-1610	1023
	1610-1760	1364
IF11	1400-1580	969
	1580-1730	969
IF12	1390-1490	644
	1490-1530	322
	1530-1710	1288

Table 59: k values for the models with the highest R² (Modes 2b, 3b) and Mode 4.

Experiment	T interval (°C)	k (g cm ⁻² s ⁻¹)		
		Mode 2b	Mode 3b	Mode 4
IF2a	1250-1380	0.000146129	0.000200681	2.89248E-05
	1380-1485	0.00039137	0.0005342	7.68089E-05
	1485-1550	0.001767081	0.002401394	0.000346933
	1550-1690	0.00014789	0.00019992	3.00475E-05
IF3a	1180-1480	0.000106058	0.000146749	2.12538E-05
	1480-1675	0.001351609	0.001839487	0.0002709
IF4	1320-1490	0.000398593	0.000559437	8.17658E-05
	1490-1590	0.001205256	0.001667182	0.000244936
	1590-1680	0.003639901	0.00498427	0.000773212
	1680-1750	0.000610504	0.000828966	0.000156847
IF5b	1240-1420	0.00013152	0.000137426	5.40859E-06
	1420-1590	0.00093023	0.000958547	2.68391E-05
	1590-1735	0.003992984	0.004063925	7.39337E-05
	1735-1770	0.001503412	0.001519443	2.20121E-05
IF7b	1250-1480	0.000778901	0.000814317	3.24024E-05
	1480-1570	0.002724782	0.002809741	8.06256E-05
	1570-1720	0.015909437	0.016239033	0.000337741
IF8	1240-1420	0.000390857	0.00041975	2.50525E-05
	1420-1590	0.002715671	0.002850571	0.000123231
	1590-1730	0.012233927	0.012589863	0.000363151
IF10	1370-1470	0.000341459	0.000366847	2.2023E-05
	1470-1610	0.001177609	0.001241597	5.82005E-05
	1610-1760	0.005408371	0.005576713	0.000179532
IF11	1400-1580	0.001098673	0.001575482	0.000233314
	1580-1730	0.004452763	0.006192376	0.001000194
IF12	1390-1490	0.002390978	0.002469695	7.39078E-05
	1490-1530	0.005605283	0.005760322	0.000147741
	1530-1710	0.015528173	0.015830921	0.000303273

Table 60: Driving force values for Mode 3b and Mode 4

Experiment	T interval (°C)	$p_{SiO^3} \cdot p_{CO}$ Mode 3b	$p_{SiO} - p_{SiO,eq}$ Mode 4
IF2a	1250-1380	0.105	0.728
	1380-1485	0.105	0.731
	1485-1550	0.105	0.729
	1550-1690	0.105	0.701
IF3a	1180-1480	0.105	0.723
	1480-1675	0.105	0.714
IF4	1320-1490	0.104	0.711
	1490-1590	0.105	0.713
	1590-1680	0.105	0.677
	1680-1750	0.105	0.556
IF5b	1240-1420	0.038	0.957
	1420-1590	0.027	0.964
	1590-1735	0.017	0.910
	1735-1770	0.010	0.705
IF7b	1250-1480	0.038	0.957
	1480-1570	0.028	0.961
	1570-1720	0.019	0.918
IF8	1240-1420	0.056	0.931
	1420-1590	0.041	0.947
	1590-1730	0.026	0.899
IF10	1370-1470	0.056	0.930
	1470-1610	0.044	0.938
	1610-1760	0.028	0.855
IF11	1400-1580	0.103	0.693
	1580-1730	0.104	0.647
IF12	1390-1490	0.029	0.966
	1490-1530	0.025	0.967
	1530-1710	0.018	0.942

Table 61: Values of k for the remaining models (Modes 1a, 1b, 2a, 3a).

Experiment	T interval (°C)	k (g cm ⁻² s ⁻¹)			
		Mode 1a	Mode 1b	Mode 2a	Mode 3a
IF2a	1250-1380	$2.89 \cdot 10^{-5}$	$1.06 \cdot 10^{-4}$	$3.97 \cdot 10^{-5}$	$5.45 \cdot 10^{-5}$
	1380-1485	$7.67 \cdot 10^{-5}$	$2.87 \cdot 10^{-4}$	$1.05 \cdot 10^{-4}$	$1.43 \cdot 10^{-4}$
	1485-1550	$3.43 \cdot 10^{-4}$	$1.30 \cdot 10^{-3}$	$4.67 \cdot 10^{-4}$	$6.34 \cdot 10^{-4}$
	1550-1690	$2.85 \cdot 10^{-5}$	$1.09 \cdot 10^{-4}$	$3.85 \cdot 10^{-5}$	$5.20 \cdot 10^{-5}$
IF3a	1180-1480	$2.12 \cdot 10^{-5}$	$7.66 \cdot 10^{-5}$	$2.94 \cdot 10^{-5}$	$4.07 \cdot 10^{-5}$
	1480-1675	$2.63 \cdot 10^{-4}$	$9.93 \cdot 10^{-4}$	$3.58 \cdot 10^{-4}$	$4.88 \cdot 10^{-4}$
IF4	1320-1490	$8.16 \cdot 10^{-5}$	$2.84 \cdot 10^{-4}$	$1.15 \cdot 10^{-4}$	$1.61 \cdot 10^{-4}$
	1490-1590	$2.41 \cdot 10^{-4}$	$8.71 \cdot 10^{-4}$	$3.34 \cdot 10^{-4}$	$4.62 \cdot 10^{-4}$
	1590-1680	$7.17 \cdot 10^{-4}$	$2.66 \cdot 10^{-3}$	$9.82 \cdot 10^{-4}$	$1.34 \cdot 10^{-3}$
	1680-1750	$1.18 \cdot 10^{-4}$	$4.50 \cdot 10^{-4}$	$1.61 \cdot 10^{-4}$	$2.18 \cdot 10^{-4}$
IF5b	1240-1420	$5.4 \cdot 10^{-6}$	$1.26 \cdot 10^{-4}$	$5.65 \cdot 10^{-6}$	$5.90 \cdot 10^{-6}$
	1420-1590	$2.67 \cdot 10^{-5}$	$9.03 \cdot 10^{-4}$	$2.75 \cdot 10^{-5}$	$2.83 \cdot 10^{-5}$
	1590-1735	$6.85 \cdot 10^{-5}$	$3.92 \cdot 10^{-3}$	$6.97 \cdot 10^{-5}$	$7.09 \cdot 10^{-5}$
	1735-1770	$1.57 \cdot 10^{-5}$	$1.49 \cdot 10^{-3}$	$1.59 \cdot 10^{-5}$	$1.60 \cdot 10^{-5}$
IF7b	1250-1480	$3.24 \cdot 10^{-5}$	$7.45 \cdot 10^{-4}$	$3.39 \cdot 10^{-5}$	$3.54 \cdot 10^{-5}$
	1480-1570	$7.99 \cdot 10^{-5}$	$2.64 \cdot 10^{-3}$	$8.24 \cdot 10^{-5}$	$8.49 \cdot 10^{-5}$
	1570-1720	$3.16 \cdot 10^{-4}$	$1.56 \cdot 10^{-2}$	$3.23 \cdot 10^{-4}$	$3.29 \cdot 10^{-4}$
IF8	1240-1420	$2.50 \cdot 10^{-5}$	$3.64 \cdot 10^{-4}$	$2.69 \cdot 10^{-5}$	$2.89 \cdot 10^{-5}$
	1420-1590	$1.22 \cdot 10^{-4}$	$2.59 \cdot 10^{-3}$	$1.29 \cdot 10^{-4}$	$1.35 \cdot 10^{-4}$
	1590-1730	$3.36 \cdot 10^{-4}$	$1.19 \cdot 10^{-2}$	$3.46 \cdot 10^{-4}$	$3.56 \cdot 10^{-4}$
IF10	1370-1470	$2.20 \cdot 10^{-5}$	$3.18 \cdot 10^{-4}$	$2.36 \cdot 10^{-5}$	$2.54 \cdot 10^{-5}$
	1470-1610	$5.75 \cdot 10^{-5}$	$1.11 \cdot 10^{-3}$	$6.07 \cdot 10^{-5}$	$6.40 \cdot 10^{-5}$
	1610-1760	$1.58 \cdot 10^{-4}$	$5.25 \cdot 10^{-3}$	$1.63 \cdot 10^{-4}$	$1.68 \cdot 10^{-4}$
IF11	1400-1580	$2.32 \cdot 10^{-4}$	$7.67 \cdot 10^{-4}$	$3.32 \cdot 10^{-4}$	$4.77 \cdot 10^{-4}$
	1580-1730	$8.99 \cdot 10^{-4}$	$3.20 \cdot 10^{-3}$	$1.25 \cdot 10^{-3}$	$1.74 \cdot 10^{-3}$
IF12	1390-1490	$7.38 \cdot 10^{-5}$	$2.31 \cdot 10^{-3}$	$7.62 \cdot 10^{-5}$	$7.87 \cdot 10^{-5}$
	1490-1530	$1.47 \cdot 10^{-4}$	$5.45 \cdot 10^{-3}$	$1.51 \cdot 10^{-4}$	$1.55 \cdot 10^{-4}$
	1530-1710	$2.91 \cdot 10^{-4}$	$1.52 \cdot 10^{-2}$	$2.97 \cdot 10^{-4}$	$3.03 \cdot 10^{-4}$

Table 62: Activation energies (kJ/mol) for experiments considered for the SiC-SiOx modeling, for models 3b and 4.

Experiment	E _a , model 3b	E _a , model 4
IF2a	281	281
IF3a	252	254
IF4	248	255
IF5b	263	204
IF7b	271	212
IF8	265	209
IF10	283	218
IF11	234	234
IF12	277	210

Considerations on model 3b

The driving force of Model 3b is proportional to $p_{SiO}^3 \cdot p_{CO}$. The order of reaction follows the reaction stoichiometry. Let us consider a similar value for the brown condensate, i.e. a reaction rate proportional to p_{SiO}^2 for Reaction 2. The DF terms will then have the expressions

$$DF_{R1} = (p_{SiO})^3 \cdot p_{CO} \quad \text{Equation 20}$$

$$DF_{R2} = (p_{SiO})^2 \quad \text{Equation 21}$$

The DF dependences on temperature are shown in Figure 255. Both the functions increase with temperature as expected, since p_{SiO} is also increasing with temperature. As it happened for Model 4, a higher inert gas amount will decrease the driving force by bringing more SiO gas further up in the condensation chamber. In fact, less condensate is generated by increasing the inert gas amount. For the SiO₂+SiC condensation, the driving force is almost constant through the whole temperature range, for experiments with $p_{SiO,in}$ close to 0.75. In fact, the starting gas composition is equal to the final products. The amount of moles in the gas will change, but the partial pressures will remain always the same.

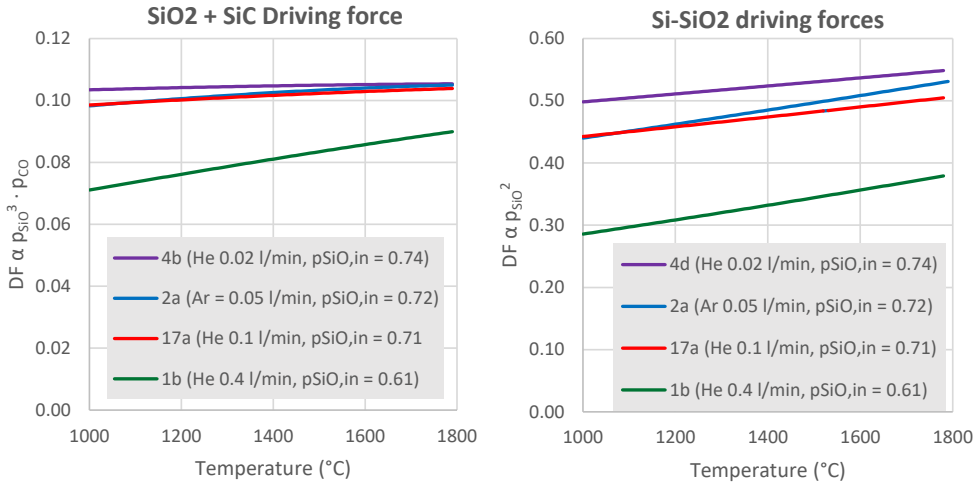


Figure 255: Driving force proportional to the reaction stoichiometries.

The driving force term in model 3b ($p_{SiO}^3 \cdot p_{CO}$) depends on the pellets charge chosen. The experiments with SiO₂-SiC pellets (IF1-4) have an almost constant DF, as confirmed from the previously discussed graphs in Figure 255. The amount of CO(g) in the starting composition makes the difference between the two cases. CO(g) is needed as a reactant during Reaction 1. As far as there is enough CO(g) in the gas, the SiO₂-SiC condensate is produced. The driving force remains higher. However, when the gas is richer in SiO(g) than CO(g), the driving force decreases. In fact, the CO(g) in the system is produced by the SiC production in the crucible (Reaction 3). CO(g) is a limiting reactant which is depleted fast and produced in small amounts. In fact, the amount of CO(g) produced by Reaction 3 was estimated at 0.1 mol, while the SiO(g) produced from the pellets is ≈ 4.5 mol. In the small-scale crucible, the SiO(g) will follow the inert gas out of the system. It can be concluded that, for model 3b, the amount of brown condensate produced is influencing the change in p_{SiO} through the crucible. A higher Si-SiO₂ production will make the DF decrease faster for the SiC-SiO_x condensation. This result agrees with the fact that experiments with higher $p_{SiO,in}$ produce less SiC-SiO_x condensate (since they produce more Si-SiO₂ condensate).

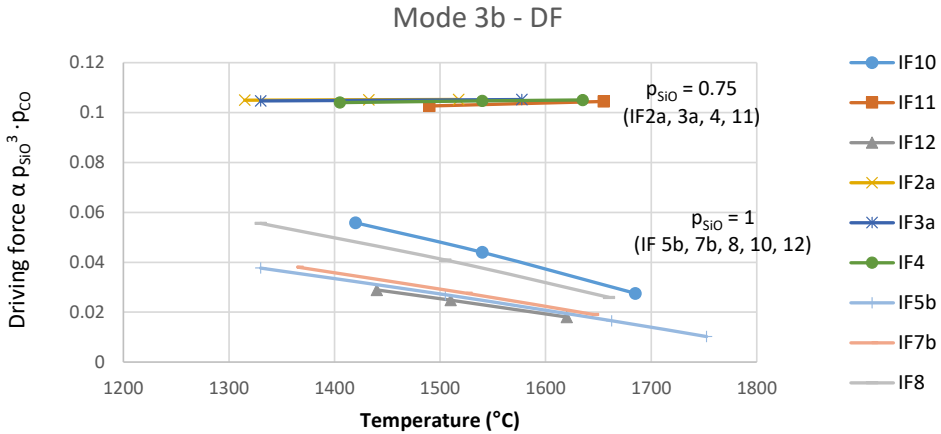


Figure 256: Driving force for experiments with $p_{SiO} = 0.75$ and $p_{SiO} = 1$.

The value of the driving force is higher for mode 4 compared to mode 3b. Figure 257 shows an example for experiment IF5b. Both decrease with T. The corresponding value of $k(T)$ are placed in the same graphs. Despite the driving force is different, $k(T)$ has the same trend, which means that the derivative of $k(T)$ is similar. In fact, the results for the activation energy, which is depending on the slope of $\ln k$ vs $1/T$, are in the same order of magnitude (279 ± 29 kJ/mol for mode 3b and 242 ± 33 kJ/mol for mode 4). However, the values of $k(T)$ differ by 2 orders of magnitude. Hence, the value of the calculated k_0 changes from $3.05 \cdot 10^5$ for mode 3b, to $1.49 \cdot 10^3$ for mode 4.

The DF for model 3b does not follow a similar trend with respect to the condensates distribution in the chamber. However, there is a good agreement with DF decreasing towards higher temperatures, which is also shared with the results from model 4. This occurs despite the values for DF between model 3 and model 4 differ by one order of magnitude.

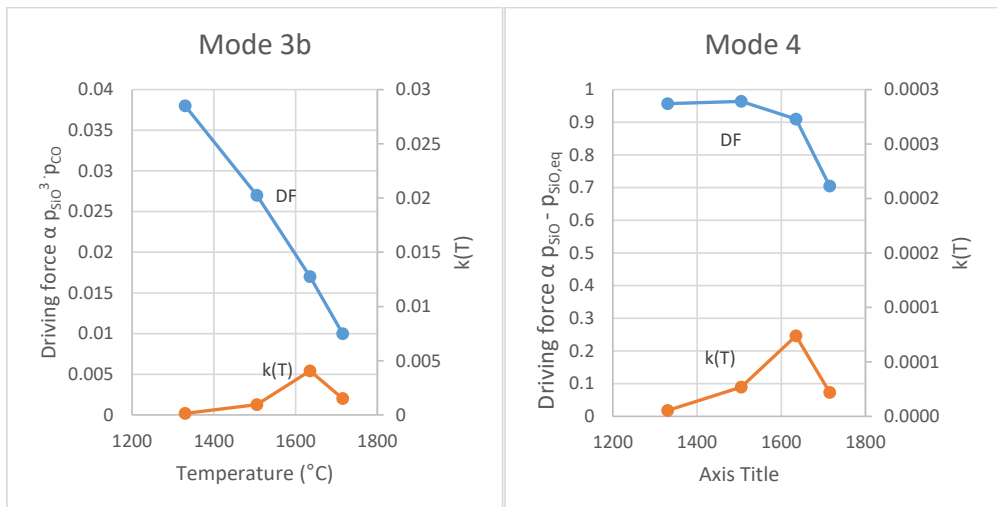


Figure 257: Comparison of driving forces for mode 3b (concentration of SiO) and mode 4 (distance from equilibrium), experiment IF5b. Driving force = Blue line; $k(T)$ = Orange line.

E. Reaction thermodynamics at 1.5 atm

K_{eq} is a function of the partial pressure of SiO(g) ($p_{SiO,eq}$) and temperature (T). $p_{SiO,eq}$ is found with the restriction on the total pressure, assuming that only CO(g) and SiO(g) are present in the gas phase, with a total pressure of 1 atm (or 1.5, when analyzing the small-scale setup). All the solid and liquid phases were assumed pure, with activities equal to one. The gas phase follows the ideal gas law. Temperature is related to a chosen K_{eq} . By interpolating points every 50°C, between 1000°C and 1800°C, one could plot the variation of p_{SiO} with respect to temperature for every reaction considered.

By changing the total pressure, the equilibrium constants remain the same, but the partial pressure in the system will change. Figure 258 shows thermodynamics of the reactions involved in the experiments. The dashed lines are referred to the system at 1 atm, whereas the continuous one at 1.5 atm. The invariant point shifts from 1811°C and $p_{SiO}=0.68$ to 1840°C and $p_{SiO}=0.63$. The system reacts with an increase in temperature after an increase in pressure, in accordance with the gas law. Reactions 3 and 4 do not shift because of the pressure, since the amount of moles of gas in the reactants and in the product coincide.

According to Le Chatelier's principle, an increase in pressure will favor the side of the reaction which produced less moles of gas. Hence, the condensation reactions will be shifted to the solid products at a higher pressure. In fact, the continuous lines are shifted to higher temperatures.

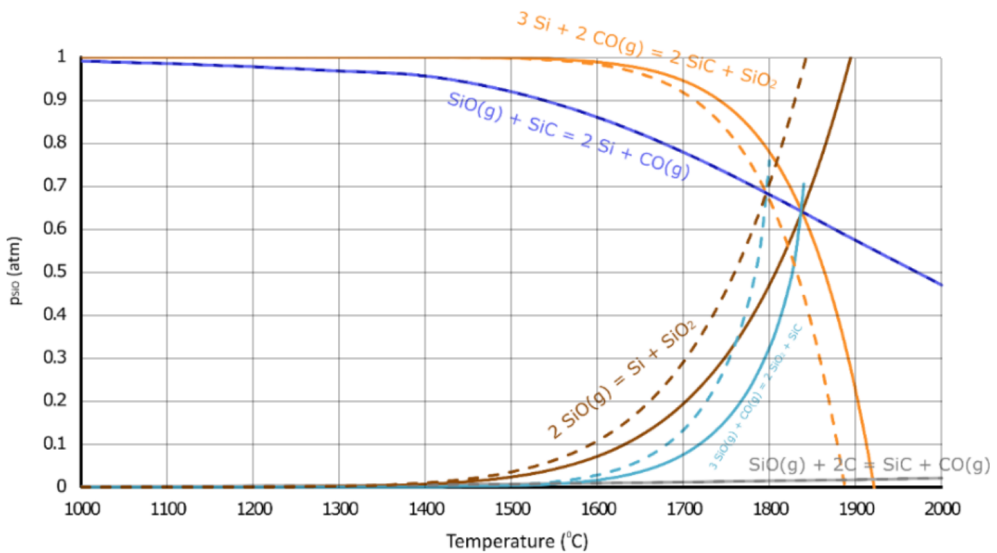


Figure 258: Thermodynamics of reaction at 1 (dashed lines) and 1.5 atm (continuous lines).

F. ImageJ® analysis on brown condensate particles

Table 63 Table 68 shows the data concerning the number of particles per picture, as well as average and standard deviation values for major axis, minor axis, particle diameter, particle area. The data are related to the position coordinate x in the sample.

Table 63: ImageJ® analysis results on number of particles and particle area, sample 1.

Position (μm)	# Ptc counted	Avg. sphere area (nm^2)	St.dev. area (nm^2)
0	415	65 629	78 012
30	370	64 270	70 631
60	330	81 273	92 990
90	216	115 806	136 060
120	253	129 000	139 376
150	157	154 529	189 663
180	126	224 222	304 758
210	185	199 919	237 139
270	147	248 578	285 951
300	146	240 322	269 880
330	160	287 363	405 454
360	142	250 613	320 705
390	126	251 548	270 791
420	127	259 677	325 630
450	116	353 914	552 392
480	153	277 680	340 404
510	137	268 124	313 279
540	125	338 688	474 678
570	102	302 412	394 858
600	117	342 667	417 156
630	107	369 813	550 406
660	104	367 933	652 475

Table 64: ImageJ® analysis results on number of particles and particle area, sample 2.

Position (µm)	# Ptc counted	Avg. sphere area (nm ²)	St.dev. area (nm ²)
0	200	322 600	398 284
30	191	303 832	354 853
60	239	311 548	423 752
90	216	277 755	300 753
120	156	426 449	515 741
150	154	414 857	462 907
180	156	399 769	485 726
210	182	367 132	377 318
240	138	513 913	603 890
270	135	650 163	653 294
300	125	443 392	471 017
330	132	539 136	585 294
360	130	522 554	650 284
390	138	607 457	819 985
420	201	280 134	410 947
450	218	235 390	342 534
480	217	354 304	513 076
510	175	557 834	667 862
540	174	556 052	695 323
570	148	645 642	935 412
600	135	557 659	676 864
630	139	456 885	519 435
660	202	316 530	361 732

Table 65: ImageJ® analysis results on number of particles and particle area, sample 3.

Position (µm)	# Ptc counted	Avg. sphere area (nm ²)	St.dev. area (nm ²)
0	399	48 060	41 784
30	300	73 433	76 787
60	235	123 889	125 990
90	175	205 623	198 175
120	129	284 380	297 889
150	133	202 105	210 637
180	93	431 548	521 224
210	147	383 435	748 282
240	741	33 818	26 326

Table 66: ImageJ® analysis results on particle size parameters, sample 1.

Position (μm)	Average major axis (nm)	Average minor axis (nm)	Average sphere diameter (nm)
0	283 ± 155	229 ± 125	256
30	282 ± 145	230 ± 119	256
60	312 ± 171	256 ± 171	284
90	373 ± 203	306 ± 169	339
120	394 ± 207	328 ± 174	361
150	418 ± 253	347 ± 209	383
180	490 ± 332	405 ± 269	447
210	473 ± 290	394 ± 241	434
270	531 ± 306	450 ± 262	490
300	513 ± 310	437 ± 272	475
330	542 ± 369	460 ± 322	501
360	511 ± 339	432 ± 296	472
390	533 ± 395	458 ± 265	495
420	522 ± 341	445 ± 296	483
450	569 ± 443	490 ± 395	530
480	546 ± 313	482 ± 294	514
510	538 ± 317	468 ± 287	503
540	581 ± 399	508 ± 350	544
570	556 ± 359	485 ± 329	520
600	602 ± 380	519 ± 333	561
630	593 ± 437	517 ± 383	555
660	589 ± 432	522 ± 383	555

Table 67: ImageJ® analysis results on particle size parameters, sample 2.

Position (µm)	Average major axis (nm)	Average minor axis (nm)	Average sphere diameter (nm)
0	589 ± 366	511 ± 307	550
30	582 ± 314	508 ± 295	545
60	580 ± 368	490 ± 314	535
90	568 ± 312	480 ± 267	524
120	678 ± 422	582 ± 363	630
150	685 ± 384	587 ± 337	636
180	653 ± 409	561 ± 358	607
210	663 ± 319	569 ± 290	616
240	741 ± 429	655 ± 401	698
270	861 ± 461	749 ± 411	805
300	706 ± 360	625 ± 348	666
330	774 ± 429	676 ± 390	725
360	740 ± 469	642 ± 415	691
390	809 ± 516	688 ± 433	749
420	541 ± 355	464 ± 305	503
450	501 ± 322	425 ± 275	463
480	597 ± 399	521 ± 358	559
510	751 ± 478	669 ± 444	710
540	757 ± 463	681 ± 426	719
570	795 ± 538	705 ± 494	750
600	777 ± 470	673 ± 410	725
630	716 ± 385	626 ± 354	671
660	594 ± 340	511 ± 299	552

Table 68: ImageJ® analysis results on particle size parameters, sample 3.

Position (µm)	Average major axis (nm)	Average minor axis (nm)	Average sphere diameter (nm)
0	251 ± 108	205 ± 93	228
30	300 ± 151	248 ± 130	274
60	386 ± 201	323 ± 169	355
90	491 ± 252	420 ± 225	455
120	566 ± 319	488 ± 276	527
150	490 ± 269	407 ± 223	449
180	676 ± 441	578 ± 372	627
210	566 ± 504	487 ± 431	527
240	213 ± 85	175 ± 72	194

G. Gauss propagation error law

The Gauss error propagation law is a simple way to estimate the deviation on a generic parameter y . A parameter could be expressed as a function of other parameters x_1, x_2, \dots, x_k .

$$y = f(x_1, x_2, \dots, x_k) \quad \text{Equation 22}$$

The deviation on parameter y is called s^2_y . If the deviations on each parameter x_i is known, s^2_y can be estimated by

$$s^2_y = \sum_{i=0}^k \left(\frac{\partial f}{\partial x_i} \right)^2 * s^2_{x_i} \quad \text{Equation 23}$$

Where s_{x_i} is the deviation on the parameter x_i . The deviation computed in this way has a 95% confidence interval.

Experimental errors

Table 69 shows the experimental errors known from the experimental analysis. The error on the particle size is depending on the particle size distribution chosen and considers the broadness of the particle size distribution. The error on temperature considers the broadness of the temperature interval. The errors known for all the experiments depend on the experimental apparatus used:

- s_t (space thickness L) = 0.5 cm
- s_{dt} (gas production time t_r) = 1 min
- s_m (condensate mass measurement m) = 0.01 g
- $s_{m\text{before}}$ (SiC substrate mass before condensation) = 1 g

The position measurements in the crucible might suffer uncertainties. $T_{\text{SiO},\text{start}}$, $T_{\text{SiO},\text{stop}}$ and $T_{\text{SiO},\text{out}}$ should be read with a confidence interval of $\pm 50^\circ\text{C}$ for the large-scale setup experiments, and $\pm 10^\circ\text{C}$ for the small scale. The uncertainty on the position measurement in the condensation chamber is ± 1 mm. While computing the position dependence on temperature in the condensation chamber, it was noticed that the temperature varies up to $10^\circ\text{C}/\text{mm}$ in the small-scale setup, and by $30\text{-}50^\circ\text{C}/\text{cm}$ in the large-scale setup.

Error computation

Error on $k(T)$, E_a and k_0

The equation for $k(T)$ is

$$k(T) = k_0 \exp\left(-\frac{E_a}{RT}\right)$$

s_{E_a} and s_{k_0} are found by the Excel worksheet regression tool.

s_k is found from

$$k = \frac{\frac{m_{\text{cond}}}{t_r}}{A * f(p_{\text{SiO}})} \quad \text{Equation 24}$$

Table 69: Errors on d_p and T for each experiment and temperature interval.

Experiment	T interval (°C)	s_T (K)
IF2a s_{d_p} (cm) = 0.15	1250-1380	65
	1380-1485	52.5
	1485-1550	32.5
	1550-1690	70
IF3a s_{d_p} (cm) = 0.40	1180-1480	150
	1480-1675	97.5
IF4 s_{d_p} (cm) = 0.30	1320-1490	85
	1490-1590	50
	1590-1680	45
	1680-1750	35
IF5b s_{d_p} (cm) = 0.35	1240-1420	90
	1420-1590	85
	1590-1735	72.5
	1735-1770	17.5
IF7b s_{d_p} (cm) = 0.40	1250-1480	115
	1480-1570	45
	1570-1720	75
IF8 s_{d_p} (cm) = 0.30	1240-1420	90
	1420-1590	85
	1590-1730	70
IF10 s_{d_p} (cm) = 0.35	1370-1470	50
	1470-1610	70
	1610-1760	75
IF11 s_{d_p} (cm) = 0.35	1400-1580	90
	1580-1730	75
IF12 s_{d_p} (cm) = 0.35	1390-1490	50
	1490-1530	20
	1530-1710	90

Which gives

$$s_k^2 = \left(\frac{\partial k}{\partial \left(\frac{m_{cond}}{t_r} \right)} * S_{\frac{m_{cond}}{t_r}} \right)^2 + \left(\frac{\partial k}{\partial A} * s_A \right)^2 + \left(\frac{\partial k}{\partial p_{SiO}} * s_{p_{SiO}} \right)^2$$

Equation 25

The errors on $\left(\frac{m_{cond}}{t_r} \right)$, A and p_{SiO} are treated in the following sections.

Error on reaction rate $\left(\frac{m_{cond}}{t_r}\right)$

$\frac{m_{cond}}{t_r}$ depends on the error on time t_r and the mass m_{cond} . They are both known from the experimental procedure.

$$s_{\frac{m_{cond}}{t_r}}^2 = \left(\frac{\partial\left(\frac{m_{cond}}{t_r}\right)}{\partial(m_{cond})} * s_{m_{cond}}\right)^2 + \left(\frac{\partial\left(\frac{m_{cond}}{t_r}\right)}{\partial(t_r)} * s_{t_r}\right)^2 = \left(\frac{1}{t_r} * s_{m_{cond}}\right)^2 + \left(-\frac{m_{cond}}{t_r^2} * s_{t_r}\right)^2 \quad \text{Equation 26}$$

Error on available surface for condensation (A)

The parameter A is coming from the multiplication of A_{cm} and L . The error on L is known from the experimental procedure.

$$s_A^2 = \left(\frac{\partial A}{\partial A_{cm}} * s_{A_{cm}}\right)^2 + \left(\frac{\partial A}{\partial h} * s_L\right)^2 = (L * s_{A_{cm}})^2 + (A_{cm} * s_L)^2 \quad \text{Equation 27}$$

The error on A_{cm} is proportional to the error on A_{tot} , since

$$A_{cm} = \frac{A_{tot}}{31}; s_{A_{cm}} = \frac{s_{A_{tot}}}{31} \quad \text{Equation 28}$$

With 31 [cm] being the crucible height.

$s_{A_{tot}}$ depends on the particle size distribution, the total mass of the silicon carbide substrate before condensation (m_{before}) and the density of SiC. It is assumed that the density of SiC has no error.

$$A_{tot} = \pi r_p^2 * n_{tot} = 4\pi r_p^2 * \frac{V_{tot}}{4\pi r_p^3} = 4\pi r_p^2 * \frac{m_{before}}{\rho * \frac{4}{3}\pi r_p^3} = \frac{3}{4} * \frac{m_{before}}{\rho * r_p} \quad \text{Equation 29}$$

$$s_{A_{tot}}^2 = \left(\frac{\partial A}{\partial m_{before}} * s_{m_{before}}\right)^2 + \left(\frac{\partial A}{\partial r_p} * s_{r_p}\right)^2 = \left(\frac{3}{4r_p * \rho} * s_{m_{before}}\right)^2 + \left(-\frac{3m}{4\rho * r_p^2} * s_{r_p}\right)^2 \quad \text{Equation 30}$$

With $s_{m_{before}} = 1$ g and $s_{r_p} = \frac{s_{dp}}{2}$

Error on partial pressure of SiO(g) (p_{SiO})

p_{SiO} can be found from the dependence of p_{SiO} on T . p_{SiO} decreases linearly with temperature through by the equation

$$p_{SiO} = \alpha T + \beta \quad \text{Equation 31}$$

α and β are assumed to have no error. Therefore, the error on p_{SiO} depends on s_T only

$$s_{p_{SiO}}^2 = \left(\frac{\partial p_{SiO}}{\partial T} * s_T\right)^2 = (\alpha * s_T)^2 \quad \text{Equation 32}$$

H. Spectra

XPS spectra

The Si-2s and O-1s electrons give a single characteristic peak, respectively at 152 and 532.5 eV. These spectra do not add supplementary information to what was already mentioned in the XPS section. These are the electrons located at internal levels, which are not actively involved in the bonds in our case. Figure 259 shows the spectra for the SiC-SiO_x condensates, but the same discussion applies also for the Si-SiO₂ condensates.

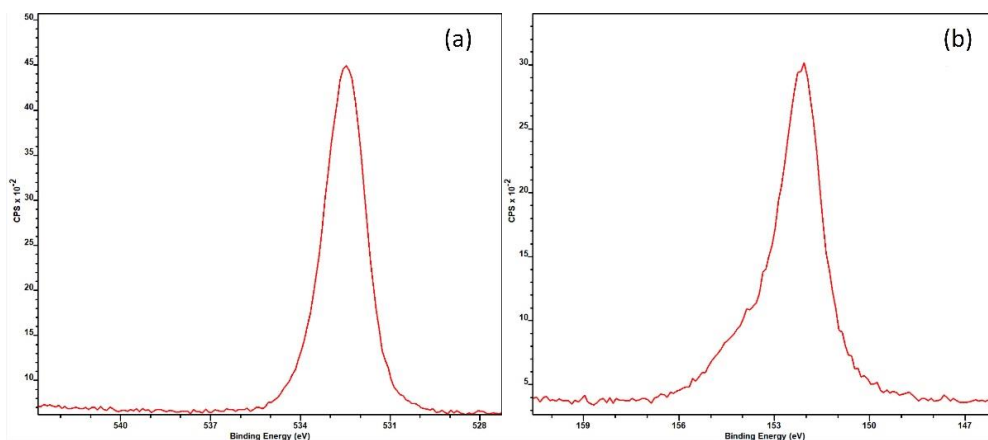


Figure 259: a) O-1s electron XPS spectrum; b) Si-2s electron XPS spectrum, sample 2.1.

XRD spectra

Figure 260 shows the XRD spectrum for Quartz B. The quantitative analysis states that the percentage of quartz is 100%. However, there are small deviations from the calculated and modeled spectrum, therefore Quartz B cannot be considered as 100% pure quartz.

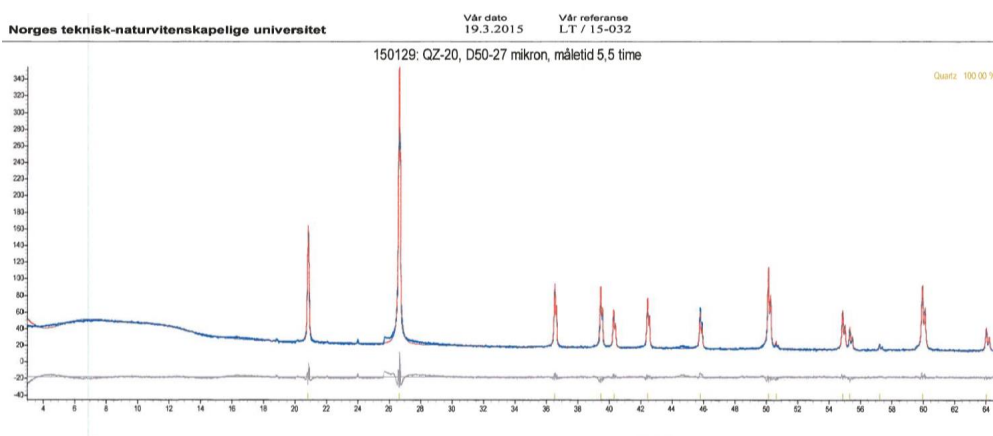


Figure 260: XRD spectrum of Quartz A

Figure 261 shows the XRD spectrum of a SiC substrate. The curve modeled by TOPAS® is the green spectrum, whereas the experimental data follow the red curve. The grey curve is the difference between the modeled and

the experimental data. The flatter the difference is, the more coherent is the model. The small vertical signs below the grey curve spot the characteristic diffraction peaks, which are produced by each polytype. Each sign corresponds to a preferential orientation of the crystal.

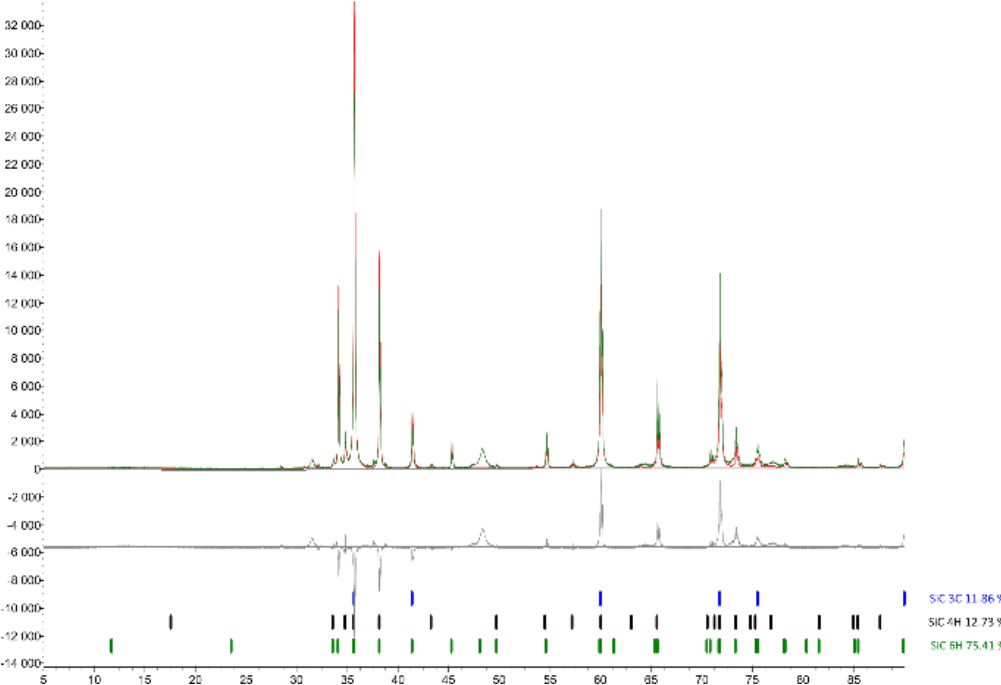


Figure 261: XRD spectrum of SiC substrate.

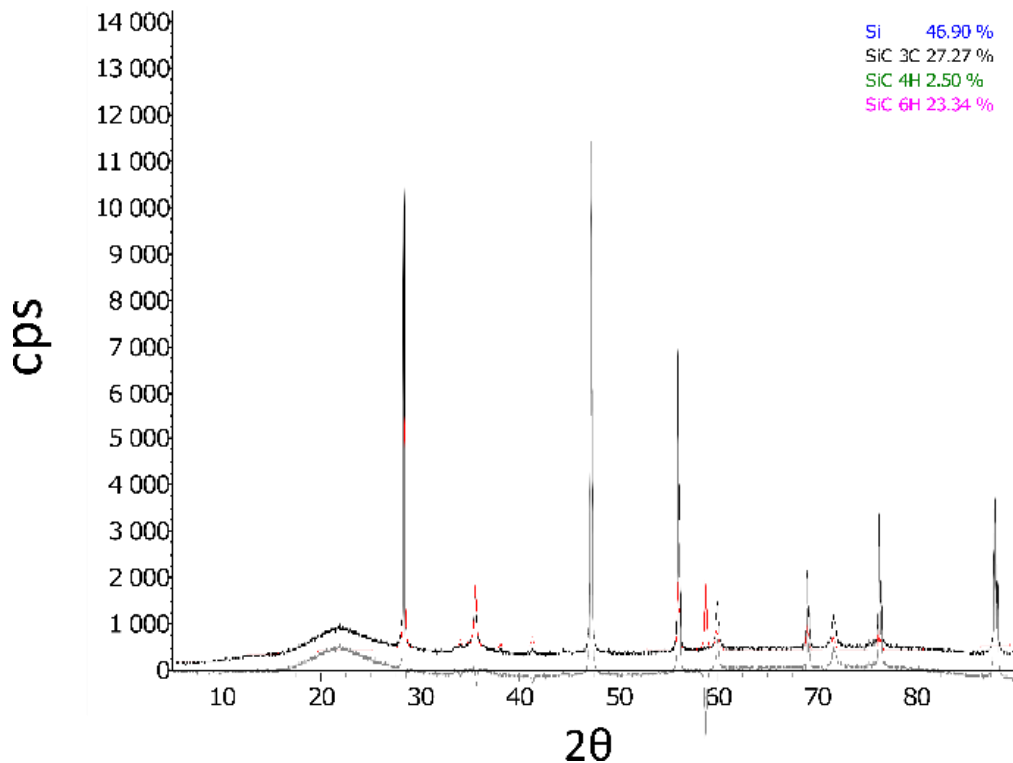


Figure 262: XRD spectrum of brown condensate from experiment R4a.

In the brown condensate sample for XRD analysis, the major differences between the calculated and the measured spectra are seen in Figure 263. The model does not fit perfectly for peaks at 57.62 (≈116 for corundum), but the peak is found. The model does not manage to reveal a peak at 47.31°, which is very close to the (022) peak for elemental Si and (113) for cristobalite. The other calculated spectra fit relatively well.

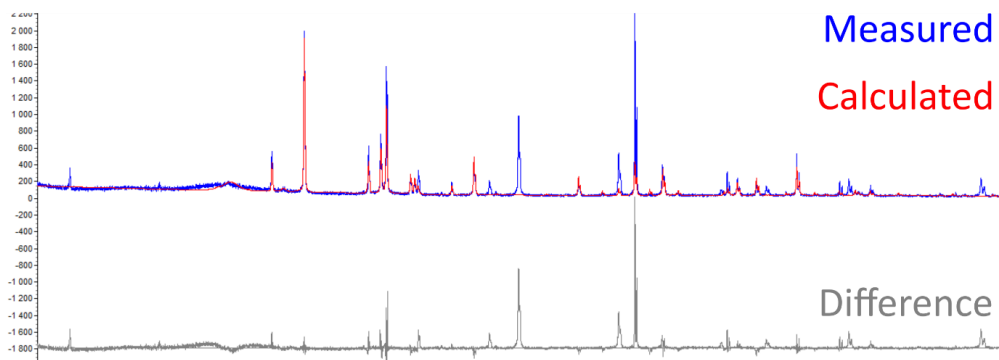


Figure 263: XRD spectrum of brown condensate sample for XRD analysis (IF7a, T = 1580-1750°C).

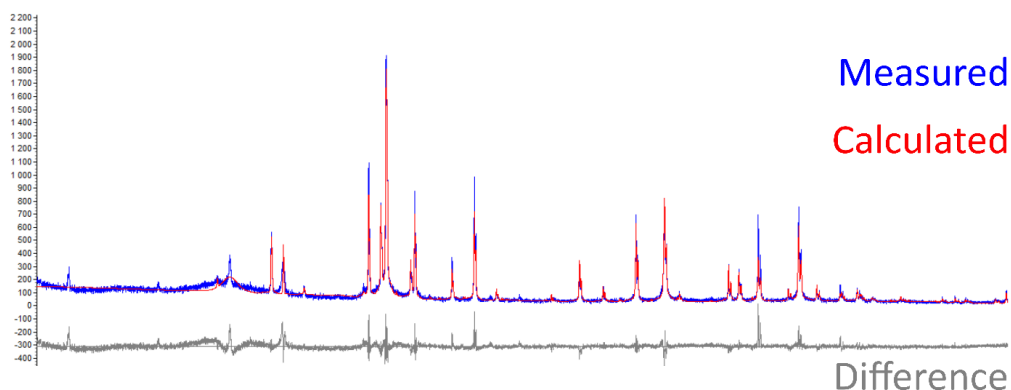


Figure 264: XRD spectrum of white condensate sample 1 (IF7b, T = 1250-1480°C).

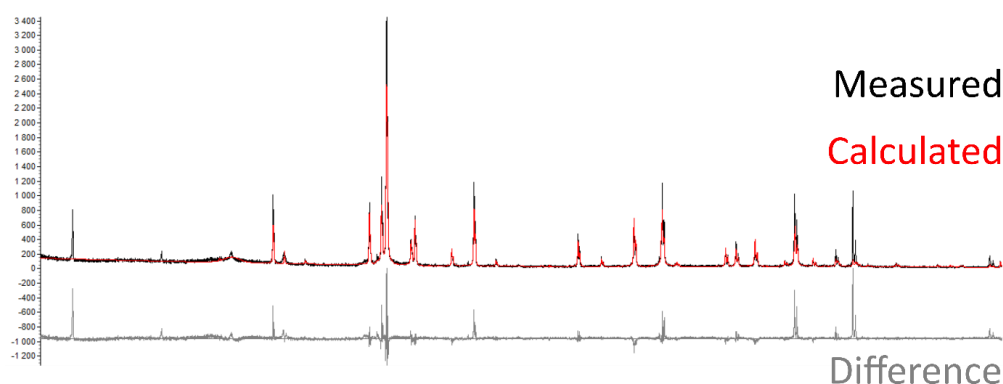


Figure 265: XRD spectrum of white condensate sample 2 (IF7b, T = 1480-1720°C).

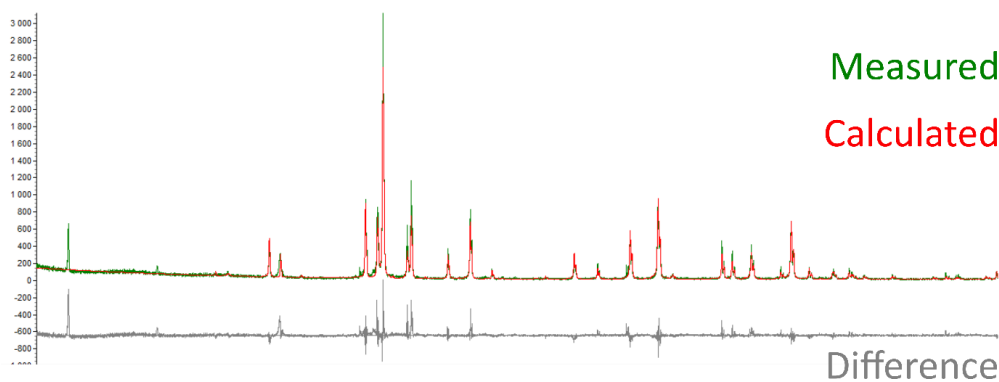


Figure 266: XRD spectrum of white condensate sample 3 (IF12, T = 1530-1710°C).

I. Estimation of SiC in Figure 209

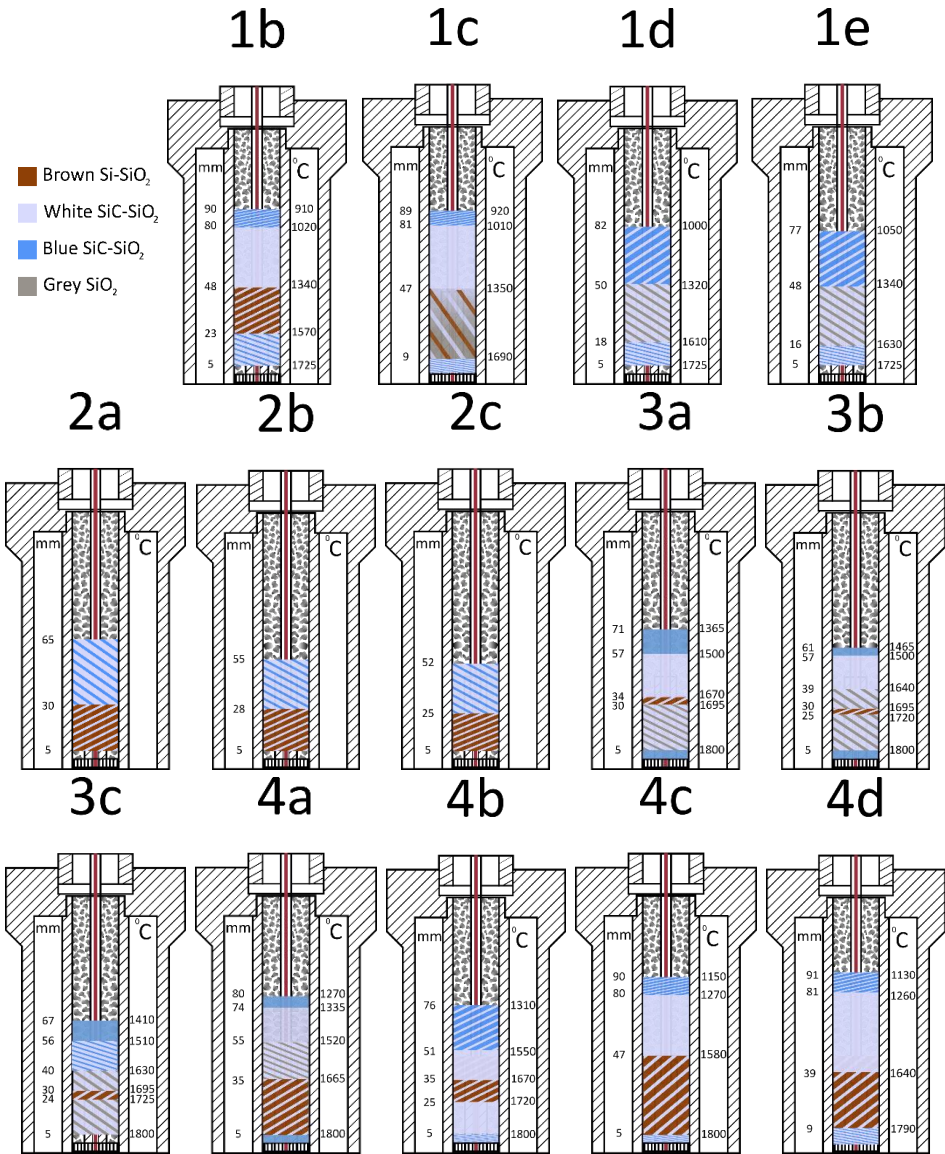
The volumes of SiC and of a Si sphere are compared, to quantify the amount of C. The moles of each phase can be calculated and related to the equilibrium composition of dissolved C in Si. Figure 209 is taken as reference for the estimation. The ratio between the sum of the SiC nanocrystals area in the picture and the area of the sphere without the nanocrystals is 15%, according to a graphic estimation by ImageJ®. Assuming the SiC

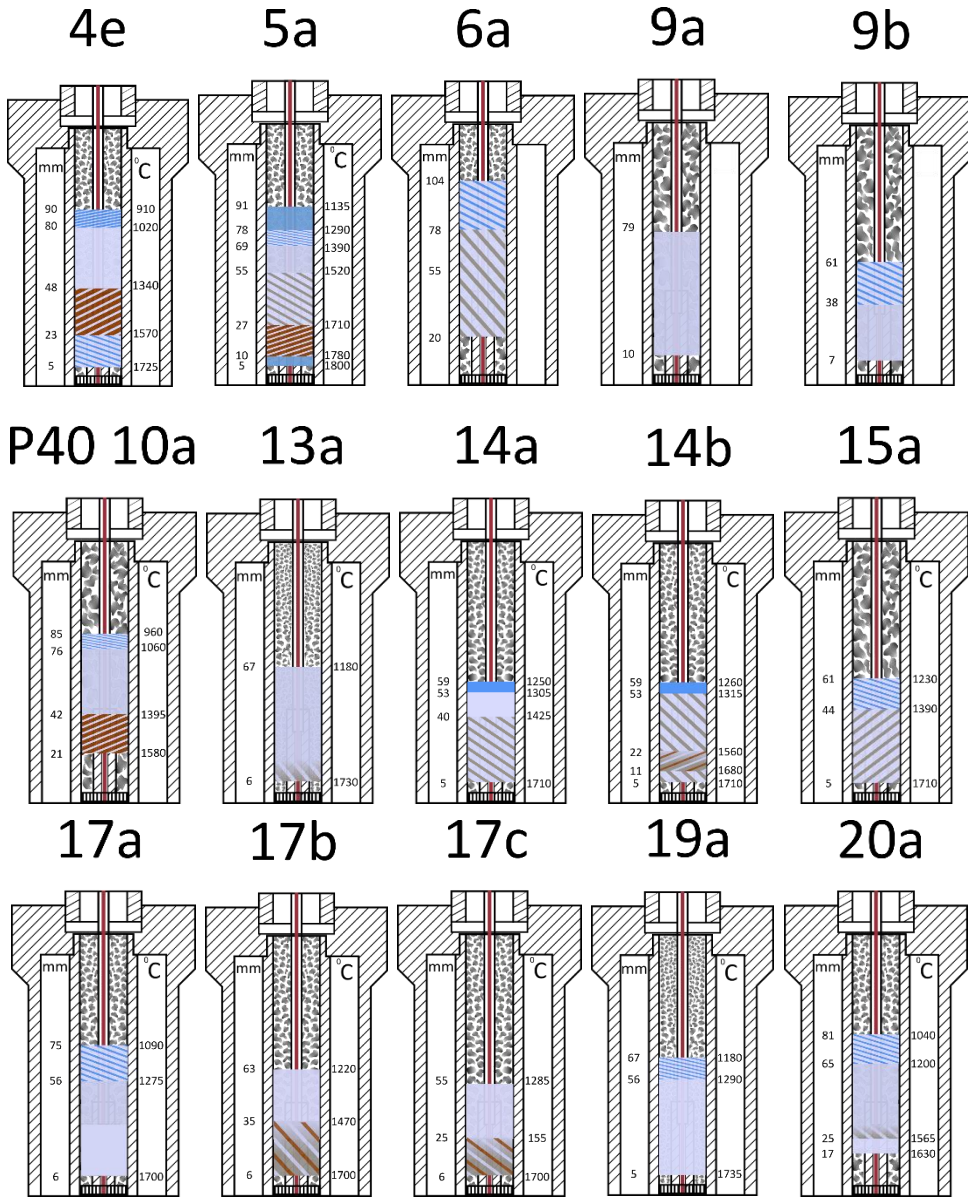
nanocrystals to be spherical, the corresponding volume ratio is 6%. Starting from a mixture of 6 vol. % SiC and 94 vol.% Si, about 5 at. % carbon is found.

J. Condensation profiles

Small scale setup

Experiments R1a is not shown, as it was interrupted earlier than expected and therefore considered not representative. The crucible of Experiment R14c was accidentally destroyed during extraction, therefore it was not possible to estimate an exact condensation profile.





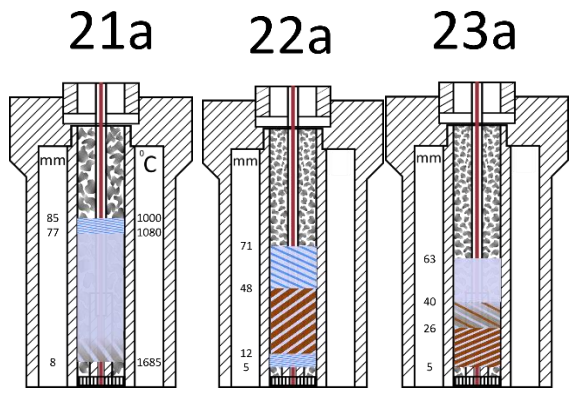


Figure 267: Condensation profiles of experiments with SiC substrates, small scale setup.

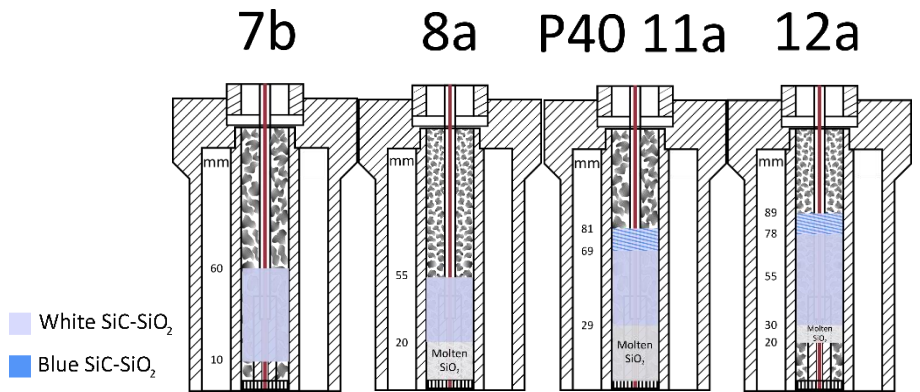
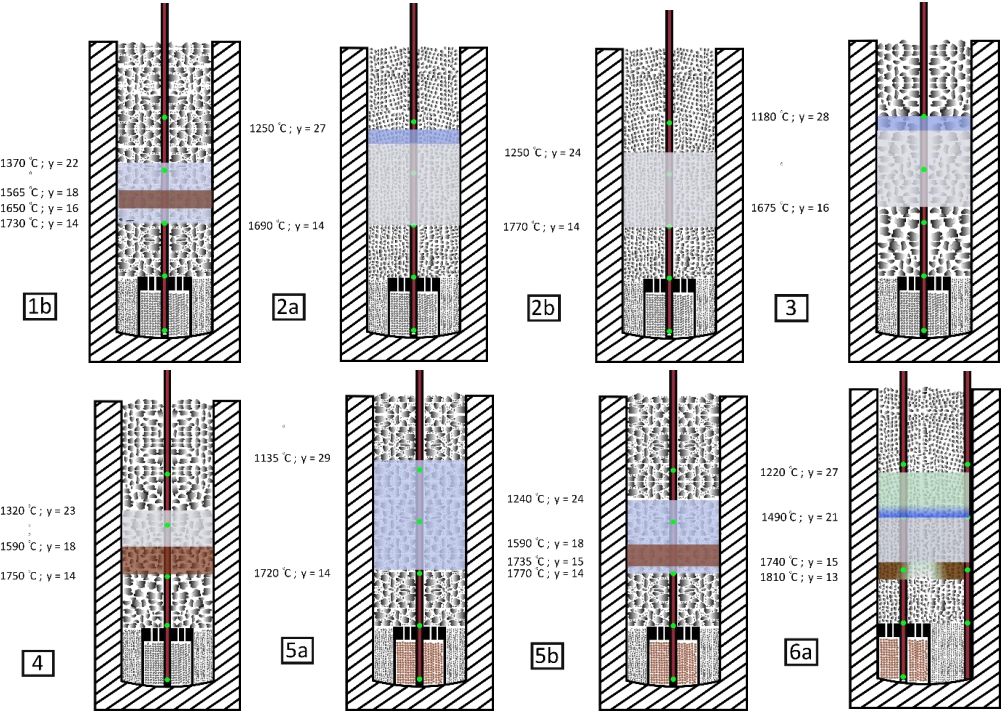


Figure 268: Condensation profiles for Quartz A experiments. Experiments R7b, R8a, R-P4011a, R12a.

Large-scale setup

The profile of Experiment IF1a was not collected, as the temperature profile was recorded by two points only, which were not enough to trace an accurate temperature gradient.



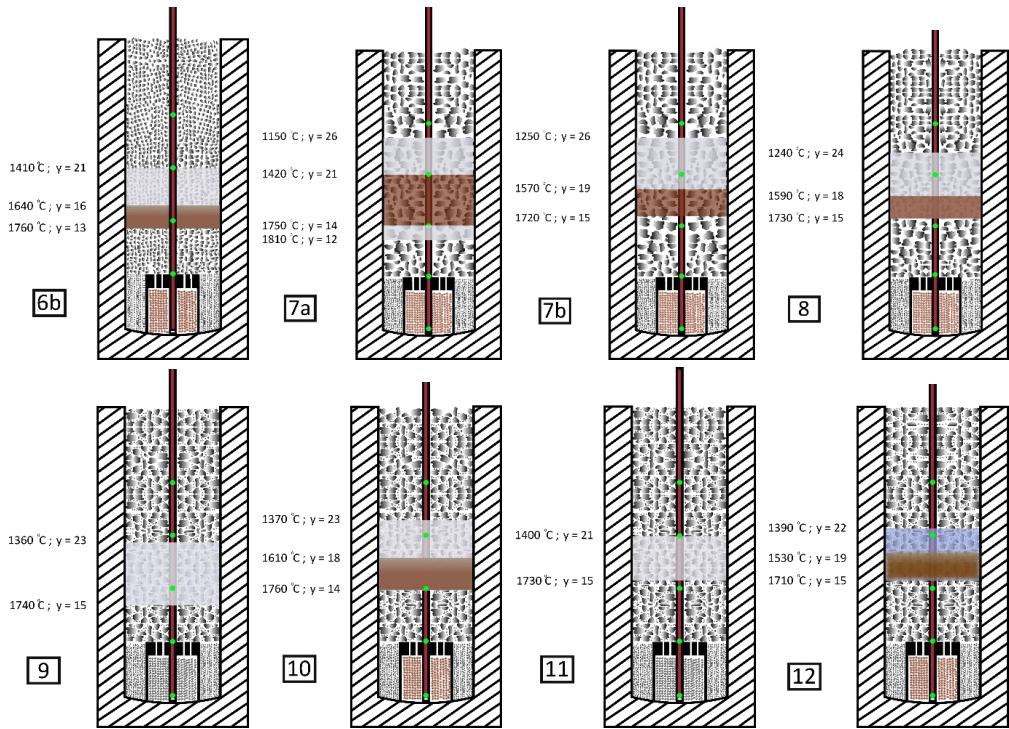


Figure 269: Temperature profiles and colors of condensates formed in experiments of large-scale setup.

ISBN 978-82-326-6352-1 (printed ver.)
ISBN 978-82-326-5929-6 (electronic ver.)
ISSN 1503-8181 (printed ver.)
ISSN 2703-8084 (online ver.)



NTNU

Norwegian University of
Science and Technology